Journal of Fluids Engineering

Published Bimonthly by ASME

VOLUME 126 • NUMBER 6 • NOVEMBER 2004

FLUIDS ENGINEERING DIVISION

Editor
JOSEPH KATZ (2005)

Assistant to the Editor
LAUREL MURPHY (2005)

Associate Editors
MALCOLM J. ANDREWS (2006)
S. BALACHANDAR (2005)
KENNETH S. BREUER (2006)
STEVEN L. CECCIO (2004)
GEORGES L. CHAHINE (2006)
WILLIAM W. COPENHAVER (2004)
THOMAS B. GATSKI (2006)
SIVIRAM GOGINENI (2006)
FERNANDO F. GRINSTEIN (2005)
HAMID JOHARI (2006)
JINKOOK LEE (2006)
M. VOLKAN ÖTÜGEN (2004)
MICHAEL W. PLESNIAK (2004)
DENNIS SIGINER (2005)
KYLE D. SQUIRES (2005)
YOSHINOBU TSUJIMOTO (2006)

PUBLICATIONS DIRECTORATE
Chair, **ARTHUR G. ERDMAN**

OFFICERS OF THE ASME
President, **HARRY ARMEN**

Exec. Director
V. R. CARTER

Treasurer
R. E. NICKELL

PUBLISHING STAFF
Managing Director, Engineering
THOMAS G. LOUGHLIN

Director, Technical Publishing
PHILIP DI VIETRO

Production Assistant
MARISOL ANDINO

(Contents continued on inside back cover)

Transactions of the ASME, Journal of Fluids Engineering (ISSN 0098-2202) is published bimonthly (Jan., Mar., May, July, Sept., Nov.) by The American Society of Mechanical Engineers, Three Park Avenue, New York, NY 10016. Periodicals postage paid at New York, NY and additional mailing offices.
POSTMASTER: Send address changes to Transactions of the ASME, Journal of Fluids Engineering, c/o THE AMERICAN SOCIETY OF MECHANICAL ENGINEERS, 22 Law Drive, Box 2300, Fairfield, NJ 07007-2300.
CHANGES OF ADDRESS must be received at Society headquarters seven weeks before they are to be effective. Please send old label and new address.

STATEMENT from By-Laws. The Society shall not be responsible for statements or opinions advanced in papers or ... printed in its publications (B7.1, Par. 3).
COPYRIGHT © 2004 by the American Society of Mechanical Engineers. Authorization to photocopy material for internal or personal use under those circumstances not falling within the fair use provisions of the Copyright Act, contact the Copyright Clearance Center (CCC), 222 Rosewood Drive, Danvers, MA 01923, tel: 978-750-8400, www.copyright.com. Request for special permission or bulk copying should be addressed to Reprints/Permission Department.

INDEXED by Applied Mechanics Reviews and Engineering Information, Inc. Canadian Goods & Services Tax Registration #126148 048.

This journal is printed on acid-free paper, which exceeds the ANSI Z39.48-1992 specification for permanence of paper and library materials. ∞™
♲ 85% recycled content, including 10% post-consumer fibers.

Downloaded 03 Jun 2010 to 171.66.16.159. Redistribution subject to ASME license or copyright; see http://www.asme.org/terms/Terms_Use.cfm

(**Contents continued**)

Journal of Fluids Engineering **Volume 126, Number 6** **NOVEMBER 2004**

TECHNICAL BRIEFS

The ASME Journal of Fluids Engineering is abstracted and indexed in the following:

Applied Science & Technology Index, Chemical Abstracts, Chemical Engineering and Biotechnology Abstracts (Electronic equivalent of Process and Chemical Engineering), Civil Engineering Abstracts, Computer & Information Systems Abstracts, Corrosion Abstracts, Current Contents, Ei EncompassLit, Electronics & Communications Abstracts, Engineered Materials Abstracts, Engineering Index, Environmental Engineering Abstracts, Environmental Science and Pollution Management, Excerpta Medica, Fluidex, Index to Scientific Reviews, INSPEC, International Building Services Abstracts, Mechanical & Transportation Engineering Abstracts, Mechanical Engineering Abstracts, METADEX (The electronic equivalent of Metals Abstracts and Alloys Index), Petroleum Abstracts, Process and Chemical Engineering, Referativnyi Zhurnal, Science Citation Index, SciSearch (The electronic equivalent of Science Citation Index), Shock and Vibration Digest, Solid State and Superconductivity Abstracts, Theoretical Chemical Engineering

Modeling of Entropy Production in Turbulent Flows

O. B. Adeyinka*
G. F. Naterer†

Department of Mechanical and Manufacturing Engineering,
University of Manitoba,
Winnipeg, Canada, R3T 2N2

This article presents new modeling of turbulence correlations in the entropy transport equation for viscous, incompressible flows. An explicit entropy equation of state is developed for gases with the ideal gas law, while entropy transport equations are derived for both gases and liquids. The formulation specifically considers incompressible forced convection problems without a buoyancy term in the y-momentum equation, as density variations are neglected. Reynolds averaging techniques are applied to the turbulence closure of fluctuating temperature and entropy fields. The problem of rigorously expressing the mean entropy production in terms of other mean flow quantities is addressed. The validity of the newly developed formulation is assessed using direct numerical simulation data and empirical relations for the friction factor. Also, the dissipation (ϵ) of turbulent kinetic energy is formulated in terms of the Second Law. In contrast to the conventional ϵ equation modeling, this article proposes an alternative method by utilizing both transport and positive definite forms of the entropy production equation. [DOI: 10.1115/1.1845551]

1 Introduction

Entropy production characterizes the energy conversion of thermofluid processes, particularly regarding the irreversible degradation of mechanical energy into internal energy. Viscous dissipation is a main frictional irreversibility in laminar flows, but other less understood irreversibilities arise with fluid turbulence. Such processes have significance in various engineering applications, ranging from flow losses in turbines to reduced effectiveness of microelectronics cooling. Sciubba [1] outlines local entropy production contours for turbomachinery design improvements. Past numerical studies of entropy production in two-dimensional laminar flows by Adeyinka and Naterer [2] have outlined the significance of the apparent entropy production difference, when analyzing convective heat transfer. A detailed review of past advances regarding entropy and the Second Law in CFD (computational fluid dynamics) has been presented by Naterer and Camberos [3].

The earliest documented effort to develop a numerical model for turbulent entropy production was outlined by Moore and Moore [4]. The Moore model assumes that turbulent fluctuations of the heat flux and viscous dissipation in the positive definite entropy equation can be modeled by adding a turbulent conductivity and turbulent viscosity to the molecular conductivity and viscosity, respectively. The Moore model has been applied to the prediction of the mean local entropy production in a bent elbow duct [5], a plane turbulent oscillating jet [6], and a jet impinging on a wall [7]. But Kramer-Bevan [8] has shown that the Moore model exhibits certain inconsistencies for confined flows with small temperature gradients close to the wall, where the production of turbulent kinetic energy is not equal to the dissipation of turbulent kinetic energy. Furthermore, other assumptions lead to difficulties when generalizing the formulation. For example, the model assumes that the production of temperature fluctuations is equal to their dissipation. Also, the viscous dissipation fluctuation is assumed to be equal to the production of turbulent kinetic energy. These shortcomings are addressed through revised modeling of the turbulence correlations in this article.

The viscous dissipation term may be neglected in the energy equation when computing the mean entropy generation based on the Moore model [4], as the evaluation depends on the velocity and temperature fields. Under certain flow conditions, previous studies have shown that CFD codes can accurately predict velocity and temperature fields when viscous dissipation is neglected. However, the viscous dissipation cannot be generally neglected when using the STTAss (small thermal turbulence assumption; [8]). In the STTAss model, it is assumed that the fluctuating component of temperature is small compared to the mean temperature, so the fluctuating temperature in the entropy transport equation can be simplified with Taylor series expansions. Those expansions are truncated after the linear terms, thereby yielding a reduced form of mean entropy production equation. But the spatial variation of the fluctuating temperature is required to accurately account for the convection of entropy in the flow. It has been shown that the transport equation model becomes inaccurate for laminar flow in the center of an adiabatic duct, where small temperature gradients may cause a cancellation [8].

Previous studies by Jansen [9] and Hauke [10] have extended entropy-based stability analysis to turbulent flows. Jansen showed that the exact Navier-Stokes equations for compressible flow could lead to an entropy inequality, through a linear combination of equations [9]. The resulting entropy expression was modeled under the assumption that the fluctuating temperature component is much smaller than the mean temperature. A modified specific entropy was also introduced. The study determined what constraints the Second Law places on the modeling of the averaged equations by linking entropy production to their solution variables.

This article extends past Reynolds averaging techniques for the momentum and scalar transport equations, to the Second Law for turbulent flows. The formulation requires instantaneous values of the velocity and temperature fields. In order to express the mean entropy generation explicitly in terms of other mean flow quantities, a closure problem is encountered, similarly as the evaluation of Reynolds stresses in the momentum equations. To our knowledge, there are no existing empirical/numerical Second Law closure models based fully on mean quantities from the conservation equations. This article addresses this shortcoming, while developing an alternative closure. Also, a new correlation for the fluctuating temperature and entropy production is derived. Furthermore, this article seeks to develop an alternative interpretation and model for the dissipation of turbulent kinetic energy, based on the Second Law.

---

*Graduate Student, Department of Mechanical and Manufacturing Engineering, University of Manitoba, 15 Gillson Street, Winnipeg, Manitoba, Canada, R3T 2N2

†Professor, Department of Mechanical and Manufacturing Engineering, University of Manitoba, 15 Gillson Street, Winnipeg, Manitoba, Canada, R3T 2N2

Contributed by the Fluids Engineering Division for publication in the JOURNAL OF FLUIDS ENGINEERING. Manuscript received by the Fluids Engineering Division December 9, 2003; revised manuscript received July 9, 2004. Review conducted by: T. Gatski.

2 Formulation of Entropy Production

In tensor form, the entropy balance for an open system, subject to mass fluxes and energy transfer across a fixed control surface, may be written as

$$\frac{\partial S}{\partial t}+\frac{\partial F_i}{\partial x_i}\equiv \dot{P}_s \geqslant 0 \tag{1}$$

where $\dot{P}_s$ is the entropy production rate and $S=\rho s$ represents the entropy per unit volume. Also, the component of the entropy flux in the x_i direction, F_i, may be expressed in terms of the velocity component and heat flux in that direction, v_i and q_i, as follows:

$$F_i=\rho v_i s+\frac{q_i}{T} \tag{2}$$

Equation (1) represents the entropy transport equation. In this form, the rate of entropy accumulation in the control volume is balanced by the net convection of entropy, entropy transfer associated with heat flow, and non-negative entropy production. Unlike the conservation of energy equation, the entropy transport equation involves an inequality, which stipulates that the rate of entropy generation must be non-negative in all thermodynamic systems.

The specific entropy s in the flux term of Eq. (1) can be obtained from the Gibbs equation as follows:

$$ds=\frac{1}{T}de+\frac{p}{\rho^2 T}d\rho \tag{3}$$

where e is the internal energy per unit mass, ρ represents density, and p is pressure. Integration of the Gibbs equation gives

$$\Delta s=\int_{T_r}^{T_s} c_v \frac{dT}{T}+\int_{\rho_r}^{\rho_s}\frac{p}{\rho^2 T}d\rho \tag{4}$$

where the subscripts r and s denote a specified initial (or reference) state and the current state, respectively. The variable c_v represents the specific heat at constant volume, which will be assumed to be constant. The impact of this constant specific volume assumption is that the formulation is limited to liquid flows or incompressible gas flows over small to moderate temperature ranges. This assumption applies to explicit evaluation of entropy in the entropy equation of state, but not upcoming transport equations for evaluating spatial variations of the entropy production rate.

For an incompressible fluid, Eq. (4) becomes

$$\Delta s=s-s_r=c_v \ln\left(\frac{T_s}{T_r}\right) \tag{5}$$

For an ideal gas,

$$s=c_v \ln\left(\frac{T_s}{T_r}\right)-R\ln\left(\frac{\rho_s}{\rho_r}\right)+s_r \tag{6}$$

Substituting the ideal gas law into Eq. (6),

$$s=c_v \ln\frac{(p_s/p_r)}{(\rho_s/\rho_r)^{\gamma}}+s_r=c_v \ln\left(\frac{p^*}{\rho^{*\gamma}}\right)+s_r \tag{7}$$

where γ is the ratio of specific heats.

When combined with the Gibbs equation, the entropy transport equation provides a way of calculating the local entropy generation for an open system. Alternatively, $\dot{P}_s$ can be formulated as [11]

$$\dot{P}_s=\frac{k}{T^2}\left(\frac{\partial T}{\partial x_i}\right)^2+\frac{\tau_{ij}}{T}\frac{\partial u_i}{\partial x_j}\geqslant 0 \tag{8}$$

where k is the thermal conductivity. Also, τ_{ij} is the viscous stress arising from velocity gradients in the fluid motion, i.e.,

$$\tau_{ij}=\mu\left[\left(\frac{\partial u_i}{\partial x_j}+\frac{\partial u_j}{\partial x_i}\right)-\frac{2}{3}\frac{\partial u_k}{\partial x_k}\delta_{ij}\right] \tag{9}$$

In Eq. (9), μ and δ_{ij} refer to dynamic viscosity and Kronecker delta, respectively. The divergence terms in Eq. (9) will vanish due to the assumption of incompressibility.

In Eq. (8), Fourier's Law has been used to represent heat conduction. Also, a Newtonian fluid is assumed for the viscous stress term. Based on these models, Eq. (8) is a positive definite expression for the entropy generation rate, since it represents a sum of squared terms [12]. Temperature T is expressed in absolute (Kelvin) units. The positive definite equation applies to both compressible and incompressible Newtonian fluids. In Eq. (8), the first term represents entropy generation due to heat transfer across a finite temperature difference, while the second term represents the local entropy generation due to viscous dissipation (i.e., degradation of mechanical energy into internal energy due to shear action).

3 Reynolds Averaged Entropy Transport Equations

For turbulent flows, the Reynolds averaged entropy equation can be obtained after combining the positive definite and entropy transport equations. The resulting combined expression, called the Reynolds averaged Clausius-Duhem equality [9,10] is written as follows:

$$\frac{\partial}{\partial t}(\rho\overline{s})+\frac{\partial}{\partial x_i}\left[\rho\overline{u_i s}+\rho\overline{u_i' s'}-\overline{\frac{k}{T}\frac{\partial T}{\partial x_i}}\right]=\overline{\frac{k}{T^2}\left(\frac{\partial T}{\partial x_i}\right)^2}+\overline{\frac{\tau_{ij}}{T}\frac{\partial u_i}{\partial x_j}} \tag{10}$$

where the overbar (i.e., $\overline{s}$) and prime (i.e., s') notations refer to mean and fluctuating components associated with the Reynolds averaging, respectively.

Since T and u_i (and consequently the viscous dissipation term) have mean and fluctuating components appearing in the denominator and numerator, modeling of Eq. (10) becomes highly complex. It becomes difficult to explicitly express the mean entropy production in terms of other mean flow variables alone. Two past approaches for expressing the mean entropy production are briefly addressed below.

A Separate Time Averaging. In the first approach, the two sides of Eq. (10) are averaged seperately. For the entropy transport equation, Reynolds averaging yields

$$\overline{\dot{P}_s}=\frac{\partial}{\partial t}(\rho\overline{s})+\frac{\partial}{\partial x_i}(\rho\overline{u_i s}+\overline{\rho u_i' s'})+k\frac{\partial}{\partial x_i}\overline{\ln\left[\overline{T}\left(1+\frac{T'}{\overline{T}}\right)\right]}\geqslant 0 \tag{11}$$

The first term in Eq. (8) can be simplified by substituting $\partial(\ln T)/\partial x_i$ for $(\partial T/\partial x_i)/T$ before time averaging. The time averaged positive definite entropy equation becomes

$$\begin{aligned}\overline{\dot{P}_s}=&\,k\frac{\partial}{\partial x_i}(\overline{\ln T})\frac{\partial}{\partial x_i}(\overline{\ln T})+k\overline{\frac{\partial}{\partial x_i}(\ln T)'\frac{\partial}{\partial x_i}(\ln T)'}+\mu\left\{\overline{\left(\frac{1}{T}\right)}\right.\\ &\left.\times\left[\left(\frac{\partial\overline{u}_i}{\partial x_j}+\frac{\partial\overline{u}_j}{\partial x_i}\right)\frac{\partial\overline{u}_i}{\partial x_j}\right]\right\}+\mu\left\{\overline{\left(\frac{1}{T}\right)}\left[\overline{\left(\frac{\partial u_i'}{\partial x_j}+\frac{\partial u_j'}{\partial x_i}\right)\frac{\partial u_i'}{\partial x_j}}\right]\right\}\\ &+2\mu\frac{\partial\overline{u}_i}{\partial x_j}\overline{\left(\frac{1}{T}\right)'\frac{\partial u_i'}{\partial x_j}}+\mu\frac{\partial\overline{u}_i}{\partial x_j}\overline{\left(\frac{1}{T}\right)'\frac{\partial u_j'}{\partial x_i}}+\mu\frac{\partial\overline{u}_j}{\partial x_i}\overline{\left(\frac{1}{T}\right)'\frac{\partial u_i'}{\partial x_j}}\\ &+\mu\left\{\overline{\left(\frac{1}{T}\right)'\left[\left(\frac{\partial u_i'}{\partial x_j}+\frac{\partial u_j'}{\partial x_i}\right)\frac{\partial u_i'}{\partial x_j}\right]}\right\}\geqslant 0\end{aligned} \tag{12}$$

A close examination of Eq. (12) reveals the physical processes leading to entropy production in turbulent flow. The first two terms on the right side are entropy production terms due to thermal fluctuations and transport. The terms in the first squared brackets represent the entropy production due to mean viscous effects. The terms in the second squared brackets represent entropy produced due to the dissipation of turbulent kinetic energy. The terms in the last squared brackets represent the mechanism of entropy produced by the interaction of fluctuating viscous effects and temperature fluctuations. The remaining terms represent the conversion of entropy production, due to mean viscous effects, to entropy production due to fluctuating viscous-temperature effects and back.

By defining the mean viscous stress and the fluctuating viscous stress, respectively, as

$$\overline{\tau}_{ij}=\mu\left[\left(\frac{\partial \overline{u}_i}{\partial x_j}+\frac{\partial \overline{u}_j}{\partial x_i}\right)\right] \tag{13}$$

$$\tau'_{ij}=\mu\left[\left(\frac{\partial u'_i}{\partial x_j}+\frac{\partial u'_j}{\partial x_i}\right)\right] \tag{14}$$

then Eq. (12) becomes

$$\overline{\dot{P}_s}=k\frac{\partial}{\partial x_i}(\overline{\ln T})\frac{\partial}{\partial x_i}(\overline{\ln T})+k\overline{\frac{\partial}{\partial x_i}(\ln T)'\frac{\partial}{\partial x_i}(\ln T)'}+\overline{\left(\frac{1}{T}\right)}\overline{\tau}_{ij}\frac{\partial \overline{u}_i}{\partial x_j}$$
$$+\overline{\left(\frac{1}{T}\right)\tau'_{ij}\frac{\partial u'_i}{\partial x_j}}+\overline{\tau}_{ij}\overline{\left(\frac{1}{T}\right)'\frac{\partial u'_i}{\partial x_j}}+\frac{\partial \overline{u}_i}{\partial x_j}\overline{\left(\frac{1}{T}\right)'\tau'_{ij}}+\overline{\left(\frac{1}{T}\right)'\tau'_{ij}\frac{\partial u'_i}{\partial x_j}}\geqslant 0 \tag{15}$$

Modeling of this equation is considered to be more complicated than modeling of the standard turbulent kinetic energy equation. No models exist at the present time (to our knowledge) for the correlations involving the $(1/T)'$ terms. Any such correlations would be difficult to validate and/or measure with a degree of accuracy.

B Combined Time Averaging. Modeling of the mean entropy generation can be simplified by the following approach, whereby the Clausius-Duhem equality is averaged. The left side of Eq. (8) is multiplied by temperature to give

$$T\dot{P}_s=\frac{k}{T}\left(\frac{\partial T}{\partial x_i}\right)^2+\tau_{ij}\frac{\partial u_i}{\partial x_j} \tag{16}$$

Kramer-Bevan [8] presented a derivation of the time averaged form of Eq. (16), with the following result:

$$\overline{T}\overline{\dot{P}}_s+\overline{T'\dot{P}'_s}=k\frac{\partial}{\partial x_i}\overline{(\ln T)}\frac{\partial \overline{T}}{\partial x_i}+k\overline{\frac{\partial}{\partial x_i}(\ln T)'\frac{\partial T'}{\partial x_i}}$$
$$+\overline{\tau}_{ij}\frac{\partial \overline{u}_i}{\partial x_j}+\overline{\tau'_{ij}\frac{\partial u'_i}{\partial x_j}} \tag{17}$$

In Eq. (17), the physical processes of conversion of entropy production, arising from mean viscous effects, to entropy production due to fluctuating viscous/temperature effects have been captured in the $\overline{T'\dot{P}'_s}$ correlation. Other terms remain as previously described for Eq. (12). This equation seems to be more straightforward than Eqs. (11) and (12), provided that suitable empirical models can be developed for the $\overline{T'\dot{P}'_s}$ and thermal gradient correlations. Kramer-Bevan [8] proposed a closure approximation for a subset of possible flow fields by using a small thermal turbulence assumption (STTAss). A detailed discussion of the STTAss will be given in an upcoming section. At this time, no model exists for the $\overline{T'\dot{P}'_s}$ correlation (to our knowledge). The following section attempts to provide such modeling.

C Fluctuating Temperature and Entropy Production Correlation. In order to derive a general, combined time averaged equation for the mean entropy generation, the $T'\dot{P}'_s$ correlation was modeled after multiplying both sides of the entropy transport equation, Eq. (1), by T. Then, time averaging is performed to yield

$$\overline{T}\overline{\dot{P}}_s+\overline{T'\dot{P}'_s}=\overline{T}\left[\frac{\partial}{\partial t}(\rho\overline{s})+\frac{\partial}{\partial x_i}(\rho\overline{u}_j\overline{s}+\overline{\rho u's'})\right.$$
$$\left.+k\frac{\partial}{\partial x_i}\overline{\ln\left[\overline{T}\left(1+\frac{T'}{\overline{T}}\right)\right]}\right]+\overline{T'\frac{\partial}{\partial x_i}(\rho u'_i\overline{s})}$$
$$+\overline{T'\frac{\partial}{\partial x_i}(\rho\overline{u}_i s')}+\overline{T'\frac{\partial}{\partial x_i}(\rho u'_i s')}$$
$$+\overline{kT'\frac{\partial}{\partial x_i}\ln\left[\overline{T}\left(1+\frac{T'}{\overline{T}}\right)\right]} \tag{18}$$

By comparing Eq. (11) with Eq. (18), it can be shown that

$$\overline{T'\dot{P}'_s}=\overline{T'\frac{\partial}{\partial x_i}(\rho u'_i\overline{s})}+\overline{T'\frac{\partial}{\partial x_i}(\rho\overline{u}_i s')}+\overline{T'\frac{\partial}{\partial x_i}(\rho u'_i s')}$$
$$+\overline{kT'\frac{\partial}{\partial x_i}\ln\left[\overline{T}\left(1+\frac{T'}{\overline{T}}\right)\right]} \tag{19}$$

Using the chain rule of calculus

$$\overline{T'\dot{P}'_s}=\rho\overline{T'u'_i}\frac{\partial\overline{s}}{\partial x_i}+\rho\overline{s}\overline{T'\frac{\partial u'_i}{\partial x_i}}+\rho\overline{T's'}\frac{\partial\overline{u}_i}{\partial x_i}+\rho\overline{u}_i\overline{T'\frac{\partial s'}{\partial x_i}}$$
$$+\overline{T'\frac{\partial}{\partial x_i}(\rho u'_i s')} \tag{20}$$

$$+\overline{kT'\frac{\partial}{\partial x_i}\ln\left[\overline{T}\left(1+\frac{T'}{\overline{T}}\right)\right]} \tag{21}$$

By assuming incompressibility, the mean and instantaneous velocity fields are solenoidal and Eq. (21) reduces to

$$\overline{T'\dot{P}'_s}=\rho\overline{T'u'_i}\frac{\partial\overline{s}}{\partial x_i}+\rho\overline{u}_i\overline{T'\frac{\partial s'}{\partial x_i}}+\overline{T'\frac{\partial}{\partial x_i}(\rho u'_i s')}$$
$$+\overline{kT'\frac{\partial}{\partial x_i}\ln\left[\overline{T}\left(1+\frac{T'}{\overline{T}}\right)\right]} \tag{22}$$

This equation for the $\overline{T'\dot{P}'_s}$ correlation is a new result for turbulent incompressible flow. It is considered that all terms in this equation can be more readily determined than the past formulations. The following section considers such modeling of terms in Eq. (22).

4 Eddy Viscosity Models of Mean Entropy Production

A few simplified models, based on the solution of the Reynolds averaged Navier Stokes equations and an eddy viscosity for mean entropy generation, have been documented in past literature [4,5,7,8]. The linear eddy viscosity model assumes a Boussinesq relationship between the turbulent stresses (or second moments) and the mean strain rate tensor through an isotropic eddy viscosity. Although these models attempt to minimize complexity, it is difficult to ascertain if the essence of relevant irreversibilities has been captured with sufficient accuracy, due to the lack of experimental data. It should be noted that no relevant experimental data regarding these turbulence correlations of entropy production has been measured and reported in the literature (to our knowledge).

Moore and Moore [4] suggest the following correlations for mean entropy production, thermal diffusion and viscous dissipation, respectively:

$$\overline{T}\overline{\dot{P}_s}=\frac{k}{\overline{T}}\left[\left(\frac{\partial\overline{T}}{\partial x_i}\right)^2+\overline{\left(\frac{\partial T'}{\partial x_i}\right)^2}\right]+\overline{\tau}_{ij}\frac{\partial\overline{u}_i}{\partial x_j}+\overline{\tau'_{ij}\frac{\partial u'_i}{\partial x_j}} \tag{23}$$

$$k\overline{\left(\frac{\partial T'}{\partial x_i}\right)^2}=k_t\left(\frac{\partial\overline{T}}{\partial x_i}\right)^2 \tag{24}$$

$$\overline{\tau'_{ij}\frac{\partial u'_i}{\partial x_j}}=\frac{\mu_t}{\mu}\overline{\tau}_{ij}\frac{\partial\overline{u}_i}{\partial x_j} \tag{25}$$

In Eqs. (24) and (25), k_t and μ_t denote the turbulent molecular conductivity and the turbulent molecular viscosity, respectively. This model misses most of the correlation in Eq. (17), due to the assumption that the temperature fluctuations are small compared to the mean temperature. Unfortunately, there is no experimental or theoretical evidence to verify that the missing terms are sufficiently small for all turbulent flows, under a range of flow conditions.

Due to these inconsistencies, particularly close to the wall, Kramer-Bevan proposed a different physically based model for the viscous dissipation correlation [8], i.e.,

$$\overline{\tau'_{ij}\frac{\partial u'_i}{\partial x_j}}=\tilde{\epsilon} \tag{26}$$

where $\tilde{\epsilon}$ is the "true" dissipation of turbulent kinetic energy. The definition of $\tilde{\epsilon}$ differs from the definition of dissipation of turbulent kinetic energy in the standard $k-\epsilon$ model (documented in Ref. [12]). The final improved model becomes

$$\overline{T}\overline{\dot{P}_s}=\frac{k+k_t}{\overline{T}}\left(\frac{\partial\overline{T}}{\partial x_i}\right)^2+\overline{\tau}_{ij}\frac{\partial\overline{u}_i}{\partial x_j}+\tilde{\epsilon} \tag{27}$$

In contrast to the Moore model, which uses the positive definite entropy equation, the small thermal turbulence model is based on time averaging of the entropy transport equation. It assumes that the fluctuating component of temperature is small compared to the mean temperature. In formulating this model, the fluctuating temperature in Eq. (11) is replaced by a Taylor series expansion of those functions. The expansions are truncated after the linear terms, thereby yielding the following equations for mean entropy production and mean specific entropy [8]:

$$\overline{\dot{P}_s}=\frac{\partial}{\partial t}(\rho\overline{s})+\frac{\partial}{\partial x_i}\left[\rho\overline{u_i s}-\frac{1}{\overline{T}}\left(\frac{c_v\mu_t}{Pr_t}+k\right)\frac{\partial\overline{T}}{\partial x_i}\right]\geqslant 0 \tag{28}$$

$$\overline{s}=s_r+c_v\ln\frac{\overline{T}_s}{T_r}-R\ln\frac{\rho_s}{\rho_r} \tag{29}$$

The turbulent Prandtl number Pr_t arises in Eq. (28) because the entropy-velocity correlation has been modeled with a Reynolds analogy. Under the STTAss, extra terms arise in the entropy transport equation, with an increase in the diffusion term. This is equivalent to adding an effective diffusivity $c_v\mu_t/\mathrm{Pr}_t$ to the thermal diffusivity in the laminar model.

5 Turbulence Modeling With the Second Law

The exact equation for the dissipation of turbulent kinetic energy (TKE) is useful to understand the meaning and importance of various terms, but usually it cannot be rigorously modeled in its full detailed form [13]. Modeling of the exact equation is traditionally carried out by drastic simplification and it usually involves a laborious empirical determination of five or more closure coefficients. This section attempts to obtain the dissipation of TKE using the Second Law under the STT Assumption. In this approach, the local entropy production in convection dominated flow can be computed based on mean quantities (velocity and temperature) obtained from the solution of the RANS equations, using both the transport and positive definite forms of the entropy equation. Since the dissipation of TKE (denoted by ϵ) appears in the positive definite mean entropy production equation, it is anticipated that its local value can be computed throughout the flow domain by the Clausius-Duhem equation, Eq. (10). A formulation for the proposed model is presented for the eddy viscosity and second moment turbulent closure.

Combining Eqs. (11), (17), and (22) we obtain the following combined entropy equation for turbulent flow:

$$\begin{aligned}\overline{T}\overline{\dot{P}_s}&=\overline{T}\left[\frac{\partial}{\partial t}(\rho\overline{s})+\frac{\partial}{\partial x_i}(\rho\overline{u_i s}+\rho\overline{u's'})+k\frac{\partial}{\partial x_i}\overline{\ln\left[\overline{T}\left(1+\frac{T'}{\overline{T}}\right)\right]}\right]\\&=k\frac{\partial}{\partial x_i}\overline{(\ln T)}\frac{\partial\overline{T}}{\partial x_i}+k\overline{\frac{\partial}{\partial x_i}(\ln T)'\frac{\partial T'}{\partial x_i}}+\overline{\tau}_{ij}\frac{\partial\overline{u}_i}{\partial x_j}+\overline{\tau'_{ij}\frac{\partial u'_i}{\partial x_j}}\\&\quad-\rho\overline{T'u'_i}\frac{\partial\overline{s}}{\partial x_i}-\rho\overline{u}_i\overline{T'\frac{\partial s'}{\partial x_i}}-\overline{T'\frac{\partial}{\partial x_i}(\rho u'_i s')}\\&\quad-\overline{kT'\frac{\partial}{\partial x_i}\ln\left[\overline{T}\left(1+\frac{T'}{\overline{T}}\right)\right]}\end{aligned} \tag{30}$$

The fourth term on the right side of Eq. (30) represents the dissipation of turbulent kinetic energy. This term, called ϵ, can be interpreted as a physical mechanism by which exergy ($T\dot{P}_s$) is destroyed in turbulent flow. This view agrees with the traditional interpretation that associates ϵ with the rate at which turbulent kinetic energy is converted to internal energy in the flow. The terms after the second equality in Eq. (30) reveal the physical processes leading to exergy destruction in turbulent flow. The total exergy destroyed in turbulent flow is the sum of the exergy destroyed due to irreversible heat transfer (terms 1, 2, and 8), viscous dissipation (terms 3 and 4), turbulent enthalpy transfer (term 5), and the work done by fluctuating temperature against turbulent entropy transfer by mass exchange (term 6 and 7). All of these irreversible processes dissipate useful mechanical energy into less useful internal energy.

It is important to note that Eq. (30) re-emphasizes the importance of maintaining the positivity of ϵ in numerical simulations. The time-averaged entropy equation does not shed much light, in regards to modeling of ϵ, except when simplified by the small thermal turbulence assumption. Complete modeling of the Clausius-Duhem equation can only be achieved through experiments, for calibrating closure coefficients when approximating the nonlinear fluctuating terms. Two approaches (linear eddy viscosity and differential second moment (DSM) closures) will be described for modeling and simplification of Eq. (30).

A Linear Eddy Viscosity Closure. The terms in the time averaged entropy equation, Eq. (30), can be determined from a linear eddy viscosity model as follows (see appendix),

$$\begin{aligned}&\frac{\partial}{\partial t}(\rho\overline{s})+\frac{\partial}{\partial x_i}\left[\rho\overline{u_i s}-\frac{1}{\overline{T}}\left(\frac{c_v\mu_t}{Pr_t}+k\right)\frac{\partial\overline{T}}{\partial x_i}\right]\\&\quad=\frac{1}{\overline{T}^2}\left[(k+\gamma k_t)\left(\frac{\partial\overline{T}}{\partial x_i}\right)^2\right]+\frac{\overline{\tau}_{ij}}{\overline{T}}\frac{\partial\overline{u}_i}{\partial x_j}+\frac{\tilde{\epsilon}}{\overline{T}}+\left\{\frac{k}{\overline{T}^2}\left(\frac{\partial T'}{\partial x_i}\right)^2\right.\\&\qquad+\frac{k}{2}\frac{\partial}{\partial x_i}\left(\frac{1}{\overline{T}}\right)\frac{\partial}{\partial x_i}\overline{(T'^2)}-\frac{\rho c_v}{\overline{T}}\left[\frac{\partial}{\partial x_i}\left(\frac{\overline{u'_i T'^2}}{\overline{T}}\right)\right.\\&\qquad\left.\left.+\overline{u}_i\frac{\partial}{\partial x_i}\left(\frac{\overline{T'^2}}{\overline{T}}\right)\right]+\frac{\rho c_v}{2\overline{T}^2}\left[\frac{\partial}{\partial x_i}(\overline{u'_i T'^2})+\overline{u}_i\frac{\partial}{\partial x_i}(\overline{T'^2})\right]\right\}\end{aligned} \tag{31}$$

The left side of Eq. (31) was developed from the entropy transport equation on the left side of Eq. (1). That expression must equal the positive definite rate of entropy production from the Second Law in Eq. (8), which becomes the right side of Eq. (31). On the left side of Eq. (31), the terms represent the transient change of mean entropy (first term) and the transport of entropy by mass and heat flow (second term in square brackets). On the right side of Eq. (31), the terms refer to entropy production associated with thermal molecular and turbulent diffusion of the mean temperature field (first term in square brackets), viscous dissipation of the mean velocity field (second term), and irreversibilities in dissipation of turbulent kinetic energy (third term). Within the braces, the terms represent entropy production corresponding to irreversible temperature fluctuations (first and second terms) and irreversible interactions between fluctuating velocity and temperature fields (remaining terms).

It is viewed that the individual terms in braces can be obtained through the following correlation governing the dynamics of T'^2 (Tennekes, Lumley [14]), i.e.:

$$\overline{u}_i \frac{\partial}{\partial x_i}\left(\frac{\overline{T'^2}}{2}\right) = \frac{\partial}{\partial x_i}\left[\frac{1}{2}\overline{u_i' T'^2} - \alpha \frac{\partial}{\partial x_i}\left(\frac{\overline{T'^2}}{2}\right)\right] - \overline{u_i' T'}\frac{\partial \overline{T}}{\partial x_i} - \alpha \overline{\left(\frac{\partial T'}{\partial x_i}\right)^2} \tag{32}$$

where α is the thermal diffusivity.

B Differential Second Moment (DSM) Closure. The differential second moment closure directly solves the transport equations for the Reynolds stresses in the momentum equation. This approach is used to obtain the scalar fluxes in turbulent flow, involving the transport of passive scalars. The computed turbulent heat flux, $\overline{T'u'}$ and Eq. ($A1$) can then be used directly in Eq. (30) to give

$$\begin{aligned}\frac{\partial}{\partial t}(\rho\overline{s}) + \frac{\partial}{\partial x_i}\left[\rho\overline{u_i s} + \frac{\rho c_v}{\overline{T}}\overline{u_i' T'} - \frac{k}{\overline{T}}\frac{\partial \overline{T}}{\partial x_i}\right] &= \frac{k}{\overline{T}^2}\left(\frac{\partial \overline{T}}{\partial x_i}\right)^2 + \rho\overline{T' u_i'}\frac{\partial \overline{s}}{\partial x_i} + \frac{\overline{\tau}_{ij}}{\overline{T}}\frac{\partial \overline{u}_i}{\partial x_j} + \frac{\tilde{\epsilon}}{\overline{T}} + \Bigg\{ \frac{k}{\overline{T}^2}\left(\frac{\partial T'}{\partial x_i}\right)^2 \\ &\quad + \frac{k}{2}\frac{\partial}{\partial x_i}\left(\frac{1}{\overline{T}}\right)\frac{\partial}{\partial x_i}(\overline{T'^2}) - \frac{\rho c_v}{\overline{T}}\left[\frac{\partial}{\partial x_i}\left(\frac{\overline{u_i' T'^2}}{\overline{T}}\right) \right. \\ &\quad \left. + \overline{u}_i\frac{\partial}{\partial x_i}\left(\frac{\overline{T'^2}}{\overline{T}}\right)\right] + \frac{\rho c_v}{2\overline{T}^2}\left[\frac{\partial}{\partial x_i}(\overline{u_i' T'^2}) + \overline{u}_i\frac{\partial}{\partial x_i}(\overline{T'^2})\right]\Bigg\}\end{aligned} \tag{33}$$

This approach dispenses with the eddy viscosity to express the turbulent shear stress in terms of mean flow quantities.

Similarities in turbulent irreversibilities can be observed in Eqs. (31) and (33). From left to right on the left side of Eq. (33), the terms represent the transient change of mean entropy (first term) and the transport of entropy by mass and heat flow (second term in square brackets). Unlike Eq. (31), the heat flow is not modeled with a turbulent conductivity in this case. On the right side of Eq. (33), the terms refer to entropy production corresponding to thermal molecular diffusion of the mean temperature field (first term), diffusive entropy transport in the mean flow field due to velocity fluctuations (second term), viscous dissipation of the mean velocity field (third term), and dissipation of turbulent kinetic energy (fourth term). In a similar way as previously described, the terms within braces represent entropy production corresponding to irreversible temperature fluctuations (first and second terms) and irreversible interactions between fluctuating velocity and temperature fields (remaining terms).

6 Turbulent Entropy Production in a Channel

The newly derived formulation for mean entropy production will be validated using direct numerical simulation data. Turbulent flow between two parallel plates at four different Reynolds numbers, based on the friction velocity, is considered in this section. Attention is focused on the positive definite model involving the dissipation of turbulent kinetic energy [right side of Eq. (33)], since the entropy transport equation requires inclusion of the viscous dissipation in the energy equation for accurate modeling.

Consider an incompressible flow in a parallel channel of length L and width D. The plates are spaced h apart. It is assumed that the width is much greater that the height. The head loss due to frictional effects in the channel is related to the Darcy's friction factor f as follows:

$$H_l = h_l g = f\frac{L\overline{u}^2}{4h} \tag{34}$$

where $\overline{u}$ and g are the mean velocity and acceleration due to gravity, respectively. It can be shown that the loss term due to viscous dissipation in the mechanical energy equation can be related to entropy production and head loss by

$$H_l = \frac{1}{\dot{m}}\int_{\forall}\tau:\nabla\vec{v}\,d\forall = \frac{1}{\dot{m}}\int_{\forall}T\dot{P}_s d\forall \tag{35}$$

where $\dot{m}$ and $\forall$ refer to the mass flow rate through the channel and differential control volume, respectively. Also, the colon symbol (:) designates matrix contraction between the shear stress and velocity gradient tensors in the viscous dissipation term. The previous result linking head loss and entropy production can be derived after combining Bernoulli's equation, Eq. (8) and the mechanical energy equation for incomressible (laminar or turbulent) flows.

By combining Eqs. (34) and (35) and substituting $d\forall = DLdy$ and $\dot{m} = \rho\overline{u}Dh$ in the resulting equation, the integral value of mean entropy production in an adiabatic channel can be related to Darcy's friction factor, i.e.

$$f = \frac{4}{\rho\overline{u}^3}\int \overline{T\dot{P}_s}dy \tag{36}$$

where ρ, $\overline{T}$, and $\dot{P}_s$ are the density, mean temperature, and entropy production rate per unit volume, respectively. The integral value of the entropy production rate is obtained from the positive definite entropy equation, based on spatial gradients of velocity, dissipation of turbulent kinetic energy and temperature. The Reynolds number based on the friction velocity Re_τ is computed with the friction velocity u_τ, half channel height δ, and the kinematic viscosity ν. Similarly, the Reynolds number based on the bulk velocity Re is computed with the mean velocity, hydraulic diameter, and the kinematic viscosity. Fluid properties are obtained at a temperature of 295 K. A useful observation is that Eq. (36) suggests that entropy production can be used as a standardized metric for loss characterization in duct flows. By using entropy production in this way, the equivalent friction factor becomes a product of the local exergy destruction integrated over the flow domain and a constant based on averaged values of the flow variables.

Darcy's friction factor is a dimensionless group defined as follows:

$$f = \frac{8\tau_w}{\rho\overline{u}^2} \tag{37}$$

The following computations with DNS data will show close agreement between friction factors calculated by Eqs. (36) and (37) with the Colebrook friction factor for channel flow. This close agreement will provide useful validation of the newly derived entropy production model for turbulent flows.

Computations of f at $\mathrm{Re}_\tau = 180$, 395, and 590 were based on direct numerical simulation (DNS) data of Moser et al. [15]. The data of Kuroda et al. [16] was used to compute f at $\mathrm{Re}_\tau = 100$. The

Table 1 Friction factors at different Re_τ

	Re_τ			
	100	180	395	590
f (based on τ_w)	0.0383	0.0325	0.0260	0.0232
f (based on present modeling)	0.0388	0.0324	0.0252	0.0225

computed friction factors based on Eqs. (36) and (37) are compared in Table 1. The present results show excellent agreement with Darcy's friction factor computed from the Colebrook equation and Eqs. (36) and (37). The Colebrook equation is documented in Ref. [17]. The results are illustrated at various Reynolds numbers based on the bulk velocity in Fig. 1. The results suggest that the present turbulence modeling of entropy production (particularly in terms of ϵ) has been accurately formulated.

Another useful validation of the new formulation is outlined in Fig. 2. A comparison with Moore's model is presented, in regards to the spatial distribution of entropy production in the channel. It is useful to observe that the integral value of entropy production computed from Moore's model in Eqs. (23) and (25), based on the production of turbulent kinetic energy, is within 1% of the newly formulated model. Although close agreement is achieved, the newly derived formulation of Eq. (33) includes additional mechanisms of turbulent entropy production, particularly involving dissipation terms. Figure 2 illustrates that past turbulence predictions with Moore's model give certain erroneous distributions of the mean entropy production. Moore's model under-predicts the entropy production closer to the wall and over-predicts entropy production away from the wall, before it decreases to zero in the middle of the channel. The additional curve in Fig. 2 shows that the viscous mean dissipation is the main component of entropy production near the wall, but other components become most significant at further distances away from the wall. In particular, the mean viscous dissipation accounts for more than 80% of the total entropy production at approximately $y^+<9$, where $y^+=yu_\tau/\nu$. This percentage decreases to zero in the center of the channel.

7 Conclusions

Modeling of turbulence correlations for the entropy transport equation is outlined in this article. Closure of the correlations involving fluctuating temperature and entropy production is accomplished through Reynolds averaging. An alternative model, which uses the small thermal turbulence assumption, is proposed for calculating mean entropy production. The validity of this STTAss model is addressed. With an eddy viscosity closure, the model resembles the corresponding laminar flow formulation, except for the eddy diffusivity added to the effective diffusivity in the diffusion component of the entropy transport equation. Also, γk_t appears in the effective diffusivity of the positive definite entropy equation, as well as T'^2 terms. In contrast to conventional modeling of the dissipation rate equation, an alternative method is developed, which involves both transport and positive definite forms of the turbulent entropy production equation.

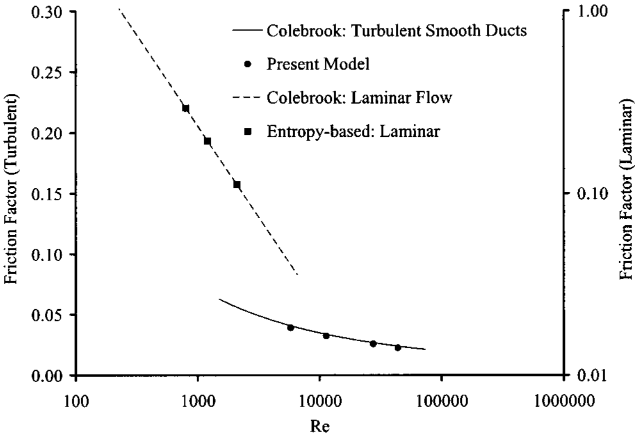

Fig. 1 Friction factor based on present entropy production modeling

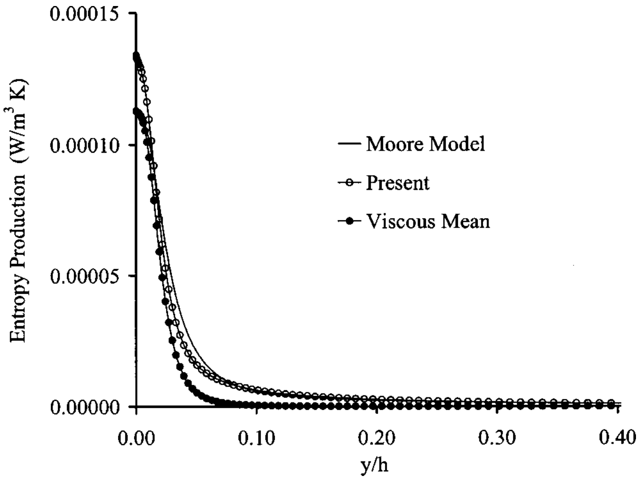

Fig. 2 Local distribution of integrated entropy production in a channel

Acknowledgments

Financial support from the Natural Sciences and Research Council of Canada and the University of Manitoba (Graduate Fellowship; O. B. Adeyinka) is gratefully acknowledged.

Nomenclature

e = thermal energy per unit mass, J/kg
c_p, c_v = specific heats, J/kgK
k = thermal conductivity, W/mK
p = pressure, Pa
$\dot{P}_s$ = entropy production rate, W/m^{3}K
s = specific entropy, J/kgK
t = time, s
T = temperature, K
u = velocity, m/s
x = cartesian coordinate
$\forall$ = volume

Greek

ρ = density, kg/m^3
μ = dynamic viscosity, kg/ms
ϕ = general scalar quantity
τ_{ij} = stress tensor

Subscripts

i, j, k = coordinate directions (tensor notation)
t = turbulent

Superscripts

$(\ )^+$ = normalized by the wall variables
$(\ )'$ = fluctuating quantity (turbulence notation)

Appendix. Derivation of Linear Eddy Viscosity Closure

The fluctuating component of the specific entropy is given by

$$s' \approx c_v \frac{T'}{\overline{T}} - R \frac{\rho'}{\overline{\rho}} \tag{A1}$$

By the Reynolds analogy,

$$\overline{T'u'} = -\frac{k_t}{\rho c_p}\frac{\partial \overline{T}}{\partial x_i} \tag{A2}$$

Also, based on the STT Assumption,

$$\frac{\partial \overline{s}}{\partial x_i} = \frac{c_v}{\overline{T}}\frac{\partial \overline{T}}{\partial x_i} \tag{A3}$$

Using Eqs. (A1)–(A3) in the first term on the right side of Eq. (22) gives

$$\rho\overline{T'u_i'}\frac{\partial \overline{s}}{\partial x_i} = -\gamma k_t\left(\frac{\partial \overline{T}}{\partial x_i}\right)^2 \tag{A4}$$

where $\gamma = c_v/c_p = 1$ for incompressible fluids.

The second term in Eq. (22), under the STT Assumption, becomes

$$T'\frac{\partial s'}{\partial x_i} \approx T'\frac{\partial}{\partial x_i}\left(c_v\frac{T'}{\overline{T}}\right) = c_v(T')^2\frac{\partial}{\partial x_i}\left(\frac{1}{\overline{T}}\right) + \frac{c_v}{\overline{T}}\left[T'\frac{\partial T'}{\partial x_i}\right] \tag{A5}$$

After time averaging,

$$\overline{T'\frac{\partial s'}{\partial x_i}} \approx c_v\overline{(T')^2}\frac{\partial}{\partial x_i}\left(\frac{1}{\overline{T}}\right) + \frac{c_v}{\overline{T}}\left[\frac{1}{2}\frac{\partial\overline{(T')^2}}{\partial x_i}\right] \tag{A6}$$

The third term in Eq. (22), under the STT Assumption, becomes

$$\begin{aligned} T'\frac{\partial}{\partial x_i}(\rho u_i's') &\approx T'\frac{\partial}{\partial x_i}\left(\rho\frac{c_v}{\overline{T}}T'u_i'\right)\\ &= \rho c_v u_i'(T')^2\frac{\partial}{\partial x_i}\left(\frac{1}{\overline{T}}\right) + \rho\frac{c_v}{\overline{T}}T'\frac{\partial}{\partial x_i}(T'u_i') \end{aligned} \tag{A7}$$

The last term in Eq. (A7) can be written as

$$T'\frac{\partial}{\partial x_i}(T'u_i') = T'\left[T'\frac{\partial u_i'}{\partial x_i} + u_i'\frac{\partial T'}{\partial x_i}\right] \tag{A8}$$

where $\overline{T'(\partial u_i'/\partial x_i)} = 0$ due to the continuity equation. The time averaged form of Eq. (A8) becomes

$$\overline{T'\frac{\partial}{\partial x_i}(T'u_i')} = \frac{1}{2}\frac{\partial}{\partial x_i}\overline{(u_i'T'^2)} \tag{A9}$$

Substituting this result back into Eq. (A7) gives

$$\overline{T'\frac{\partial}{\partial x_i}(\rho u_i's')} \approx \rho c_v\overline{u_i'(T')^2}\frac{\partial}{\partial x_i}\left(\frac{1}{\overline{T}}\right) + \frac{\rho c_v}{2\overline{T}}\overline{(u_i'T'^2)} \tag{A10}$$

The final form of the $\overline{T'\dot{P}_s'}$ correlation, under the small thermal turbulence assumption, becomes

$$\begin{aligned} \overline{T'\dot{P}_s'} = {} & -\gamma k_t\left(\frac{\partial \overline{T}}{\partial x_i}\right)^2 + \rho c_v\frac{\partial}{\partial x_i}\left(\frac{\overline{u_i'T'^2}}{\overline{T}}\right) + \rho c_v\overline{u}_i\frac{\partial}{\partial x_i}\left(\frac{\overline{T'^2}}{\overline{T}}\right)\\ & -\frac{\rho c_v}{2\overline{T}}\frac{\partial\overline{(u_i'T'^2)}}{\partial x_i} - \frac{\rho c_v\overline{u}_i}{2\overline{T}}\frac{\partial\overline{(T'^2)}}{\partial x_i} \end{aligned} \tag{A11}$$

Equations (17), (28), and (A11) can be combined under the STT Assumption. After several algebraic manipulations,

$$\begin{aligned} & \frac{\partial}{\partial t}(\rho\overline{s}) + \frac{\partial}{\partial x_i}\left[\rho\overline{u_i s} - \frac{1}{\overline{T}}\left(\frac{c_v\mu_t}{Pr_t} + k\right)\frac{\partial \overline{T}}{\partial x_i}\right]\\ & = \frac{1}{\overline{T}^2}\left[(k+\gamma k_t)\left(\frac{\partial \overline{T}}{\partial x_i}\right)^2\right] + \frac{\overline{\tau}_{ij}}{\overline{T}}\frac{\partial \overline{u}_i}{\partial x_j} + \frac{\tilde{\epsilon}}{\overline{T}} + \left\{k\left(\frac{\partial T'}{\partial x_i}\right)^2\right.\\ & \quad + \frac{k}{2}\frac{\partial}{\partial x_i}\left(\frac{1}{\overline{T}}\right)\frac{\partial}{\partial x_i}\overline{(T'^2)} - \frac{\rho c_v}{\overline{T}}\left[\frac{\partial}{\partial x_i}\left(\frac{\overline{u_i'T'^2}}{\overline{T}}\right)\right.\\ & \quad \left.\left. + \overline{u}_i\frac{\partial}{\partial x_i}\left(\frac{\overline{T'^2}}{\overline{T}}\right)\right] + \frac{\rho c_v}{2\overline{T}^2}\left[\frac{\partial}{\partial x_i}\overline{(u_i'T'^2)} + \overline{u}_i\frac{\partial}{\partial x_i}\overline{(T'^2)}\right]\right\} \end{aligned} \tag{A12}$$

This result represents the turbulent entropy transport equation, based on a linear eddy viscosity closure.

References

[1] Sciubba, E., 1997, "Calculating Entropy with CFD," Mech. Eng. (Am. Soc. Mech. Eng.), **119**(10), pp. 86–88.

[2] Adeyinka, O. B., and Naterer, G. F., 2002, "Apparent Entropy Production Difference with Heat and Fluid Flow Irreversibilities," Numer. Heat Transfer, Part B, **42**, pp. 411–436.

[3] Naterer, G. F., and Camberos, J. A., 2003, "Entropy and the Second Law in Fluid Flow and Heat Transfer Simulation," J. Thermophys. Heat Transfer, **17**(3), pp. 360–371.

[4] Moore, J., and Moore, J. G., 1983, "Entropy Production Rates from Viscous Flow Calculations, Part I. A Turbulent Boundary Layer Flow," ASME Paper 83-GT-70, ASME Gas Turbine Conference, Phoenix, AZ.

[5] Moore, J., and Moore, J. G., 1983, "Entropy Production Rates from Viscous Flow Calculations, Part II. Flow in a Rectangular Elbow," ASME Paper 83-GT-71, ASME Gas Turbine Conference, Phoenix, AZ.

[6] Cervantes, J., and Solorio, F., 2002, "Entropy Generation in a Plane Turbulent Oscillating Jet," Int. J. Heat Mass Transfer, **45**, pp. 3125–3129.

[7] Drost, M. K., and White, M. D., 1991, "Numerical Predictions of Local Entropy Generation in an Impinging Jet," ASME J. Heat Transfer, **113**, pp. 823–829.

[8] Kramer-Bevan, J. S., 1992, "A Tool for Analysing Fluid Flow Losses," M.Sc. Thesis, University of Waterloo, Canada.

[9] Jansen, K. E., 1993, "The Role of Entropy in Turbulence and Stabilized Finite Element Methods," Ph.D. Thesis, Stanford University, CA.

[10] Hauke, G., 1995, "A Unified Approach to Compressible and Incompressible Flows and a New Entropy-Consistent Formulation of the K-Epsilon Model," Ph.D. Thesis, Stanford University, CA.

[11] Bejan, A., 1996, *Entropy Generation Minimization: The Method of Thermodynamic Optimization of Finite-Time Systems and Finite-Time Processes*, CRC Press, Boca Raton, FL.

[12] Naterer, G. F., 2002, *Heat Transfer in Single and Multiphase Systems*, CRC Press, Boca Raton, FL.

[13] Hanjalić, K., and Jakirlić, S., 2002, "Second Moment Turbulent Closure Modelling," *Closure Strategies for Turbulent and Transitional Flows*, Part A, Chap. 2, Cambridge University, Cambridge, England.

[14] Tennekes H., and Lumley, J. L., 1981, *A First Course in Turbulence*, MIT, Cambridge, MA.

[15] Moser, R. D., Kim, J., and Mansour, N. N., 1999, "Direct Numerical Simulation of Turbulent Channel Flow up to $\mathrm{Re}_\tau=590$," Phys. Fluids, **11**(4), pp. 943–945.

[16] Kuroda, A., Kasagi, N., and N. Hirata, M., 1990, "A Direct Numerical Simulation of the Fully Developed Turbulent Channel Flow," *Numerical Methods in Fluid Dynamics*, M. Yasuhara et al., eds., Vol. 2, Jap. Soc. Comp. Fluid Dyn., pp. 1012–1017.

[17] White, F. M., 1988, *Fluid Mechanics*, 4th ed., McGraw-Hill, NY.

On the Grid Sensitivity of the Wall Boundary Condition of the k-ω Turbulence Model

L. Eça
Instituto Superior Técnico,
Department of Engineering,
Avenida Rovisco Pais, 1 Lisbon,
1049-001 Portugal

M. Hoekstra
Maritime Research Institute Netherlands,
P.O. Box 28 6700AA,
Wageningen, The Netherlands

This paper presents a study on the k-ω turbulence model with regard to the numerical implementation of the ω boundary condition at a solid wall, where ω tends to infinity. Three different implementations are tested in the calculation of a simple two-dimensional turbulent flow over a flat plate. Grid refinement studies in grids with different near-wall grid line spacings are performed to assess the numerical uncertainty of the predicted drag coefficient C_D. The results are compared with the predictions of several alternative algebraic, one-equation, and two-equation eddy-viscosity turbulence models. For the same level of grid refinement, the estimated uncertainty of C_D obtained with the k-ω model is one order of magnitude larger than for all the other models. [DOI: 10.1115/1.1845492]

1 Introduction

The use of eddy-viscosity turbulence models in the Reynolds averaged Navier-Stokes equations is still common practice in the numerical calculation of complex turbulent flows. Nowadays, one of the most popular eddy-viscosity models is the two-equation eddy-viscosity k-ω model proposed by Wilcox [1] in a version that removes the sensitivity to the free-stream boundary conditions, like the ones proposed in [2] and [3].

One of the major advantages claimed for the k-ω model is the ability to compute the k and ω transport equations in the near-wall region without the use of any damping functions. On the other hand, ω goes to infinity at the wall, which can hardly be considered as a strong point of the model. Proposals for implementation of the ω boundary condition at a solid wall are available in the open literature.

Usually a finite value for ω is imposed at the wall, either derived from the distance of the first grid node to the wall [2] or from the so-called rough-wall condition [1]. The numerical implementation of the latter has been discussed in [4] and [5].

The ω wall boundary condition proposed by Menter in [2] is formally grid dependent, because it involves explicitly the grid spacing adjacent to the wall. Conversely, the rough-wall boundary condition is dependent on the roughness selected, even for roughness values well below the hydrodynamically smooth limit, as the results presented in [4] show. Therefore, in the present study we have investigated also our own alternative to the numerical implementation of the ω boundary condition at a solid wall, which is an attempt to remove the grid dependency.

Our aim is to investigate the consequences of the ω wall boundary condition for the convergence of meaningful viscous flow quantities with grid refinement and to estimate the numerical uncertainty obtained with the near-wall discretizations typically used in viscous flow calculations. In order to avoid unnecessary complications, we have selected a simple two-dimensional (2D) incompressible flow over a flat plate as the test case.

Four grid refinement studies, using different near-wall grid line spacings, have been carried out for the so-called BSL and SST versions of the k-ω model, proposed in [2], as well as the version based on a turbulent, non-turbulent analysis (TNT) version [3] with the three numerical implementations of the ω wall boundary condition mentioned above.

For comparison, the same studies were also performed for the algebraic Cebeci and Smith method [6], the one-equation models proposed by Menter [7] and by Spalart and Allmaras [8], and for the low-Reynolds k-ϵ model proposed by Chien [9].

The paper is organized in the following way: Section 2 presents the numerical implementations of the ω boundary condition tested. For the sake of completeness, the procedure to estimate the numerical uncertainty of a given solution is briefly described in Section 3. The results obtained for the 2D incompressible flow over a flat plate are presented and discussed in Section 4 and the conclusions of this study are summarized in Section 5.

2 Wall Boundary Condition for ω

According to Wilcox [1], the exact solution[1] of ω in the viscous sublayer is

$$\omega = \frac{6\nu}{\beta y_n^2} \quad \text{for } y_n^+ < 2.5, \tag{1}$$

where y_n is the distance to the wall, β is a constant of the model equal to 0.075, and $y_n^+ = u_\tau y_n/\nu$, u_τ being the friction velocity. So at the wall where $y_n = 0$, ω goes to infinity. This is an awkward boundary condition from the numerical point of view, requiring at least a decision on its practical implementation.

In [1], Wilcox suggests the use of 7 to 10 grid nodes in the viscous sublayer to obtain an accurate implementation of the ω wall boundary condition. But this is not a very attractive proposal, because one has to ensure that all the selected grid nodes are in the viscous sublayer; moreover there is some arbitrariness in the number of nodes chosen. An alternative would be to apply Eq. (1) in all the grid nodes that have $y_n^+ < 2.5$, but with two major drawbacks:

- Since the number of grid nodes satisfying $y_n^+ < 2.5$ is solution dependent, it may invoke convergence difficulties due to oscillations between consecutive iterations.
- The use of this type of switches leads to scatter in the data obtained from grid refinement studies [10].

Therefore, in the present study we consider the following three alternatives for the numerical implementation of the ω boundary condition at a smooth surface:

Contributed by the Fluids Engineering Division for publication in the JOURNAL OF FLUIDS ENGINEERING. Manuscript received by the Fluids Engineering Division September 9, 2003; revised manuscript received May 26, 2004. Review conducted by: T. Gatski.

[1] This is the exact solution of the ω transport equation when only diffusion and dissipation are retained and the eddy-viscosity is set equal to 0.

- BC1: Specify ω at the first grid node away from the wall in accordance with Eq. (1) as

$$(\omega)_2 = \frac{6\nu}{0.075(y_n^2)_2}. \tag{2}$$

- BC2: Specify ω at the wall from

$$(\omega)_1 = \frac{60\nu}{0.075(y_n^2)_2}, \tag{3}$$

as suggested by Menter in Ref. [2].

- BC3: Use the rough-wall boundary condition to obtain the ω wall value.

$$(\omega)_1 = \frac{2500\nu}{k_s^2}, \tag{4}$$

where k_s is the typical roughness size.

The alternative BC1 yields a formally grid-independent boundary condition provided $(y_n)_2$ is in the range where Eq. (1) is valid. Although the value of $(\omega)_1$ is irrelevant in BC1, it is fixed with Eq. (3) when needed in, e.g., postprocessing.

Hellsten [5] has found that the constant in BC2 should preferably be chosen somewhat smaller, viz. 36 instead of 60, to improve the consistency of the predictions of the wall friction. In our tests we have maintained Menter's original version, however.

In [4], the alternative BC3 has been tested for fixed values of $k_s^+ = u_\tau k_s / \nu$, which implies varying k_s for a given surface. However, in practical situations a uniform k_s is more realistic. Therefore, in the present study we have selected a constant k_s value, corresponding to $k_s^+ = 1$ at the inlet of the computational domain. So we have used

$$(\omega)_1 = \frac{2500}{\nu}(u_\tau^2)_{\text{inlet}} \tag{5}$$

all along the wall.

It may be mentioned that we have included the alternative BC3 only for comparison purposes; it is already known that it does not reproduce the smooth wall solution [4,5].

3 Uncertainty Estimation

The basis of our procedure for the estimation of the uncertainty U of the solution on a given grid is the standard grid convergence index (GCI) method [11] which says

$$U = F_s |\delta_{\text{RE}}|. \tag{6}$$

F_s is a safety factor and δ_{RE} is the error estimation obtained by Richardson extrapolation

$$\delta_{\text{RE}} = \phi_i - \phi_o = \alpha h_i^p, \tag{7}$$

where ϕ_i is the numerical solution of any local or integral scalar quantity on a given grid (designated by the subscript $_i$), ϕ_o is the estimated exact solution, α is a constant, h_i is a parameter which identifies the representative grid cell size, and p is the observed order of accuracy.

There are three unknowns in Eq. (7): ϕ_o, α, and p. Therefore, three geometrically similar grids are required to estimate δ_{RE}. If solutions on more than three grids are available, more than one grid triplet can be chosen to estimate δ_{RE}. It is our experience that these estimates can vary a lot. Therefore, we compute ϕ_o, α, and p in such cases with a least-squares root approach that minimizes the function

$$S(\phi_o, \alpha_j, p_j) = \sqrt{\sum_{i=1}^{n_g} [\phi_i - (\phi_o + \alpha h_i^p)]^2}, \tag{8}$$

where n_g is the number of grids available. The minimum of Eq. (8) is found by setting the derivatives of Eq. (8) with respect to ϕ_o, p, and α equal to zero. The details on the solution of Eq. (8) are given in, [10].

Our experience with the GCI method has shown that its application in monotonic convergent solutions which exhibit an observed order of accuracy significantly larger than the theoretical order of accuracy may be troublesome [12]. Therefore, we have considered an alternative based on an error representation with a power series with fixed exponents, which we have tested before in [10]. Thus when the observed order of the accuracy is larger than 2, we consider an alternative representation of the error estimation given by

$$\delta_{\text{RE2}} = \phi_i - \phi_o = \alpha_1 h_i^2 + \alpha_2 h_i^3. \tag{9}$$

Equation (9) is also solved in the least-squares root sense as described in [10].

The standard deviation of the fit U_s is used as one of the contributions of the uncertainty.

$$U_s = \sqrt{\frac{\sum_{i=1}^{n_g} [\phi_i - (\phi_o + \alpha h_i^p)]^2}{n_g - 3}} \tag{10}$$

for Eq. (7) and

$$U_s = \sqrt{\frac{\sum_{i=1}^{n_g} (\phi_i - (\phi_o + \alpha_1 h_i^2 + \alpha_2 h_i^3))^2}{n_g - 3}}, \tag{11}$$

for Eq. (9).

We can summarize our procedure for the estimation of the numerical uncertainty, valid for a nominally second-order accurate method, as follows:

1. The observed order of accuracy is estimated with the least-squares root technique to identify the apparent convergence condition according to the definition given above.
2. For $0.5 < p \leqslant 2$
   - The uncertainty is estimated with the GCI, Eq. (6), using $F_s = 1.25$ and the numerical error estimated with Richardson extrapolation, Eq. (7), using the least-squares root technique.
   - The standard deviation of the fit U_s, Eq. (10), is added to the uncertainty.
3. For $2 < p \leqslant 3$
   - The uncertainty is estimated with the GCI, Eq. (6), using
     $$U = 1.25\max(|\delta_{\text{RE}}|, |\delta_{\text{RE2}}|).$$
   - The standard deviation of the fit U_s, obtained from Eq. (10) or (11), is added to the uncertainty.
4. For $0 < p \leqslant 0.5$ or $p > 3$
   - U is set equal to the maximum difference between the solutions obtained in the available grids multiplied by a factor of safety, $F_s = 3$.
5. For $p < 0$ the uncertainty estimation fails.

This means that we adopt the GCI for $0.5 \leqslant p \leqslant 3$, but we refer to Eq. (9) in addition to Eq. (7) in some circumstances. For p above 3 the use of the Richardson extrapolation may lead to unacceptably small uncertainty levels. For $0 < p < 0.5$, on the other hand, δ_{RE} becomes excessively large and so the GCI will be over conservative. In both cases we prefer to use the maximum difference between the data of the selected solutions to estimate the uncertainty.

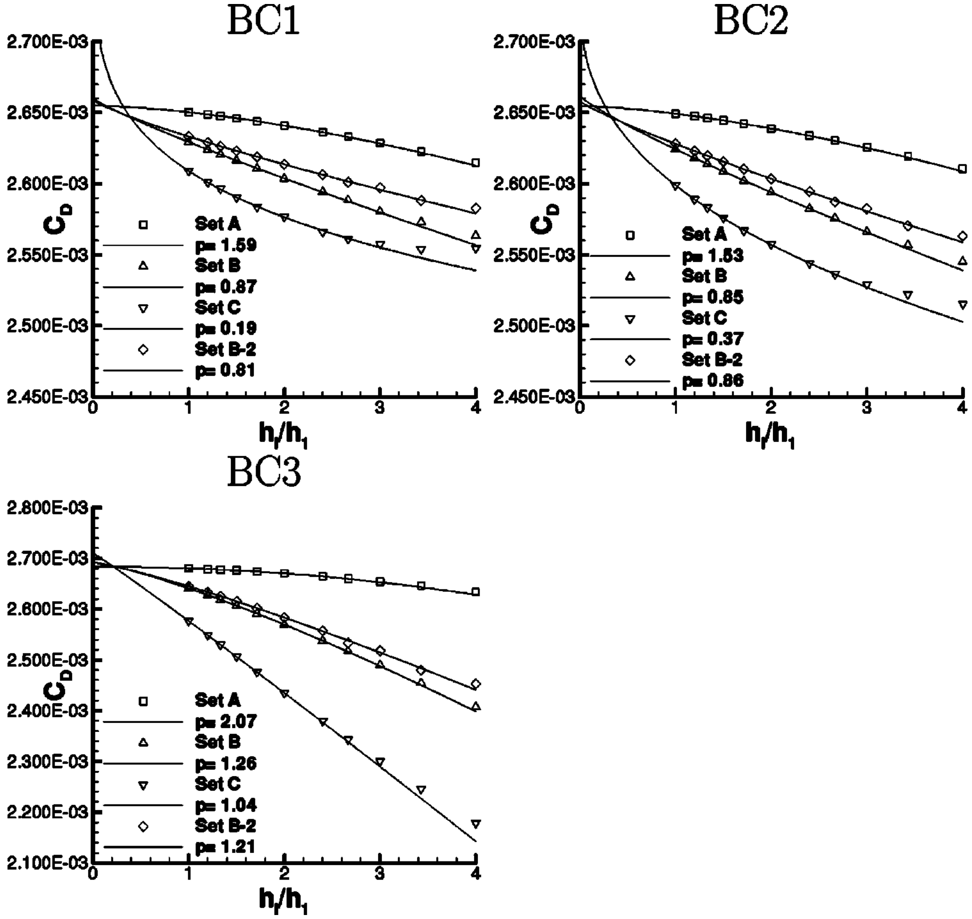

Fig. 1 Convergence of the friction resistance coefficient with the grid refinement. SST version of the k-ω model.

4 Results

4.1 General. The selected test case is a 2D, incompressible, turbulent flow on a flat plate. The computational domain is a rectangle with the inlet located at $\mathrm{Re}_x = 1.07\times 10^6$ and the outlet at $\mathrm{Re}_x = 1.1\times 10^7$. The outer boundary is located at $y/L = 0.04$, which is about four boundary-layer thicknesses[2] at the outlet away from the flat plate. L stands for the x value at the outlet.

The flow field is computed with a 2D code [14] based on a discretization procedure similar to PARNASSOS, [15]. Theoretically, the discretization of the continuity and momentum equations is second-order accurate. However, the numerical solution of all the turbulent quantities transport equations is only first-order accurate, because we have applied first-order upwind schemes to the convective terms of the turbulent quantities transport equations. The calculations are performed with all the terms of the Reynolds-averaged Navier-Stokes equations and so the pressure is also considered to be an unknown. At the inlet boundary, the boundary conditions are specified from standard boundary-layer profiles. The inlet eddy-viscosity profile is the same for all the turbulence models tested. A detailed description of the boundary conditions applied at the four boundaries is given in [16].

The calculations were performed on four sets of 11 geometrically similar Cartesian grids. The finest grids have 241×241 grid nodes and the coarsest ones 61×61 grid nodes. The grids are stretched toward the plate as well as to the inflow boundary using the one-sided function proposed by Vinokur in [17]. The stretching parameter defines the ratio between the distance of the first and second grid nodes and the equidistant spacing.[3] We have selected a stretching parameter of 0.2 for the x direction and four different ones for the y direction: 0.001 for set A, 0.005 for set B, 0.01 for set C. Set B-2 has a similar stretching as set B, but it has an equally spaced distribution in the viscous sub-layer, as suggested in [18]. The typical values of the maximum y^+ at the first grid node away from the wall are given in Table 1 for the four grid sets. It is clear that most of the grids of set C do not satisfy the commonly accepted value of $y^+ < 1$. However, our aim is to evaluate the dependence of the solution uncertainty on the near-wall grid line spacing and so we have also considered cases with $y^+ > 1$.

All the calculations were performed with 15 digits precision and the solution was carried out to machine accuracy. Therefore, the iterative and round-off errors are negligible compared with the discretization error.

We have selected one global and two local flow quantities to illustrate the convergence of the flow field and its numerical uncertainty:

- The total friction resistance coefficient C_D obtained by integration of the shear stress at the wall.
- The axial velocity component U^1 and the eddy-viscosity ν_t at $x = 0.8774$ L, $y = 2.034\times 10^{-4}$ L, which corresponds to a location in the log-law region $y^+ \simeq 100$.

The uncertainty in U^1 and ν_t is estimated at a location which

---

[2] The boundary-layer thickness is estimated from the experimental results of Wieghardt and Tillman [13].

[3] A stretching parameter value of 1 yields therefore an equidistant distribution.

Table 1 Typical values of the maximum y^+ at the first grid node away from the wall

$N_x \times N_y$	Set A	Set B	Set C	Set B-2
241	0.08	0.39	0.77	0.38
201	0.09	0.46	0.93	0.45
181	0.10	0.52	1.03	0.51
161	0.12	0.58	1.16	0.57
141	0.14	0.67	1.33	0.65
121	0.16	0.79	1.56	0.76
101	0.19	0.95	1.89	0.91
91	0.24	1.06	2.38	1.14
81	0.24	1.20	2.38	1.14
71	0.24	1.38	2.38	1.14
61	0.33	1.62	3.23	1.52

Table 2 Friction resistance coefficient and its uncertainty estimates for the SST k-ω model in the 241×241 grids

				Finest grid, 241×241					
				BC1					
	SST			BSL			TNT		
Grid Set	C_D $\times 10^3$	U (%)	p	C_D $\times 10^3$	U (%)	p	C_D $\times 10^3$	U (%)	p
A	2.6502	0.22	1.59	2.7199	0.16	1.71	2.6649	0.31	6.74
B	2.6293	1.47	0.87	2.6978	1.51	0.82	2.6431	0.80	1.06
C	2.6089	3.71	0.19	2.6763	3.54	0.10	2.6221	2.93	0.29
B-2	2.6332	1.23	0.81	2.7018	1.19	0.79	2.6478	0.50	1.17
				BC2					
	SST			BSL			TNT		
Grid Set	C_D $\times 10^3$	U (%)	p	C_D $\times 10^3$	U (%)	p	C_D $\times 10^3$	U (%)	p
A	2.6492	0.26	1.53	2.7188	0.20	1.62	2.6639	0.39	5.40
B	2.6242	1.80	0.85	2.6924	1.85	0.81	2.6379	1.11	1.00
C	2.5988	4.80	0.37	2.6657	4.65	0.32	2.6120	4.03	0.49
B-2	2.6281	1.43	0.86	2.6964	1.40	0.84	2.6426	0.72	1.14
				BC3					
	SST			BSL			TNT		
Grid Set	C_D $\times 10^3$	U (%)	p	C_D $\times 10^3$	U (%)	p	C_D $\times 10^3$	U (%)	p
A	2.6803	0.15	2.07	2.7516	0.11	2.29	2.6955	0.39	7.36
B	2.6408	2.42	1.26	2.7099	2.44	1.26	2.6548	1.93	1.37
C	2.5767	6.50	1.04	2.6423	6.57	1.04	2.5894	5.63	1.13
B-2	2.6449	2.22	1.21	2.7142	2.21	1.21	2.6597	1.70	1.35

Table 3 Friction resistance coefficient and its uncertainty estimates for the SST k-ω model in the 121×121 grids

				Coarsest grid, 121×121					
				BC1					
	SST			BSL			TNT		
Grid Set	C_D $\times 10^3$	U (%)	p	C_D $\times 10^3$	U (%)	p	C_D $\times 10^3$	U (%)	p
A	2.6409	0.75	1.42	2.7122	0.58	1.48	2.6629	0.29	2.10
B	2.6037	4.65	0.31	2.6729	4.15	0.07	2.6250	—	<0
C	2.5765	—	<0	2.6447	—	<0	2.5965	—	<0
B-2	2.6135	3.54	0.22	2.6830	3.08	0.06	2.6350	1.92	0.69
				BC2					
	SST			BSL			TNT		
Grid Set	C_D $\times 10^3$	U (%)	p	C_D $\times 10^3$	U (%)	p	C_D $\times 10^3$	U (%)	p
A	2.6388	0.84	1.38	2.7100	0.67	1.42	2.6608	0.34	1.97
B	2.5939	5.63	0.36	2.6626	5.17	0.16	2.6150	4.50	0.06
C	2.5573	—	<0	2.6244	—	<0	2.5769	—	<0
B-2	2.6034	4.64	0.33	2.6724	4.25	0.23	2.6246	2.75	0.69
				BC3					
	SST			BSL			TNT		
Grid Set	C_D $\times 10^3$	U (%)	p	C_D $\times 10^3$	U (%)	p	C_D $\times 10^3$	U (%)	p
A	2.6703	0.76	1.71	2.7433	0.60	1.82	2.6930	0.39	2.28
B	2.5696	6.89	1.10	2.6368	6.91	1.10	2.5901	6.59	1.10
C	2.4347	21.3	0.70	2.4951	21.2	0.70	2.4517	17.3	0.81
B-2	2.5833	13.3	0.58	2.6511	13.6	0.57	2.6041	10.1	0.70

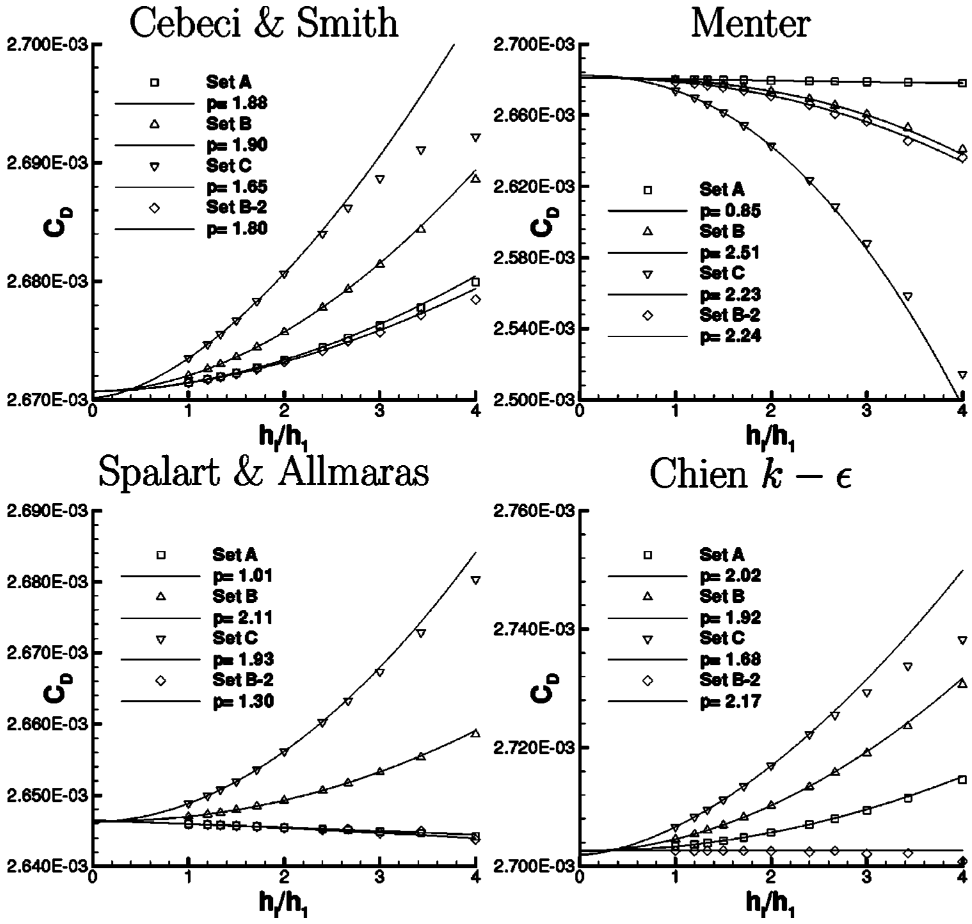

Fig. 2 Convergence of the friction resistance coefficient with the grid refinement. Algebraic Cebeci and Smith model, one-equation models of Menter and Spalart and Allmaras and Chien's k-ϵ model.

does not coincide with a grid node. A third-order interpolation scheme based on the blending of bilinear and biquadratic basis functions is applied to determine U^1 and ν_t at the selected location. The resistance coefficient is calculated using the trapezoidal rule for integration of the skin friction coefficient C_f, which is evaluated with a one-sided two-point scheme for the U^1 derivative with respect to y at the wall.

For all these flow variables we have estimated the uncertainty of the solution on

- The finest grid of 241×241 grid nodes, using the data of the six finest grids covering a grid refinement ratio of 2.
- The 121×121 grid using the data of the six coarsest grids which also cover a grid refinement ratio of 2.

Table 4 Friction resistance coefficient and its uncertainty estimates for the algebraic Cebeci and Smith model, one-equation models of Menter and Spalart and Allmaras and Chien's k-ϵ model in the 241×241 grids

Finest grid, 241×241						
	Cebeci and Smith			Menter		
Grid Set	C_D $\times 10^3$	U (%)	p	C_D $\times 10^3$	U (%)	p
A	2.6715	0.03	1.88	2.6803	0.05	0.85
B	2.6721	0.06	1.90	2.6798	0.07	2.51
C	2.6735	0.16	1.65	2.6739	2.23	0.42
B-2	2.6714	0.03	1.80	2.6788	0.11	2.24
	Spalart and Allmaras			Chien's k-ϵ		
Grid Set	C_D $\times 10^3$	U (%)	p	C_D $\times 10^3$	U (%)	p
A	2.6460	0.02	1.01	2.7034	0.04	2.02
B	2.6470	0.03	2.11	2.7046	0.09	1.92
C	2.6488	0.12	1.93	2.7066	0.22	1.68
B-2	2.6460	0.02	1.30	2.7026	0.01	—

Table 5 Friction resistance coefficient and its uncertainty estimates for the algebraic Cebeci and Smith model, one-equation models of Menter and Spalart and Allmaras and Chien's k-ϵ model in the 121×121 grids

Coarsest grid, 121×121						
	Cebeci and Smith			Menter		
Grid set	C_D $\times 10^3$	U (%)	p	C_D $\times 10^3$	U (%)	p
A	2.6734	0.14	1.59	2.6795	0.07	0.99
B	2.6757	0.28	0.87	2.6735	0.43	2.28
C	2.6806	—	<0	2.6427	1.87	2.30
B-2	2.6732	0.25	1.02	2.6710	0.89	1.58
	Spalart and Allmaras			Chien's k-ϵ		
Grid set	C_D $\times 10^3$	U (%)	p	C_D $\times 10^3$	U (%)	p
A	2.6455	0.03	1.60	2.7057	0.15	1.94
B	2.6493	0.16	1.91	2.7102	0.38	1.81
C	2.6562	0.67	1.44	2.7170	2.35	0.08
B-2	2.6454	0.19	6.42	2.7026	0.20	—

4.2 Friction Resistance Coefficient C_D. The calculation of the friction resistance is usually one of the goals of a viscous flow calculation. Therefore, it is an excellent flow parameter to assess the convergence properties of the solution.

As expected, the results obtained with the three versions of the k-ω model [(BSL), (SST), (TNT)] are not exactly equal. However, there was so much similarity in the behavior of the three versions with respect to grid convergence and their reaction on the different numerical implementations of the ω boundary condition at the wall, that it suffices to discuss the results obtained with the SST version only. Nevertheless, we have included the data obtained with the other two versions in the tables.

The convergence of C_D with the grid refinement using the three numerical implementations of the wall ω boundary condition is illustrated in Fig. 1. The line fits to the data plotted in the three sub figures have been derived with the least-squares root approach applied to the six finest grids.

Tables 2 and 3 present the values of C_D, the estimates of the

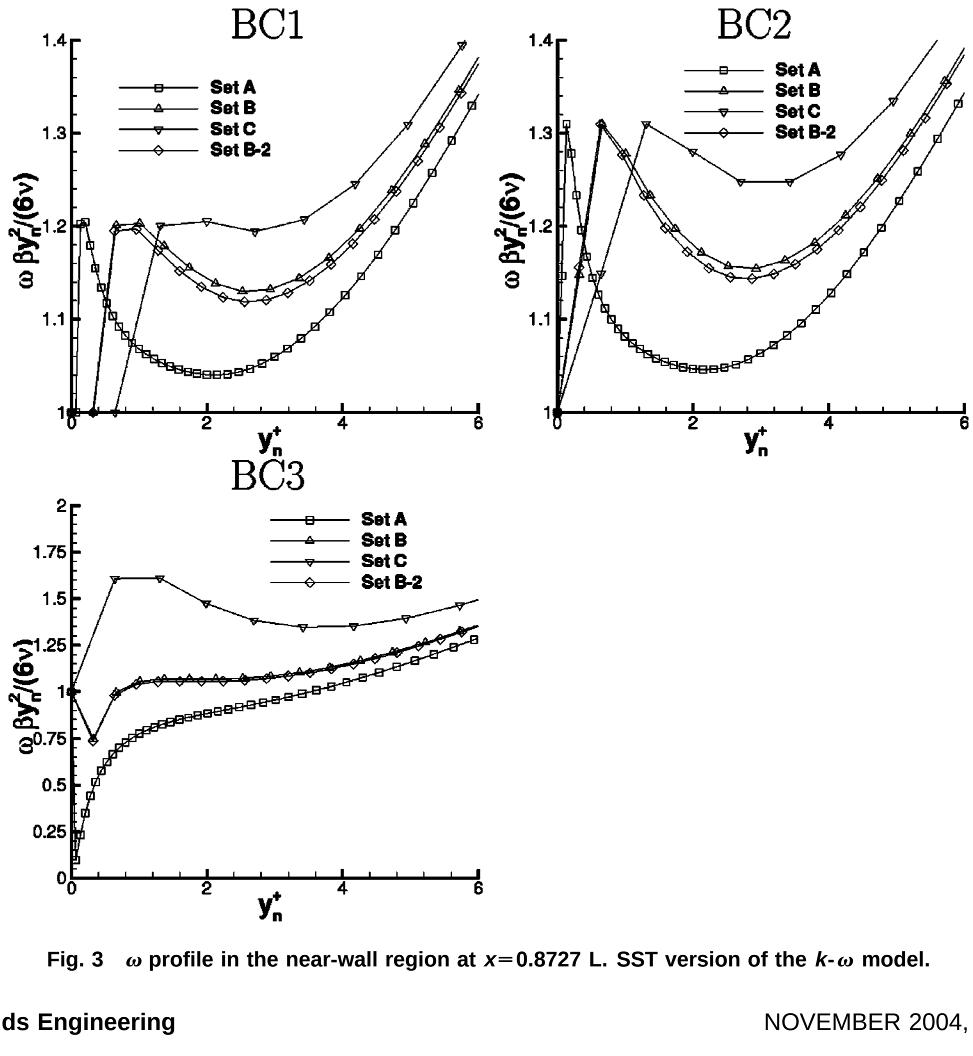

Fig. 3 ω profile in the near-wall region at $x=0.8727$ L. SST version of the k-ω model.

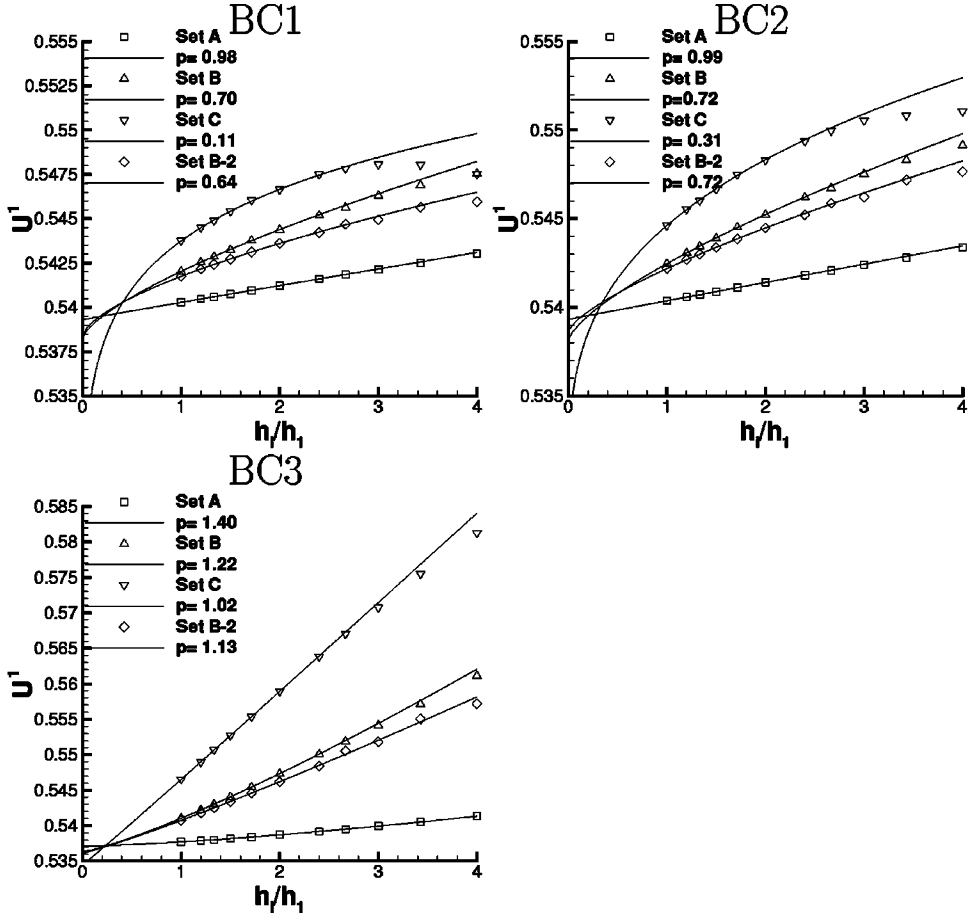

Fig. 4 Convergence of U^1 at $x=0.8774$ L, $y=2.034\times10^{-4}$ L with the grid refinement. SST version of the k-ω model.

uncertainty U, and the observed order of accuracy p, for the two selected discretization levels in the four grid sets.

The overall tendencies observed in the convergence of the drag coefficient are similar for the three implementations of the ω wall boundary condition. Notably, the implementations BC1 and BC2 show essentially the same behavior.

The near-wall grid line spacing is of course an essential parameter for the accuracy of the skin friction determination. This is evident from the fact that the uncertainty is smaller for the coarsest grid of set A than for the finest grids of the sets B, C, and B-2.

A careful comparison of the performance of the BC1, BC2, and BC3 boundary conditions shows the following additional trends:

- Naturally, in each grid set the estimated uncertainty increases with the near-wall grid line spacing for all the tested boundary conditions. This effect is accompanied by an increase of the observed order of accuracy with the reduction of the near-wall grid line spacing.
- The comparison of grid sets B and B-2 shows that the use of an equally spaced grid in the viscous sublayer does not produce any significant improvement in the accuracy of the solution.
- As expected (see [4]), the rough-wall ω wall boundary condition BC3 does not lead to the same results as the other two implementations. The highest levels of uncertainty are obtained for this ω wall boundary condition. However, it exhibits the smallest dependence of the observed order of accuracy on the near-wall grid line spacing.
- Several cases do not exhibit an observed order of accuracy in the expected range, $1\leqslant p\leqslant 2$. As mentioned above, the order of accuracy tends to decrease with the increase of the near-wall grid line spacing. This is particulary evident for the results obtained in the coarsest grid of set C, where several cases exhibit apparent divergence. However, there are also cases where the observed order of accuracy is significantly larger than 2. It is our experience that the observed order of accuracy [10] is extremely sensitive to

Table 6 Uncertainty estimates for U^1 at $x=0.8774$ L, $y=2.034\times10^{-4}$ L. SST, BSL, and TNT k-ω models in the 241×241 grids.

	SST U(%)			BSL U(%)			TNT U(%)		
Grid Set	BC1	BC2	BC3	BC1	BC2	BC3	BC1	BC2	BC3
A	0.23	0.24	0.14	0.26	0.28	0.19	0.89	0.90	0.65
B	0.87	1.00	1.09	0.99	1.09	1.17	1.80	1.86	1.55
C	1.59	2.03	2.77	1.70	2.14	2.84	2.14	2.58	3.29
B-2	0.78	0.82	1.06	0.73	0.82	1.13	1.54	1.53	1.54

Table 7 Uncertainty estimates for U^1 at $x=0.8774$ L, $y=2.034\times10^{-4}$ L. Cebeci and Smith algebraic model (CS), one-equation models of Menter (MT), and Spalart and Allmaras (SA) and Chien's k-ϵ (KE) model in the 241×241 grids.

Grid Set	U(%)			
	CS	MT	SA	KE
A	0.02	0.07	0.03	0.01
B	0.01	0.07	0.04	0.03
C	0.04	0.12	0.07	0.08
B-2	0.02	0.06	0.03	0.01

small disturbances in the data. Therefore, these results indicate that there are difficulties with the near-wall convergence of ω.

In order to assess the grid convergence performance of the k-ω model in comparison with other models, a similar study has been conducted for four alternative eddy-viscosity turbulence models: the algebraic model of Cebeci and Smith, the one-equation models of Menter and Spalart and Allmaras, and Chien's k-ϵ model. The results obtained with these four models are presented in Fig. 2 and Tables 4 and 5.

There are two main differences in the convergence properties obtained with the three versions of the k-ω model as opposed to the other four eddy-viscosity turbulence models

- The estimated uncertainty level for the k-ω models is one order of magnitude larger than for the other eddy-viscosity models. This is clearly a numerical penalty of the near wall behavior of ω.
- The equally spaced grid in the near-wall region significantly improves the accuracy of the drag prediction for the algebraic Cebeci and Smith model, one-equation Spalart and Allmaras model, and Chien's k-ϵ model. However, in the k-ω models and in Menter's one-equation model there is only a minor effect of the near-wall equally spaced grid. This result must be related to the use of the von Karman length-scale in the dissipation term of Menter's one-equation model and to the ω solution in the near-wall region for the k-ω model, respectively.

It can be noticed that the observed order of accuracy of the drag coefficient is less dependent on the grid line spacing for these turbulence models than for the k-ω models. Nevertheless, there are still some cases where the observed order of accuracy is significantly different from the expected value, specially for the grids with the largest near-wall spacing.

It is also worthwhile to observe that even in such a simple turbulent flow the differences between the predictions of the various turbulence models are larger than the numerical uncertainty level.

4.3 ω Profile in the Near-Wall Region. The convergence properties of C_D obtained with the k-ω models must be influenced by the near-wall ω profile. Let us therefore have a look at the behavior of ω in the viscous sublayer as a function of y_n^+ at the

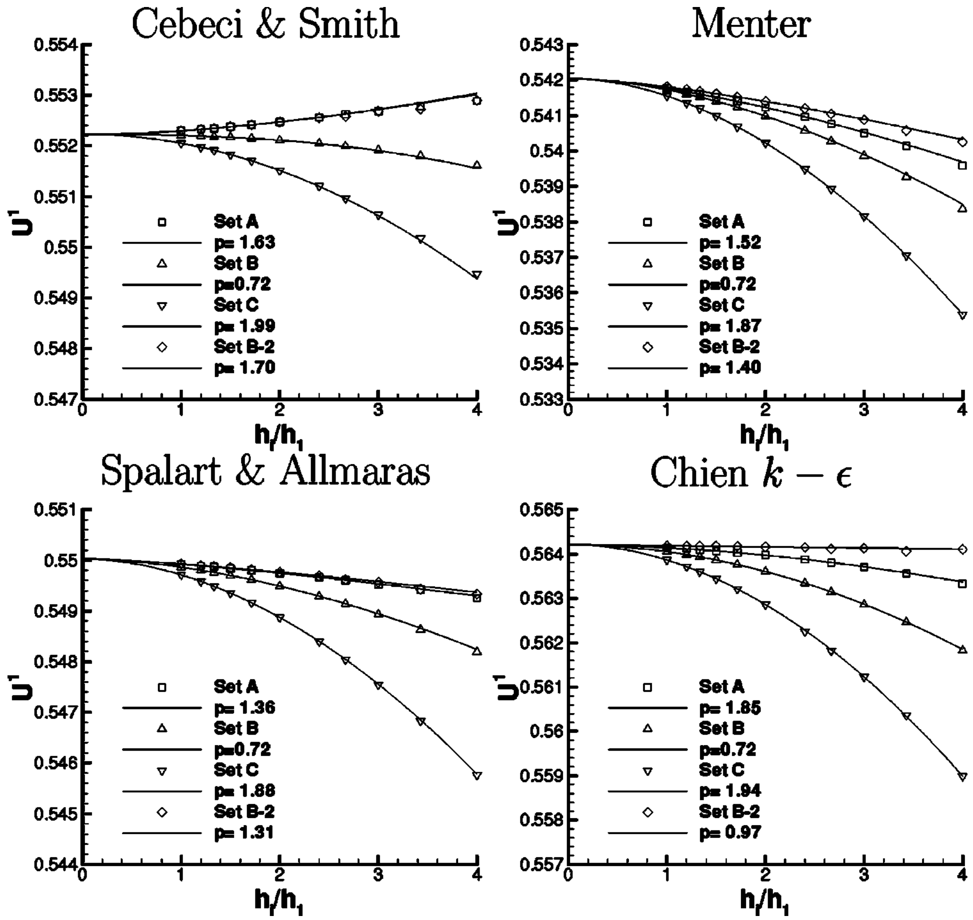

Fig. 5 Convergence of U^1 at $x=0.8774$ L, $y=2.034\times10^{-4}$ L with the grid refinement. Algebraic Cebeci and Smith model, one-equation models of Menter and Spalart and Allmaras and Chien's k-ϵ model.

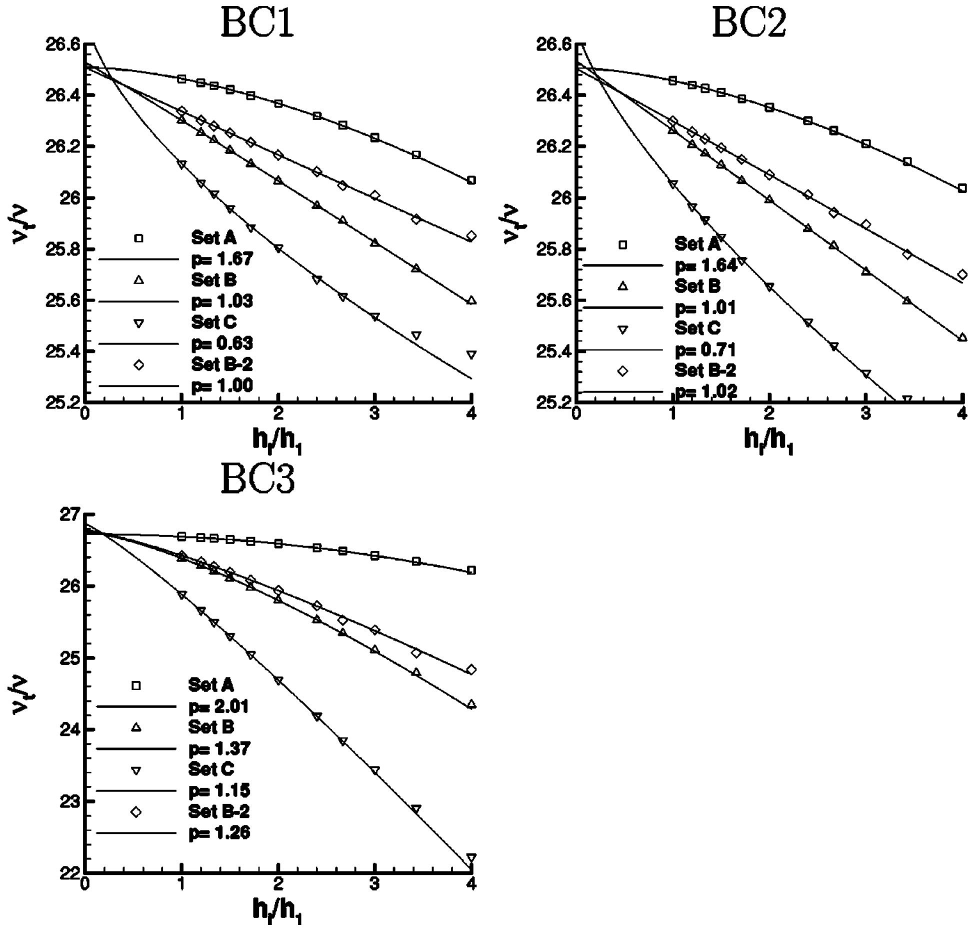

Fig. 6 Convergence of ν_t at $x=0.8774$ L, $y=2.034\times10^{-4}$ L with the grid refinement. SST version of the k-ω model.

representative location $x=0.8727$ L, which coincides with a grid line in the finest grid of the four grid sets. In Fig. 3 we have plotted the quantity

$$\omega^* = \frac{\omega\beta y_n^2}{6\nu},$$

which according to Eq. (1) should smoothly tend to 1 at the wall. ω^* has been explicitly set to 1 at the wall for all the profiles.

The results plotted in Fig. 3 are a clear indication of the difficulties with the k-ω model. There is an inaccurate solution of ω in the near-wall region. Although the solution improves with the grid refinement, the basic anomaly near the wall persists. The two alternatives BC1 and BC2 are again very similar, but the alternative BC1 exhibits smaller values of ω^*. This is reasonable because the ω transport equation is also solved at the first grid node away from the wall for the alternative BC2, whereas in the boundary condition BC1 the transport equation is solved only for the second grid node away from the wall. Also the rough-wall boundary condition shows a clear dependence on the near-wall grid line spacing.

4.4 U^1 in the Log-Law Region. As stated by Wilcox in [1], the effects of a numerically inaccurate ω wall boundary condition can distort the entire boundary-layer solution. Therefore, we have also checked the convergence properties of the U^1 velocity field in the present study. To illustrate the results we have selected a location in the log-law region at $x=0.8774$ L, $y=2.034\times10^{-4}$ L, where $y^+\simeq100$. As for C_D, graphical results are given for the SST version of the k-ω model only.

The convergence of the local value of U^1 with the grid refinement is illustrated in Fig. 4, while Table 6 presents the estimated uncertainty for the finest grid of the four grid sets with the SST, BSL, and TNT versions of the k-ω model.

In general, the results show the same trends as found above for

Table 8 Uncertainty estimates for ν_t/ν at $x=0.8774$ L, $y=2.034\times10^{-4}$ L. SST, BSL and TNT k-ω models in the 241×241 grids.

	SST U(%)			BSL U(%)			TNT U(%)		
Grid Set	BC1	BC2	BC3	BC1	BC2	BC3	BC1	BC2	BC3
A	0.21	0.23	0.16	0.16	0.19	0.12	0.55	0.04	0.57
B	1.08	1.29	1.76	1.14	1.31	1.75	0.72	0.90	1.46
C	2.90	3.03	4.77	2.98	3.06	4.75	2.22	2.41	4.34
B-2	0.82	0.98	1.67	0.74	0.94	1.65	0.39	0.56	1.33

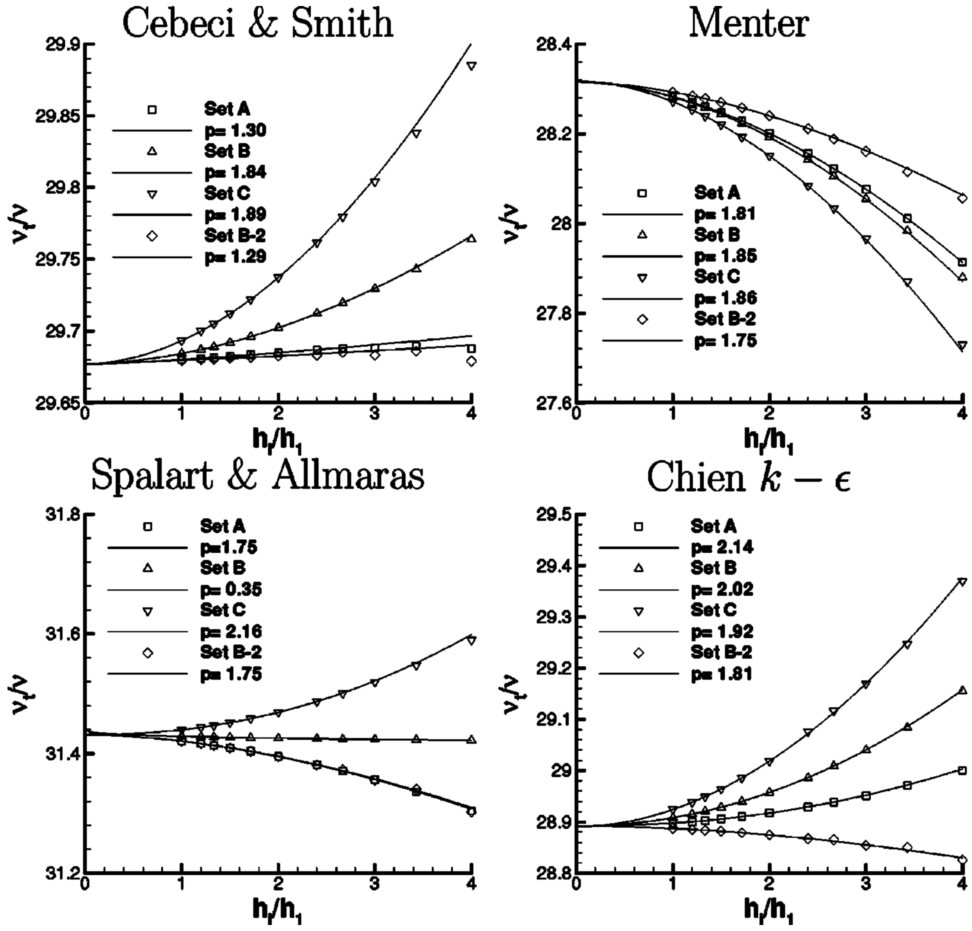

Fig. 7 Convergence of ν_t at $x=0.8774$ L, $y=2.034\times10^{-4}$ L with the grid refinement. Algebraic Cebeci and Smith model, one-equation models of Menter and Spalart and Allmaras and Chien's k-ϵ model.

C_D, with very similar solutions for the two boundary condition implementations based on the near-wall analytical solution of ω, BC1, and BC2.

The observed order of accuracy for U^1 is close to 1 on the four grid sets for the rough-wall boundary condition. On the other hand, p is clearly below 1, but increasing with a decrease of the near wall grid spacing ($p_A > P_B > p_C$) in the results obtained with the BC1 and BC2 implementations.

The estimated exact solution, i.e., U^1 at $h_i/h_1=0$, obtained from the four grid sets is far from being coincident; this holds for all three numerical implementations of the ω wall boundary condition.

The results of the grid refinement studies performed for the other four turbulence models considered in this study are presented in Fig. 5 and in Table 7.

Table 9 Uncertainty estimates for ν_t/ν at $x=0.8774$ L, $y=2.034\times10^{-4}$ L. Cebeci and Smith algebraic model (CS), one-equation models of Menter (MT), and Spalart and Allmaras (SA) and Chien's k-ϵ (KE) model in the 241×241 grids.

Grid Set	U(%)			
	CS	MT	SA	KE
A	0.03	0.15	0.03	0.07
B	0.07	0.21	0.03	0.15
C	0.01	0.15	0.04	0.03
D	0.01	0.10	0.04	0.02

As for the drag coefficient, the level of the estimated uncertainty for these four turbulence models is at least one order of magnitude lower than the values obtained for the three versions of the k-ω model. This result confirms Wilcox's statement that the effects of the numerical difficulties with the ω wall boundary condition are not limited to the near-wall region.

It is also important to emphasize that the observed order of accuracy obtained for U^1 is clearly above 1 in most of the convergence studies performed with the algebraic, one-equation, and k-ϵ models. Furthermore, in the solutions obtained with these four models there is a remarkably good agreement between the estimated exact solution U^1 for $h\rightarrow 0$ obtained from the four grid sets.

Also here, the differences obtained between the predictions of the various turbulence models are larger than the estimated numerical uncertainty.

4.5 ν_t in the Log-Law Region. The differences between all the predictions compared above are a consequence of the selection of the turbulence model that defines the eddy-viscosity ν_t. Therefore, we have also checked the convergence properties of the eddy-viscosity field. The location selected to illustrate the results of ν_t is the same as used in the previous section for U^1.

The convergence properties obtained with the SST version of the k-ω model are illustrated in Fig. 6 and Table 8 presents the estimated uncertainty for the three versions of the k-ω model.

There is a remarkable resemblance between the results obtained for the eddy-viscosity and for the drag coefficient. The trends discussed above for C_D hold for the ν_t data as well. This result confirms the importance of the numerical properties of the turbulence model in the quality of the solution of the continuity and momentum equations in a turbulent flow.

For the sake of completeness, we also present the ν_t convergence properties obtained for the other four turbulence models tested. Figure 7 presents the convergence of ν_t at the selected location with the grid refinement and Table 9 presents the uncertainty estimates in the finest grids of each grid set.

There is once more a strong correlation between the convergence properties of ν_t and C_D. The level of uncertainty in the predictions performed with the algebraic, one-equation, and k-ϵ models is again one order of magnitude smaller than in the results of the k-ω models.

5 Conclusions

This paper presents a numerical study on the accuracy of turbulent flow calculations with the eddy-viscosity k-ω model in three of its most popular versions: the TNT, BSL, and SST versions, which are free of problems with the definition of the free-stream boundary conditions.

We have tested three different implementations of the ω wall boundary condition, where $\omega \rightarrow \infty$, based on the analytical near-wall solution of ω and on the so-called rough-wall boundary condition.

Grid convergence studies have been performed for a simple 2D incompressible turbulent flow over a flat plate using different near-wall grid line spacings. The numerical uncertainty of meaningful viscous flow quantities, like the friction resistance coefficient, was estimated with a practical procedure based on a least-squares root implementation of the grid convergence index method.

In order to assess the performance of the k-ω models, the same grid refinement studies have been performed for four well-known eddy-viscosity models: The algebraic Cebeci and Smith model, the one-equation models proposed by Menter and Spalart and Allmaras, and the low-Reynolds k-ϵ model proposed by Chien.

From the results obtained in this study we draw the following conclusions:

- The k-ω model is more sensitive to the near-wall grid line spacing than all the other eddy-viscosity turbulence models tested. For the same level of grid refinement, the k-ω leads to levels of numerical uncertainty which are typically one order of magnitude larger than the other four eddy-viscosity turbulence models tested. In other words, for the same accuracy, the k-ω models require a much finer grid near the wall than other models.
- The three implementations of the ω boundary condition at a solid wall suffer from the same problem: the inaccurate solution of the ω transport equation in the near-wall region. This problem does not vanish with the grid refinement and so none of these three implementations of the ω wall boundary condition is completely satisfactory.
- It was reconfirmed that the ω rough-wall boundary condition does not reproduce the smooth wall solution for roughness values well below the hydrodynamically smooth limit. Furthermore, the rough-wall ω boundary condition is more sensitive to the near-wall grid line spacing than the alternatives based on the near-wall analytical solution.
- Imposing ω at the first grid node away from the wall (which formally removes the grid dependency of the boundary condition) is a viable alternative to the specification of a finite ω value at the wall. But effectively, it does not improve the behavior of the solution.
- The use of an equally spaced grid in the viscous sublayer may improve the numerical accuracy of viscous flow calculations with eddy-viscosity turbulence models for a given grid density. However, the amount of improvement appeared to be dependent on the turbulence model selected.
- In the flat-plate-flow test case the numerical errors were consistently smaller than the modeling errors (i.e., the differences between the results of various turbulence models).

References

[1] Wilcox, D. C., 1998, *Turbulence Modeling for CFD*, 2nd ed., DWC Industries, La Canada, California.
[2] Menter, F. R., 1994, ''Two-Equation Eddy-Viscosity Turbulence Models for Engineering Applications,'' AIAA J., **32**, pp. 1598–1605.
[3] Kok, J. C., 1999, ''Resolving the Dependence on Free-stream values for the k-ω Turbulence Model,'' NLR-TP-99295, http://www.nlr.nl/public/library/1999/99295-tp.pdf
[4] Thivet, F., Daouk, M., and Knight, D., 2002, ''Influence of the Wall Condition on k-ω Turbulence Model Predictions,'' AIAA J., **40**, pp. 179–181.
[5] Hellsten, A., 1998, ''On the Solid-Wall Boundary Condition of ω in the k-ω Type Turbulence Models,'' *Report B-50*, Helsinki University of Technology, Laboratory of Aerodynamics, ISBN 951-22-4005-X; http://www.aero.hut.fi/Englanniksi/index.html
[6] Cebeci, T., and Smith, A. M. O., 1984, *Analysis of Turbulent Boundary Layers*, Academic Press, New York.
[7] Menter, F. R., 1997, ''Eddy Viscosity Transport Equations and Their Relation to the k-ϵ Model,'' J. Fluids Eng.,**119**, pp. 876–884.
[8] Spalart, P. R., and Allmaras, S. R., 1992, ''A One-Equations Turbulence Model for Aerodynamic Flows,'' *AIAA 30th Aerospace Sciences Meeting*, Reno, La Recherche Aerospatiale, 121, pp. 5–21.
[9] Chien, K. Y, 1982, ''Prediction of Channel and Boundary-Layer Flows with a Low-Reynolds-Number Turbulence Model,'' AIAA J., **20**(1), pp. 33–38.
[10] Eça, L., and Hoekstra, M., 2002, ''An Evaluation of Verification Procedures for CFD Applications,'' *24th Symposium on Naval Hydrodynamics*, Fukuoka, Japan, Office of Naval Research, National Research Council, Washington.
[11] Roache, P. J., 1998, *Verification and Validation in Computational Science and Engineering*, Hermosa Publishers, Albuquerque, New Mexico.
[12] Eça, L., and Hoekstra M., 2003, ''An Example of Uncertainty Estimation in the Calculation of a 2-D Turbulent Flow,'' *4th Marnet-CFD Workshop*, Haslar, Qinetia, UK.
[13] Coles, D. E., and Hirst, E. A., eds., 1968, ''Computation of Turbulent Boundary-Layers,'' *Proceedings of AFOSR-IFP-Stanford Conference*, Vol. 2, Stanford University, California.
[14] José, M. Q. B., Jacob, and Eça, L., 2000, ''2-D Incompressible Steady Flow Calculations with a Fully Coupled Method,'' *VI Congresso Nacional de Mecânica Aplicada e Computacional*, Aveiro, José M. Q. B. Jacob, Universidade de Aviero, Portugal.
[15] Hoekstra, M., and Eça, L., 1998, ''PARNASSOS: An Efficient Method for Ship Stern Flow Calculation,'' *Third Osaka Colloquium on Advanced CFD Applications to Ship Flow and Hull Form Design*, Osaka, Japan.
[16] Eça, L., 2002, ''Comparison of Eddy-Viscosity Turbulence Models in a 2-D Turbulent Flow on a Flat Plate,'' IST Report D72-16, Instituto Superior Técnico, Lisbon, Universidade Tecnica de Lisboa, Portugal.
[17] Vinokur, M., 2002, ''On One-Dimensional Stretching Functions for Finite-Difference Calculations,'' J. Comput. Phys., **50**, pp. 215–234.
[18] Di Mascio, A., Paciorri, R., and Favini, B., 2002, ''Truncation Error Analysis in Turbulent Boundary Layers,'' J. Fluids Eng., **124**, pp. 657–663.

Alexander Yakhot
The Pearlstone Center for Aeronautical Engineering Studies, Department of Mechanical Engineering, Ben-Gurion University of the Negev, Beersheva 84105, Israel

Leopold Grinberg
Department of Mechanical Engineering, Ben-Gurion University of the Negev, Beersheva 84105, Israel

Nikolay Nikitin
Institute of Mechanics, Moscow State University, 1 Michurinski prospekt, 119899 Moscow, Russia

Simulating Pulsatile Flows Through a Pipe Orifice by an Immersed-Boundary Method

A pulsatile laminar flow of a viscous, incompressible fluid through a pipe with a sudden constriction (an orifice) was simulated by an immersed-boundary method. A fluid is forced to move by an imposed sinusoidally varying pressure difference, $\Delta p(t)$. For a pulsatile flow through a pipe orifice, an oscillating recirculation bubble develops behind the orifice. The induced flow rate, $Q(t)$, the recirculation bubble length, $L_b(t)$, as well as their phase shift (ϕ_Q, ϕ_L) with respect to the imposed pressure difference were computed for different constriction ratios and the Womersley (Ws) number. [DOI: 10.1115/1.1845554]

1 Introduction

A numerical study of the fundamental hydrodynamic effects in complex geometries is a challenging task when discretizing Navier–Stokes equations in the vicinity of complex geometry boundaries. The use of boundary-fitted, structured or nonstructured grids can help to deal with this problem, although the numerical algorithms implementing such grids are usually inefficient in comparison to those using simple rectangular meshes. This disadvantage is particularly pronounced when simulating nonsteady incompressible flows if the Poisson equation for the pressure has to be solved at each time step. Iterative methods used for complex meshes have low convergence rates, especially for fine grids. On the other hand, very efficient and stable algorithms for solving Navier–Stokes equations in rectangular domains have been developed. These algorithms use fast direct methods for solving the Poisson's equation for the pressure [1]. These difficulties led to the development of various approaches that rely on formulating complex geometry flows on simple rectangular domains.

One approach is based on the immersed-boundary (IB) method as introduced by Peskin [2] during the early seventies. At present, immersed-boundary-based methods are considered to be a powerful tool for simulating complex flows. In the present study, we applied an immersed-boundary method for simulating time-dependent flows through a pipe orifice.

Immersed-boundary methods were originally used to reduce simulating complex geometry flows to those defined on simple (rectangular) domains. To understand the basic method, consider a flow of an incompressible fluid around an obstacle Ω (S is its boundary) placed onto a rectangular domain (Π). The flow is governed by the Navier–Stokes and incompressibility equations with the no-slip boundary condition on S. The fundamental idea behind IB methods is to describe a flow problem, defined in $\Pi - \Omega$, by solving the governing equations inside an entire rectangular Π *without* an obstacle, which allows using simple rectangular meshes. To impose the no-slip condition on an obstacle surface S (which becomes an internal surface for the rectangular domain where the problem is formulated), a forcing term **f** (an artificial body force) is added to the Navier–Stokes equations as follows:

$$\frac{\partial \mathbf{u}}{\partial t} = -(\mathbf{u}\nabla)\mathbf{u} - \nabla p + \nu \nabla^2 \mathbf{u} + \mathbf{f}. \tag{1}$$

The purpose of the forcing term in Eq. (1) is to impose the no-slip boundary condition at the point $\mathbf{x}_S$ which defines the immersed boundary S. Formally, the solution to Eq. (1) is identical to that without the source term only if $\mathbf{f} \equiv 0$ everywhere outside the obstacle. This requirement is very difficult to satisfy when implementing IB numerical schemes. Therefore, one can expect that only an approximate equivalency of the two solutions will be obtained. The peculiarity of IB methods is that the no-slip boundary condition is not imposed at the initial stage but instead is gradually attained during the time-advanced computing procedure. In other words, the obstacle's boundary "gets built up" inside the surrounding fluid. For this reason, IB methods are sometimes called "virtual body" methods.

Introducing an artificial force in (1) is crucial for implementing immersed-boundary approaches. In addition, the boundary S does not coincide with the grid points of a rectangular mesh where the velocity values are computed. This means that in order to impose the no-slip boundary condition, numerical algorithms require that the node velocity values be interpolated onto the boundary points. Thus, the performance and effectiveness of any IB method depends on both the source force (**f**) and the computation data exchange (inter- and extrapolation) between the grid and the immersed (virtual) boundary points.

References of different immersed-boundary methods can be found in recently published paper [3]. We note "a direct forcing" approach, which was suggested by Mohd-Yusof [4] for numerical schemes using spectral methods. Fadlun et al. [5] and Kim et al. [6] developed the idea of direct forcing for implementing finite-volume methods on a staggered grid. Our present study is based on a direct forcing approach suggested by Kim et al. [6]. These authors contributed two basic ideas towards introducing direct forcing for the immersed-boundary methods for finite-volume-based numerical schemes on a staggered grid. One was a new numerically stable interpolation procedure for evaluating forcing, and the other introduced a mass source/sink to enhance the solution's accuracy. In Ref. [6], forcing and the mass source/sink are applied at the grid points only on the immersed body and not inside the flow. Both 'direct forcing' methods of [5,6] were applied for time-stepping numerical schemes in which the step of imposing the no-slip condition is followed by the pressure correction step, thus changing the velocity at the boundary points by $O(\Delta t^2)$.

Numerous experimental investigations have been focused on fully developed periodic pipe flows with sinusoidally varying pressure gradients (or flow rates). Numerical investigations of pulsatile flows in a pipe have received considerable attention for decades. Low-speed (laminar) pulsatile flows have been studied in order to analyze flows through small pipes or in the blood circulation systems. However, unsteady pulsatile flows through a pipe with constrictions, which is of practical engineering and biomedical importance, have received only meagre attention. Complex cardiovascular flows such as a stenosis in blood vessels, flows through artificial valves have similar features for relatively simple

---

Contributed by the Fluids Engineering Division for publication in the JOURNAL OF FLUIDS ENGINEERING. Manuscript received by the Fluids Engineering Division July 24, 2003; revised manuscript received March 26, 2004. Review conducted by: Jeffrey Marshall.

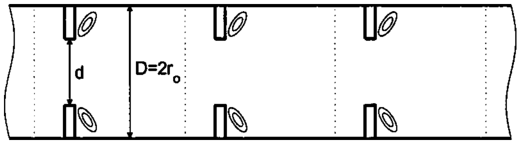

Fig. 1 Schematic design of a pipe with an orifice

geometry flows through a pipe orifice. Such flows are accompanied by separation, recirculation and stagnation, and secondary vortex motion. Laminar flows are comparatively simple for numerical (or analytical) analysis and are a natural choice to provide basic studies of fundamental hydrodynamic effects in pulsatile flows.

2 Flow Through a Pipe Orifice

We consider an incompressible fluid forced by a pulsating pressure difference to move through a pipe with periodically distributed orifices. A schematic drawing of the pipe is presented in Fig. 1, where the computational domain is marked by dashed lines. The governing Navier–Stokes equations with the added forcing term **f** are

$$\frac{\partial \mathbf{u}}{\partial t}=\frac{\Delta p}{\rho L}e_z-\nabla\Pi-(\mathbf{u}\cdot\nabla)\mathbf{u}+\nu\nabla^2\mathbf{u}+\mathbf{f}, \tag{2}$$

subjected to the incompressibility constraint

$$\nabla\cdot\mathbf{u}=0. \tag{3}$$

We consider an axisymmetric two-dimensional flow, namely the velocity field $\mathbf{u}=[u_r(r,z,t),0,u_z(r,z,t)]$ and $\nabla\Pi=(\partial\Pi/\partial r,0,\partial\Pi/\partial z)$. In Eq. (2), we split the pressure gradient into two terms, when the pressure difference, $\Delta p(t)$, is prescribed by

$$\Delta p(t)=\Delta p_0[1+\gamma_p\sin(\omega t)], \tag{4}$$

where Δp_0 is a prescribed pressure difference across a computational domain. The computational domain length, L, was set large enough to exclude the influence of the periodicity conditions. In all computations, a fully developed Poiseuille velocity profile has been established at the outlet. Computing divergence of Eq. (2), to impose an incompressibility Π is obtained from the Poisson equation: $\nabla^2\Pi=-\mathrm{div}[(\mathbf{V}\cdot\nabla)\mathbf{V}]$. In our computations Π was assumed to be periodic in z-direction, which means that it does not contribute to the pressure difference, $\Delta p(t)$. In Eq. (4), γ_p and ω are the amplitude and the frequency of the pressure difference oscillations, respectively.

2.1 Numerical Scheme. For solving the governing equations (2) we use a three-level time splitting scheme, Adams–Bashforth and Crank–Nicolson discretization of the nonlinear and viscous terms:

a) explicit step

$$\frac{\mathbf{u}^*-\mathbf{u}^l}{\Delta t}=\frac{\Delta p}{\rho L}\mathbf{e}_z-\left[\frac{3}{2}(\mathbf{u}^l\cdot\nabla)\mathbf{u}^l-\frac{1}{2}(\mathbf{u}^{l-1}\cdot\nabla)\mathbf{u}^{l-1}\right]-\nabla\Pi^l+\mathbf{f}^{l+1/2}, \tag{5}$$

b) viscous step

$$\frac{\mathbf{u}^{**}-\mathbf{u}^*}{\Delta t}=\nu\frac{1}{2}(\nabla^2\mathbf{u}^l+\nabla^2\mathbf{u}^{**}), \tag{6}$$

c) pressure correction step

$$\frac{\mathbf{u}^{l+1}-\mathbf{u}^{**}}{\Delta t}=-\nabla\phi,\qquad \nabla\cdot\mathbf{u}^{l+1}=0. \tag{7}$$

It is readily seen from Eqs. (5)–(7), that upon executing a time step, the advanced-in-time pressure gradient is

$$\nabla p^{l+1}=-\frac{\Delta p}{\rho L}\mathbf{e}_z+\nabla\Pi^{l+1}, \tag{8}$$

where

$$\nabla\Pi^{l+1}=\nabla\Pi^l+\nabla\left(\phi-\Delta t\frac{\nu}{2}\nabla^2\phi\right). \tag{9}$$

Following the immersed-boundary approach developed by Kim et al. [6], a provisional velocity field, $\tilde{\mathbf{u}}$, is first computed from

$$\frac{\tilde{\mathbf{u}}-\mathbf{u}^l}{\Delta t}=\frac{\Delta p}{\rho L}\mathbf{e}_z-\left[\frac{3}{2}(\mathbf{u}^l\cdot\nabla)\mathbf{u}^l-\frac{1}{2}(\mathbf{u}^{l-1}\cdot\nabla)\mathbf{u}^{l-1}\right]+\nu\nabla^2\mathbf{u}^l-\nabla\Pi^l. \tag{10}$$

Let us denote by $\mathbf{x_f}$ the grid points nearest to the boundary surface and located inside the immersed body. At these points, the values $\tilde{\mathbf{u}}=\mathbf{u_f}$ are re-evaluated by choosing $\mathbf{u_f}$ to satisfy the no-slip boundary condition $\tilde{\mathbf{u}}=0$ for the provisional velocity at the boundary *surface points* $\mathbf{x}=\mathbf{x}_S$. For that purpose, $\mathbf{u_f}$ is computed by interpolating the velocity values of $\tilde{\mathbf{u}}$, obtained at the staggered grid points of a computational cell containing the immersed-boundary, onto the boundary point $\mathbf{x}=\mathbf{x}_S$. Then, the forcing term in Eq. (5) is computed from

$$\mathbf{f}^{l+1/2}=\frac{\mathbf{u_f}-\mathbf{u}^l}{\Delta t}-\frac{\Delta p}{\rho L}\mathbf{e}_z+\left[\frac{3}{2}(\mathbf{u}^l\cdot\nabla)\mathbf{u}^l-\frac{1}{2}(\mathbf{u}^{l-1}\cdot\nabla)\mathbf{u}^{l-1}\right]-\nu\nabla^2\mathbf{u}^l+\nabla\Pi^l \tag{11}$$

at $\mathbf{x}=\mathbf{x_f}$, otherwise (at $\mathbf{x}\neq\mathbf{x_f}$), $\mathbf{f}^{l+1/2}=0$.

The incompressibility constraint Eq. (7) leads to the Poisson equation[1] for ϕ. We recall that according to the immersed-boundary technique, the Helmholtz equation (6) for a provisional velocity field, $\mathbf{u}^{**}$, and the Poisson equation for ϕ are defined in the entire computational domain without the obstacle (an orifice). We assume the periodicity in z-direction for both $\mathbf{u}^{**}$ and ϕ. At the pipe's wall we impose no-slip conditions for $\mathbf{u}^{**}$ and the Neumann conditions for ϕ, $\phi_r(r=R,z)=0$. All variables are assumed to be axisymmetric. The standard Poiseuille parabolic velocity profile, $u_z^0=1-r^2$, is used as the initial conditions.

2.2 Accuracy of the No-Slip Boundary Condition. When implementing the no-slip boundary condition, the immersed-boundary method introduces an error. To estimate this error, the L_2-norm of the velocity components with respect to the values prescribed at the boundary points have to be monitored in time. For an axisymmetric flow with motionless boundaries, as considered in this paper, $\mathbf{u}=(u_r,u_z)$. The L_2-norm error in the no-slip condition for each velocity component is defined in the root-mean square form

$$L_2(w)=\sqrt{\frac{1}{N_b}\sum_{i=1}^{N_b}w_i^2}, \tag{12}$$

where $w=u_r$ or u_z and N_b is the number of selected points specifying the boundary. Results of computations can be considered reliable only if the no-slip boundary condition is satisfied with reasonable accuracy.

To control the accuracy, the fluid velocity was monitored on the immersed boundary surface. Figure 2 shows the $L_2(u_r)$ and $L_2(u_z)$ norms computed at the orifice's surface for a steady flow. One can see that the no-slip boundary condition is imposed with machine accuracy. In the Introduction we noted that, applying the immersed-boundary method, the no-slip condition is gradually attained during the time-stepping computing procedure. Steady flows are relatively simple to simulate by the immersed-boundary

---

[1] The forcing points are located on the immersed boundary or inside the body. Therefore, the cell containing the immersed boundary does not satisfy the mass conservation and a source/sink, q, must be introduced for these near-boundary cells. This means that in Eq. (7) the incompressibility constraint should be, speaking generally, written as $\nabla\cdot\mathbf{u}^{l+1}=q$. For details see Ref. [6].

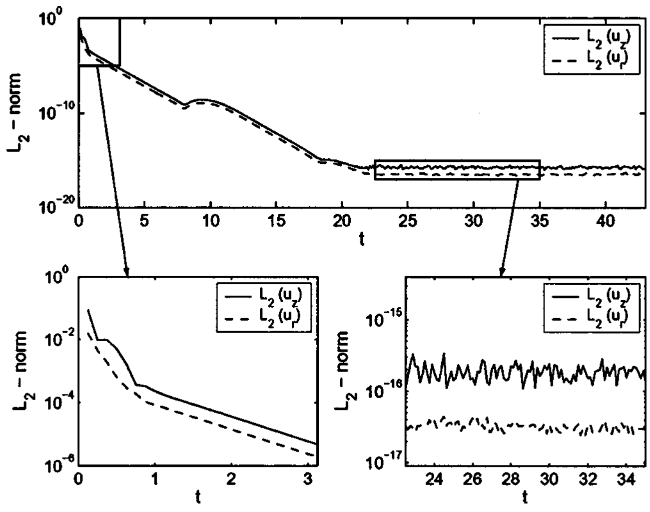

Fig. 2 L_2-norm error in the no-slip boundary condition; steady flow

method. For the pulsatile flow considered in this paper, Fig. 3 shows the typical time-history of the L_2-norm error in the no-slip condition. To clearly show the second-order error in the no-slip condition, the L_2-norm is plotted in Fig. 4 against Δt^2. Accurate implementation of the no-slip boundary condition is important for predicting the development of a recirculating bubble behind an orifice. The size of recirculation regions can be estimated by means of zero-vorticity contours. The computations performed by us confirm the existence of two secondary eddies at the orifice-wall corners in addition to the main recirculation bubble (see Fig. 5). One can see that the rear secondary eddy at the corner is extremely small. Such small eddies always take place for flows through orifices and over forward- or backward-facing steps. For flow through a pipe orifice, even for moderate Reynolds numbers, the size of the upstream eddy is much smaller than that of the main downstream eddy [7]. The prediction of small secondary corner eddies is an important test for spacial resolution used for calculations. In our case, it is also a test for demonstrating the capability of the applied direct forcing immersed-boundary approach.

2.3 Verification of the Numerical Scheme. The numerical scheme has been applied for simulating a steady laminar flow through a pipe orifice [7] (the results obtained in Ref. [7] are also cited by White [8]). As noted earlier, in all calculations, the computational domain length, L, has been set large enough and the fully developed Poiseuille velocity profile has been established at the outlet. Therefore, despite the imposed periodicity in the z-direction, our calculations are equivalent to those that specify the Poiseuille velocity profile at pipe's inlet–outlet. In Ref. [7], numerical solutions of the Navier–Stokes equations have been obtained using the vorticity-stream function formulation, and the finite-difference equations were solved by iterations. Mills [7] employed a special treatment of the sharp orifice corners using Thom's approximation for the wall vorticity.

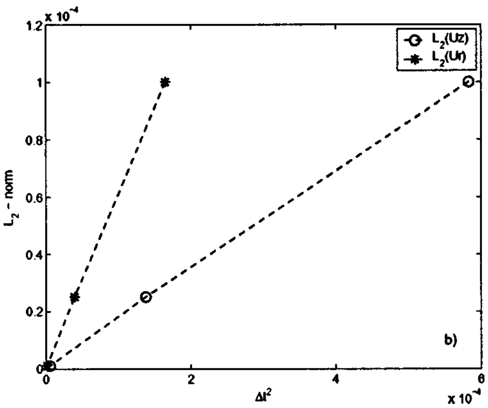

Fig. 4 L_2-norm error in the no-slip boundary condition vs Δt^2; pulsatile flow

In this study, we calculated the discharge coefficient C_d through a pipe orifice as is defined in Ref. [7]:

$$C_d=\frac{1}{2}\sqrt{\frac{\rho U_m^2}{2(p_1-p_2)}\left[\left(\frac{D}{d}\right)^4-1\right]},\tag{13}$$

where, D is the pipe's diameter, d is the orifice's inner diameter, U_m is the mean velocity, p_1-p_2 is the pressure drop across the orifice computed using the integration path of Ref. [7]. The discharge coefficient for different Reynolds numbers ($\mathrm{Re}_0=2\,\mathrm{Re}_m$) is shown in Fig. 6. One can see that our results are in very good agreement with the experimental data presented in Ref. [7].

In Fig. 7 we show streamlines and vorticity contours for a creeping flow, $\mathrm{Re}_m=0.01$. As in Ref. [7], the flow pattern is per-

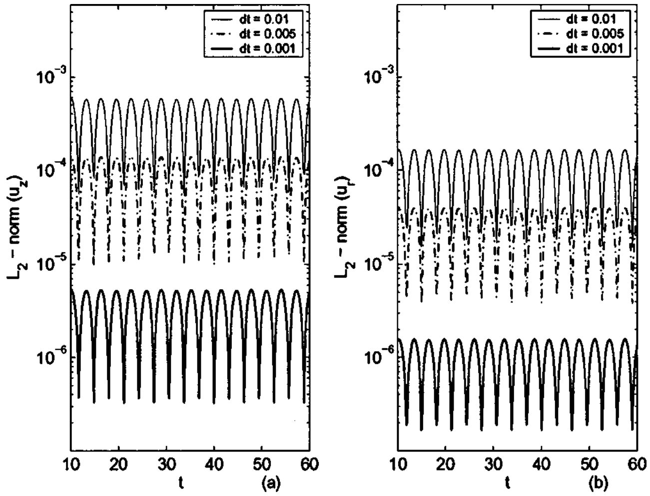

Fig. 3 Time history of the L_2-norm error in the no-slip boundary condition; pulsatile flow

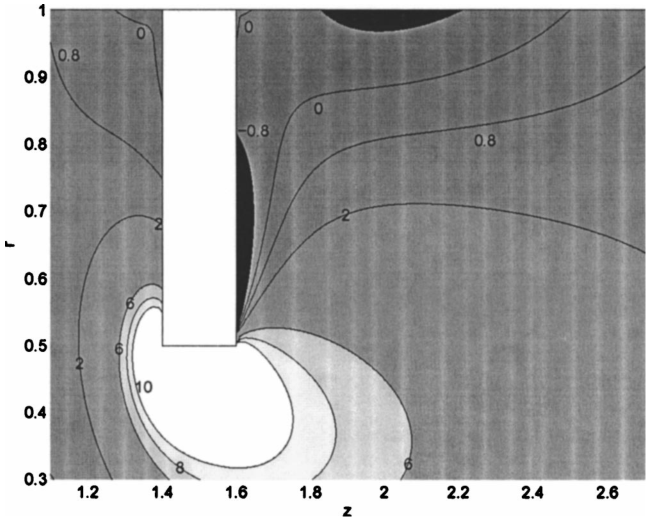

Fig. 5 Vorticity contours

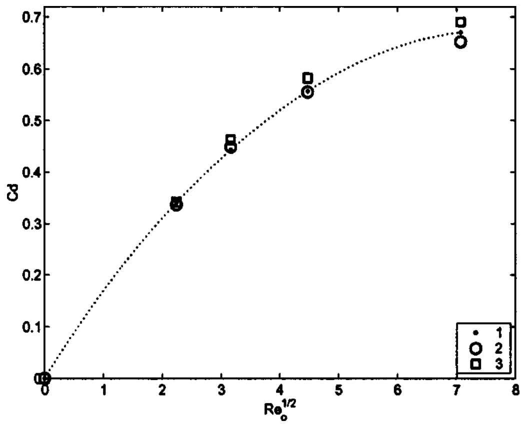

Fig. 6 Discharge coefficient, C_d. 1—experiment, 2—present, 3— Ref. [7].

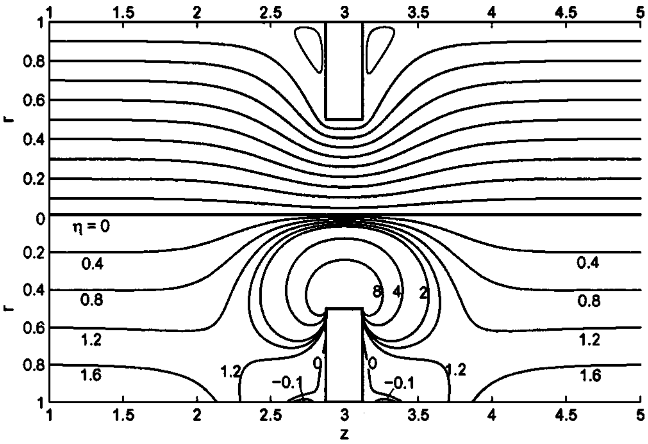

Fig. 7 Creeping flow. Streamlines and vorticity contours, $Re_m = 0.01$.

fectly symmetric with two small eddies present in the orifice-wall corners. The size of the eddies is about half of that of the orifice size.

Sisavath et al. [11] recently numerically studied a creeping flow through a ring-type constriction in a pipe. Davis [12] derived a semianalytical (though quite cumbersome) solution for the total velocity in the form of a disturbance flow to the steady Poiseuille flow. Sisivath et al. presented the results of Wang [13] for a flow through a thin annular disc. In Figs. 8(*a*) and 8(*b*) we compare our results with those obtained by Sisavath et al. [11] and in Refs. [12,13]. The results of Refs. [12,13] are reproduced by us as presented in Ref. [11]. In Ref. [12], the additional pressure drop due to the constriction, Δp_c, and the maximum (centerline) velocity excess, ΔU_c, have been computed for orifice ratios $d/D = 0.2 \div 0.9$. Sisivath et al. [11] suggested a simple approximation for the excess pressure drop, Δp_c. Very good agreement of the results obtained by Davis [12] with those in Ref. [11] was found for d/D between 0.4 and 0.6. For severe constrictions $(d/D < 0.25)$, the discrepancy is large. Sisavath et al. [11] explained this by possible substantial numerical errors in implementing the semianalytical solution in Ref. [12].

In Figs. 8(*a*) and 8(*b*) we present the results obtained for a pressure drop, Δp_c, and the centerline velocity, ΔU_c, excesses due to the pipe constriction that were computed for two orifice widths, $h = 1/32$ and $h = 1/64$. One can see that the results are practically identical which indicates that in our calculations the orifice width was set small enough for comparing our results with those of Davis [12] and Wang [13] obtained for an annular zero thickness orifice and reproduced in Ref. [11]. In Fig. 8(*a*) we show results for the pressure drop excess, Δp_c. The solid line in Fig. 8(*a*) corresponds to the approximation suggested in Ref. [11]:

$$\frac{r_1^3 \Delta p_c}{8\mu Q_0} = 3[1 - (d/D)^2], \tag{14}$$

where $r_1 = d/2$. In Fig. 8(*b*) the centerline velocity excess, ΔU_c, is compared with that of [12] (cf. Table 1 in [12]). The agreement, as can be seen, is excellent.

3 Results and Discussion

3.1 Flow Characteristics. We have used the mean velocity, U_m, and the pipe radius, r_0, as the characteristic velocity and length, respectively. The balance between the local and convective acceleration, inertia and viscous forces in the governing equations (2) is characterized by the nondimensional parameters:

- $\omega^* = \dfrac{\omega r_0}{U_m} \propto \dfrac{\partial \mathbf{u}/\partial t}{(\mathbf{u}\cdot\nabla)\mathbf{u}}$ local versus convective acceleration
- $\mathrm{Re}_m = \dfrac{U_m D}{\nu} \propto \dfrac{(\mathbf{u}\cdot\nabla)\mathbf{u}}{\nu\nabla^2\mathbf{u}}$

Reynolds number, nonlinear versus viscous terms

- $Ws^2 = \dfrac{\omega r_0^2}{\nu} = \dfrac{\omega^* \mathrm{Re}_m}{2} \propto \dfrac{\partial \mathbf{u}/\partial t}{\nu\nabla^2\mathbf{u}}$ Womersley number

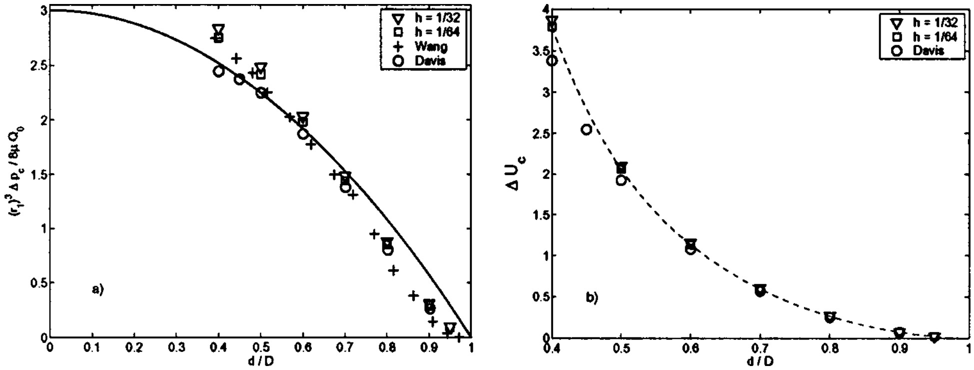

Fig. 8 Creeping flow. Dimensionless (a) pressure drop Δp_c and (b) maximum velocity excess ΔU_c vs d/D.

The Womersley number, $Ws = r_0(\omega/\nu)^{1/2}$, is a measure of oscillating effects in a flow. In this section we present different characteristics (Z) in the form of $Z = Z(Ws;\mathrm{Re}_m)$. Hereafter, the asterisk for ω is omitted and all parameters are nondimensionalized. The following comments might be useful for interpretation of the results. Let us consider two classes of results:

i. Z is independent of Re_m: nonlinear effects are negligible;
ii. Z is independent of Ws at given Re_m: flow is quasi-stationary.

From the first class, one can distinguish flows with $\omega \gg 1$, when the induced local acceleration is much larger than the convective one. We call such flows "fully oscillating" flows. An incompressible viscous fluid that is forced to move under a pulsating pressure difference has several features. One is that an oscillating fluid has a phase shift, ϕ, with respect to the imposed pressure difference. There are fundamental differences between a pulsating flow induced by low- or high-frequency pressure gradient oscillations. The first limiting case of low-frequency oscillations, where the Womersley number, Ws, is small, means that the velocity varies very slowly with time, and the derivative term $\partial u/\partial t$ in the governing equation of motion can, therefore, be neglected. Thus, the viscous term in the governing equation is balanced by the imposed pressure gradient term. Consequently, the velocity varies periodically in the same phase as the pressure gradient. A flow induced by slow pressure oscillations can be considered as a quasi-stationary flow. In contrast, for high-frequency oscillations, where Ws is large, the viscous term can be neglected everywhere except in the very narrow layers near the walls. The width of these layers is of the order of magnitude of the depth of penetration of the viscous wave, $\delta \propto (\nu/\omega)^{1/2}$. This case is typical for boundary layers when at a certain distance from the wall the fluid moves as if it was frictionless. This implies that the unsteady term $\partial \mathbf{u}/\partial t$ in the governing equations is balanced (except in the narrow δ-layer) by the imposed oscillating pressure gradient term, i.e., the terms $\rho \partial u/\partial t$ and $-\partial p/\partial z$ are of the same order of magnitude. Therefore, at a large distance from the wall the fluid is forced to move with a phase shift (lag) of 90° with respect to the exciting pressure gradient.

The pulsating flow in a pipe without an orifice is well-known since Sexl's paper [9] published in 1930. In this case, a flow is fully developed, $\mathbf{V} = (0,0,w)$, the nonlinear term in Eq. (2) vanishes, $\Pi \equiv 0$, and the solution for $w(r,t)$ reads [8]

$$w(r,t) = \frac{\Delta p_0}{4\mu L}(r_0^2 - r^2) + \mathcal{R}eal[\hat{w}(r)e^{-i\omega t}], \tag{15}$$

where

$$\hat{w}(r) = \frac{\Delta p_0 \gamma_p}{\rho L \omega}\left[\frac{J_0(r\sqrt{i\omega/\nu})}{J_0(r_0\sqrt{i\omega/\nu})} - 1\right]. \tag{16}$$

In the past, numerical implementation of the expression (16), which includes a Bessel function with an imaginary argument, was carried out by hand using tables, which required quite cumbersome calculations. Now fortunately, this can be easily calculated using standard computer software. This solution obviously shows that the flow rate $Q(t) = 2\pi\int_0^{r_0} w(r,t) r dr$ has a phase shift with respect to the imposed oscillating pressure and, therefore, can be written as

$$Q(t) = Q_0[1 + \gamma_Q \sin(\omega t + \phi_Q)]. \tag{17}$$

For a flow through a pipe orifice, the velocity field is not fully developed, which means that $\mathbf{V} = [u(r,z,t),0,w(r,z,t)]$, and the convective (nonlinear) term in Eq. (2) is not equal to zero. The latter means that a solution to (2) cannot be written as $\mathbf{V} = \mathbf{V}_0(r,z) + \hat{\mathbf{V}}(r,z)e^{i\omega t}$, and, speaking generally, is not phase-shifted with respect to the imposed pressure. However, for flows with relatively low Reynolds numbers, one can expect that the nonlinear term will weakly contribute to the flow global characteristics. In this study, we present any computed property, $Z(t)$, in the form

$$Z(t) = Z_0(1 + \gamma_Z \delta_Z(t)), \tag{18}$$

where $\delta_Z(t)$ is a periodic function; $\delta_Z^{\max}$ and $\delta_Z^{\min}$ are $+1$ and -1, respectively. To estimate the phase shift between a computed property, $Z(t)$, and the imposed pressure difference oscillations, $\Delta p(t)$, we approximate $Z(t)$ by $\tilde{Z}(t)$

$$Z(t) \approx \tilde{Z}(t) = Z_0(1 + \gamma_Z \sin(\omega t + \phi_Z)). \tag{19}$$

For low-Reynolds number flows and negligibly minor nonlinear effects, a phase $(\Delta p, Z)$-plane instantaneous states plot is very close to the phase $(\Delta p, \tilde{Z})$-plane trajectory. This trajectory being properly nondimensionalized by

$$\begin{aligned} \alpha_p(t) &= \frac{\Delta p(t) - \Delta p_0}{\gamma_p \Delta p_0} \equiv \sin(\omega t), \\ \beta_{\tilde{Z}}(t) &= \frac{\tilde{Z}(t) - Z_0}{\gamma_Z Z_0} \equiv \sin(\omega t + \phi_Z). \end{aligned} \tag{20}$$

is a phase shift ellipse defined in [10]. The $(\alpha_p, \beta_{\tilde{Z}})$-phase plane ellipse, Eq. (20), deserves some comments. It is defined in the $Ox'y'$ coordinate system by

$$\frac{x'^2}{a^2} + \frac{y'^2}{b^2} = 1, \quad a = \sqrt{2}\cos\left(\frac{\phi_Z}{2}\right), \quad b = \sqrt{2}\sin\left(\frac{\phi_Z}{2}\right), \tag{21}$$

where

$$x' = \frac{\sqrt{2}}{2}(\alpha_p + \beta_{\tilde{Z}}), \quad y' = \frac{\sqrt{2}}{2}(-\alpha_p + \beta_{\tilde{Z}}), \tag{22}$$

and $a = -\sqrt{2}\cos(\phi_Z/2)$ for $\phi_Z > \pi$.

The limiting case of very slow oscillations $(Ws \ll 1)$ means that the induced velocity field has no phase shift with respect to the imposed pressure oscillations, i.e., $\phi_Z = 0$ and $a = 1$, $b = 0$. The latter implies that the $(\alpha_p, \beta_{\tilde{Z}})$-phase plane trajectory is a degenerate ellipse flattened into an almost straight line $\beta_{\tilde{Z}}(t) = \alpha_p(t)$, which means completely in-phase trajectories. Increasing Ws leads to increased phase shift ϕ_Z, which widens the flattened ellipse up to a circle $(\phi_Z = \pi/2, a = b = 1)$. Further increasing Ws may be followed by increased phase shifts up to $\phi_Z = \pi$ and $a = 0$, $b = 1$. This is the case when the $(\alpha_p, \beta_{\tilde{Z}})$-phase plane trajectory is degenerated into a straight line $\alpha_p(t) + \beta_{\tilde{Z}}(t) = 1$. As follows from this expression, $\alpha_p(t)$ and $\beta_{\tilde{Z}}(t)$ trajectories are opposite in phase. Finally, we note that for $0 < \phi_Z < \pi$, the phase plane time trajectory of the $(\alpha_p, \beta_{\tilde{Z}})$ instantaneous states is *counter-clockwise*, but for $\phi_Z > \pi$ it is *clockwise*.

In Fig. 9, the phase shift, ϕ_Q, is shown as a function of the Womersley number, Ws, for moderate constriction, $d/D = 0.75$. One can see that the data scattering is insufficient, which means that the phase shift is practically independent of the Reynolds number. In other words, for the considered range of Reynolds numbers, the nonlinear effects are negligible for $d/D = 0.75$ and the phase shift of the induced flow rate differs slightly from that for an oscillating flow in a pipe [9]. In Fig. 10 we present the phase shift data for $d/D = 0.5$. From Fig. 10, we can clearly see the dependency on the Reynolds number and that the phase shifts are decreased in comparison with those obtained for a pipe flow. In Figs. 11 and 12, we present the amplitude, γ_Q, of the induced flow rate for different Reynolds numbers as a function of the Womersley number, Ws. Independence of γ_Q on the Reynolds number shows that the contribution of nonlinear terms is negligible. This is clearly seen for practically the entire range of the considered Womersley numbers at a moderate constriction, $d/D = 0.75$. For a relatively large constriction, $d/D = 0.5$, Fig. 12, this can be observed for $Ws > 4$. On the contrary, from Fig. 12, one can see that for slow oscillations $(Ws < 3)$ γ_Q does depend on the

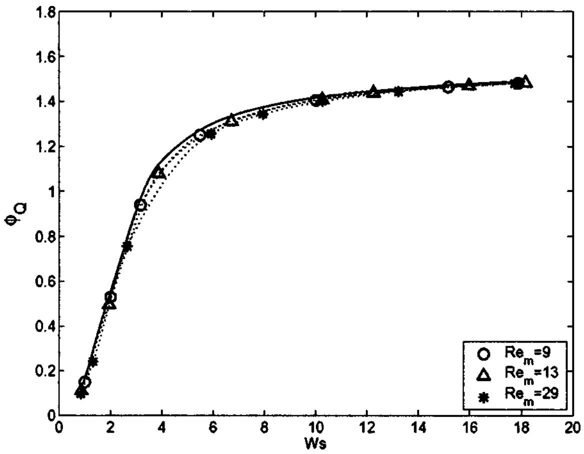

Fig. 9 ϕ_Q vs Ws, $d/D=0.75$, solid line—Sexl [9]

Reynolds number. For comparison, in Figs. 11 and 12, we show by the dashed line the γ_Q/γ_p ratio for a pulsatile flow in a circular pipe, as derived from Sexl's solution (15). It can be shown from Eqs. (15)–(17) that for a pulsating flow in a pipe, $\gamma_Q \rightarrow \gamma_p$ and $\gamma_Q \rightarrow 0$ for slow and fast imposed pressure oscillations, respectively. Indeed, for very slow oscillations (with no local acceleration), the viscous forces due to the induced velocity field are balanced by the imposed pressure oscillations. This means that the amplitude of the induced oscillations is proportional to γ_p, and, consequently, $\gamma_Q \propto \gamma_p$. (The equality $\gamma_Q=\gamma_p$ at $\omega \ll 1$ is a matter of proper nondimensionalization.) For a flow through a pipe orifice, one can expect that $\gamma_Q=\alpha_d \gamma_p$ at $\omega \ll 1$, when α_d depends on the constriction ratio d/D. From Fig. 11, we find $\alpha_d \approx 1.0$ for $d/D=0.75$, which means that the nonlinear effects are negligibly weak. For "a fully oscillating" flow ($Ws \gg 1$), the local acceleration term, $\partial u/\partial t$, is dominant. Moreover, $\partial u/\partial t \propto \omega$ and, as a result, the amplitude of the induced oscillations is proportional to $1/\omega$, and, therefore, $\gamma_Q \rightarrow 0$ for $Ws \gg 1$.

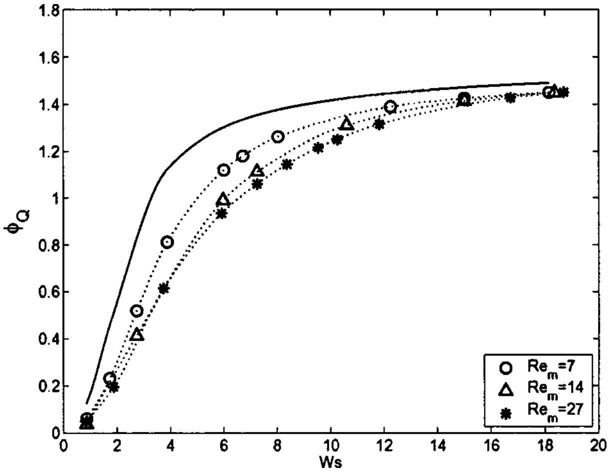

Fig. 10 ϕ_Q vs Ws, $d/D=0.5$, solid line—Sexl [9]

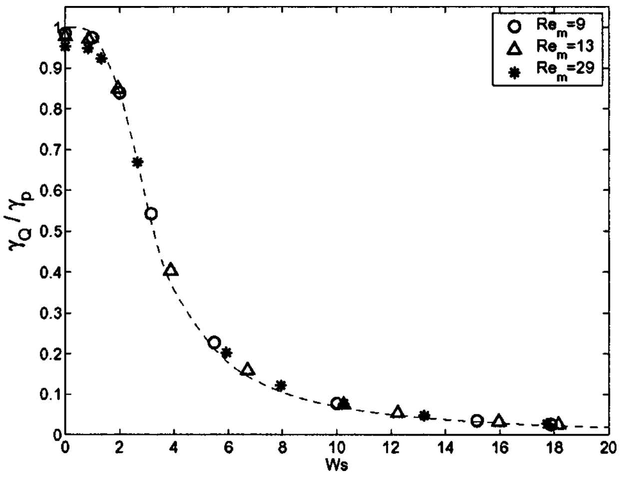

Fig. 11 γ_Q/γ_p vs Ws, $d/D=0.75$

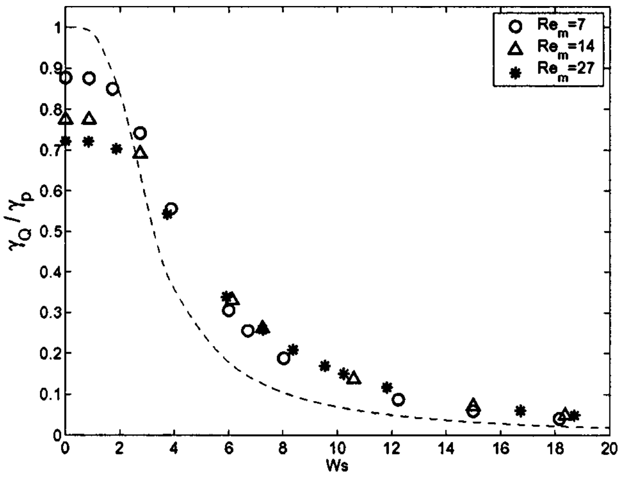

Fig. 12 γ_Q/γ_p vs Ws, $d/D=0.5$

For a flow through a pipe with a ring-type constriction (an orifice), a recirculating flow (a bubble) develops behind an orifice. The recirculation bubble length (L_b) oscillates in time, however, due to the nonlinear effects, one cannot expect that $L_b(t)$ behaves likewise Eq. (17). Our calculations showed that for the range of the parameters considered in this study L_b is of the form $L_b(t) = L_{b0}[1+\gamma_L \delta(t)]$; $\delta(t)$ is a periodic function (very close to $\sin(\omega t+\phi_L)$); and $\delta_{\max}$ and $\delta_{\min}$ are $+1$ and -1, respectively. The time-averaged recirculating bubble length (L_{b0}) is independent of the Womersley number [10]. In Fig. 13 we show the length of this bubble, $L_{b0}=l_0+k_L \mathrm{Re}_m$, which grows linearly with the Reynolds number. Moreover, a small recirculating bubble (l_0) exists for creeping flow ($\mathrm{Re} \approx 0$) also, which agrees with the previous calculations cited in White [8]. The constants k_L and l_0 for different constriction ratios are presented in Table 1.

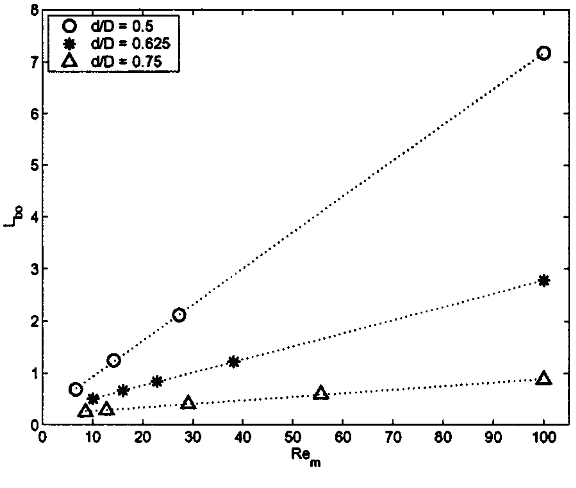

Fig. 13 $\gamma_L L_{b0}$ vs Re_m, $Ws<3$

Table 1 $L_{b0}=l_0+k_L \mathrm{Re}_m$; k_L, l_0 for different constriction ratios, d/D

d/D	k_L	l_0
0.5	0.069	0.233
0.625	0.025	0.249
0.75	0.007	0.194

The absolute amplitude ($\gamma_L L_{b0}$) of the oscillating separation bubble for $Ws<3$ is shown in Fig. 14. The separation bubble growth reveals the linear dependency on Re_m, and, therefore, such regimes could be considered as quasi-stationary. From Fig. 14, we can see that for relatively small constrictions ($d/D>0.75$) and low-Reynolds numbers ($\mathrm{Re}_m<15$), the absolute amplitude ($\gamma_L L_{b0}$) of the oscillating separation bubble is very small, in fact less than 0.02. To estimate the phase shift (ϕ_L) between the $L_b(t)$ and $\Delta p(t)$ trajectories, we use the approximation defined in Eq. (19) for $Z\equiv L_b$. In Figs. 15 and 16, the phase shift, ϕ_L, is shown as a function of the Womersley number, Ws, for constrictions of $d/D=0.75$ and $d/D=0.5$, respectively. One can see that the data is practically independent of the Reynolds number for $\mathrm{Re}<14$. Note that $\phi_L>\pi$ for relatively fast oscillations ($Ws>7$), indicating that the induced oscillations of the recirculation bubble and the imposed pressure oscillations are opposite in phase. Figures 15 and 16 show that the phase shift is practically independent of the Reynolds number for $\mathrm{Re}<9$. We can see that for the limiting case of very fast oscillations ($Ws\gg 1$), $\phi_L\rightarrow 5\pi/4$.

In Figs. 17 and 18 we show $L_b(t)$ versus $\Delta p(t)$ and $L_b(t)$ versus $Q(t)$ instantaneous phase plane states, respectively. In Fig. 17, the arrows mark the time trajectories, which are counterclockwise and clockwise for $Ws=3$ and 11, respectively. According to our calculations, relatively low-oscillation regimes ($Ws<3$) can be considered as quasi-steady. In Fig. 18 both trajectories are counter-clockwise due to the phase shift between the induced flow and separation bubble oscillations was less than π. The states marked by "a" and "b" have the same recirculation bubble length, but belong to the cycle branches of decreasing and increasing bubbles, respectively. In Fig. 18, we can see that for high oscillation flows, the deceleration cycle is characterized by increasing separation bubbles.

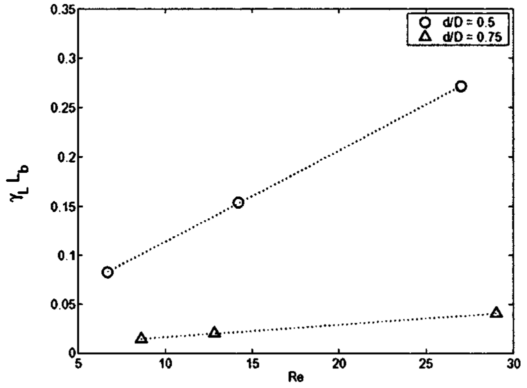

Fig. 14 L_{b0} vs Re_m

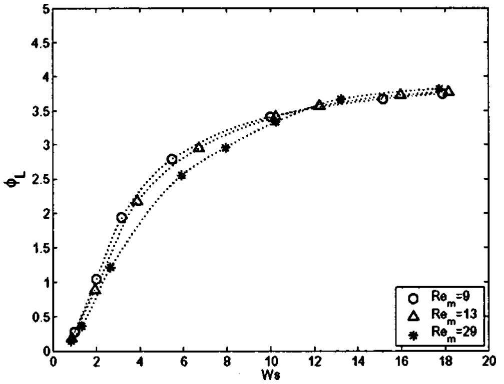

Fig. 15 ϕ_L vs Ws, $d/D=0.75$

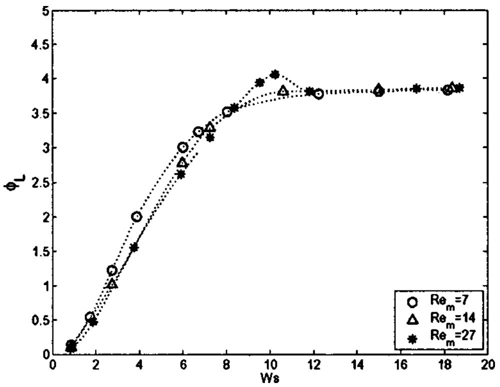

Fig. 16 ϕ_L vs Ws, $d/D=0.5$

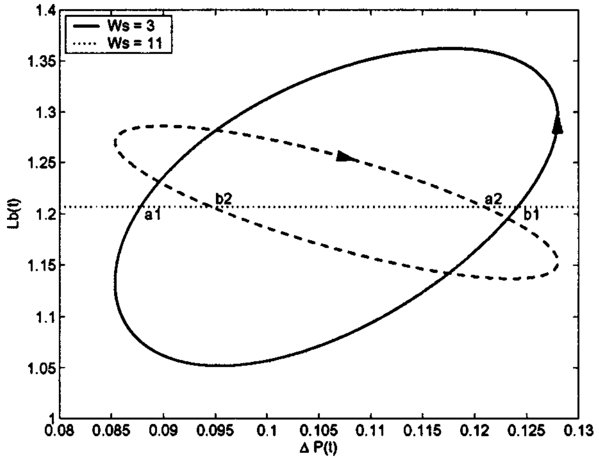

Fig. 17 $L_b(t)$ vs $\Delta p(t)$, $\mathrm{Re}_m=14$, $d/D=0.5$

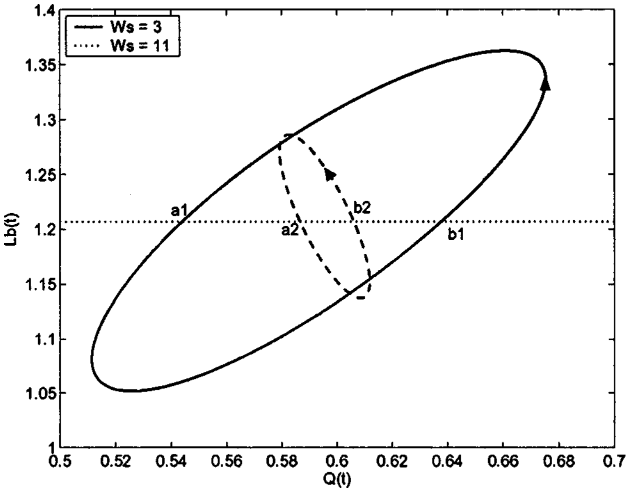

Fig. 18 $L_b(t)$ vs $Q(t)$, $\mathrm{Re}_m=14$, $d/D=0.5$

4 Summary

In this paper, a pulsatile laminar flow of a viscous, incompressible fluid through a pipe with a sudden constriction (an orifice) was simulated by an immersed-boundary method. The flow is driven by an imposed sinusoidally varying pressure difference, $\Delta p(t)$ and governed by the balance between the local acceleration, inertia and viscous forces. Flow characteristics (Z) are presented in the form of $Z=Z(Ws;\mathrm{Re}_m)$, where the Wormersley number, Ws, is a measure of oscillating effects.

For a pulsatile flow through a pipe orifice, an oscillating recirculation bubble develops behind the orifice. The induced flow rate, $Q(t)$, the recirculation bubble length, $L_b(t)$, as well as their phase shift (ϕ_Q, ϕ_L) with respect to the imposed pressure difference have been computed for different constriction ratios, Womersley (Ws) and Reynolds (Re_m) numbers. The presented results allow to distinguish regimes with negligibly minor nonlinear effects and those which can be considered as quasi-steady ones.

Acknowledgments

This research was supported by The Israel Science Foundation Grant 159/02 and in part by CEAR of The Hebrew University of Jerusalem. The work of N.N. was also supported in part by Russian Foundation for Basic Research under Grant No. 02-01-00492.

References

[1] Swarztrauber, P. N., 1974, ''A Direct Method for the Discrete Solutions of Separable Elliptic Equations,'' SIAM (Soc. Ind. Appl. Math.) J. Numer. Anal., **11**, 1136–1150.
[2] Peskin, C. S., 1972, ''Flow Patterns Around Heart Valves: A Numerical Method,'' J. Comput. Phys., **10**, 252–271.
[3] Balaras, E., 2004, ''Modeling Complex Boundaries Using an External Force Field on Fixed Cartesian Grids in Large-Eddy Simulations,'' Comput. Fluids, **33**, 375–404.
[4] Mohd-Yusof, J., ''Combined Immersed Boundaries/B-Splines Method for Simulations of Flows in Complex Geometries,'' *CTR Ann. Res. Briefs*, NASA Ames/Stanford University, 1997.
[5] Fadlun, E. A., Verzicco, R., Orlandi, P., and Mohd-Yusof, J., 2000, ''Combined Immersed-Boundary Finite-Difference Methods for Three-Dimensional Complex Flow Simulations,'' J. Comput. Phys., **161**, 35–66.
[6] Kim, J., Kim, D., and Choi, H., 2001, ''An Immersed-Boundary Finite-Volume Method for Simulations of Flow in Complex Geometries,'' J. Comput. Phys., **171**, 132–150.
[7] Mills, R. D., 1968, ''Numerical Solutions of Viscous Flow Through a Pipe Orifice at Low Reynolds Numbers,'' J. Mech. Eng. Sci., **10**, 133–140.
[8] White, F. M., *Viscous Fluid Flow*, McGraw-Hill, New York, 1991.
[9] Sexl, T., 1930, ''Über den von E. G. Richardson entdeckten annulareffekt,'' Z. Phys., **61**, 349.
[10] Yakhot, A., and Grinberg, L., 2003, ''Phase Shift Ellipses for Pulsating Flows,'' Phys. Fluids, **15**, 2081–2083.
[11] Sisavath, S., Jing, X., Pain, C. C., and Zimmerman, R. W., 2002, ''Creeping Flow Through an Axisymmetric Sudden Contraction or Expansion,'' J. Fluids Eng., **124**, 273–278.
[12] Davis, A. M. J., 1991, ''Creeping Flow Through an Annular Stenosis in a Pipe,'' Q. Appl. Math., **49**, 507–520.
[13] Wang, C. Y., 1996, ''Stokes Flow Through a Tube With Annular Fins,'' Eur. J. Mech. B/Fluids, **15**, 781–789.

Numerical Simulation of Incompressible Laminar Flow over Three-Dimensional Rectangular Cavities

H. Yao
E-mail: h.yao@qub.ac.uk

R. K. Cooper
E-mail: rcooper@qub.ac.uk

S. Raghunathan
E-mail:sraghunathan@qub.ac.uk

School of Aeronautical Engineering,
Queens University Belfast,
Ashby Building, Stranmillis Road,
BT9 5AG, UK

This paper presents results of investigations of unsteady incompressible flow past three-dimensional cavities, where there is a complex interaction between the external flow and the recirculating flow inside the cavity. A computational fluid dynamics approach is used in the study. The simulation is based on the solution of the unsteady Navier-Stokes equations for three-dimensional incompressible flow by using finite difference schemes. The cavity is assumed to be rectangular in geometry, and the flow is assumed to be laminar. Typical results of computation are presented, showing the effects of the Reynolds number, cavity geometry, and inflow condition on the cavity flow fields. The results show that high Reynolds numbers, with deep cavity and shallow cavity flows can become unsteady with Kelvin-Helmholtz instability oscillations and exhibiting a three-dimensional nature, with Taylor-Görtler longitudinal vortices on the floor and longitudinal vortex structures on the shear layer. At moderate Reynolds numbers the shallow cavity flow is more stable than deep cavity flows. For a given Reynolds number the flow structure is affected by the thickness of the inflow boundary layer with a significant interaction between the external flow and the recirculating flow inside the cavity. [DOI: 10.1115/1.1845531]

1 Introduction

Fluid flow past cavities on solid surfaces is a topic of significant interest in a range of engineering applications. Aircraft configurations include cavities as an integral part of design, manufacture, and performance. Examples of such configurations include landing-gear wells, bomb bays, uncovered cavities to house optical instruments, and junctions between surfaces, to name a few. Cavity phenomena can also be observed on a much larger scale, for example, around the channel gates or harbor entrances [1,2]. The presence of a cavity generates unsteady velocity, density, and pressure fluctuation [3], the impact of which may extend downstream of the cavity. Large levels of pressure fluctuation associated with cavity flows result in buffeting (i.e., a response of the structure to pressure fluctuation) leading to structural failure. Development of control techniques to reduce the adverse effect of cavity flows requires a fundamental understanding of aerodynamics of complex flow over such a geometry [4]. Cavity flow is also a topic relevant to aeroacoustics (noise generation) and transition studies.

During the past decades, both experimental and computational studies have been conducted into the cavity-flow physics. These studies were mainly focused on compressible, particularly supersonic flows (see, for example, [5–11]). Although there have been some studies considering incompressible cavity flow, these were mainly focused on flow inside or around two-dimensional (2D) cavities (see, for example, [12–15]), and there has been very few investigations on flow *inside* a three-dimensional (3D) cavity known as a lid-driven cavity (see, for example, [16–19]).

The computational study of 2D incompressible cavity flow began in the 1960s. Early studies assumed steady flows. Examples of these studies include the pioneering work by Burggraf [20], by Weiss and Florsheim [21], and by Pan and Acrivos [22]. More recent studies on steady cavity flow can be found from Nallasamy and Prasad [23]. For unsteady incompressible cavity flow, Mehta and Lavan [12] calculated the flow in a 2D channel with a rectangular cavity. They solved the Navier-Stokes (NS) equations for a laminar flow in terms of the stream function and vorticity for the Reynolds number from 1 to 1500 and cavity length-to-depth ratios of 0.5, 1.0, and 2.0. Wood [15] investigated the use of a multi-grid approach to calculate 2D viscous flow within rectangular cavities. Gustafson and Halasi [24] studied the time-dependent solution of the 2D lid-driven cavity problem for moderate to high Reynolds numbers. Pereira and Sousa [14] investigated the computation of unsteady flow, with a moderate Reynolds number, past a 2D open shallow rectangular cavity. The computation results revealed the destabilization of the flow field and the eddy shedding from the recirculating region due to the coexistence of the unstable shear layer with the recirculating flow field. The roll-up of the separating layer is a result of the Kelvin-Helmholtz (K-H) instability.

Unlike the 2D incompressible cavity flow, research on 3D cavity flow, so far has appeared, to be limited to the study of the flow fields within the cavity driven by a moving lid (i.e., lid-driven cavity flow) [19]. Experimentally, Aidun et al. [25] investigated the global stability of a lid-driven cavity with throughflow by flow visualization studies. Maull and East [26] reported their experimental results considering flow within 3D deep cavities using three different low-speed wind tunnels. Further, East [27] found that under certain conditions regular oscillations at particular frequencies can be observed inside the cavity. Pan and Acrivos [22] provided visualizations of the flow in a lid-driven cavity with a width-to-length ratio of 1. More recently, Koseff and Street [19,28,29] studied a shear-driven, recirculating flow in a lid-driven cavity. They found that the flow was three-dimensional and exhibited regions where Taylor-type instabilities and Taylor-Görtler-like vortices (i.e, Taylor-Görtler longitudinal vortices (TGL)) were present [30].

Based on a computational fluid dynamics (CFD) approach, De Vahl and Mallison [31] first demonstrated the 3-D structure of a lid-driven cavity flow numerically for a rectangular cavity at $R_e = 100$. Freitas et al. [30] simulated flow in a 3-D cavity and studied the nonlinear transport phenomena in a complex recirculating

---

Contributed by the Fluids Engineering Division for publication in the JOURNAL OF FLUIDS ENGINEERING. Manuscript received by the Fluids Engineering Division September 13, 2003; revised manuscript received July 7, 2004. Review conducted by: S. Balachandar.

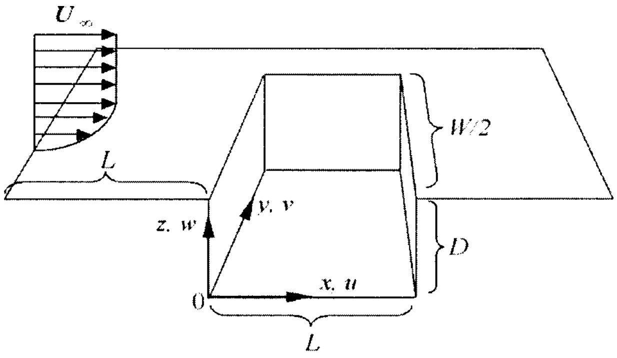

Fig. 1 Geometry of the rectangular half-span cavity used for computation

flow [32] for large Reynolds numbers (e.g., $R_e=3{,}200$). In their computational results the TGL vortices were observed and have a good agreement with the experimental results [32]. Cortes and Miller [17] also studied the lid-driven cavity flow based on a numerical method. Chiang, Hwang, and Sheu studied the end-wall corner vortices in a lid-driven cavity [16] and revealed the major role played by the end vortices in the spanwise transport.

Flows past cavities are susceptible to oscillations. The oscillations observed at high Mach numbers are influenced by compressibility wave or free surface wave effects, and by the coupling of the oscillations of the shear layer over the cavity with the flow inside the cavity. Some flow oscillations appear to be controlled, wholly or in part, by the acoustic modes of the cavity [3]. For incompressible flows, the oscillations (i.e., the K-H instability) are caused by the interaction between the shear layer and the recirculating flow within the cavity. Due to the K-H instability in the shear layer, unsteady vortical structures are generated, which convect across the cavity to produce fluctuations in velocity, density, and pressure, leading to the destabilization of the flow field [33]. A laminar boundary layer flow over a cavity may undergo transition in the shear layer to turbulence downstream of the cavity (e.g., [5,34–36]). Lid-driven cavity flow only models the flow field inside the cavity and does not take into consideration the interaction between the shear layer and the recirculating flow inside the cavity [10].

This paper presents a numerical study into the problem of incompressible laminar flow passing a 3D rectangular cavity with a view to understanding the complex nature of the flow and the 3D structure of shear layer. The study was based on the solution of the unsteady 3D incompressible NS equations by using finite difference schemes. The study included on the flow field the effects of Reynolds numbers, cavity geometry, from open deep cavity to open shallow cavity; and different inflow conditions, particularly laminar Blasius boundary layer inflow with different boundary layer thickness.

This paper is organized as follows. Section 2 introduces the methodology used in the study, including the governing equations and numerical methods. Section 3 addresses the validation results of the code that is used to carry out the simulation. In Sec. 4, the results of computation of incompressible laminar flow past 3D rectangular cavities are presented. Finally, in Sec. 5, a summary of the investigations presented in the paper is provided.

2 Methodology

2.1 The Cavity. Figure 1 shows the geometric configuration of the rectangular cavity used for computation. The cavity has length L, width W, and depth D, and has the characteristic of an open cavity (i.e., $D/L>0.1$ [33]). The Cartesian coordinate system is used to define the problem, as shown in Fig. 1. Following convention, the three axis directions, x, y, and z, are also referred to as longitudinal, lateral, and normal directions, respectively. Because simulating the half-cavity flow is valid and cost-effective [4,9,30], it is assumed that the flow is symmetric with respect to the longitudinal-normal center plane (i.e., the x-z plane at $y=0$), therefore only a half span of the cavity is chosen for the computational domain. This will be considered in the discussion of the results.

2.2 Governing Equations. The governing equations are based on the 3D, unsteady, incompressible NS equations. In Cartesian coordinates, these equations can be written, in a nondimensional form, as

$$\nabla\cdot\vec{u}=0 \tag{1}$$

$$\frac{\partial\vec{u}}{\partial t}+\vec{u}\cdot\nabla\vec{u}=-\nabla p+\frac{1}{R_e}\nabla^2\vec{u} \tag{2}$$

where, based on reference length L, free stream velocity U_∞ and density ρ_∞, $\vec{u}=\vec{u}(\vec{x},t)$ is the nondimensional velocity vector, which is a function of the nondimensional coordinate vector $\vec{x}$ and the nondimensional time t; $p=p(\vec{x},t)$ is the nondimensional pressure; and $R_e=U_\infty L/\nu$ is the Reynolds number, where L is the length of the cavity and ν is the kinematic viscosity.

One of the primary difficulties for solving Eqs. (1) and (2) is to couple changes in the velocity field with changes in the pressure field while satisfying the continuity condition, Eq. (1). To overcome this difficulty, a pressure Poisson equation is established to obtain the pressure field [37]. The Poisson equation is formed by taking the divergence of the momentum equation, Eq. (2), giving

$$\nabla^2 p=\nabla\cdot\left(\frac{1}{R_e}\nabla^2\vec{u}-\vec{u}\cdot\nabla\vec{u}\right)-\nabla\cdot\left(\frac{\partial\vec{u}}{\partial t}\right) \tag{3}$$

At any time step, the pressure field is obtained by solving Eq. (3) based on the velocity field obtained at a previous time step. The obtained pressure field is then used to derive a new velocity field, which is then used to obtain a new pressure field. This iteration process continues until the obtained velocity field satisfies the required continuity condition. In this method, the velocity and pressure are indirectly coupled.

2.3 Numerical Method. The second-order implicit Crank-Nicolson finite difference scheme is implemented in the present computation, with second-order accuracy in both time and space. To ensure the time accuracy, which is of particular importance for computing unsteady flows, a sub-iteration method [8] has been used. At each time step the computation involves the solution of a linear algebraic system with a tridiagonal matrix. This can be efficiently solved using the alternating direction implicit method, which is the method employed in the present computation.

With reference to Fig. 1, a laminar Blasius boundary layer inflow condition is considered. The inflow condition is specified along the free stream flow direction (i.e., the x direction), assuming that the y and z component velocities v and w are zero.

The flow variables at the outflow boundary and outer boundaries are specified by zero normal derivatives at each subiteration step (i.e., $\partial\vec{u}/\partial t+C\partial\vec{u}/\partial n=0$). No-slip boundary condition is used on solid surfaces. At the plane of symmetry (i.e., the x-z plane with $y=0$), the component velocity v is set to be zero and the other flow variables are obtained by extrapolation. The entire flow field above the cavity is initialized with the inflow condition, and the flow field within the cavity is initialized to zero. The initial pressure is set to its free stream value.

A nonuniform grid is used for all three directions. Specifically, 3D Cartesian grids are generated with clustering of nodes near walls and in the shear layer region. These clustered nodes account for greater gradients in velocity and pressure in these regions. Figure 2 shows an example, in which the grid resolution in the longitudinal, lateral and normal directions for the computation domain of the cavity with $D/L=0.25$ and $W/L=3$ is $130\times 74\times 71$.

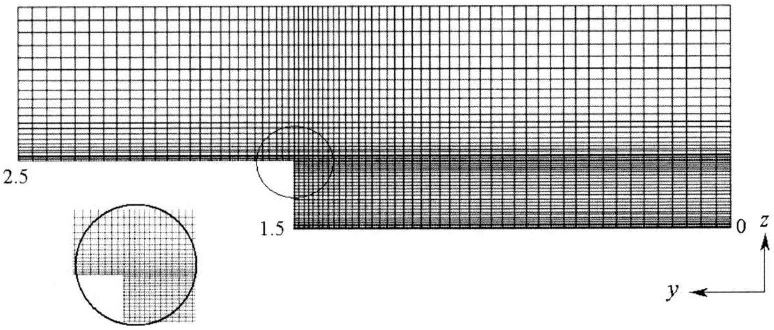

(a) Grids on the $y-z$ plane

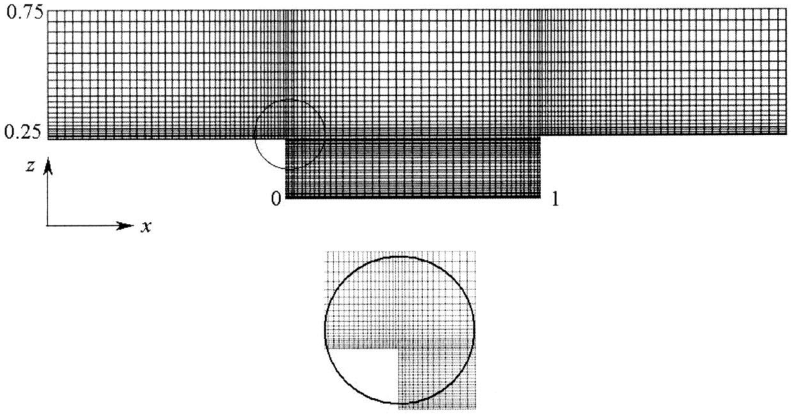

(b) Grids on the $x-z$ (i.e. symmetry) plane at $y=0$

Fig. 2 Grid structures for computation

3 Code Validation

The code has been examined using both analytical and numerical examples, including: (a) a cubical lid-driven cavity of unit length, with a Reynolds number $R_e=1000$, compared to the predictions by other methods [16]; (b) flat plate boundary layer flow, compared to the laminar Blasuis flat solution; and (c) flow past a 2D open rectangular cavity, compared to the predictions by Forristal [38] validated by the commercial software package FLUENT and by experiments. All those validation studies indicate good agreements between the results produced by the present code and the predications published by other researchers [41]. Computational results based on different grid resolutions and time steps are compared, to show that the results presented in this paper are grid independent [42].

The code has been further validated for the problem of viscous flow in a 3D lid-driven rectangular cavity, studied by Chiang et al. [16] and by Freitas et al. [30]. The results of computation based on the present code were proven to be very close to those reported in [16]. As an example, Fig. 3 shows the TGL vortices predicted by the present method on the y-z planes at $x=0.6$. These results are very similar to those observed in [16]. Furthermore, the TGL vortex structure captured by the present code also conforms to those predicted by Freitas et al. [30].

4 Results and Discussion

Open cavity flows arise, typically, at $D/L>0.14$ and are characterized by unsteady velocity, density, and pressure fluctuation. Open cavities are commonly classified into "deep" (with $D/L \geqslant 1$) and "shallow" (with $D/L<1$). Open cavity flow fields are remarkably complicated, with the internal and external regions that are coupled via self-sustained shear layer oscillations.

This section describes the Results of computation of incompressible laminar flow past a 3D open rectangular cavity, based on the CFD approaches described above are shown in Figures 4–12, the geometry of the cavity was rectangular cavity (Fig. 1). Throughout the computations, a grid size of 130×74×71 has been used for the computation domain and symmetry about $y=0$ is assumed. The following flow fields have been considered:

1. "Deep" cavities, with varying Reynolds numbers, assuming a thin boundary layer inflow;
2. "Deep" cavities, with two different inflow conditions—thin boundary layer inflow and laminar Blasius boundary layer inflow, for a given Reynolds number;

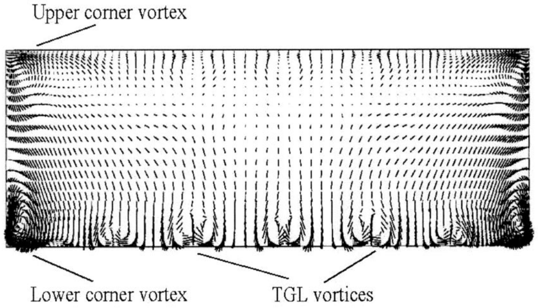

Fig. 3 Velocity vectors on the y-z planes at $x=0.6$, for flow in a 3D lid-driven rectangular cavity, with $D/L=1$, $W/L=3$, and $R_e=1{,}500$, $t=246$. The results are in good agreement with those predicted in [16]

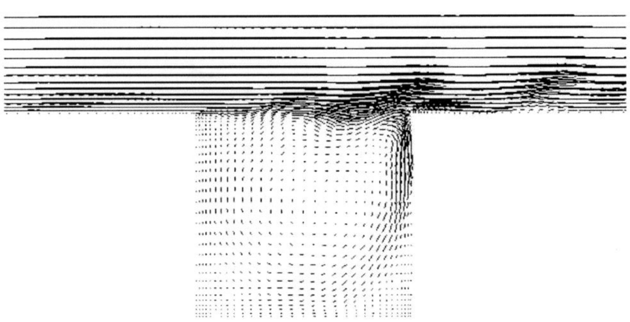

(a) $R_e = 3,000$

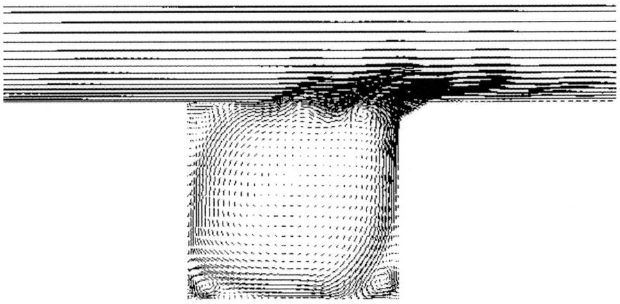

((b) $R_e = 10,000$

Fig. 4 Instantaneous velocity vectors on the *x-z* plane at *y* =0.2, for laminar flow past a 3D open deep rectangular cavity at *t*=274

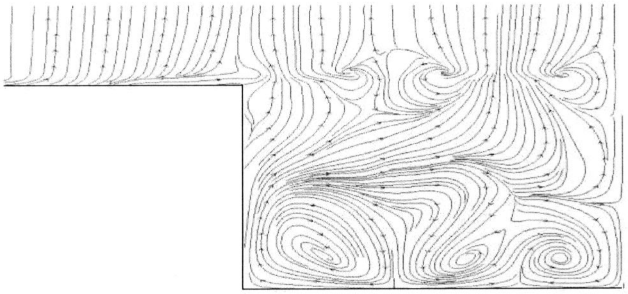

(a) $R_e = 3,000$

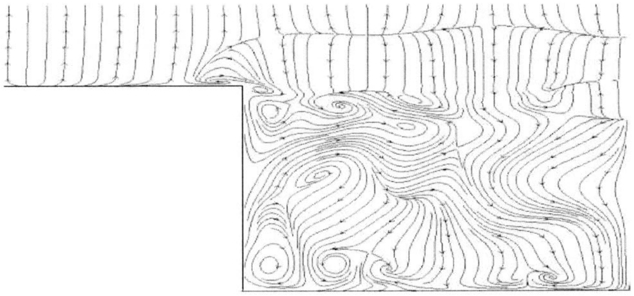

(b) $R_e = 10,000$

Fig. 5 Instantaneous cross flow fields on the *y-z* plane at *x* =0.6, for laminar flow past a 3D open deep rectangular cavity, at *t*=274

3. "Shallow" cavities, with varying D/L ratios and varying Reynolds numbers, assuming a laminar Blasius boundary layer inflow.

This research aims to understand the effects of the cavity geometry, Reynolds number, and the upstream boundary layer thickness on the flow fields for laminar flow past a 3D rectangular cavity.

4.1 Open Deep Cavity Flows.

Two aspects of open deep cavity flows are discussed in the following sections. The results compared to $D/L=1$ and $W/L=3$. This study is focused on two aspects: (1) The effect of the Reynolds number on the flow fields and (2) the effect of the inflow condition on the flow fields, for a given Reynolds number. For the second problem, the effect of the boundary-layer thickness at upstream lip of cavity on the flow structure has been investigated.

4.1.1 Effect of Reynolds Numbers.

In computation of laminar flow past the cavity with varying Reynolds numbers from 3000 to 10,000, a uniform inflow condition (i.e., inflow velocity U_∞ is constant at $x=-1$) was assumed so that a thin laminar boundary layer was developed at the lip of the cavity.

The streamwise instantaneous velocity vectors, corresponding to the Reynolds number $R_e=3000$, and 10,000, respectively [Figs. 4(*a*) and 4(*b*)], indicate the K-H instability in the shear layer, due to the interaction between the external flow and the recirculating flow within the cavity. This instability is promoted by the inflection in the velocity $u(z)$ profile of the shear layer, and is particularly strong in a free shear layer. The lid driven cavity flow may have such inflections, due to the TGL vortices (see below), but the corresponding instability is weaker. As shown from Figs. 4, the larger the Reynolds number, the stronger the K-H instability. In Fig. 4(*a*), with Reynolds number $R_e=3000$, the K-H instability was weak and the primary eddy was small. As the Reynolds number was increased, the K-H instability became stronger, as indicated by the increasingly violent shear layer oscillations, and the primary eddy became larger. It can be noticed that, as the Reynolds number was increased, the occurrence of the K-H instability was located close to the front wall of the cavity. Vortex pairing and merging could be observed in the shear layer. In addition, two secondary vortices can be seen in Fig. 4(*b*) at the lower corners of the cavity. Both vortices were weak at a low Reynolds number $R_e=3000$.

The cross flow is a typical phenomena of 3D flow fields, which could not be accurately simulated by 2D model. Figures 5(*a*) and 5(*b*) present the instantaneous cross-flow field on the y-z plane at $x=0.6$, corresponding to the Reynolds number $R_e=3000$ and 10,000, respectively. The differences in the cross-flow structure between the lid-driven cavity flow and the flow past the cavity can be identified by comparing the figure to Fig. 3, which showed the cross-flow velocity vectors for a 3D lid-driven rectangular cavity of the same geometry. Specifically, comparing Fig. 5(*a*) with Fig. 3, both being on the same y-z plane $(x=0.6)$, one can notice that, for the flow past the cavity, the lower corner vortex was located farther away from the corner than the same corner vortex found in the lid-driven cavity. A further important difference between Figs. 5(*a*) and 3 is that the TGL vortices, which were observed in the flows inside the lid-driven cavity with $R_e=1500$, appear in the flow past the cavity with $R_e=3000$ rather than $R_e=1500$. In other words, a higher Reynolds number may be required for the occurrence of the TGL vortices in the flow past the cavity, in comparison to the flow in the lid-driven cavity. This is due to the lower velocities inside the cavity and more effective dissipation, for flow past the cavity.

In Figs. 5, at nondimensional time $t=274$, it can be seen clearly that the TGL vortices exist on the floor and longitudinal vortices exist near the top of the cavity. The figure has captured some interesting vortex structures occurring within and around the cavity, including the longitudinal corner vortices, TGL vortices and the vortices in the free shear layer of the cavity. These are typical 3D flow structures.

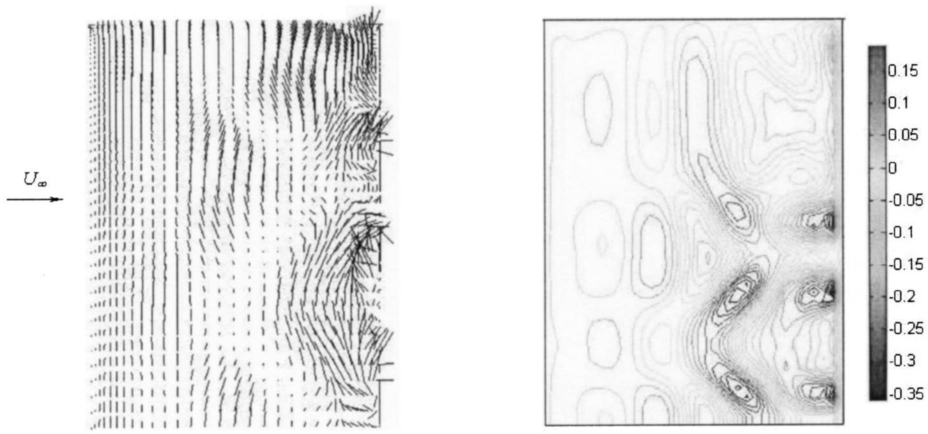

(a) Vorticity vectors (b) Contours of velocity w

Fig. 6 Instantaneous flow fields on the x-y plane at $z=0.99$, for laminar flow past a 3D open deep rectangular cavity, at $t=274$, $R_e=3000$

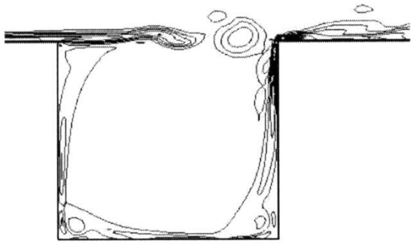

(a) $\delta = 0.06$

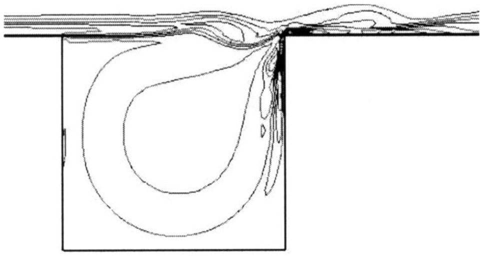

(b) $\delta = 0.11$

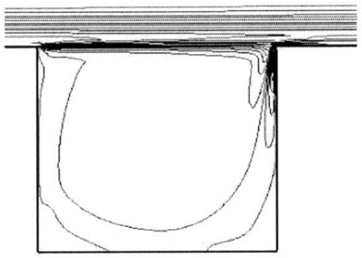

(c) $\delta = 0.21$

Fig. 7 Instantaneous vorticity contours on the x-z plane at $y=0.2$, for laminar flow past a 3D open deep rectangular cavity, with three boundary layer thicknesses (δ) at upstream lip of cavity, $R_e=10{,}000$, $t=288$

The instability on the free shear layer is not the same as the TGL phenomena. It is due to vortex stretching of the K-H vortex structures due to the velocity $u(z)$ profile. The flow is extremely unstable, as shown by Fig. 5. The transverse K-H vortex core kinks in a wave up and down. The lower portion is in a region of lower velocity u, and vice versa; so the vortex is stretched to a lambdalike shape (e.g., in plan view, see Fig. 6). The vortex induced velocities have a downward component on the lower (slowed) section and thus amplify the instability. Clearly these shear layer vortices strongly influence the flow down the rear wall and floor of the cavity, possibly dominating the TGL vortex structure. The interaction between these two phenomena may account for the alternate weakening and strengthening of the vortices.

In summary, the flow is dominated by several interacting features. The high velocity gradient flow in the shear layer above the cavity produced small vortex structures causing the K-H instability. These vortices are unstable and tend to kink and stretch, leading to longitudinal vortices, a typical 3D flow structure, which partially eject to form the boundary layer downstream of the cavity. A type of wall jet flows down the rear wall of the cavity, driving the main cavity vortex. It is clear that free shear layer is a complex 3D structure, with both K-H instability and TGL vortices interacting. This flow would become turbulent at some higher Reynolds number and thus strongly affect the boundary layer downstream of the cavity.

4.1.2 Effect of Upstream Boundary Layer Thickness. This section presents selected results of computation of laminar flow past the cavity, assuming a laminar Blasius boundary layer inflow, with varying boundary layer thickness at upstream lip of cavity at $x=-0.1$. The boundary layer thickness δ is expressed relative to the length of the cavity (i.e., L). In particular, the cavity flow fields with $\delta=0.06$, 0.11, and 0.21 were studied, respectively, assuming a Reynolds number $R_e=10{,}000$. The uniform inflow, discussed above, is equivalent to a boundary layer inflow with a thickness $\delta=0.06$ at upstream lip of cavity.

Figures 7 show the instantaneous vorticity contours for $\delta=0.06$, 0.11, and 0.21, respectively. Shown in the figures are the flows on the x-z plane at $y=0.2$, at the nondimensional time $t=288$.

Figure 7(a) corresponds to $\delta=0.06$, showing the K-H instability in the shear layer due to the interaction between the external flow and the recirculating flow inside the cavity. It reveals a vortex formed from the shear layer near the rear wall of the cavity. Figure 7(b) corresponds to $\delta=0.11$, clearly showing that the oc-

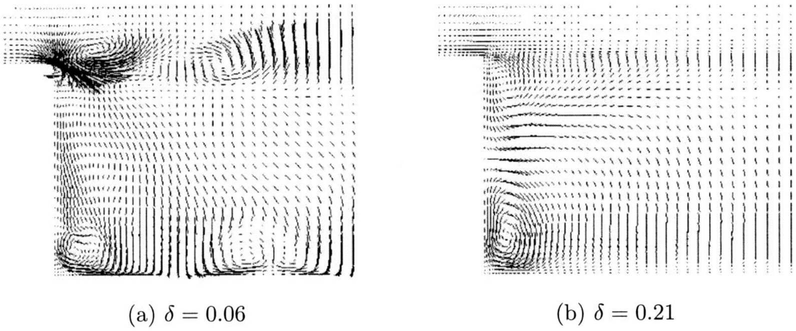

(a) $\delta = 0.06$ (b) $\delta = 0.21$

Fig. 8 Instantaneous cross flow velocity vectors on the y-z plane at $x=0.8$, for laminar flow past a 3D open deep rectangular cavity, with two boundary layer thicknesses (δ) at upstream lip of cavity, $R_e=10{,}000$, $t=288$

currence of the K-H instability was moved closer to the rear wall of the cavity than it was found in Fig. 7(*a*). Again, some interaction between the flow in the cavity and the shear layer was seen. But in Fig. 7(*c*), corresponding to $\delta=0.21$, there was no obvious shed vortex formation, and the shear layer directly impinged on the downstream boundary of the cavity. Compared to Figs. 7(*a*) and 7(*b*), Fig. 7(*c*) for $\delta=0.21$, shows a more stable flow field in terms of much smaller oscillations in the shear layer. In this case the flow is almost steady.

Figures 8(*a*) and 8(*b*) show the instantaneous cross flow velocity vectors on the y-z plane at $x=0.8$ for $\delta=0.06$ and $\delta=0.21$, respectively. Figure 8(*a*) indicates longitudinal vortices at the floor of the cavity and in the shear layer above the cavity. This indicates that the cavity flow fields can be complex and can exhibit a strong three-dimensional nature. Figure 8(*b*) shows that the cross flow became much weaker than that shown in Fig. 8(*a*)—actually, it looks like a 2D cavity flow except the left hand side wall, where upper and lower corner vortices are visible. As a conclusion, given the Reynolds number, the cavity flow structure is affected by the boundary layer thickness; the flow becomes more unstable and complex as the boundary layer thickness decreases. It is probable that the flow would not be symmetrical about the midplane (i.e., $y=0$ plane). However the flow structures would be similar to those computed, especially in the corners.

4.2 Open Shallow Cavity Flows.

The above section studied laminar flow past open deep rectangular cavities. This section extends this study, investigating laminar flow past open shallow rectangular cavities, with a geometry shown in Fig. 1 with $D/L<1$. This study aimed to discover the differences in flow characteristics between the open deep cavity flow and the open shallow cavity flow. For this, two problems have been addressed: (1) The effect of the shallow cavity geometry, particularly the D/L ratio, on the flow fields, for a given Reynolds number; and (2) the effect of the Reynolds number on the flow fields, for a given D/L ratio. The results of computation have been compared to the open deep cavity results, described in Sec. 4.1, under the same flow conditions.

4.2.1 Effect of Depth-to-Length Ratio. The influence of the cavity geometric D/L ratio on the flow fields was studied, for laminar flow past an open shallow rectangular cavity, for a given Reynolds number. In particular, two D/L ratios were considered, which were $D/L=0.5$ and $D/L=0.25$, respectively; in both cases, the width-to-length ratio of the cavity was $W/L=3$. The following presents the results obtained at the Reynolds number $R_e=3000$, assuming a laminar Blasius boundary layer inflow.

Case 1: $D/L=0.5$. Figure 9 shows the instantaneous flow fields (streamlines) at $t=204$. Specifically, in Fig. 9, part (*a*) indicates the flow field on the x-z plane at $y=0.2$ and part (*b*) is a cross flow field on the y-z plane at $x=0.7$. Figure 9(*a*) shows the vortices inside the cavity, including the primary vortex and a secondary vortex upstream. In addition, a K-H vortex is formed in the front of the cavity in the free shear layer. Since the K-H and the primary vortices rotate in a clockwise direction, a saddle point exists in the flow field between their cores. These vortex phenomena have also been found in 2D open shallow cavities [39].

Comparing Fig. 9(*a*) with the results for the open deep cavity, as shown in Fig. 4(*a*) for $D/L=1$ with the same Reynolds num-

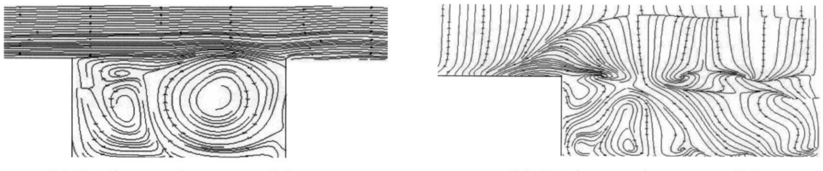

(a) On the x-z plane at $y=0.2$ (b) On the y-z plane at $x=0.7$

Fig. 9 Instantaneous flow fields, for laminar flow past a 3D open shallow rectangular cavity with $D/L=0.5$ and $R_e=3000$, at $t=204$

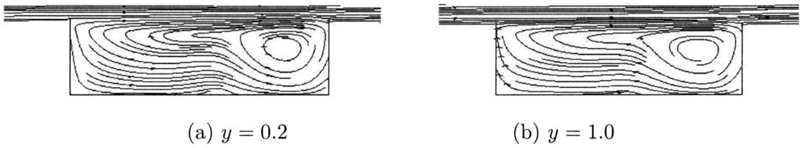

(a) $y = 0.2$ (b) $y = 1.0$

Fig. 10 Instantaneous flow fields on x-z planes, for laminar flow past a 3D open shallow rectangular cavity with $D/L=0.25$ and $R_e=3000$, at $t=204$

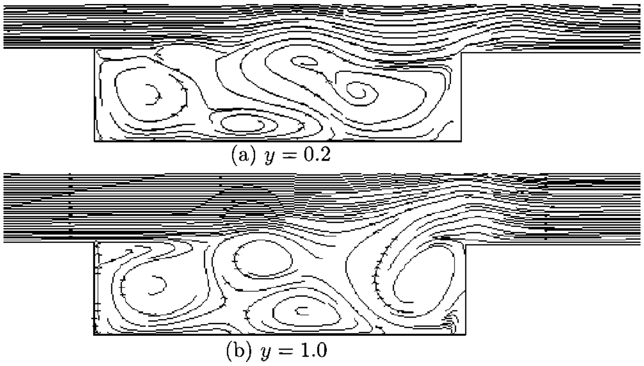

Fig. 11 Instantaneous flow fields on *x*-*z* planes, for laminar flow past a 3D open shallow rectangular cavity with $D/L = 0.25$ and $R_e = 10{,}000$, at $t = 80$

ber, two observations may be obtained. First, a weaker K-H instability was observed in the shear layer for the shallow cavity, than observed for the deep cavity. Second, for the shallow cavity, the primary vortex moved toward the rear wall of the cavity, thereby leaving room for a much larger secondary vortex to be formed in the upstream and the further formation of the tertiary vortex. It is believed that these differences are due to the change in the D/L ratio. These observations are very similar to those found for flows with 2D rectangular cavities (e.g., [15,40]).

Figure 9(*b*) shows the instantaneous cross flow field on the y-z plane at $x = 0.7$. The longitudinal vortices were found at the top and floor of the cavity. The structural similarity between Fig. 5(*a*) (for the deep cavity at the $x = 0.6$ plane) and Fig. 9(*b*) (for the shallow cavity at the $x = 0.7$ plane) may indicate a further difference between the deep cavity flow and shallow cavity flow. The TGL vortices would appear in a location closer to the rear wall for the shallow cavity. TGL vortices are visible on the floor due to the movement of the primary vortex towards the end of the cavity. The flow exhibits 3D nature.

Case 2: $D/L = 0.25$. Figure 10(*a*) shows flow fields on the x-z planes at (a) $y = 0$ and (b) $y = 1.0$, respectively. As can be seen, the flow structures at these two planes were similar. In fact, this similarity has also been found between the flow structures at other planes for which visualizations have also been performed. Thus, the size of the primary vortex, located downstream in the cavity, did not change significantly with the planes except for the plane at $y = 1.2$. This may explain why there was no significant shear layer oscillation being found in these flow fields. These are considerably different from the observations obtained earlier for the cavity with a smaller $D/L = 0.5$, in Case 1. These indicate that, in the case with $D/L = 0.25$ and $R_e = 3000$, the flow tends to be stable, and thus exhibits a 2D nature.

For the shallow cavity $D/L = 0.25$ the viscous effects due to the flow seem to damp the longitudinal vortices, and also K-H instability, thus making the flow nearly two-dimensional, in the range about $0 < y < 1.2$. The proximity of the floor may also tend to reduce vertical velocity w in the shear layer, thus inhibiting K-H instability. Note that the boundary layer at the lip is virtually identical for all cases of D/L, so it must be the differing flow inside the cavity that is influencing the free shear layer growth.

Based on the above two case studies, it is not difficult to find the major differences between the shallow cavity flow field and the deep cavity flow field. Given the same Reynolds number, it appears that the flow field tends to become increasingly stable as the D/L ratio is decreased. In other words, the shallow cavity flow field seems to be more stable than the deep cavity flow field in terms of a weaker K-H instability in the shear layer, at a Reynolds number that is not large. However, the shallow cavity flow fields may exhibit more complex vortical structures than the deep cavity flow fields, as indicated by the formation of a larger secondary vortex and a new tertiary vortex in the cavity. Moreover, as will be shown next, as the Reynolds number is increased, the shallow cavity flow field can become as unstable as the deep cavity flow field.

4.2.2 Effect of Reynolds Numbers. This section studies the influence of the Reynolds number on the open shallow cavity flow fields, for the cavity with $D/L = 0.25$ and $W/L = 3$. In particular, a Reynolds number $R_e = 10{,}000$ is considered, assuming a laminar Blasius boundary layer inflow.

Figures 11(*a*) and 11(*b*) present the instantaneous flow fields on two x-z planes at $y = 0.2$ and $y = 1$, respectively. Both figures show the primary vortex and a secondary vortex upstream. In addition, a tertiary vortex can be found in the middle of the cavity below the free shear layer. Differences in the flow structure between these two planes could be easily found. The stronger oscillation is seen at $y = 1$ plane. It is quit different from 2D cavity flows.

Compared to Fig. 10 with $R_e = 3000$, the K-H instability which was not observed there reappeared in the shear layer in the $R_e = 10{,}000$ case, with the latter particularly showing a stronger K-H instability due to the higher Reynolds number.

Figure 12 shows the instantaneous cross flow velocity vectors for $R_e = 10{,}000$. Two y-z planes, at $x = 0.8$ and $x = 1.7$, are indicated. Figure 12(*a*) shows a complex flow structure, and the longitudinal vortices were found at the floor and the top of the cavity. These vortices, interacting with the changing primary vortex along the lateral direction, caused the oscillation in the shear layer at the lateral direction. These oscillations were propagated downstream. This is evident in Fig. 12(*b*), corresponding to the cross flow on the $x = 1.7$ plane, which is aft of the cavity. It shows the boundary layer downstream of the cavity contains the longitudinal vortices, as well as components of the K-H vortices. This indicates that, at the higher Reynolds number, the shallow cavity flow fields become highly unsteady and complex, and exhibit a strong 3D nature. Like the deep cavity flow, the shallow cavity flow would become turbulent at some higher Reynolds number and thus strongly affect the boundary layer downstream of the cavity.

As a summary, Table 1 presents all of the computations conducted, showing the computation conditions and a brief description of the flow characteristics associated with each condition.

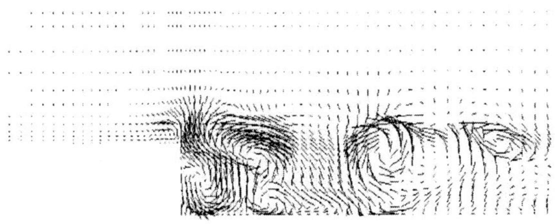

(a) $x = 0.8$

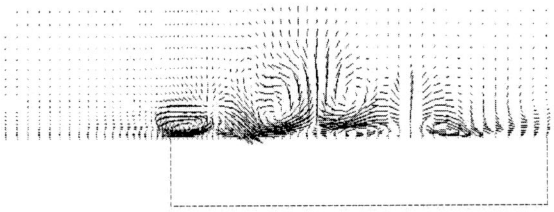

(b) $x = 1.7$

Fig. 12 Instantaneous cross flow velocity vectors on *y*-*z* planes, for laminar flow past a 3D open shallow rectangular cavity with $D/L = 0.25$ and $R_e = 10{,}000$, at $t = 204$

Table 1 Summary of computations for laminar flow past a 3D open rectangular cavity.

Cavity class	D/L	R_e	Inflow	δ	Flow characteristics
Deep	1	3000	Thin boundary layer	0.10	Unstable, 3D
Deep	1	10,000	Thin boundary layer	0.06	Unstable, 3D
Deep	1	10,000	Boundary layer	0.11	Unstable, 3D
Deep	1	10,000	Boundary layer	0.21	Stable, 2D
Shallow	0.5	3000	Boundary layer	0.10	Unstable, 3D
Shallow	0.25	3000	Boundary layer	0.10	Stable, 2D
Shallow	0.25	10,000	Boundary layer	0.10	Unstable, 3D

5 Conclusions

This paper studied incompressible laminar flow over 3D open rectangular cavities based on the solution of the unsteady 3D incompressible NS equations using finite difference schemes. A CFD code was developed for this study; the code was validated.

The cavity flow fields were studied against: (1) different inflow conditions, i.e., laminar Blasius boundary layer inflow with different boundary layer thickness δ; (2) different Reynolds numbers R_e; and (3) different cavity geometry D/L, particularly the open deep cavity $D/L \geqslant 1$ and the open shallow cavity $D/L < 1$.

The following observations were made from the study, for laminar flow past a 3D rectangular cavity:

1. At high R_e, typically, $R_e = 10{,}000$, both deep cavity flow and shallow cavity flow can become unsteady and complex, with K-H instability oscillations in the shear layer and exhibiting a three-dimensional nature, with TGL vortices on the floor and longitudinal vortex structures on the shear layer. It can not be simulated by a 2D model.
2. The shallow cavity flow may exhibit a more complex vortical structure, with primary, secondary, and tertiary vortices within the cavity. At low/moderate R_e (e.g., $R_e = 3000$), the shallow cavity flow appears to be more stable than the deep cavity flow. In other words, a higher R_e is required for the shallow cavity flow to become unsteady than for the deep cavity flow.
3. Given an R_e, the flow structure is affected by the thickness of the inflow boundary layer. The flow becomes increasingly unstable as the thickness δ decreases. At a high R_e, for a small δ, the strong K-H instability and vortex stretching cause a complex 3D flow, implying a high potential of turbulence developing downstream.
4. In comparison to the flow in the lid-driven cavity, the flow past the cavity involves several important flow phenomena, including the shear layer oscillations due to the interaction between the external flow and the recirculating flow inside the cavity, and the influence of the free shear layer on the boundary layer downstream of the cavity. Bedsides, it is found that a higher R_e may be required for the occurrence of the K-H and longitudinal vortices in the flow past the cavity, due to the lower velocities inside the cavity and more effective dissipation.

This research has indicated that as the Reynolds number increases, the open cavity flow would become highly unsteady and complex, which would strongly affect the boundary layer downstream of the cavity. At some higher Reynolds number, the flow would go into the transitional and turbulent regions. Further studies are being undertaken towards higher Reynolds numbers beyond turbulent/transition region.

References

[1] Ball, J. W., 1959, ''Hydraulic Characteristics of Gates Slots,'' J. Hydraul. Div., Am. Soc. Civ. Eng., **85**(HY10), pp. 81–114.
[2] Miles, J. W., and Lee, Y. K., 1959, ''Helmholtz Resonance of Harbors,'' J. Fluid Mech., **67**(3), pp. 445–467.
[3] Rockwell, D., and Naudascher, E., 1978, ''Review-Self-Sustaining Oscillations of Flow Past Cavities,'' ASME J. Fluids Eng., **100**, pp. 152–165.
[4] Suhs, N. E., 1987, ''Computation of Three-Dimensional Cavity Flow at Subsonic and Supersoic Mach Numbers,'' NASA TP-2683.
[5] Baysal, O., Srinivasan, S., and Stallings, R. L., Jr., 1988, ''Unsteady Viscous Calculations of Supersonic Flows Past Deep and Shallow Three-Dimensional Cavities,'' AIAA Paper 88-0101.
[6] Baysal, O., and Stallings, Jr., R. L., 1988, ''Computational and Experimental Investigation of Cavity Flowfields,'' AIAA J., **26**(1), pp. 6–7.
[7] Chokani, N., and Kim, I., 1991, ''Suppression of Pressure Oscillations in an Open Cavity by Passive Pneumatic Control,'' AIAA Paper 91-1729.
[8] Morgenstern, Jr., A., and Chokani, N., 1994, ''Hypersonic Flow Past Cavities,'' AIAA J., **32**(12), pp. 2387–2393.
[9] Rizzetta, D. P., 1988, ''Numerical Simulation of Supersonic Flow Over a Three-Dimensional Cavity,'' AIAA J., **26**(7), pp. 799–807.
[10] Sinha, S. N., Gupta, A. K., and Oberai, M. M., 1982, ''Laminar Separating Flow over Backsteps and Cavities Part II: Cavities,'' AIAA J., **20**(3), pp. 370–375.
[11] Srinivasan, S., Baysal, O., and Plentovich, E. B., 1988, ''Navier-Stokes Calculations of Transonic Flows Past Open and Transitional Cavities,'' ASME J. Fluids Eng., **66**, pp. 169–179.
[12] Mehta, U. B., and Lavan, Z., 1969, ''Flow in a Two-Dimensional Channel with a Rectangular Cavity,'' NASA CR 1245.
[13] O'Brien, V., 1972, ''Closed Streamlines Associated with Channel Flow over a Cavity,'' Phys. Fluids, **15**(12), pp. 2089–2097.
[14] Pereira, J. C. F., and Sousa, J. M. M., 1995, ''Experimental and Numerical Investigation of Flow Oscillations in a Rectangular Cavity,'' ASME J. Fluids Eng., **117**, pp. 68–74.
[15] Wood, W. A., 1996, ''Multigrid Approach to Incompressible Viscoue Cavity Flows,'' NASA TM-110262.
[16] Chiang, T. P., Hwang, R. R., and Sheu, W. H., 1997, ''On End-Wall Corner Vortices in a Lid-Driven Cavity,'' ASME J. Fluids Eng., **119**, pp. 201–204.
[17] Cortes, A. B., and Miller, J. D., 1994, ''Numerical Experiments with the Lid-Driven Cavity Flow Problem,'' Comput. Fluids, **23**(8), pp. 1005–1027.
[18] Iwatsu, R., Hyun, J. M., and Kuwahara, K., 1993, ''Numerical Simulations of Three-Dimensional Flows in a Cubic Cavity with an Oscillating Lid,'' ASME J. Fluids Eng., **115**, pp. 680–686.
[19] Koseff, J. R., and Street, R. L., 1984, ''On End Wall Effects in a Lid-Driven Cavity Flow,'' ASME J. Fluids Eng., **106**, pp. 385–389.
[20] Burggraf, O. R., 1966, ''Numerical Prediction of Unsteady Flowfield in an Open Cavity,'' J. Fluid Mech., **24**, pp. 113–151.
[21] Weiss, R. F., and Florsheim, B. H., 1965, ''Flow in a Cavity at Low Reynolds Number,'' Phys. Fluids, **8**(9), 1631–1635.
[22] Pan, F., and Acrivos, A., 1967, ''Steady Flows in Rectangular Cavities,'' J. Fluid Mech., **28**(4), pp. 643–655.
[23] Nallasamy, M., and Prasad, K. K., 1977, ''On Cavity Flow at High Reynolds Numbers,'' J. Fluid Mech., **79**(2), pp. 391–414..
[24] Gustafson, K., and Halasi, K., 1986, ''Vortex Dynamics of Cavity Flows,'' J. Comput. Phys., **64**, pp 279–319.
[25] Aidun, C. K., Triantafillopoulos, N. G., and Benson, J. D., 1991, ''Global Stability of a Lid-Driven Cavity with Throughflow: Flow Visualization Studie,'' Phys. Fluids A, **3**(HY10), pp. 2081–2091.
[26] Maull, D. J., and East, L. F., 1963, ''Three-Dimensional Flow in Cavities,'' J. Fluid Mech., **16**(4), pp. 620–632.
[27] East, L. F., 1966, ''Aerodynamically Induced Resonance in Rectangular Cavities,'' J. Sound Vib., **3**(3), pp. 277–287.
[28] Koseff, J. R., and Street, R. L., 1984, ''The Lid-Driven Cavity Flow: A Synthesis of Qualitative and Quantitative Observations,'' ASME J. Fluids Eng., **106**, pp 390–398.
[29] Koseff, J. R., and Street, R. L., 1984, ''Visualization Studies of a Shear Driven Three-Dimensional Recirculating Flow,'' ASME J. Fluids Eng., **106**, pp. 21–29.
[30] Freitas, C. J., Street, R. L., Findikakis, A. N., and Kosseff, J. R., 1985, ''Numerical simulation of Three-Dimensional Flow in a Cavity,'' Int. J. Numer. Methods Fluids, **5**, pp. 561–575.
[31] de Vahl Davis, G., and Mallison, G. D., 1976, ''An Evaluation of Upwind and Central Difference Approximations by a Study of Recirculating flow,'' Comput. Fluids, **4**, pp. 29–43.
[32] Freitas, C. J., and Street, R. L., 1988, ''Non-Linear Transport Phenomena in a Complex Recirculating Flow: A Numerical Investigation,'' Int. J. Numer. Methods Fluids, **8**, pp. 769–802.
[33] Komerath, N. M., Ahuja, K. K., and Chambers, F. W., 1987, ''Prediction and Measurement of Flows over Cavities-A Survey,'' AIAA Paper 87-0166.
[34] Baldmin, B. S., and Lomax, H., 1978, ''Thin Layer Approximation and Algebraic Model for Separated Turbulent Flows,'' AIAA Paper 78-257.
[35] Bardina, J., Ferziger, J. H., and Reynolds, W. C., 1984, ''Improved Turbulence

Models Based on LES of Homogeneous Incompressible Turbulent Flow,'' Report TF-19, Dept. of Mechanical Engineering, Stanford.
[36] Hankey, W. L., and Shang, J. S., 1980, ''Analysis of Pressure Oscillation in an Open Cavity,'' AIAA J., **18**(8), pp. 892–898.
[37] Rogers, S. E., and Kwak, D., 1990, ''Upwind Difference Scheme for the Time-Accurate Incompressible Navier-Stokes Equations,'' AIAA J., **28**, pp. 253–262.
[38] Forristal, R., 2000, ''Unsteady Flow over Cavities,'' Ph.D. Thesis, School of Aeronautical Engineering, The Queen's University of Belfast, Belfast, UK.
[39] Neary, M. D., and Stsphanoff, K. D., 1987, ''Shear-Layer-Driven Transition in a Rectangular Cavity,'' Phys. Fluids, **30**(10), pp. 2936–2946.
[40] Hardin, J. C., and Pope, D. S., 1995, ''Sound Generation by Flow over a Two-Dimensional Cavity,'' AIAA J., **33**(3), pp. 407–412.
[41] Yao, H., Cooper, R. K., and Raghannathan, S., 2000, ''Computation of Incompressible Flow Over Three-Dimensional Cavities,'' *Advances in Fluid Mechanics III*, (Proc. 3rd International Conference on Advances in Fluid Mechanics), Rohman, M. and Brebbin, C. A. eds., WIT Press, Southampton, UK, pp. 125–133.
[42] Yao, H., ''Incompressible Flow Over a Three-Dimensional cavity,'' Ph.D. Thesis, School of Aeronautical Engineering, The Queen's University of Belfast, December 2002.

B. Brunone*
Professor of Hydraulics
e-mail: brunone@unipg.it

M. Ferrante
Assistant Professor

M. Cacciamani
Post Graduate Student

University of Perugia,
Dipartimento di Ingegneria Civile
ed Ambientale, Via G. Duranti, 93,
06125, Perugia, Italy

Decay of Pressure and Energy Dissipation in Laminar Transient Flow

In the present paper, some peculiar characteristics of transient laminar flow are discussed. After presenting a review of the existing literature, attention is focused on transient energy dissipation phenomena. Specifically, results of both laboratory and numerical experiments are reported, the latter by considering one-dimensional (1D) along with two-dimensional (2D) models. The need of modifying a criterion for simulating unsteady friction proposed some years ago by one of the writers, and extensively used for water-hammer calculations, is pointed out. Differences between accelerating and decelerating flows as well as between transients in metallic and plastic pipes are also highlighted. [DOI: 10.1115/1.1839926]

Keywords: Transient, Laminar, Energy, Dissipation, Viscoelasticity

1 Introduction

The main motivation for the attempts of improving models of unsteady-state friction in pressurized pipe systems is the need for simulating properly the very large decay and rounding of pressure peaks after the end of a complete closure manoeuvre. For transients in single pipe systems—i.e., a constant diameter pipe supplied by a constant level reservoir upstream and with a manoeuvre valve placed at the downstream end section—such an interest is mainly academic. As a matter of fact, in such a system, there is a strong link between the time when the extreme values of the transient pressure occur and the duration of the maneuvre. On the contrary, in more complex systems, involving many branches and/or loops such as may be found in many industrial process systems, cooling water systems for power plants and combined potable and firewater systems, a proper evaluation of pressure peak decay is of technical interest. In fact, in such systems the extreme values of transient pressures take place after the end of the maneuvre and are due to the overlapping of pressure waves coming from different parts of the systems [1]. Consequently, to neglect decay of pressure peak during transients is not safe, since extreme values of pressure strongly depend on the chosen criterion for computing unsteady-state friction. Since one-dimensional (1D) models based on the quasi steady-state approximation for evaluating friction term, do not capture the mentioned strong attenuation phenomena at all, they do not allow a proper evaluation of such extreme pressures. Moreover, such models may give rise to a valuable time shift between numerical and experimental pressure time-histories.

Due to powerful computational tools available nowadays, two-dimensional (2D) models are an actual choice with respect to 1D unsteady-state models and related unsteady friction formulas. As a matter of fact, they give much better results since they do not postulate simple energy dissipation mechanisms as those assumed when the quasi steady-state approach is followed. On the other hand, within a 2D frame, it is hard to treat properly complex boundary conditions, as well as it is quite arbitrary to extend uniform turbulence models to transient flows. In practice, mainly to save computer memory capacity, quasi 2D models are used where pressure head is assumed as constant over the cross-section. In any case, all 2D models lack the inherent conciseness that makes 1D models more successful both in research activity and when solving technical problems.

Even though in engineering applications laminar pipe flow occurs less frequently than the turbulent one, in the present work, attention is focused on nonperiodic (*water-hammer*) laminar transients for the following main reasons: (i) Unsteady laminar pipe flow is mathematically tractable; and (ii) as mentioned earlier, results do not depend on the chosen unsteady-state turbulence model.

The aims of the present paper are as follows: (i) to point out peculiarities of laminar transients with respect to those with higher initial Reynolds numbers; (ii) to discuss effects of flow acceleration−deceleration on energy dissipation for a given base flow; and (iii) to highlight some aspects of transients in plastic pipes versus those in metallic ones. As a matter of fact, somehow related to research efforts in the field of unsteady friction modeling is the large debate concerning differences between accelerating and decelerating flows with respect to a steady-state one with the same value of the instantaneous discharge.

The paper is organized as follows. In Sec. 2, an overview of the existing literature—mainly focused on laminar flow—is reported (a review up to early 1980s may be found in Shuy and Apelt [2]). The proposed methodology for evaluating unsteady laminar friction is illustrated in Sec. 3. The results of laboratory tests and numerical simulations—by means of both 1D and 2D models—are discussed in Sec. 4, for both metallic and plastic pipes. In the concluding section, some remarks are outlined.

2 Modeling of the Friction Term in Laminar Transients

Any aspect of fluids behavior is strongly related to the flow regime. Modeling of transients in closed conduits is not an exception and then research efforts have been addressed towards the investigation of the unsteady-state flow regimes. Main point in the present context is whether stability of transient laminar flow can be simply assessed by means of the criterion valid for uniform flow (i.e., as long as the instantaneous Reynolds number is smaller than 2000−2500 the flow is laminar) or not. The position of such a problem is very arduous: ''The terms ''stable flow'' and ''unstable flow'' may become unclear for the case of time-dependent base flows which change substantially with time,'' as pointed out by Drazin and Reid [3]. Moreover, as some experimental results

---

*Corresponding author. Telephone: +39 075 5853617; Fax +39 075 5853892.

Contributed by the Fluids Engineering Division for publication in the JOURNAL OF FLUIDS ENGINEERING. Manuscript received by the Fluids Engineering Division November 10, 2003; revised manuscript received July 31, 2004. Associate Editor: Hamid Johari.

show [4], acceleration may delay transition to turbulence giving rise to the so-called *relaminarization*. At present, no conclusive result has been achieved, particularly when nonlinear transients—i.e., transients with a nonconstant acceleration as water hammer flow is—are considered. As a matter of fact, most of the available results concern periodic (e.g., Ref. [5]) or constant-acceleration (e.g., Ref. [6]) flows. Consequently, in the present paper, as well as in all contributions cited below, the assumption of a stable laminar transient flow is made, implicitly assuming the validity of the mentioned criterion for uniform flow.

The quasi-analytical solution proposed by Zielke [7,8] is a miliary stone in simulating transient laminar flow by means of 1D models. In Zielke's solution, the instantaneous value of the friction term at a computational section, J_Z, is the sum of a quasi-steady component, J_s—given by the Poiseuille equation—and an unsteady-state component, $J_{Z,u}$, depending on weighted past velocity changes:

$$\begin{aligned} J_z(x,t) &= J_s(x,t)+J_{z,u}(x,t) \\ &= \frac{32\nu}{gD^3}V(x,t)+\frac{16\nu}{gD^2}\int_0^t \frac{\partial V}{\partial t}(x,t)W(x,t-y)dy. \end{aligned} \quad (1)$$

Zielke's solution was successfully checked by considering laboratory test carried out by Holmboe and Rouleau [9]. Even though such a test provides the standard example used for comparing unsteady friction calculations for many years, it must be pointed out that its duration is quite short since only four periods of the transient were reported in the paper.

Fundamental results due to Zielke were recalled by Achard and Lespinard [10] who presented two approximation procedures to handle practical problems. Shuy [11] and Ghilardi and Barbero [12] derived different approximate equations for wall shear stress, τ_w, in terms of the instantaneous mean velocity and acceleration. In Prado and Larreteguy's model [13]—obtained for the particular case of an infinite pipe with an imposed time-dependent pressure gradient along the pipe axis—τ_w is a function of both V and some weighted mean velocities.

Numerical solution of Eq. (1) requires the storage of all computed past velocities but in practice, since weighting function is small when time is large, numerical integration of W can be truncated. Consequently, several approximate expressions of the weighting function W have been proposed. The first of them is due to Trikha [14] who approximated the function W by the sum of three exponential terms whose coefficients were obtained by fitting the exact values in the original formulation of W by Zielke. Such terms are introduced at each computational time, but only the change in velocity since the previous time step is needed. A larger computer storage is required by the approximate relationships obtained by Suzuki et al. [15] and Schohl [16], where function W is a sum of five exponential terms. In the present paper, the original formulation by Zielke will be considered. An approximate solution for an oscillatory laminar flow in a pipe was proposed by Stavitsky and Maccagno [17] who pointed out significant differences between the actual friction coefficient and the one evaluated within the quasi steady-state approach.

With regard to turbulent flows, since no analytical solution is available, the unsteady-state component of the friction term, J_u, has been expressed in terms of the instantaneous acceleration by means of laboratory data based relationships. Starting from the classical papers by Daily et al. [18] and Carstens and Roller [19], different expressions of J_u have been proposed relatively easy to include in 1D numerical models. On the other hand, most of such unsteady friction models lack generality, such that they do not provide reliable results—in terms of both pressure peak decay and phase shift—for transient conditions different from those considered when building up the model. Within 1D unsteady friction models, the most widely used in water hammer applications is the one proposed by one of the writers and Greco and Golia since it allows to produce reasonable agreement with experimental pressure traces and it can be easily included in any numerical procedure based on the Method of Characteristics (MOC) without increasing the computational burden [20]. In such a model, herein referred to as the *k model*, the unsteady-state component of friction term, $J_{k,u}$, is given by the following relationship [21,22]:

$$J_{k,u}(x,t)=\frac{k}{g}\left(\frac{\partial V(x,t)}{\partial t}-a\,\frac{\partial V(x,t)}{\partial x}\right) \quad (2)$$

Equation (2) was obtained on the basis of both theoretical and experimental findings. Specifically, in the momentum equation two additional terms were introduced, both function of local acceleration, $\partial V/\partial t$, to take into account the difference with respect to uniform flow conditions of the shape of velocity profiles and the friction term, respectively:

$$\frac{\partial h}{\partial x}+\frac{V}{g}\frac{\partial V}{\partial x}+\frac{1}{g}\frac{\partial V}{\partial t}+\frac{\eta}{g}\frac{\partial V}{\partial t}+\frac{\phi}{g}\frac{\partial V}{\partial t}+J_s=0 \quad (3)$$

In Eq. (3), $\eta=(\int_A u^2 dA/V^2A)-1$ is the excess over unity of the Coriolis momentum flux correction coefficient, whereas $\phi/g\partial V/\partial t=J-J_s$ is the difference between the actual friction term and the one obtained within the quasi steady-state approach. By analyzing the experimental velocity profiles given by Hino et al. [5,23], with regard to the lumped term $(\eta+\phi)/g\partial V/\partial t$, it was pointed out that: (i) A significant correction with respect to uniform flow conditions holds when $V(\partial V/\partial t)>0$; and (ii) a constitutive equation can be put in the form $\eta+\phi=k(1-a(\partial V/\partial x)/\partial V/\partial t)$ where $\partial V/\partial t/\partial V/\partial x$ is the propagation speed of a given value of V. The k model has been extensively checked by other researches with good results (e.g., Bergant and Simpson [24], Wylie [25], Bughazem and Anderson [26,27], Vitkosky et al. [28], Louriero and Ramos [29]). Moreover it was extended by Pezzinga [30] and Bergant et al. [31] also to ''upstream transients'' (i.e., caused by the operation of a valve or a pump placed at the upstream end section of the pipe). It is also consistent with the extended thermodynamics derivation of unsteady-state pipe flow equation proposed by Axworthy et al. [32].

In the original formulation [21,22], the decay coefficient k was assumed as a constant for low initial Reynolds number transients and was estimated within a trial and error procedure by considering numerical and experimental pressure traces. With regard to the special case of uniform acceleration, for transient laminar flows, Vardy and Brown (VB) [33] obtained the theoretically based value $k_{\mathrm{VB}}=0.0345$, irrespective of the value of the initial Reynolds number, $N_0=V_0D/\upsilon$. By comparing quasi 2D and 1D numerical model results, Pezzinga [30,34] developed Moody diagramlike charts for k. With regard to laminar transients, Pezzinga [34] pointed out that, with respect to turbulent flows, coefficient k is constant with N_0 and ε/D and is dependent only on the characteristic parameter of the pipe, $y_0=gJ_0L/aV_0$. As a matter of fact, for a given y_0, the value of k_P can be obtained from plots due to Pezzinga [34].

Any 1D unsteady-state friction model can be tested by considering the results of quasi 2D numerical models [35,36]. In the model by Vardy and Hwang [36]—specifically considered in the present paper—the following expression of the friction term, J_{VH}, is used:

$$J_{\mathrm{VH}}(x,t)=\frac{4\mu}{\rho g D}\,\frac{u_{nr}(x,t)}{\Delta r_{nr}/2} \quad (4)$$

according to the proposed discretization of the flow into a finite number, nr, of cylinders.

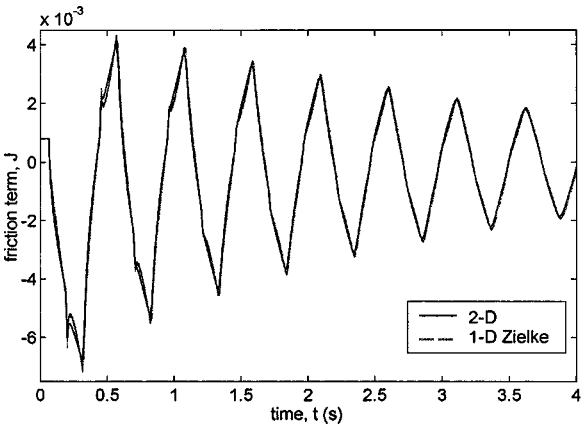

Fig. 1 Numerical experiment. Friction term at mid-length section given by the Zielke's model and quasi 2D Vardy and Hwang's one (copper pipe; $T=0.14$ s and $N_0=1134$)

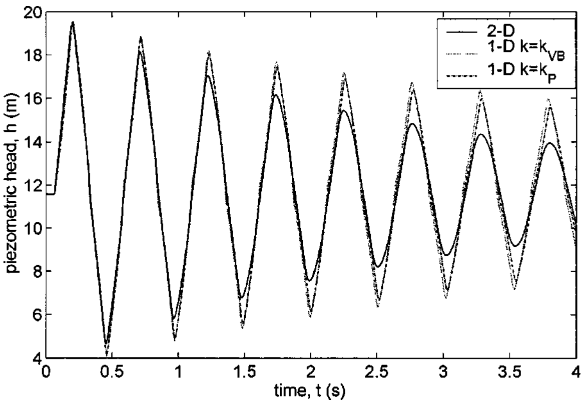

Fig. 3 Numerical experiment. Pressure time-history at mid-length section given by quasi 2D Vardy and Hwang's model and 1D one with: $k=k_{VH}$ and $k=k_P$ (copper pipe; $T=0.14$ s and $N_0=1134$)

3 A New Procedure for Unsteady Laminar Friction

In this part, the results of some preliminary numerical experiments are shown referring to the single copper pipe ($L_c=141.07$ m; $D_c=20$ mm; $a_c=1120$ m/s) at WEL (*Water Engineering Laboratory*) of the Department of Civil and Environmental Engineering of the University of Perugia (I), that will be described in the next section.

As an example, in Figs. 1 and 2, results from the Zielke's model and the quasi 2D Vardy and Hwang's one are compared for the transient with $N_0=1134$ caused by the complete closure of the end valve with a duration $T=0.14$ s. In the plots, J and h are the friction term and the piezometric head at mid-length section ($x=42$ m), respectively, whereas t is time from the beginning of the transient. Graphs of Figs. 1 and 2 confirm the very good agreement between the two considered models in terms of both energy dissipation (Fig. 1) and decay and rounding of pressure peaks (Fig. 2). Moreover there is a very good temporal match between the two pressure time-histories since no phase shift takes place. Due to the very good agreement between these two models, only the Vardy and Hwang's model has been considered for all subsequent numerical tests, since it allows for a simpler evaluation of the friction term by means of Eq. (4).

In Fig. 3 results from the quasi 2D Vardy and Hwang's model of Figs. 1 and 2 are compared with those given by the 1D model based on Eq. (2) with a constant value of coefficient k; specifically with $k=k_{VB}=0.0345$ and $k=k_P=0.042$ (personal communication). As it can be seen from the plots in Fig. 3, the 1D model does not capture the pressure peak decay at all even though a specific unsteady-state friction formula has been used as well as two different values of k are considered. Moreover, further numerical tests (not shown) carried out assuming other different constant values of k confirm the behavior of transient pressure traces shown in Fig. 3. Such a result differs from what was obtained by Bergant et al. [31] who simulated well laminar transients by means of Eq. (2), but with regard to flow conditions—i.e., the value of N_0—very close to the limit of existence of the viscous regime in steady-state flow.

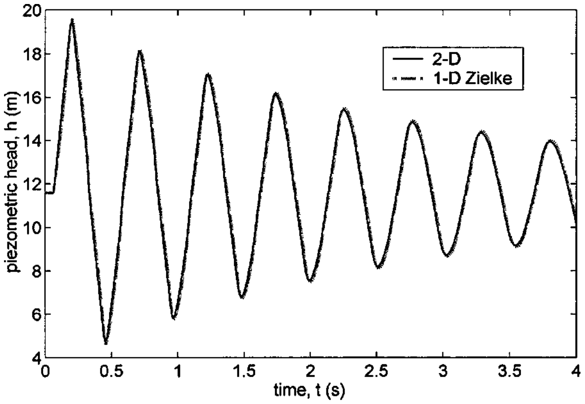

Fig. 2 Numerical experiment. Pressure time-history given by the Zielke's model and quasi 2D Vardy and Hwang's one (copper pipe; $T=0.14$ s and $N_0=1134$)

As a consequence, since the hypothesis of a constant value of the decay coefficient k for laminar transients has to be neglected, the following functional relationship has been assumed:

$$k=k(x,t) \tag{5}$$

to be determined by means of both numerical and laboratory experiments.

As it has been shown in Ref. [21], when the continuity equation:

$$\frac{a^2}{g}\frac{\partial V}{\partial x}+V\left(\frac{\partial h}{\partial x}+J_0\right)+\frac{\partial h}{\partial t}=0 \tag{6}$$

is coupled with the momentum equation (3), i.e., when the additional term $(\eta+\phi)/g\,\partial V/\partial t$ is introduced, some changes occur in the characteristics equations. Specifically, following the well-known procedure [37], by assuming $V \ll a$, within MOC, the equation of the positive characteristic line becomes:

$$\frac{dx}{dt}=\frac{a}{1+k} \tag{7}$$

and the compatibility equations become:

$$dh+\frac{a}{g}dV+J_s dx=0 \tag{8}$$

along the positive characteristic line, and

$$dh-\frac{a}{g}(1+k)dV+J_s dx=0 \tag{8'}$$

along the negative characteristic line ($dx/dt=-a$).

As a consequence, at any computational point and time, one can consider k as the only unknown in Eq. (8′) if values of h and V are known since they are given by another model. Specifically, in the present paper the quasi 2D Vardy and Hwang's model is used for evaluating V and h, at any computational point and time for the considered transient and pipe system.

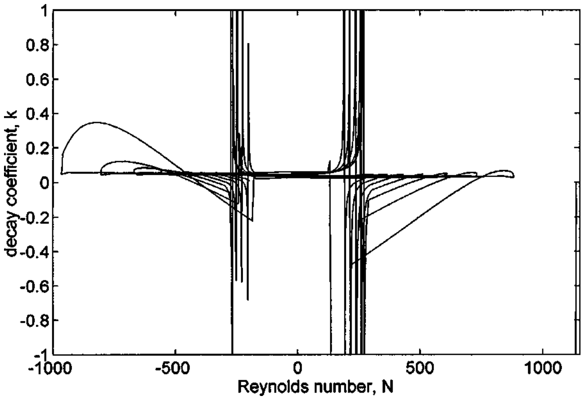

Fig. 4 Numerical experiment. Decay coefficient, *k*, vs instantaneous Reynolds number, *N*, at mid-length section (copper pipe; $T=0.14$ s and $N_0=1134$)

For example, in Fig. 4, the values of the decay coefficient at the mid-length section, obtained by means of the described procedure, are depicted versus the local instantaneous Reynolds number, *N*, for transient of Figs. 1–3. It must be stressed that the aim of such a numerical experiment is to point out peculiarities of laminar transients with respect to turbulent ones. Specifically, for laminar transients, as in Eq. (1) flow time-history has to be taken into account to properly model energy dissipation, when Eq. (3) is considered, coefficient *k* cannot be assumed as a constant. In order to check the numerical procedure giving rise to the curves in Fig. 4, it has been verified that the two pressure traces—i.e., the one given by the 1D model with $k(x,t)$ and the one obtained by means of the 2D model—are almost indistinguishable (not shown).

Plots in Fig. 4 merit some comments. Firstly, the curves point out a significant variation of *k* with *N*, and then in time. This may justify bad results achieved by assuming a constant value of *k* (Fig. 3). Secondly, in the first phases of the transient, *k* may reach values much higher than the ones obtained for transients with higher initial Reynolds number; moreover, *k* decreases significantly with time. Thirdly, negative values of *k* take place in some phases of the transient. Finally, for a given value of *N*, *k* is different depending on the change of *V*.

With regard to the last comments, a deeper analysis of the results points out that the following different cases may happen:

accelerating flow (case 1)

$$\frac{\partial|V|}{\partial t}>0 \quad \text{with} \quad \tau_w>\tau_{w,s}\Rightarrow\{|J|>|J_s|;\mathrm{sgn}(J)=\mathrm{sgn}(J_s);k>0\} \tag{9}$$

In this case, unsteady-state friction is larger than the one obtained within the staedy-state approach, i.e., by considering the Poiseuille's formula with the same instantaneous value of *V*.

Condition (9) is necessary but not sufficient. As a matter of fact, when flow decelerates, different cases may occur as shown in Fig. 5. In such a figure, velocity profiles in the upper plots, given by the quasi 2D model are reported along with ones obtained for the same value of *V*, by means of the Poiseuille's formula. In the lower plots, the zone close to the wall—bounded by a circle in the upper plots—is magnified to show the local behavior of the velocity gradient, and then of τ. Three different cases in Fig. 5 may be described as follows:

decelerating flow [case 2a—Fig. 5(*a*)]

$$\frac{\partial|V|}{\partial t}<0 \quad \text{with} \quad \tau_w>\tau_{w,s}\Rightarrow\{|J|>|J_s|;\mathrm{sgn}(J)=\mathrm{sgn}(J_s);k>0\} \tag{9$'$}$$

decelerating flow [case 2b—Fig. 5(b)]

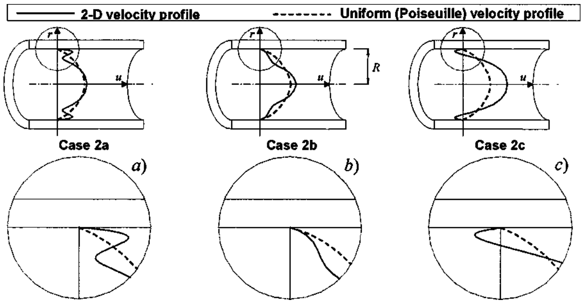

Fig. 5 Behavior of local velocity field close to the wall for laminar decelerating flows

$$\frac{\partial|V|}{\partial t}<0 \quad \text{with} \quad \tau_w<\tau_{w,s}\Rightarrow\{|J|<|J_s|;\mathrm{sgn}(J)=\mathrm{sgn}(J_s);k<0\} \tag{9$''$}$$

decelerating flow [case 2c—Fig. 5(c)]

$\partial|V|/\partial t<0$ but $\mathrm{sgn}(J)\neq\mathrm{sgn}(J_s)\Rightarrow$ no general rule can be stated for *k*, as defined by Eq. (2).

Such a behavior of the unsteady-state friction term agrees with results of experimental tests in a smooth circular pipe by Kurokava and Morikawa [38]. Main findings of their study—based on local velocity measurements carried out by means of a hot film anemometer—may be summarized as follows: (i) In laminar regime, the transient friction factor, λ_u, is larger than the quasi-steady one when the flow accelerates; such a result is in agreement with those by Cocchi [39] who proposed the expression: $\lambda_u=980/N$ instead of the Poiseuille one $\lambda_s=64/N$; (ii) due to the presence of random fluctuations, no precise evaluation of λ_u was possible for decelerated flows; and (iii) significant differences existed between laminar and turbulent transient flows, for a given value of velocity change. The latter finding discourages to extend to laminar regime results—somewhat very conflicting—obtained for turbulent flows (e.g., Daily et al. [18] and Shuy [40]). As a consequence of the present state-of-the-art, in the writers' opinion, local velocity field in transient conditions merits further analysis from both numerical and experimental points of view due to lack of not very conclusive results. In such a context, a secondary role can be played by some available analytic solutions. As a matter of fact, the ones proposed by Szymanski [41] and Das and Arakeri [42], for example, may be used only if the time-history of the axial pressure gradient and flow rate—this being very unfrequent in any practical case—are respectively, known.

4 Laboratory Experiments

In spite of the large body of literature about laminar transients, the scarcity of experimental data is quite evident. As a consequence, in the present section, some tests were carried out at WEL for both metallic and plastic pipes. At WEL, two different pipe systems are available. The first one, the already mentioned copper pipe, is mainly used for laminar flow. The second one comprises a high-density polyethylene pipe ($L_{pl}=352.00$ m; $D_{pl}=93.8$ mm; $a_{pl}=335.9$ m/s) which is more devoted to turbulent flows. At WEL an air vessel is used as a constant head supply reservoir; the prescribed pressure is maintained by varying the speed of the submerged pumps placed in the recycling reservoir. For both pipe systems, transients are caused by the closure of a ball valve placed at the downstream end section and discharging into a free surface tank. Pressure measurements were made at the supply reservoir, at the end section of the pipe as well as at a mid-length section. Pressure transducers were of the strain-gauge type, with an accuracy of 0.15% of the full-scale and a time response of about 1 ms. Recording range ($r.r.$) of transducers is chosen according to the maximum overpressure. Specifically, for transients in the copper pipe (Figs. 6 and 7) $r.r.$ is of 20 m of water, with a measurement

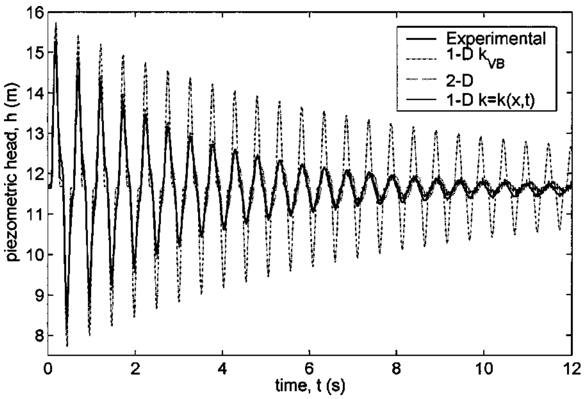

Fig. 6 Numerical and experimental pressure time-histories at mid-length section (copper pipe; $T=0.11$ s and $N_0=815$)

uncertainty of 0.03 m, whereas for transients in the polyethylene pipe (Fig. 8), *r.r.* is of 10 m of water, with a measurement uncertainty of 0.015 m. Calibration of pressure transducers has been checked by means of a pressure calibrator according to the European Guidelines on the "Calibration of Electromechanical Manometers" by EA (*European co-operation for Accreditation*) confirming data in the manufacturer certificate. Steady-state discharges were measured by means of discharge magnetic meters calibrated by means of the volumetric method. During tests in the copper pipe, water temperature was equal to 17°C, whereas it was equal to 18.3°C during those in the polyethylene pipe.

Pressure time-histories in Figs. 6 and 7 refer to transients in the copper pipe; with the floor of WEL chosen as the reference datum for piezometric head. In Fig. 6 transient, the duration of the closure, *T*, is equal to 0.11 s and the initial Reynolds number, N_0, is equal to 815, whereas for the Fig. 7 transient, it is $T=0.14$ s and $N_0=1339$. In Figs. 6 and 7, experimental data are compared with the numerical simulations obtained by means of: (i) The quasi 2D model by Vardy and Hwang; (ii) the 1D model with $k=k_{\mathrm{VB}}$; and (iii) the 1D model with $k=k(x,t)$. The curves in Figs. 6 and 7 confirm the reliability of the proposed procedure and the possibility of capturing all characteristics of laminar transients by using a more sophisticated unsteady-state 1D friction model.

Further tests were carried out on the polyethylene pipe. Figure 8 refers to a transient with $T=0.12$ s and $N_0=2020$, with the measurement section placed at $x=127$ m. The experimental pressure trace along with numerical results are reported in the graph, obtained by: (i) 2D Vardy and Hwang's model; (ii) *k* constant model [$k=k_{\mathrm{VB}}$, $k=0.25$, and $k=0.50$]; and (iii) the $k(x,t)$ model. In Fig. 8 significant discrepancies between experimental and numerical pressure time-histories in terms of both shape and decay of pressure peaks can be noticed. Such a finding disagrees apparently with what was shown in Ref. [43] where, with regard to higher N_0 transients, quite reliable numerical simulations were carried out for transients taking place in the same polyethylene pipe by means of the 1D model with *k* as a constant ($k=0.11-0.25$). More precisely, in Ref. [43] the pressure peak decay was well simulated whereas the shape of the pressure trace was not. Even though an in-depth analysis of transients in viscoelastic pipes is beyond the scope of this paper, two preliminary remarks can be made. Firstly, for the considered tests, the failure of the 1D model with *k* as a constant and larger than the mentioned values [38], could be due to peculiarities of laminar transients with respect to turbulent ones. In other words, as in metallic pipes for turbulent transients, the *k* constant model allows to simulate properly pressure peak decay whereas the variability of *k* with space and time must be taken into account for laminar transients, in viscoelastic pipes pressure peak decay can be modeled with a *k* constant model only in turbulent transients. Secondly, the failure of the 2D model, that for laminar transients can be assumed as an exact model, could be ascribed to the fact that energy dissipation due to viscoelasticity effects are much larger than those due to unsteady friction.

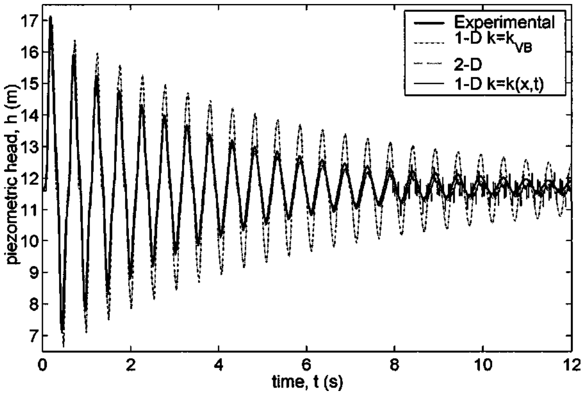

Fig. 7 Numerical and experimental pressure time-histories at mid-length section (copper pipe; $T=0.14$ s and $N_0=1339$)

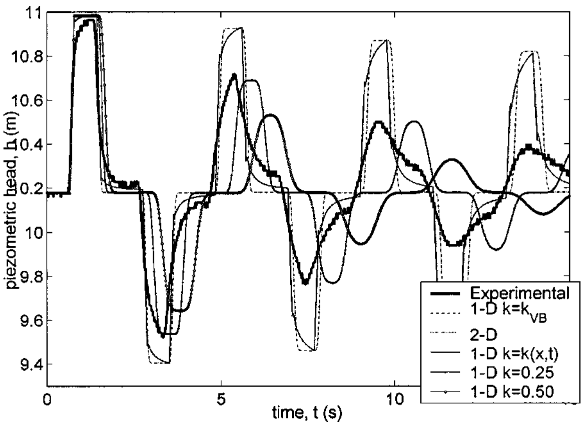

Fig. 8 Numerical and experimental pressure time-histories at mid-length section (polyethylene pipe; $T=0.12$ s and $N_0=2020$)

5 Conclusions

Numerical and experimental results for laminar transient flows are discussed with particular attention to energy dissipation phenomena. In the first part of the paper, performance of existing 1D and quasi 2D models for laminar transients has been checked by means of numerical experiments. In such a context, a 1D model previously proposed by one of the writers—herein referred to as the *k* model—has been modified. Specifically, unlike turbulent flows, the variability of the decay coefficient with space and time must be taken into account in order to simulate effectively laminar transients. As a consequence—provided that boundary conditions are properly stated—2D MOC models are more appropriate for highly transient laminar flows. In the second part, new laboratory tests have been presented for both metallic and plastic pipes, the former confirming reliability of the proposed model, the latter the peculiarity of laminar transients in plastic pipes with respect to those both in metallic pipes and with higher initial Reynolds number.

Acknowledgments

This research was partially supported by the Italian Ministry of University and Technological Research, project "*Hydrodynamic characterization of transients in hydro-systems with applications* *for the diagnosis of pressurised pipe networks*.'' The writers extend special appreciation to F. Calabresi for his valuable assistance in numerical simulations. The writers gratefully acknowledge comments of the three anonymous reviewers and the associate editor who helped to improve the original version of this manuscript.

Nomenclature

A = pipe cross-section
D = pipe internal diameter
J = friction term
L = pipe length
N = Reynolds number$=VD/\nu$
R = pipe radius
T = duration of the closure
V = mean flow velocity
W = weighting function in Zielke's solution
a = pressure wave speed
g = gravitational acceleration
h = piezometric head
k = decay coefficient in Eq. (2)
$r.r.$ = recording range
t = time
u = axial velocity component
x = spatial co-ordinate
y_0 = characteristic parameter of the pipe$=gJ_0L/aV_0$
Δr = radial thickness of the cylinder in the Vardy and Hwang's model
ε = equivalent sand roughness
ϕ = excess over unity of the Coriolis momentum flux correction coefficient
η = coefficient of the term difference between J and J_s
λ = friction factor
μ = absolute viscosity
ν = kinematic viscosity
ρ = density
τ = shear stress

Subscripts

c = copper pipe
P = Pezzinga's calculations
pl = polyethylene pipe
VB = Vardy and Brown's solution
VH = Vardy and Hwang's model
Z = Zielke's solution
s = steady-state
u = unsteady-state
w = pipe wall
0 = initial condition

References

[1] Karney, B. W., and Brunone, B., 1999, ''Water Hammer in Pipe Network: Two Case Studies,'' Proc., CCWI'99 Int. Conf. on 'Water Industry Systems: Modelling and Optimization Applications', D. A. Savic and G. A. Walters, eds., Exeter (UK), 1, pp. 363–376.
[2] Shuy, E. B., and Apelt, C. J., 1983, ''Friction Effects in Unsteady Pipe Flows,'' Proc., 4th Int. Conf. on 'Pressure Surges', H. S. Stephens et al., eds., Bath (UK), BHRA, pp. 147–164.
[3] Drazin, P., and Reid, W., 1991, *Hydrodynamics Stability*, Cambridge University Press, Cambridge, MA.
[4] van de Sande, E., Belde, A. P., Hamer, A. P., and Hiemstra, W., 1980, ''Velocity Profiles in Accelerating Pipe Flows Started From Rest,'' Proc., 3rd Int. Conf. on '*Pressure Surges*', H. S. Stephens et al., eds., Canterbury (UK), BHRA, pp. 1–14.
[5] Hino, M., Masaki, S., and Shuji, T., 1976, ''Experiments on Transition to Turbulence in an Oscillatory Pipe Flow,'' J. Fluid Mech., **75**, part 2, pp. 193–207.
[6] Lefebvre, P. J., and White, F. M., 1989, ''Experiments on Transition to Turbulence in a Constant-Acceleration Pipe Flow,'' ASME J. Fluids Eng., **111**, pp. 428–432.
[7] Zielke, W., 1966, ''Frequency-Dependent Friction in Transient Pipe Flow,'' Ph.D. thesis, The University of Michigan, Ann Arbor.
[8] Zielke, W., 1968, ''Frequency-Dependent Friction in Transient Pipe Flow,'' J. Basic Eng., **90**(1), pp. 109–115.
[9] Holmboe, E. L., and Rouleau, W. T., 1967, ''The Effect of Viscous Shear on Transients in Liquid Lines,'' J. Basic Eng., **89**(1), pp. 174–180.
[10] Achard, J. L., and Lespinard, G. M., 1981, ''Structure of the Transient Wall-Friction Law in One-Dimensional Models of Laminar Pipe Flows,'' J. Fluid Mech., **113**, pp. 283–298.
[11] Shuy, E. B., 1995, ''Approximate Wall Shear Equation for Unsteady Laminar Pipe Flows,'' J. Hydraul. Res., **33**(4), pp. 457–469.
[12] Ghilardi, P., and Barbero, G., 1996, ''Energy Dissipation Modelling in Transient Laminar Flow,'' Proc., XXV Convegno di Idraulica e Costruzioni Idrauliche, Turin (I), II, pp. 23–32 (in Italian).
[13] Prado, R. A., and Larreteguy, A. E., 2002, ''A Transient Shear Stress Model for the Analysis of Laminar Water-Hammer Problems,'' J. Hydraul. Res., **40**(1), pp. 45–53.
[14] Trikha, A. K., 1975, ''An Efficient Method for Simulating Frequency-Dependent Friction in Transient Liquid Flow,'' ASME J. Fluids Eng., **97**(1), pp. 97–105.
[15] Suzuki, K., Taketomi, T., and Sato, S., 1991, ''Improving Zielke's Method of Simulating Frequency-Dependent Friction in Laminar Liquid Pipe Flow,'' ASME J. Fluids Eng., **113**(4), pp. 569–573.
[16] Schohl, G. A., 1993, ''Improved Approximate Method for Simulating Frequency-Dependent Friction in Transient Laminar Flow,'' ASME J. Fluids Eng., **115**(3), pp. 420–424.
[17] Stavistky, D., and Macagno, E., 1980, ''Approximate Analysis of Unsteady Laminar Flow,'' J. Hydraul. Res., **106**(HY12), 1973–1980.
[18] Daily, J. W., Hankey, W. L., Olive, R. W., and Jordaan, J. M., 1956, ''Resistance Coefficients for Accelerated and Decelerated Flows Through Small Tubes and Orifices,'' Trans. ASME, **78**(5), pp. 1071–1077.
[19] Carstens, M. R., and Roller, J. E., 1959, ''Boundary-Shear Stress in Unsteady Turbulent Pipe Flow,'' J. Hydraul. Res., **85**(HY2), pp. 67–81.
[20] Ghidaoui, M. S., Zhao, M., Mc Innis, D. A., and Axworthy, D. H., 2004, ''A Rewiew of Waterhammer Theory and Practice,'' J. Applied Mech. Reviews (to be published).
[21] Brunone, B., Golia, U. M., and Greco, M., 1991, ''Some Remarks on the Momentum Equation for Fast Transients,'' Proc., Int. Meeting on 'Hydraulic Transients and Water Column Separation', IAHR, E. Cabrera and M. A. Fanelli, eds., Valencia (E), pp. 201–209.
[22] Brunone, B., Golia, U. M., and Greco, M., 1995, ''The Effects of Twodimensionality on Pipe Transients Modeling,'' J. Hydraul. Eng., **121**(12), pp. 906–912.
[23] Brunone, B., and Golia, U. M., 1991, ''Some Considerations on Velocity Profiles in Unsteady Pipe Flows,'' Proc., Int. Conf. on 'Entropy and Energy Dissipation in Water Resources', V. P. Sing and M. Fiorentino, eds., Maratea (I), pp. 481–487.
[24] Bergant, A., and Simpson, A. R., 1994, ''Estimating Unsteady Friction in Transient Cavitating Pipe Flow,'' Proc., 2nd Int. Conf. on 'Water Pipeline Systems', D. S. Miller, ed., Edinburgh (UK), bHrGroup, pp. 3–15.
[25] Wylie, E. B., 1996, ''Frictional Effects in Unsteady Turbulent Pipe Flow,'' *Applied Mechanics in the Americas*, M. Rysz et al., eds., 5, University of Iowa, Iowa City, Iowa, pp. 29–34.
[26] Bughazem, M. B., and Anderson, A., 1996, ''Problems With Simple Models for Damping in Unsteady Flow,'' Proc., 7th Int. Conf. on 'Pressure Surges and Fluid Transients in Pipelines and Open Channels', A. Boldy, ed., bHrGroup, pp. 537–548.
[27] Bughazem, M. B., and Anderson, A., 2000, ''Investigation of an Unsteady Friction Model for Waterhammer and Column Separation,'' Proc., 8th Int. Conf. on 'Pressure Surges', A. Anderson, ed., The Hague (NL), bHrGroup, pp. 483–495.
[28] Vitkosky, J. P., Lambert, M. F., Simpson, A. R., and Bergant, A., 2000, ''Advances in Unsteady Friction Modelling in Transient Pipe Flow,'' Proc., 8th Int. Conf. on 'Pressure Surges', A. Anderson, ed., The Hague (NL), bHrGroup, pp. 471–481.
[29] Louriero, D., and Ramos, H., 2003, ''A Modified Formulation for Estimating the Dissipative Effect of 1-D Transient Pipe Flow,'' Proc., Int. Conf. on 'Pumps, Electromechanical Devices and Systems Applied to Urban Water Management PEDS 2003', Cabrera, E. and Cabrera, E., Jr., eds., Swets & Zeitlinger, Lisse, II, pp. 755–763.
[30] Pezzinga, G., 2000, ''Evaluation of Unsteady Flow Resistances by Quasi-2D or 1D Models,'' J. Hydraul. Eng., **126**(10), pp. 778–785.
[31] Bergant, A., Simpson, A. R., and Vitkovsky, J., 2001, ''Developments in Unsteady Pipe Flow Friction Modelling,'' J. Hydraul. Res., **39**(3), pp. 249–257.
[32] Axworthy, D. H., Ghidaoui, M. S., and McInnis, D. A., 2000, ''Extended Thermodynamics Derivation of Energy Dissipation in Unsteady Pipe Flow,'' J. Hydraul. Eng., **126**(4), 276–287.
[33] Vardy, A., and Browne, J., 1996, ''On Turbulent, Unsteady, Smooth-Pipe Friction,'' Proc., 7th Int. Conf. on 'Pressure Surges and Fluid Transients in Pipelines and Open Channels', A. Boldy, ed., bHrGroup, pp. 289–311.
[34] Pezzinga, G., 1999, ''Quasi-2D Model for Unsteady Flow in Pipe Networks,'' J. Hydraul. Eng., **125**(7), pp. 676–685.
[35] Bratland, O., 1986, ''Frequency-Dependent Friction and Radial Kinetic Energy Variation in Transient Pipe Flow,'' Proc., 5th Int. Conf. on 'Pressure Surges', BHRA, pp. 95–101.
[36] Vardy, A. E., and Hwang, K., 1991, ''A Characteristic Model of Transient Friction in Pipes,'' J. Hydraul. Eng., **29**(5), pp. 669–684.
[37] Wylie, E. B., and Streeter, V. L., 1993, *Fluid Transients in Systems*, Prentice Hall, Englewood Cliffs, NJ.

[38] Kurokawa, J., and Morikawa, M., 1986, ''Accelerated and Decelerated Flows in a Circular Pipe,'' Bull. JSME, **29**(249), pp. 758–765.
[39] Cocchi, G., 1988, ''An Experiment on Unsteady-State Friction,'' Proc., Accademia delle Scienze di Bologna, series XIV, V, pp. 203–210 (in Italian).
[40] Shuy, E. B., 1996, ''Wall Shear Stress in Accelerating and Decelerating Turbulent Pipe Flows,'' J. Hydraul. Res., **34**(2), pp. 173–183.
[41] Szymansky, P., 1932, ''Quelques solutions exactes des èquations de l'hydrodynamique du fluid visqueux dans le cas d'un tube cylindrique,'' J. Math. Pures Appl., **97**(11), pp. 67–107.
[42] Das, D., and Arakeri, J. H., 2000, ''Unsteady Laminar Duct Flow With a Given Volume Flow Rate Variation,'' ASME J. Appl. Mech., **67**, pp. 274–281.
[43] Brunone, B., Karney, B. W., Mecarelli, M., and Ferrante, M., 2000, ''Velocity Profiles and Unsteady Pipe Friction in Transient Flow,'' J. Water Resour. Plan. Manage., **126**(4), pp. 236–244.

Swirling Gas–Liquid Two-Phase Flow—Experiment and Modeling Part I: Swirling Flow Field

L. Gomez
R. Mohan
O. Shoham
The University of Tulsa,
600 S. College Ave.,
Tulsa, OK 74104

Compact cyclonic separators are based on swirling flow, whereby the phases are separated due to the centrifugal forces generated by the flow. This phenomenon is common in several compact separators used by the oil, process, and aerospace industries. The objective of this paper is to study experimentally the hydrodynamics of the continuous liquid phase under swirling two-phase flow, such as that occurring in the lower part of the Gas–Liquid Cylindrical Cyclone (GLCC©[1]) compact separator and develop a model to characterize it. Local LDV measurements for a swirling flow field have been analyzed and utilized to develop cyclone and pipe swirling flow field prediction correlations. The developed correlations, including the axial, tangential, and radial velocity distributions, have been tested and validated against data from other studies, showing good agreement. The velocity field correlations can be used to analyze swirling two-phase flow in cyclonic separators and pipes. In part II of this two-part paper, correlations are developed for the turbulent quantities, and core characteristics and stability for swirling two-phase flow. [DOI: 10.1115/1.1849253]

1 Introduction

Compact multiphase cyclonic separators, such as the Gas–Liquid Cylindrical Cyclone (GLCC), are becoming increasingly popular as an attractive alternative to conventional separators. Compact cyclonic separators operate based on centrifugal forces generated by swirling two-phase flow, as opposed to the gravity-based conventional separators. Swirling flow is generated in the GLCC by an inclined and tangential inlet, as shown in Fig. 1. Cyclonic separators are simple, compact, possess low weight, low-cost, require little maintenance, have neither moving nor internal parts and are easy to install and operate. More than 700 GLCC units have already been installed and put to use in the field for various applications in the United States and around the world in the past decade, as reported by Gomez et al. [1].

Figure 2(*A*) presents a schematic of the velocity field in the lower part of the GLCC, namely, the axial and tangential velocities. The radial velocity is an order of magnitude smaller than the other two components. As can be seen, due to the swirling flow, a flow reversal in the axial velocity occurs near the axis of the GLCC. This phenomenon is demonstrated in Figs. 2(*B-1*) and 2(*B-2*), which present velocity field flow visualization with dye injection. In Fig. 2(*B-1*), the blue dye is injected at the axis of the cyclone, whereby it diffuses upward following the flow reversal at the axial region. On the other hand, in Fig. 2(*B-2*), the red dye is injected near the wall and follows the downward velocity in the wall region.

A lack of understanding of the complex multiphase hydrodynamic flow behavior in cyclonic compact separators has inhibited complete confidence in its design and prevented its widespread application. In particular, the prediction of two-phase swirling flow characteristics, such as the continuous-phase velocity field, is required for the proper analysis and design of cyclonic separators. This is the gap that the present study addresses. Correlations have been developed for the continuous-phase flow field, which are required for the analysis of the effect of swirling on the motion of the dispersed-phase (that is coupled with the continuous phase) for the determination of the dispersed-phase void fraction.

2 Literature Review

A pioneering experimental study on local measurements in swirling flow was carried out by Nissan and Bresan [2]. Ito et al. [3] investigated swirl decay in a tangentially injected swirling flow. Velocity field in decaying swirling flow through a pipe was studied by Algifri et al. [4] using a hot-wire probe. Kitoh [5] studied swirling flows generated with guide vanes. It was shown that the swirl intensity decays exponentially in the axial direction. Later, Yu and Kitoh [6] developed an analytical method to predict the decay of swirling flow in a straight pipe.

In a study by Chang and Dhir [7], the turbulent flow field in a tube was investigated by injecting air tangentially into the tube. Profiles for mean velocities in the axial and tangential directions, as well as the Reynolds stresses, were obtained. Kurokawa [8] utilized a Laser Doppler Velocimeter (LDV) and a pitot-tube probe to characterize swirling flow. He confirmed the existence of a complex velocity profile in swirling flow, distinguishing three regions for the tangential velocity component: a forced vortex near the centerline (core region), a free vortex near the wall (wall region), and an intermediate region (annulus region). Erdal [9] measured tangential and axial velocity distributions, as well as their corresponding velocity fluctuations, using a Laser Doppler Velocimeter (LDV) system. He used two liquids of 1 and 7 cP viscosity. However, neither analysis nor correlations development for the turbulent quantities were conducted.

As can be seen from the above literature review, not many studies, either experimental analyses or theoretical development, have been published on swirling two-phase flow. This is the need that the present study attempts to address. In this study, the data acquired by the previous investigators, as mentioned above, are collected, presented, and used to develop correlations for the continuous-phase velocity field, which are important in the prediction of the dispersed-phase characteristics occurring in swirling two-phase flow that takes place in cyclonic separators, such as the GLCC.

---

[1] Gas–Liquid Cylindrical Cyclone (GLCC©)—Copyright The University of Tulsa, 1994.

Contributed by the Fluids Engineering Division for publication in the JOURNAL OF FLUIDS ENGINEERING. Manuscript received by the Fluids Engineering Division May 27, 2003; revised manuscript received June 8, 2004. Associate Editor: Joseph Katz.

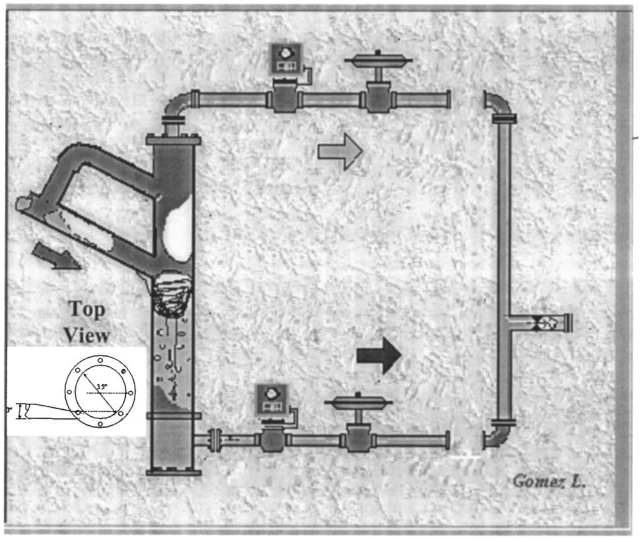

Fig. 1 Schematic of GLCC separator

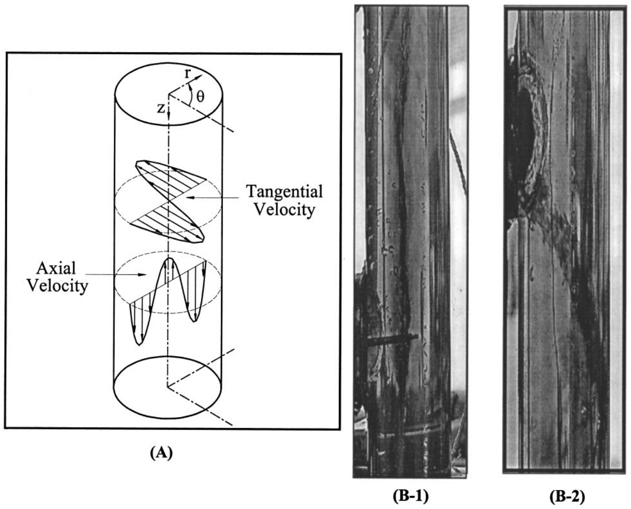

(A)

(B-1)

(B-2)

Fig. 2 Schematic of swirling flow field and cyclone coordinate system

3 Experimental Program

Data from several investigators, namely, Algifri et al. [4], Kitoh [5], Chang and Dhir [7] and Erdal [9] are collected and presented here with the purpose of developing correlations or validating existing correlations to characterize and predict swirling flow behavior. First, swirling flow data in cyclonic separators will be presented. For this case the swirling flow is generated by a tangential inlet. Second, data for swirling flow in a straight pipe will be presented, where the swirl is induced by vanes installed inside the pipe.

3.1 Flow Field in Cyclonic Separators. In this section the Erdal [9] local measurement results of the flow field are presented, followed by the results for turbulent quantities. The local measurement results of the swirling flow field are presented in the form of contour plots. These plots help to shed more light on the hydrodynamic structure of the swirling flow.

3.1.1 Velocity Contour Plots. Figures 3 and 4 show contour plots of the axial and tangential velocity distributions measured at 24 axial locations below the cyclonic separator inlet, respectively. The results are normalized with respect to U_{av}, where U_{av} is the average bulk velocity, namely, the volumetric flow rate per unit area.

The axial velocity contour plots presented in Fig. 3 show clearly an upward flow reversal region, with negative axial velocity, in the core region around the cyclone axis. The flow reversal region is not axisymmetric and has a helical shape. The magnitude of both the upward (reverse flow) and downward (outer region) flow decrease as the flow moves downward.

The tangential velocity, shown in Fig. 4, is positive on the left-hand side and is negative on the other side (right). This is due to the rotation of the flow. As can be seen, the tangential velocity is high near the wall region and it decays toward the centerline. The location of zero or low tangential velocity has also a helical path, similar to the one observed in the axial velocity contours.

3.1.2 Velocity Profiles. The variation of the axial and tangential velocity profiles with axial position is presented in Figs. 5 and 6, respectively. As can be seen, both the axial and tangential profiles vary along the cyclone axis, mainly due to the decay of the swirl. In general, the data show that the flow is not symmetric with respect to the pipe axis, whereby the reverse flow region whips around with a helical shape. This is due to the nonsymmet-

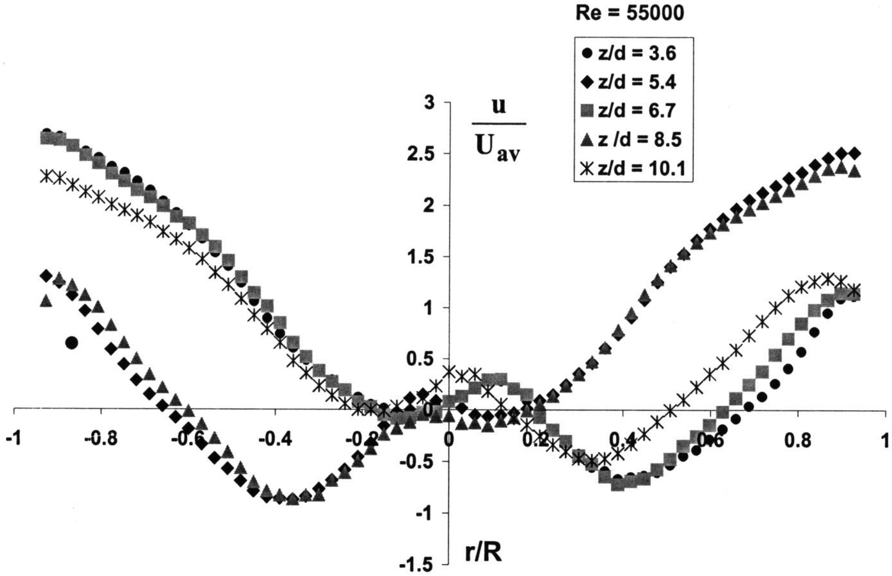

Fig. 5 Variation of axial velocity profile with axial position after Erdal [9]

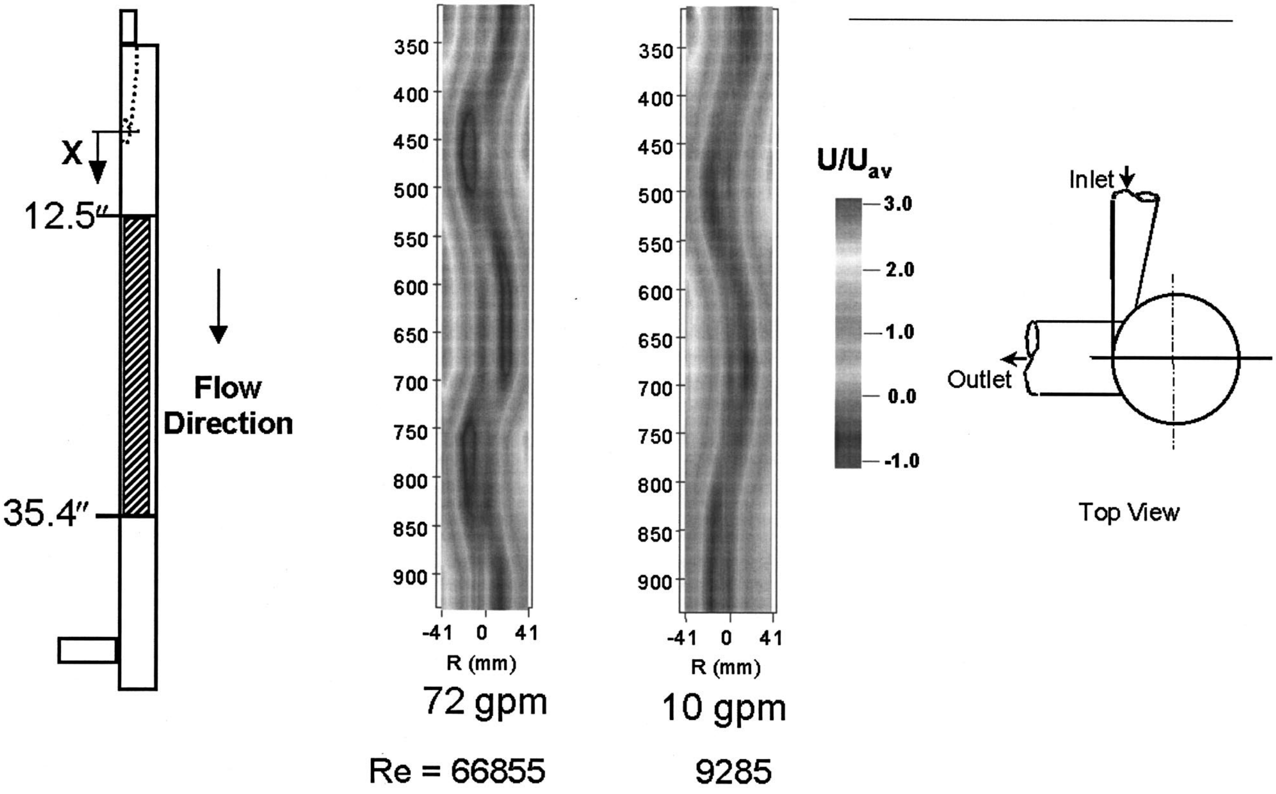

Fig. 3 Axial velocity for single inclined gradually reducing nozzle area inlet configuration after Erdal [9]

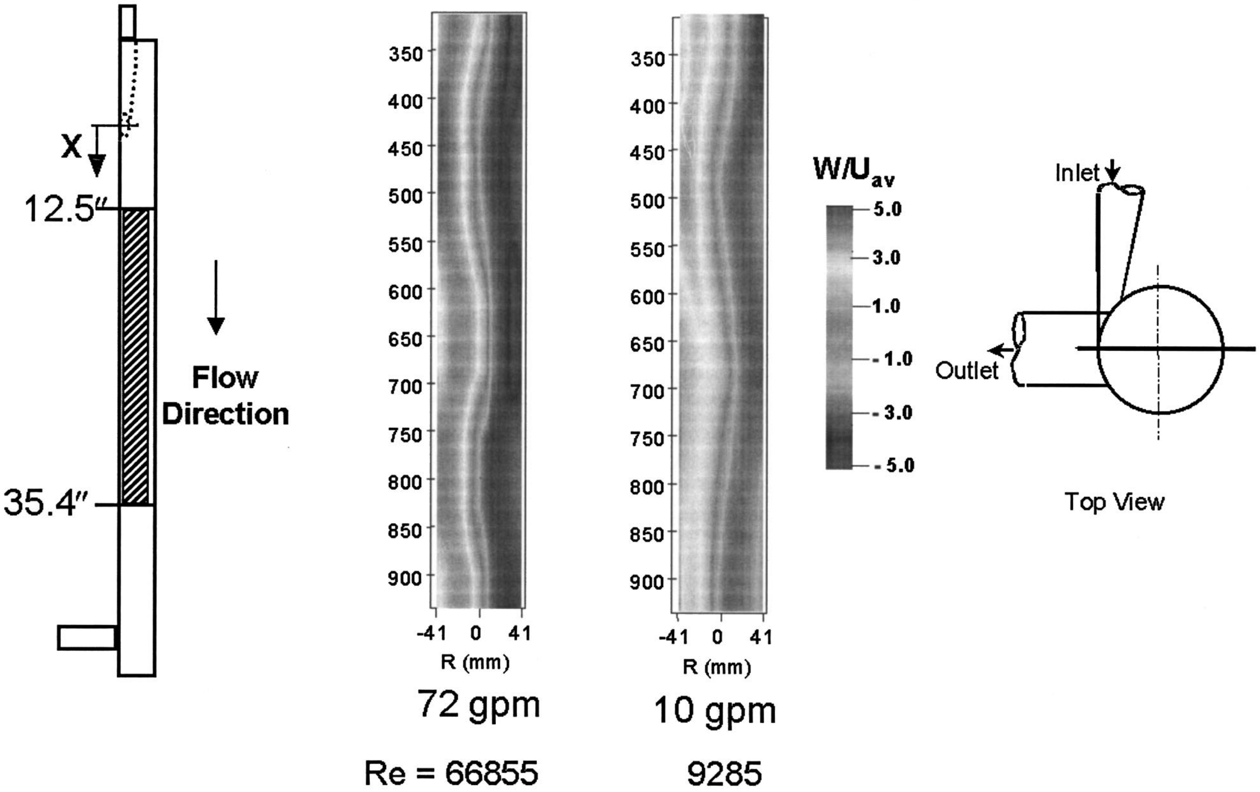

Fig. 4 Tangential velocity for single inclined gradually reducing nozzle area inlet configuration after Erdal [9]

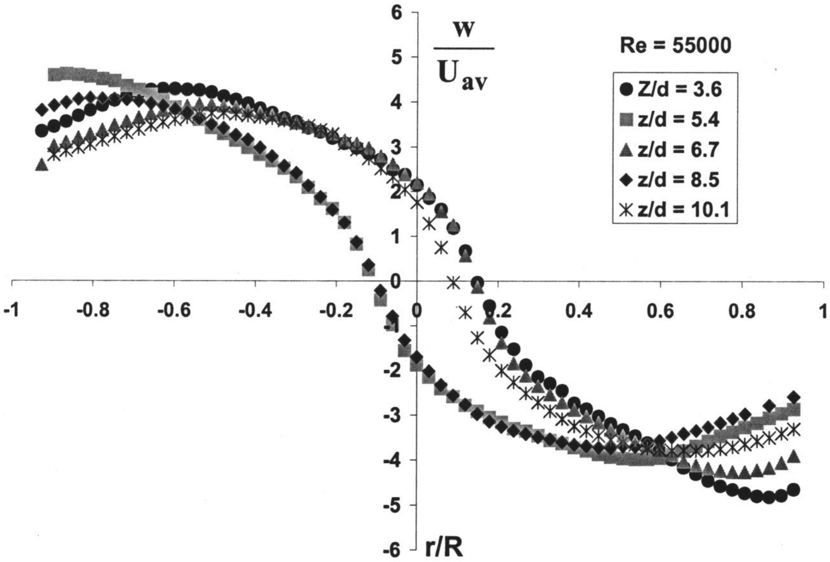

Fig. 6 Variation of tangential velocity profile with axial position after Erdal [9]

ric inlet of the GLCC. When the flow is injected through symmetrical inlet arrangement (e.g., two or four), this helical shape is eliminated and the flow becomes more symmetrical around the cyclone centerline Erdal [9].

3.2 Velocity Field in Straight Pipe. In this section the data collected from the literature as reported by Algifri et al. [4], Kitoh [5], and Chang and Dhir [7] are presented in terms of the flow field and turbulent quantities, similar to the way the Erdal [9] data were presented for the cyclones.

3.2.1 Axial Velocity Distribution. Figures 7 and 8 show the profiles of axial mean velocity, u, after Kitoh [5] and Chang and Dhir [7], respectively. The axial mean velocity, u, normalized with respect to U_{av}, is given at various locations along the pipe axis. The data show a low or negative upward velocity in the core region surrounded by relatively high downward velocity in the annular region. The presented data show that the flow is approximately axisymmetric and that the reverse flow occurs at the central region for all cases.

3.2.2 Radial Velocity Distribution. The radial mean velocity distributions, v, estimated from the continuity equation and normalized with respect to U_{av}, are given in Figs. 9 and 10. The experimental results indicate that the radial velocity component is three order of magnitudes $O(100-1000)$ smaller, as compared to the average axial or tangential velocities.

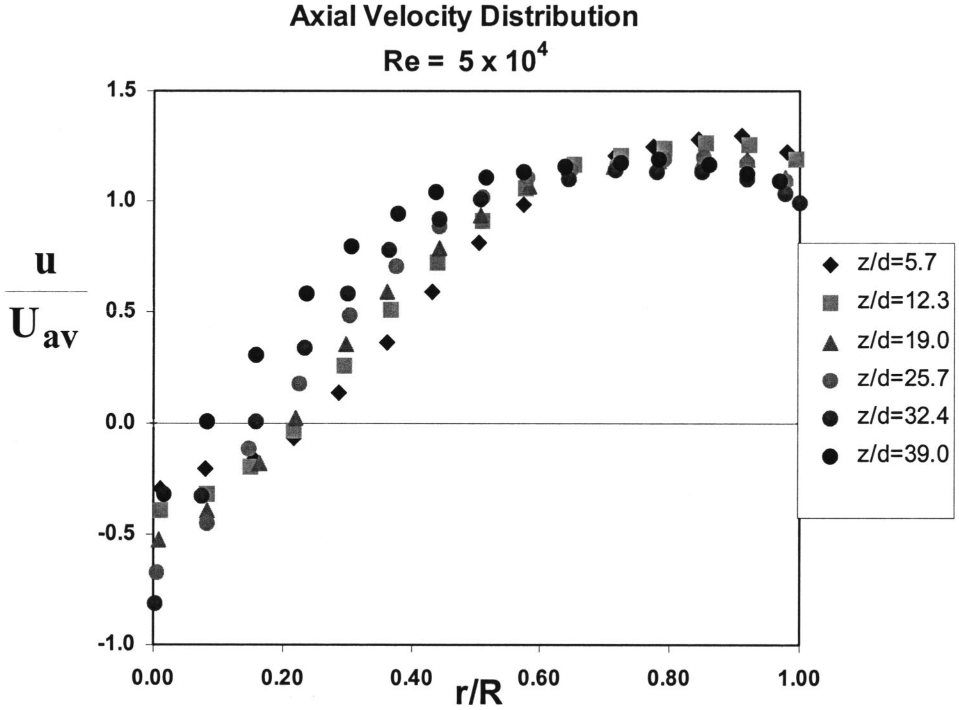

Fig. 7 Axial velocity distribution after Kitoh [5]

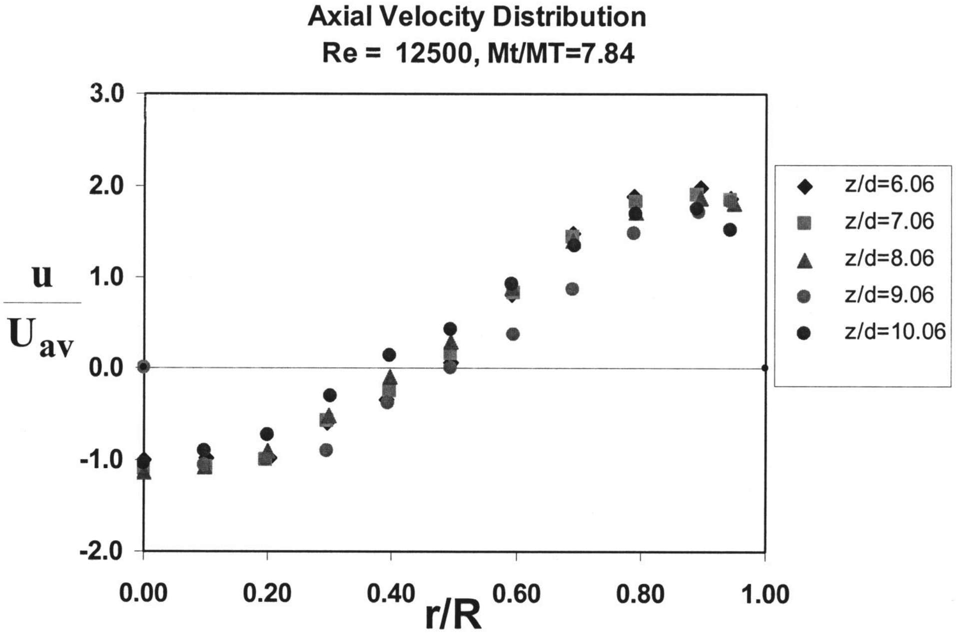

Fig. 8 Axial velocity distribution after Chang and Dhir [7]

It can also be seen that the magnitude of the radial velocity increases with increasing swirl intensity and that the location where the radial velocity is maximum shifts toward the pipe centerline, where the swirl intensity is maximum. The radial velocity occurs due to the variations of the axial velocity in the direction of the flow.

3.2.3 Tangential Velocity Distribution. The tangential mean velocity, w, normalized with respect to U_{av}, is plotted in Figs. 11, 12, and 13. These figures show that the mean tangential velocity increases with radial position in the core region, and reaches a maximum value; thereafter it decreases with radial position in the annular region and near the wall. The velocity gradient near the wall is steep, thus, the tangential velocity rapidly decreases to zero at the wall. From these figures it can also be seen that the tangential velocity indeed has a shape of a Rankine vortex, which has a three-region structure consisting of the core (forced vortex), annular (transition), and wall (free vortex) regions. The wall region is thin, with a very narrow boundary layer.

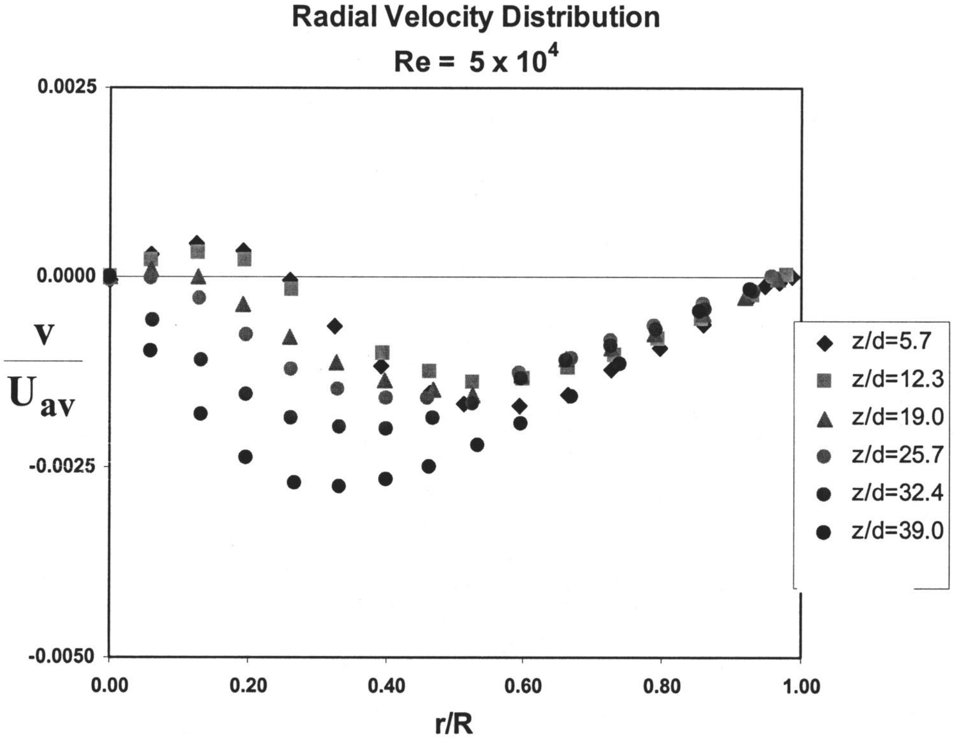

Fig. 9 Radial velocity distribution after Kitoh [5]

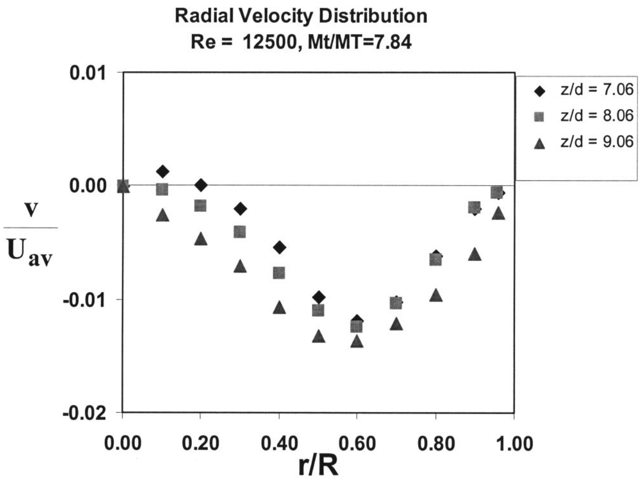

Fig. 10 Radial velocity distribution after Chang and Dhir [7]

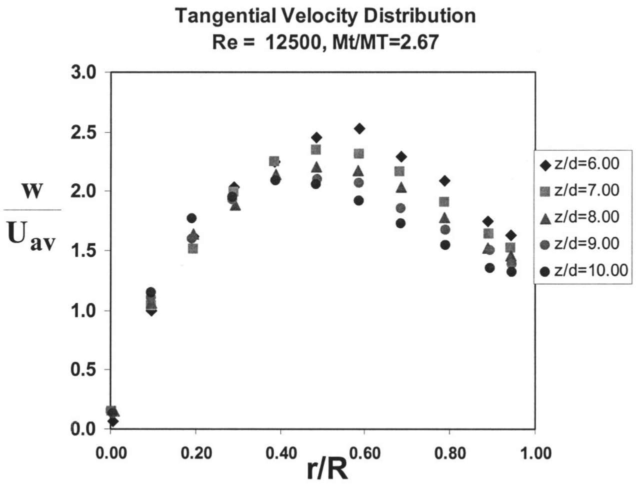

Fig. 13 Tangential velocity distribution after Chang and Dhir [7]

4 Swirling Flow Mechanistic Model

Typical axial and tangential velocity profiles are shown schematically in Fig. 2. Indeed, the data that were presented in the experimental program section confirm these hydrodynamic flow behavior. Based on several sets of swirling flow experimental data available in the literature, Mantilla [10] and later Erdal [9] modified an existing swirl intensity correlation, proposed originally by Chang and Dhir [7], to predict the flow field, as given in the next section.

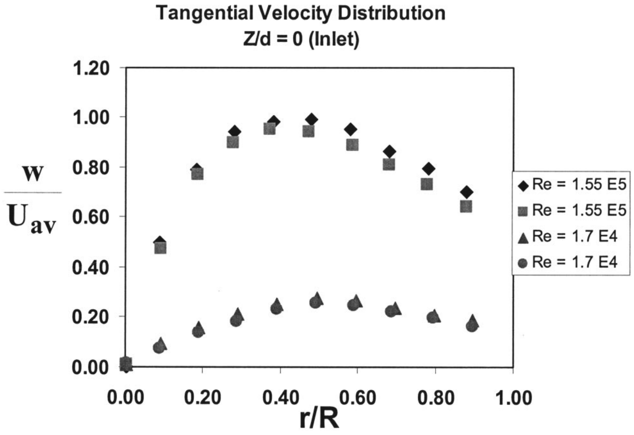

Fig. 11 Tangential velocity distribution after Algifri [4]

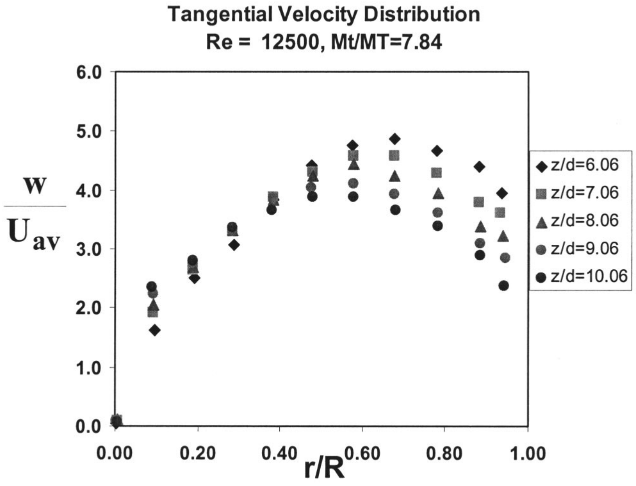

Fig. 12 Tangential velocity distribution after Chang and Dhir [7]

4.1 Swirl Intensity Decay Number. The swirling motion decays as a result of wall friction. The swirl intensity concept is used to characterize this decay. For axisymmetric single-phase flow, the swirl intensity, Ω, is defined as the ratio of the tangential to total momentum flux at any axial location, namely

$$\Omega=\frac{2\pi\rho\int_0^R u_z u_\theta r\,dr}{\pi\rho R^2 U_{av}^2} \tag{1}$$

The numerator of Eq. (1) corresponds to the tangential momentum flux integrated over the pipe cross-sectional area, while the denominator is the total momentum flux based on the average bulk velocity. The Erdal [9] correlation for the swirl intensity is given by

$$\Omega=0.67\,\mathrm{Re}^{0.13}\Bigg(\frac{M_t}{M_T}\Bigg(1-\exp\Bigg(-\frac{n}{2}\Bigg)\Bigg)\Bigg)^{2}\Bigg)^{0.93} \\ \times\exp\Bigg[-\frac{1}{2}\Bigg(\frac{M_t}{M_T}\Bigg(1-\exp\Bigg(-\frac{n}{2}\Bigg)\Bigg)\Bigg)^{4}\Bigg)^{0.35}\mathrm{Re}^{-0.16}\Bigg(\frac{z}{d_{sep}}\Bigg)^{0.7}\Bigg] \tag{2}$$

where n is the number of tangential inlets and M_t/M_T is the ratio of the tangential momentum flux to the total momentum flux at the inlet, as given by

$$\frac{M_t}{M_T}=\left(\frac{u_{Linlet}\cos\beta}{U_{av}}\right)=\frac{u_{t\ is}}{U_{av}} \tag{3}$$

where u_{Linlet} is the liquid velocity at the inlet and β is the inlet inclination angle. The liquid velocity at the inlet can be calculated from the nozzle analysis developed by Gomez [11], which can then be used to compute the tangential velocity of the liquid at the inlet slot, $u_{t\ is}$. The Reynolds number in Eq. (2) is defined as for pipe flow, based on the bulk velocity and the diameter of the cyclone.

4.2 Swirling Flow Velocity Distribution. The swirl intensity is related, by definition, to the local axial and tangential velocities. Therefore, it is assumed that for a specific axial location, the swirl intensity prediction can be used to calculate these velocity profiles.

4.2.1 Mean Axial Velocity Profile. Mantilla [10] developed a correlation for the axial velocity profile, as follows:

$$\frac{u_z}{U_{av}}=\frac{2}{C}\left(\frac{r}{R}\right)^3-\frac{3}{C}\left(\frac{r}{R}\right)^2+\frac{0.7}{C}+1, \tag{4}$$

where

$$C=3\left(\frac{r_{rev}}{R}\right)^2-2\left(\frac{r_{rev}}{R}\right)^3-0.7, \tag{5}$$

$$\frac{r_{rev}}{R}=0.5-0.65\exp\left(-\frac{\Omega}{0.6}\right) \tag{6}$$

The reversal flow radius (or the so-called capture radius), r_{rev}, is the radial location for which the axial velocity u_z is zero.

4.2.2 Mean Tangential Velocity Profile. The tangential velocity distribution, except in the vicinity of the wall, can be approximated by a Rankine Vortex type. Algifri et al. [4] proposed the following equation for the tangential velocity profile:

$$\frac{u_\theta}{U_{av}}=\frac{T_m}{\left(\frac{r}{R}\right)}\left\{1-\exp\left[-B\left(\frac{r}{R}\right)^2\right]\right\} \tag{7}$$

where u_θ is the local tangential velocity, T_m is related to the maximum moment of the tangential velocity, and B is related to the radial location of this maximum velocity. Correlations presented by Mantilla [10], based on experimental data, are used to determine the values of T_m and B, as follows:

$$T_m=0.9\Omega-0.05, \tag{8}$$

$$B=3.6+20\exp\left(-\frac{\Omega}{0.6}\right) \tag{9}$$

4.2.3 Mean Radial Velocity Profile. As a result of the high swirl intensity, a reduction of the axial velocity near the centerline occurs, that might reverse the axial flow near the centerline of the pipe. Due to the swirl intensity decay, variations of the axial velocity component cause variations in the radial velocity component to satisfy continuity conditions. Thus, with knowledge of the axial velocity distribution, and using the continuity equation, the mean radial velocity distribution is obtained, as presented by Gomez [12]:

$$u_r=\frac{1}{r}\int_0^r\frac{\partial(ru_z)}{\partial z}dr \tag{10}$$

$$\frac{u_r}{U_{av}}=-\frac{R}{20}\left(\frac{dC}{C^2}\right)\left[64\left(\frac{r}{R}\right)^4-60\left(\frac{r}{R}\right)^3-11\left(\frac{r}{R}\right)^2+7\left(\frac{r}{R}\right)\right] \tag{11}$$

where

$$dC=\left[6\left(\frac{r_{rev}}{R}\right)-6\left(\frac{r_{rev}}{R}\right)^2\right]dr_{rev} \tag{12}$$

$$d\Omega=-0.35\,\mathrm{Re}^{-0.16}\left(\frac{M_t}{M_T}\left(1-\exp\left(-\frac{n}{2}\right)\right)^4\right)^{0.35}\left(\frac{z}{d_{sep}}\right)^{-0.3}\Omega \tag{13}$$

$$dr_{rev}=\frac{13}{12}d\Omega\exp\left(-\frac{\Omega}{0.6}\right) \tag{14}$$

where C and r_{rev}/R are the same as that used in the calculation of the mean axial velocity (Eqs. 5 and 6).

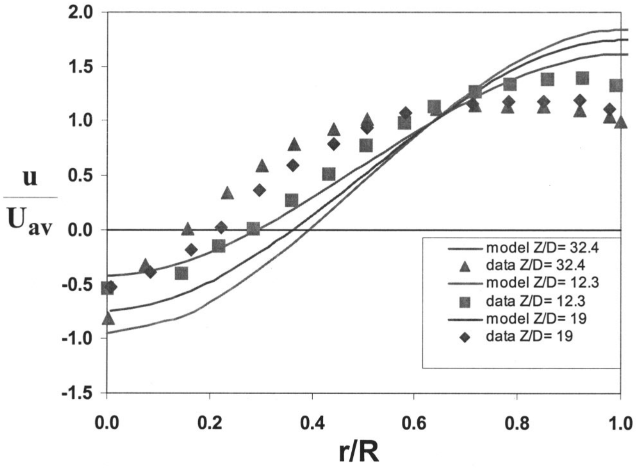

Fig. 14 Mean axial velocity comparisons for Kitoh data [5]

5 Simulation and Results

In this section, the developed swirling flow velocity distribution correlations are tested against data from different published studies for the continuous-phase swirling flow. The developed correlations for axial, tangential, and radial velocity profiles are evaluated against the data presented by Algifri [4], Kitoh [5], and Chang and Dhir [7], as summarized by Gomez [12]. In this section, only Kitoh [5] data are used in this comparison.

Mean Axial Velocity Profile: Figure 14 presents a comparison between the developed correlation and experimental data for the mean axial velocity. Good agreement is observed between the data and the predictions.

Mean Tangential Velocity Profile: A comparison between the developed correlation and experimental data for the mean tangential velocity is shown in Fig. 15. Very good agreement is observed between the data and the predictions.

Mean Radial Velocity Profile: Figure 16 presents a comparison between the correlation for the mean radial velocity, developed in this study, against experimental data. The comparisons show fair agreement with respect to both trend and magnitude.

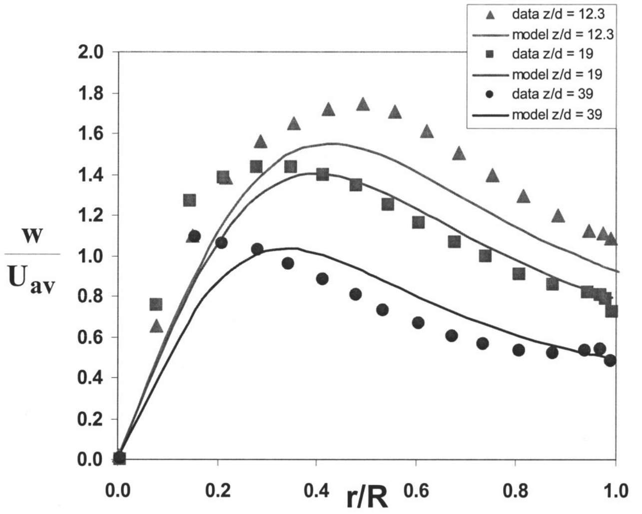

Fig. 15 Mean tangential velocity comparisons for Kitoh data [5]

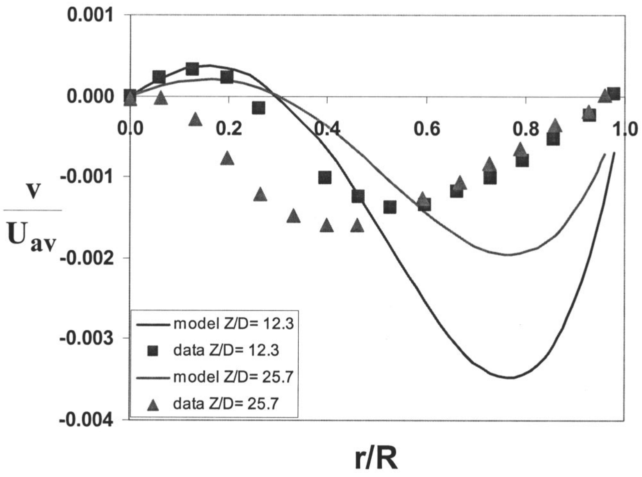

Fig. 16 Mean radial velocity comparisons for Kitoh data [5]

6 Conclusions

The hydrodynamics of dispersed two-phase swirling flow in the lower part of the cyclone and in a straight pipe were studied both experimentally and theoretically. Following are the main conclusions of the study:

- Published local LDV measurements for swirling flow field have been analyzed and utilized to develop and validate cyclone and pipe swirling flow field prediction correlations. The correlations include the axial, tangential and radial velocity distributions.
- The developed correlations for the continuous-phase swirling flow field have been tested against data from other studies, not used in the development of the correlations. All the correlations, including the axial, tangential, and radial velocity distributions show good agreement with the data.
- The following are concluded with respect to the swirling flow velocity field:

i. *Mean Axial Velocity Profile:* A low or negative upward velocity in the centerline region surrounded by relatively high downward velocity in the wall region.

ii. *Mean Tangential Velocity Profile:* The mean tangential velocity increases with the radial position from the centerline toward the wall, reaching a maximum value; thereafter it decreases with the radial position near the wall region. The tangential velocity indeed exhibits the shape of a Rankine vortex.

iii. *Mean Radial Velocity Profile:* The mean radial velocity distribution is estimated from the continuity equation. The experimental results indicate that the radial velocity component is three orders of magnitude $O(100-1000)$ smaller as compared to the average axial or tangential velocities.

Acknowledgment

The authors wish to thank the US-DOE (Contract No. DE-FC26-03NT15416) and the Tulsa University Separation Technology Projects (TUSTP) members for supporting this project.

Nomenclature

B = radial location of the maximum velocity
C = coefficient
d = diameter (m)
M = momentum (Newton)
r = radial direction
R = pipe radius (m)
Re = Reynolds number
T_m = parameter related to maximum moment of tangential velocity
u = continuous-phase velocity (m/s)
U_{av} = average bulk velocity (m/s)
z = axial direction

Greek Letters

β = inclination angle measured from horizontal
θ = tangential direction of cylindrical coordinates
ρ = density (kg/m^3)
Ω = swirl intensity

Subscripts

av = average
inlet = inlet
is = inlet slot
L = liquid
r = radial direction of cylindrical coordinates
rev = flow reversal
sep = separator
t = tangential
T = total
z = axial direction of cylindrical coordinates

References

[1] Gomez, L., Mohan, R., Shoham, O., and Kouba, G., 2000, "Enhanced Mechanistic Model and Field Application Design of Gas–Liquid Cylindrical Cyclone Separator," SPE J., **5**, pp. 190–198.
[2] Nissan, A. H., and Bresan, V. P., 1961, "Swirling Flow in Cylinders," AIChE J., **7**, pp. 543–547.
[3] Ito, S., Ogawa, K., and Kuroda, C., 1979, "Decay Process of Swirling Flow in a Circular Pipe," Int. Chem. Eng., **19**, pp. 600–611.
[4] Algifri, A. H., Bhardwaj, R. K., and Rao, Y. V. N., 1988, "Turbulence Measurements in Decaying Swirl Flow in a Pipe," Appl. Sci. Res., **45**, pp. 233–250.
[5] Kitoh, O., 1991, "Experimental Study of Turbulent Swirling Flow in a Straight Pipe," J. Fluid Mech., **225**, pp. 445–479.
[6] Yu, S. C. M., and Kitoh, O., 1994, "General Formulation for the Decay of Swirling Motion Along a Straight Pipe," Int. Commun. Heat Mass Transfer, **21**, pp. 719–728.
[7] Chang, F., and Dhir, V. K., 1994, "Turbulent Flow Field in Tangentially Injected Swirl Flows in Tubes," Int. J. Heat Fluid Flow, **15**, pp. 346–356.
[8] Kurokawa, J., 1995, "Gas–Liquid Flow Characteristics and Gas-Separation Efficiency in a Cyclone Separator," ASME FED-Vol. 225, Gas Liquid Flows, pp. 51–57.
[9] Erdal, F., 2001, "Local Measurements and Computational Fluid Dynamic Simulations in a Gas–Liquid Cylindrical Cyclone Separator," Ph.D. dissertation, The University of Tulsa.
[10] Mantilla, I., 1998, "Bubble Trajectory Analysis in GLCC Separators," M.S. thesis, The University of Tulsa.
[11] Gomez, L. E., 1998, "A State-of-the Art Simulator and Field Application Design of Gas–Liquid Cylindrical Cyclone Separators," M.S. thesis, The University of Tulsa, 1998.
[12] Gomez, L. E., 2001, "Dispersed Two-Phase Swirling Flow Characterization for Predicting Gas Carry-Under in Gas–Liquid Cylindrical Cyclone Compact Separator," Ph.D. dissertation, The University of Tulsa.

Swirling Gas–Liquid Two-Phase Flow—Experiment and Modeling Part II: Turbulent Quantities and Core Stability

L. Gomez

R. Mohan

O. Shoham

The University of Tulsa,
600 S. College Ave.,
Tulsa, OK 74104

In Part I of this two-part paper on swirling gas–liquid two-phase flow, correlations have been developed for the continuous liquid-phase velocity field under swirling conditions, such as that occurring in the lower part of the Gas–Liquid Cylindrical Cyclone (GLCC©[1]) compact separator. The developed correlations, including the axial, tangential, and radial velocity distributions, are applicable for swirling flow in both cyclones and pipe flow. The first objective of this paper is to extend the study of Part I by developing correlations for the turbulent quantities of the continuous liquid phase, including the turbulent kinetic energy and its dissipation rate and Reynolds shear stresses. The second objective is to study experimentally and theoretically two-phase swirling flow gas-core characteristics and stability. The first objective has been met utilizing local LDV measurements acquired for swirling flow. The developed turbulent quantities correlations have been tested against data from other studies, showing good agreement. For the second objective, experimental data have been acquired under swirling two-phase flow conditions. A model for the prediction of the gas-core diameter and stability in swirling flow field has been developed, based on the turbulent kinetic energy behavior predicted by the developed correlations. Good agreement is observed between the model predictions and the data. [DOI: 10.1115/1.1849254]

1 Introduction

Compact multiphase cyclonic separators, such as the Gas–Liquid Cylindrical Cyclone (GLCC) operate based on centrifugal forces generated by swirling two-phase flow, as opposed to the gravity based conventional separators. A review of applications of compact cyclonic separators in the field is given by Gomez et al. [1]. Figure 1 represents a schematic of the swirling flow velocity field in the lower part of a cyclone, namely, the axial and tangential velocities.

In Part I of this two-part paper, correlations have been developed for the continuous liquid-phase velocity field under swirling conditions, including the axial, tangential, and radial velocity distributions, which are applicable for both cyclones and pipe flow.

For a proper prediction of the hydrodynamic flow behavior in the cyclone, correlations must be developed for the turbulent quantities. The turbulent quantities are required for the analysis of bubble/droplet breakup and coalescence, e.g., inlet gas bubble entrainment and remixing at the GLCC entrance region.

2 Literature Review

Experimental studies on local measurements in swirling flow were carried out by Nissan and Bresan [2] and Ito et al. [3]. Turbulent quantities in decaying swirling flow through a pipe were studied by Algifri et al. [4]. Kitoh [5] and Yu and Kitoh [6] studied swirling flows generated with guide vanes and developed an analytical method to predict the decay of swirling flow in a straight pipe.

Reynolds stress data for turbulent flow were presented by Chang and Dhir [7] for swirling flow generated by injecting air tangentially into a tube. Kurokawa [8] utilized a Laser Doppler Velocimeter (LDV) and a pitot-tube probe to characterize swirling flow. Erdal [9] utilized a Laser Doppler Velocimeter (LDV) to measure swirling flow velocity field and the corresponding velocity fluctuations in a cyclone with an inclined tangential inlet.

A review of the above literature indicates that no correlations for the turbulent quantities have been developed on swirling two-phase flow. In this study, the data acquired by the previous investigators, as mentioned above, are presented and used to develop correlations for the turbulent quantities, which are important in the prediction of the behavior of the dispersed-phase in swirling two-phase flow.

3 Experimental Program

Data from several investigators, namely, Algifri [4], Kitoh [5], Chang and Dhir [7] and Erdal [9] are collected and presented here with the purpose of developing correlations or validating existing correlations to characterize and predict swirling flow behavior. Similar to Part I, first, swirling flow turbulent quantities data in cyclonic separators with a tangential inlet will be presented. Then, data for swirling flow in a straight pipe, induced by vanes installed inside the pipe, will be presented.

3.1 Turbulent Quantities in Cyclonic Separators. The two-component LDV system used by Erdal [9] is also capable of determining the standard deviation of the sampled data, which represents the turbulent fluctuations ($\sqrt{\overline{(u')^2}}$ and $\sqrt{\overline{(w')^2}}$). The statistical quantities, such as the mean velocity ($\overline{\nu}$) and the standard deviation (σ_ν) of the data are calculated with the equations given below:

$$\overline{\nu}=\frac{\Sigma\,\nu T}{\Sigma\,T}, \tag{1}$$

$$\sigma_\nu=\sqrt{\left(\frac{\Sigma\,\nu^2 T}{\Sigma\,T}-\overline{\nu}^2\right)}. \tag{2}$$

---

[1] Gas–Liquid Cylindrical Cyclone (GLCC©—Copyright The University of Tulsa, 1994.

Contributed by the Fluids Engineering Division for publication in the JOURNAL OF FLUIDS ENGINEERING. Manuscript received by the Fluids Engineering Division May 27, 2003; revised manuscript received June 8, 2004. Associate Editor: Joseph Katz.

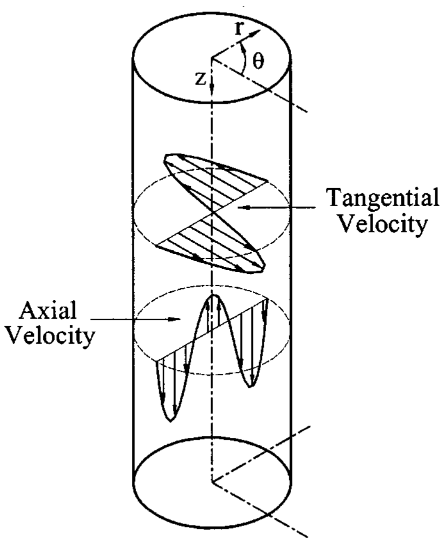

Fig. 1 Schematic of Swirling Flow Field and Cyclone Coordinate System

Therefore, axial and tangential velocity fluctuations can be directly determined from the LDV data. The measurements show that fluctuations in the axial and tangential directions have the same order of magnitude. To obtain an estimate of the turbulent kinetic energy, the radial velocity fluctuations are approximated, assuming it to be the average of the axial and tangential velocity fluctuations. The radial velocity fluctuations and turbulent kinetic energy are calculated by the following equations:

$$\sqrt{\overline{(v')^2}} = \frac{1}{2}\left(\sqrt{\overline{(u')^2}} + \sqrt{\overline{(w')^2}}\right), \tag{3}$$

$$k = \tfrac{1}{2}\left(\overline{(u')^2} + \overline{(v')^2} + \overline{(w')^2}\right). \tag{4}$$

3.1.1 Turbulent Kinetic Energy Contour Plots. The calculated turbulent kinetic energy distributions, k, normalized with U_{av}^2 are presented in contour plots in Fig. 2. As can be seen, a maximum local peak value of k occurs around the centerline, which initially increases axially as the flow moves downward. However, there exists an axial location where the turbulence starts decreasing, and eventually the turbulent intensity converges to the value of swirling-free pipe flow. The high turbulence center region exhibits large instability of the flow near the centerline.

3.1.2 Turbulent Intensities. Figures 3 and 4 present the axial and tangential turbulent intensities, or normal Reynolds stresses, at one axial location, $z/d = 3.6$ below the inlet, for different Reynolds numbers, Re$=$9200 and Re$=$55 000, respectively. The Reynolds number is global, based on the axial bulk velocity U_{av}. Both figures exhibit low (flat) intensity distribution near the wall region and high intensities around the centerline, and both demonstrate the effect of the Reynolds number on the intensity.

A very peculiar behavior is exhibited by both turbulent kinetic energy and Reynolds shear stresses in the core region, as shown in Figs. 5 and 6, respectively, at Re$=$55 000 and various values of z/d. As can be seen, both quantities tend to increase with the axial location. The reason for this behavior is that as the swirl decays with axial position, the turbulent energy dissipation increases. Also, both normal stresses show low (flat) intensity near the wall region, while at the core region high intensities are observed.

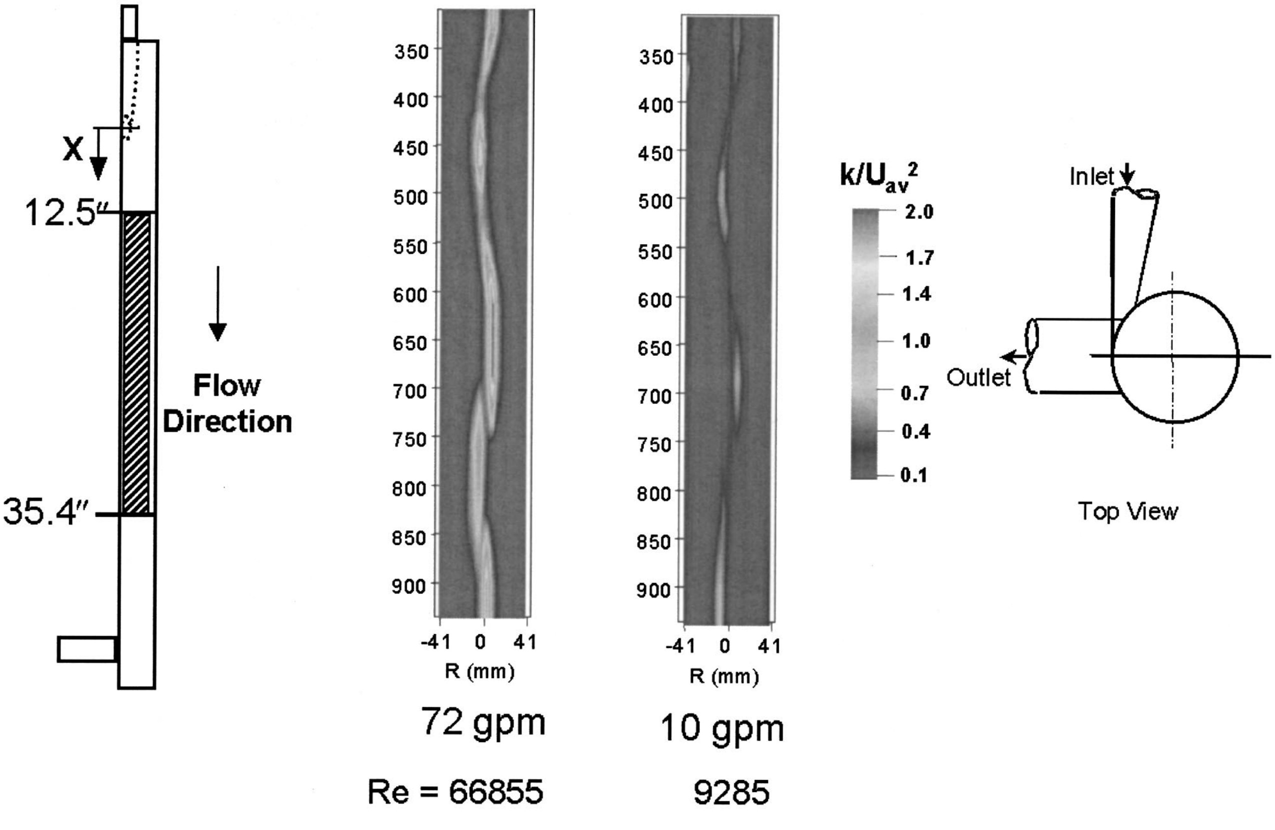

Fig. 2 Turbulent Kinetic Energy for Gradually Reducing Inlet Nozzle Configuration after Erdal [9]

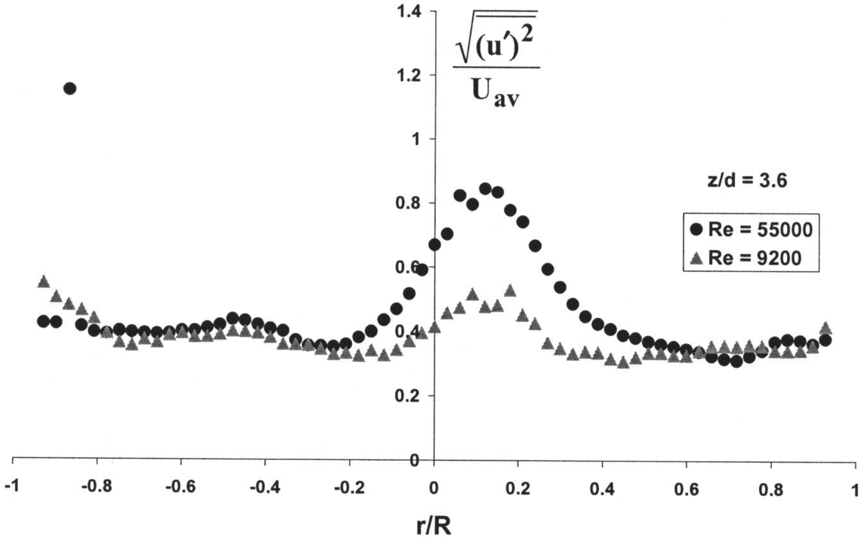

Fig. 3 Axial Normal Reynolds Stress Distribution after Erdal [9]

3.2 Turbulent Quantities in Straight Pipe. The same experimental datasets, as described in the flow field section, are also utilized for the presentation of the turbulent intensity and Reynolds stresses. Since Erdal [9] used a two-component LDV system, only the $\overline{u'w'}$ values were reported, while other investigators have provided a complete set of data of turbulent flow.

3.2.1 Turbulent Intensities. Figures 7, 8, and 9 (after Algifri et al. [4]) show the radial distribution of the normal stresses $\sqrt{\overline{u'^2}}$, $\sqrt{\overline{v'^2}}$, and $\sqrt{\overline{w'^2}}$, normalized with U_{av}. This is followed by a brief summary of Kitoh's discussion on turbulent swirling flow phenomena, which are later confirmed by the Chang and Dhir [7] and Erdal [9] data that are presented in this study.

The data reveal that turbulent intensity has a large magnitude. In a normal (swirl-free) pipe flow, all the components of the turbulent intensities are observed to have high values in the vicinity of the pipe wall, whereas the swirling has a tendency to increase these intensities in the region close to the axis of the pipe. Among the three components, $\sqrt{\overline{v'^2}}$, the radial component shows the most significant increase, becoming three times larger than that of swirling-free pipe flow, for Kitoh's data [5]. This might be the reason for the performance enhancement exhibited in heat transfer applications operating under swirling flow. While the turbulent intensity in the annular region reduces gradually as the swirl decays, it increases in the core region. In the core region very low-frequency motion prevails, while in the outer regions (annular and wall) the fluctuations include high-frequency motion, as expected in turbulent flow. This peculiar frequency observed in the core region might be the result of an inertial wave generated by the rotating motion, which prevails as the flow is nondissipative. Thus, the tangential velocity in swirling flow has a significant influence on the flow structure.

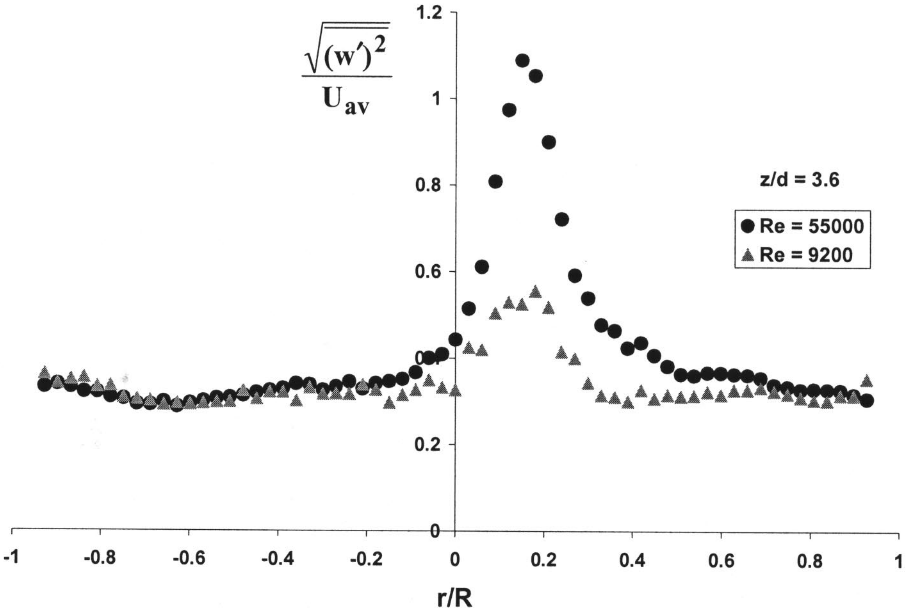

Fig. 4 Tangential Normal Reynolds Stress Distribution after Erdal [9]

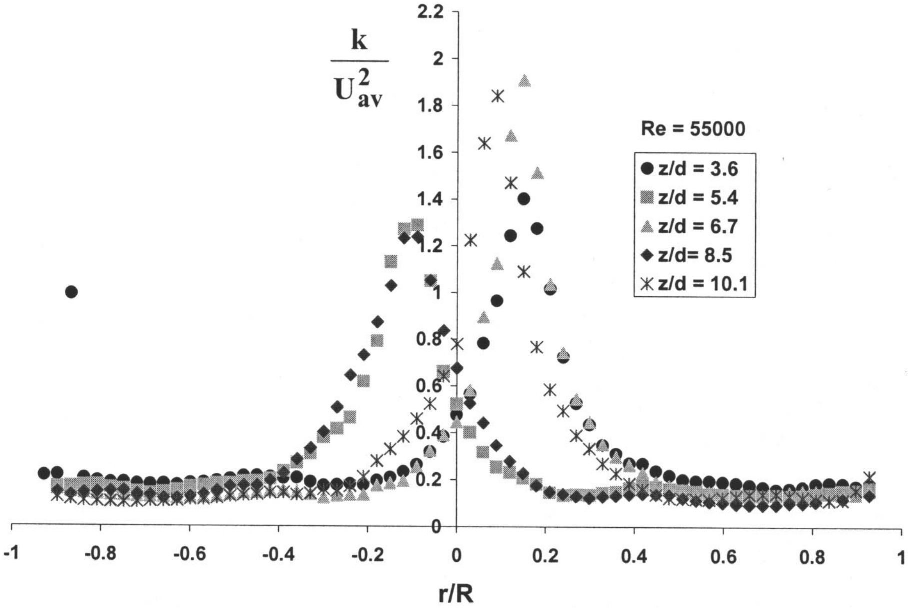

Fig. 5 Turbulent Kinetic Energy Distribution after Erdal [9]

3.2.2 Turbulent Kinetic Energy. The turbulent kinetic energy, *k*, is analyzed in this study, aimed at developing turbulent flow correlations, instead of using normal Reynolds stress expressions. Figures 10 and 11 show the turbulent kinetic energy, *k*, normalized with U_{av}^2, for Algifri et al. [4] and Kitoh [5], respectively.

Reynolds Stresses: The radial distributions of the Reynolds shear stresses are shown in Figs. 12, 13, and 14 (after Algifri et al. [4]). The figures display the dependence of the Reynolds shear stress on the Reynolds number and the axial location. Generally, the Reynolds stress component $\overline{u'v'}$ decreases in magnitude as the swirl decays and changes its sign (see Fig. 12). It is negative near the wall or annular region, where the flow slows down, but it is positive in the core region, where the axial velocity increases in the axial direction. As can be seen from Fig. 13, the component $\overline{v'w'}$ presents a change in its sign from the pipe centerline toward the wall. This is due to the nature of flow in the core and the outer regions. The magnitude of $\overline{v'w'}$ is negative and large in the annular region, while it is small and positive in the core region. It can also be noticed that the location where $\overline{v'w'}$ changes its sign has a tendency to move toward the wall as the swirl decreases, which is similar to the distribution of the mean tangential velocity given in the previous section. For the case of swirl-free pipe, the component $\overline{v'w'}$ does not exist.

Since angular momentum is transferred in the downstream direction, the magnitude of $\overline{u'w'}$ should be mostly positive, decreasing as the swirl decays. Also, as can be seen from Fig. 14, in the region around the pipe centerline where the forced vortex behavior of the tangential velocity is dominant, $\overline{u'w'}$ has a large positive value. However, in the outer region where the tangential velocity is of the free-vortex type, small values of $\overline{u'w'}$ do exist.

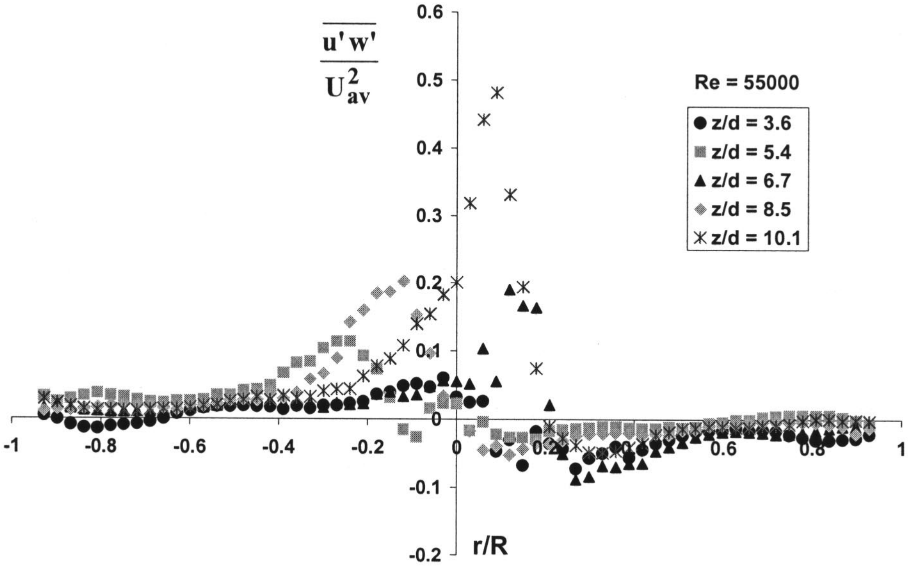

Fig. 6 Reynolds Shear Stress Distribution after Erdal [9]

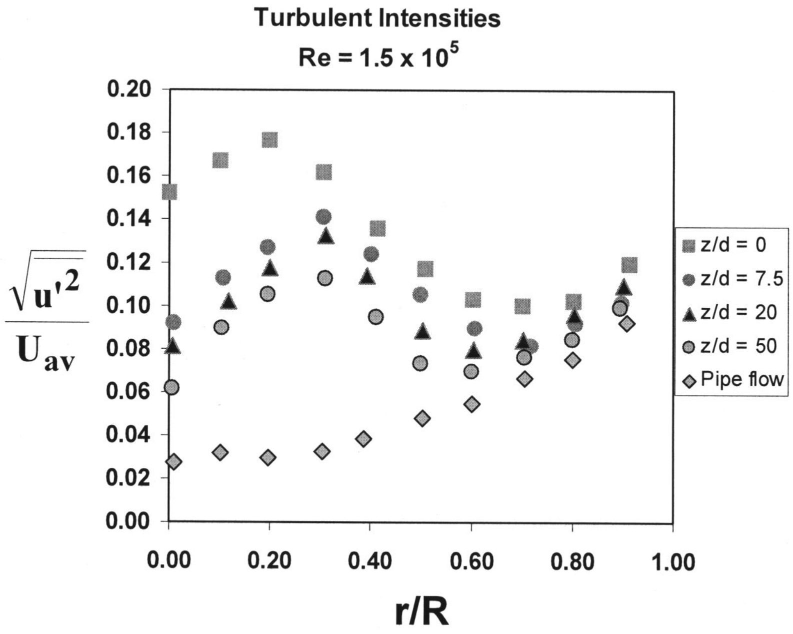

Fig. 7 Axial Normal Stress Distribution after Algifri et al. [4]

4 Swirling Flow Mechanistic Model

Typical axial and tangential velocity profiles in swirling flow are shown schematically in Fig. 1. In part I of this two-part paper, correlations were developed for the flow field, including the axial, tangential and radial velocity profiles. In this section, correlations are developed for the corresponding turbulent quantities, including the turbulent kinetic energy and its dissipation rate and Reynolds shear stresses. First, the important concept of the swirl intensity, presented in part I, is reviewed here as it is required for the calculation of the turbulent quantities correlations.

4.1 Swirl Intensity Decay Number. Based on several sets of swirling flow experimental data Mantilla [10] and later Erdal [9] modified an existing swirl intensity correlation, proposed originally by Chang and Dhir [7], to predict the flow field. The swirling motion decays as a result of wall friction. The swirl intensity concept is used to characterize this decay. For axisymmetric single-phase flow, the swirl intensity, Ω, is defined as the ratio of the tangential to total momentum flux at any axial location, namely

$$\Omega=\frac{2\pi\rho\int_0^R u_z u_\theta r dr}{\pi\rho R^2 U_{av}^2} \tag{5}$$

The numerator of Eq. (5) corresponds to the tangential momentum flux integrated over the pipe cross sectional area, while the de-

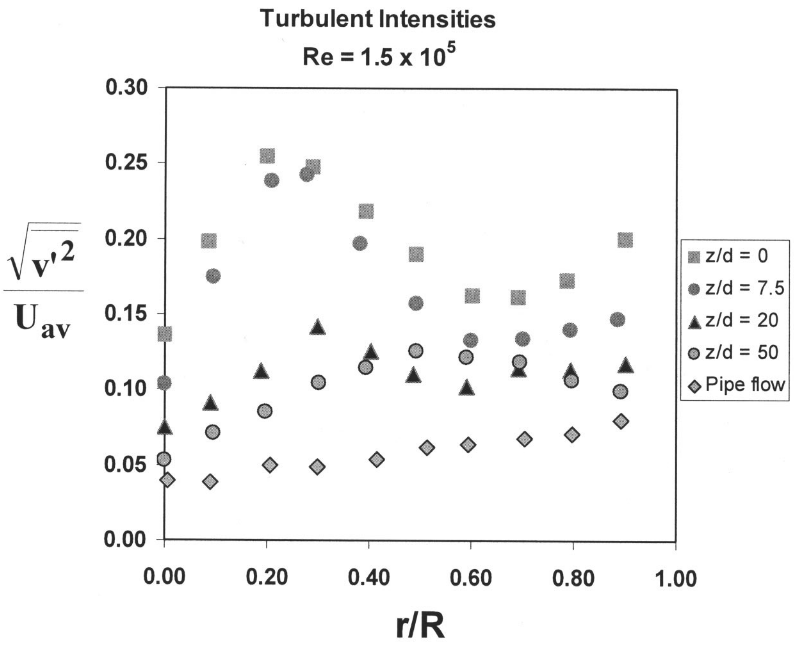

Fig. 8 Radial Normal Stress Distribution after Algifri et al. [4]

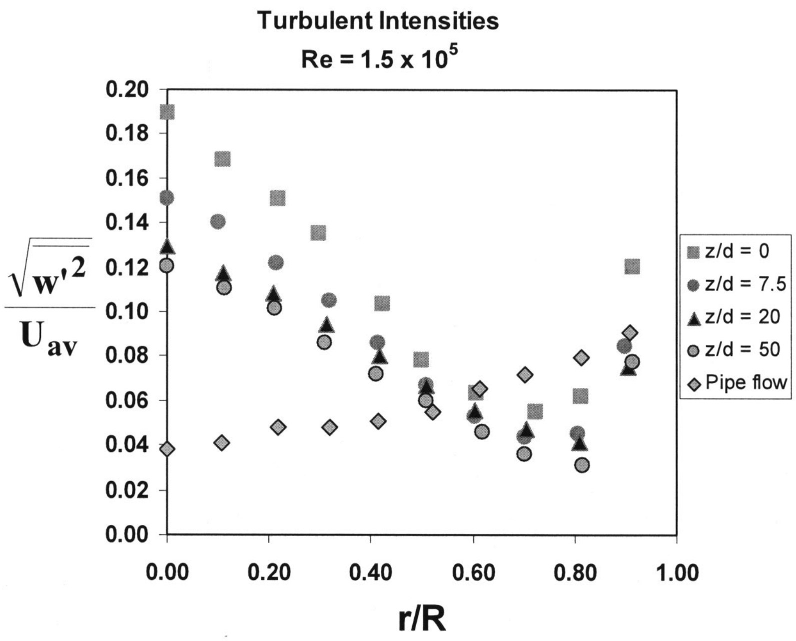

Fig. 9 Tangential Normal Stress Distribution after Algifri et al. [4]

nominator is the total momentum flux based on the average bulk velocity. The Erdal [9] correlation for the swirl intensity is given by:

$$\Omega = 0.67\,\mathrm{Re}^{0.13}\left(\frac{M_t}{M_T}\left(1-\exp\left(-\frac{n}{2}\right)\right)^{2}\right)^{0.93} \times \exp\left[-\frac{1}{2}\left(\frac{M_t}{M_T}\left(1-\exp\left(-\frac{n}{2}\right)\right)^{4}\right)^{0.35}\mathrm{Re}^{-0.16}\left(\frac{z}{d_{sep}}\right)^{0.7}\right] \quad (6)$$

where n is the number of tangential inlets and M_t/M_T is the ratio of the tangential momentum flux to the total momentum flux at the inlet, as given by

$$\frac{M_t}{M_T}=\left(\frac{u_{L\ inlet}\cos\beta}{U_{av}}\right)=\frac{u_{t\ is}}{U_{av}} \quad (7)$$

where $u_{L\ inlet}$ is the liquid velocity at the inlet and β is the inlet inclination angle. The liquid velocity at the inlet can be calculated from the nozzle analysis developed by Gomez [11], which can then be used to compute the tangential velocity of the liquid at the

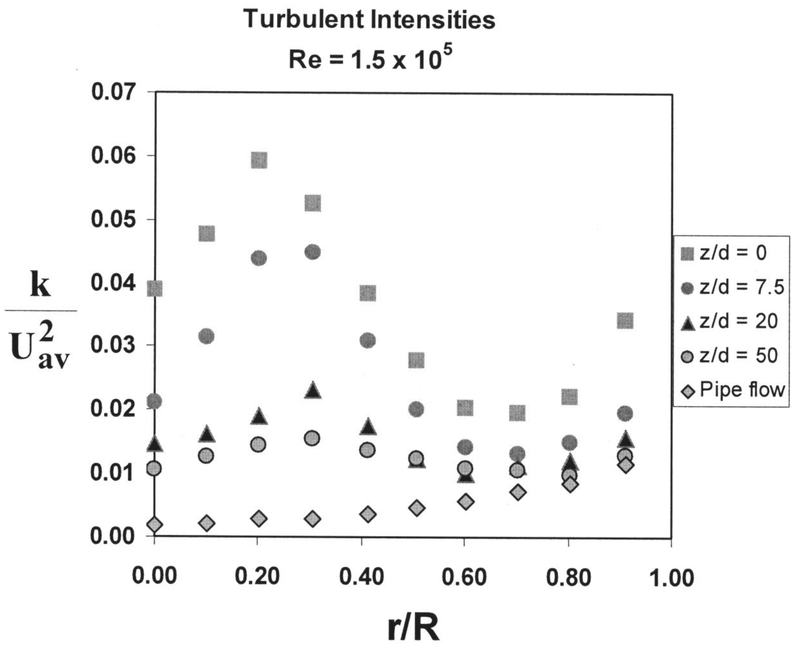

Fig. 10 Turbulent Kinetic Energy after Algifri et al. [4]

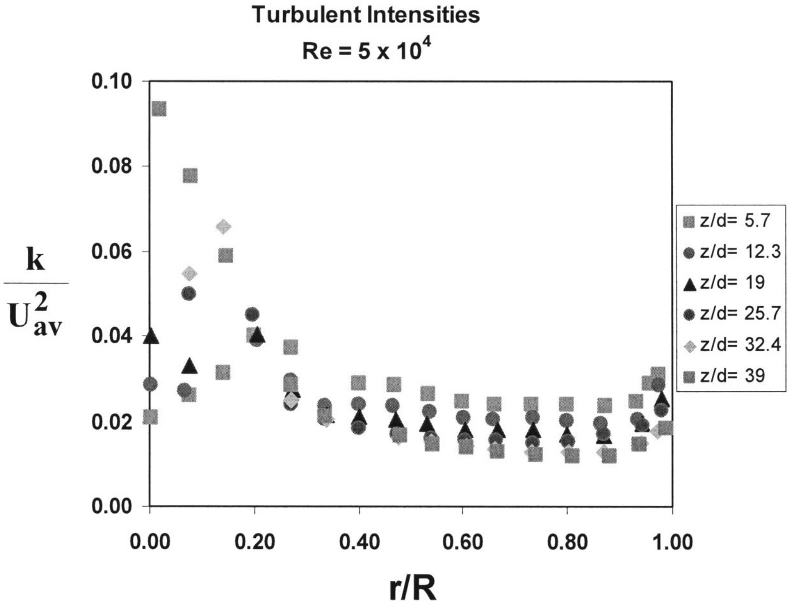

Fig. 11 Turbulent Kinetic Energy after Kitoh [5]

inlet slot, $u_{t\,is}$. The Reynolds number in Eq. (6) is defined as for pipe flow, based on the bulk velocity and the diameter of the cyclone.

4.2 Continuous-Phase Turbulent Quantities Correlations. In swirling flow, turbulence exhibits an anisotropic behavior. The turbulent quantities of the continuous-phase are required to complete the two-phase swirling flow model for the calculation of the interfacial phenomena. The hypothesis is that as turbulence dissipates, it affects the formation of the interfacial area concentration. Therefore, the turbulent intensity, eddy viscosity, and energy dissipation rate distributions have to be known for an analysis of the gas core. Details are given by Gomez [12].

4.2.1 Reynolds Shear Stresses. Correlations are developed for the radial distributions of the Reynolds shear stresses for the swirling continuous-phase, aimed at determining the eddy viscosity of this phase. The parameters of these correlations are based on experimental observations that high anisotropic turbulent behavior occurs in swirling flow among the three Reynolds stress components, $\overline{u_i' u_j'}$. This behavior is observed in the core region around the pipe axis, where the tangential velocity exhibits a forced vortex, affecting the behavior of the Reynolds stresses. Hence, the value of T_m and B are selected as correlating parameters, which are related to the maximum magnitude and location of the tangential velocity, respectively. Following are the correlations for the three Reynolds stress components, normalized with respect to the average bulk velocity, U_{av}^2. The values of the coefficients are given in Table 1.

$$-\frac{\overline{u'v'}}{U_{av}^2}=\frac{T_m}{B}\cdot\left[\mathrm{a}\cdot\left(\frac{r}{R}\right)^4-\mathrm{b}\cdot\left(\frac{r}{R}\right)^3+\mathrm{c}\cdot\left(\frac{r}{R}\right)^2+\mathrm{d}\cdot\left(\frac{r}{R}\right)-\mathrm{f}\right] \quad (8)$$

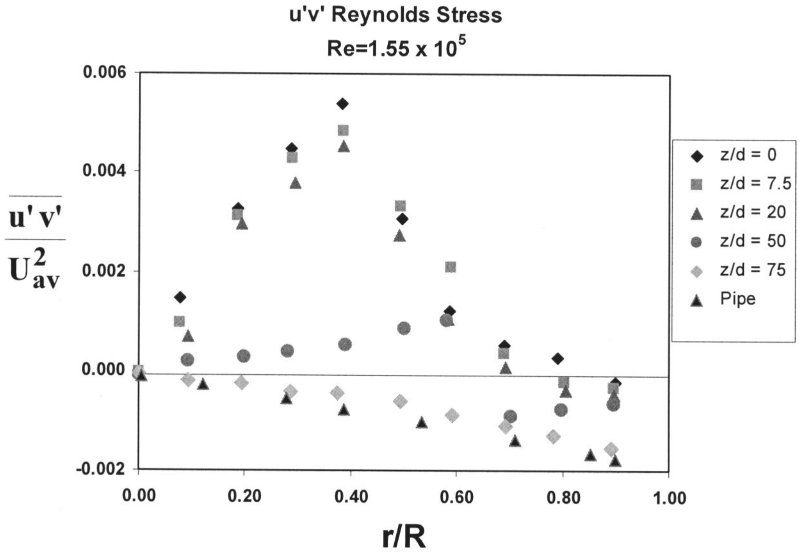

Fig. 12 Reynolds Shear Stress $\overline{u'v'}$ Distribution after Algifri et al. [4]

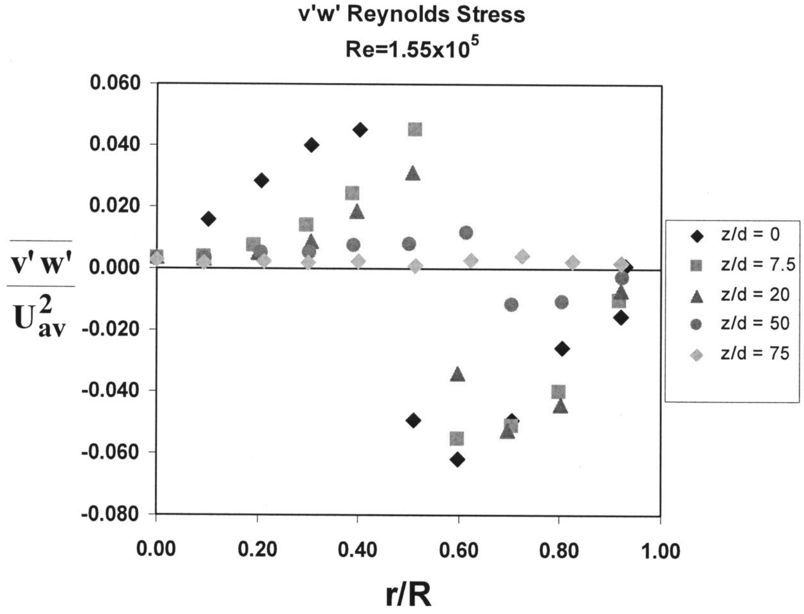

Fig. 13 Reynolds Shear Stress $\overline{v'w'}$ Distribution after Algifri et al. [4]

$$-\frac{\overline{u'w'}}{U_{av}^2}=\frac{T_m}{B}\cdot\left[\mathrm{a}\cdot\left(\frac{r}{R}\right)^4-\mathrm{b}\cdot\left(\frac{r}{R}\right)^3+\mathrm{c}\cdot\left(\frac{r}{R}\right)^2-\mathrm{d}\cdot\left(\frac{r}{R}\right)+\mathrm{f}\cdot e^{\mathrm{n}\cdot\Omega}\right] \tag{9}$$

$$-\frac{\overline{\nu'w'}}{U_{av}^2}=\frac{T_m}{B}\cdot\left[\mathrm{a}\cdot\left(\frac{r}{R}\right)^4-\mathrm{b}\cdot\left(\frac{r}{R}\right)^3+\mathrm{c}\cdot\left(\frac{r}{R}\right)^2-\mathrm{d}\cdot\left(\frac{r}{R}\right)+\mathrm{f}\right] \tag{10}$$

4.2.2 Eddy Viscosity Calculation for Swirling Flow. The Boussinesq eddy viscosity hypothesis defines the interaction between the Reynolds stresses and the gradients of the mean velocities. Also, it is well known that the turbulent kinetic energy, k, and its dissipation rate, ε, are related to the turbulent eddy viscosity, υ_t, through a dimensional Kolmogorov relationship (which is widely used in the standard k-ε model–isotropic concept). For the case of swirling flow, the distribution of the Reynolds stress components exhibit a different magnitude and behavior, as the swirl decays. This results in different magnitudes of the three eddy viscosity components, caused by the anisotropic behavior of the turbulent flow. The values of the eddy viscosities are derived from the Boussinesq eddy viscosity model, once the Reynolds shear stresses and the velocity field are known, and are given by

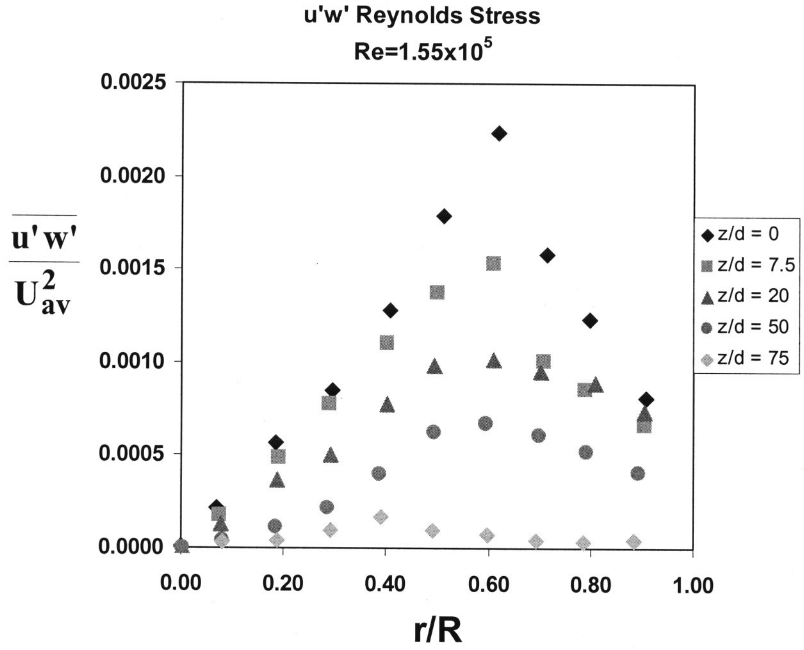

Fig. 14 Reynolds Shear Stress $\overline{u'w'}$ Distribution after Algifri et al. [4]

Table 1 Reynolds stress coefficients

	a	b	c	d	f	n
$\overline{u'v'}$	0.3304	0.6158	0.1177	0.1295	0.0059	⋯
$\overline{u'w'}$	0.7935	2.0297	1.8388	0.6549	0.0352	0.0314
$\overline{v'w'}$	1.2954	2.4614	1.3188	0.1942	1.6390	⋯

$$\upsilon_{tzr} = -\frac{\overline{u'v'}}{\dfrac{\partial u_z}{\partial r}} \tag{11}$$

$$\upsilon_{t\theta r} = -\frac{\overline{v'w'}}{r\dfrac{\partial}{\partial r}\left(\dfrac{u_\theta}{r}\right)} \tag{12}$$

$$\upsilon_{t\theta z} = -\frac{\overline{u'w'}}{\dfrac{\partial u_\theta}{\partial z}} \tag{13}$$

Experimental observations demonstrate that close to the wall the anisotropy among the three eddy viscosity components becomes weak, as discussed by Algifri et al. [4]. It is also observed from the data that in the annular region the magnitude of $\upsilon_{t\theta z}$ is larger than $\upsilon_{t\theta r}$ and υ_{tzr}. This leads to the conclusion that in order to satisfy Kolmogorov theory, a modification has to be made to account for anisotropic turbulent flow. One simple way is to use an ad hoc coefficient, so that the k-ε model relationship can still hold. This coefficient may or may not have functionality with other turbulent parameters, as was demonstrated by Kobayashi and Yoda [13]. Due to the high degree of empiricism of these coefficients and with no validation done, this method is disregarded in the present investigation. Instead, a tensor analysis is carried out, similar to the method of determining the principal stress direction, for calculating an equivalent magnitude of the eddy viscosity acting in the principal stress direction.

4.2.3 Turbulent Kinetic Energy Correlation for Swirling Flow. From the experimental data for the turbulent quantities, it can be seen (Fig. 5) that the turbulent kinetic energy exhibits an increasing maximum near the pipe centerline, as the flow moves downward. However, at some particular location along the axial direction, the magnitude of maximum turbulent kinetic energy starts decreasing. A transition zone occurs between the two regions that is dependent on the swirl intensity and the Reynolds number. As the swirl intensity decreases and decays completely, the turbulent kinetic energy also decreases until it converges to a magnitude similar to that of swirl-free pipe flow. It is also observed that these maxima location shift around the cyclone axis in an oscillatory manner.

The minima values of the kinetic energy exhibit an opposite behavior, as compared to the maxima values. The minima have almost a zero magnitude, increasing slowly with axial position as the swirl intensity decreases, until converging to swirl-free pipe flow values, as well.

The above experimental observations have been used in this study to develop an empirical correlation for the turbulent kinetic energy, normalized with respect to U_{av}^2. The correlation is dependent on the initial swirl intensity and its decay, and on the Reynolds number. The developed correlation also captures the oscillatory phenomenon of the maximum kinetic energy value.

The location of the maximum of the turbulent kinetic energy in the radial direction is modeled with a periodical type equation, correlated with experimental data, which can predict the whipping behavior of the core, as follows:

$$\frac{r_{shift}}{R} = -0.22\cdot\exp[-0.6\cdot(\ln\Omega - 0.8)^2] \times \sin(23.088\cdot\Omega - 10.091) - 0.022\,74 \tag{14}$$

The parameters given below are used to determine the magnitude of the kinetic energy, $k(r,z)$, in the entire flow domain:

$$Yk_{\min} = 0.18\cdot[1 - \exp(-0.5467\cdot\Omega\cdot\mathrm{Re}^{-0.009\,79})] \tag{15}$$

$$A_K = 3.202\times 10^{-5}\cdot\exp\left[0.7\cdot\left(\frac{M_t}{M_T}\right)\right] - 3.342\times 10^{-3} \times\sin\left(0.908\cdot\left(\frac{M_t}{M_T}\right) - 0.0238\right) + 3.23\cdot 10^{-3} \tag{16}$$

$$B_K = 1.126\cdot\{0.5\cdot\tanh[5000\cdot(\Omega - 2)] + 0.5\} \tag{17}$$

$$Yk_{\max} = A_K\,\mathrm{Re}^{0.45}\cdot\exp[-0.83\cdot(\ln\Omega - 0.5415)^2] + B_K\left(\frac{r_{shift}}{R}\right) + Yk_{\min} \tag{18}$$

$$n = \frac{133.009\Omega}{\mathrm{Re}} \tag{19}$$

$$\vartheta = 0.1292\cdot\exp(-0.0784\cdot\Omega) \tag{20}$$

The final equation for the turbulent kinetic energy correlation, normalized with respect to U_{av}^2, is given by:

$$\frac{k}{U_{av}^2} = (Yk_{\max} - Yk_{\min})\cdot\exp\left[-\frac{1}{2}\left(\frac{\dfrac{r}{R} - \dfrac{r_{shift}}{R}}{\vartheta}\right)^2\right] + Yk_{\min}\cdot\exp\left[n\cdot\left(\frac{r}{R}\right)^2\right] \tag{21}$$

4.2.4 Turbulent Energy Dissipation Calculation for Swirling Flow. For a complete eddy viscosity turbulent model, at least two turbulent quantities have to be specified. In the present study, the two specified turbulent quantities are the Reynolds shear stresses and the turbulent kinetic energy. As was discussed above, the k-ε model provides a relationship between the turbulent eddy viscosity and the turbulent kinetic energy through the energy dissipation, ε, as given below, where, $C_\mu = 0.09$.

$$\varepsilon = C_\mu \frac{k^2}{\upsilon_t} \tag{22}$$

The energy dissipation expresses the rate of dissipation of the turbulent kinetic energy. The importance of the energy dissipation in a two-phase dispersion is manifested in the generation of the interfacial area, namely, breakup and coalescence of bubbles/droplets.

A particular problem is presented in swirling flow, due to the anisotropic behavior of the turbulent flow. In order to solve Eq. (22) for ε, the isotropic turbulent eddy viscosity, υ_t, must be known. As the flow is anisotropic, the turbulent eddy viscosity is a tensor, as given by Eqs. (11) to (13). To overcome this problem, a method similar to tensor analysis is adopted, for determining equivalent isotropic turbulent eddy viscosity acting in the principal direction from the different eddy viscosity components. Thus, the Reynolds stress tensor is expressed as follows:

$$\overline{u_i' u_j'} = \begin{pmatrix} \overline{u'^2} & \overline{u'v'} & \overline{u'w'} \\ \overline{u'v'} & \overline{v'^2} & \overline{v'w'} \\ \overline{u'w'} & \overline{v'w'} & \overline{w'^2} \end{pmatrix} \tag{23}$$

The turbulent kinetic energy is defined as the sum of the normal Reynolds stresses, and is given below:

$$k=\frac{1}{2}(\overline{u'^2}+\overline{v'^2}+\overline{w'^2}) \tag{24}$$

Equivalent tensor components are defined below to express the eddy viscosity values for the different directions, so that the equivalent value of the eddy viscosity acting in the principal direction can also be obtained, namely,

$$\upsilon_{t\ \ ij}=\begin{pmatrix} \xi_{\overline{u'^2}} & \upsilon_{zr} & \upsilon_{\theta z} \\ \upsilon_{zr} & \xi_{\overline{\upsilon'^2}} & \upsilon_{\theta r} \\ \upsilon_{\theta z} & \upsilon_{\theta r} & \xi_{\overline{w'^2}} \end{pmatrix} \tag{25}$$

where the parameters used are defined below:

$$\xi=\frac{\overline{u_i'^2}\cdot R}{U_{av}} \tag{26}$$

$$c_1=\frac{\overline{u'^2}}{\overline{w'^2}} \quad \text{and} \quad \overline{\nu'^2}=\frac{1}{2}(\overline{u'^2}+\overline{w'^2}) \tag{27}$$

The value of $c_1=1.13$ is used in this study, obtained from experiments. The three roots of the cubic polynomial equation, given below, are the three principal equivalent eddy viscosity values,

$$\delta^3-I_1\delta^2+I_2\delta-I_3=0 \tag{28}$$

where the invariants, I, are defined in this study as follows:

$$I_1=\frac{2R}{U_{av}}k \tag{29}$$

$$I_2=\frac{16}{9}\frac{c_1}{(c_1+1)^2}\frac{R^2}{U_{av}^2}\cdot k^2+\frac{8}{9}\frac{1}{(c_1+1)}\frac{R^2}{U_{av}^2}\cdot k^2$$
$$+\frac{8}{9}\frac{c_1}{(c_1+1)}\cdot\frac{R^2}{U_{av}^2}k^2-(\upsilon_{\theta r}^2+\upsilon_{\theta z}^2+\upsilon_{zr}^2) \tag{30}$$

$$I_3=\frac{4}{3}\frac{c_1}{(c_1+1)}\frac{R}{U_{av}}k\left(\frac{8}{9}\frac{1}{(c_1+1)}\frac{R^2}{U_{av}^2}k^2-\upsilon_{\theta r}^2\right)$$
$$+\upsilon_{zr}\left(\upsilon_{zr}\frac{4}{3}\frac{1}{(c_1+1)}\frac{R}{U_{av}}k-\upsilon_{\theta z}\upsilon_{\theta r}\right)$$
$$+\upsilon_{\theta z}\left(\upsilon_{zr}\upsilon_{\theta r}-\frac{2}{3}\frac{R}{U_{av}}k\upsilon_{\theta z}\right) \tag{31}$$

Once the three roots of Eq. (28) are obtained, the equivalent turbulent eddy viscosity is defined by the magnitude of the principal direction components.

$$\upsilon_{t\ \ eqv}=\sqrt{\delta_1^2+\delta_2^2+\delta_3^2} \tag{32}$$

In cases where $\delta_1=\delta_2=\delta_3$, isotropic turbulent flow will occur. Finally, the energy dissipation rate is determined by the well-known k-ε equation as:

$$\varepsilon=C_\mu\frac{k^2}{\upsilon_{t\ eqv}} \tag{33}$$

5 Gas-Core Stability Model

The mechanisms of the stability of single-phase swirling flow can be related to the turbulent intensity, as demonstrated by the experimental data. The offset location from the centerline of the maximum peak of the turbulent kinetic energy is observed. Thus, it is assumed that the turbulent kinetic energy can be used to develop a model to predict the stability of the gas-core in two-phase swirling flow, as well.

The stability of the gas core is the key to defining the dominant swirling two-phase flow pattern. Thus, one might think that high intensity swirling flow would enhance the gas–liquid separation due to the surge motion of the lighter fluid toward the gas-core region, which also becomes wider as the swirl intensity increases.

The developed model for the prediction of the gas-core stability is based on the above-mentioned phenomena. Using the derivative of the turbulent kinetic energy correlation (given by Eq. (21)) with respect to swirl intensity parameter, one can obtain the slope of the turbulent kinetic energy to analyze the stability of the gas core. Gomez [12] defined the swirling two-phase flow pattern as follows:

- For positive slope of the gas core and very low swirl intensity (less than 0.8), the gas core behaves as a **No Gas-Core−High Bubble Dispersion**.
- For positive slope of the gas core and moderate swirl intensity (between 0.8 and 1.5), **Weak Gas-Core−High Bubble Dispersion** is present.
- For slope approaching zero value as swirl intensity increasing up to values around 2 to 3, for this case **Whipping Gas-Core−Low Bubble Dispersion** is the dominant swirling flow pattern.
- Finally, for negative slope at high swirl intensity (larger than 4) **Stable Gas-Core−No Bubble Dispersion** is the present swirling flow pattern.

The diameter of the core can be determined similar to the analysis presented by Barrientos et al. [14]. The Young–Laplace equation can be used to define the normal stresses at the interface (jump conditions), as given below:

$$\tau_n\cdot n|_{r=r_c}^{liquid}-\tau_n\cdot n|_{r=r_c}^{gas}=\frac{\sigma}{r_c} \tag{34}$$

Assuming that the gas-core interface rotates as a rigid body with an angular velocity ω_1, and that the normal stress at the inner side of the gas-core is that of an ideal fluid, while at the liquid side the normal stress can be expressed using the radial velocity gradient and the hydrostatic pressure yields the following expression for the gas-core diameter:

$$\tau_n\cdot n|_{r=r_c}^{liquid}=-\rho_L gz+2\mu\left.\frac{\partial u_r}{\partial r}\right|_{r=r_c}$$

$$\text{and}\quad \tau_n\cdot n|_{r=r_c}^{gas}=-(P_g+\tfrac{1}{2}\rho_g\omega_1^2rc^2) \tag{35}$$

where r_c the gas core radius and P_g is the gas static pressure.

6 Simulation and Results

In this section, the developed correlations for swirling flow turbulent quantities are tested against data from different published studies for the continuous-phase. Also, the validation of the hypothesis of the core-stability model against the experimental data is presented.

6.1 Continuous-Phase Turbulent Quantities. As mentioned above, the turbulent flow properties are important in the two-phase swirling dispersion process to define the interfacial area by means of breakup and coalescence processes.

6.1.1 Turbulent Kinetic Energy. Figures 15 and 16 present the performance of the developed normalized turbulent kinetic energy correlation with the data of Erdal [9]. Figure 15 gives the radial distribution of the turbulent kinetic energy at different axial positions. As can be seen, the developed correlation captures the physical phenomenon of the helical shifting of the maximum turbulent kinetic energy along the axis of the cyclone. Figure 16 presents the same comparison in contour plot form.

A comparison between the entire Erdal [9] data and the developed correlation for the helical radial oscillation of the maximum turbulent kinetic energy around the cyclone axis, as a function of the swirl intensity, is shown in Fig. 17. The figure demonstrates

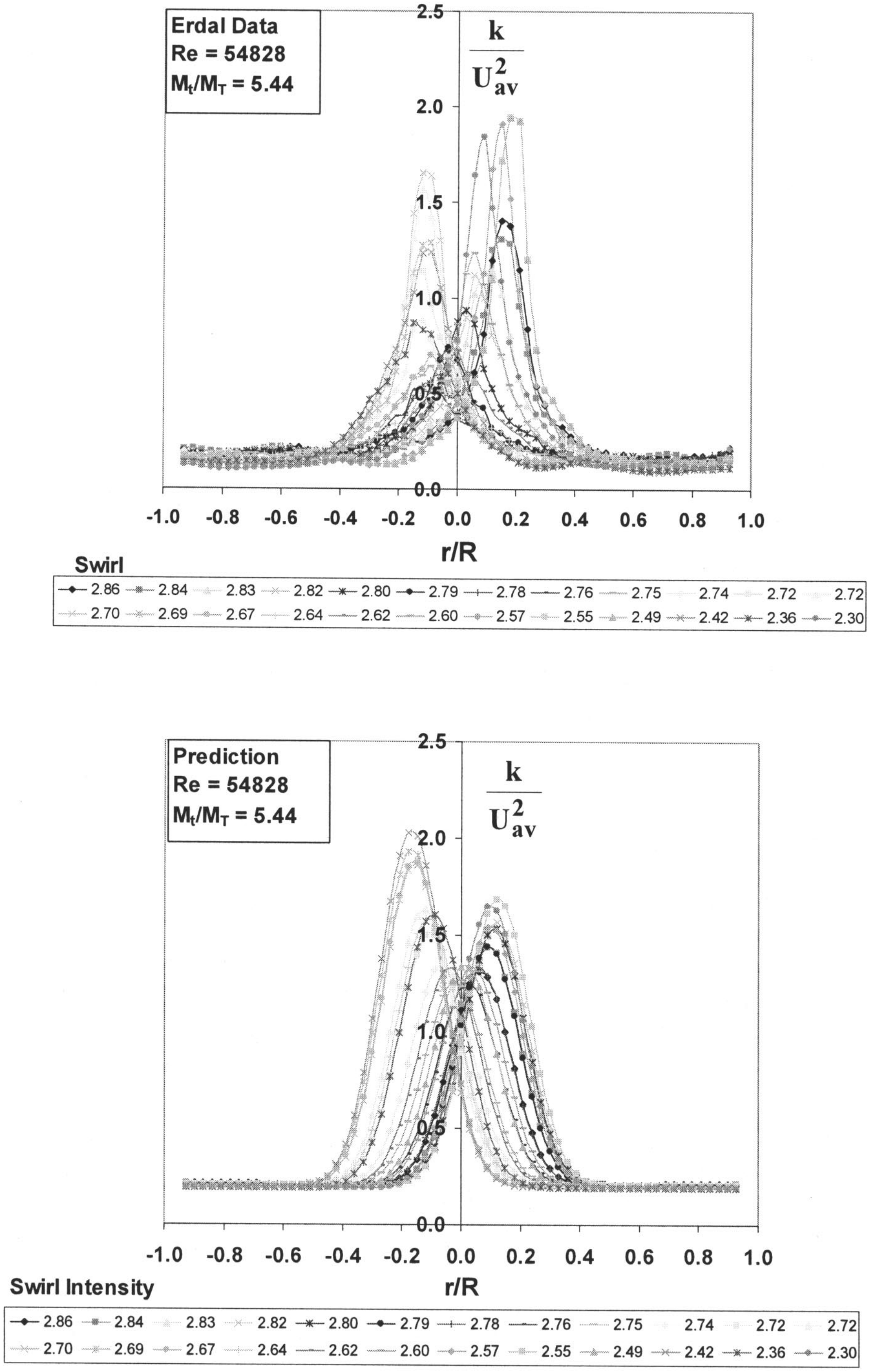

Fig. 15 A comparison of Turbulent Kinetic Energy Radial Distribution

that for low swirl intensity corresponding to locations far below the inlet, high fluctuations occur due to flow instability. However, as the swirl intensity increases (corresponding to locations near the inlet) the radial oscillation of the maximum turbulent kinetic energy decreases, since the flow becomes more stable. Figures 18, 19, and 20 show the comparison of maximum and minimum magnitudes of the turbulent kinetic energy as function of swirl intensity and Reynolds number. Figure 18 shows the comparison for low Reynolds numbers (Re=9137) at moderate swirl intensity (M_t/M_T=5.44), while Fig. 19 is for high Reynolds numbers (Re =54 828) at both moderate and high swirling intensities. A comparison of the turbulent kinetic energy for the same value of M_t/M_T=10.88, for both low and high Reynolds numbers, is presented in Fig. 20. Excellent performance is observed in all three figures.

Finally, the developed correlation for the turbulent kinetic energy is compared against the data of Kitoh [5] for very low swirl intensity (less than 0.8), as can be seen in Fig. 21. Note that these data have not been used in the correlation development. As can be seen, the correlation performs well against the additional data, capturing the decay of the turbulent kinetic energy as the swirl intensity tends to zero.

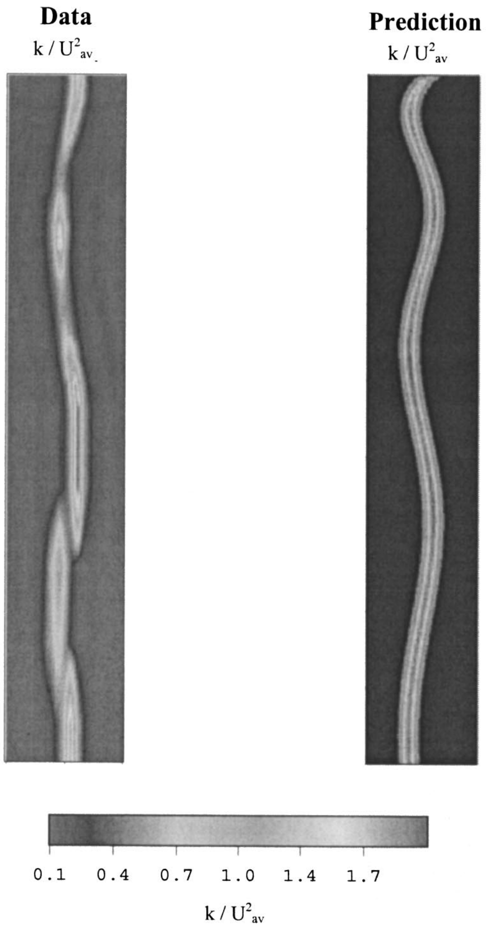

Fig. 16 Contour Plot Comparison of Turbulent Kinetic Energy Radial Distribution

6.1.2 Reynolds Shear Stresses. Comparisons between the developed correlations for the three Reynolds shear stress components and Kitoh [5] experimental data, for Re=50 000 and $M_t/M_T=2.37$, are presented in Figs. 22, 23, and 24 for the $\overline{u'v'}$, $\overline{u'w'}$, and $\overline{v'w'}$ components, respectively, As can be seen, the good performance of the correlations confirm that the location and the maximum value of the tangential velocity are indeed the proper correlating parameters for the Reynolds shear stress correlations, as proposed in this study.

6.2 Gas-Core Stability Model. Figure 25(*a*) shows data and simulation results of turbulent single-phase swirling flow kinetic energy contour plots. As the swirling intensity increases, with values between 3 to 6 (similar to the case shown in Fig. 19), the gas-core tends to stabilize in the centerline, as shown in Fig. 25(*b*) 1. For high values of swirl intensity, larger than 6, the core remain stable around the centerline. At low swirling intensities, between 1.5 to 3 (similar to the case shown in Fig. 20), the peak-offset location from the centerline increases, which is related to whipping gas-core phenomenon, as shown in Fig. 25(*b*) 2. For cases where the swirl intensity are lower than 1.5 (similar to the case presented in Fig. 21), no gas-core forms but rather high bubble dispersion.

7 Conclusions

The hydrodynamics of dispersed two-phase swirling flow in the lower part of the Gas–Liquid Cylindrical Cyclone (GLCC) and in a straight pipe were studied both experimentally and theoretically. Following are the main conclusions of the study:

- Published local LDV measurements for swirling flow field have been analyzed and utilized to develop and validate cyclone and pipe swirling flow field prediction correlations for the turbulent kinetic energy and Reynolds shear stresses.
- The developed correlations for the continuous-phase swirling flow turbulent quantities have been tested against data from other studies, not used in the development of the correlations. The correlations show good agreement with the data.
- The hypothesis that the swirling flow turbulent kinetic energy behavior exhibits the same mechanism as that of the gas-core. A

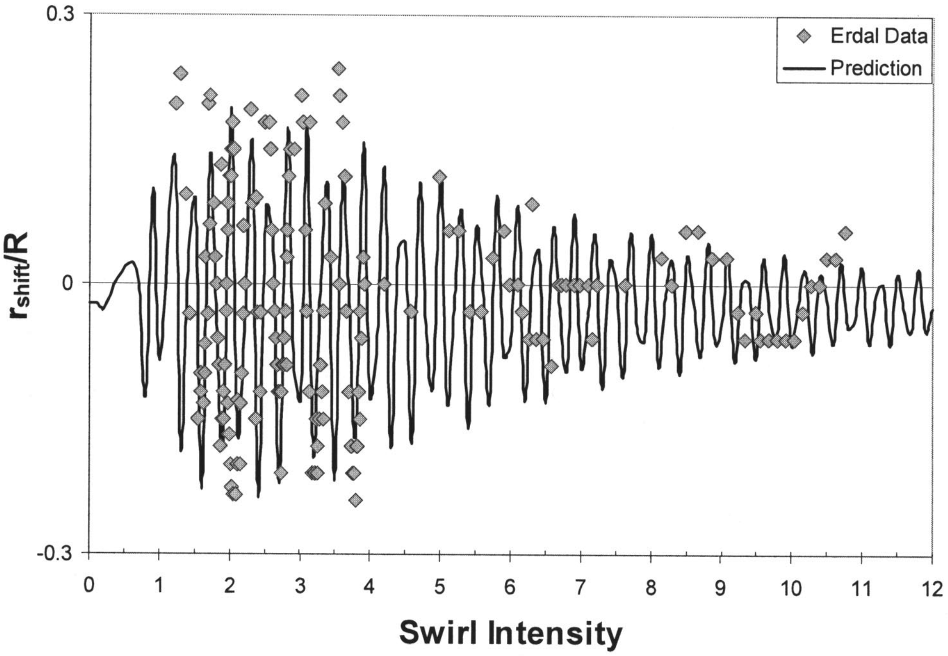

Fig. 17 A comparison of Helical Radial Oscillations of the Maximum Turbulent Kinetic Energy With Swirl Intensity

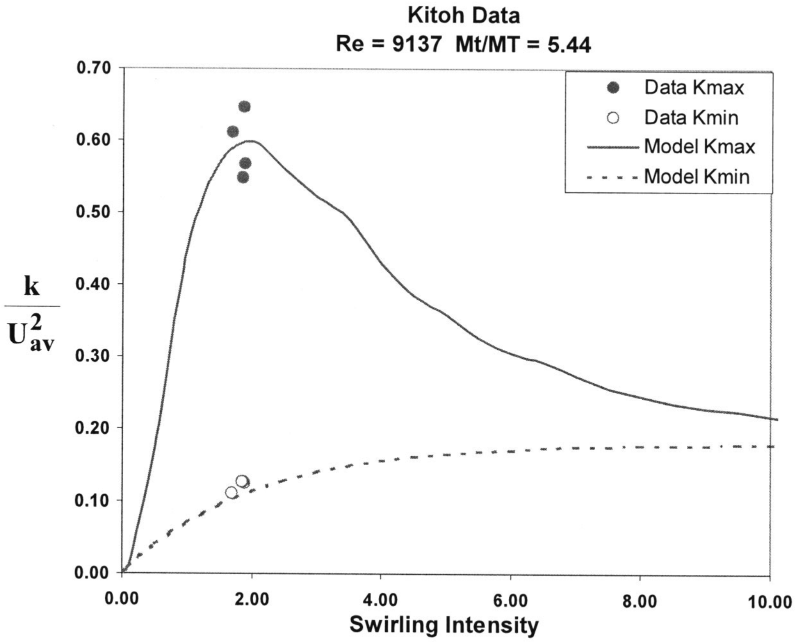

Fig. 18 Turbulent Kinetic Energy Comparison—Moderate Swirling Intensity

model for the prediction of the gas-core diameter and stability in swirling flow field has been developed, based on the turbulent kinetic energy behavior predicted by the developed correlation. It was also confirmed that the stability of the gas-core can be used to define the dominant swirling two-phase flow pattern in cylindrical cyclone separators.

- The following are concluded with respect to the swirling flow turbulent quantities:

i. *The turbulent kinetic energy:* The turbulent kinetic energy exhibits an increasing maximum near the center, as the flow moves downward. As the swirl intensity decreases and decays completely, the turbulent kinetic energy also decreases until it converges to a magnitude similar to swirl-free pipe flow kinetic energy. In this study, a correlation is developed for the turbulent kinetic energy that captures the oscillatory phenomenon of the maximum kinetic energy value around the centerline, which can predict the whipping behavior of the core.

ii. *Reynolds Stress Components:* The three Reynolds stress components, $\overline{u'v'}$, $\overline{v'w'}$ and $\overline{u'w'}$ have different trends and magnitudes. Correlations are developed for all three components. The important observation is that large anisotropic turbulent behavior among the three components is present, where the anisotropy becomes weak very close to the wall.

iii. *Turbulent Energy Dissipation:* The energy dissipation in a two-phase dispersion is manifested in the generation of the interfacial area, namely, breakup and coalescence of bubbles/droplets. A particular problem is presented in swirling flow, due to the anisotropic behavior of the turbulent flow. In order to satisfy

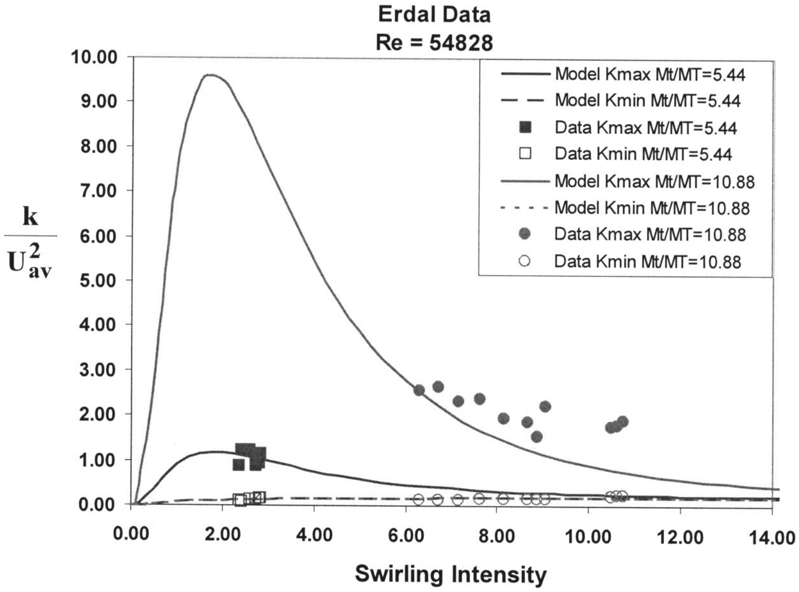

Fig. 19 Turbulent Kinetic Energy Comparison—Different M_t/M_T

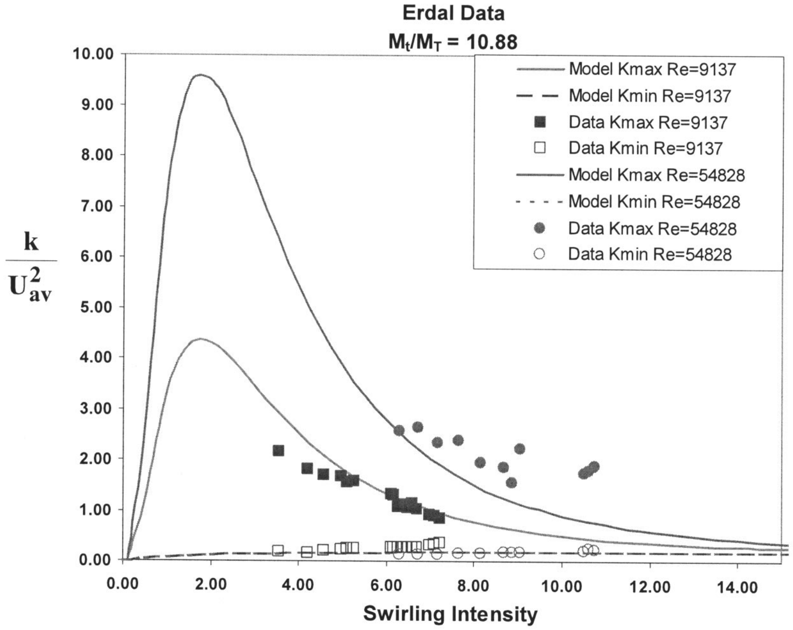

Fig. 20 Turbulent Kinetic Energy Comparison—Low and High Reynolds Number

Boussinesq eddy-viscosity approximation, a method similar to tensor analysis is adopted, for determining equivalent isotropic turbulent eddy viscosity acting in the principal direction, from the different eddy viscosity values resulting from Reynolds stress tensor.

Acknowledgment

The authors wish to thank the US-DOE (Contract No. DE-FC26-03NT15416) and Tulsa University Separation Technology Projects (TUSTP) members for supporting this project.

Nomenclature

B = radial location of the maximum velocity
C_μ = constant for k-ε model
d = diameter (m)
g = acceleration due to gravity (m/s^2)
k = kinetic energy (m^2/s^2)
M = momentum (Newton)
P = pressure (Pa)
r = radial direction
R = pipe radius (m)
Re = Reynolds number

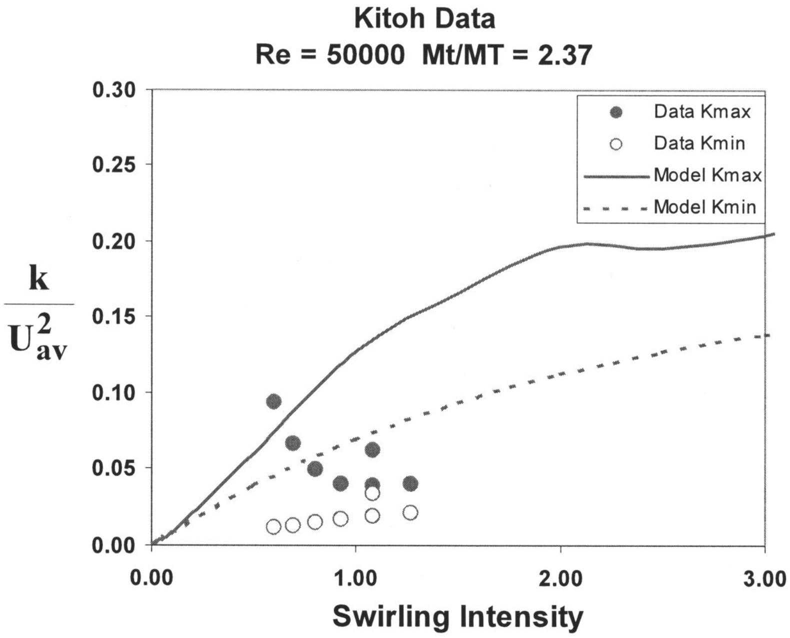

Fig. 21 Turbulent Kinetic Energy Comparison—Very Low Swirling Intensity

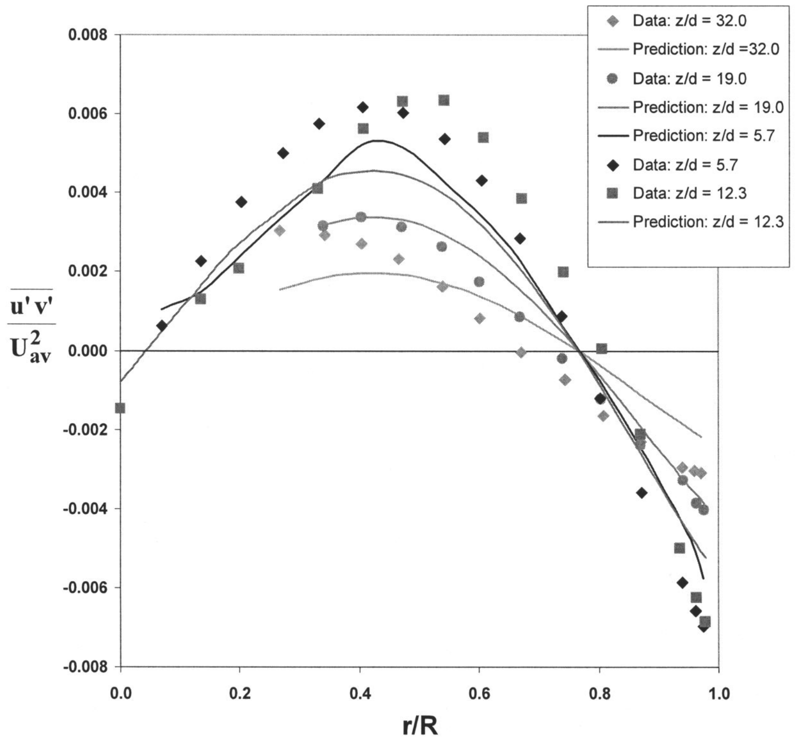

Fig. 22 Reynolds Shear Stress $\overline{u'v'}$ Comparison with Kitoh [5] Data (Re=50,000 and M_t/M_T=2.37)

T_m = parameter related to maximum moment of tangential velocity
u = axial and continuous-phase velocity (m/s)
U_{av} = average bulk velocity (m/s)
v = radial velocity (m/s)
w = tangential velocity (m/s)
Yk = Turbulent kinetic energy parameter
z = axial direction

Greek Letters

β = inclination angle measured from horizontal
ϵ = kinetic energy dissipation rate (m^2/s^3)
θ = tangential direction
ρ = density (kg/m^3)
σ = surface tension (Newton/m)
T = total burst time (s)

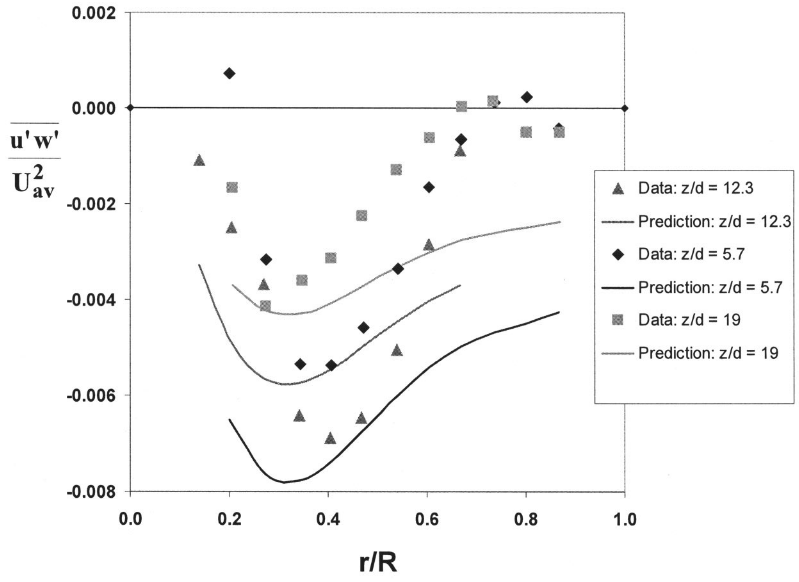

Fig. 23 Reynolds Shear Stress $\overline{u'w'}$ Comparison with Kitoh [5] Data (Re=50 000 and M_t/M_T=2.37)

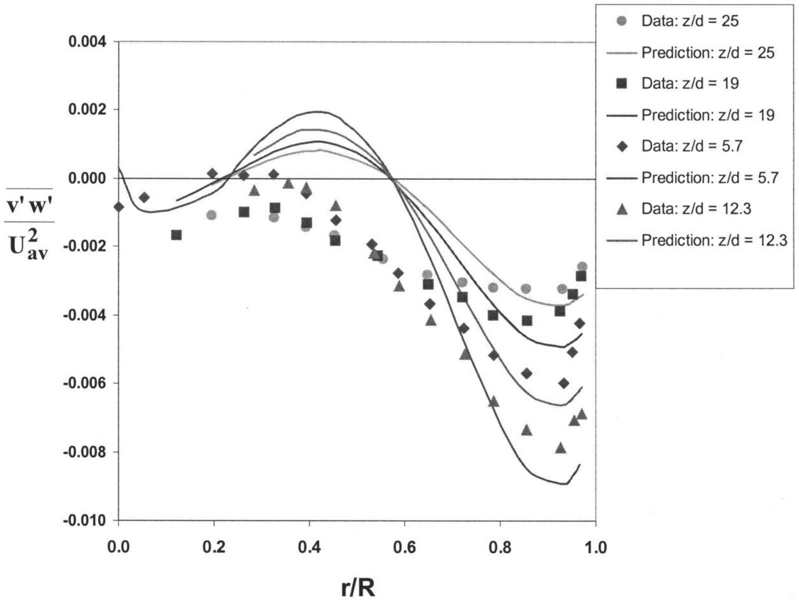

Fig. 24 Reynolds Shear Stress $\overline{v'w'}$ Comparison with Kitoh [5] Data (Re=50 000 and M_t/M_T=2.37)

τ = shear stress (Pa)
υ_t = turbulent eddy viscosity (kg/m s)
μ = dynamic viscosity (kg/m s)
ω = angular velocity (1/s)
Ω = swirl intensity

Superscripts

$\overline{}$ = mean value of the variable
$'$ = turbulent disturbance

Subscripts

av = average
c = core
eqv = equivalent
g = gas
$inlet$ = inlet
is = inlet slot
L = liquid
max = maximum
min = minimum
r = radial direction of cylindrical coordinates
sep = separator
$shift$ = location of maximum of turbulent kinetic energy with respect to centerline
t = tangential
T = total
z = axial direction of cylindrical coordinates

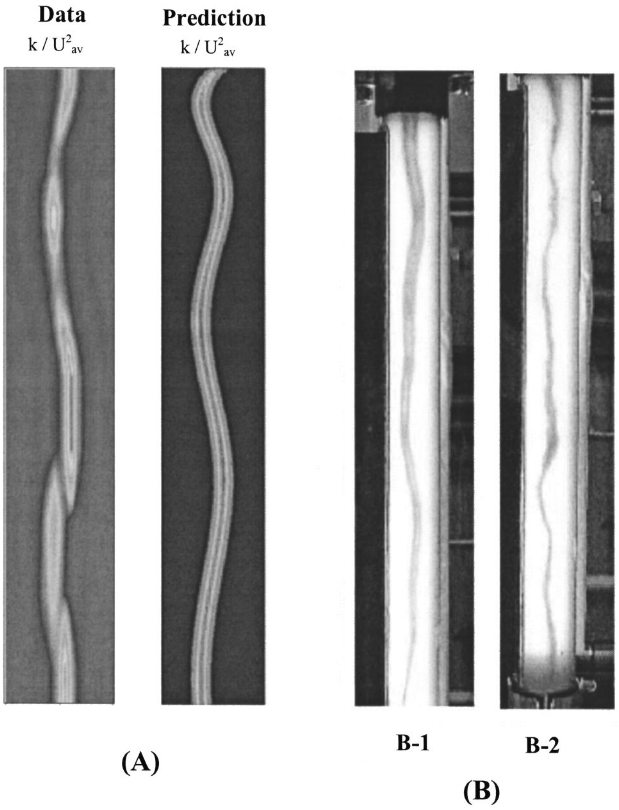

Fig. 25 Results for Gas-Core Stability

References

[1] Gomez, L., Mohan, R., Shoham, O., and Kouba, G., 2000, "Enhanced Mechanistic Model and Field Application Design of Gas–Liquid Cylindrical Cyclone Separator," SPE J., **5**, pp. 190–198.
[2] Nissan, A. H., and Bresan, V. P., 1961, "Swirling Flow in Cylinders," AIChE J., **7**, pp. 543–547.
[3] Ito, S., Ogawa, K., and Kuroda, C., 1979, "Decay Process of Swirling Flow in a Circular Pipe," Int. Chem. Eng., **19**, pp. 600–611.
[4] Algifri, A. H., Bhardwaj, R. K., and Rao, Y. V. N., 1988, "Eddy Viscosity in Decaying Swirl Flow in a Pipe," Appl. Sci. Res., **45**, pp. 287–302.
[5] Kitoh, O., 1991, "Experimental Study of Turbulent Swirling Flow in a Straight Pipe," J. Fluid Mech., **225**, pp. 445–479.
[6] Yu, S. C. M., and Kitoh, O., 1994, "General Formulation for the Decay of Swirling Motion Along a Straight Pipe," Int. Commun. Heat Mass Transfer, **21**, pp. 719–728.
[7] Chang, F., and Dhir, V. K., 1994, "Turbulent Flow Field in Tangentially Injected Swirl Flows in Tubes," Int. J. Heat Fluid Flow, **15**, pp. 346–356.
[8] Kurokawa, J., 1995, "Gas–Liquid Flow Characteristics and Gas-Separation Efficiency in a Cyclone Separator," ASME FED-Vol. 225, Gas Liquid Flows, pp. 51–57.
[9] Erdal, F., 2001, "Local Measurements and Computational Fluid Dynamic

Simulations in a Gas–Liquid Cylindrical Cyclone Separator,'' Ph.D. dissertation, The University of Tulsa.

[10] Mantilla, I., 1998, ''Bubble Trajectory Analysis in GLCC Separators,'' M.S. thesis, The University of Tulsa.

[11] Gomez, L. E., 1998, ''A State-of-the Art Simulator and Field Application Design of Gas-Liquid Cylindrical Cyclone Separators,'' M.S. thesis, The University of Tulsa.

[12] Gomez, L. E., 2001, ''Dispersed Two-Phase Swirling Flow Characterization for Predicting Gas Carry-Under in Gas-Liquid Cylindrical Cyclone Compact Separator,'' Ph.D. dissertation, The University of Tulsa.

[13] Kobayashi, T., and Yoda, M., 1987, ''Modified k-e Model for Turbulent Swirling Flow in a Straight Pipe,'' JSME Int. J., **30**, p. 66.

[14] Barrientos, A., Sampaio, R., and Concha, F., 1993, ''Effect of the Air Core on the Performance of a Hydrocyclone,'' *XVIII International Mineral Processing Conference*, Sydney, pp. 267–270.

An Evaluation of Impeller Blade Torque During an Impeller–Diffuser Interaction

Kevin A. Kaupert
Ebara Cryodynamics International,
350 Salomon Circle,
Sparks, NV
89434

An evaluation of the torque on an impeller blade interacting with a diffuser blade is presented. Comparisons of time averaged quantities are made between computed and measured results. The calculation of the impeller blade torque was based on the axial moment from fluid forces acting on a control volume surrounding an impeller blade passage. Unsteady flow field contributions were incorporated in the computational model. Results are compared to numerical predictions of the impeller blade torque based on pressure and shear stress terms integrated over the blade and wall surfaces. From the fluid forces perspective the major contribution to the time averaged impeller torque originated on the impeller inlet and outlet control surfaces. Contrarily the major contribution to the unsteady impeller torque originated in the unsteady flow field within the impeller control volume. [DOI: 10.1115/1.1839929]

1 Introduction

Turbomachinery represents a mature advanced technology. Design techniques continually strive to improve machinery performance by increasing efficiency and power concentration without sacrificing reliability [1,2]. Improved machinery performance can be accomplished with better predictability of the torque for a rotating impeller.

The force and moment imparted to a fluid by a rotating impeller blade are a synthesis of the complex interaction between centrifugal, Coriolis, viscous, and blade forces all acting in an unsteady fashion. The necessity of unsteady flow for an impeller to transfer energy to a fluid is well established [3,4] and inclusion of unsteady forces and resulting moments is a requirement for a complete numerical model.

To circumvent the inclusion of unsteady flow calculations in an impeller it is common place to calculate the flow field in the rotating frame of reference, perhaps even isolating the impeller from the diffuser. In the case of an isolated rotating impeller the torque required can be described by considering the rate of change of fluid angular momentum between the impeller inlet and outlet. In a simplified form this can be expressed with the Euler turbomachinery equation. Commonly the Euler equation is evaluated during the initial design phases of an impeller as an estimate of impeller torque and consequently energy transferred to the flow. Neglected in the application of the Euler turbomachinery equation are impeller moment terms that stem from,

- unsteady flow,
- flow field nonuniformity,
- external fields (i.e., gravity),
- fluid viscosity.

Given the complexity of evaluating each of these influences it is clear why the Euler turbomachinery equation is a preferred design approximation, but oversimplified. The neglected unsteady flow field that arises in a rotating impeller interacting with the stationary system is well documented to be a significant contributor to unsteady impeller blade forces and moments [5–7]. This interaction must be modeled using unsteady techniques. Numerically numerous efforts have been made to incorporate this interaction into design methods with Reynolds averaged Navier–Stokes solvers [8] or even with intricate vorticity elements and panel methods [9]. But no open literature has reported the individual influence of the above listed 4 points on impeller blade torque. This must be evaluated in the design of advanced turbomachinery. The novelty of the following investigation then lies in the quantitative evaluation of each term that provides the impeller blade torque and applies this information to the design of an industrial high-pressure pump.

2 Theoretical Considerations

2.1 Control Volume. Fig. 1 depicts the control volume V used in the analysis. Represented is the impeller of an impeller–diffuser-return vane combination. The inlet control surface S_1 has a unit normal $\mathbf{n}_1$ parallel to the z-axis of rotation. The outlet control surface S_2 has a unit normal $\mathbf{n}_2$ perpendicular to the axis of rotation. Shear and pressure influences are indicated on S_1 and S_2. The wall pressure and wall shear stress adjacent to the hub surface S_{wh} and adjacent to the shroud surface S_{ws} are indicated by P_{wh}, P_{ws} and τ_{wh}, τ_{ws}. The influence of the location for the control surfaces S_1 and S_2 was investigated by moving their position up and downstream. While this changed the magnitudes of the quantities computed along the control surfaces and within the control volume, the general tendencies remained in tact. Results for only one position of S_1 and S_2 that were very close to the impeller inlet and outlet are described for presentation simplicity.

2.2 Axial Moment (Torque) From Blade and Wall Forces The axial moment on a shaft axis resulting from impeller forces is a consequence of,

- blade surface pressure,
- blade surface shear,
- hub and shroud surface pressure,
- hub and shroud surface shear.

This is expressed mathematically in Fig. 2 for the control volume described in Fig. 1. $\mathbf{e}_z$ is the unit vector taken parallel to the machinery z-axis. The surface pressure terms represent the moment to overcome the pressure acting on each infinitesimal surface area dS_S on the blade and walls. The unit normal vector perpendicular to dS_S is $\mathbf{n}_S$. The surface shear terms represent the moment to overcome the shear force from blade and wall rotation. This shear force acts on the infinitesimal blade surface area dS_S in the direction of the unit parallel vector $\mathbf{t}_S$. The sum of the dot product of the surface forces and associated moments is taken along the z-axis of rotation to provide the shaft torque required to rotate the blade.

Contributed by the Fluids Engineering Division for publication in the JOURNAL OF FLUIDS ENGINEERING. Manuscript received by the Fluids Engineering Division May 27, 2003; revised manuscript received July 9, 2004. Associate Editor: Edward W. Graf.

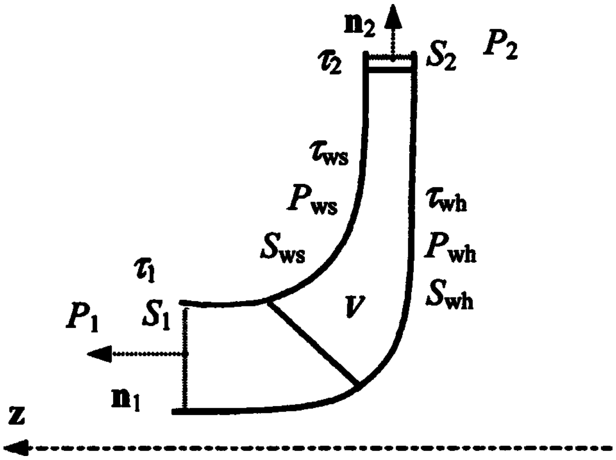

Fig. 1 Control volume and control surfaces in the impeller

2.3 Axial Moment (Torque) From Fluid Forces. The moment on a shaft axis M_{zf} resulting from the reaction forces of flowing fluid contains five influences inside the control volume V, shown in Fig. 2 as Eq. (2) [10]. All five of these terms are unsteady. Eq. (2) represents the unsteady flow field that causes the axial blade moment represented by Eq. (1). It is useful to solve the individual terms of Eq. (2) as these can be manipulated in a given industrial design to reduce detrimental moment and force fluctuations on a pump impeller.

It has been commonplace to approximate M_{zf} in this equation by neglecting all terms except the velocity terms on the control surfaces S_1 and S_2 to provide,

$$M_{\mathrm{zf}}=\left[\int_{S_1}\mathbf{r}_1\times\mathbf{v}_1 dm_{\mathrm{S1}}-\int_{S_2}\mathbf{r}_2\times\mathbf{v}_2 dm_{\mathrm{S2}}\right]\cdot\mathbf{e}_{\mathrm{z}} \tag{3}$$

Separating out the vector components along the control surfaces of Fig. 1 the equation further simplifies to,

$$M_{\mathrm{zf}}=\int_{S_1} r_1 v_{\theta 1} dm_{\mathrm{S1}}-\int_{S_2} r_2 v_{\theta 2} dm_{\mathrm{S2}} \tag{4}$$

With the assumption of uniform circumferential and meridional velocity over the control surfaces a form of the Euler turbomachinery equation is obtained as,

$$M_{\mathrm{zf}}=m(v_{\theta 1}R_{1-\mathrm{ave}}-v_{\theta 2}R_{2-\mathrm{ave}}) \tag{5}$$

Axial Moment from Blade and Wall Surface

$$M_{\mathrm{zb}}=[\underbrace{\int_{S_{\mathrm{s}}}\mathbf{r}_{\mathrm{s}}\times(\mathbf{n}_{\mathrm{s}}P_{\mathrm{s}}dS_{\mathrm{s}})}_{\boxed{\text{surface pressure}}}+\underbrace{\int_{S_{\mathrm{s}}}\mathbf{r}_{\mathrm{s}}\times(\mathbf{t}_{\mathrm{s}}\tau_{\mathrm{s}}dS_{\mathrm{s}})}_{\boxed{\text{surface shear}}}]\bullet\mathbf{e}_{\mathrm{z}} \tag{1}$$

Axial Moment from Fluid Forces (reaction forces to the flowing fluid)

$$M_{\mathrm{zf}}= \tag{2}$$

$$[-\frac{\partial}{\partial t}\left(\int_V \mathbf{r}\times\rho\mathbf{v}\,dV\right) \quad \text{Unsteady velocity term in flow region } V,$$

$$+\int_{S_1}\mathbf{r}_1\times\mathbf{v}_1\,dm_{S1}-\int_{S_2}\mathbf{r}_2\times\mathbf{v}_2\,dm_{S2} \quad \text{Velocity terms on control surfaces } S,$$

$$+\int_{S_1}\mathbf{r}_1\times(-\mathbf{n}_1P_1dS_1)+\int_{S_2}\mathbf{r}_2\times(-\mathbf{n}_2P_2dS_2) \quad \text{Pressure terms along control surfaces } S,$$

$$+\int_V \mathbf{r}\times\rho\mathbf{g}\,dV \quad \text{Gravity term in flow region } V,$$

$$+\int_{S_1}\mathbf{r}_1\times(-\mathbf{t}_1\tau_1dS_1)+\int_{S_2}\mathbf{r}_2\times(-\mathbf{t}_2\tau_2dS_2)]\bullet\mathbf{e}_z \quad \text{Shear terms along control surfaces } S.$$

Fig. 2 The expression for the axial moment (torque) in terms of blade contributions and fluid contributions

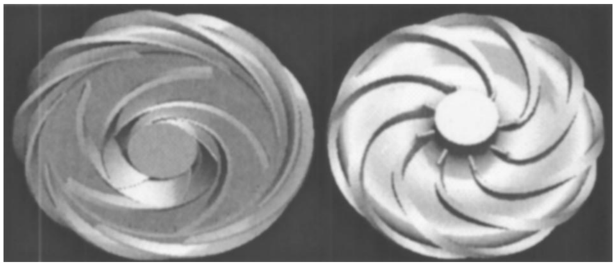

Fig. 3 Geometry of the tested impeller and combined diffuser–return vane. Shroud removed for viewing.

where $R_{1-\mathrm{ave}}$ and $R_{2-\mathrm{ave}}$ are geometric functions that are often approximated by $R_{1-\mathrm{ave}}\approx\mathrm{Sqrt}[0.5(R^2_{1-\mathrm{hub}}+R^2_{1-\mathrm{shroud}})]$ and $R_{2-\mathrm{ave}}\approx\mathrm{Sqrt}[0.5(R^2_{2-\mathrm{hub}}+R^2_{2-\mathrm{shroud}})]$. In this article the situation for the geometry of Fig. 1 provides the more exact values of $R_{2-\mathrm{ave}}=R_2$ and $R_{1-\mathrm{ave}}=2(R^3_{1-\mathrm{shroud}}-R^3_{1-\mathrm{hub}})/3(R^2_{1-\mathrm{shroud}}+R^2_{1-\mathrm{hub}})$. The uniform velocity assumption of Eq. (5) is equivalent to stating the circumferential and meridional velocity are area averaged across the S_1 and S_2 control surface, not mass averaged which Eq. (4) requires. While such simple forms as Eq. (5) are useful in a first design iteration they are too oversimplified for the design of modern fluid machinery which must incorporate the full governing flow physics.

Computational fluid mechanics offers the opportunity to include models for all the terms present in Eq. (2) to determine the axial moment from fluid forces. This is particularly useful for computations with coupled component interactions that generate sizable unsteady flow.

3 Numerical Method

The numerical computations were performed using the commercially available Numeca Fine Turbo code version 4.14 which performs Reynolds averaging of the Navier–Stokes equations in strong conservative form. Three turbulence models were independently applied, the Baldwin–Lomax, the standard $k-\varepsilon$, and a high Reynolds number nonlinear $k-\varepsilon$ model. While each of these gave a slightly different result the general tendencies remained consistent. The results presented here are based on the standard $k-\varepsilon$ model. The structured numerical grid for a single impeller blade passage consisted of 159841 nodes while a single diffuser–return vane passage had 219069 nodes. Several other grid sizes were evaluated to model the geometry with greater and less node numbers. It was found that grid independence was established for the listed node numbers. Grid independence was determined quantitatively as impeller torque variations of less than 1% and with a reasonable y^+ resolution of the boundary layer. The iterative calculations were stopped when a mass flow convergence of better than 0.15% was maintained for 500 cycles and the root mean square global residual (the sum of all the residual fluxes) on the grid was below -6. The artificial viscosity was held at the lowest value possible to obtain this convergence and was not varied among the time steps. Liquefied natural gas at a temperature of $-165°\mathrm{C}$ and density of 450 kg/m^3 was the working fluid. This fluid was treated as compressible but always remained in liquid form. The geometry parameters of interest for the pump were,

- the impeller–diffuser gap was 5% of the impeller outlet radius,
- the impeller blade solidity was 1.5,
- the pump dimensionless specific speed was 0.35,
- the diffuser inlet blade angle was 9°,
- the impeller rotating speed was held constant.

The impeller and diffuser–return vane are seen in Fig. 3.

The interface plane between the rotating impeller and stationary diffuser was treated in two steps. First a steady flow computation was performed that applies a mixing plane approach for pitch averaging of flow parameters across the interface. The result of this steady computation was applied as an initial guess for the unsteady flow computation. The impeller grid was then rotated through 10 time steps and the entire flow field solved for each time step. The interface was treated as a connected boundary between the impeller and diffuser grid. To provide an accurate boundary layer solution, values of $y^+ < 10$ are obtained over a large portion of the wetted surfaces. This was required to provide adequate resolution of the boundary layer used in the evaluation of surface shear stress.

For the unsteady computation simplifications were made to the actual machine to obtain periodicity which is industrially not viable due to synchronization of the impeller–diffuser interaction. Domain scaling was applied. The number of diffuser–return vanes $Z_\mathrm{d} = 10$ was made an integer factor of the impeller blades $Z_\mathrm{i} = 5$. In reality $Z_\mathrm{d} = 8$ and $Z_\mathrm{i} = 5$, as seen in Fig. 3. The number of impeller time steps calculated was 10, which corresponds to 10 steps for 1/5 of a full rotation or every 7.2°. Periodicity was assumed for the remaining 4/5 of a rotation. The boundary conditions imposed on the periodic sections are defined by $F_k(r, \theta_k, z, t) = F_k(r, \theta_k \pm \text{blade pitch},\ z, t)\ k = 1,2, \ldots$ with F_k as some flow property in a cylindrical coordinate system. At the impeller–diffuser interface a nonmatching connected boundary was applied as the grids do not match at the interface for each time step. A comparison of the results from the time averaged domain scaling method and the separate mixing plane method revealed that the computed impeller torque was within ±1.9% at the flow rates corresponding to 65%, 100%, and 125% bep. The inlet and outlet boundary conditions were far enough upstream and downstream to be held constant for each of the flow rates calculated. Overall the major sources of flow field unsteadiness modeled are the impeller–diffuser interaction, the impeller blade wake, and the boundary layer development. The influence of leakage from clearance flows and seals was neglected. The computational results provide the unsteady quantities within the entire control volume required for a full evaluation of Eq. (2). The domain scaling approach is, however, clearly recognized as having an unsteady interaction with the diffuser that was synchronized. The magnitude of the unsteady flow field from such an approach with a 10 bladed diffuser will be larger than that expected in reality with an 8 bladed diffuser. Thus the results presented here should be viewed as a worst case scenario for design to bracket the upper limit on the impeller torque fluctuations. This is then a usefull design approach that provides a relatively quick computation and an upper limit on the expected unsteady flow field magnitude even though the frequency of excitation will not match reality. But the frequency of excitation can be easily found with a standard interference diagram of the blade rows.

4 Test Stand Measurements

The designed impeller and diffuser–return vane combination in Fig. 3 was manufactured and tested in a 10-stage high-pressure pump. The test fluid was liquefied natural gas at a temperature of −165°C. The drive was a submerged cryogenic motor with a power rating of 1.1 MW. This motor was a two-pole machine running at 3000 rpm from a 6 kV voltage source. A solid model view of the multistage pump is seen in Fig. 4. The differential pressure of the pump was measured between the inlet and discharge using pressure transducers capable of ±0.8% full-scale accuracy. The flow rate was measured with an orifice plate arrangement to ±2% full-scale accuracy. The torque on the shaft of the pump was determined from the measured motor input power and the measured rotational speed of the pump shaft. In the comparison to numerical results compensation for uncalculated hydraulic and mechanical losses (i.e., leakage, bearings, and motor) have been included. This compensation was based on extensive industrial testing experience coupled with previous results from water tests and liquid nitrogen tests where the use of a dynamometer was technically feasible. Using this method the shaft torque was determined to be accurate within ±2%. All of the measured data are time averaged quantities, which are used to provide validation for the steady state numerical results.

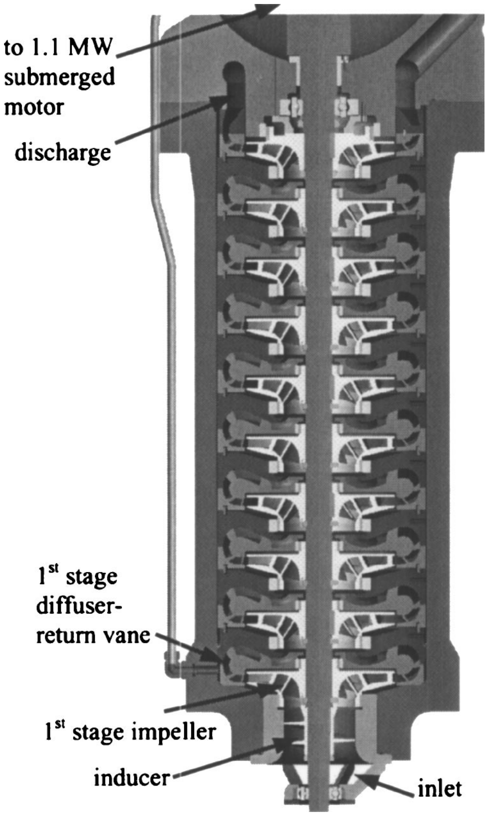

Fig. 4 Solid model view of the 10 stage pump hydraulics that were used to obtain measurments

5 Results

General numerical results are first provided as a foundation for further analysis since these results are applied to calculate the axial moment from fluid forces in Eq. (2). Shown in Fig. 5 is the time averaged total pressure coefficient ψ. As expected the impeller raises the total pressure. In the diffuser–return vane a slight drop in total pressure is experienced due to dissipation.

From the 10 impeller positions corresponding to the 10 time steps at 7.2° rotation, the tangential velocity at the bep flow rate is shown in Fig. 6 on the mid blade height position across the circumference. These profiles, along with the meridional velocity,

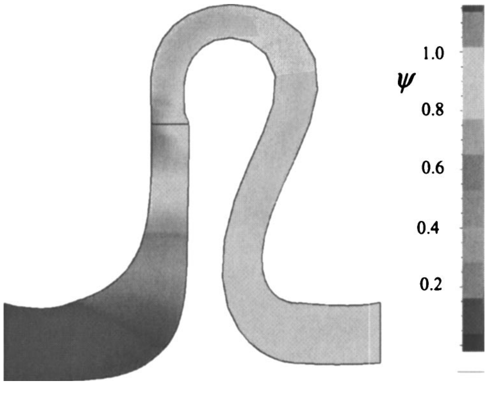

Fig. 5 Circumferential averaged total pressure coefficient

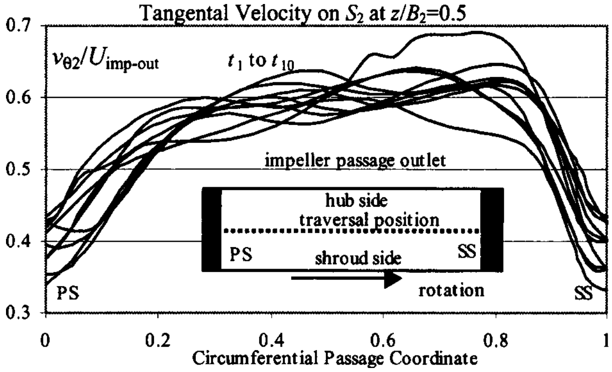

Fig. 6 Tangential velocity for 10 time steps at the bep flow along a traversal of control volume outlet surface S_2

which is not shown, are assumed to be a constant value across the entire impeller outlet surface in the area averaged Euler turbomachinery Eq. (5). This is seen not to be the case and the error associated with the area averaging procedure is summarized in Sec. 6.4.

In the final analysis the overall measured performance of the pump is a validation of the global parameters computed in the numerical model. Figure 7 compares the predicted and measured global characteristics of the pressure coefficient and normalized efficiency at several operating points. Agreement is reasonable with part load calculations showing more deviation from the measurements.

6 Axial Moment From Fluid Forces

For the geometry depicted by Fig. 1 simplifications to Eq. (2) are possible.

1. The pressure term acting on the S_2 control surface causes a force perpendicular to the rotation axis. This force does not contribute to the axial moment on the impeller. The pressure term acting on the S_1 control surface causes a force parallel to the z-axis. This also does not contribute to the axial moment. Both pressure terms are, therefore, zero.

2. The pump had a vertical orientation meaning the gravity vector was parallel to the axis of rotation. The cross product of the gravity vector with the radius vector was perpendicular to the z-axis. No moment contribution along the z-axis was made. The gravity term is therefore zero.

The three remaining moment terms result from the action of,

(1) viscous shear stress on the S_1 and S_2 control surfaces,
(2) fluid velocity on the S_1 and S_2 control surfaces,
(3) unsteady fluid velocity in the control volume V.

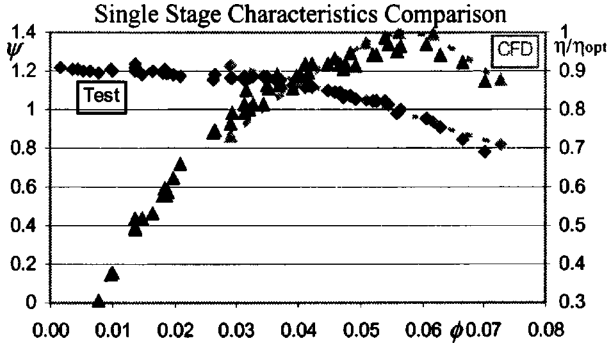

Fig. 7 Comparison of the measured and computed single stage characteristics in LNG

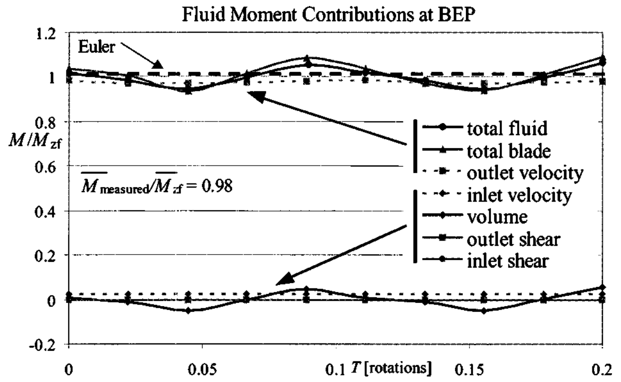

Fig. 8 Comparison of moment contribution terms at bep over 1/5 rotation

The shear stress terms are simplified by the numerical grid arrangement so that the expressions to evaluate the shear stress on the control surface S_2 and S_1 are, respectively,

$$\tau_{r\theta}=\mu\sum_{S_2}\left[R_2\frac{\partial}{\partial r}\left(\frac{v_\theta}{R_2}\right)+\frac{1}{R_2}\frac{\partial v_r}{\partial \theta}\right]$$
$$\tau_{zr}=\mu\sum_{S_1}\left[\frac{\partial v_r}{\partial z}+\frac{\partial v_z}{\partial r}\right] \qquad (6)$$

The numerical differentiation was carried out on the control surfaces using a central difference technique.

6.1 Best Efficiency Point. Figure 8 reveals a graphical comparison of the above three contributions to the axial moment from fluid forces, made dimensionless by the total steady moment $\overline{M}_{\rm zf}$ generated by the fluid forces from the domain scaled computation. The sum of the three fluid contributions $M_{\rm zf}$ is also plotted to reveal the relative importance of each term. The straight dashed line on the graph indicates the value of moment determined from the area averaged Euler equation (5). The experimentally measured steady moment value $M_{\rm measured}$ is 2% below the time averaged axial moment from the domain scaled computation. To be noted is that the impeller–diffuser interaction is well documented to have the least influence on the flow field near the best efficiency point [11]. This operating point represents the best case regarding the magnitude of unsteadiness and related machinery vibrations as recognized by industry [12]. Also of interest is that the unsteady contributions are approximately in phase with each other, rising to their peak as the impeller blade trailing edge was in radial alignment with the diffuser blade leading edge.

6.1.1 Viscous Shear Stress Contribution. The action of shear stress can be seen to be a minor contributor to the total fluid generated moment. The small value of viscosity for liquefied natural gas (approximately 1/4 of water) is partially responsible for the small magnitude of moment to overcome viscous shear forces. In the case of more viscous fluids this term will be more significant.

6.1.2 Fluid Velocity Control Surfaces Contribution. The velocity term on the outlet control surface S_2 is the major contributor to the steady fluid generated moment. The S_1 inlet contribution is shown as much less but will depend on the preswirl for a given application. A comparison between this surface contribution and the Euler equation (5) shows the values are within 4% of each other over the 1/5 rotation. Mathematically these values differ only in the procedure of averaging, being mass or area averaged. As will be seen this level of agreement will not be the case for off-design operation as the flow field gradients and unsteadiness become influential.

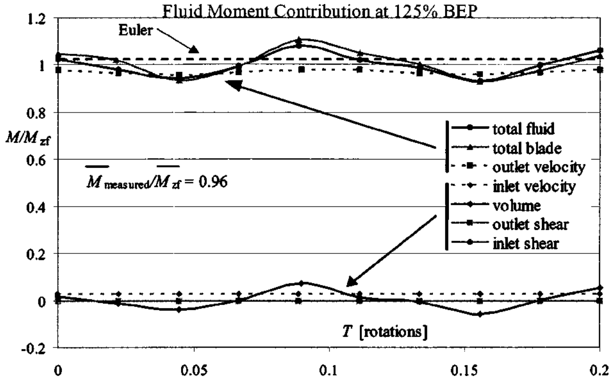

Fig. 9 Comparison of moment contribution terms at 120% bep over 1/5 rotation

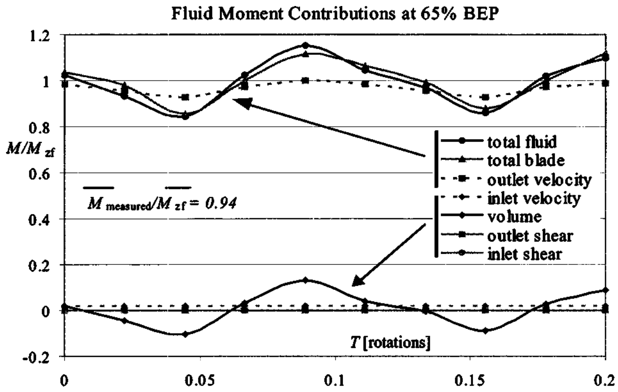

Fig. 10 Comparison of moment contribution terms at 65% bep over 1/5 rotation

6.1.3 Fluid Velocity Control Volume Contribution. The control volume contribution to the axial moment fluctuates at an amplitude of nearly 5% the total fluid moment. This is due primarily to the impeller–diffuser interaction, without this interaction the term would be near zero with only the unsteady boundary layer and impeller wake contributions. It can also be seen that the control volume contribution is responsible for approximately 75% of the unsteady fluctuation amplitude in the total axial moment. The contribution of the fluid velocity on the control surfaces in Sec. 6.1.2 provides the other 25%. This indicates the unsteady velocity in the control volume is primarily responsible for the unsteady axial moment.

6.1.4 Blade Moment. Revealed in Fig. 8 is also the resulting axial moment from the summation of pressure and shear forces acting on the surfaces of the blade and walls, hub and shroud. According to Eq. (1) this must equal the axial moment from fluid forces and serves as a consistency check. Within the numerical uncertainty of the discrete summation procedure, round off, and convergence residuals this can be stated to be true. The discrepancy over the time interval provided is a maximum of 1.4%.

6.2 Over Load: 125% Bep.

Fig. 9 represents the same moment contribution terms at 125% bep flow rate operation. The experimentally derived steady moment value $\overline{M}_{\text{measured}}$ is 4% below the calculated total steady moment. While no significant flow field instabilities were found to occur in the impeller or diffuser, the impeller–diffuser angular momentum exchange and flow angles are mismatched resulting in local regions of larger flow field gradients than at bep.

6.2.1 Viscous Shear Stress Contribution. The sum of the shear stress contributions increases in magnitude by 25% over the bep flow rate case. The reason for this growth is increased secondary flow due to off-design behavior. As depicted in Fig. 9 the viscous contribution, however, remains small enough to be considered negligible.

6.2.2 Fluid Velocity Control Surfaces Contribution. The velocity term on the control surface S_2 is again the major contributor to the steady fluid generated moment. A comparison to the Euler equation (5) is also shown. The terms are within 7% of each other over the 1/5 rotation. Discrepancies are now slightly larger than the bep case as none uniform flow fields have formed which need to be evaluated with a mass averaged procedure.

6.2.3 Fluid Velocity Control Volume Contribution. The amplitude of the unsteady velocity fluctuation inside the control volume V contributes up to 8% of the total fluid moment, which is a slight increase over the bep case. The percentage contribution to the unsteady total moment amplitude remains near 75% while the fluid velocity contribution on the control surfaces is 25%. This is due to both contributions rising in amplitude concurrently.

6.3 Part Load: 65% Bep.

Shown in Fig. 10 are the contributions to the fluid generated moment at a flow rate of 65% bep. The experimentally derived steady moment value $\overline{M}_{\text{measured}}$ is 6% below the calculated total steady moment. At this flow rate various flow field instabilities have formed including impeller inlet and outlet recirculation that are causing the overprediction of the measured value.

6.3.1 Viscous Shear Stress Contribution. The shear stress contribution increases in magnitude by nearly 150% over the bep flow rate case. Reasons for this large growth in magnitude are the existence of both impeller inlet and outlet recirculation which represent regions of large flow field gradients not encountered near bep. However, as depicted in Fig. 10 the shear stress contribution still remains small enough to be considered negligible.

6.3.2 Fluid Velocity Control Surfaces Contribution. The velocity term on the control surface S_2 is again the major contributor to the fluid generated steady moment. In comparison to the Euler equation (5) the average of the S_2 term is 26% higher over the 1/5 rotation. Discrepancies are larger than the bep case as large flow field gradients and secondary flow have formed which require a mass, not area, averaging procedure.

6.3.3 Fluid Velocity Control Volume Contribution. The unsteady moment amplitude from the control volume contributes up to 13% of the total fluid moment, which is significantly more than the bep case. The contribution to the unsteady total moment amplitude is however not changed over the bep case, remaining at near 75% while the fluid velocity contribution on the control surface is near 25%. This is again due to both contributions rising in amplitude concurrently.

6.4 Summary.

Table 1 compares the three unsteady blade moment contributions at the three analyzed operating points. These are compared as the percentage of the total fluid generated moment. The off-design operating points show a greater unsteadiness. The unsteady motion in the control volume term is seen as

Table 1 Comparison of unsteady axial moment from fluid forces as a percentage of the steady value

Operating Point	Viscous	Control Surface	Control Volume
bep	≤1%	1%	5%
125% bep	≤1%	2%	8%
65% bep	≤1%	3%	13%

Table 2 Comparison of contributions to the steady blade moment. Discrepancy between area averaged Euler equation and steady blade moment is also compared.

Operating Point	Viscous	Control Surface	Control Volume	Euler
bep	$\leqslant 1\%$	99%	$\leqslant 1\%$	104%
125% bep	$\leqslant 1\%$	99%	$\leqslant 1\%$	107%
65% bep	$\leqslant 1\%$	99%	$\leqslant 1\%$	74%

the largest contributor to unsteady impeller moment although the relative contribution sizes remain fairly equal at near 0%:25%:75%.

Table 2 compares the steady values of the three moment contributions. Since the volume contribution was based on the derivative of velocity with respect to time a 0% contribution is expected. Also shown for comparison is the evaluation of the area averaged Euler equation (5) determined from control surface averaged values. As expected near bep agreement is reasonable while further removed from bep the area averaging method of Eq. (5) falters.

7 Conclusions

This article provides insight into the physical mechanisms in the fluid that are responsible for the moment on an impeller blade during the impeller–diffuser interaction. The largest contribution to the steady blade moment stems from the velocity contribution on the control surface S_2 at the impeller outlet. The largest contribution to the unsteady blade moment originates from the unsteady velocity in the entire impeller volume V. This may already seem an intuitive pre-determined conclusion; in this article it has been quantified.

The amplitude of the unsteady impeller moment is about 5% the steady value at the bep flow rate and rises in amplitude for off-design conditions to 13% the steady value at 65% bep flow rate. Here the unsteady velocity in the control volume contributes 75% of the moment fluctuation magnitude; the outlet control surface provides the other 25%. For the design of high power concentration turbomachinery these quantities are not negligible and must be included in all design evaluations involving impeller torque including rotordynamic simulations.

Comparisons reveal the computed steady moment values on the impeller blade to be in reasonable agreement with measurements. Furthermore the agreement in the moment is reasonable when compared to the area averaged Euler turbomachinery equation near the bep flow rate. At 65% bep flow rate the area averaged Euler equation shows a discrepancy of approximately 0.75 times smaller. This comes from the area averaging approach of the Euler equation when in actuality mass averaging is required.

Finally the current investigation evaluates one radial gap size between one impeller–diffuser combination. The results presented here should not be generalized without evaluating several other impeller–diffuser combinations from other industries. However the relative importance of all the terms in Eq. (2) for the axial moment generated from fluid forces has been highlighted. The outlook is to manipulate these terms in turbomachinery design to obtain reduced impeller moment fluctuations in high power concentration applications for greater machine reliability. The most obvious way to manipulate these terms is by increasing the radial gap size but other methods such a decreasing the blade loading or reducing the amount of unsteady secondary flow are also available in the design process.

Nomenclature

bep = best efficiency point
$\mathbf{e}$ = unit vector in the subscript direction
$\mathbf{g}$ = gravitational acceleration
M = moment
m = mass flow rate
$\mathbf{n}$ = unit vector normal to control surface
P = pressure
r = radius
S = control surface
$\mathbf{t}$ = unit vector parallel to surface in shear direction
V = control volume
v = absolute velocity
Z = blade number
ψ = pressure coefficient ($\Delta P/0.5\rho U^2_{\text{imp-out}}$)
ϕ = flow coefficient ($Q/A_{\text{imp-out}}U_{\text{imp-out}}$)
η = hydraulic efficiency
ρ = density
τ = shear stress
μ = viscosity
— = time averaged quantity

Subscripts

d = diffuser
i = impeller
s = surface
ws = wall shroud
wh = wall hub
z = direction
zf = z direction, fluid generated
zb = z direction, blade generated
1 = inlet control surface
2 = outlet control surface
θ = circumferential direction

References

[1] Florjancic, D., 2000, ‘‘The Future of the Pump Industry,’’ *Proceedings of the 17th International Pump Users Symposium*, Houston, TX, March.
[2] Cooper, P., 1997, ‘‘Perspective: The New Face of R&D—A Case Study of the Pump Industry,’’ ASME J. Fluids Eng., **118**, No 4, December, pp. 654–664.
[3] Dean, C. D., 1959, ‘‘On the Necessity of Unsteady Flow in Fluid Machines,’’ J. Basic Eng., March, pp. 24–28.
[4] Traupel, W., 1966, *Thermische Turbomaschinen*, Springer Verlag, Heidelberg.
[5] Kaupert, K. A., and Staubli, T., 1998, ‘‘Ecoulement Instationnaire dans une Roue d'une Pompe Centrifuge,’’ Houille Blanche , **3/4**, (3/4), pp. 45–51.
[6] González, J., Fernández, J., Blanco, E., and Santolaria, C., 2002, ‘‘Numerical Simulation of the Dynamic Effects Due to Impeller-Volute Interaction in a Centrifugal Pump,’’ ASME J. Fluids Eng., **124**, pp. 348–355.
[7] Dong, R., Chu, S., and Katz, J., 1997, ‘‘Effect of Modification to Tongue and Impeller Geometry on Unsteady Flow, Pressure Fluctuations, and Noise in a Centrifugal Pump,’’ ASME J. Turbomach., **119**, pp. 506–515.
[8] Sun, J., and Tsukamoto, H., 2001, ‘‘Off Design Performance Prediction for Diffuser Pumps, Institute of Mechanical Engineers,’’ Journal of Power Energy—Part A, **215**, pp. 191–201.
[9] Wang, H., and Tsukamoto, H., 2003, ‘‘Experimental and Numerical Study of Unsteady Flow in a Diffuser Pump at Off-Design Conditions,’’ ASME J. Fluids Eng., **125**, pp. 767–778.
[10] Vavra, M., 1960, *Aero-Thermodynamics and Flow in Turbomachines*, Wiley, New York.
[11] Arndt, N. K. E., Acosta, A. J., Brennen, C. E., and Caughey, T. K., 1989, ‘‘Experimental Investigation of Rotor Stator Interaction in a Centrifugal Pump With Several Vaned Diffusers,’’ ASME J. Turbomach., **112**, pp. 98–108.
[12] API 610 1995, *Centrifugal Pumps for Petroleum, Heavy Duty Chemical, and Gas Industry Services*, 8th ed., American Petroleum Institute, August, Washington, USA.

Transonic and Low Supersonic Flow Losses of Two Steam Turbine Blades at Large Incidences

S.-M. Li
Research Associate

T.-L. Chu
Graduate Student Research Assistant

Y.-S. Yoo
Research Associate

W. F. Ng
Endowed Professor

Department of Mechanical Engineering, Virginia Polytechnic Institute and State University, Blacksburg, VA 24060

A linear cascade experiment was conducted to investigate transonic and low supersonic flow losses of two nozzle blades for the steam turbines. In the experiment, flow incidences were changed from $-34°$ *to* $35°$ *and exit Mach numbers were varied from 0.60 to 1.15. Tests were conducted at Reynolds numbers between* 7.4×10^5 *and* 1.6×10^6*. Flow visualization techniques, such as shadowgraph, Schlieren, and surface color oil were used to document the flows. Measurements were made by using downstream traverses with Pitot probe, upstream total pressure probe, and sidewall static pressure taps. The losses were found to be rather constant at subsonic flows. At transonic and low supersonic flows, the losses increased steeply. The maximum relative increase of the losses was near 700% when the Mach numbers increased from 0.6 to 1.15. However, the maximum relative increase of the losses was only about 100% due to very large variation of incidences. It is important to note that the effect of Mach numbers on losses was much greater than that due to the very large incidences for the transonic and low supersonic flows. A frequently used loss correlation in the literature is found not suitable to predict the losses of the tested blades for the transonic and low supersonic flows. From the current experimental data and some data in the literature, a new correlation for the shock related losses is proposed for transonic and low supersonic flows of turbine cascades. Comparison is made among the existing correlation and the new correlation, as well as the data of the current two cascades and other three turbine cascades in the literature. Improved agreement with the experimental data of the five cascades is obtained by using the new correlation as compared with the prediction by using the frequently used loss correlation in the literature.* [DOI: 10.1115/1.1839927]

Keywords: Transonic and Low Supersonic Flow, Large Flow Incidence, Shock Loss, Linear Cascade, Steam Turbine

Introduction

Steam turbines frequently operate at off-design conditions, such as idling, variable speed, and varying loading. At off-design conditions, flow entering each stage of a turbine can be far off from the design incidences. A transonic and low supersonic flow coupled with a large incidence, possibly leading to a large flow separation on the turbine blade, poses a real challenge for turbine designers. Aerodynamic loss data and their correlations based on turbine cascade experiments are essential for the aerodynamic design and analysis, especially to account for a complete operating range at the initial stage of a whole turbine design process. In addition, transonic and low supersonic flows of turbine cascades with large incidences are also a challenge for CFD analysis. The aerodynamic loss data of transonic and low supersonic flows with large flow separations are also important for the validations of CFD codes.

Over the years, many experimental studies have been carried out to investigate the effects of flow incidences on the performance of turbine cascades, and good results have been obtained, such as Jouini et al. [1], Benner et al. [2], Goobie et al. [3], Hodson and Dominy [4]. However, the aerodynamic loss data for transonic and low supersonic flows at very large incidences are very limited for turbine cascades in the literature.

Many loss correlations for turbine blades have been derived and improved in the past, such as Ainley and Mathieson [5], Craig and Cox [6], Martelli and Boretti [7], and Chen [8]. The most widely used empirical loss system for axial flow turbines is that due to Ainley and Mathieson [5] published in 1951. This loss system was subsequently updated to reflect the improved understanding of some aspects of the flows. The most notable and widely accepted improvement was made by Dunham and Came [9] in 1970. In 1981, Kacker and Okapuu [10] further refined Ainley–Mathieson/Dunham–Came correlation [5,9] to account for the effects of shock waves and channel acceleration of turbine blades at higher Mach numbers. In addition, Kacker–Okapuu correlation [10] also accounted for the advances in turbine design over the past three decades since Ainley and Mathieson [5] (1951). Until recently, Kacker and Okapuu correlation [10] is still frequently used in the literature.

In summary, new data are needed in the area of transonic and low supersonic flows of turbine blades at very large incidences, and periodic revisions are necessary for empirical loss correlations to reflect the recent trends in turbine design. This research is to address the limitation of the data for transonic and low supersonic flows of turbine blades at very large incidences. From the current experimental data, an effort is also made on the shock related loss correlation for transonic and low supersonic flows of turbine cascades.

A linear turbine cascade experiment was carried out in the transonic wind tunnel at Virginia Polytechnic Institute and State University (VPI&SU). Two nozzle blade profiles used for high-pressure steam turbines were tested at the very large incidences (from $-35°$ to $+34°$). Exit Mach numbers were varied from 0.6 to

---

Contributed by the Fluids Engineering Division for publication in the JOURNAL OF FLUIDS ENGINEERING. Manuscript received by the Fluids Engineering Division June 20, 2003; revised manuscript received June 9, 2004. Associate Editor: William W. Copenhaver.

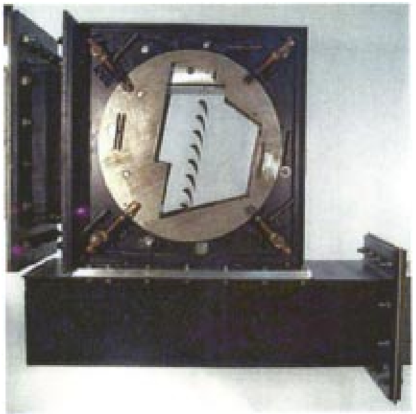

Fig. 1 Cascade test-section

1.15. Flow visualization techniques, such as shadowgraph, Schlieren, and surface color oil were applied to aid in interpreting the data. Measurements such as total pressure and wall static pressure were made to obtain total pressure loss coefficients. The frequently used loss correlation by Kacker and Okapuu [10] was compared with the current experimental data. The comparison shows that the loss model by Kacker and Okapuu [10] severely underestimates the losses of the transonic and low supersonic flows. From the present experimental data and some data in the literature, a new shock related loss correlation is proposed for transonic and low supersonic flows of turbine cascades. The comparison of the new loss correlation is made with the experimental data of the current two cascades and three other turbine cascades in the literature. The comparison of the current experimental data with those of the three cascades in the literature serves as a further validation for the present experiment. In addition, the comparison of the new correlation with the data of the current two cascades and the three turbine cascades in the literature also serves as a validation of the new correlation.

Experimental Techniques

Wind Tunnel and Cascades. The transonic wind tunnel at VPI&SU is a blow-down type. A four-stage reciprocating compressor is used to pressurize air into two storage tanks. Upon discharge from the storage tanks, the air passes through an activated-alumina dryer where the air is de-humidified. Upon entering the test-section of the wind tunnel, the flow is straightened via a flow straightening component and then is made homogeneous by a mesh-wired component. When the tunnel is started to run, a butterfly valve is adjusted to maintain a constant mass flow and constant total pressure with a control computer. Typically the valve is able to maintain a constant mass flow rate and constant total pressure for up to 15 s.

A picture of the test-section is shown in Fig. 1. The test-section has an inlet cross-section with the dimensions of 152 by 234 mm. A cascade with a blade span of 152 mm is mounted on two circular Plexiglasses with a diameter of 457 mm and then is assembled into the test-section. The cascade can be rotated to achieve various flow incidences from −45° to +50°. The flow control techniques for cascade flow periodicity, such as adjustable endwall contours, tailboards, and endwall boundary layer suction, etc., were not used in this experiment. As compared with usual cascade facilities, more blade numbers were used for the cascades in the current experiment to obtain good flow periodicity. A total of 11 to 12 blades were installed for each cascade in this experiment. Flow visualization and traversing data of the cascade wakes showed that an acceptable flow periodicity was obtained in this experiment.

Table 1 Blade specification

Parameter\Type	Blade A	Blade B
Chord (mm)	66	51
Pitch (mm)	31	38
Inlet Blade Angle, β_1	85°	76.4°
Exit Flow Angle, α_2	12°	12°
Solidity (c/s)	2.15	1.34
Gauging (o/s)	0.2	0.2

Two turbine blade profiles were tested in the current cascade experiment. The two blade profiles are proprietary and are not allowed to be published. The geometry parameters of the two cascades are listed in Table 1. Figure 2 illustrates the definition of the geometry parameters used in this paper. The pictures of the blades are shown in Figs. 3–5 for Blade A and shown in Fig. 1 for Blade B. The two blade profiles, Blades A and B were used for impulse-type nozzles of high-pressure steam turbines. Blade A was purposely designed for structural strength necessary for high pressure drops, and Blade B was designed for maximum efficiency of moderate- to low-pressure drop. The two cascades had the same gauging (0.2) and exit metal angles (12°). However, the blade chords, solidities, pitches, and inlet metal angles of the two cascades were different, as listed in Table 1.

Measurement Techniques. The measurements of upstream total pressure were completed using a Pitot probe positioned at 305 mm upstream of the test-section in the wind tunnel. The pitchwise traverse of a Pitot probe was applied at an axial location of 25% of the blade chord downstream from the blade trailing edges. The traversing probe was aligned in the approximated mean flow directions and the traverse of the probe was made to cover at least two middle blade passages of the cascades. The traversing speed of six seconds per pitch was found to be suitable for both the frequency response of the probe and the period of time of the blow-down operation of the wind tunnel at the constant upstream flow conditions.

The measurements of downstream wall static pressures were made with static pressure taps on the sidewalls of the cascades. The size of the pressure taps was 1.6 mm in diameter and they were uniformly spaced in the pitchwise direction of the cascades. Six of the pressure taps were installed for each blade passage. The axial locations of the pressure taps were aligned on the same axial location of the head of the traversing probe. In addition, four static pressure taps were located upstream of the cascades to obtain the upstream static pressure and to verify the uniformity of the inlet flows to the cascades.

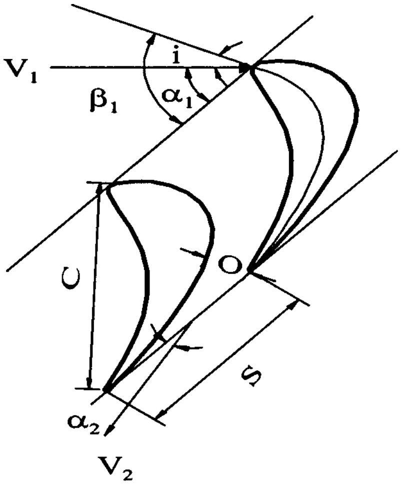

Fig. 2 Nomenclature of blade geometry

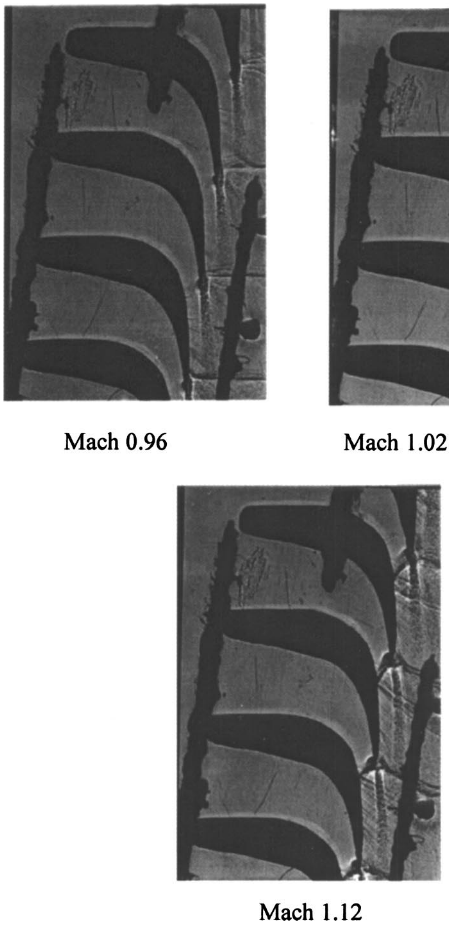
Mach 0.96

Mach 1.02

Mach 1.12

Fig. 3 Shadowgraphs at design incidence of 5° (Mach 0.96, Mach 1.02, and Mach 1.12)

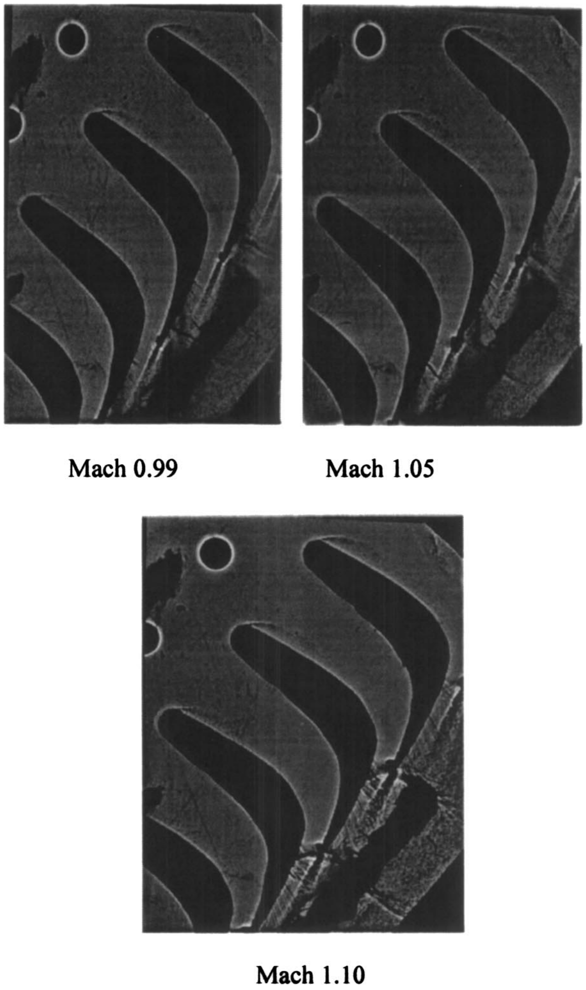
Mach 0.99

Mach 1.05

Mach 1.10

Fig. 4 Shadowgraphs at 35° incidence (Mach 0.99, Mach 1.05, and Mach 1.10)

A relative humidity sensor was positioned upstream of the cascades together with a thermocouple to record the total temperature. The effects of relative humidity on flow loss measurements had been studied with the transonic wind tunnel at VPI&SU before the current experiment and had been found to be negligible when the relative humidity was below 10%. Accordingly, the relative humidity for the current experiment was controlled to be less than 10%.

The data acquisition was performed by two commercial acquisition systems, LeCroy and PSI. Three flow visualization techniques: Shadowgraph, Schlieren, and color surface oil flow, were applied to document the flows. For brevity, only some shadowgraph–Schlieren results will be presented in this paper. The complete flow visualization results can be found in Chu [11].

Total pressure loss coefficients were calculated using the measured data at the inlet and exit of the cascades. The total pressure and wall static pressure at each point of the downstream station were used in determining the local total pressure loss coefficient and the exit Mach number. The local total density was obtained by using the ideal gas state equation. The local static density and flow velocity were then calculated according to the local Mach number. A correction was applied to correct the local data when the probe traverse experienced a supersonic condition. This correction was made according to the well-known Rayleigh formula for supersonic Pitot probe to obtain the real exit Mach numbers and total pressures. A mass-weighted average was made along the two middle blade passages of the cascades to obtain the mean values of total pressure loss coefficients and exit Mach numbers.

The current experiment was performed for the Reynolds numbers from 7.4×10^5 to 1.6×10^6 based on the blade chords and the blade exit flow conditions. The Reynolds numbers and the Mach numbers were not independently controlled in the experiment, but were coupled due to the change of the operating conditions of the wind tunnel. The inlet turbulence intensities to the cascades were found to be less than 1% in the current experiment.

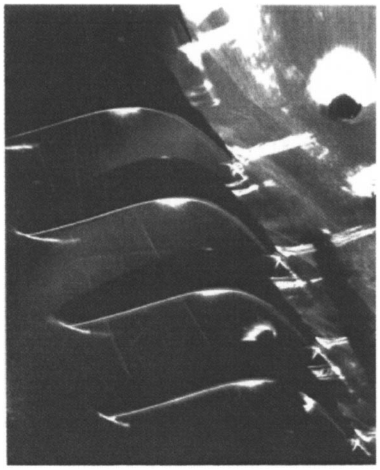

Fig. 5 Schlieren at −25° incidence (Mach 1.12)

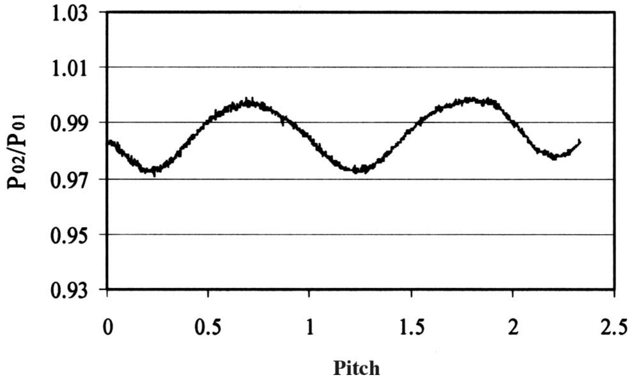

Fig. 6 A sample of the probe traverse data: Total pressure ratio of exit over inlet

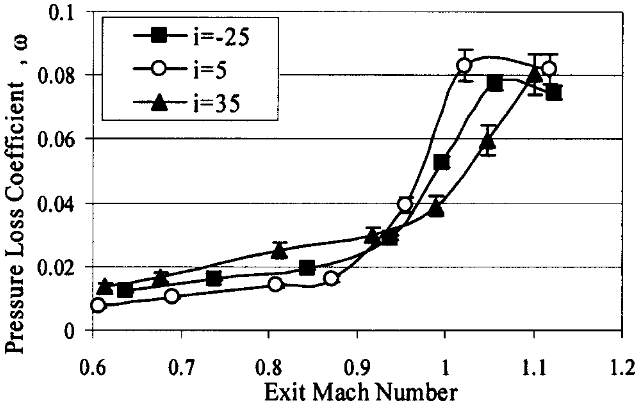

Fig. 7 Pressure loss coefficients with exit Mach numbers and incidences, Blade A (*i*=−25, 5, and 35°)

The major quantities were estimated to have the following uncertainties due to the errors of the instruments and the measurements: total and static pressures, ±1%; incidence angles: ±1°; mass-averaged total-pressure loss coefficients, ±2%; Mach numbers: ±1%. Another major source of the uncertainty of the data was due to the flow aperiodicity of the cascades. The uncertainty due to the flow aperiodicity was estimated by the relative difference between the two averaged values of a quantity on each of the two middle blade passages. The total uncertainty of the flow quantity was obtained by summing the errors due to the instruments and the measurements, as well as the error due to the flow aperiodicity.

Results

Blade A. Shadowgraphs at the design incidence of 5° are shown in Fig. 3 for the three exit Mach numbers, 0.96, 1.02, and 1.12. Good flow periodicity was recorded by the shadowgraphs for all three Mach numbers. At the Mach number of 0.96, a distinctive normal shock appeared at the trailing edge on the suction surface of each blade. This shock interacted with the wake of its adjacent blade. At the Mach number of 1.02, an additional branch of shock appeared at the trailing edge on the pressure side and impinged on the suction surface of the adjacent blade. When the Mach number was beyond 0.96, it was expected that the shock increased to the maximum strength and then tended to diminish to an oblique shock. However, due to the small difference of the Mach numbers between 1.02 and 1.12, no large difference of the shock patterns is distinguished from the shadowgraphs.

Shadowgraphs at the extremely positive incidence of 35° are shown in Fig. 4 for the three exit Mach numbers, 0.99, 1.05, and 1.10. For all three Mach numbers, a flow separation at the leading edge was recorded on the suction surface of each blade. At the extreme positive incidence, the shock pattern is similar to that at the design incidence. However, the location of the shock at the extreme positive incidence occurred earlier on the suction surface and the strength of the shock appeared weaker when the Mach numbers were below 1.05. The additional branch of the shock on the pressure side of the trailing edge started to generate at the higher Mach number, 1.10.

A Schlieren picture at the extremely negative incidence (−25°) is presented in Fig. 5 for the exit Mach number of 1.12. One feature of the flow was the flow separation on the pressure side at the leading edge. It is expected that the separated flow would reattach at some point on the pressure surface because of a strong flow acceleration occurring towards the trailing edge. However, the reattachment point is not clearly observable from the picture. In addition, an additional branch of the shock on the pressure side of the trailing edge was not observed at the tested Mach numbers.

Figure 6 is a sample of the traversing data with the downstream probe presented in the form of a total pressure ratio of the exit over the inlet. The periodicity of the traversing data along the cascade pitches supports the observation with the flow visualizations. It should be mentioned that the periodicity of some traversing data was not as good as shown in Fig. 6. The uncertainty due to the aperiodicity of the flows is included in the total uncertainty of the data, as was mentioned earlier in this paper. The total errorbars of the data will be presented at each data point in the following figures of this paper.

Figure 7 displays the variation of total pressure loss coefficients versus exit Mach numbers for three incidences, the extremely negative incidence of −25°, the design incidence of 5°, and the extremely positive incidence of 35°. Despite the extremities of the incidences, the distributions of loss coefficients versus Mach numbers are similar for all the incidences tested. The profiles of the loss coefficients can be clearly distinguished into three regions: Subsonic, transonic, and supersonic.

In the subsonic region at the exit Mach numbers below 0.90, the flow was dominated by viscous losses. The loss coefficients were relatively insensitive to the Mach numbers. The lowest loss happened at the design incidence and the highest loss occurred at the extremely positive incidence (35°). The loss level at the design incidence was around 50% of that at the extremely positive incidence.

In the transonic and supersonic regions for the exit Mach numbers beyond 0.90, the presence of the strong shock waves caused the losses to increase in a steep gradient. The maximum loss increase was about 700% when the Mach number increased from 0.6 to 1.15 (from a loss coefficient of about 0.01 at the subsonic flow to about 0.08 at the transonic and low supersonic flows). On the other hand, the maximum loss increase due to the very large variation of the incidences was only about 100% and occurred at the subsonic flow (from a loss coefficient of about 0.01 at 5° incidence to about 0.02 at 35° incidence). It is important to note that the effect of the Mach numbers on the losses was dominant for the transonic and low supersonic flows, while the effect of the very large incidence variation was secondary.

At the design incidence of 5°, as shown in Fig. 7, the steep increase of the losses occurred at the exit Mach numbers between 0.87 and 1.02, and then the losses peaked weakly at the Mach number of 1.02. An explanation for this behavior can be made according to the shadowgraphs shown in Fig. 3. At the Mach number of 0.96, the flow separated at the trailing edge due to strong interaction between the distinctive normal shock and the blade boundary layers. The interaction between the shock of a blade and the flow wake of the adjacent blade made the wake mixing stronger. Both the separated flow and the stronger wake mixing were responsible for the steep increase of the losses. When the Mach number went higher, an additional branch of the shock started to appear on the pressure side of each blade and to interact

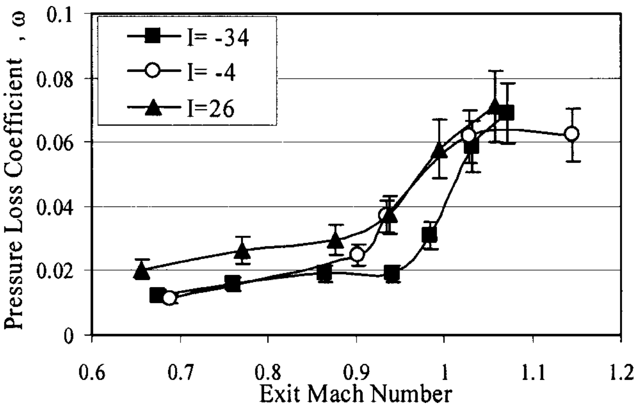

Fig. 8 Pressure loss coefficients with exit Mach numbers and incidences, Blade B ($i=-34$, −4, and 26°)

with the boundary layer on the suction surface of the adjacent blade. The flow interaction due to the additional branch of the shock resulted in a continuing increase of the losses. When the Mach number was getting higher, the strength of the shocks was expected to continue to increase to its maximum and then to diminish to an oblique shock. Subsequently, the loss coefficient at the Mach number of 1.12 was 0.081, a little lower than that at the Mach number of 1.02.

Regarding the effect of the incidence angle variation, as was shown in Fig. 7, the loss pattern for the transonic and low supersonic flows was reversed as compared with that for the subsonic flows. For the transonic and low supersonic flows, the loss curves of the two extreme incidences (−25° and 35°) drop below that of the design incidence, with 5° incidence having the highest loss level while 35° incidence having the lowest loss level. As has also been noted earlier in this session of this paper, at the extreme incidences, the shock was weaker and the generation of the additional branch of the shock was delayed to higher Mach numbers. For transonic and low supersonic flows, shock and its interaction with blade boundary layers–wakes were the dominant source of the flow losses. At the extreme incidences, both the weaker shock and the later generated additional branch of the shock were responsible for the lower loss levels. For the subsonic flows, on the contrary, the flow separation at the blade leading edge was the major contribution to the losses. Even though no shadowgraphs were taken for the subsonic flows, it is reasonable to assume that the subsonic flow separation occurred at the blade leading edge for both the extremely positive and negative incidences, similar to the leading edge flow separations shown earlier in this session for the transonic and supersonic flows (Figs. 4 and 5). At the design incidence, no separation or relatively small separation is expected at the blade leading edge. Consequently, the subsonic loss level was always the lowest at the design incidence and always the highest at one of the extreme incidences.

Blade B. For brevity, the flow pictures of shadowgraph–Schlieren for Blade B will not be presented in this paper. Full documentation of the pictures can be found in Chu [11]. The blade profile of Blade B is displayed in Fig. 1. The pressure loss coefficients as a function of the exit Mach numbers are shown in Fig. 8 for three incidences. The three incidences included the extremely negative incidence of −34°, the design incidence of −4°, and the extremely positive incidence of 26°. When compared with the loss pattern of Blade A shown in Fig. 7, it is noticed that both Blades A and B behave similar for the flow losses in most aspects. The profile of the loss coefficients for Blade B can be also distinguished in three regions: The subsonic region at the exit Mach numbers below 0.90, the transonic and supersonic regions at the Mach number beyond 0.90.

The hollow circles in Fig. 8 represent the loss profile for the design incidence and the remaining two symbols for the two extreme incidences. In the subsonic region, the loss level of the design incidence was the lowest among the three incidences and approximately 50% of the loss level at the extremely positive incidence. In the transonic and supersonic regions, the loss curve of the design incidence peaked weakly at a Mach number between 1.0 and 1.2.

In the subsonic region, as shown in Fig. 8, the loss level at the negative incidence behaved closely to that at the design incidence. In the transonic region, the loss level of the negative incidence became the lowest among the three incidences. At the Mach number of 1.07, the loss of the negative incidence started to exceed that of the design incidence. Due to the limitation of the facility, no data were obtained at higher Mach numbers.

The extremely positive incidence was found to have the maximum loss level among all three incidences, as shown in Fig. 8. In the subsonic region, the loss level of the positive incidence was almost twice of that at the design incidence. In the transonic and low supersonic regions, the loss level of the positive incidence was close to that of the design incidence.

For all three incidences, as shown in Fig. 8, the losses in the subsonic region were relatively insensitive to the Mach numbers. For the transonic and low supersonic flows, the presence of the shock waves and their interactions with the blade boundary layers–wakes caused the losses to increase in a steep gradient. The maximum increase of the losses was about 600% when the Mach numbers increased from 0.6 to 1.1 (from a loss coefficient of 0.012 at $M=0.67$ to a loss coefficient of 0.071 at $M=1.10$). Under subsonic conditions, however, the loss level differed only by 100% due to the very large incidence variation. At the transonic and supersonic flows, the effect of the large variation of incidence angles on the losses was much smaller than that at the subsonic flows. The same conclusion for Blade B can be drawn as compared with the case for Blade A in that for the transonic and low supersonic flows the effect of Mach numbers on the flow losses was dominant and the effect of the large incidence variation was secondary.

Further Comparison of Blades A and B. The pictures of the two blades are shown in Figs. 3–5 for Blade A and in Fig. 1 for Blade B. The two blade profiles appear quite different, with Blade A having a larger curvature on the suction surface approaching the trailing edge, while Blade B having a straight-backed profile toward the trailing edge. The throat–pitch ratios of the two cascades, however, are identical, suggesting that some similar flow accelerating conditions existed in the two cascades. In addition, the cascade solidity of Blade A is significantly larger than that of Blade B. For further comparison, the experimental data of both Blades A and B have been put together at each incidence and are shown in Figs. 9–11.

Figure 9 shows the flow losses of both blade profiles at their design incidences. When the exit Mach numbers were below 0.9, Blades A and B appeared to have almost the same loss level. However, when the Mach numbers exceeded unity, Blade A had higher losses. The larger the cascade solidity is, the narrower the blade passage is, and the stronger the shock interactions are with the blade boundary layer–wake for the transonic and low supersonic flows. Therefore, Blade A generated higher loss than Blade B in the transonic and supersonic regions.

Figure 10 shows the losses of both blade profiles at the extremely negative incidences. When the exit Mach number was below 0.85, the loss levels for the two blade profiles were close to each other. When the Mach numbers were beyond 0.85, the loss level of Blade A started to exceed that of Blade B. Thus, similar to the situation at the design incidences, Blade B could operate more efficiently than Blade A at the extremely negative incidences. The larger cascade solidity of Blade A was also responsible for the higher losses in the transonic and low supersonic regions.

Figure 11 shows the losses of both blade profiles at the extremely positive incidences. In the subsonic region, the loss levels

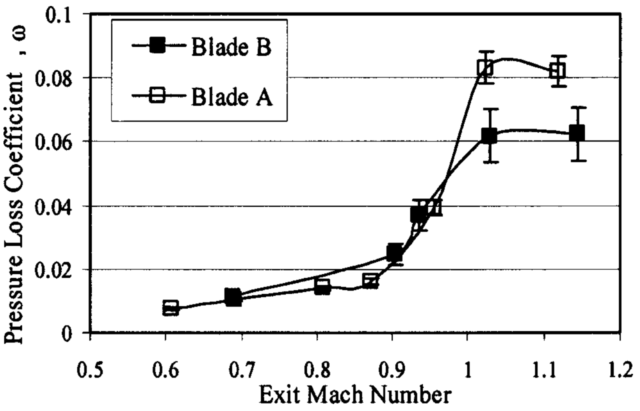

Fig. 9 Comparison of test data at design incidences (Blades A and B)

for the two blade profiles were close to each other. When the Mach numbers went higher into the transonic and supersonic regions, the loss level of Blade A was obviously lower than that of Blade B. These observations are somewhat consistent with the unpublished data in another experiment (Mindock, [12]). At the extreme positive incidence, as presented earlier in this paper, the shock was weaker as compared with the design incidence at the same Mach number and the additional branch of the shock started to generate later to higher Mach number. In addition, Blade A was tested with 9° higher than Blade B for the extremely positive incidences. Therefore, Blade A had weaker shock and more delayed generation of the additional shock branch than Blade B. The weaker shock and the later generated additional shock branch were responsible for the lower loss level of Blade A in the transonic and supersonic regions. Due to the larger solidity of Blade A, its loss had the tendency to exceed that of Blade B at higher Mach number, as shown in Fig. 11.

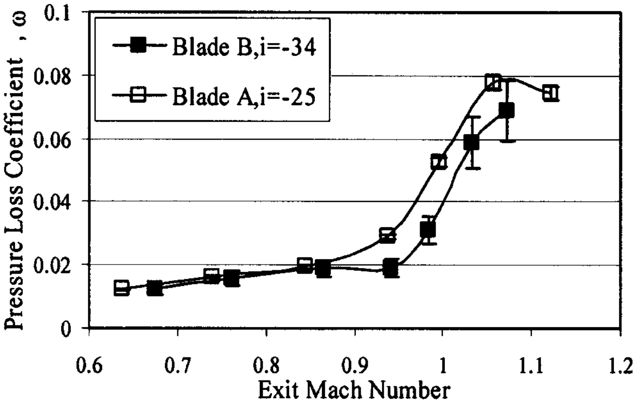

Fig. 10 Comparison of test data at extreme negative incidences (Blade A, $i=-25$ and Blade B, $i=-34$)

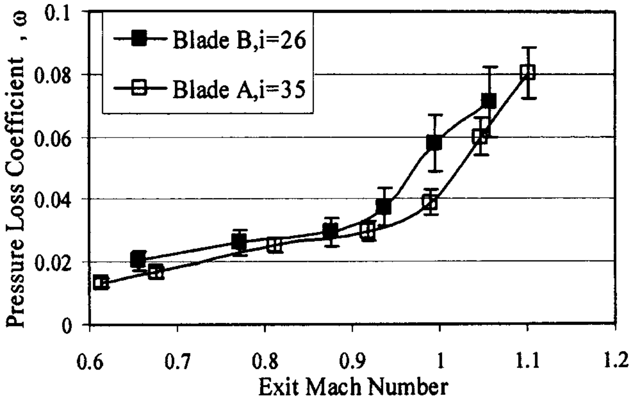

Fig. 11 Comparison of test data at extreme positive incidences (Blade A, $i=35$ and Blade B, $i=26$)

The above comparison in this subsection together with those in the two earlier subsections has revealed some common points for both blade profiles. As was shown in Figs. 7 and 8, the subsonic losses were always the lowest at the design incidences and always the highest at the extremely positive incidences. In particular, the subsonic loss level was relatively constant with respect to the variation of the transonic and low supersonic flow losses. When the Mach numbers increased from 0.9 to 1.15, the losses increased steeply. The maximum increase in the losses was about 700% when the Mach numbers increased from 0.6 to 1.15. On the contrary, the losses due to the very large variation of the incidences only differed by 100%, much smaller as compared with the steep increase due to the Mach number variation from the subsonic to the transonic and low supersonic conditions. Therefore, for both cases the effect of the Mach numbers was much more predominant than that of the very large incidence variation.

In the literature, some loss correlations for off-design conditions of turbine blades are obtained based on the low speed experiments, in which the losses at the off-design incidences always appear much higher than those at the design incidences. This is true for subsonic flows. According to the currently experimental data, however, this is not true at the transonic and low supersonic flows. Under the transonic and low supersonic conditions, the effect of the Mach numbers was predominant and the effect of the very large incidence variation was secondary. For this reason, the large incidences did not necessarily generate higher losses than the design incidences at the transonic and low supersonic conditions. Therefore, the off-design loss correlations for turbine blades derived from the low speed experiments are questionable when applied for transonic and low supersonic flows even at very large incidences.

Loss Correlation

Kacker–Okapuu Correlation. Two-dimensional losses of transonic turbine cascades are mainly associated with blade boundary layers, boundary layer separation, shock waves, flow mixing in the wakes, interaction between shocks and boundary layers, and interaction between shocks and wakes [16]. For convenient discussion in this paper, the two-dimensional losses are classified as (1) nonshock related losses, including those due to blade boundary layers, boundary layer separation, and flow mixing in the wakes, but excluding any effects caused by shock-boundary-layer interaction and shock-wake interaction; (2) shock related losses, including those generated by shocks themselves, boundary layer separation due to shock-boundary-layer interaction, and wake mixing due to shock-wake interaction.

The frequently used Kacker–Okapuu correlation for transonic turbine losses is presented as follows [10]:

$$Y_{p,ko}=0.914 f_{(\mathrm{Re})} Y_{\mathrm{shock}}\left\{\frac{2}{3} Y_{p,amdc} K_p + Y_{\mathrm{hubshock}}\right\} + Y_{\mathrm{TET}} \quad (1)$$

$$Y_{\mathrm{shock}}=1+60(M_2-1)^2 \quad (2)$$

$$K_p=1-\left[\frac{M_1}{M_2}\right]^2 1.25(M_2-0.2) \quad (3)$$

$Y_{p,amdc}$ in Eq. (1) is the Ainley–Mathieson/Dunham–Came loss correlation. The multiplier 2/3 is a correction factor to account for the later improvement in blade designs over the last three decades since Ainley and Mathieson (1951) [5]. K_p is a correction factor for the loss increase due to the channel acceleration of a turbine cascade. Y_{hubshock} is a combined effects of blade shock on inner end wall flow and the blade channel flow of a cascade when the

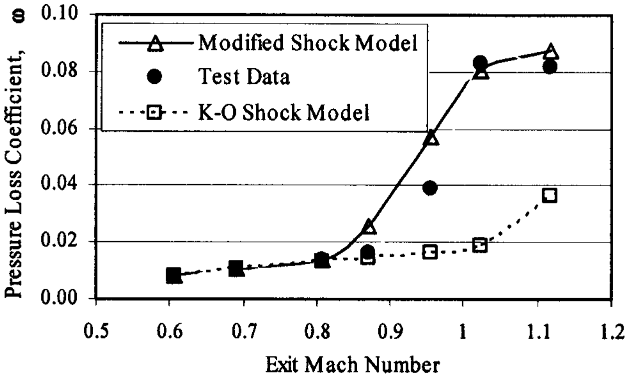

Fig. 12 Comparison of test data with correlations for blade A at design incidence (5°)

inlet Mach number is larger than 0.4. For all tested conditions of the present experiment, the inlet Mach numbers are less than 0.4 and thus $Y_{\text{hubshock}}=0$. Y_{TET} is the trailing edge loss due to tailing edge thickness but without shock effects included. For the two currently tested blades, Y_{TET} is found to be less than 0.2% of the overall losses. $f_{(\text{Re})}$ is a correction factor for Reynolds Number's effects and has the value of unity when Reynolds number is between 2×10^5 and 10^6. Equation (2) is the loss correlation for shock wave effects when the exit Mach number exceeds unity. When the Mach number is less than unit, $Y_{\text{shock}}=1$. Actually, Eq. (2) is the only factor to account for the shock related losses.

When Kacker–Okapuu correlation is applied to predict the total pressure loss coefficients in this paper, the following relation is used to transfer the data from one definition to another for the total pressure loss coefficients:

$$\omega=\frac{Y\left[1-\left(1+\frac{k-1}{2}M_2^2\right)^{k/k-1}\right]}{1+Y\left[1-\left(1+\frac{k-1}{2}M_2^2\right)^{k/k-1}\right]} \tag{4}$$

Figures 12 and 13 present the comparison between the currently experimental data and the prediction by using Kacker–Okapuu correlation of Eq. (1). For both the blade profiles, as shown in Figs. 12 and 13, Kacker–Okapuu correlation is able to estimate the losses satisfactorily at the exit Mach numbers below 0.90. When the Mach numbers are beyond 0.90, Kacker–Okapuu correlation severely underestimates the losses, by as much as 300%. These results show that Kacker–Okapuu correlation works very well when shock waves are not present. Thus, Kacker–Okapuu correlation will be kept unchanged for subsonic flows throughout this paper. When the Mach numbers were beyond 0.90, however, as displayed earlier in this paper, the cascades entered the transonic and supersonic regions and the shocks were generated in the blade passages. Consequently, the shocks and their interaction with the blade boundary-layers/wakes produced steep increase in the losses. Therefore, the severe underestimation of the losses by Kacker–Okapuu correlation at the transonic and supersonic flows is due to the inability of the correlation accounting for the shock related losses, that is, due to Eq. (2). As originally noted by Kacker and Okapuu in Ref. [10], Eq. (2) in their correlation is only an assumption made due to the lack of valid experimental data for transonic and supersonic conditions. Thus, Eq. (2), the correlation for shock related loss, should be modified.

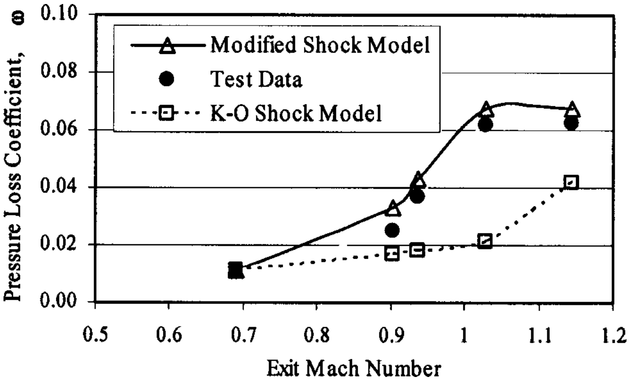

Fig. 13 Comparison of test data with correlations for blade B at design incidence (−4°)

New Correlation for Shock Wave Related Losses. Equation (2), the correlation of shock related losses, includes two pieces of information: (a) The onset Mach number at which the shock related loss starts at transonic and supersonic flows; (b) the profile of the shock related loss variation versus Mach number. The comparison made earlier in this paper between the current experiment and the correlation suggests that the onset of the shock related losses in Kacker–Okapuu correlation should be corrected to lower Mach number, instead of the Mach number 1.0. This is reasonable because the nominal exit Mach number of a cascade represents a mean value of the exit Mach numbers of the cascade. When the nominal exit Mach number approaches 1.0, a local Mach number of the cascade flow could be far beyond 1.0, representing the possibility of the generation of shocks and the interactions between the shocks and the blade boundary layers–wakes. This is why the experiment in this paper displays the steep increase in losses in the transonic and low supersonic regions and the shock related losses started at a much lower Mach number than 1.0.

One may consider that Eq. (2), the correlation for shock related losses could work well if the onset Mach number of the shock related losses was changed to some lower Mach number. For this consideration, some modification has been made for the onset Mach number to a lower Mach number in the following way

$$Y_{\text{shock}}=1+60\left(\frac{M_2}{M_{2\text{on}}}-1\right)^2 \tag{5}$$

When $M_{2\text{on}}$ of Eq. (5) is set to some lower Mach numbers and Eq. (5) is applied for the loss prediction of the two cascades, it is realized that Eq. (5) still very much underestimates the steep increase in the shock related losses. Therefore, a new correlation representing the shock related losses is needed and will be proposed in this paper to replace Eqs. (2) and (5) while the rest of Eq. (1) is kept the same.

The new correlation includes three aspects: (a) The onset Mach number of the shock related losses; (b) the profile of the shock related losses having a maximum when Mach number changes; (c) the offset Mach number of the shock related losses at which Mach number no shock related losses are generated.

The onset Mach number is considered to be related to the critical exit Mach number of a cascade at which a local Mach number of the cascade flow approaches unit. The critical exit Mach number of a turbine cascade can be determined by its geometry and flow parameters, such as the blade profile, cascade gauging (o/s), and flow angles. It is realized that the smaller the cascade gauging, the larger the curvature of the blade suction surface, and the smaller the blade exit angle α_2. In correlating so many factors with the onset Mach number, it is found that the gauging of a turbine cascade can be the most significant parameter or the representative one that determines the onset Mach number, that is, the onset Mach number is approximated only proportional to the cascade gauging. Based on the current experimental data and some data in the literature, a correlation for the onset Mach number is obtained as follows

$$M_{\text{on}}=0.8\frac{o}{s}+0.63 \tag{6}$$

The concept of the offset Mach number, on the other hand, is proposed based on two facts: (a) The loss profile measured in the current experiment, and (b) the theory on an ideal, one-dimensional, compressible flow through a nozzle. As shown in this experiment, the losses of the two turbine cascade increase steeply in the transonic and low supersonic region. The flow losses continue to increase to the maximum in the transonic and low supersonic region and then decrease when the Mach number continues to increase. Based on the theory for an ideal, one-dimensional, compressible flow through a nozzle, the flow can approach the supersonic condition isentropically at the exit of the nozzle, without any shock waves generated. For such a one-dimensional nozzle, this isentropic, supersonic Mach number, without shock waves, is unique and depends only on the area ratio of the exit over the throat of the nozzle (if we consider the thermal characteristic of the fluid to be constant). The offset Mach number of the shock related losses of a turbine cascade should be related to this isentropic, supersonic exit Mach number of the turbine blade nozzle. The area ratio of the exit over the throat of a turbine cascade is approximated as the ratio of the sine of the sum between the half blade trailing wedge angle and the blade exit angle over the sine of the blade exit angle. Considering that the wedge angle of a blade trailing edge is usually not available at the initial stage of a turbine design process, it will not be practical to use the trailing edge wedge angle in the loss correlation. Consequently, a very simple approximation is made for the offset Mach number as follows

$$M_{\mathrm{off}} = M_{\mathrm{on}} + 0.55 \tag{7}$$

Regarding the profile of shock related losses versus Mach number, some considerations are exploited from the current experimental data and some additional data in the literature. Accordingly, the shock related losses are expected to start mildly from the critical Mach number or the onset Mach number of a cascade, followed by a steep increase due to the strong, normal shocks, the multibranches of shocks, and their interaction with the blade boundary layers–wakes. After the Mach number increases to the location having the maximum shock related loss, the flow loss goes down due to the weakened shocks and interactions. It is noticed that the data presented by Martelli and Boretti [7] and Chen [8] have displayed some evidences that the shock related losses behave some symmetrically in the profile around the Mach number of the maximum loss in the transonic and low supersonic regions. Therefore, the profile of the shock related losses is proposed as follows:

$$Y_{\mathrm{shock}} = 1 + K_{\mathrm{sh}}\left[1 + \cos\left(\frac{M_2 - M_{\mathrm{on}}}{M_{\mathrm{off}} - M_{\mathrm{on}}} 2\pi - \pi\right)\right], \quad M_{\mathrm{on}} \leq M_2 \leq M_{\mathrm{off}} \tag{8}$$

$$Y_{\mathrm{shock}} = 1, \quad \mathrm{M}_2 < M_{\mathrm{on}} \text{ or } M_2 > M_{\mathrm{off}} \tag{8a}$$

The correction factor K_{sh} is correlated to the solidity of a cascade as follows:

$$K_{\mathrm{sh}} = K_{\mathrm{shs}}\sigma + K_o \tag{9}$$

Cascade solidity has a large effect on blade boundary layer and consequently is a major factor of effect on flow loss. A turbine cascade with a given blade exit angle has an optimal solidity at which the flow loss is minimum. This optimal characteristic of loss versus solidity is related to nonshock related loss and has been included in $Y_{p,amdc}$, the Ainley–Mathieson/Dunham–Came loss correlation in Eq. (1). However, Eq. (9) accounts for the different flow physics: the larger the cascade solidity is, the narrower the blade passage is, and the stronger the shock interactions are with the blade boundary layer/wake. Therefore, a cascade with larger solidity generates higher shock related loss than a cascade with a smaller solidity. Based on the current experimental data, we obtain $K_{\mathrm{shs}} = 1.0$ and $K_o = 0$.

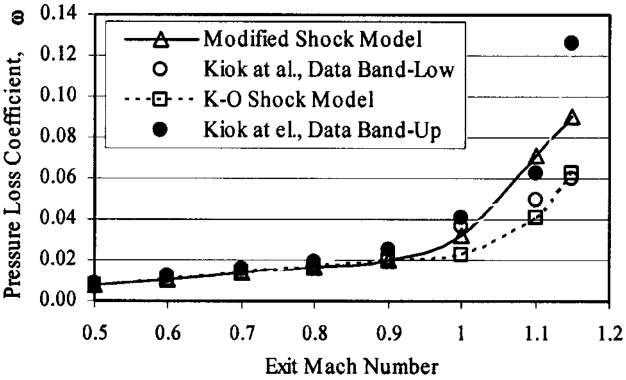

Fig. 14 Comparison of correlations with test data by Kiock et al. [13]

The new shock related loss correlation, as represented by Eqs. (8) and (8*a*), together with the related Eqs. (6), (7), and (9) is proposed to replace Eq. (2), the shock related loss correlation of Kacker–Okapuu.

Comparison Between the New Correlation and Kacker–Okapuu. The predicted losses based on Eqs. (8) and (8*a*), the new shock related loss correlation, are added into Figs. 12 and 13 for the two cascades presented in this paper. It is shown in the figures that much improved agreement is obtained between the new correlation and the experiment for both blade profiles while, as pointed out earlier in this paper, the original Kacker–Okapuu correlation severely underpredicts the transonic and supersonic losses for the two cascades. In particular, the predicted locations of the maximum loss in the transonic and low supersonic regions, based on the new correlation, agree quite well with the experimental data of the two cascades.

To further examine Eqs. (8) and (8*a*), the new shock related loss correlation, a comparison was made among the new correlation, the original Kacker–Okapuu correlation, and the experimental data of three different turbine cascades in the literature. The experiments for the three cascades in the literature were performed and published by Kiock et al. [13], Mee et al. [14], and Detemple-Laake [15], separately. All the loss data published in the literature, whenever presented in the form of the loss coefficient *Y*, have been transferred to the form of the loss coefficient ω, according to Eq. (4).

The data presented by Kiock et al. [13] were obtained in four different European wind tunnels and are presented in the form of an upper and lower limit in this paper. The upper and lower limit of the data and the prediction results with both the original Kacker–Okapuu correlation and the new correlation are presented in Fig. 14. It is shown that both the original Kacker–Okapuu correlation and the new correlation have a good agreement with the experiment at the subsonic flow, as expected. In the transonic and low supersonic regions, the original Kacker–Okapuu correlation also underestimates the losses, even though the underestimation in this case is not as severely as those for the two cascades presented in this paper. It is noted that the new correlation gives the improved agreement with the experiment through the whole transonic and low supersonic range.

Figure 15 shows the comparison of both the original Kacker–Okapuu correlation and the new correlation with the experiment by Mee et al. [14]. The experimental data have been obtained at two Reynolds numbers, 1 000 000 and 2 000 000 and the test data of both conditions are displayed in the figure. The predicted results are displayed at the averaged Reynolds number, 1 500 000. As shown in Fig. 15, the original Kacker–Okapuu correlation, like before, underestimates the losses in the whole transonic and

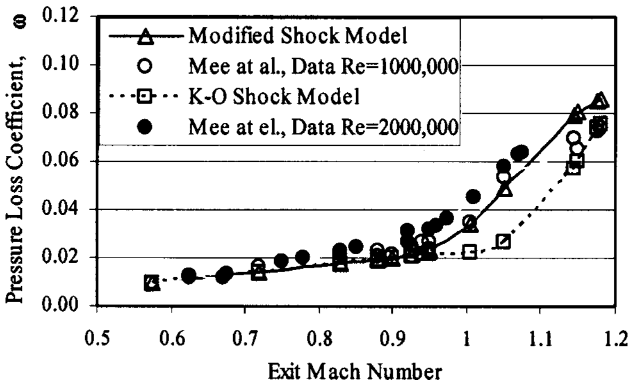

Fig. 15 Comparison of correlations with test data by Mee et al. [14] model)

low supersonic range. On the contrary, the new correlation attains better agreement with the experiment through the complete transonic and low supersonic range.

Figure 16 shows the comparison of the original Kacker–Okapuu correlation and the new correlations with the experiment by Detemple-Laake [15]. As there is no absolute loss level of the data published by Detemple-Laake [15], the loss coefficient, ω at the exit Mach number of 0.9 has been assumed to be 0.025 in order to obtain the absolute loss levels for the other data points presented by Detemple-Laake [15]. In this case, the original Kacker–Okapuu correlation matches quite well with the experiment even though there is still some underestimation of the losses. On the other hand, the new correlation also has quite a good agreement with the experiment data for most of the conditions recorded. However, the new correlation underestimates the loss at the point of the highest Mach number tested. This local underestimation by the new correlation is likely due to the simple approximation of the offset Mach number by Eq. (7).

In summary, through Figs. 12–16, the original Kacker–Okapuu correlation generally underestimates the losses of the three cascades in the literature and severely underestimates the losses of the current two cascades in transonic and low supersonic range. On the contrary, the new correlation proposed for shock related losses gives better and even much better agreement between the prediction and the experimental data for the five cascades in almost all test points.

Since the new correlation matches with the current experimental data very well, the agreement and the improvement of the agreement between the new correlation and the three experiments in the literature also serve as a further validation for the current experiment.

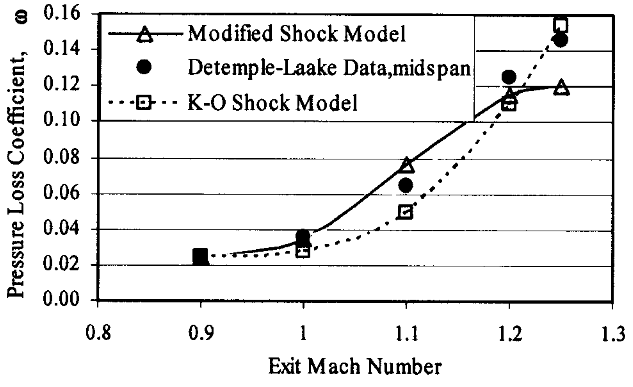

Fig. 16 Comparison of correlations with test data by Detemple-Laake [15]

Summary and Conclusions

- The effects of exit Mach numbers and two extreme flow incidences on the flow losses were investigated for two nozzle blade profiles of the high-pressure steam turbines in a linear cascade experiment. Flow incidences were varied from −34° to 35° and Mach numbers were tested from 0.6 to 1.15.
- For the subsonic flows, the losses were found rather constant with respect to Mach numbers. For both blade profiles tested, the subsonic losses were always the lowest at their design incidences and always the highest at their extremely positive incidences.
- When the flow changed from the subsonic to the transonic and low supersonic conditions, the losses increased steeply. When the Mach number increased from 0.6 to 1.15, the maximum loss increase was about 700%. However, the maximum loss variation due to the very large incidence variation was only about 100%. Therefore, the effect of the Mach numbers was predominant and the effect of very large incidences was secondary under the transonic and low supersonic conditions.
- Regarding the secondary effect of the very large incidence variation, the maximum loss variation (only about 100%) occurred at the subsonic flows. Under the transonic and low supersonic conditions, the loss variation due to the very large incidence variation was even smaller and in particular, the large off-design incidences even did not produce higher losses than the design incidences.
- Some off-design loss correlations for turbine blades in the literature are obtained based on the low speed experiments, in which the losses at the off-design incidences always appear much higher than those at the design incidences. This is true at subsonic flows. According to the current experiment, however, this is not necessarily true at transonic and low supersonic flows. The off-design loss correlations for turbine blades in the literature derived from the low speed experiments are questionable when applied for transonic and low supersonic flows even at very large incidences.
- The frequently used loss correlation by Kacker and Okapuu [10] with its original shock loss model severely underestimates the losses at the transonic and low supersonic flows and should be corrected for future applications.
- A new correlation for the shock related losses has been proposed and then applied to the two cascades presented in this paper and the other three cascades in the literature. As compared with the original Kacker–Okapuu loss correlation, an improved and even much improved agreement with the experimental data for the five cascades has been obtained by using the new correlation.
- Since the new correlation matches with the current experimental data very well, the agreement and the improvement of the agreement between the new correlation and the three experiments in the literature can also serve as a further validation for the current experiment.

Acknowledgments

The authors wish to acknowledge Demag Delaval Turbomachinery Corp. as the project sponsor, and to thank Mr. Mike Mindock of Demag Delaval Turbomachinery for his guidance during this research. Our thanks are extended to the anonymous reviewers for their very insightful and steering criticisms which made the paper much improved than the original manuscript, especially made the section of "Loss Correlation" of this paper completely updated.

Nomenclature

c = Blade chord

$f_{(\mathrm{Re})}$ = Reynolds' number correction to the loss coefficient, Eq. (1)

k = ratio of specific heats

K_o, K_p, K_{sh}, K_{shs} = Correction factors

o = Cascade throat width

s = Cascade pitch

P_o = Stagnation pressure

M = Mach number

M_{on} = Onset Mach number for shock related losses, Eq. (6)

M_{off} = Offset Mach number for shock related losses, Eq. (7)

V = Velocity

x = Axial distance from blade trailing edge

y = Pitch-wise axis of coordinate

Y = Mass averaged total pressure loss coefficient, $Y=[\int(P_{o1}-P_{o2})\rho_2V_2/(P_{o2}-p_2)dy/\int\rho_2V_2dy]$

Y_{hubshock} = Loss coefficient, Eq. (1)

$Y_{p,ko}$ = Kacker–Okapuu loss coefficient

Y_{shock} = Shock loss correlation

Y_{TET} = Trailing edge loss coefficient

α = Flow angle, measured from circumferential direction

β = Blade metal angle, measured from circumferential direction

i = Incidence, $(\beta_1-\alpha_1)$

ρ = Density

ω = Mass averaged total pressure loss coefficient, $\omega=[\int((P_{o1}-P_{o2})/P_{o1})\rho_2V_2dy/\int\rho_2V_2dy]$

Subscripts

1 = Cascade inlet

2 = Cascade exit

References

[1] Jouini, D. B. M., Sjolander, S. A., and Moustapha, S. H., 2001, "Aerodynamic Performance of A Transonic Turbine Cascade at Off-Design Conditions," ASME J. Turbomach., **123**, pp. 510–518.

[2] Benner, M. W., Sjolander, S. A., and Moustapha, S. H., 1997, "Influence of Leading-Edge Geometry on Profile Losses in Turbines at Off-Design Incidences: Experimental Results and Improved Correlation," ASME J. Turbomach., **119**, pp. 193–200.

[3] Goobie, S., Moustapha, S. H., and Sjolander, S. A., 1989, "An Experimental Investigation of the Effect of Incidence on the Two-Dimensional Performance of an Axial Turbine Cascade," ISABE Paper No. 89-7019.

[4] Hodson, H. P., and Dominy, R. G., 1986, "The Off-Design Performance of a Low Pressure Steam Turbine Cascade," ASME Paper No. 86-GT-188.

[5] Ainley, D. G., and Mathieson, G. C. R., 1951, "A Method of Performance Estimation for Axial Flow Turbines," British ARC, R&M 2974.

[6] Craig, H. R. M., and Cox, H. J. A., 1971, "Performance Estimate of Axial Flow Turbines," Proc. Inst. Mech. Eng., **185**, No. 32, pp. 407–424.

[7] Martelli, F., and Boretti, A. A., 1987, "Transonic Profile Losses in Turbine Blades," Institute of Mech. Engrs, C266.

[8] Chen, S., 1987, "A Loss Model for the Transonic Flow Low-Pressure Steam Turbine Blades," Institute of Mech. Engrs. C26.

[9] Dunham, J., and Came, P. M., 1970, "Improvements to the Ainley/Mathieson Method of Turbine Performance Prediction," ASME J. Eng. Power, **92**, pp. 252–256.

[10] Kacker, S. C., and Okapuu, U., 1982, "A Mean Line Prediction Method for Axial Flow Turbine Efficiency," ASME J. Eng. Power, **104**, pp. 111–119.

[11] Chu, T. L., 1999, "Transonic Flow Losses of Two Steam Turbine Blades at Large Incidences," M.S. thesis, Department of Mechanical Engineering, Virginia Tech.

[12] Mindock, Mike, 2001, personal communication.

[13] Kiock, R., Lehthaus, F., Baines, N. C., and Sieverding, C. H., 1986, "The Transonic Flow Through a Plane Turbine Cascade as Measured in Four European Wind Tunnels," ASME J. Eng. Gas Turbines Power, **108**, pp. 277–284.

[14] Mee, D. J., Baines, N. C., Oldfield, M. L. G., and Dickens, T. E., 1992, "An Examination of the Contributions to Loss on a Transonic Blade Cascade," ASME J. Turbomach., **114**, pp. 155–162.

[15] Detemple-Laake, E., 1991, "Detailed Measurements of the Flow Field in a Transonic Turbine Cascade," ASME Paper, 91-GT-29.

[16] Lakshminarayana, B., 1996, *Fluid Dynamics and Heat Transfer of Turbomachinery*, Wiley, New York, p. 558.

S. Mauri
e-mail: sebastiano.mauri@bluewin.ch

J. L. Kueny

F. Avellan

LMH—Laboratory for Hydraulic Machines,
EPFL—Swiss Federal Institute of Technology,
Av. Cour 33bis, Lausanne 1007,
Switzerland

Werlé–Legendre Separation in a Hydraulic Machine Draft Tube

The three-dimensional turbulent flow in a compact hydraulic machine elbow draft tube is numerically investigated for several operating conditions, covering an extended range around the best efficiency point. Comparisons with the experimental data are presented as validation. The interest is focused on the experimentally observed pressure recovery drop occurring near the best efficiency point. The flow is first analyzed locally by means of a topological analysis, then globally with an energetic approach. The study provides evidence for the role played by a Werlé–Legendre separation originating in the bend. The separation is due to the contrasting flow angles imposed by the blades, and the angle resulting from the secondary flow. [DOI: 10.1115/1.1839930]

Introduction

Draft tubes are components which act to convert a maximum of dynamic pressure into static pressure. A measure of the efficiency of these devices is the static pressure recovery obtained. A large number of hydraulic turbomachinery installations are ageing. Thus, there is potential during refurbishment to implement changes in the design for improved efficiency and associated power output as well as greater operating stability. Usually the runner and guide vanes are focused upon in the refurbishment process. Due to capital construction costs the spiral casing and the draft tube are seldom modified. Unfavorable flow behavior occurs when the runner and the draft tube are unsuitably matched. This can sacrifice flow stability and reduce the optimal operating range of the machine. Typically a sudden drop of the pressure recovery in the draft tube is observed near the best efficiency operating condition. The comprehension of this unexplained phenomenon is the objective of the present study. For this aim an extended range of operating conditions is numerically investigated. After the description of the model, a grid convergence study is presented, then comparisons with experimental data are briefly shown as validation. The flow is first analyzed globally with an energetic approach, then locally by means of a topological analysis. The framework introduced by Tobak and Peake [1] is adopted to describe the topological evolution of the flow in the draft tube as the flow rate is varied. A debate on the terminology can be found in Hornung and Perry [2] and other references cited therein.

Case

Experimental studies are carried out on a vertical axis reduced scale model (1:10) of an existing water turbine at the test rig facilities of the EPFL—Laboratory for Hydraulic Machines. A high specific speed Francis runner supplies the symmetrical draft tube with a single pier (Fig. 1). The numerical flow analysis is carried out at a constant head for 14 flow rates ranging from 90% to 110% of the best efficiency discharge. The Reynolds number based on the inlet mean velocity and diameter is $\mathrm{Re}_D \sim 1.5\, 10^6$. The inlet conditions are experimentally investigated on the symmetry axis diameter at six operating points by means of the local density approximation (LDA) technique. The three components of the velocity and the turbulent kinetic energy profile (Fig. 2) are obtained through two positions of a two-dimensional (2D) laser probe, [4]. The measurement uncertainties are estimated to be less than 3%. The other conditions are linearly interpolated from the measurements.

Modeling. Three-dimensional (3D) steady Reynolds-averaged Navier–Stokes (RANS) flow computations with the standard k-ϵ turbulence model and logarithmic wall functions are performed. The flow in the draft tube is simulated using the commercial code CFX-TASCFLOW 2.10. Details on the code are given in Refs. [5,6]. The computation is considered converged to the steady solution when the value of the maximal normalized equation residual is less than 10^{-4}. The fluid properties are set to the values corresponding to the water at atmospheric conditions. The calibration of modeling parameters has been performed in previous studies, see Refs. [7,8], and is here briefly summarized. The inlet profile is specified at the inlet using a cubic spline. A linear interpolation is applied to the circumference. The radial component is imposed as $C_r = C_r \tan(\theta r/R)$. The inclination of the velocity vector in the radial direction is, therefore, determined by the geometry of the cone. This theoretical profile performs better than the profile extrapolated from the relatively few and wiggly measured values. The influence of the radial component is important in spite of its small magnitude. The nearest measurement point is at 0.076 inlet diameter from the wall. The extrapolation of the velocity profile from the last measurement point to the wall has a strong influence on the flow prediction in the draft tube. The influence of the momentum thickness on the efficiency of a diffusor is well known. The velocity components at the wall are set as a factor of the velocity at the nearby interior measurement point. Best results with respect to measurements are achieved with a factor of 0.9. The standard k-ϵ model assumes that $\epsilon = k^{3/2}/L_\epsilon$. For the determination of ϵ from the measured turbulent kinetic energy, the length scale L_ϵ defining the size of the largest eddies must be specified. This parameter has an important influence on the overall flow. $L_\epsilon = 0.002\,\mathrm{D}$ leads to the best results. Several models of the outlet region show a limited influence on the upstream flow. The domain is, therefore, simply prolonged with a downstream channel of length 2 D. At the outlet the flow is considered developed. Several two-equation turbulence models and one second-order closure scheme have been tested. While the two-equation turbulence models perform similarly, the Reynolds-stress model does not increase agreement with the experimental results in spite of the theoretically greater potential. A structured multiblock mesh discretizes the geometry of the draft tube model. A butterfly topology with a C-shaped grid around the pier is used. The y^+ values of the first grid points lie in the validity range of the model.

Verification. An a posteriori numerical error estimation based on the generalized Richardson extrapolation not requiring any restriction to integer refinement and applicable to solution functionals is carried out. Following Roache [10] the more conservative Grid Convergence Index is also reported. The flow rate in the left channel obtained with three meshes is compared at $\varphi^* = 0.994$ in

---

Contributed by the Fluids Engineering Division for publication in the JOURNAL OF FLUIDS ENGINEERING. Manuscript received by the Fluids Engineering Division October 30, 2002; revised manuscript received February 25, 2004. Associate Editor: Edward W. Graf.

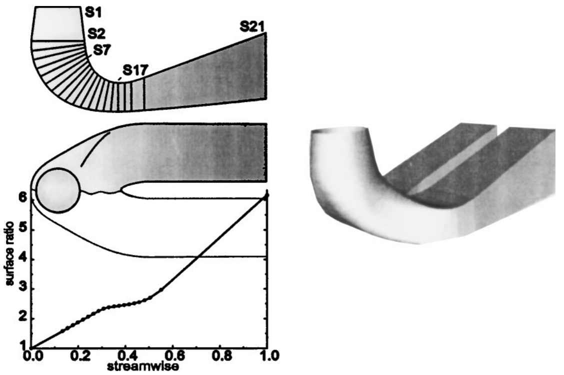

Fig. 1 Investigated geometry. Cross area evolution. Sections definition.

Table 1. The number of nodes corresponds to the effective number of points in the draft tube geometry (double nodes at the block interfaces are counted only once, the downstream channel is not considered). The grid refinement is reported simply in terms of total number of grid points used in the two meshes as $r_{ij} = (N_i/N_j)^{1/3}$. The meshes have the same topology but the grid refinement is not uniform in the space. This may give an inaccurate estimation of the accuracy depending on whether the grid refinement occurs in the critical areas or not. Depending on the mesh resolution at the inlet the resulting flow rate will change and must be corrected to retrieve the measured value by multiplying the velocity field by a factor. The slight differences in the inlet boundary conditions introduce an additional inaccuracy. The meshes seem to be in the asymptotic range; the actual asymptotic rate of convergence is indeed $p=1.98$, to be compared with the theoretical order $p=2$. These results are expected to be only partially representative for other operating conditions due to the important flow differences. The results at the points $\varphi^*=0.919$–1.108 are compared in Table 2. The mesh with $N_3=328{,}360$ nodes insures a GCI smaller than 7% for all operating points. The results obtained with these meshes show the same flow topology and compare very similar with respect to the measured velocity and pressure profiles on several sections. The coarser mesh is, therefore, adequate for our purposes.

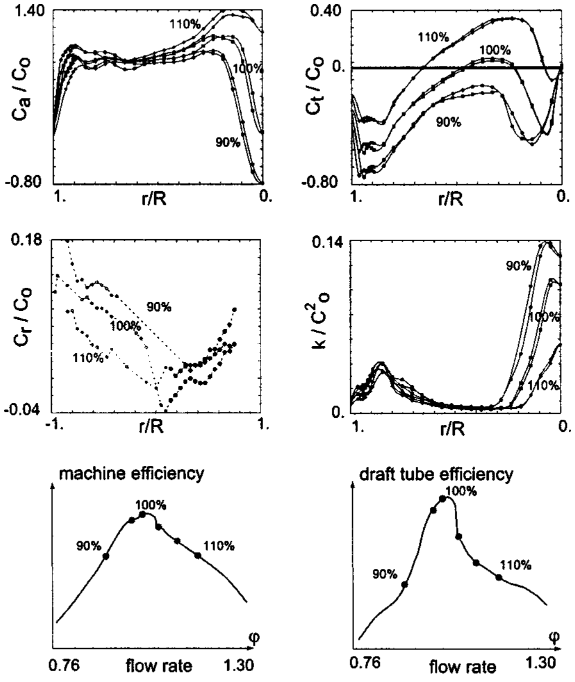

Fig. 2 Measured velocity and kinetic energy inlet profiles (filled points correspond to the external radius). C_a: Axial velocity component, C_t: Circumferential velocity component, C_r: Radial velocity component, k: Turbulent kinetic energy, C_0: Mean sectional velocity magnitude. Machine and draft tube efficiency with the main operating points.

Table 1 $\varphi^*=0.994$. *N*: Number of nodes, *l*: Flow rate in the left channel [%], *E*: Estimated fractional error, *GCI*: grid convergence index. Values for *E*, *GCI* are reported in [%] using $p=2$ as order of the discretization.

$N_1=1{,}107{,}237$	$N_2=633{,}720$	$N_3=328{,}360$
$l_1=63.232$	$l_2=63.309$	$l_3=63.445$
$E_{12}=0.27$	$E_{12}=0.39$	$E_{23}=0.60$
$GCI_{12}=0.81$	$GCI_3=1.17$	$GCI_{23}=1.82$

Table 2 (a) $\varphi^*=0.919$ (b) $\varphi^*=1.108$. See caption in Table 1.

	(*a*)	
$l_1=72.526$	$l_2=72.544$	$l_3=72.576$
$E_{12}=0.06$	$E_{12}=0.08$	$E_{23}=0.12$
$GCI_{12}=0.17$	$GCI_{12}=0.24$	$GCI_{23}=0.37$
	(*b*)	
$l_1=65.094$	$l_2=65.367$	$l_3=65.886$
$E_{12}=0.93$	$E_{12}=1.44$	$E_{23}=2.23$
$GCI_{12}=2.80$	$GCI_{12}=4.06$	$GCI_{23}=6.71$

Validation

The comparison with measurements is not emphasized here, the objective being the characterization of the "numerical flow." Only the recovery factor and the velocity field at the draft tube outlet are shown. Several other comparisons on the whole geometry have been performed showing that while the main flow features and trends are correctly captured, locally important differences occur, see, Refs. [7–9]. The recovery factor is compared with the measurements in Fig. 3. The global behavior is fairly well predicted. The pressure recovery drop takes place at the same flow rate observed experimentally, however, the computations overestimate the recovery factor over the whole range, with a maximal difference of 14% of the measured value. Near the best efficiency conditions the maximal difference is 6%. The velocity field at the draft tube outlet is compared for the two extreme operating points in Fig. 4.

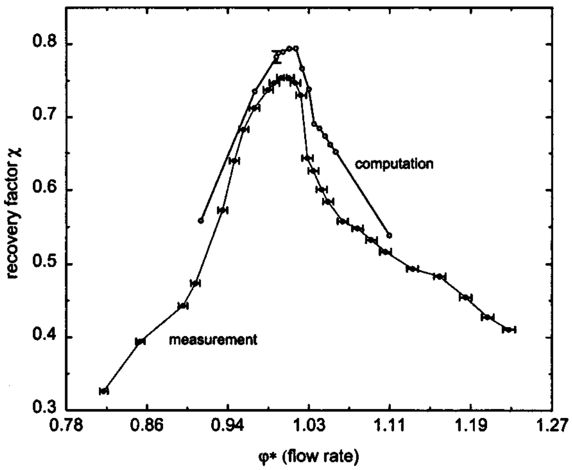

Fig. 3 Static pressure recovery. Comparison measurement-computation. The GCI is reported for $\varphi^*=0.994$.

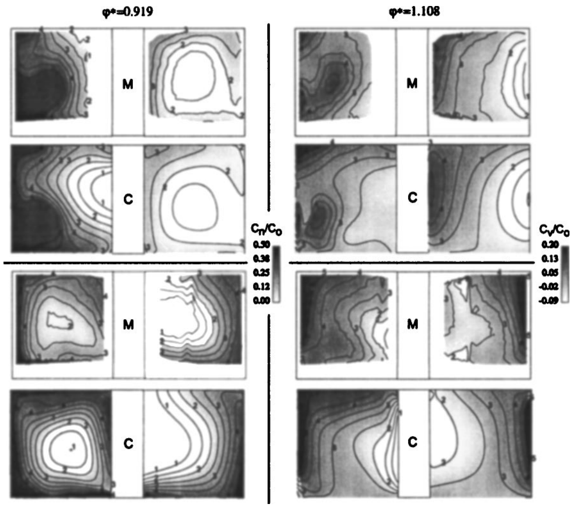

Fig. 4 Comparison measurements (M)-computation (C) at the draft tube outlet. Normal (C_n) and vertical (C_v) velocity components, C_0: mean sectional velocity magnitude. $\varphi^*=0.919$ and $\varphi^*=1.108$. The measurements do not cover the whole channels' surface.

Static Pressure Recovery. The specific static pressure energy recovery is summarized in Fig. 5 over the whole computed operating range. Most of the recovery occurs in the cone. The efficiency drop taking place in the second half of the bend is clearly visible in the range $\varphi^*=1.021$–1.049. This deficiency is partially recovered in the last part. The domain is split into two symmetrical parts allowing a comparison between the left and the right channel, even upstream at the pier's leading edge. The recovery drops on the left side due to a flow acceleration, while on the right channel the pressure recovery is very small in the straight diffuser, indicating an unfavorable flow situation. The flow rate distribution in the channels is shown in Fig. 6. The right channel is clearly blocked in the efficiency drop region.

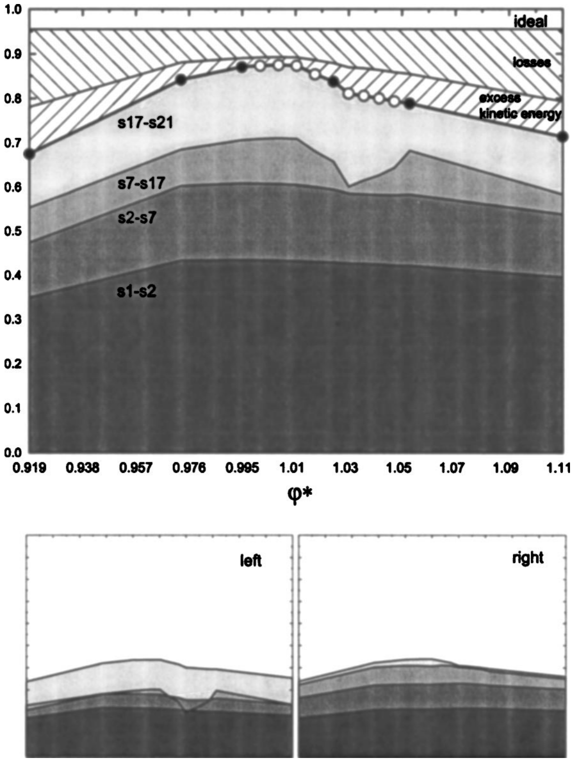

Fig. 5 Computed local mean specific static pressure coefficient. The recovery occurring in the cone (s1-s2), first half of the bend (s2-s7), second half of the bend (s7-s17) and diffuser (s17-s21) and in the left- and right-side of the draft tube are distinguished.

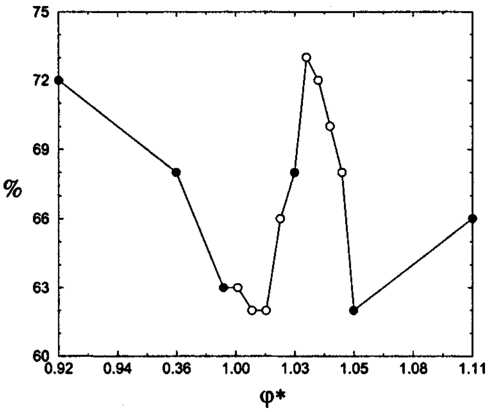

Fig. 6 Predicted flow rate percentage in the left channel over the operating range

Flow Topology. The main characteristics of the skin friction lines are investigated. Experimentally the flow patterns at the wall can be obtained by means of the oil film method. The power of topological visualization is that, given the singular (critical) points and their principal tangent curves, an observer can visually infer the shape of other tangent curves and hence the structure of the whole vector field. A representation of the global topology is much more readily visualized than the original data set. The main flow characteristics are summarized in Fig. 7, where the change of the flow direction in the right channel due to the increase of the secondary flow introduced by the bend, and to the change of the rotation direction at the inlet (Fig. 2), is put in evidence by means of separation lines. These are lines drawn in the flow toward which other trajectories are asymptotic. A universal definition of separation in a three-dimensional flow is still subject of debate. The specification of separation by means of a reverse flow or vanishing wall shear stress is usually inadequate in three-dimensional flows. A necessary condition for the occurrence of flow separation is the convergence of skin friction lines onto a separation line. The regions of flow separation are important because of the reduced kinetic energy and the consequent blockage effect that these regions can introduce. The point before the efficiency drop shows local (not passing through any critical point) separation lines at the surface. After the drop the flow stemming from the cone region situated at the outer side with respect to the

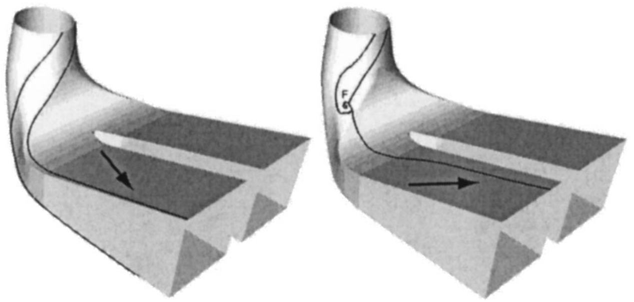

Fig. 7 Predicted separation lines and flow direction in the right channel before ($\varphi^*=0.994$) and after ($\varphi^*=1.021$) the efficiency drop

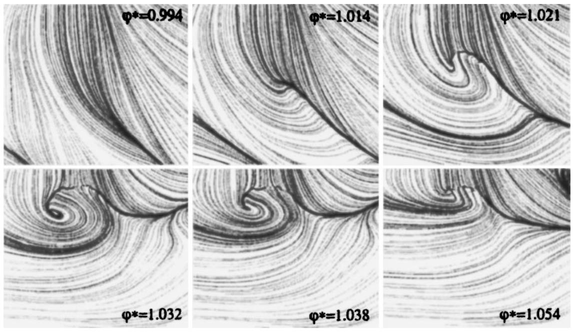

Fig. 8 Computed skin friction lines, onset on the surface of a focus in company with a saddle point. Before the efficiency drop: $\varphi^*=0.994$, $\varphi^*=1.014$, after: $\varphi^*=1.021$, $\varphi^*=1.032$, $\varphi^*=1.038$, $\varphi^*=1.054$.

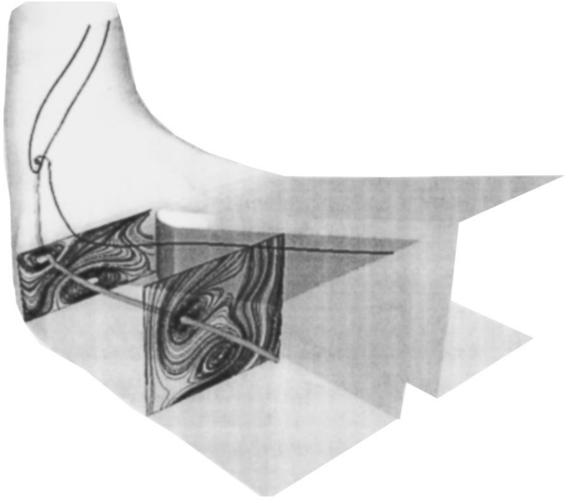

Fig. 10 Predicted vortex evolution. Before the drop: $\varphi^*=1.014$, after: $\varphi^*=1.021$, $\varphi^*=1.027$, $\varphi^*=1.032$, $\varphi^*=1.038$. The last picture summarizes the first four operating conditions (lighter core: $\varphi^*=1.014$, darker core: $\varphi^*=1.032$).

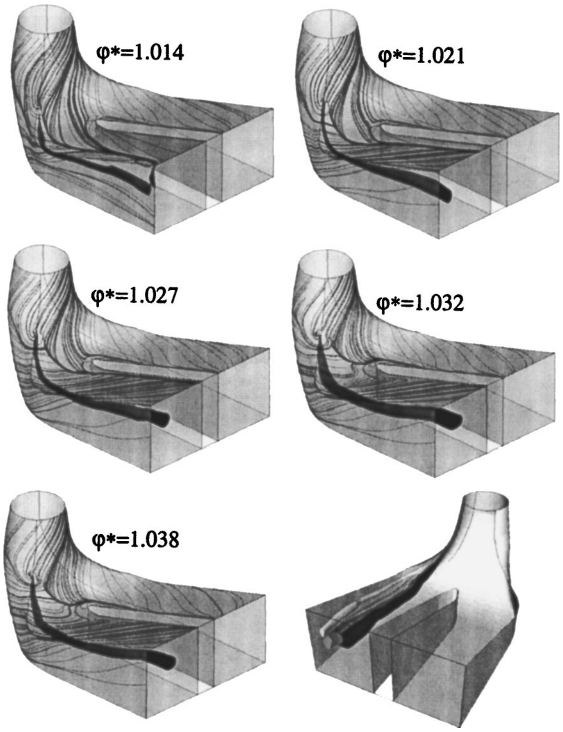

Fig. 11 Interpretation of Fig. 8. S: Saddle, F: Focus, N: Node.

bend curvature is forced by the secondary flow to the inner side, while the flow angle imposed by the blade geometry remains constant for all operating points. The collision of these two flow directions leads to the onset on the surface of a focus in company with a saddle point leading to a global Werlé–Legendre separation (see also Fig. 8, showing the wall region where the onset of the critical points occurs). In this particular form of separation one leg of the line of separation emanating from the saddle point winds into the focus to form the curve on the surface from which the dividing surface stems. The focus on the wall extends into the fluid as a concentrated vortex filament, while the surface rolls up around the filament. This flow behavior was first hypothesized by Legendre in 1965 and confirmed by the experiments of Werlé (1962). The cooperation between these two scientist is described in Ref. [3]. As the flow rate reaches a critical value the flow bifurcates, breaking the symmetry of the precedent flow and adopting a form of lesser symmetry in which dissipative structures arise to absorb just the amount of excess available energy that the more symmetrical flow no longer was able to absorb. The flow pattern in the inner domain can be seen in Fig. 9, where the vortex core originating from the focus and the tangential streamlines on two cross-sections are shown. There is a practical difficulty to define the separation region delimited by the stream surface originating from the line of separation. A simple separation region extraction algorithm is used to define a volume. Streamlines are started from the zone at the wall where separation occurs. A streamline is then equidistantly divided and from each point the intersection of the corresponding normal plane with all other streamlines is computed. From each group of points the mean point is calculated and used to define a new line and the procedure is repeated until the desired convergence is achieved. From each cloud of points, corresponding to the intersection of the normal plane of this mean line with all streamlines, the best fitting ellipse to the external points of the cloud is computed. The resulting tube with elliptic sections approximates the separation zone. In this case the separation forms a swirling structure. The vortex evolution is shown in Fig. 10. Just prior to the drop the separated region is small and attached to the sidewall. Then the vortex structure is formed and moves toward the center of the section and increases its size and strength until $\varphi^*=1.032$, then begins to decay and at $\varphi^*=1.054$ the focus disappears (Fig. 11). The relationship to the flow rate distribution shown in Fig. 6 and to the pressure recovery illustrated in Fig. 5 is evident.

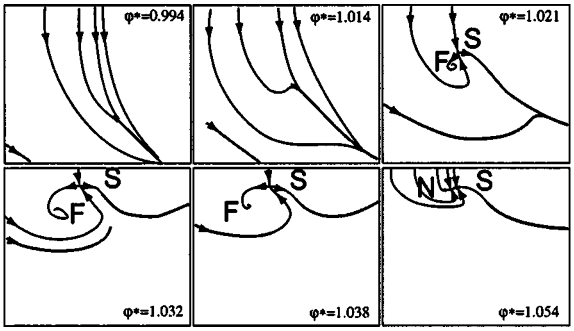

Fig. 9 Computed vortex core and separation line, $\varphi^*=1.021$

Conclusion

The origin of the static pressure recovery drop can be clearly localized in the bend region by means of an energetic analysis.

The study of the skin friction lines in this region shows the onset of a global Werlé–Legendre separation as the flow rate reaches a critical value. The topological structure of the skin friction field bifurcates with the emergence of a saddle point and a focus in the surface pattern. The evolution of the vortex region originating in the focus is visualized in the inner flow clearly illustrating how the separation blocks the right channel leading to a flow acceleration in the other channel. The static pressure recovery is strongly affected, leading to an important loss in the overall machine efficiency.

Acknowledgments

This study is established within the Flindt project (Eureka No. 1625) whose participants are EPFL, Electricite de France, Alstom Power, General Electric Canada, VA Tech Escher Wyss, and Voith Hydro who are gratefully acknowledged. The project is also supported by the Swiss Federal Commission for Technology and Innovation (PSEL) and the German Ministry of Science and Technology (BMBF). The authors wish to thank G. Ciocan and J. Arpe for the experimental data and the staff of the Laboratory for Hydraulic Machines for providing support in the experimental and numerical work.

Nomenclature

A_{ref} = Reference section area
C = Velocity field
C_0 = Mean local normal velocity
$D=0.4\,[\text{m}]$ = Runner outlet diameter
$E_{k_o}=\langle C^2/2\rangle_{\text{Q}}$ = Inlet mean kinetic specific energy
$e_{p_i}=E_{p_i}/E_{k_o}$ = Local mean specific static pressure energy coefficient
$E_{p_i}=\langle p/\rho\rangle_{\text{Q}_\text{i}}$ = Local mean static pressure specific energy
ϵ = Turbulent disspation rate
k = Turbulent kinetic energy
L_ϵ = Turbulent eddy length scale
Q = Flow rate
r = Radius
R = Inlet radius
$\text{Re}_D=C_0D/\upsilon$ = Reynolds number
y^+ = Nondimensional distance from the wall
$\chi=((1/\rho)\Delta P_{dt})/(0.5(Q/A_{\text{ref}})^2)$ = Pressure recovery factor
ΔP_{dt} = Mean wall pressure difference between draft tube inlet and outlet
υ = Water kinematic viscosity
φ = Flow rate coefficient
φ^* = Flow rate coefficient divided by the φ of the best efficiency point
ρ = Water density
θ = Half cone opening angle
$\langle f\rangle_Q=(1/Q)\times\int_A f\vec{c}.\vec{n}dA$ = Volume flow weighted surface average

References

[1] Tobak, M., and Peake, D. J., 1982, ''Topology of Three-Dimensional Separated Flows,'' Annu. Rev. Fluid Mech., **14**, pp. 61–85.
[2] Hornung, H., and Perry, A. E., 1984, ''Some Aspects of Three-Dimensional Separation, Part I: Streamsurface Bifurcations,'' Z. Flugwiss. Weltraumforsch., **8**, Heft 2, pp. 77–87.
[3] Délery, J. M., 2001, ''Toward the Elucidation of Three-Dimensional Separation,'' Annu. Rev. Fluid Mech., **33**, pp. 129–54.
[4] Ciocan, G. D., Kueny, J.-L., and Avellan, F., 2000, ''Optical Measurement Techniques for Experimental Analysis of Hydraulic Turbines Rotor-Stator Interaction,'' Proceedings of 2000 ASME Fluids Engineering Conference, Boston, June 11–15.
[5] Raw, M. J., Galpin, P. F., and Hutchinson, B. R., 1989, ''A Colocated Finite Volume Method for Solving the Navier-Stokes Equations for Incompressible and Compressible Flows in Turbomachinery: Results and Applications,'' Proceedings Thirty-Sixth Annual General Meeting Canadian Aeronautics and Space Institute, Ottawa Ontario, III.
[6] AEA Technology Engineering Software Limited, 2000, ''CFX-TASCflow Theory Documentation Version 2.10,'' Waterloo, Ontario, Canada N2L 5Z4.
[7] Mauri, S., Kueny, J.-L., and Avellan, F., 2000, ''Numerical Prediction of the Flow in a Turbine Draft Tube—Influence of the Boundary Conditions,'' Proceedings of 2000 ASME Fluids Engineering Conference, Boston, June 11–15.
[8] Mauri, S., 2002, ''Numerical Simulation and Flow Analysis of an Elbow Diffuser,'' Ph.D. thesis EPFL $N°$2527, Lausanne, http://lmhwww.epfl.ch/Publications/Theses/Mauri/MauriPhD.html
[9] Mauri, S., Kueny, J.-L., and Avellan, F., ''Flow Simulation in an Elbow Diffuser: Verification and Validation,'' Proceedings of the 21st IAHR Symposium on Hydraulic Machinery and Systems, Lausanne, Switzerland, 9–12 September, 2002, pp. 231–240.
[10] Roache, P. J., 1997, ''Quantification of Uncertainty in Computational Fluid Dynamics,'' Annu. Rev. Fluid Mech., **29**, pp. 123–160.

Time Resolved Concentration Measurements in an Axial Flow Mixer

J. E. Campbell
R. W. Coppom
J. E. Guilkey
J. C. Klewicki
P. A. McMurtry

Physical Fluid Dynamics Laboratory,
Department of Mechanical Engineering,
University of Utah,
Salt Lake City, UT 84112

Experimental results are reported providing information on the downstream mixing evolution in axial pipe flow mixers where a scalar is introduced into the pipe via a coaxial injection tube. Experiments were conducted in a 25.4 mm diameter water pipe flow loop $(25{,}700>R_D>28{,}500)$*, in which a fluorescein dye was coaxially injected. The injection tube diameter was 1.5 mm. Three velocity ratios,* $V_R=0.5$*, 1.0, and 2.0 were explored, where* $V_R=V_{jet}/V_{main}$*. The present results indicate that the effects of velocity ratio on the scalar concentration statistics are mainly evident in the first several outer pipe diameters downstream. In the far field, velocity ratio effects are shown to be insignificant on the concentration statistics. All cases showed a similar trend of an initial increase in variance at the centerline as the injected fluid begins mixing with the main pipe flow. This is followed by a region of rapid "exponential-like" decay, followed by a much slower decay rate after approximately 50 pipe diameters. Space-time correlations of the scalar concentration between far field locations verify the low wavenumber motions as predicted by the recent theory of Kerstein and McMurtry [A. Kerstein and P. McMurtry, "Low-wave-number statistics of randomly advected passive scalars," Phys. Rev. E* ***50****, 2057 (1994)], and are consistent with the slower than exponential downstream mixing rate.*

[DOI: 10.1115/1.1845491]

1 Introduction

Axial flow mixers are commonplace in a number of industrial applications, largely due to their simplicity of design and relative ease of implementation. However, owing to the complexity of the underlying turbulent mixing processes, the behavior of these devices remains poorly understood.

The work of Nye and Brodkey [1] was one of the earliest studies to focus on the downstream evolution of the scalar variance and scalar spectrum. These authors used dye injection and optical measurement to make concentration measurements of dye injected coaxially into the main pipe flow. Measurements were made at up to 36 diameters downstream and indicated an exponential decay of the scalar variance. Hartung and Hibby [2] performed a similar fundamental study, the difference being the way the two scalars were introduced into the pipe. The pipe was initially divided down the center resulting in two separated streams. Concentration measurements were made out to 80 pipe diameters downstream of the initial mixing location and showed an exponential rate of decay throughout the measurement region. Several subsequent studies have been performed, focusing primarily on optimal design of mixing configurations in pipes, (e.g. Forney et al. [3], Ger and Holley [4], Fitzgerald and Holley [5], Edwards et al. [6], O'Leary and Forney [7], Sroka and Forney [8], and Forney [9].)

Most of the early studies on scalar mixing in pipes focused on the scalar variance decay and the relation to Corrsin's [10] theory for scalar variance decay in stirred tanks. The studies of Nye and Brodkey, Hibby and Hartung, among others exhibited consistency with this theory. Much subsequent theory has involved relating Corrsin's theory for mixing in stirred tanks to pipe flow mixing by approximating the mixing evolution as a series of stirred tanks with the dimensions of the pipe diameter moving along at the mean fluid velocity [11].

More recently, an analytical study by Kerstein and McMurtry [12] predicted that the scalar variance decay in pipe mixing should transition from an exponential decay to a power-law decay in the far field: a prediction not observed in any previous experimental mixing studies. The transition to power-law decay was associated with the emergence of long-wavelength scalar fluctuations. These fluctuations were shown to grow with the square root of downstream distance and would eventually be much larger than any characteristic scale of the fully developed turbulent velocity field. To experimentally investigate this theory, Guilkey et al. [13] devised a set of experiments that allowed for a very idealized initial scalar field in the pipe, providing an experimental analogue of the Kerstein-McMurtry theory. Using a flow seeded with a caged fluorescein dye, Guilkey et al. were able to selectively uncage or "mark" regions of the flow at regular intervals. This generated an initial scalar concentration similar to that used in the Kerstein-McMurtry analysis. Measurements made at up to 120 pipe diameters downstream showed a clear transition from exponential to power-law decay, confirming the predictions of the McMurtry-Kerstein theory. To further investigate this behavior and to explain the lack of a region of power-law decay in any of the previous works addressed above, additional experiments were performed looking at potential variations relating to how the scalar was injected into the main flow [14,15]. With the exception of the work of Hartung and Hibby [2], none of the studies cited above reported variance decay statistics beyond a few tens of pipe diameters downstream, a key reason why the transition to a slower mixing rate was not observed. These later experimental studies [14,15] successfully explained differences among previous studies and showed evidence that the initial conditions could be manipulated to delay or expedite the onset of the transition to power-law scalar variance decay.

The motivation behind the present study is to continue the investigation of mixing in pipe flow reactors and broaden the knowledge base of the downstream mixing evolution in configurations more commonly encountered in practice. The application here is the mixing downstream of a coflow, axial injector. A specific aim of this paper is to explore the exponential to power-law transition of the variance decay with respect to different velocity ratios V_R, examine the development of the long-wavelength axial variations in the scalar field, and better understand the flow phys-

---

Contributed by the Fluids Engineering Division for publication in the JOURNAL OF FLUIDS ENGINEERING. Manuscript received by the Fluids Engineering Division August 11, 2003; revised manuscript received July 24, 2004. Review conducted by: M. Volkan Ötügen.

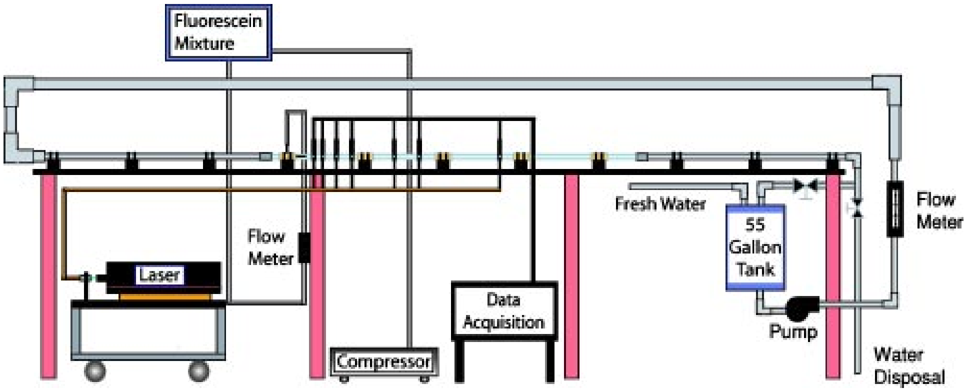

Fig. 1 Flow facility schematic

ics leading to the behavior of the higher-order concentration statistics in the near field of the injector. This work has some overlap with the early pioneering work of Nye and Brodkey. Because, however, of the improved measurement techniques and a reporting of measurements much farther downstream, the current study provides findings relevant to mixing in this configuration.

The present effort focuses on the study of scalar mixing associated with dye injected into a primary pipe flow through a coflowing pipe of much smaller diameter. Given this configuration, it is relevant to provide some perspective with regard to the rather extensive body of literature that exists on flow field structure in coflowing jets in both confined [16–19] and sudden expansion [20–30] configurations. In particular, a number of previous investigations have explored the velocity and vorticity field interactions in the near field, and the impact of various inflow conditions and geometry effects on the downstream flow development [at least up to $O(10)$ inner jet diameters]. As characterized by Ko and Kwan [21], what has been traditionally called the near field of the coaxial jet can be conceptualized as comprising three primary zones. With downstream distance from the exit plane these are (i) the initial merging zone, (ii) the intermediate zone, and (iii) the fully merged zone. Broadly speaking, the nomenclature for these zones refers to the interactions between the shear layers bounding the central and annular jets, as well as the erosion of the central jet core. It is well-documented that the ‘‘large scale’’ coherent motions in these shear layers are highly relevant to the near field development. Similarly, the extent of the intermediate zone (at the end of which the central core is completely eroded) is generally only about 3–6 inner diameters from the exit plane [30].

Given this context, it is thus important to note that in the present experiments the first measurement location is about 1.5 outer pipe diameters (or equivalently about 25 inner diameters) downstream of the exit plane of the inner jet. Thus, near field effects (as traditionally defined) on the flow-field development are not explicitly examined herein. Similarly, a distinguishing characteristic of the present work is that it explores the time resolved behavior of the scalar field up to very large distances downstream. There is an increasing body of evidence indicating that the scalar field can exhibit behaviors (i) at scales both smaller and within the range of the dynamical scales [31] and (ii) at scales much larger than the dynamical motions [13–15], and that none of these observations are rationally derivable from an understanding of the velocity field alone. In the present study, the development of very large scale scalar length scales [$O(10)$ outer diameters] and their potential dependence on practically adjustable parameters (e.g., the injected stream flow rate) are explored for a configuration commonly found in a number of practical applications.

2 Experimental Procedures

2.1 Experimental Setup. As shown schematically in Fig. 1, the facility employed consisted of a 31 m long flow loop. The 6.1 m long test section consisted of five 1.22 m sections of 25.4 mm inner diameter (I.D.) quartz pipe. The quartz pipe sections were connected by brass couplers that were designed to facilitate a smooth section-to-section transition. The test section was located 150 outer pipe diameters from the nearest bend to assure fully-developed flow and avoid unwanted entrance effects. A centrifugal pump was used to drive the main flow up to an average velocity of 2 m/s. A series of valves enabled the system to be run in either a recirculating or a ‘‘flushing’’ mode. In the flushing mode, an attached 208 L water reservoir allowed the experiment to be run for roughly 6 min. All mixing experiments were run in the ‘‘flushing’’ mode, that enabled the dye containing water to be drained. During characterization and calibration, the facility was run in the recycling mode to conserve water.

A 3 mm outer diameter, 1.5 mm I.D. stainless steel injector was located coaxially and at the beginning of the test section. The injector was inserted into the facility at the first brass coupling joining the PVC recirculation piping to the quartz test section. The injector was used to introduce a diluted fluorescein mixtured ($\approx$4.00e-4 M in water) into the main flow. Fluorescein was chosen due its characteristic of fluorescing when excited by 488 nm light as produced by the argon laser (0.5 W continuous wave) employed. The injector was 19.7 cm ($x/d=131$) in length to assure fully developed flow at the injector exit. The injector flow was fed by an attached PVC pressure vessel. This vessel acted as a fluorescein reservoir with a capacity of 34 L and was pressurized to 138 kPa (20 psi) using a portable air compressor. Flow meters were attached to both the main and injected flows to achieve the desired average velocity of above 1 m/s for the main flow and up to 2 m/s for the injected flow, see Fig. 1.

Data were acquired in the form of centerline instantaneous concentration along the pipe axis and diametral plane flow visualizations. Centerline scalar concentration measurements were taken at the seven downstream locations listed in Table 1. A Coherent Innova 70-4 argon laser was used to generate a 488.0 nm beam at 0.5 W. This beam was focused into a custom-built fiber optic bundle, which then split into seven separate fiber-optic lines, each of which terminated at the different downstream locations. The individual beams were oriented through and perpendicular to the axis of the quartz tube (see Fig. 1).

Using standard laser induced fluorescence (LIF) techniques [32], seven optical sensors were built to interrogate the intensity of the passive scalar, fluorescein. The maximum absorption fre-

Table 1 Locations for the seven downstream sensors

Sensor number	1	2	3	4	5	6	7
x/D	1.50	7.63	15.50	25.25	48.56	75.06	120.06

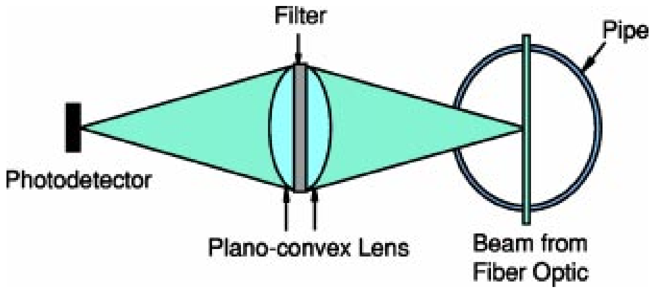

Fig. 2 Custom LIF sensor schematic

quency of fluorescein is 492 nm. Therefore, a single-line laser frequency of 488 nm was chosen as the closest option available. The emission frequency of fluorescein peaks near 520 nm. The wavelength of interest was only that emitted by the fluorescein. The exclusive acquisition of the desired light (rather than the laser excitation) was accomplished using two planoconvex lenses and a long-pass filter, which effectively blocked any scattered light below 508 nm. The desired light was focused onto a photodetector as seen in Fig. 2. The photo detector, 3.1 mm in diameter, linearly correlated the light intensity into a corresponding voltage between 0 and 9 V. Neutral-density filters were used to avoid saturation of the photo-detectors during all experiments.

The Schmidt number, $\mathrm{Sc}=\nu/D_m$, where D_m is the molecular diffusivity of fluorescein in water, is approximately 600 [32]. Using an estimate of the dissipation rate, ϵ, the Kolmogorov length scale was estimated as $\eta=0.1$ mm. Using this value of η, the Kolmogorov frequency was calculated to be approximately 1600 Hz $[f_k=U/(2\pi\eta)]$. However, the factor limiting the resolution of the small structure of the flow was the size of the optical sensor, which was approximately 3.1 mm. This spatial limitation only makes it possible to resolve frequencies up to about 360 Hz. Therefore, the sampling rate of 2000 Hz is well above the Nyquist criterion for resolving the smallest possible frequencies, given these limitations.

The quartz tubing used for the test section creates a visual distortion of the internal flow due to the convex surface of the tube. To account for this, a 76.2 cm long Plexiglas box was built that encompassed the quartz pipe and could be moved to different locations along the test section. This box was filled with a sodium-thiocynate mixture of a concentration sufficient to match the index of refraction of the quartz pipe. The box was then covered to prevent evaporation, which would alter the concentration.

2.2 Calibration. Prior to data collection, calibration of the LIF measurement system was performed to verify the linearity of the sensors and to determine the proper operating intensity range for the individual sensors; especially to avoid sensor saturation. Starting with a pure water recirculating system, measured quantities of fluorescein were added, allowed time to mix (≈ 5 min), and then light intensity measurements were taken for 10 s and averaged. This process was used to construct the individual calibration curves subsequently employed for conversion from voltage to arbitrary, but, self-consistent, relative concentration values. Figure 3 shows a sample result from this calibration procedure. After observing a repeatable linear relationship between concentration and voltage for all the sensors (with linear curve-fit R^2 values between 0.982 and 0.997), it was determined that linear extrapolation, when necessary, was acceptable. Such extrapolation was only required for sensors 1, 2, and 3.

2.3 Data Collection and Processing. The seven photodetectors were sampled simultaneously using an analog to digital converter operated via laptop computer. All signals were sampled at 2 kHz for 60 s. According to the analysis of Klewicki and Falco [33] in a boundary layer the sampling durations of the present study were sufficient to obtain statistical convergence of the kurtosis to within $\pm 5\%$.

Processing the data began by converting the acquired voltage time series to a corresponding relative concentration time series using the linear calibration curves for each sensor. The data were then low-pass filtered at a cutoff frequency of 450 Hz. The 60 s filtered concentration time-series data were then processed for statistical moments and correlations. Power spectral densities of the time series were calculated using an averaging block size of 2^{12} points.

2.4 Error Analysis. The primary sources of error in the data result from electronic noise in the various components. These include unsteadiness in the output of the interrogation laser, drift

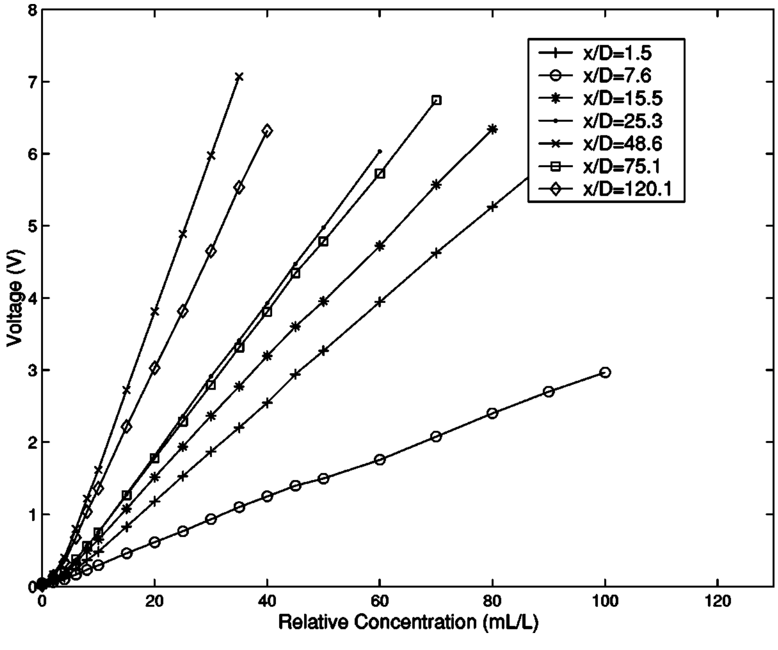

Fig. 3 Typical calibration curve for the seven sensors employed

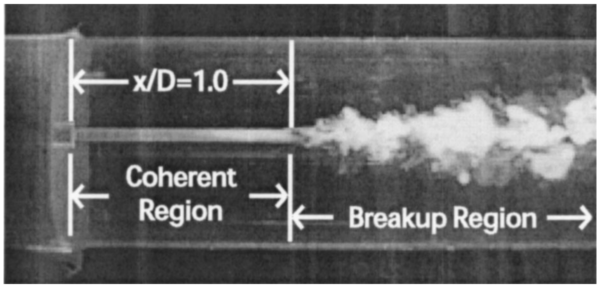

Fig. 4 Flow visualization showing the rapid transition from coherent jet to the break-up region. $R_d=1550$

in the photodetector signal, and noise in the data acquisition system. The particular significance of any one of these sources is reflected in their contribution to the overall signal uncertainty. To estimate the overall signal noise, data collected for the calibration curves of Fig. 3 were analyzed in the same manner as the time varying data. Namely, for the calibration data, a fully mixed condition exists, so any variation from the mean signal can be attributed to noise in the data collection system. Thus the normalized variance of the time varying data relative to the normalized variance of the calibration data gives one an effective signal to noise ratio. In Fig. 10, the variances of the calibration data are included for $V_R=2.0$ to demonstrate their relative values. Signal-to-noise ratio ranged from a high of 2949.1 to a low of 3.6.

3 Experimental Results

Experimental results are provided for three different velocity ratios between the jet and the free stream, $V_R=0.5,1.0,2.0$. For each case the main flow was fixed at approximately 2 m/s. This corresponds to a main flow Reynolds number of approximately 30,000 for all three runs. The Reynolds number for the injection jet was 1064 (laminar), 2126 (transitional), and 3546 (turbulent) for the three data sets reported.

3.1 Flow Visualizations. To provide a context for interpreting the statistical results that follow and better understand the initial flow development (as well as what impact this initial develepoment may have on the statistical results that follow), diametral plane visualizations were conducted. These visual analyses were carried out over a range of velocity ratios, V_R, and jet Reynolds numbers. Of particular interest was the length of the coherent jet exiting the injector and the transition to a jet break-up zone. Varying experimental parameters resulted in a range of behaviors seen in Figs. 4 and 5. An analysis of the visual data showed little affect of the velocity ratio on the coherent region. The key factor in the coherent region structure was observed to be the injection jet Reynolds number. A region of jet instability was observed that correlated with the transition of the jet from laminar to turbulent. Figures 4 and 5 illustrate this phenomena. The visualization of Fig. 4, at $R_d=1550$, reveals a distinct coherent jet region prior to jet breakup. On the other hand, Fig. 5 ($R_d=3310$) shows that the coherent jet region exists for only a few inner jet diameters. The flow visualizations represented in these figures were taken at primary stream flow rates less than that of the concentration experiments to better illustrate the behavior of the jet breakup, although higher main flow velocities revealed this same structure, leading to the hypothesis that these behaviors were most importantly influenced by the flow in the injection tube transitioning to turbulence.

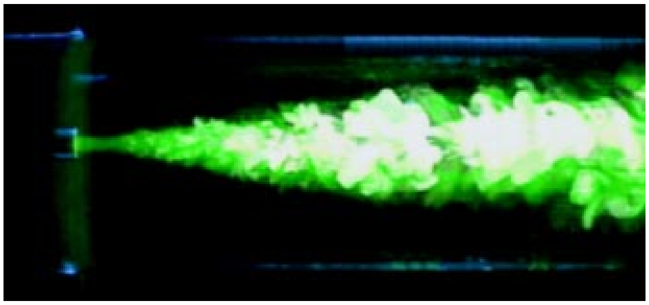

Fig. 5 Flow visualization showing reduced coherent core region. $R_d=3130$

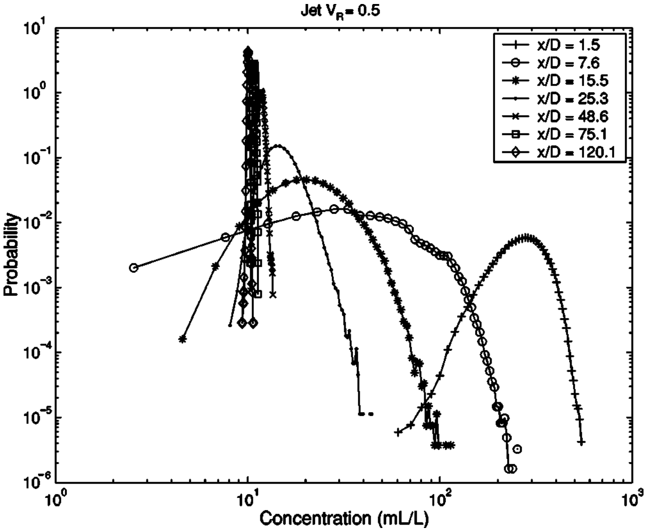

Fig. 6 Probability density function of concentration. $V_R=0.5$

Velocity profiles determined by particle image velocimetry (not shown) reveal that for all velocity ratios, the overall velocity profile in the pipe had returned to approximate a fully developed state by an x/D location of 3 (corresponding to about 45 inner jet diameters. The primary difference between the different velocity ratios is the structure of the wake downstream of the injector. However, the measured velocity profiles indicate that velocity ratio effects are limited to the first few outer pipe diameters downstream. This is explored further in the statistical analysis of the scalar field evolution below.

3.2 Statistical Analysis of the Scalar Field Evolution. Quantitative features of the scalar field evolution are now analyzed. These involve an examination of the evolution of the probability density function (pdf) of the concentration, along with spectral analyses. The pdf contains all single point statistical information. Figures 6, 7, and 8 show the evolution of the scalar pdf at different downstream locations. At the first measurement station ($x/D=1.5$) the pdf reveals the high mean concentration value near the unmixed jet concentration. Subsequent evolution reveals the dilution of the scalar along the centerline. The mean shifts to lower values and approaches a constant value at the fully mixed concentration. The variance at the centerline increases between the first two measurement stations due to introduction of pure water to the scalar, then decreases as the jet stream and main flow continue to mix toward a uniform concentration. Each case reveals a peak of a high concentration near the injector, a wide range of values including unmixed main stream water at the second station, followed by an evolution resulting in a delta distribution at the final mixed concentration. The highest velocity ratio (Fig. 8) shows a noticeably narrower distribution at the first station and a lower probability of unmixed fluid at the second station. If a measurement were made right at the exit of the injector, the pdf would be delta distribution (zero variance) centered around the undiluted concentration.

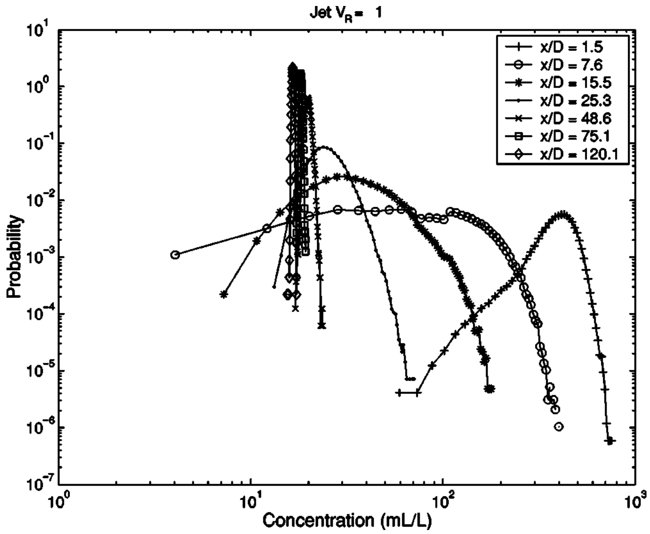

Fig. 7 Probability density function of concentration. $V_R=1.0$

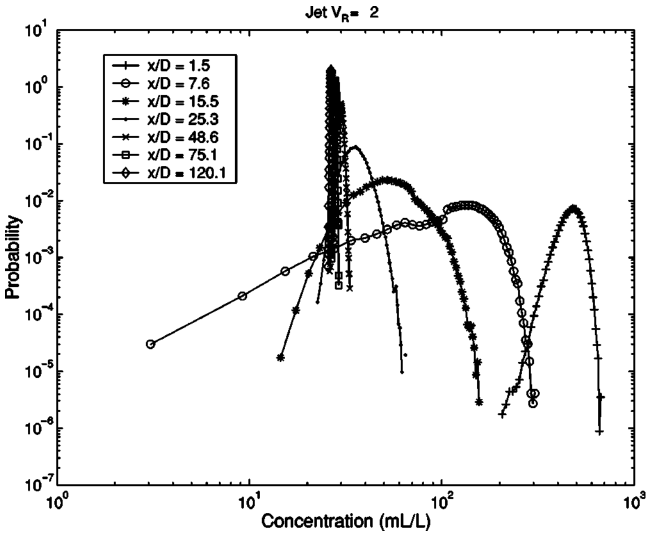

Fig. 8 Probability density function of concentration. $V_R=2.0$

Figure 9 shows the pdf at the last measurement station ($x/D=120.1$) with the concentration normalized by the rms (the normalized pdfs of the other runs show a similar behavior). As the fluid in the pipe approaches a fully mixed state, the scalar pdf approaches a Guassian as shown in Fig. 9. These observations are quantified in the following discussion.

3.2.1 Scalar Variance Decay. The scalar variance is a key indicator of the extent of mixing and is studied here for the different velocity ratios. The scalar variance at the centerline is presented here normalized by the local mean centerline concentration, $\overline{c^2}/C^2$. The variance was calculated over the entire 60 s signal. Figures 10 and 11 present these data in semilog and log-log coordinates. The differing velocity ratio flows all produced the same general trends. An initial increase in the variance along the centerline is observed over the first two sensors (1.5 and 7.6 L/D, respectively) as the uniform scalar from the injection jet begins to mix with the main flow. Following this is a region of rapid variance decay, up to approximately 50 pipe diameters, as a more uniform concentration is approached. Beyond this, the rate of variance decay decreases substantially. Figure 10, indicates that the initial steep drop is approximately exponential between about 20 and 50 pipe diameters. Beyond 50 L/D the rate of decay is slower than exponential. Also shown in this figure is the data of Guilkey et al. [13] The scalar field was initialized in the pipe when the flow was fully developed in a way that resulted in alternate transverse bands of fluorescein and fluorescein-free fluid across the pipe and with a length of one pipe diameter. The initial variance was thus at its peak at the first measurement station. A clear exponential decay is evident in the initial mixing.

A log-log plot of the decay is shown in Fig. 11. As discussed in the Introduction, previous theory, backed by experimental work using idealized initial conditions (shown here with the data of

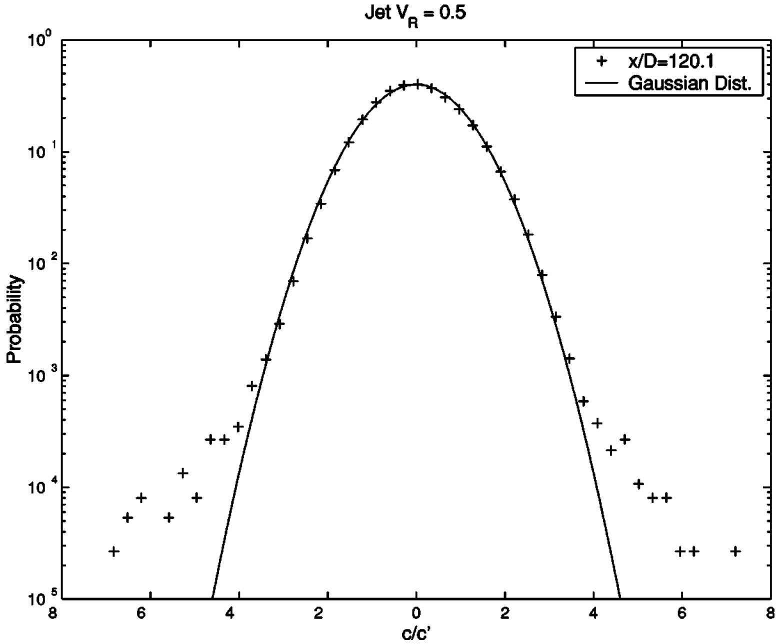

Fig. 9 Probability density function of concentration at last measurement station ($x/D=120.1$). Scaled by the rms

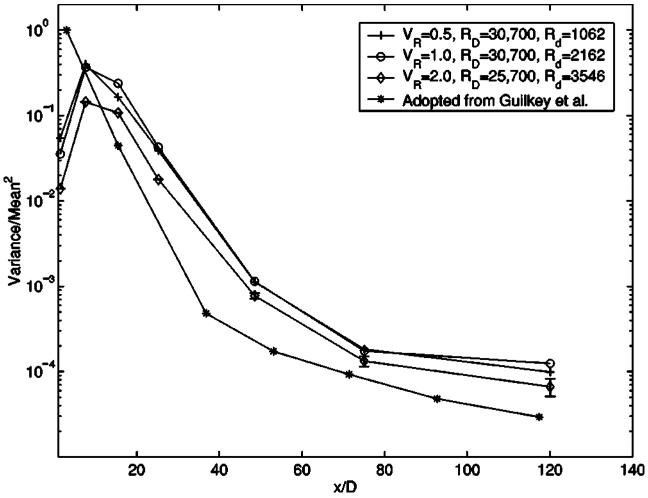

Fig. 10 Normalized scalar variance versus x/D on log-linear coordinates

Guilkey et al. included in the figure) has indicated a transition to power law decay in the far downstream in pipe flow mixing. A specific power-law form is not observed here, but the clear transition to a slower decay rate is evident. In this mixing configuration, the mean concentration at the centerline is continually decreasing downstream due to entrainment of pure water. This is one possible reason for the departures from purely exponential to power-law decay as seen in other pipe mixing configurations. This process of continual dilution is not present, for example, in a closed stirred tank or in the pipe flow mixing configurations studied by Guilkey and coworkers [13–15]. However, the transition from a rapid mixing rate to a slower mixing rate is still apparent in the mixing in this configuration. These results, combined with previously studied different mixing configurations for pipe flow indicate that the transition to a slower mixing rate is a generic feature of downstream axial mixing in pipes.

To further investigate the mechanisms involved in this mixing transition, the centerline concentration times series is shown at four different x/D for $V_R=1$ in Fig. 12. An important feature of the scalar field evolution depicted in the time-series is the emergence of a low frequency scalar fluctuation with downstream development. At $x/D=1.5$, the characteristic fluctuations of the scalar field were observed to be much less than the pipe diameter. By $x/D=120.1$, scalar wavelengths as long as 0.7 m are apparent, which corresponds to 33.5D. This increase in the scalar length scale to lengths much greater than the pipe diameter is predicted by the theory of Kerstein and McMurtry [12], and is consistent with the transition to a slower rate of variance decay. These results point to the development of long wavelength scalar fluctuations as a general characteristic of axial mixing in the far field and are associated with the transition to a slower scalar variance decay rate.

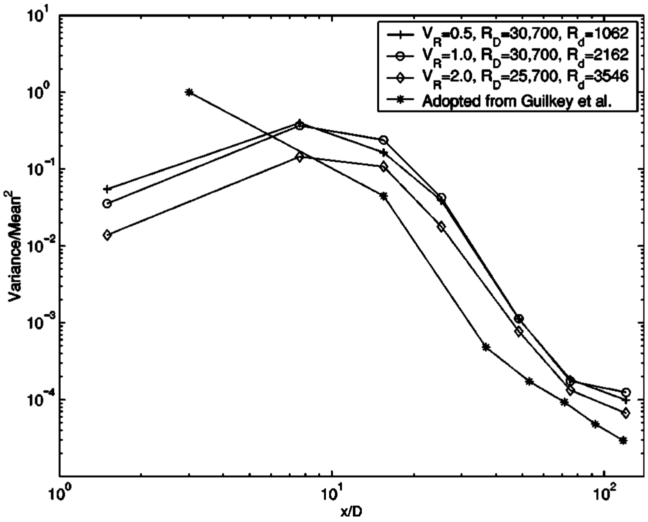

Fig. 11 Normalized scalar variance versus x/D on log-log coordinates

As can be seen from Figs. 11 and 10, the behavior of the normalized variance exhibited only subtle variation for differing velocity ratios. The velocity ratio of 2.0, however, attained a lower peak magnitude than the velocity ratios of 0.5 and 1.0. This difference in amplitude can be attributed to the difference in flow conditions of the jet. For the velocity ratio of 2.0, the jet flow was turbulent ($R_d=3546$), while for the velocity ratios of 0.5 and 1.0 the jet flow was laminar ($R_d=1062$) and transitional ($R_d=2126$), respectively. Also, the wake structure at the exit of the jet is different for the three different velocity ratios. These effects combine to reveal differences in mixing behavior in the first few pipe diameters downstream. To understand these near field effects, more measurements would be required in the near field of the injector. These are not available for this experiment so this question is left open for further investigation. The current work, however, is focused on the far-field mixing and these results suggest that velocity ratio effects are not significant in the far field.

3.2.2 Higher Order Moments. To further characterize the mixing behavior as the flow developed downstream, the third and fourth central moments (skewness, $\overline{c^3}/\overline{c^2}^{3/2}$ and kurtosis, $\overline{c^4}/\overline{c^2}^{2}$) of the concentration fluctuations were computed as a function of axial location. As can be seen in Fig. 13, the skewness undergoes

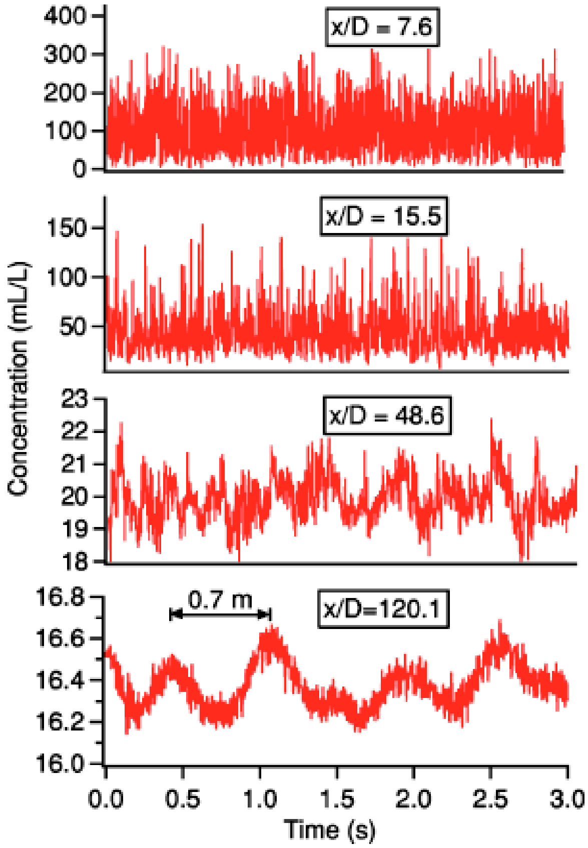

Fig. 12 Centerline concentration time series for $V_R=1.0$, plotted for increasing x/D. (Note change of scale with x/D)

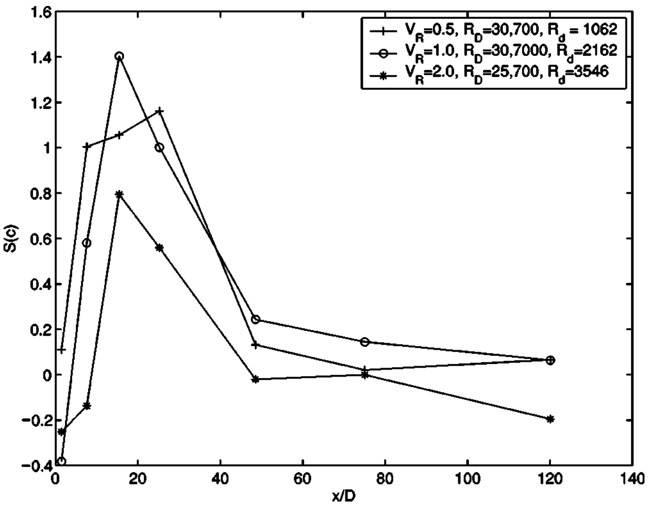

Fig. 13 Skewness of the concentration fluctuations plotted as a function of *x*/*D*

a large initial increase. This is a result of the introduction of pure water from the main channel into the centerline measurement area, as also seen directly in the pdfs. As mixing procedes, a more uniform concentration develops, centered around he mean value. By $x/D \sim 60-80$ the skewness approaches zero.

The kurtosis also initially increases, indicating high probability of experiencing concentrations toward the tails of the pdf. As mixing proceeds downstream, by about an $x/D \sim 50$, the kurtosis is nearing its Gaussian value of 3.0. It is interesting to note that the appearance of the Gaussian distribution correlates with the emergence of the low-wave-number scalar fluctuations. (See Fig. 14.)

3.3 Spectral Analysis. Examination of the concentration time series (presented above) shed insight into the length and time scales associated with the concentration field with downstream distance. The qualitative behavior of the long wavelength scalar length scale development can be viewed from a more quantitative perspective by observing scalar spectra.

As seen in Fig. 15, the scalar spectral shape changes dramatically with x/D. The primary evident feature is the downstream depletion of the spectral intensity at intermediate frequencies, and is taken to indicate spectral intensity transport from these intermediate frequencies to both higher and lower frequencies. Note that by $x/D=75$, a low frequency (long wavelength) contribution to the scalar spectrum is clearly evident. This is followed by a drop to a fairly flat region preceding the decay at higher frequencies. The dynamical velocity fluctuations are restricted by the pipe diameter. For the flow case shown, the frequency associated with an outer diameter sized eddy is approximately 40 Hz. This observation is consistent with the Kerstein-McMurtry theory and the experimental work of Guilkey et al. [13] The low frequency fluctuations can communicate only through a turbulent diffusivity mechanism with a length scale on the order of the pipe diameter, leading to the transition from an exponential to decay, to a slower form. Although theory predicts a transition to a power-law decay,

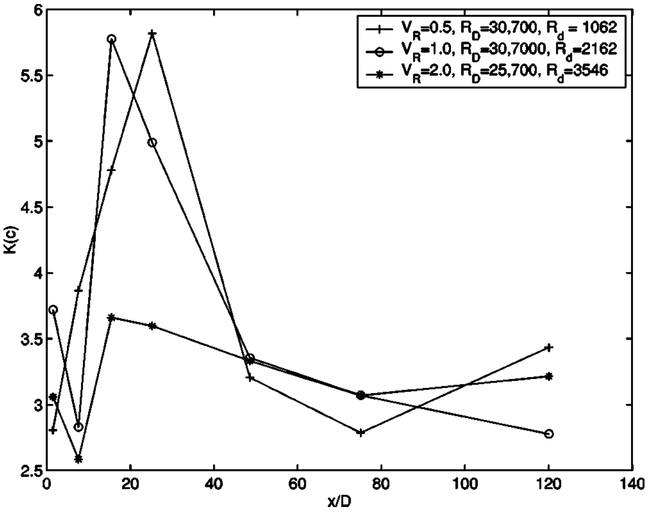

Fig. 14 Kurtosis of the concentration fluctuations plotted as a function of *x*/*D*

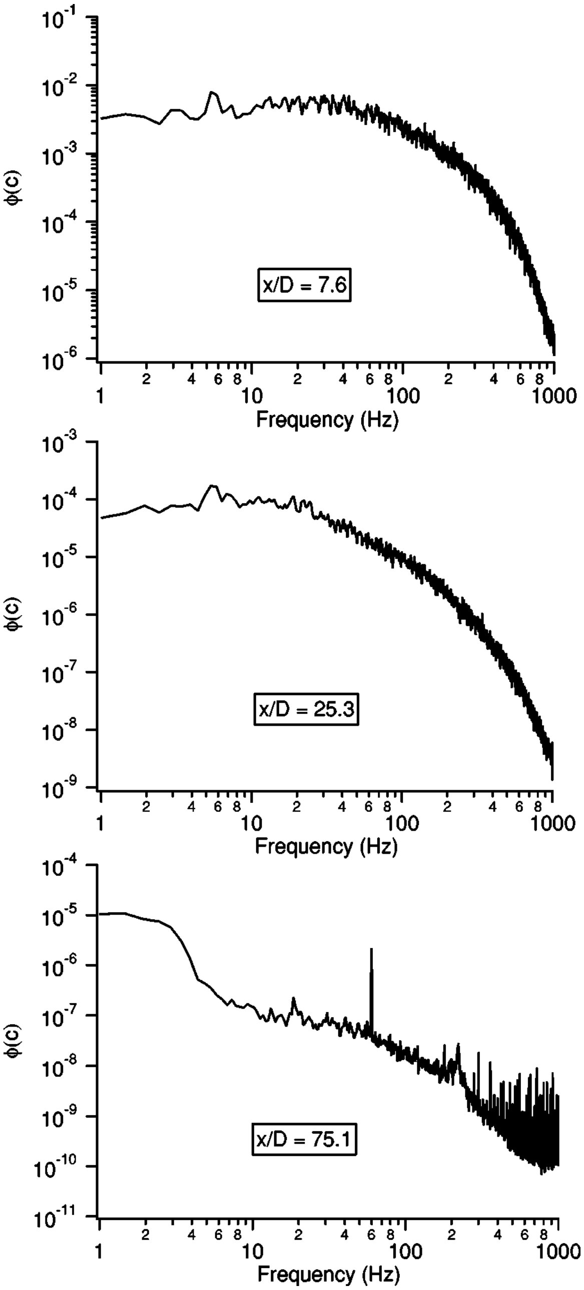

Fig. 15 Concentration power spectral densities as a function of *x*/*D*. Development in the far field reveals indicates the depletion of spectral intensity at midrange frequencies owing to spectral transfer to both higher and lower frequencies

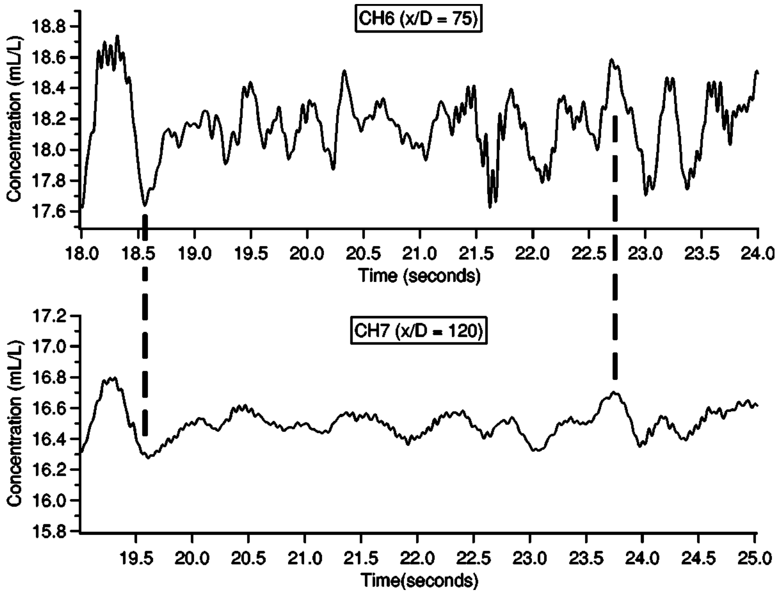

Fig. 16 Concentration time series of sensors 6 and 7. Note the same *y*-scale windows size, but different ranges, as well as the shifted time range (*x* axis)

the theory does not take into account of additional entrainment of pure fluid into the marked scalar stream. Due to this increased level of complexity, the transitional nature of this configuration has yet to be fully characterized.

3.4 Correlations. Observation of the time series for sensors 6 and 7, with the signals shifted to account for the time required to travel between the sensors, reveals the propagation of long-lived, low-frequency scalar structures (see Fig. 16). Also apparent in Fig. 16 is the conversion of intermediate frequencies to both higher and lower frequencies from sensors 6 and 7 as discussed above relative to the spectral analysis. For model experiments this phenomenon was predicted by Kerstein and McMurtry [12] and verified by Guilkey et al. [13]. The seven simultaneously sampled signals seen in Fig. 12, allowed the space-time structure of the signals to be explored. The centerline concentration correlation coefficient

$$R_{a-b}(\Delta t)=\frac{\overline{C_a(t)C_b(t+\Delta t)}}{C_a'\times C_b'} \tag{1}$$

was determined, for any pair of sensors, (a,b). In the above equation, C_a and C_b represent the concentration measured for the upstream and downstream sensors, respectively, and C_a' and C_b' represent the root-mean-square (RMS) value of the entire time series for sensors 1 and 2. Space-time autocorrelations between sensors 5-6, 5-7, 6-7, and 1-4 are seen in Fig. 17. The expected value of Δt was predicted by taking the convected length, or the length between the sensors, and dividing it by the fluid velocity (e.g., through the use of Taylor's hypothesis). A strong correlation between the expected value of Δt and the calculated value of Δt indicates a coherent advection of scalar structures between the sensors. An increase in the peak width and correlation value with an increasing x/D seen in Fig. 17 indicates that the low-frequency content is becoming more prevalent as the flow develops downstream. Examination of Fig. 16 indicates that between sensors 6 and 7 the low frequency scalar structures are propagated downstream with little distortion.

Correlations between sensors 5, 6, and 7 are shown because they were the only plots with a peak value within 5% of that predicted by Taylor's hypothesis. The correlation plot for sensors 1 and 4 displays the lack of similar structure between the two sensors. The lack of correlation between sensors 1 through 4 indicates that the low-frequency structures had not developed to a sufficient state and only become prevalent after sensor 4. This propagation of low-frequency structures is characteristic of the downstream mixing region and indicates that the mixing evolution in this region is very slow. This slow mixing evolution in the downstream region gains importance for industrial mixing/reaction applications whose effectiveness is sensitive to incomplete mixing owing, for example, to cost or environmental concerns.

4 Conclusions

An experimental facility and measurement system for the study of axial flow mixers has been constructed, calibrated, and tested. This experimental facility allowed for the examination of the effects of velocity ratio for a fixed outer to inner pipe diameter ratio of 14.5.

Effects of velocity ratio were limited to the first few pipe diameters. This is due to the velocity profile returning to an approximately fully developed state after 2-3 outer pipe diameters (approximately 50 inner pipe diameters), for the velocity ratios studied here. The scalar statistics and mixing behavior in the far field showed minimal effect of the initial velocity ratio.

The scalar variance decay initially experienced a rapid increase, as pure water from the main pipe was transported to the centerline. This rapid increase was followed by a rapid, approximately exponential decrease. After about 50 pipe diameters, the variance decay transitioned to a much slower decay rate. In more ideal mixing cases in pipes, Guilkey et al. [13] showed the initial decrease in variance to be clearly exponential, followed by a power law. This is in accordance with Corrsin's theory [10] for the near field and the Kerstein McMurtry theory in the far field. [12] The departure from the ideal case seen in these experiments is attributed to the continual entrainment of pure water to the mixing region during the downstream development. The emergence of the predicted low-frequency scalar fluctuations was clearly evident in all cases and consistent with the transition to a slower rate of variance decay. This was demonstrated by a direct measurement of the scalar time series and a correlation analysis performed between the seven downstream locations. The scale of these struc-

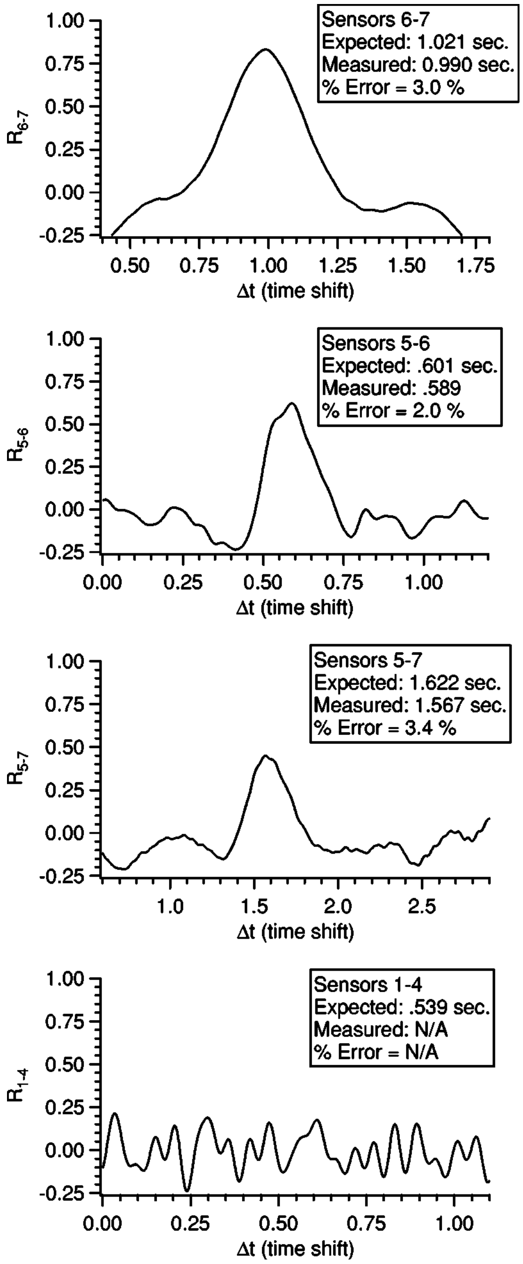

Fig. 17 Correlation plots between sensors 6-7, 5-7, 5-6, and 1-4

tures is significantly larger than the diameter of the pipe (and therefore characteristic velocity scales), thus contributing to their slow decay.

Measurements of the scalar probability density function and their associated higher order moments revealed a structure initially characterized by entrainment of pure water into the region, yielding high values of skewness and kurtosis. Subsequently, the pdf evolved towards a Guassian distribution, with Guassian statistics emerging with the transition to a slower mixing rate and development of low-frequency scalar fluctuations.

Acknowledgments

The authors gratefully acknowledge funding by the NSF-REU program under Grant No. CTS 0120061, Dr. C. F. Chen and Dr. M. Plesniak grant monitors.

References

[1] Nye, J., and Brodkey, R., 1967, ‘‘The Scalar Spectrum in the Viscous-Convective Subrange,’’ J. Fluid Mech., **29**, pp. 151–163.
[2] Hartung, K. H., and Hibby, J. W., 1972, ‘‘Beschleunigung der Turbulenten Mischung in Rohren,’’ Chem. Eng. Technol., **44**, 1051–1056.
[3] Forney, L., Nafia, N., and Vo, H., 1996, ‘‘Optimum Jet Mixing in a Tubular Reactor,’’ AIChE J., **42**(11), 3113–3122.
[4] Ger, A. M., and Holley, E. R., 1976, ‘‘Comparison of Single-Point Injections in Pipe Flow,’’ J. Hydraul. Div., Am. Soc. Civ. Eng., **102**, 731–745.
[5] Fitzgerald, S. D., and Holley, E. R., 1981, ‘‘Jet Injections for Optimum Mixing in Pipe Flow,’’ J. Hydraul. Div., Am. Soc. Civ. Eng., **107**, 1179–1195.
[6] Edwards, A. C., Sherman, W. D., and Breidenthal, R. E., 1985, ‘‘Turbulent Mixing in Tubes with Transverse Injection,’’ AIChE J., **31**, 516–518.
[7] O'Leary, C. D., and Forney, L. J., 1985 ‘‘Optimization of In-line Mixing at a 90 Degree Tee,’’ Ind. Eng. Chem. Process Des. Dev., **24**, 332–338.
[8] Sroka, L. M., and Forney, L. J., 1989, ‘‘Fluid Mixing with a Pipeline Tee-:Theory and Experiment,’’ AIChE J., **35**, 406–414.
[9] Forney, L., 1986, ‘‘Jet Injection for Optimum Pipeline Mixing,’’ *Encyclopedia of Fluid Mechanics Volume 2-Dynamics of Single-Fluid Flows and Mixing*, N.P. Cheremisinoff, ed., Gulf Publishing Company, Houston.
[10] Corrsin, S., 1964, ‘‘The Isotropic Turbulent Mixer: Part II. Arbitrary Schmidt Number,’’ AIChE J., **10**, 870–877.
[11] Smith, J., 1981, *Chemical Engineering Kinetics*, Mcgraw-Hill New York.
[12] Kerstein, A., and McMurtry, P., 1994, ‘‘Low-Wave-Number Statistics of Randomly Advected Passive Scalars,’’ Phys. Rev. E, **50**, 2057–2063.
[13] Guilkey, J., Kerstein, A., McMurtry, P., and Klewicki, J., 1997, ‘‘Mixing Mechanism in Tubrulent Pipe Flow,’’ Phys. Fluids, **9**, 717–723.
[14] Guilkey, J., McMurtry, P. A., and Klewicki, J. C., 1997, ‘‘Effect of Inlet Conditions on Scalar Statistics in Pipe Mixing,’’ AIChE J., **43**, 1947–1962.
[15] Hansen, L., Guilkey, J., McMurtry, P., and Klewicki, J., 2000, ‘‘The Use of Photoactivatable Fluorophores in the Study of Turbulent Pipe Mixing: Effects of Inlet Geometry,’’ Meas. Sci. Technol., **11**, 1235–1250.
[16] Choi, D., Gessner, R., and Oates, G., 1986, ‘‘Measurements of Confined, Coaxial Jet Mixing With Pressure Gradient,’’ ASME J. Fluids Eng., **108**, 39–46.
[17] Habib, M., and Whitelaw, J., 1979, ‘‘Velocity Characteristics of a Confined Coaxial Jet,’’ ASME J. Fluids Eng., **101**, 521–529.
[18] Curtet, R., and Ricou, F., 1964, ‘‘On the Tendency to Self-Preservation in Axisymmetric Ducted Jets,’’ ASME J. Basic Eng., **86**, 765–776.
[19] Razinsky, E., and Brighton, J., 1971, ‘‘Confined Jet Mixing for Nonseparating Conditions,’’ ASME J. Basic Eng., **93**(2), 333–349.
[20] Champagne, F., and Wygnanski, I., 1971, ‘‘An Experimental Investigation of Coaxial Turbulent Jets,’’ Int. J. Heat Mass Transfer, **14**, 1445–1464.
[21] Ko, N. W. M., and Kwan, A. S. H., 1976, ‘‘The Initial Region of Subsonic Coaxial Jets,’’ J. Fluid Mech., **73**, 305–332.
[22] Kwan, A. S. H., and Ko, N. W. M., 1977, ‘‘The Initial Region of Subsonic Coaxial Jets. Part 2.,’’ J. Fluid Mech., **82**, 273–287.
[23] Ko, N. W. M., and Chan, W. T., 1979, ‘‘The Inner Region of Annular Jets,’’ J. Fluid Mech., **93**, 549–584.
[24] Ko, N. W. M., and Lam, K. M., 1984, ‘‘Further Measurements in the Initial Region of an Annular Jet,’’ J. Sound Vib., **92**, 333–348.
[25] Au, H., and Ko, N. W. M., 1987, ‘‘Coaxial Jets of Different Mean Velocity Ratios. Part 2.,’’ J. Sound Vib., **116**, 427–443.
[26] Dahm, W., Frieler, C., and Tryggvason, G., 1992, ‘‘Vortex Structure and Dynamics in the Near Field of a Coaxial Jet,’’ J. Fluid Mech., **241**, 371–402.
[27] Buresti, G., Talamelli, A., and Pentagna, P., 1994, ‘‘Experimental Characterization of the Velocity Field of a Coaxial Jet Configuration’’ Exp. Therm. Fluid Sci., **9**, 135–146.
[28] Wicker, R. B., and Eaton, J. K., 1994, ‘‘Near Field of a Coaxial Jet With and Without Axial Excitation,’’ AIAA J., **32**, 542–546.
[29] Warda, H. A., Kassab, S. Z., Elshorbagy, K. A., and Elsaadawy, E. A., 1999, ‘‘An Experimental Investigation of the Near-Field Region of a Free Turbulent Coaxial Jet Using LDA’’ Flow Meas. Instrum., **10**, 15–26.
[30] Sadr, R., and Klewicki, J. C., 2003, ‘‘An Experimental Investigation of the Near-Field Flow Development in Coaxial Jets,’’ Phys. Fluids, **15**, 1233–1246.
[31] Warhaft, Z., 2003, ‘‘Passive Scalars in Turbulent Flows,’’ Annu. Rev. Fluid Mech., **32**, 203–240.
[32] Koochesfahani, M., and Dimotakis, P., 1986, ‘‘Mixing and chemical reactions in a turbulent liquid mixing layer,’’ J. Fluid Mech., **170**, 83–112.
[33] Klewicki, J., and Falco, R., 1989, ‘‘On Accurately Measuring Statistics Associated with Small-Scale Structure in Turbulent Boundary Layers Using Hot-Wire Probes,’’ J. Fluid Mech., **219**, 119–142.

L. Wilson

Arunn Narasimhan*

S. P. Venkateshan†

Heat Transfer and Thermal Power Laboratory,
Department of Mechanical Engineering,
Indian Institute of Technology Madras,
Chennai, Tamil Nadu 600036, India

Turbulent Flow Hydrodynamic Experiments in Near-Compact Heat Exchanger Models With Aligned Tubes

Hydrodynamic experiments measuring longitudinal pressure-drop versus flow rate are conducted for turbulent flow of air (channel hydraulic diameter based Reynolds number range of 2300 to 6860) through near-compact heat exchanger models with rod bundles having aligned (inline) arrangement. Effects of the flow (Re), the geometry parameters, and number of rods of the test models on the nondimensional pressure-drop ξ *are studied in detail. Treating the near compact heat exchanger model as a porous medium, a dimensional pressure-drop* $(\Delta P/L)$ *versus average velocity of flow (U) model similar in content to a non-Darcy porous medium model, is shown to fit the experimental data with fair accuracy. Variation in form drag related to, and induced by the flow and geometric parameters are shown to be the reason for the pressure-drop variations of different models. The relation between the porous medium type model* $(\Delta P/L$ *versus U) and the "*ξ *versus Re" model is discussed with careful attention to the differences in the two transitions viz. laminar to turbulent and viscous-drag to form-drag dominated flow inside the models. A proposed correlation for predicting* ξ*, ably capturing all of the form effects induced by the flow and geometric parameters, is found to give predictions with* $\pm 20\%$ *accuracy.* [DOI: 10.1115/1.1845553]

Introduction

Compact heat exchangers, with high surface-to-volume ratio α normally greater than 700 $\mathrm{m}^2/\mathrm{m}^3$ and D_M less than or equal to 6 mm [1,2], are useful in engineering applications such as air conditioning systems [2], air borne power plants, and cooling applications [3]. The hydrodynamic parameter of chief interest is the overall pressure-drop across the compact heat exchangers, as pressure-drop penalty paid for an increase in heat transfer coefficient in heat exchangers can be quite high. However, heat exchangers with α values falling reasonably below that of compact heat exchangers (α=100 to 300 $\mathrm{m}^2/\mathrm{m}^3$) and D_M ranging over 6 mm also find themselves useful in many practical applications such as heat exchangers for low grade energy, the cool ability of nuclear reactors following a loss-of-core cooling accident, the decay of heat removal from spent fuel storage tanks, and steam generators in nuclear plants [4]. The advantage of these near-compact heat exchangers is the smaller overall pressure-drop.

Zukauskas [5] reported data for air and water, in the turbulent and transitional regimes, flowing through rod bundles with fixed rod diameter ($d=19$ mm) and small relative transverse spacing (a <1.1). Recent reviews on compact heat exchangers [1,6] and turbulent cross flow over rod bundles [7] reveals lack of experimental data in the turbulent flow configuration for rod bundles having rod diameters less than 5 mm, one of the criterion for compact heat exchangers, [1] and the model D_M ranging between 6 and 19 mm, which we term, *near*-compact heat exchanger. Numerical simulation [8] done for turbulent flow of air (with Re range of 5000 and 100,000) over a single (aligned) row of rods of fixed diameter shows the effect of increase in the relative longitudinal spacing (b) is to increase the overall pressure drop. However, for $b>3$, the configuration loses its compactness and cannot be treated as a near-compact heat exchanger.

Taking cue from the literature, which shows a dearth of useful research data, this paper reports hydrodynamic pressure-drop experiments in rod bundles in aligned (inline) arrangement within a rectangular test section forming a near-compact heat exchanger model (with α value ranging between 100 and 300 $\mathrm{m}^2/\mathrm{m}^3$), studied for fully developed turbulent flow configuration. Experiments were performed in turbulent flow through rod bundle models having three different diameters ($d=2,3,4$ mm), selected with a wide range in the characterizing geometric parameters for aligned arrangement.

One of the objectives is to treat these near-compact heat exchanger models as porous media and to delineate the effects of the geometry of the rod bundles as a *form* resistance of the porous medium, which predominate the viscous resistance for high velocities. This approach of viewing compact and near compact heat exchangers as porous medium, although not new [9], has evoked recent interests [10,11]. For instance, frictional losses and convection heat transfer in sparse, periodic cylinder arrays under laminar air cross flow was evaluated in the recent studies by Martin et al. [12–14] based on a clear distinction between fluid continuum and porous continuum. A comparison of pressure drop versus flow rate results with the Ergun [9] and non-Darcy (quadratic in velocity) type porous medium flow relations was made to examine their validity. Results suggest that the Ergun equation (which is known to be valid for a packet bed of spheres only) and the non-Darcy equation do not correlate well with the numerical results.

Experimental Setup

Figure 1 shows schematically, the experimental setup. A reciprocating compressor (Make-Kirloskar, Model No-TC 500, capacity 0 kPa to 600 kPa) provides a steady continuous discharge of compressed air, free of pulsation and with minimum agitation, which is sent through a pressure regulator (range 14 kPa to 1040 kPa), which regulates the discharge to be at 1.5 bar (150 kPa)

---

*Corresponding author; e-mail: arunn@iitm.ac.in

†E-mail: spv@iitm.ac.in

Contributed by the Fluids Engineering Division for publication in the JOURNAL OF FLUIDS ENGINEERING. Manuscript received by the Fluids Engineering Division November 28, 2003; revised manuscript received June 4, 2004. Review conducted by: M. Volkan Ötügen.

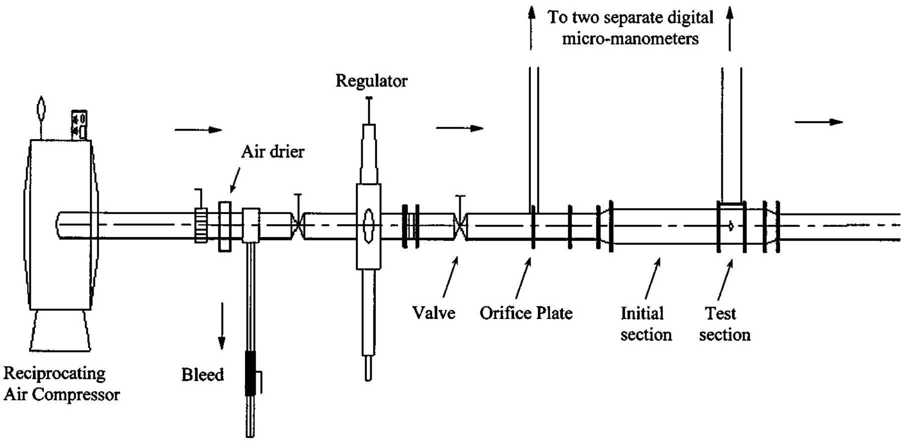

Fig. 1 Schematic diagram of the experimental setup

throughout the experiments. A valve controls the discharge of air from the regulator to the test section before entering which air passes through an orifice plate measuring the discharge and a desiccant air dryer (Make-Sanpar, Model No-SHD AA 040, capacity 0 to 15 CFM) with 5 μm air filter to remove moisture and dirt up to 99% (this drier was used for most of our experiments, based on the air humidity on a particular day). The test section is a flow channel of rectangular cross section ($LBW = 120 \times 30 \times 50$ mm^3) into which the test models with the aligned rod arrangement are inserted. The inner walls of the test section are coated with a noncorrosive paint having a smooth surface finish. The test section is sandwiched between an initial and final section of sufficient length (3 m and 0.5 m, respectively) and of similar rectangular geometry (see Fig. 1) to ensure fully developed flow conditions [15].

In the installation of the test models inside the test section, all potential leaks (for instance, between the outer walls of the model and the inner walls of the test section) are properly sealed. Static pressure taps (made of 1 mm bore stainless steel tubes) across the test section are positioned at 108 mm intervals along the length of the upper wall of the flow channel and this is the magnitude of length L in Fig. 2, for all of the models. Pressure measurements on the taps were done by digital micromanometer (manufactured by Furness Controls Ltd., USA, ±0.45% full scale accuracy). The calibration of the orifice meter measuring the discharge is done using the procedure listed in [16] and the accuracy of the orifice meter is determined to be 0.25% for full-scale reading. Discharge pressure measurements were carried out by another micromanometer connected to the orifice plate, measuring a range of flow rates from 0.0015 m^3/sec to 0.00405 m^3/sec (U between 0.8 and 3 m/s). For ensuring isothermal experimental conditions and for correcting the dry air density (ρ) and viscosity (μ), the dry air temperature at the inlet and outlet of the test section are measured using Resistance Temperature Detectors connected to a thermal systems indicator (model No: DQ 100). The dry air temperature difference between inlet and outlet of the test section is found to be negligible for all experiments.

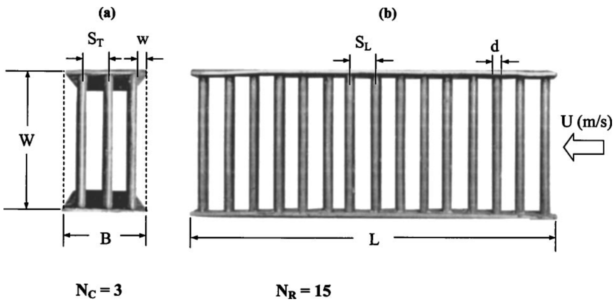

Fig. 2 Photograph of a test model marked with the relevant geometric parameters

Table 1 Characteristic parameters of test models

Model size: $L \times B \times W = 108 \times 30 \times 50$ mm^3												
Model	d (mm)	S_T (mm)	S_L (mm)	w (mm)	$a = S_T/d_t$	$b = S_L/d_t$	$c = w/d_t$	N_R	N_C	α (m^2/m^3)	D_M (mm)	Ψ
1	2	7	8	2.5	3.5	4	1.25	15	4	200.11	15.1	0.0478
2	2	8	10	1.5	4	5	0.75	12	4	181.69	16.6	0.0383
3	2	7	10	2.5	3.5	5	1.25	12	4	181.66	16.6	0.0383
4	2	6	9	1.5	3	4.5	0.75	13	5	209.03	13.2	0.0523
5	2	8	7	1.5	4	3.5	0.75	17	4	211.62	14.3	0.0537
6	2	10	8	3	5	4	1.5	15	3	175.90	18.6	0.0354
7	2	10	7	3	5	3.5	1.5	17	3	185.31	17.7	0.0402
8	2	10	6	3	5	3	1.5	20	3	200.11	16.3	0.0478
9	3	6	6	4	2	2	1.33	19	4	281.59	9.1	0.136
10	3	7	7	3	2.33	2.33	1	16	4	253.43	10.1	0.114
11	3	8	8	4.5	2.66	2.66	1.50	15	3	209.96	13.9	0.0801
12	4	7	7	1.5	1.75	1.75	0.38	16	4	302.45	6.8	0.205
13	4	8	8	4	2	2	1	15	3	243.19	10.5	0.143
14	4	9	9	2.5	2.5	2.5	0.63	13	3	224.45	11.4	0.123
15	2	14	14	0	7	7	0	8	3	100.37	31.57	0.171

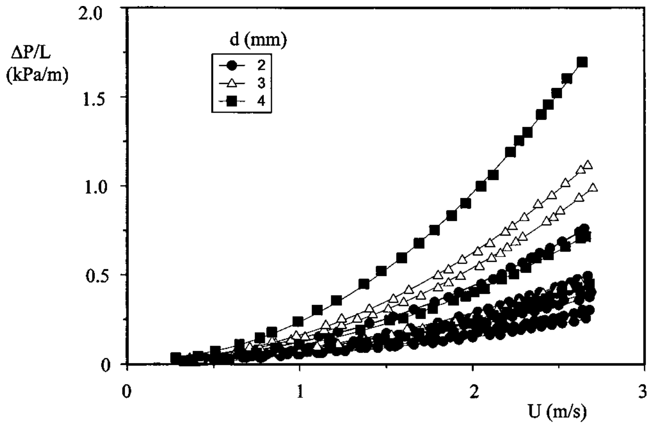

Fig. 3 Longitudinal pressure drop versus average velocity for all of the models

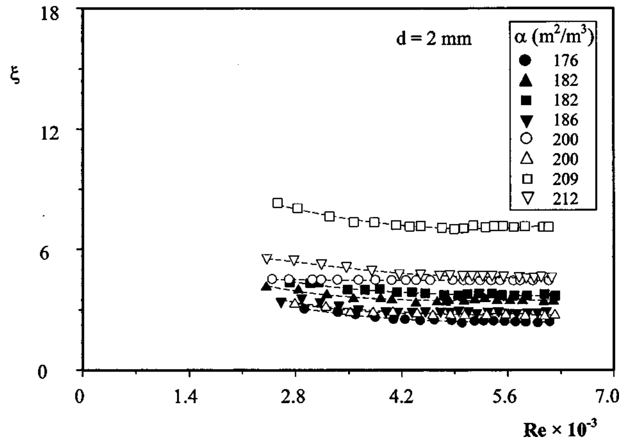

Fig. 4 Nondimensional pressure drop ξ versus Re for models having 2 mm diameter rod bundles

Model Parameters and Uncertainty

Experiments were performed on 15 different near compact heat exchanger models constructed with an aligned arrangement of aluminum rods positioned by riveting to two side structures of 1 mm thickness. The test models are periodically cleaned by soaking in dilute acids to remove fouling on the surface of the aluminum rods. Following convention [2,17], the models are characterized using nondimensional parameters whose definitions and values are detailed in Table 1. A typical model used in the experiments is displayed in Fig. 2, a channel hydraulic diameter (D) based Reynolds number defined as

$$\mathrm{Re}=\frac{\rho D U}{\mu} \tag{1}$$

and a nondimensional pressure drop defined as

$$\xi=\frac{\Delta P/L}{\rho \mathrm{U}^2/2D} \tag{2}$$

are used to study the hydrodynamic characteristics of the models. The hydraulic experiments are conducted with air, flowing under isothermal conditions of $T_{\mathrm{in}}=30°\mathrm{C}$ with $\rho=1.14\ \mathrm{kg/m^3}$ and $\mu=18.5\times10^{-6}\ \mathrm{Nsm^{-2}}$ for the average velocity (U) range of 0.28 m/s to 2.7 m/s [Re, Eq. (1), from 638 to 6860]. This velocity range covers both the transition and fully turbulent flow regime for the rectangular channel used.

The individual uncertainties in calculating the area of the test section (A) and hydraulic diameter of the duct (D) are 0.24% and 0.27%, respectively. The uncertainty in discharge measurement using the orifice plate and pressure drop using the micromanometer are 0.25% and 0.5%, respectively. The uncertainty "u" of a quantity R, which is a function of several variables $x_1 \ldots x_N$, can be found with good accuracy using a root-sum-square combination [16] as $u_R=\{\Sigma_{i=1}^{N}[(\partial R/\partial x_i)u_i]^2\}^{0.5}$ where u_i is the uncertainty in the generic variable x_i. Using this relation and following the procedure listed in [18], the uncertainty for Re, Eq. (1), is found for all of the models (with three different diameter rods) to be varying between 0.441% and 0.448% within the experimental Re range of 638 to 6860. A similar procedure yields 0.88% as the maximum uncertainty of the nondimensional pressure-drop ξ, Eq. (2).

Results and Discussions

Figure 3 shows the experimental results of longitudinal pressure drop versus channel average cross sectional velocity for all of the 14 near-compact heat exchanger models tested. For all of the models, the pressure-drop dependence on velocity is linear in the lower velocity regime ($U<1$ m/s, $\mathrm{Re}<2300$) where the incoming fluid is still in the transition (from laminar to turbulent flow) regime (p. 280, Fig. 6.5, [15]). However, although the results are grouped for three different diameters of the rods that are used in the different models, they all reveal the quadratic nature of the pressure-drop dependence on velocity, for higher velocities. With γ and β as constants, we may use an equation of the form

$$\frac{\Delta P}{L}=\gamma U+\beta U^2 \tag{3}$$

to curve fit the experimental results satisfactorily as shown in Fig. 3. Following porous media parlance [10] and setting the constants $\gamma=\mu/K$ and $\beta=\rho C$, Eq. (3) takes the form

$$\frac{\Delta P}{L}=\frac{\mu}{K}U+\rho C U^2 \tag{4}$$

where K and C are, respectively, the permeability and form coefficient of the porous medium, to be determined from isothermal hydraulic experiments.

The drag offered by the first term in the right-hand side (RHS) of Eq. (4) is because of the viscous friction arising from the contact and shear of the fluid over the solid surfaces of the rod bundle models. In our experiments, this contact surface includes the bounding walls of the test section as well, for all of the models tested. For lower velocities ($U<1$ m/s), the fluid has better contact with the surfaces resulting in the dominance of "viscous drag," which varies linearly with average velocity (U). Hence, for lower velocities, the pressure-drop data for all of the models follow almost a linear relation with average velocity (U).

Proceeding from left to right in Fig. 3, it is evident that for higher velocities the pressure drop for all of the models deviates from being proportional U. Although this can be seen as a characteristic of the fully developed turbulent flow ($U>1$ m/s, $\mathrm{Re}>2300$) entering the test section, the models when viewed as a porous medium can also be interpreted using Eq. (4). For increasing velocity ($U>1$ m/s, $\mathrm{Re}>2300$), the magnitude of the second term on the RHS of Eq. (4), identified as the "form drag," gains dominance over the first term, thus we enter the fully turbulent regime where for any particular rod bundle model (porous medium) inside the test section, flow separation and wake effects dominate due to the *form* of the rod bundles (porous medium). In Eq. (4), this form drag effect is lumped as a coefficient C [in Eq. (3) as β] proportional to U^2.

Taking Eq. (3) as a guiding hydraulic model, we proceed to delineate the parameters that influence β, the form drag coefficient. Using the conventional notations of Eqs. (1) and (2) for Re and friction factor, Fig. 4 portrays for several α ($\mathrm{m^2/m^3}$) values, the nondimensional pressure drop versus Reynolds number for the

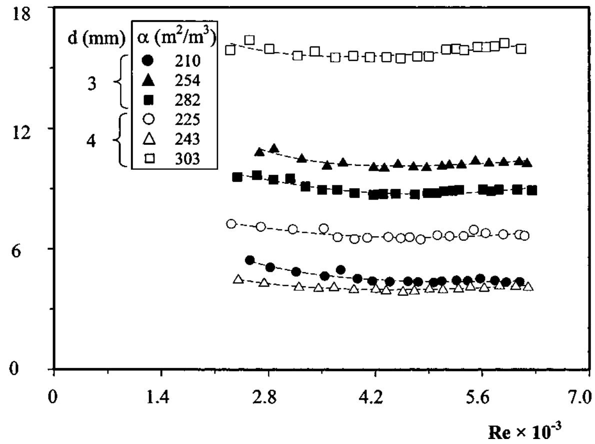

Fig. 5 ξ versus Re for models having 3 and 4 mm diameter rod bundles

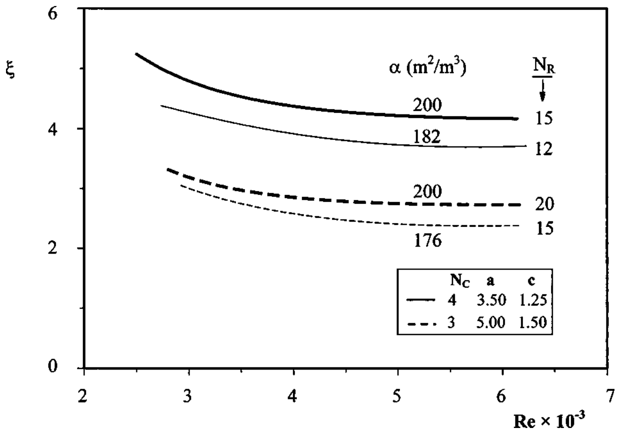

Fig. 7 Effect of N_C and N_R on ξ

2 mm rod bundle models. Although for increasing α, we add more solid material, increasing the viscous contact resistance for the flow, in Fig. 4 we do not find a direct relation between α and ξ. What happens is the form drag influencing parameters (such as d, N_R, N_C, a, b, c) override the viscous drag, which is directly proportional to α and U. Further, this quadratic effect also varies from model to model (increase in the pressure drop for the same velocity) as evident from the "spread" of the results and does not follow a direct relation with either α (Figs. 4 and 5) or the diameter of the rods (Fig. 3). This suggests that the quadratic amplification should be because of the drag effects resulting from the nature of the rod bundles that depend on U^2 and gets dominated for higher velocities. This drag effect is because of the complex influence of all of the other model parameters such as a, b, c, N_R, N_C and is lumped as β in Eq. (3) [or for constant density, as C in Eq. (4)].

Figure 6 reveals the effect of "a" and "c" on ξ for two models having identical N_C, N_R, "b" and surface to volume ratio (α, m^2/m^3). The fully developed turbulent flow with a flattened velocity profile [$u(y)$ flattened from the almost parabolic one for the fully developed laminar flow case] enters the model in the test section as shown in Figs. 2(a) and 2(b). By increasing "a," the transverse cross-sectional spacing between the rod rows is increased and for a fixed N_C, this results in the reduction of "c," the wall clearance. For a cross section [Fig. 2(a)], this result in more unobstructed flow near the axis with higher velocity and is further aided by the tubes crowding in the low velocity region near the walls due to the reduction in c. For aligned rod rows with a fixed mass flow rate, the overall effect is the reduction of longitudinal pressure-drop as more flow can be accommodated near the axis with higher average velocity. Hence, the model with a larger "a" and smaller "c" experience a lower pressure drop. Hence, the corresponding dashed line curve in Fig. 6 is below the continuous curve for smaller "a" and larger "c" model. This effect is fully valid even if the wall clearance "c" goes to zero.

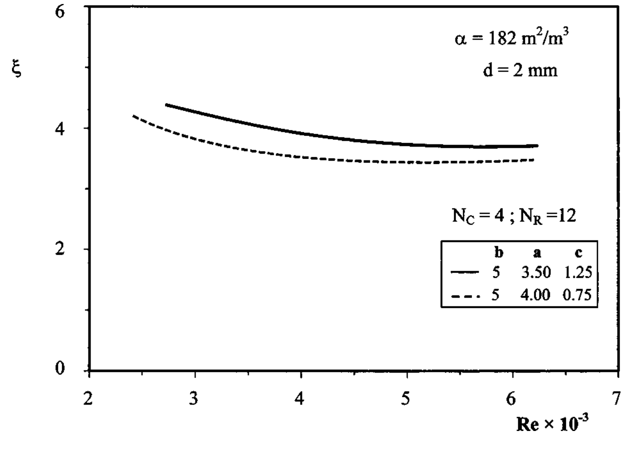

Fig. 6 Effect of "a" and "c" on ξ for constant surface to volume ratio α

It is to be kept in mind however that the above reasoning for the effects of "a" and "c" is valid only as long as both N_C and N_R remain fixed. For instance, in Fig. 7, the models having identical "α" values (first and third curve from top) do so by maintaining their product of N_C and N_R constant. Since N_C is no more a constant, increasing "a" need not necessarily reduce "c," the wall clearance. In fact, both "a" and "c" increase as we go from the first to the third curve. Reducing N_C (thus increasing "a") reduces the solid obstruction per cross section, in spite of probable increase in "c," the wall clearance, resulting in reduced pressure drop (ξ) for models with aligned rod arrangement.

Notice further that the ξ results for the four models in Fig. 7 are grouped for $N_C = 4$ (top two curves) and $N_C = 3$ (bottom two curves). The pairs individually reveal the effect of N_R: for increasing N_R, "b" reduces, reducing the spacing between two successive tubes along the flow direction (see Fig. 2). For an aligned arrangement of rods, this results in the downstream rod to be pushed into the wake and recirculation zone of the upstream rod causing ξ to increase. In the limit of $b \rightarrow 0$, the rods along the flow direction will merge together, forming a continuous sheet of solid material. This configuration is akin to a stack of parallel plate channels. Although, the incoming flow is turbulent, the nature of the flow through the individual passages (whether laminar or turbulent) depends on the respective passage hydraulic diameter. However, the overall longitudinal pressure drop across the model in this limit of $b \rightarrow 0$ is bound to be lower as the wake effects between successive rods are completely eliminated, resulting in the reduction of *form* drag. However, the surface viscous resistance (hence the viscous drag) is still present and is further amplified because of the increase in solid surface (N_R is very high). In addition, by comparing the topmost and bottommost curves, it is evident that for constant $N_R (= 15)$, ξ increases with increase in N_C. Further, the two bottom curves (with $N_C = 3$) have N_R equal to 15 and 20 while the top group (with $N_C = 4$) has N_R equal to 12 and 15. Comparing them, we may conclude that the effect of variation in N_C is stronger than that of the variation in N_R.

Figure 8 summarizes the pressure-drop results for models with rod bundles having diameters 3 and 4 mm. The first two curves from the top have $N_C = 4$ and the corresponding models experience higher pressure drop when compared to the bottom two curves having $N_C = 3$. This effect, consistent with the earlier explanation about N_C under Fig. 7, apparently holds merit irrespec-

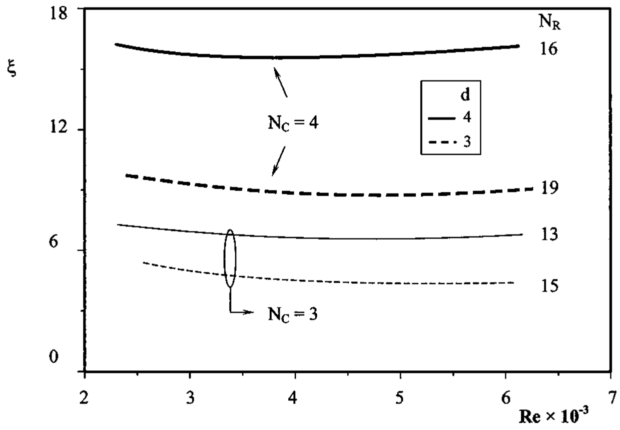

Fig. 8 Effect of diameter of tubes, N_C and N_R on ξ for rods with two different diameters

tive of the diameters of the individual rods. However, it is to be kept in mind that when the diameter of the individual rods becomes comparable to the cross-sectional width W, the effect of N_C should become redundant. This effect is already apparent in Fig. 8, if we compare the individual curves with identical N_C: As diameter increases (from 3 mm to 4 mm), pressure drop increases, as the frontal cross-sectional area is obstructed by more solid material.

In light of the above discussions, using Eqs. (1) and (2), the experimental results for all of the tested models can be fitted using the simple model equation

$$\xi = \frac{E}{\mathrm{Re}} + F \tag{5}$$

where E and F are constants to be determined from the curve-fits. Curve fits are performed on the experimental results in Figs. 4 and 5 using Eq. (5) allowing E and F to take independent values for each of the models. The comparative results are within 10% as shown in Fig. 9. Further, the curve fits yield E as a constant for all the models, equal to 300, while F takes different values for each of the models. This is expected since we are using experimental results under fully developed turbulent flow, in which case we expect the pressure drop to be proportional to U^2, leading to dominant changes in F for models with a different aligned arrangement of the rods. Further, as discussed from Figs. 6 through 8, these changes in F are effected purely by the *form* of the rod arrangement leading to variation in the "*form drag*" induced by the wake and separation behind each of the rods because of the influence of various geometric parameters such as "*a*" (and N_C), "*c*," "*b*" (and N_R) and diameter "*d*" of the rods of the models. Hence we relate the influence of all of the geometrical parameters to F through an empirical correlation of the form

$$F = \frac{40\left(\dfrac{b(1+2c)}{a}\right)^{1/4}\dfrac{N_R}{\sqrt{\psi}}}{(\alpha D_M)^6} \tag{6}$$

which predicts the F from the curve-fits within 15% accuracy.

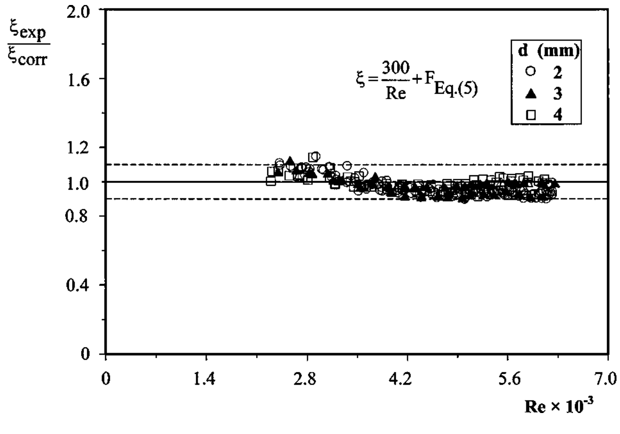

Fig. 9 Comparison of the ξ prediction using Eq. (5) with the experimental ξ results

In Eq. (6), Ψ is the volumetric solidity of the model equal to the ratio of the total volume of solid (rods) V_s, and the total volume V of the model. D_M is the model based hydraulic diameter defined following heat exchanger parlance [17], as

$$D_M = \frac{4A_f L}{A_s} \tag{7}$$

where A_f is the minimum frontal flow area of the model [see Fig. 2(*a*)] and, as defined in the nomenclature, A_s is the surface area offering resistance to flow—which includes all of the rod surfaces, top and bottom wall surfaces, and two side wall surfaces minus the area where the rods are attached to them. For a "plain" model without the rod bundles (i.e., for $d=0$), Eq. (7) will reduce to the conventional channel hydraulic diameter D [15], used to define Re in Eq. (1). Keep in mind however that A_s in Eq. (7) can be different from the heat transfer area used in defining D_M in [17] and [15] but is always equal to the surface area used while defining α, the surface to volume ratio of the compact heat exchanger models.

The nondimensional group αD_M in Eq. (6) can be interpreted in two ways. It can be viewed as a nondimensional volume ratio, with the product of A_s and D_M in the numerator, and the total volume of the model V in the denominator. Alternately, substituting for D_M from Eq. (7) and $\alpha = A_s/V$ and expanding $A_f\{=(B-dN_C)W\}$ and $A(=B\times W)$ results

$$\alpha D_M = \frac{4A_f}{A} = 4\phi = 4\left(1 - \frac{N_C}{B/d}\right) \tag{8}$$

where ϕ can be interpreted as a transverse (frontal) surface porosity of the models. When $N_C=0$, Eq. (8) yields $\phi=1$, i.e., there are no rods obstructing the frontal flow cross section and when $N_C = B/d$, $\phi=0$, i.e., no flow results as we have the cross section covered with solid.

Using Eq. (8) in Eq. (6) results in

$$F = 0.01\left(\frac{\left(\dfrac{b(1+2c)}{a}\right)^{1/4}\dfrac{N_R}{\sqrt{\psi}}}{(\phi)^6}\right) \tag{9}$$

An immediate observation from Eq. (8) is as N_C increases for a fixed model breadth B and diameter of rod d, the surface porosity ϕ decreases and this in Eq. (9) leads to a large increase in F [notice ϕ in Eq. (9), is raised to power 6 in the denominator]. When F is substituted into Eq. (5), we observe an increase in the nondimensional pressure drop, consistent with the strong influence of N_C on the experimental pressure-drop results that we observed in Figs. 7 and 8. Further, Eq. (9) is consistent with the other observations such as the weak increase in pressure drop for increase in N_R observed in Fig. 7 when N_C is fixed and the combined effect of "*a*" and "*c*" on the pressure drop identified in Fig. 6, while the other parameters (*d*, *b*, N_R, and N_C) remain fixed. Finally, the strength of changing N_C overriding the effects of "*a*" and "*c*" as observed in Fig. 7 is also predicted correctly by Eq. (9).

Using Eq. (9) to calculate F, Eq. (5) becomes a predictive tool for finding pressure drop across models with rods in aligned arrangement encountering turbulent flow. The results of the predictions from Eq. (5) agree within ±20% with our experimental results, as shown in Fig. 10. Additional comparisons with previously

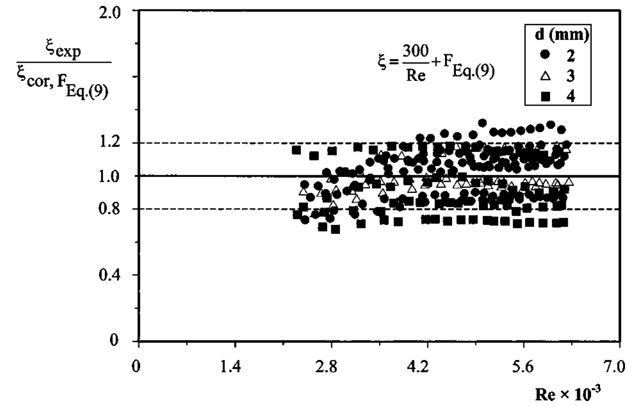

Fig. 10 Comparison of the ξ prediction from Eq. (5) using F from Eq. (9), with the experimental ξ results

published results are performed for the model, Eq. (5), along with the proposed correlation Eq. (9) in Fig. 11. The continuous lines in Fig. 11 are the predictions using Eq. (9), while the dotted lines are using correlations in [7] (Zukauskas, 1987) and the dashed lines are using correlations in the recent (2002) extensions of Martin [22], which uses pressure-drop correlations from [23]. (Gaddis and Gnielinski, 1985). The model numbers (from Table 1) for which these correlations yield their respective predictions are shown to the right of each curve.

The comparisons in Fig. 11 shows only the predictions from Eq. (9) are good because the proposed correlation, Eq. (9), stand out from the other correlations in three ways: (i) a new parameter, namely, the wall clearance effect, is introduced in our models. The parameter "c" in the correlation, Eq. (9), captures the effect of wall clearance which is not seen in any of the earlier correlations; (ii) The tube diameters we have used are 2, 3, and 4 mm, which are not the ranges suggested by the earlier correlations (for instance, the correlations in [22] and [23] are claimed for diameter range greater than 7.9 mm); and (iii) The range for parameter "a" has been extended in our models up to 7 (see Table 1, a' range from 1.75 to 7)—Zukauskas [7] has it for 1 through 2.5, while [22] claim it up to 6 although the original reference [23] claims it only up to 3 (few experiments were done for a>3 and up to 6).

Hence, even when appropriate models (model-numbers 9 and 14) with $a=2$ and $a=2.5$ are chosen for comparison (first and second data set from the top, in Fig. 11), because their diameters ($d=3$ and 4, respectively) and wall clearance $c(\neq 0)$ are different from parameter ranges for earlier correlations, it is difficult as such, to use the proposed correlation, Eq. (9), to "verify" earlier correlations. Likewise, using model-number 15, a specific model designed with wall clearance $c=0$, the comparison between our proposed correlation and that of [22] and [23] is marginally agreeable. The differences are due to the difference in tube diameters ($d=2$ mm, for model-number 15) and the range for "a" (=7, for model-number 15). Further, from Fig. 6.19 of [7] one may find, Zukauskas's data for "a" and "b" equal to 2.5 is extended into the low Reynolds numbers range by the present work.

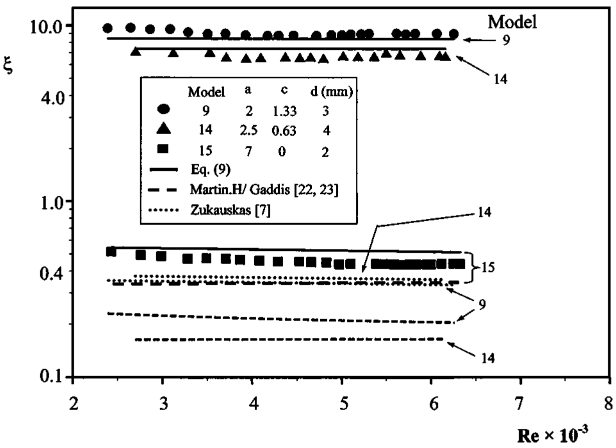

Fig. 11 Comparison of the ξ prediction using Eq. (9) with that of other published results by [7,22,23]

Expanding Eq. (5) by substituting for ξ and Re from Eqs. (2) and (1), respectively, and rearranging,

$$\frac{\Delta P}{L}=\frac{\mu}{(2D^2/E)}U+\rho\left(\frac{F}{2D}\right)U^2 \qquad (10)$$

Comparing Eq. (10) with Eq. (4), we find K and C of Eq. (4) equal to $2D^2/E$ and $F/2D$, respectively. In other words, the near compact heat exchanger models with aligned rod arrangement tested for fully turbulent flow configuration can in the outset be treated as a porous medium. As the model dependent parameter E turns out to be a constant in the curve fits using Eq. (5), the permeability $K=2D^2/E$ remains a constant for all of the models tested in the fully turbulent regime (Re>2300). For a chosen fluid under turbulent flow through a model configuration, even the variations in K (due to variations in Ψ) will always be overshadowed by the dominance of the second term in the RHS of Eq. (4). Since $C=F/2D$, the geometric parameters such as d, a (and N_C), c, b (and N_R) due to their capacity to alter the flow characteristics within the model because of their *form*, predominantly influence only the form coefficient C of Eq. (4) through F, which can be found using the correlation in Eq. (9).

The above exercise reveals the nature of the drags involved the turbulent flow experiments, Eq. (10), to be consistent with the porous medium interpretation of Eq. (3). However, we must keep in mind that Eq. (3) is *only* a model and *can* be used to interpret more than one physical phenomenon satisfactorily. For instance, the similarity in content of Eqs. (3) and (10) has led researchers to believe [19] that "transition" from laminar to turbulent flow (marked by global, channel hydraulic diameter D based Re to be greater than 2300) through a porous medium like configuration [governed by Eq. (10)] implies transition from viscous drag [first term in the RHS of Eq. (3)] to form drag [second term in the RHS of Eq. (3)] dominated flow regime inside the porous medium. However, as mentioned in [20], the transition from viscous drag ($D_\mu=\mu U/K$) to form drag ($D_C=\rho C U^2$) dominated flow in a porous medium is better predicted based on the criterion

$$\lambda=\left(\frac{D_C}{D_\mu}\right)=\left(\frac{\rho K C}{\mu}U\right)>1 \qquad (11)$$

Using $K=2D^2/E$ and $C=F/2D$ from Eq. (10) we find for isothermal turbulent air flow experiments that even for the model with lowest F tested (Model 7, $F=3.1$), at $U_{\min}=0.8$ m/s, λ is 18.28, which satisfies Eq. (11). This implies the flow inside the rod bundles (viewed as a porous medium) is already form drag dominated, well within the channel flow transition regime itself ($U<1$ m/s and Re<2300)—i.e., the flow is yet to become fully turbulent in the initial channel section. This shows that the claim made by [19] is not correct. This was heuristically pointed out in [20] and [21] as well. The transition to turbulence (determined based on channel hydraulic diameter based Re to be greater than 2300) in the initial flow section is not a criterion for transition to form drag dominated flow regime inside a porous medium test section as observed in [19]. The flow inside the porous medium like rod bundle models can already be form drag dominated owing to the influence of various *form* parameters such as d, a (and N_C), c, b (and N_R) of the rod arrangement inside the models. This is clearly validated by our experimental results.

Conclusions

Hydrodynamic pressure-drop experiments were conducted in the turbulent flow regime for near-compact heat exchanger models (α, 100 to 300 m^2/m^3), with rod bundles of three different diameters in various aligned arrangements. The diameter range used in the present study ($d=2,3,4$ mm) are different from the earlier results, to accommodate D_M to be greater than 6 mm, complying with the near-compact heat exchanger configurations. The pressure-drop results were curve fitted using a nondimensional pressure drop versus Re model, Eq. (5), which is similar in content to a dimensional, low permeability, non-Darcy flow, porous medium model, Eq. (4). Treating the rod bundle models as a porous medium, the ''viscous drag'' of the rod bundles is found to be a fixed value losing strength, as expected, with the gaining dominance of the ''form drag,'' for higher Re (>2300) turbulent flow.

Connecting the various form drag inducing parameters such as d, a (and N_C), c, b (and N_R) of the rod arrangement inside the models to the form coefficient F in Eq. (5) [or C in Eq. (4)], a predictive correlation for F is proposed in Eq. (9). Using Eq. (9) for calculating F, the model Eq. (5) predicts within $\pm 20\%$, the experimental pressure drop results, thus serving as a hydraulic predictive tool for finding pressure drop across rod bundle models with rods in aligned arrangement encountering fully developed turbulent flow. Comparisons of proposed correlation, Eq. (9), with earlier published results [7,22,23] reveal the effect of a new parameter, the wall clearance effect, ''c,'' and also the effects of ''a'' and small tube-diameter d, in our models. The range for parameter ''a'' is studied for 7, an extension from earlier results.

Based on the porous medium transition parameter λ, Eq. (11), the experimental results also validate the transition to form-drag dominated regime inside the rod bundle models (when treated as a porous medium) happens well before the global turbulent regime for the initial section of the flow channel.

Nomenclature

A = cross-sectional area of inlet duct, m
A_f = frontal flow area, $\{=(B-dN_C)W\}$, Eq. (7), m
A_s = surface area offering resistance to flow, $\{=(\pi dWN_RN_C)+(2LB)-(2N_RN_C\pi d^2/4)\}$, Eq. (7), m
a = relative nondimensional transverse spacing, Fig. 2 $(=S_T/d)$
B = depth of the rod bundle, Fig. 2, mm
b = relative nondimensional longitudinal spacing, Fig. 2 $(=S_L/d)$
C = form-coefficient of the porous medium, Eq. (4), m^{-1}
c = relative nondimensional wall clearance, Fig. 2 $(=w/d)$
D = hydraulic diameter of the rectangular cross section, $\{=4A/P\}$, m
D_M = model based hydraulic diameter, $\{=4A_fL/A_s\}$, Eq. (7), m
d = diameter of a rod used in the models, Fig. 2, mm
K = permeability of the porous medium, Eq. (4), m^2
L = length of rod bundle, Fig. 2, mm
N_R = number of rod rows in the model, along the longitudinal (flow) direction, Fig. 2
N_C = number of rod rows in the model, along the transverse direction, Fig. 2
P = perimeter of inlet duct, m
$\Delta P/L$ = longitudinal pressure-drop across rod bundles, Pa/m
Re = Reynolds Number, Eq. (1)
S_T = transverse spacing, Fig. 2, mm
S_L = longitudinal spacing, Fig. 2, mm
U = average velocity in the rectangular channel, Fig. 2, m/s
V = total model volume $(=L\times B\times W)$, mm^3
W = width of the rod bundle, Fig. 2, mm
w = frontal wall clearance/spacing, Fig. 2, mm

Greek symbols:

α = surface to volume ratio of the model (rod bundle), (m^2/m^3)
β = form drag coefficient, Eq. (3)
γ = viscous drag coefficient, Eq. (3)
ϕ = transverse surface porosity of the model (rod bundle) $(=A_f/A)$, Eq. (9)
ξ = nondimensional pressure drop, Eq. (2)
Ψ = volumetric solidity of the model (rod bundle) $(=V_s/V)$, Eq. (6)

References

[1] Shah, R. K., and Sekulic, D. P., 2003, *Fundamentals of Heat Exchanger Design*, Wiley, NY.
[2] Kays, W. M., and London, A. L., 1984, *Compact Heat Exchangers*, 3rd ed., McGraw-Hill, NY.
[3] Lage, J. L., Weinert, A. K., Price, D. C., and Weber, R. M., 1996, ''Numerical Study of Low Permeability Micro-Porous Heat Sink for Cooling Phased-Array Radar Systems,'' Int. J. Heat Mass Transfer, **39**, pp. 3622–3647.
[4] Sung-Ho, Kim, and Mohamed, S. EL-Gnek, 1989, ''Heat Transfer Experiments for Low Flow of Water in Rod Bundles,'' Int. J. Heat Mass Transfer, **32**(7), pp. 1321–1326.
[5] Zukauskas, A. A., 1972, ''Heat Transfer From Tubes in Cross Flow,'' Adv. Heat Transfer, **8**, pp. 93–169.
[6] Fraas, A. P., 1988, *Heat Exchanger Design*, 2nd ed., Wiley, NY.
[7] Zukauskas, A. A., 1987, ''Convective Heat Transfer in Cross Flow,'' Chap. 6 in S. Kakaç, S., Shah, R. K., and Aung, W., eds., *Handbook of Single Phase Convective Heat Transfer*, Wiley, NY.
[8] Safwat Wilson, A., and Khalil Bassiouny, M., 2000, ''Modeling of Heat Transfer for Flow Across Tube Banks,'' Chem. Eng. Prog., **39**, pp. 1–14.
[9] Ergun, S., 1952, ''Fluid Flow Through Packed Columns,'' Chem. Eng. Prog., **48**, pp. 89–94.
[10] Nield, D. A., and Bejan, A., 1999, *Convection in Porous Media*, 2nd ed., Springer-Verlag, NY.
[11] Lage, J. L., and Narasimhan, A., 2000, ''Porous Media Enhanced Forced Convection: Fundamentals and Applications,'' *Handbook of Porous Media*, K. Vafai, ed., Marcel Dekker, NY, **8**, pp. 357–394.
[12] Martin, A. R., Saltiel, C., and Shyy, W., 1998a, ''Heat Transfer Enhancement With Porous Inserts in Recirculating Flows,'' ASME J. Heat Transfer, **120**, pp. 458–467.
[13] Martin, A. R., Saltiel, C., and Shyy, W., 1998b, ''Convective and Radiative Internal Heat Transfer Augmentation With Fiber Arrays,'' Int. J. Heat Mass Transfer, **41**, pp. 3431–3440.
[14] Martin, A. R., Saltiel, C., and Shyy, W., 1998c, ''Frictional Losses and Convective Heat Transfer in Sparse Periodic Cylinder Arrays in Cross Flow,'' Int. J. Heat Mass Transfer, **41**, pp. 2383–2397.
[15] Bejan, A., 1995, *Convection Heat Transfer*, 2nd ed., Wiley, NY.
[16] Holman, J. P., 2001, *Experimental Methods for Engineers*, 7th ed., McGraw-Hill, NY.
[17] Kays, W. M., and Crawford, M. E., 1993, *Convective Heat and Mass Transfer*, 3rd ed., McGraw-Hill, NY.
[18] Lage, J. L., Antohe, B. V., and Nield, D. A., 1997, ''Two Types of Nonlinear Pressure-Drop Versus Flow-Rate Relation Observed for Saturated Porous Media,'' ASME J. Fluids Eng., **119**, pp. 700–706.
[19] Ward, J. C., 1964, ''Turbulent Flow in Porous Media,'' J. Hydraul. Div., Am. Soc. Civ. Eng., **90HY5**, pp. 1–12.
[20] Lage, J. L., and Antohe, B. V., 2000, ''Darcy's Experiments and the Deviation to Nonlinear Flow Regime,'' ASME J. Fluids Eng., **122**, pp. 619–625.
[21] Lage, J. L., 1998, ''The Fundamental Theory of Flow Through Permeable Media: From Darcy to Turbulence,'' *Transport Phenomena in Porous Media*, D. B. Ingham and I. Pop, eds., Pergamon, NY, pp. 1–30.
[22] Martin, H., 2002, ''The Generalized Léveque Equation and its Practical Use for the Predication of Heat and Mass Transfer Rates From Pressure Drop,'' Chem. Eng. Sci., **57**, pp. 3217–3223.
[23] Gaddis, E. S., and Gnielinski, V., 1985, ''Pressure Drop in Cross Flow Across Tube Bundles,'' Int. Chem. Eng., **25**, pp. 1–15.

Axisymmetric Stagnation-Point Flow and Heat Transfer of a Viscous Fluid on a Moving Cylinder With Time-Dependent Axial Velocity and Uniform Transpiration

R. Saleh
Ph.D. student and lecturer,
Faculty of Engineering, Azad Univ.,
Mashhad, Iran

A. B. Rahimi[1]
Professor,
e-mail: rahimiab@yahoo.com
P.O. Box No. 91775-1111,
Faculty of Engineering,
Ferdowsi University of
Mashhad, Mashhad, Iran

The unsteady viscous flow and heat transfer in the vicinity of an axisymmetric stagnation point of an infinite moving cylinder with time-dependent axial velocity and with uniform normal transpiration U_o *are investigated. The impinging free stream is steady and with a constant strain rate* k. *An exact solution of the Navier–Stokes equations and energy equation is derived in this problem. A reduction of these equations is obtained by use of appropriate transformations for the most general case when the transpiration rate is also time-dependent but results are presented only for uniform values of this quantity. The general self-similar solution is obtained when the axial velocity of the cylinder and its wall temperature or its wall heat flux vary as specified time-dependent functions. In particular, the cylinder may move with constant speed, with exponentially increasing–decreasing axial velocity, with harmonically varying axial speed, or with accelerating–decelerating oscillatory axial speed. For self-similar flow, the surface temperature or its surface heat flux must have the same types of behavior as the cylinder motion. For completeness, sample semisimilar solutions of the unsteady Navier–Stokes and energy equations have been obtained numerically using a finite-difference scheme. Some of these solutions are presented for special cases when the time-dependent axial velocity of the cylinder is a step-function, and a ramp function. All the solutions above are presented for Reynolds numbers,* $Re = ka^2/2\upsilon$, *ranging from 0.1 to 100 for different values of dimensionless transpiration rate,* $S = U_o/ka$, *where* a *is cylinder radius and* υ *is kinematic viscosity of the fluid. Absolute value of the shear-stresses corresponding to all the cases increase with the increase of Reynolds number and suction rate. The maximum value of the shear- stress increases with increasing oscillation frequency and amplitude. An interesting result is obtained in which a cylinder moving with certain exponential axial velocity function at any particular value of Reynolds number and suction rate is axially stress-free. The heat transfer coefficient increases with the increasing suction rate, Reynolds number, Prandtl number, oscillation frequency and amplitude. Interesting means of cooling and heating processes of cylinder surface are obtained using different rates of transpiration. It is shown that a cylinder with certain type of exponential wall temperature exposed to a temperature difference has no heat transfer.* [DOI: 10.1115/1.1845556]

Keywords: Stagnation Flow, Time-Dependent Axial Movement, Time-Dependent Heat Transfer, Transpiration, Exact Solution

1 Introduction

The task of finding exact solutions for Navier–Stokes equations is a difficult one due to nonlinearity of these equations. Hiemenz [1] has obtained an exact solution of the Navier–Stokes equations governing the two-dimensional stagnation-point flow on a flat plate. The analogous axisymmetric stagnation-point flow was investigated by Homann [2]. Results of the problem of stagnation flow against a flat plate for asymmetric cases were presented by Howarth [3] and Davey [4]. Wang [5] was first to find exact solution for the problem of axisymmetric stagnation flow on an infinite stationary circular cylinder. Gorla [6–10], in a series of papers, studied the steady and unsteady flows and heat transfer over a circular cylinder in the vicinity of the stagnation-point for the cases of constant axial movement, and the special case of axial harmonic motion of a nonrotating cylinder. This special case is only for small and high values of the frequency parameter using perturbation techniques. Recently, Cunning, Davis, and Weidman [11] have considered the stagnation flow problem on a rotating circular cylinder with constant angular velocity, including the effects of suction and blowing with constant rate. Takhar, Chamkha, and Nath [12] have also investigated the unsteady viscous flow in the vicinity of an axisymmetric stagnation-point of an infinite circular cylinder when both the cylinder and the free-stream velocities vary as a same function of time. Their self-similar solution is

---

[1] Corresponding author.

Contributed by the Fluids Engineering Division for publication in the JOURNAL OF FLUIDS ENGINEERING. Manuscript received by the Fluids Engineering Division October 31, 2002; revised manuscript received November 12, 2003. Corresponding author.

only for the case when both the cylinder and the free-stream velocities vary inversely as a linear function of time and by taking an average value for the Reynolds number.

The effects of cylinder movement with time-dependent axial velocity, and time-dependent heat transfer in general, specially with different types of harmonic oscillation which are of interest in certain manufacturing processes, have not yet been considered. In the present analysis, the unsteady viscous flow and heat transfer in the vicinity of an axisymmetric stagnation point of an infinite cylinder with time-dependent axial movement and with uniform transpiration is considered, though the reduction of the Navier–Stokes equations and the energy equation is obtained for the most general case of time-dependent transpiration rate. Our motivation is to generalize the problem of stagnation-point flow and heat transfer of a fluid on a moving cylinder. An exact solution of the Navier–Stokes equations and the energy equation is obtained. The general self-similar solution is obtained when the axial velocity of the cylinder and its surface temperature or heat flux vary in a prescribed manner. The cylinder may perform different types of motion: it may move with constant speed, with exponentially increasing–decreasing axial velocity, with harmonically varying axial speed, or with accelerating–decelerating oscillatory axial speed. The cylinder surface temperature and its surface heat flux may have the same behavior as the cylinder motion.

Sample distributions of shear-stresses, and temperature fields at Reynolds numbers ranging from 0.1 to 100 are presented for different forms of cylinder movement and different values of Prandtl numbers and selected values of uniform suction and blowing rates. Particular cases of these results are compared with existing results of Wang [5] and Gorla [7,9,10], Correspondingly. For completeness, some semisimilar solutions of the Navier–Stokes equations and energy equation are obtained and results for a few examples of cylinder axial motion in the form of a step-function, and a ramp function are presented for different values of flow parameters.

2 Problem Formulation

Flow is considered in cylindrical coordinates (r,φ,z) with corresponding velocity components (u,v,w), see Fig. 1. We consider the laminar unsteady incompressible flow and heat transfer of a viscous fluid in the neighborhood of an axisymmetric stagnation-point of an infinite circular cylinder when it moves axially with a velocity that varies with time. An external axisymmetric radial stagnation flow of strain rate $\bar{k}$ impinges on the cylinder of radius a, centered at $r=0$. A uniform normal transpiration U_o at the cylinder surface may occur, where $U_o>0$ corresponds to suction into the cylinder, though the formulation of the problem is for the more general case of time-dependent transpiration rate. The unsteady Navier–Stokes and energy equations in cylindrical polar coordinates governing the axisymmetric flow and heat transfer are given by [5–10]:

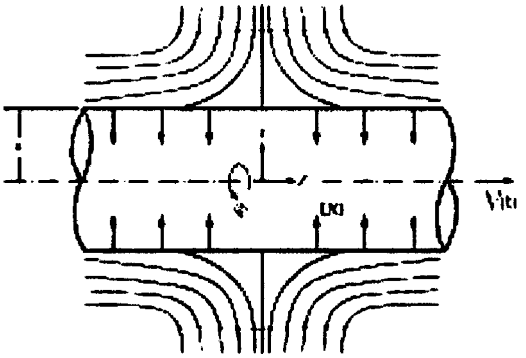

Fig. 1 Schematic diagram of an axially moving cylinder under radial stagnation flow in the fixed cylindrical coordinate system (r,φ,z)

Mass:

$$\frac{\partial}{\partial r}(ru)+r\frac{\partial w}{\partial z}=0 \tag{1}$$

Momentum:

$$\frac{\partial u}{\partial t}+u\frac{\partial u}{\partial r}+w\frac{\partial u}{\partial z}=-\frac{1}{\rho}\frac{\partial p}{\partial r}+\upsilon\left(\frac{\partial^2 u}{\partial r^2}+\frac{1}{r}\frac{\partial u}{\partial r}-\frac{u}{r^2}+\frac{\partial^2 u}{\partial z^2}\right) \tag{2}$$

$$\frac{\partial w}{\partial t}+u\frac{\partial w}{\partial r}+w\frac{\partial w}{\partial z}=-\frac{1}{\rho}\frac{\partial p}{\partial z}+\upsilon\left(\frac{\partial^2 w}{\partial r^2}+\frac{1}{r}\frac{\partial w}{\partial r}+\frac{\partial^2 w}{\partial z^2}\right) \tag{3}$$

Energy:

$$\frac{\partial T}{\partial t}+u\frac{\partial T}{\partial r}+w\frac{\partial T}{\partial z}=\bar{\alpha}\cdot\left[\frac{1}{r}\frac{\partial}{\partial r}\left(r\frac{\partial T}{\partial r}\right)+\frac{\partial^2 T}{\partial z^2}\right] \tag{4}$$

where p, ρ, υ, and $\bar{\alpha}$ are the fluid pressure, density, kinematic viscosity, and thermal diffusivity. The boundary conditions for velocity field are:

$$r=a:\quad u=-U_o,\quad w=V(t) \tag{5}$$

$$r\to\infty:\quad u=-\bar{k}\left(r-\frac{a^2}{r}\right)-\frac{aU_o}{r},\quad w=2\bar{k}z \tag{6}$$

in which, (5) are no-slip conditions on the cylinder wall and relations (6) show that the viscous flow solution approaches, in a manner analogous to the Hiemenz flow, the potential flow solution as $r\to\infty$, Ref. [11].

For the temperature field we have:

$$\begin{aligned} r=a:\quad &\text{(i)}\quad T=T_w(t)\quad \text{for defined wall temperature}\\ &\text{(ii)}\quad \frac{\partial T}{\partial r}=-\frac{q_w(t)}{k}\quad \text{for defined wall heat flux}\\ r\to\infty:\quad &T\to T_\infty \end{aligned} \tag{7}$$

where k is the thermal conductivity of the fluid and $T_w(t)$ and $q_w(t)$ are temperature and heat flux at the wall cylinder, respectively.

A reduction of the Navier–Stokes equations is obtained by the following coordinate separation of the velocity field:

$$u=-\bar{k}\frac{a}{\sqrt{\eta}}f(\eta,\tau),\quad w=2\bar{k}f'(\eta,\tau)z+H(\eta,\tau),\quad p=\rho\bar{k}^2a^2P \tag{8}$$

where $\tau=2\bar{k}t$ and $\eta=(r/a)^2$ are dimensionless time and radial variables and prime denotes differentiation with respect to η. Transformations (8) satisfy (1) automatically and their insertion into (2) and (3) yields a coupled system of differential equations in terms of $f(\eta,\tau)$ and $H(\eta,\tau)$ and an expression for the pressure:

$$\eta f'''+f''+\mathrm{Re}\left[1-(f')^2+ff''-\frac{\partial f'}{\partial\tau}\right]=0 \tag{9}$$

$$\eta H''+H'+\mathrm{Re}\left[fH'-f'H-\frac{\partial H}{\partial\tau}\right]=0 \tag{10}$$

$$P-P_o=-\left[\frac{f^2}{2\eta}+\frac{1}{\mathrm{Re}}f'+2\left(\frac{z}{a}\right)^2\right] \tag{11}$$

In these equations, primes indicate differentiation with respect to η and $\mathrm{Re}=\overline{ka}^2/2\upsilon$ is the Reynolds number. From conditions (5) and (6), the boundary conditions for (9) and (10) are as follows:

$$\begin{aligned} &\eta=1:\ \ f=s(\tau),\ \ f'=0,\ \ H=V(\tau) \\ &\eta\rightarrow\infty:\ \ f'=1,\ \ H=0 \end{aligned} \tag{12}$$

in which, $s(\tau)=U_o(\tau)/\overline{ka}$ is the dimensionless wall-transpiration rate.

To transform the energy equation into a nondimensional form for the case of defined wall temperature, we introduce

$$\Theta=\frac{T(\eta,\tau)-T_\infty}{T_w(\tau)-T_\infty} \tag{13}$$

Making use of (8) and (13), the energy equation may be written as:

$$\eta\Theta''+\Theta'+\mathrm{Re}\cdot\mathrm{Pr}\left(f\Theta'-\frac{\partial\Theta}{\partial\tau}-\frac{dT_w/d\tau}{T_w-T_\infty}\Theta\right)=0 \tag{14}$$

with the boundary conditions as:

$$\Theta(1,\tau)=1,\ \ \Theta(\infty,\tau)=0 \tag{15}$$

For the case of defined wall heat flux, we introduce

$$\Theta=\frac{T(\eta,\tau)-T_\infty}{aq_w(\tau)/2k} \tag{16}$$

Now making use of (8) and (16), the energy equation may be written as:

$$\eta\Theta''+\Theta'+\mathrm{Re}\cdot\mathrm{Pr}\left(f\Theta'-\frac{\partial\Theta}{\partial\tau}-\frac{dq_w/d\tau}{q_w}\Theta\right)=0 \tag{17}$$

with the boundary conditions as:

$$\Theta'(1,\tau)=-1,\ \ \Theta(\infty,\tau)=0 \tag{18}$$

Here, Eqs. (9), (10), and (14) or (17) are for different forms of $s(\tau)$, $V(\tau)$, $T_w(\tau)$, or $q_w(\tau)$ functions and have been solved numerically with Re and Pr as parameters. For the sake of brevity, only results for $s(\tau)=\text{constant}$ are shown in this paper.

For $U_0(\tau)=\text{constant}\,[s(\tau)=\text{constant}]$ none of the boundary conditions of Eq. (9) are functions of time, and assuming steady-state initial conditions for this equation, we have:

$$\tau=0\rightarrow\frac{\partial f'}{\partial\tau}=0$$

Therefore, in this case Eq. (9) is reduced to the form:

$$\eta f'''+f''+\mathrm{Re}[1-(f')^2+ff'']=0 \tag{19}$$

Steady-state solutions are obtained by solving this equation. Since none of the boundary conditions on f is time-dependent, then this function does not change with respect to time and the result of steady-state solution ($\tau=0$) is the same as the solution for all the later times ($\tau>0$). Thus $f(\eta,\tau)=f(\eta)$ and consequently Eq. (9) can be reduced to Eq. (19).

Equation (19) is the same as the one obtained by Wang [5] and its solution is known. Here, Eqs. (10), (14), and (17) are solved for different forms for $V(\tau)$ functions and prescribed values of surface temperature or surface heat flux. In what follows, first the self-similar equations and the exact solutions for some particular $V(\tau)$, $T_w(\tau)$, and $q_w(\tau)$ functions are presented and then, for completeness, the semisimilar equations and their numerical solutions are obtained and sample results for Eq. (10) are presented.

3 Self-Similar Equations

Equations (10) and (14) or (17) can be reduced to a system of ordinary differential equations if we assume that the function $H(\eta,\tau)$ in (10) and $\Theta(\eta,\tau)$ in (14) or (17) are seperable as:

$$\begin{aligned} &H(\eta,\tau)=V(\tau)\cdot h(\eta) \\ &\Theta(\eta,\tau)=\theta(\eta)\cdot Q(\tau) \end{aligned} \tag{20}$$

Substituting these separation of variables into (10) and (14) or (17), correspondingly gives:

$$\eta\frac{h''}{h}+\frac{h'}{h}+\mathrm{Re}\left(f\frac{h'}{h}-f'\right)=\frac{\mathrm{Re}}{V(\tau)}\frac{dV(\tau)}{d\tau} \tag{21}$$

$$\eta\frac{\theta''}{\theta}+\frac{\theta'}{\theta}+\mathrm{Re}\cdot\mathrm{Pr}(f\theta'/\theta)=\mathrm{Re}\cdot\mathrm{Pr}\left(\frac{dQ/d\tau}{Q}+\frac{dT_w/d\tau}{T_w-T_\infty}\right) \tag{22}$$

or for defined wall heat flux:

$$\eta\frac{\theta''}{\theta}+\frac{\theta'}{\theta}+\mathrm{Re}\cdot\mathrm{Pr}(f\theta'/\theta)=\mathrm{Re}\cdot\mathrm{Pr}\left(\frac{dQ/d\tau}{Q}+\frac{dq_w/d\tau}{q_w}\right) \tag{23}$$

The general solution to the differential equations in (21) and (22) or (23) with τ as an independent variable are as the following:

$$V(\tau)=b\cdot\mathrm{Exp}[(\alpha+i\beta)\tau] \tag{24}$$

$$Q(\tau)=\frac{c\cdot\mathrm{Exp}[(\gamma+i\delta)\tau]}{T_w(\tau)-T_\infty},\quad \text{for defined wall temperature} \tag{25}$$

$$Q(\tau)=\frac{c\cdot Exp[(\gamma+i\delta)\tau]}{q_w(\tau)},\quad \text{for defined wall heat flux} \tag{26}$$

Here, $i=\sqrt{-1}$ and b, α, and β and also c, γ, and δ are constants. Substituting these solutions into the differential equations in (21) and (22) or (23) with η as an independent variable results in:

$$\eta h''+h'+\mathrm{Re}[fh'-f'h-\alpha h-i\beta h]=0 \tag{27}$$

$$\eta\theta''+\theta'+\mathrm{Re}\cdot\mathrm{Pr}(f\theta'-\gamma\theta-i\delta\theta)=0 \tag{28}$$

The axial velocity boundary conditions are:

$$\eta=1:\ \ h=1 \tag{29}$$

$$\eta\rightarrow\infty:\ \ h=0 \tag{30}$$

For the above defined wall temperature and wall heat flux, respectively, one obtains:

$$\Theta(1,\tau)=1=\theta(1)\cdot Q(\tau)\rightarrow\theta(1)=1,Q(\tau)=1\rightarrow T_w(\tau)-T_\infty=c\cdot \text{Exp}[(\gamma+i\delta)\tau] \tag{31}$$

$$\Theta'(1,\tau)=-1=\theta'(1)\cdot Q(\tau)\rightarrow\theta'(1)=-1,Q(\tau)=1\rightarrow q_w(\tau)=c\cdot \text{Exp}[(\gamma+i\delta)\tau]$$

$$\Theta(\infty,\tau)=0=\theta(\infty)\cdot Q(\tau)\rightarrow\theta(\infty)=0 \tag{31a}$$

Note that, in (24) $b=0$ corresponds to the case of a cylinder with no axial movement, wang [5]. If $b\neq 0$ and $\alpha=\beta=0$, (24) gives the case of a uniformly moving cylinder with constant axial velocity, Gorla [7]. $b\neq 0$, $\beta\neq 0$, and $\alpha=0$, corresponds to the case of a moving cylinder with a harmonic velocity in its own plane, Gorla [9]. The case of $b\neq 0$, $\alpha\neq 0$, $\beta\neq 0$ is the most general case which is considered in this paper. If $b=\alpha=\beta=0$ and $c\neq 0$, $\gamma=\delta=0$, Eqs. (31) correspond to the result of Gorla [10] which is for a stationary cylinder. Other combinations of values of c, γ, and δ in Eqs. (31) give different time-dependent wall temperature and heat flux functions.

To obtain solution of Eqs. (27) and (28), it is assumed that the functions $h(\eta)$ and $\theta(\eta)$ are complex functions as:

$$h(\eta)=h_1(\eta)+ih_2(\eta) \tag{32}$$

$$\theta(\eta)=\theta_1(\eta)+i\theta_2(\eta) \tag{33}$$

Substituting (32) and (33) into (27) and (28), the following coupled system of differential equations are obtained:

$$\begin{cases}\eta h_1''+h_1'+\text{Re}(fh_1'-f'h_1-\alpha h_1+\beta h_2)=0\\ \eta h_2''+h_2'+\text{Re}(fh_2'-f'h_2-\alpha h_2-\beta h_1)=0\end{cases} \tag{34}$$

$$\begin{cases}\eta\theta_1''+\theta_1'+\text{Re}\cdot\text{Pr}(f\theta_1'-\gamma\theta_1+\delta\theta_2)=0\\ \eta\theta_2''+\theta_2'+\text{Re}\cdot\text{Pr}(f\theta_2'-\gamma\theta_2-\delta\theta_1)=0\end{cases} \tag{35}$$

The boundary conditions for functions f, h, and θ become:

$$\eta=1:\ \ f=s,\ \ f'=0,\ \ h=1,\ \ \theta=1\quad(\text{or}\ \ \theta'=-1) \tag{36}$$

$$\eta\rightarrow\infty:\ \ f'=1,\ \ h=0,\ \ \theta=0 \tag{37}$$

where $s=U_o/\overline{k}a$ is the dimensionless wall-transpiration rate which is assumed uniform. Hence, the boundary conditions on functions h_1 and h_2 are:

$$\eta=1:\ \ h_1=1,\ \ h_2=0,\ \ \theta_1=1,\ \ \theta_2=0\quad(\text{or}\ \ \theta_1'=-1,\theta_2'=0) \tag{38}$$

$$\eta\rightarrow\infty:\ \ h_1=0,\ \ h_2=0,\ \ \theta_1=0,\ \ \theta_2=0 \tag{39}$$

The coupled system of Eqs. (34) and (35) along with boundary conditions (38) and (39) have been solved by using the fourth-order Runge–Kutta method of numerical integration along with a shooting method, Press et al. [13]. First, Eq. (19) was solved by guessing initial values for $f''(1)$ and intergrating until the convergence reached. Then, the initial values of $h_1'(1)$, $h_2'(1)$ and $\theta_1'(1)$, $\theta_2'(1)$ [or $\theta_1(1)$, $\theta_2(1)$] were guessed and the integration was repeated until convergence was obtained. The value of $h_2(\eta)=0$ and $\theta_2(\eta)=0$ was assumed initially and then by repeating the integration of these two systems of equations, final values of $h_1(\eta)$, $h_2(\eta)$, and $\theta_1(\eta)$, $\theta_2(\eta)$ were obtained. In these computations the grid size was chosen 0.001 and the truncation error was set at 1E-9.

The axial velocity is:

$$V(\tau)=b\ \text{Exp}(\alpha\tau)[\cos(\beta\tau)+i\sin(\beta\tau)] \tag{40}$$

and thus, the $H(\eta,\tau)$ function from definition (20) becomes:

$$H(\eta,\tau)=b\ \text{Exp}(\alpha\tau)[(h_1\cos(\beta\tau)-h_2\sin(\beta\tau))+i(h_1\sin(\beta\tau)+h_2\cos(\beta\tau))]. \tag{41}$$

4 Semi-Similar Equations

Equations (10), (14), and (17) may be solved directly for any chosen $V(\tau)$, $T_w(\tau)$, and $q_w(\tau)$ functions. The solutions obtained this way, are called semisimilar solutions. These equations, along with boundary conditions (12), (15), and (18), were solved by using a central finite-difference method which lead to a tri-diagonal matrix. Assuming steady-state for $\tau<0$, the solution starts from $V(0)$, $T_w(0)$ or $q_w(0)$ and marching through time, time-dependent solutions for $\tau>0$ were obtained. Sample axial velocity profiles will be presented in later sections.

5 Shear-Stress

The shear-stress at the cylinder surface is calculated from:

$$\sigma=\left[\mu\frac{\partial w}{\partial r}\right]_{r=a} \tag{42}$$

where μ is the fluid viscosity. Using definition (8), the shear-stress at the cylinder surface for semisimilar solutions becomes

$$\sigma=\frac{2\mu}{a}[2\overline{k}f''(1)\cdot z+H'(1,\tau)] \tag{43}$$

Axial surface shear-stress for self-similar solutions is presented by the following form:

$$\sigma=\frac{2\mu}{a}\{2\overline{k}f''(1)\cdot z+b\ \text{Exp}(\alpha\tau)[(h_1'(1)\cos(\beta\tau)-h_2'(1)\sin(\beta\tau))+i(h_1'(1)\sin(\beta\tau)+h_2'(1)\cos(\beta\tau))]\} \tag{44}$$

The real and imaginary parts of the shear-stress at $z=0$ are indeed the same but with a phase difference of $\pi/2$. Thus, there is no need for presentation of both of these parts. Some numerical values of real component will be presented later for a few examples of axial velocities.

6 Heat Transfer Coefficient

The wall heat transfer coefficient and rate of heat transfer for defined wall temperature case are given by:

$$\begin{aligned}h=\frac{q_w}{T_w-T_\infty}&=\frac{-k\left(\dfrac{\partial T}{\partial r}\right)_{r=a}}{T_w-T_\infty}\\ &=-\frac{2k}{a}\Theta'(1,\tau)\quad\text{for semi-similar case}\\ &=-\frac{2k}{a}[\theta_1'(1)+i\theta_2'(1)]\quad\text{for self-similar case}\end{aligned} \tag{45}$$

$$q_w=-\frac{2k}{a}\Theta'(1,\tau)(T_w-T_\infty)\quad\text{for semi-similar case}$$

$$q_w=-\frac{2k}{a}c\ \text{Exp}(\gamma\tau)[\{\theta_1'(1)\cos(\delta\tau)-\theta_2'(1)\sin(\delta\tau)\}+i\{\theta_1'(1)\sin(\delta\tau)+\theta_2'(1)\cos(\delta\tau)\}]\quad\text{for self-similar case} \tag{46}$$

And for defined wall heat flux case:

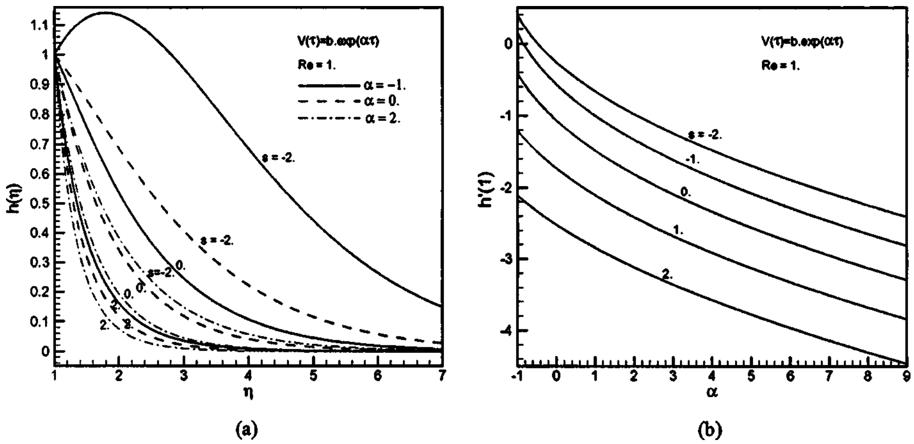

Fig. 2 Sample profiles of, (*a*) $h(\eta)$, (*b*) axial shear-stress parameter, for cylinder with accelerating and decelerating exponential axial velocity for selected values of suction and blowing rates

$$h=\frac{q_w}{T_w-T_\infty}=\frac{2k}{a}\frac{1}{\Theta(1,\tau)} \quad \text{for semi-similar case}$$

$$=\frac{2k}{a}\left(\frac{1}{\theta_1(1)+i\theta_2(1)}\right) \quad \text{for self-similar case} \tag{47}$$

$$(T_w-T_\infty)=\frac{a}{2k}\Theta(1,\tau)q_w \quad \text{for semi-similar}$$

$$(T_w-T_\infty)=\frac{a}{2k}c\,\mathrm{Exp}(\gamma\tau)[\{\theta_1(1)\cos(\delta\tau)-\theta_2(1)\sin(\delta\tau)\}+i\{\theta_1(1)\sin(\delta\tau)+\theta_2(1)\cos(\delta\tau)\}] \quad \text{for self-similar case} \tag{48}$$

From (45) and (47), it is seen clearly that for self-similar cases, the wall heat transfer coefficient is not a function of time contrary to the fact that wall temperature and wall heat flux are time-dependent.

7 Presentation of Results

In this section, the solution of the self-similar Eqs. (27) and (28) and the semi-similar Eqs. (10), (14), and (17) along with surface shear-stresses for different functions of axial velocity and prescribed values of surface temperature or surface heat flux, and selected values of suction and blowing rates are presented.

Sample profiles of the $h(\eta)$ function for $V(\tau)$ in accelerating and decelerating exponential form at Re=1. are presented in Fig. 2(*a*), for selected values of suction and blowing rates. It is interesting to note that as α increases, the depth of the diffusion of the fluid velocity field decreases. For $\alpha<0$, at any rate of suction and for the absolute value of α greater than a certain value, the fluid velocity in the vicinity of the cylinder cannot decrease with the same rate as the cylinder axial velocity and, therefore, in this region the fluid velocity is greater than the cylinder velocity. Note, $\alpha=0$ indicates the case of a moving cylinder with constant axial velocity, Ref. [7]. Further, it is seen that as the blowing rate decreases or when suction rate increases, the depth of the diffusion of the fluid velocity decreases and vice versa. Also it is evident from this Figure that the boundary layer becomes very small for high suction rates and the effect of α is negligible on the thickness of this layer. On the contrary, high rates of blowing thickens the boundary layer and in this case α has a strong effect on it. The axial shear-stress parameter on the surface of the cylinder for an exponential axial velocity in terms of accelerating rate at Re=1 displayed in Fig. 2(*b*) for different rates of suction and blowing show that with increasing value of α this parameter and the slope of the curves decrease. This means that the absolute value of

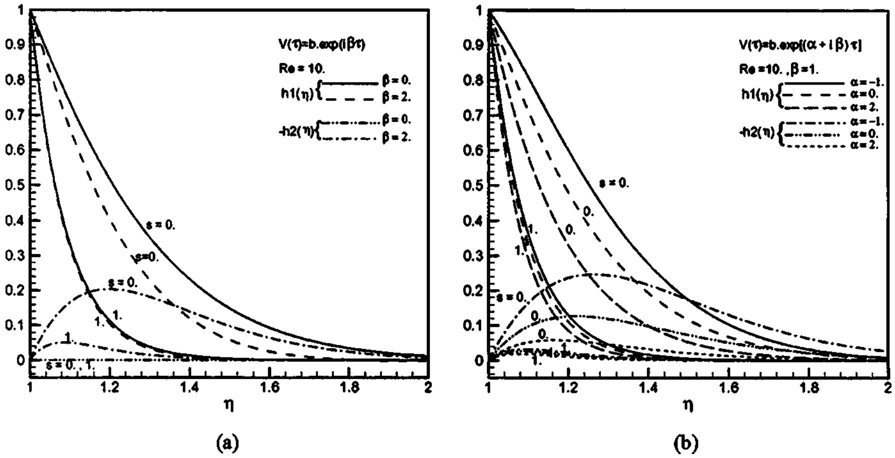

Fig. 3 Sample profiles of $h_1(\eta)$ and $h_2(\eta)$ for cylinder with (*a*) axial harmonic oscillation, (*b*) accelerating and decelerating oscillatory motion for selected values of α, β and suction rates

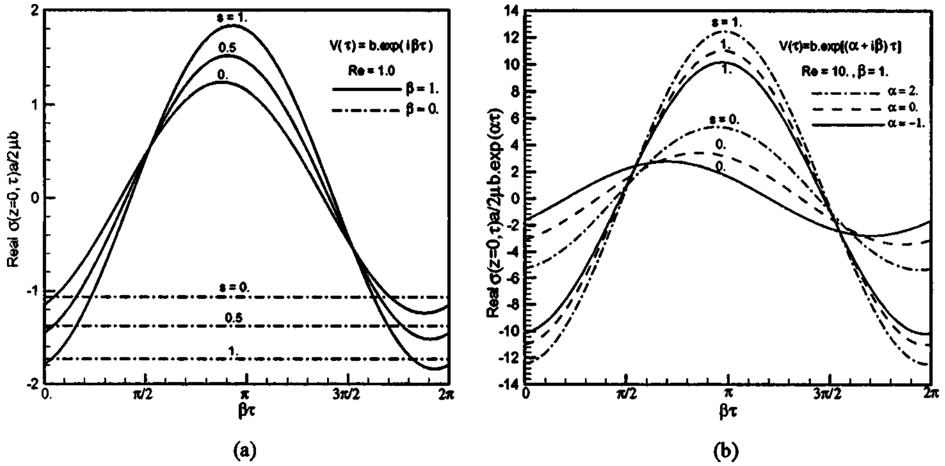

Fig. 4 Real part of axial shear-stress at $z=0$ for cylinder with (*a*) harmonic oscillation for $\beta=0$, 1, (*b*) accelerating and decelerating oscilllatory motion for $\alpha=-1$, 0, 2, and $\beta=1$, for selected values of suction rates

shear-stress increases with increasing α and its sensitivity decreases with respect to variations of α. Further, it is concluded that as suction rate increases, the absolute value of the axial shear-stress increases. The practical application of this result is that by providing blowing on the surface of a cylinder, reduction of resistance against its axial movement inside a fluid can be achieved. It is also interesting to note that at any Reynolds number and suction rate, there is a particular value of negative α for which the value of shear-stress is zero. This is to be expected since the movement of the cylinder in the fluid and the natural effect of decay of viscosity are happening in the same manner, then no shear is exerted on the cylinder by the fluid. This interesting result opens the way for an analysis into flows for which a cylinder moving with certain combination of Reynolds number, α, and suction rate is axially stress-free.

Sample profiles of the $h(\eta)$ function at Re=10 are given in Fig. 3(*a*), for pure harmonic motion of the cylinder with different frequencies and suction rates. The case of $\beta=0$ is the same as in Ref. [7] and clearly the imaginary part of $h(\eta)$ is zero. As in the foregoing discussion, we observe that the thinning of the diffusion of the velocity field with increasing values of both β and suction rate is evident. Samples of the $h(\eta)$ function for an accelerating and decelerating oscillatory motion are presented in Fig. 3(*b*), for selected values of α, β, and suction rates. Again, the rapid thinning of the diffusion of the fluid velocity is observed, but now with increasing values of α and suction strength. Further, it is seen from both Figs. 3(*a*) and 3(*b*) that with increasing rate of suction the effects of α and β fade away.

The real part of axial shear-stress at $z=0$ on the surface of the cylinder with pure harmonic and accelerating and decelerating oscillatory motion at Re=1 and 10 is displayed in Fig. 4, for selected values of α, β, and suction rate. This shear-stress is for a complete period between 0 and 2π. From Fig. 4(*a*), the maximum of the absolute value of the shear-stress increases with increasing values of both β and suction rates. Here, $\beta=0$ corresponds to the case of constant axial velocity, as in Ref. [7]. From Fig. 4(*b*), the maximum absolute value of the axial shear-stress increases when the value of α and suction rate increase. Further, $\alpha=0$ corresponds to the shear-stress of the pure oscillation case that was obtained by Gorla [9] by using perturbation methods and only for very high and very low frequencies. Also from these Figures, the shear-stress and the axial velocity, $V(\tau)$, have phase differences. Comparing Figs. 4(*a*) and 4(*b*), it is evident that the surface shear-stress increases with increasing values of Reynolds number.

Figure 5 presents the semisimilar solution for different forms of time-dependent axial velocity in which the function $H(\eta,\tau)$ is shown in terms of η and for different nondimensional time values and Reynolds numbers for zero suction. The process of obtaining

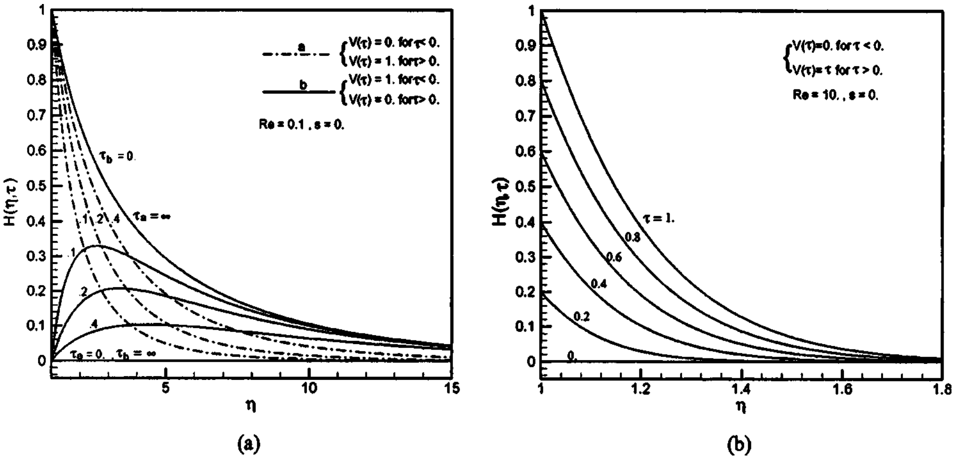

Fig. 5 Sample profiles of $H(\eta,\tau)$ for (*a*) step-function, (*b*) linear function, for selected values of time steps

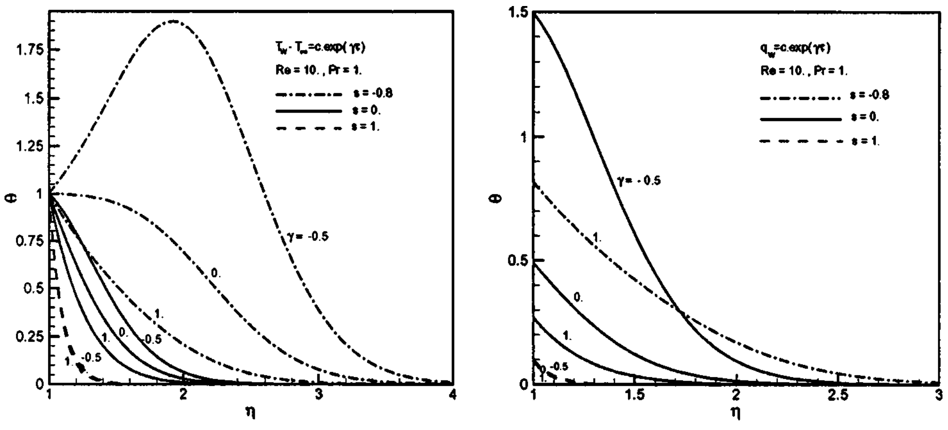

(a)

(b)

Fig. 6 Sample profiles of $\theta(\eta)$ for, (*a*) wall temperature, (*b*) wall heat flux, varying exponentialy with time, for Re=10, Pr=1, and s=0, 1, −0.8

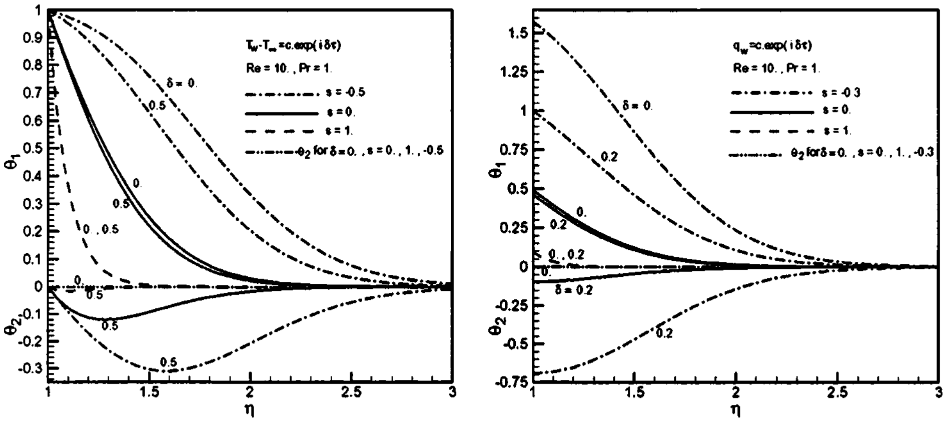

(a)

(b)

Fig. 7 Sample profiles of $\theta_1(\eta)$ and $\theta_2(\eta)$ for, (*a*) wall temperature, (*b*) wall heat flux, varying harmonically with time, for Re=10, Pr=1, and selected values of suction and blowing rates

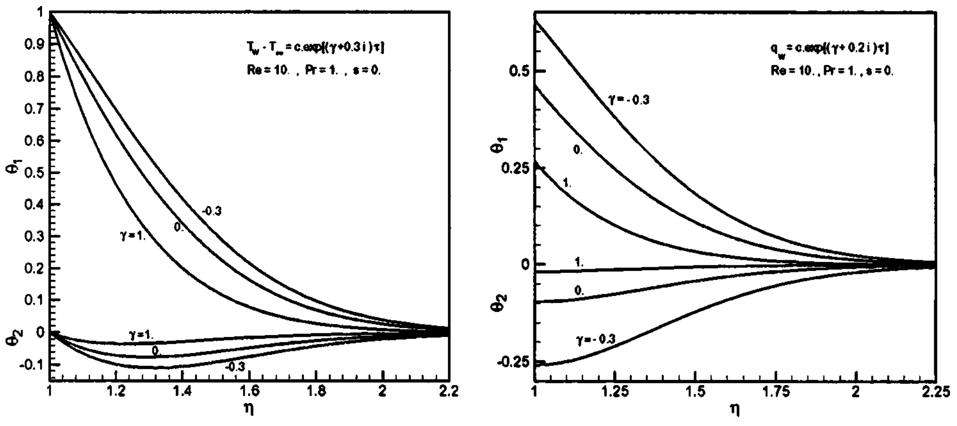

(a)

(b)

Fig. 8 Sample profiles of $\theta_1(\eta)$ and $\theta_2(\eta)$ for, (*a*) wall temperature, (*b*) wall heat flux, varying with accelerating and decelerating oscillatory function of time, for Pr=1, and Re=10, and *s* =0, and selected values of γ and δ

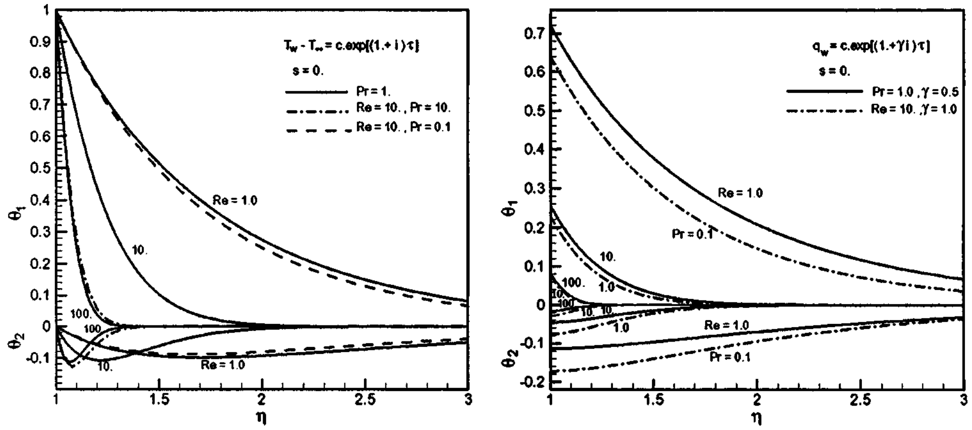

(a) (b)

Fig. 9 Sample profiles of $\theta_1(\eta)$ and $\theta_2(\eta)$ for, (a) wall temperature, (b) wall heat flux, varying with accelerating oscillatory function of time, for Re=1, 10, 100, and Pr=0.1, 1.0, 10, and $s=0$, and $\gamma=0.5$, 1 and $\delta=1$

these solutions is explained in Sec. 4. The solution of two step-functions is shown simultaneously in Fig. 5(*a*), in the first one the axial velocity of the cylinder at $t<0$ is equal to zero and at $t\geqslant 0$ its value becomes one suddenly. But in the second function the axial velocity of the cylinder at $t<0$ is one and at $t\geqslant 0$ becomes zero, suddenly. The interesting point in the solution of these two functions is that the solution starts from a steady state and when $t\rightarrow\infty$ it reaches the steady state again which is the solution of the other function at $t<0$. The ramp function is shown in Fig. 5(*b*) in which as time passes and along with increasing velocity, the thickness of the boundary layer increases.

Sample profiles of the $\theta(\eta)$ function for wall temperature and wall heat flux, both varying exponentially with time at Re=10 and Pr=1 are presented in Fig. 6, for selected values of γ and suction rate. From Fig. 6(*a*) it is seen that for $\gamma>0$ the absolute value of the initial slope of the temperature increases with increasing values of γ and suction rate, and considering Eq. (45), in fact the coefficient of heat transfer increases. Also, from Fig. 6(*b*), the temperature on the surface of the cylinder decreases with increasing values of γ and suction rate, and considering Eq. (47), in fact the coefficient of heat transfer increases. Further, as suction rate increases, the effect of variation of γ fades away. Therefore, it can be concluded that suction provides a means for cooling the surface, and blowing provides a means for heating the surface of the cylinder. This is rather obvious since in former case there is more contact of free stream fluid with the cylinder and in the latter case relatively less contact of free stream fluid with cylinder takes place. Note that in Fig. 6(*a*) for $\gamma<0$ and any particular value of suction rate, as the absolute value of γ increases beyond certain value, the fluid in the vicinity of the cylinder is not cooled as fast as the cylinder wall and, therefore, the flow temperature here is greater than the wall temperature. It is interesting to note that at any suction rate there is a certain value of negative γ for which the slope of the temperature on the surface becomes zero and therefore there is no heat transfer. This is to be expected since the natural diffusion of temperature difference in the fluid and the reduction of the temperature of the cylinder surface are happening in the same manner, then no heat is transferred between the fluid and the cylinder. From both of these figures and for $\gamma=0$, and zero suction, the results of Gorla [10] are obtained.

Sample profiles of the $\theta_1(\eta)$ and $\theta_2(\eta)$ functions for wall temperature and wall heat flux both varying harmonically with time at Re=10 and Pr=1 are given in Fig. 7, for selected values of δ and suction rate. It is noted in Fig. 7(*a*) that as the absolute value of oscillation frequency increases, the absolute values of the initial slope of $\theta_1(\eta)$ and $\theta_2(\eta)$ increase. Also increase of suction rate decreases the depth of the diffusion of temperature field rapidly, and the effect of δ fades away. From Fig. 7(*b*), the $\theta_1(\eta)$ and $-\theta_2(\eta)$ functions and their depth of diffusion decrease with increasing suction rate, also increase of oscillation frequency causes $\theta_1(\eta)$ and $\theta_2(\eta)$ to decrease. Note from Figs. 6(*b*) and 7(*b*) that high suction rate can be used to prevent high wall temperatures in case of high heat transfer. For $\delta=0$, the results in Ref. [10] are deduced from Figs. 7(*a*) and 7(b).

Sample profiles of the $\theta_1(\eta)$ and $\theta_2(\eta)$ functions for wall temperature and wall heat flux both varying with accelerating and decelerating oscillatory functions of time at Re=10 and Pr=1 is depicted in Fig. 8, for selected values of γ and δ and zero suction. In Fig. 8(*a*), the thinning of the depth of the diffusion and increase of the absolute value of the initial slope of the $\theta(\eta)$ function with increasing γ is evident. In Fig. 8(*b*), as γ increases, both real and imaginary parts of $\theta(\eta)$ and its depth of diffusion decrease in absolute value. With the role of increasing γ in both of these Figures and considering the Eqs. (45) and (47), it is found that the wall coefficient of heat transfer increases with increasing value of this parameter.

Sample profiles of the $\theta_1(\eta)$ and $\theta_2(\eta)$ functions for wall temperature and wall heat flux varying with accelerating oscillatory function of time are depicted in Fig. 9, for different values of Prandtl numbers, Reynolds numbers and zero suction. From Fig. 9(*a*), it is noted that as Prandtl number increases (Re=10, Pr=0.1, 1.0, 10) and Reynolds number increases (Pr=1, Re=1, 10, 100), the depth of diffusion of the temperature field decreases and the absolute value of the initial slope of temperature meaning wall coefficient of the heat transfer increases. In Fig. 9(*b*), as Prandtl number increases (Re=10, Pr=0.1, 1, 10) and Reynolds number increases (Pr=1, Re=1, 10, 100), both real and imaginary parts of the $\theta(\eta)$ function and its depth of diffusion decrease in absolute value and, therefore, considering Eq. (47), the wall coefficient of heat transfer increases. So in cooling processes, higher Prandtl number and Reynolds number fluids are preferred.

8 Conclusions

An exact solution of the Navier–Stokes equations and energy equation is obtained for the problem of stagnation-point flow on a circular cylinder with uniform normal transpiration rate. The formulation of the problem, though, is for the more general case of time-dependent transpiration rate. A general self-similar solution is obtained when the cylinder has different forms of time-dependent axial motions, wall temperature and wall heat flux including: constant axial velocity, exponential axial velocity, pure harmonic movement, and both accelerating and decelerating oscillatory motion. Also, some sample semisimilar solutions for the same problem have been presented when the circular cylinder is moving with different types of time-dependent axial velocity. Axial component of fluid velocity and surface axial shear stress on the cylinder are obtained in all the above situations, and for different values of the Reynolds numbers and transpiration rates. Absolute value of axial shear-stresses corresponding to all the cases increases with increase of the Reynolds number and suction rate. Also, the maximum value of shear-stress increases with increase of oscillation frequency and accelerating and decelerating parameter in the exponential amplitude function. In defined wall temperature case, heat transfer coefficient increases with the increase of Reynolds number, Prandtl number, oscillation frequency and suction rate, whereas the depth of the diffusion of temperature field decreases. In the case of defined wall heat flux, the wall nondimensional temperature, $\theta(1)$, and its depth of diffusion decreases and heat transfer coefficient increases with increase of the Reynolds number, Prandtl number, oscillation frequency and suction rate. So, increase of suction rate can be used as a means of cooling the surface and increase of blowing rate can be used as a means of heating the surface. It is shown that by providing blowing on the surface of a cylinder, reduction of resistance against its axial movement inside a fluid can be achieved. It is also shown that a cylinder moving axially in an exponential manner is axially stress-free for certain combinations of the Reynolds number, suction rate and rate of this exponential function. An interesting result is also obtained showing that a cylinder with certain type of exponential wall temperature exposed to a temperature difference has no heat transfer. The wall coefficient of heat transfer is found to be independent of time, though, the temperature field is time-dependent.

References

[1] Hiemenz, K., 1911, ‘‘Die Grenzchicht an einem in den gleichformingen Flussigkeitsstrom eingetauchten geraden Kreiszylinder,’’ Dinglers Polytechnic J., **326**, pp. 321–410.

[2] Homann, F. Z., 1936, ‘‘Der Einfluss grosser Zahighkeit bei der Strmung um den Zylinder und um die Kugel,’’ Z. Angew. Math. Mech., **16**, pp. 153–164.

[3] Howarth, L., 1951, ‘‘The Boundary Layer in Three-Dimensional Flow. Part II. The Flow Near a Stagnation Point,’’ Philos. Mag., **42**, pp. 1433–1440.

[4] Davey, A., 1951, ‘‘Boundary Layer Flow at a Saddle Point of Attachment,’’ J. Fluid Mech., **10**, pp. 593–610.

[5] Wang, C., 1974, ‘‘Axisymmetric Stagnation Flow on a Cylinder,’’ Q. Appl. Math., **32**, pp. 207–213.

[6] Gorla, R. S. R., 1977, ‘‘Unsteady Laminar Axisymmetric Stagnation Flow Over a Circular Cylinder,’’ Development in Mechanics, **9**, pp. 286–288.

[7] Gorla, R. S. R., 1978, ‘‘Nonsimilar Axisymmetric Stagnation Flow on a Moving Cylinder,’’ Int. J. Eng. Sci., **16**, pp. 392–400.

[8] Gorla, R. S. R., 1978, ‘‘Transient Response Behavior of an Axisymmetric Stagnation Flow on a Circular Cylinder Due to Time-Dependent Free Stream Velocity,’’ Lett. Appl. Eng. Sci., **16**, pp. 493–502.

[9] Gorla, R. S. R., 1979, ‘‘Unsteady Viscous Flow in the Vicinity of an Axisymmetric Stagnation-Point on a Cylinder,’’ Int. J. Eng. Sci., **17**, pp. 87–93.

[10] Gorla, R. S. R., 1976, ‘‘Heat Transfer in an Axisymmetric Stagnation Flow on a Cylinder,’’ Appl. Sci. Res., **32**, pp. 541–553.

[11] Cunning, G. M., Davis, A. M. J., and Weidman, P. D., 1998, ‘‘Radial Stagnation Flow on a Rotating Cylinder With Uniform Transpiration,’’ J. Eng. Math., **33**, pp. 113–128.

[12] Takhar, H. S., Chamkha, A. J., and Nath, G., 1999, ‘‘Unsteady Axisymmetric Stagnation-Point Flow of a Viscous Fluid on a Cylinder,’’ Int. J. Eng. Sci., **37**, pp. 1943–1957.

[13] Press, W. H., Flannery, B. P., Teukolsky, S. A., and Vetterling, W. T., 1997, *Numerical Recipes*, *The Art of Scientific Computing*, Cambridge University Press, Cambridge.

An Active Flap Deployment System for Blade–Disturbance Interaction Alleviation

Carter T. Nelson*

Othon K. Rediniotis†

Department of Aerospace Engineering, Texas
A&M University, College Station, TX
77843-3141

A new, actively deployable trailing edge flap system is introduced and an experimental investigation is undertaken to determine its effects on the disturbances created during blade–disturbance interactions (BDI), with blade–vortex interaction (BVI) alleviation being the ultimate objective. Experimental tests were conducted using a two-dimensional (2D) wind tunnel setup incorporating a pressure instrumented airfoil section with a deployable 20% trailing edge flap and an upstream vortex generator to produce the disturbance. Results of this study showed that the disturbances, caused by BDI events, to the pressure distribution over the airfoil occur mostly at the leading edge. Carefully synchronized deployment of the trailing edge flap during BDI events resulted in a reduction of this pressure disturbance. The aeroelastic response of the active flap was modeled via unsteady linear theory and the model was validated experimentally. The aeroelastic model shows good agreement with experimental results, which supports its use as a preliminary design tool for the actuation parameters of the active flap system.

[DOI: 10.1115/1.1839928]

Introduction

There are numerous sources of noise associated with rotorcraft. However, the two most dominant of these sources are: (a) Due to transonic effects, which produce high speed impulsive (HSI) noise, and (b) due to blade–vortex interactions (BVI) [1]. Blade–vortex interaction noise typically occurs at slower flight speeds when the rotorcraft is maneuvering or performing a landing. Since this later often occurs in highly populated areas, it has become a source of annoyance to the general public. Further, reducing the noise levels produced during maneuvering has military significance in minimizing rotorcraft detectability.

A well-known common feature of finite length lifting surfaces is the formation of a tip vortex. In most aircraft configurations, this vortex trails off into the wake and there is little interaction with the aircraft. However, due to the geometry of rotor blades, there is the potential for significant interaction between the wake produced by one rotor blade and a rotor blade that subsequently passes through it. Moreover, multiple interactions are possible as a particular blade rotates through the entire azimuthal range. Further, interactions occur on both the advancing and retreating sides of the rotor disk and their corresponding aerodynamic natures are inherently different.

The effective angle at which a particular vortex filament interacts with a rotor blade varies greatly with radial distance and azimuthal angle, but two limiting cases exist as shown in Fig. 1. In the first, the vortex filament is perpendicular to the leading edge of the rotor blade, and the overall nature of the flow is three-dimensional and steady. The second case is for parallel interaction, in which case the flow is two-dimensional and unsteady. In terms of the intensity of noise produced by these interactions, the parallel interaction is more severe [2]. It is for this reason that the parallel interaction has received the most attention in the field of BVI research and it is this limiting case which is studied in this work.

Numerous studies have been carried out to examine the BVI phenomena both analytically and experimentally. Probably one of the earliest attempts to compute BVI noise is that of Widnall [2] and Widnall and Martinez [3]. In this approach, Fourier transforms were used to represent the vortex-induced velocity field as a series of sinusoidal gusts. The formulation derived was able to predict the far field noise generated and compared reasonably well with experimental results.

Hardin and his associates have modeled the two-dimensional BVI event using potential flow, incompressible Navier–Stokes, and Euler codes [4–6]. The results from these computations were more or less synthesized in a later report [7], in which a formulation was derived to provide an estimate for the sound generated by a 2D BVI event. From an examination of this formula, various concepts for reducing noise were proposed, including reducing incoming vortex strength, reducing blade lift, reducing interaction length, and increasing miss distance. Lee [8] numerically examined the effects that a porous leading edge has on the reduction of noise and showed some potential for noise reduction, although the results were purely analytical and the concept was not experimentally tested.

A numerical study of the effects of leading and trailing edge flaps was carried out by Hassan et al. [9] using a 2D full potential code. Although the study did not include viscous effects such as formation of secondary vortices, which may occur during a parallel BVI event, the results indicate that for a subcritical case, a trailing edge flap alone is adequate in attenuating noise. However, for supercritical cases, it becomes necessary to use a leading edge flap as well. Criticality here refers to the presence of supersonic flow over the airfoil. In this latter case, the trailing edge flap becomes less effective due to the presence of upper and lower surface regions of supercritical flow which reduce the trailing edge flap's ability to alter the leading-edge pressure fluctuations.

Numerous experimental tests have also been conducted to examine both the general aerodynamics of the 2D and three-dimensional (3D) BVI phenomena, as well as the effectiveness of various means of noise reduction. Experiments on actual rotating vmodels (3D) have been performed by Lorber [10,11], Splettstoesser et al. [12], and Martin et al. [13]. These tests demonstrated that the most dominant source regions of noise are at the azimuth angles corresponding to parallel BVI interactions, with those occurring on the advancing side to be the worst.

Static 2D experiments have also been conducted to examine

---

*Graduate Research Assistant, currently with the Boeing Company.

†Associate Professor.

Contributed by the Fluids Engineering Division for publication in the JOURNAL OF FLUIDS ENGINEERING. Manuscript received by the Fluids Engineering Division June 2, 2003; revised manuscript received March 29, 2004. Associate Editor: Hamid Johari.

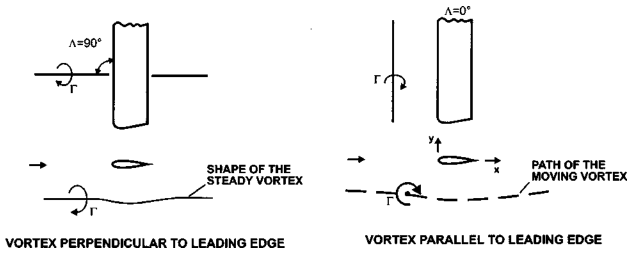

Fig. 1 The two limiting cases of blade–vortex interaction

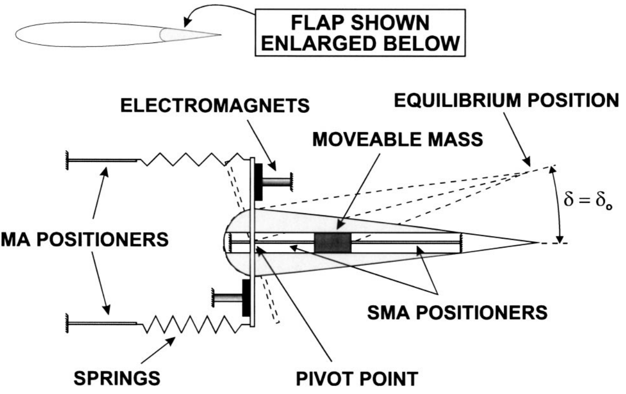

Fig. 2 Schematic of the Active Flap Deployment System concept

more closely the effect of the BVI event on the pressure distribution over the blade. Low speed (i.e., subsonic, incompressible) experiments have been carried out by Booth [14,15], Booth and Yu [16], Straus et al. [17], and Seath et al. [18]. These experiments have demonstrated that the perturbations in the pressure distribution over the airfoil due to BVI mainly occur at the leading edge. High speed, transonic experiments were also conducted by Lee and Bershader [19] and Kalkhoran et al. [20]. The results again illustrate the leading edge nature of the BVI disturbance.

Various BVI noise attenuation concepts have also been experimentally tested. In an attempt to reduce the strength of the interacting vortex, various wing tip devices were examined by Smith and Sigl [21]. While there was some vortex attenuation seen for several of the tips, due to the passive nature of the devices, they performed poorly at off-design conditions. A Higher Harmonic Control (HHC) approach, which pitched the entire rotor blade at a specific azimuthal angle, was examined by Brooks et al. [22]. Some noise reduction was observed; however, the HHC system was heavy and complicated. Although theoretically HHC or related IBC (individual blade control) systems can be set for arbitrary flight conditions by varying frequency content, amplitude and phase, HHC has limitations on frequency content, since it relies on fixed-frame actuation. Dawson and Straub [23] used a cam-driven, impulsively moved flap to reduce BVI on a model rotor. A trailing edge flap concept was tested by Marcolini et al. [24] and Simonich et al. [25], and demonstrated the potential of a TEF in reducing noise. The present work is motivated partially by the potential of a TEF to reduce BDI and ultimately BVI noise and partially by its potential to reduce impulsive blade–wing loads during blade–wing-disturbance interactions. A new TEF concept is introduced with potential for higher efficiency, compactness and versatility than previously introduced systems and its effectiveness in pressure impulse reduction during BVI and BDI is demonstrated. It should be noted that, as just mentioned, we are examining the potential of a TEF to reduce the impulsive pressure spikes on the blade surface during BVI and BDI. Reduction of these pressure signatures is assumed to lead to noise reduction. Although this is a reasonable conjecture, noise reduction is not rigorously demonstrated here. Moreover, the introduction of a new noise source associated with the TEF itself should be noted, that could reduce the effectiveness of the TEF in overall noise reduction. More details on the present work can be found in Ref. [26].

The Active Flap Deployment System

In simple terms, the principle of operation of the trailing edge flap relies on the fact that the unsteady deployment of the flap produces an unsteady pressure distribution that counteracts the pressure fluctuations produced by the BDI. In addition to examining the aerodynamic potential of a trailing-edge flap in reducing blade–disturbance and blade–vortex interaction, a second issue must also be addressed: How will the flap be deployed? Due to issues related to weight, center of gravity location, frequency response, reliability, practical transfer of hydraulic fluid to the blade, and to a lesser degree extremely confining space inside a typical helicopter rotor blade as well as the high *g*-loadings, most conventional means of actuation, such as hydraulics, can not be readily employed. It is for this reason that some nonconventional means of actuation have appeared in the literature. A common theme in these proposals is the incorporation of different types of induced-strain actuators based on such materials as piezoelectrics, shape-memory alloys (SMA), magnetostrictive solids, and magnetorheological fluids, with piezoelectrics and SMAs being the most popular. A piezoelectric, bimorph-based actuator was implemented by Walz and Chopra [27] and tested in nonrotating experiments. While flap deflection angles of up to 16° were reported, the relatively weak loads provided by the piezoelectric material was a major drawback in this approach. Shape memory alloys have the potential of providing much more usable actuation force compared to piezoelectrics, but are limited in frequency response. Current maximum SMA frequency responses are on the order of 5 Hz, which falls short of the deployment response needed for the TEF which would be on the order of the rotor blade rotation rate, and is generally significantly higher. Further, if SMA were employed as direct actuators, their useful life would be shortened by the high usage demand placed on them.

In order to overcome the frequency response problem and prolong the SMA life span, a flap actuation system was conceived that combined conventional actuation with SMA-based actuator parameter tuning. The concept has been called the Active Flap Deployment System (AFDS) and is conceptually illustrated in Fig. 2. The actual driving force for actuation is a set of springs, which are unevenly pre-tensioned such that the equilibrium position of the flap is at some deflected angle δ_o. The flap is held at its undeflected position by electromagnets until an actuation is desired. A deployment is carried out by first turning off the electromagnets. When this occurs, the flap will begin an oscillatory motion about the equilibrium position. By quickly re-energizing the electromagnets when the flap has completed one oscillation, the flap is again held at the undeflected position. In Fig. 3, the free response of the AFDS is shown (not numerical, but actual experimental results) for a case when the electromagnets are turned off but not re-energized. As can be seen, the flap exhibits a damped oscillation about an equilibrium angle of about 8°. Also shown is a typical deployment case for which the electromagnets are used to capture the flap and hold it at the undeflected position. The later constitutes what would be a single deployment of the AFDS.

The AFDS is basically a mass-spring-damper system with a forcing function resulting from the aerodynamic moment on the flap. The differential equation of motion is:

$$I_\delta\ddot{\delta}+C_\delta\dot{\delta}+K_\delta\delta=M \tag{1}$$

where I_δ is the flap mass moment of inertia about the pivot axis, C_δ is the damping coefficient, K_δ is the torsional stiffness, and M is the aerodynamic moment. The flap angle δ is defined as positive for upward trailing edge deflection and the dots represent differentiation with respect to time. Thus, in order to achieve different

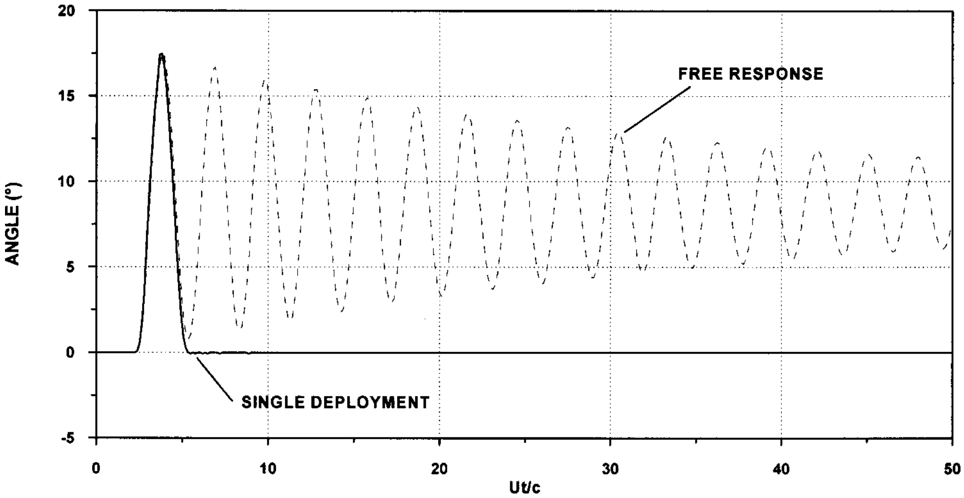

Fig. 3 Free response of the AFDS system and a single deployment

deployment schedules, the various parameters in the equation of motion can be modified. The mass moment of inertia can be altered by incorporating a moving mass into the trailing edge flap. By using SMA positioners to change the distance of this mass from the flap pivot point, different values of I_δ can be achieved. The torsional spring constant can be changed by either varying the moment arm of the springs, or, in an actual in-blade implementation of the system as discussed later, by using nonlinear springs or SMA springs. These modifications can be made to tune the performance of the system for changing flight conditions. Further, the frequency of the modifications would be much less than the rotational frequency of the rotor blade. Since the SMAs do not directly actuate the flap, but are only used to tune the response of the system, their limited frequency response is overcome and their useful life is extended.

The AFDS version illustrated in Fig. 2 represents the experimental setup used in this work and is obviously not compact enough to fit inside a blade. However, reconfiguring it into an in-blade system can be achieved via good design, and is not a matter of operation principle. To illustrate this point we offer a possible system configuration such that it can be accommodated inside a blade. The two schematics of Fig. 4 illustrate ways of accommodating all means of parameter variation (stiffness, moment of inertia and amplitude of oscillation) inside the blade–flap. The electromagnet/lever arm assembly was omitted in the second schematic to avoid clutter. The torsional spring could be nonlinear, which, combined with the linear SMA actuator, can result in variation of the torsional stiffness. In the last sentence, "linear" refers to the mode of actuation (versus, for example, "torsional" SMA actuator), and not the SMA thermomechanical behavior, which is hysteretic and nonlinear. Another design would be to fabricate the spring out of SMA (SMA springs are even readily available in the market). By varying the martensitic volume fraction of the spring (for example through electrical heating of the SMA) the stiffness can be varied all the way from that corresponding to 100% martensite (material stiffness as low as 20 GPa) to that corresponding to 100% austenite (material stiffness as high as 80 GPa); a factor of 4.

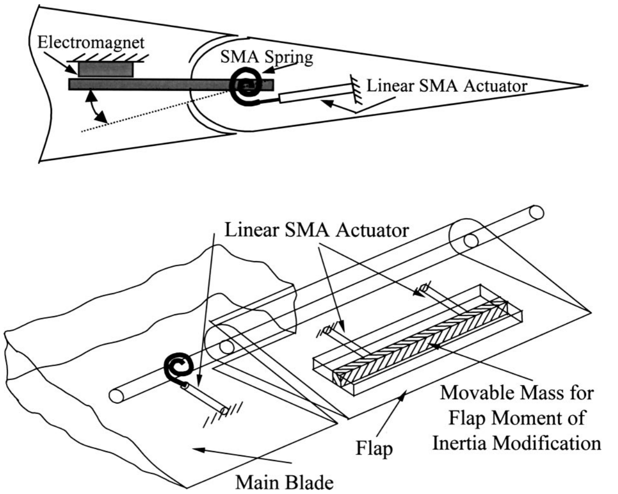

Fig. 4 Schematics illustrate ways of accommodating all means of parameter variation (stiffness, moment of inertia, and amplitude of oscillation) inside the blade–flap

The linear SMA actuators–positioners can be made extremely compact, with power densities (output power per unit volume) significantly exceeding known existing actuators, by two orders of magnitude in some cases. The high energy density, high transformation stress and strain of SMAs result in high actuator compactness, force and stroke, respectively. Electrical heating and convection cooling of the SMAs, in turn, results in actuation frequencies significantly higher than what SMAs have traditionally been thought to be capable of (we have achieved actuation frequencies as high as 20 Hz [28,29]). However, for the specific application discussed in this work, only low actuation frequencies are necessary (an order of magnitude smaller than 1 Hz). Electrical power will have to be routed from the fuselage to the blade through hub sliprings. Another alternative has recently been developed [30], in which the chemical energy of fuel is used for the heating of the SMA and could potentially result in a stand-alone actuator that could be totally embedded in the blade (including the power source). Detailed discussions of SMA actuation issues, such as SMA actuation curves, heating and cooling times of the SMA, SMA fatigue life and actuator-load (fluid dynamics loading) interaction can be found in some of our SMA related work [28–32].

A significant benefit of the AFDS, compared to other flap actuation means is explained below. Consider a different actuation system for the flap, for example, a stepper motor that drives the flap with the specified schedule $\delta(t)$. First, one needs to determine what is the optimal $\delta(t)$ schedule that has the most effect in reducing BDI–BVI. Once the schedule is determined it becomes the input to the flap actuator controller. The objective of the controller is to properly command the actuator so that the flap executes the specified schedule $\delta(t)$. In the case of the stepper motor actuation system, there is no "aeroelastic problem." The controller commands the flap to perform exactly the schedule, and

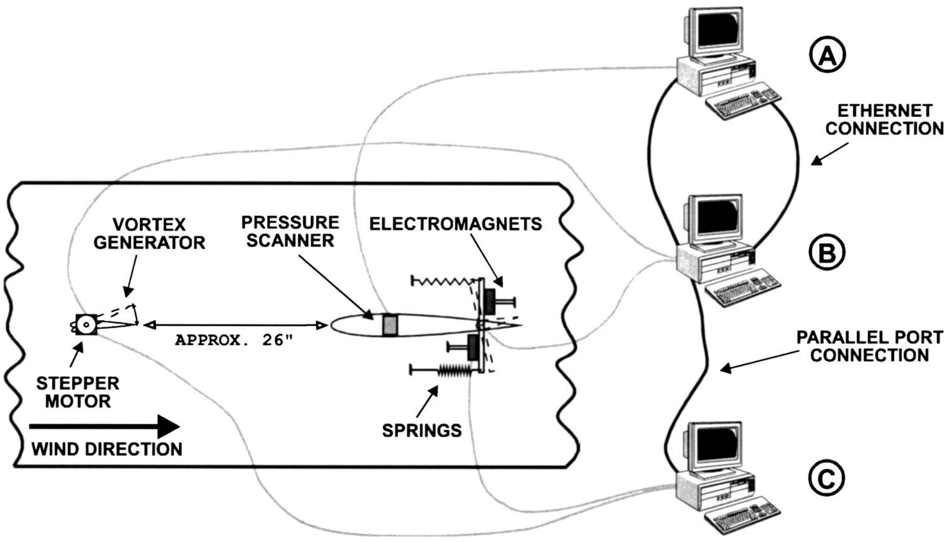

Fig. 5 Schematic of wind tunnel experiment test section setup

the flap and its motion is not "allowed" to respond to its aerodynamic loading. The system has no dynamics and no aeroelasticity (assuming the flap itself is stiff) and is certainly simpler that the AFDS presented in the manuscript. However, such a stepper motor actuation system is "oblivious" to the dynamics and aerodynamics (loading) of the flap and rather than taking advantage of its dynamics–aerodynamics, it uses brute force to command the flap to the desired angle. One of the penalties this system pays is that, exactly because it does not take advantage of the flap dynamics–aerodynamics, it spends more energy than necessary and is thus inefficient. On the other hand, the AFDS considers the flap dynamics and aerodynamics and takes advantage of them. The penalty for that is that it is more complex and introduces an aeroelastic problem that has to be solved in order to determine the AFDS parameters, such as the system's stifnesses, mass moments of inertia, etc., in order to achieve the prescribed flap schedule $\delta(t)$. This is what the aeroelastic model described later does. Also, the model uses insight, especially into the nature of Wagner's function $\phi_w(s)$, to perform an "order reduction" or an approximation of engineering value of the original, computationally intensive aeroelastic model, with only a small sacrifice in model accuracy (code B). It should be noted that the model discussed here will ultimately have to take into account issues that arise in high Ma numbers and are not considered here, such as flutter and shock wave effects over the blade.

Experimental Facilities and Instrumentation

In order to study the aerodynamics of the two-dimensional blade–disturbance interaction, a nonrotating experiment was constructed in the Texas A&M University Low Turbulence Wind Tunnel. This facility is an open circuit wind tunnel with a test section of 0.46 m×0.46 m and a contraction ratio of 20:1. The tests were conducted at wind tunnel velocities ranging from 13 to 26 m/s, which resulted in a Reynolds number range from 0.25×10^6 to 0.5×10^6 based on the chord of the main airfoil. A blockage correction factor was calculated from the method outlined in Rae and Pope [33]. The freestream velocity measured by the pitot tube was corrected to account for the flow acceleration due to the airfoil blockage.

The layout of the experimental setup is shown in Fig. 5. A NACA 0012 airfoil section with a chord of $1'$ was used to model a section of a rotor blade. Housed within the airfoil was a Pressure Systems ESP-32 electronic pressure scanner. This pressure scanner has 32 differential pressure ports with a range of $+/-20$ in. H_2O (approximately $+/-5$ kPa). It was placed within the airfoil section in order to minimize the tubing lengths running to the airfoil surface and thus reduce any pressure lag and attenuation errors in the system. For the tubing length and diameter used here, and the measurement bandwidth of interest, these effects were found to be negligible, based on the work in Ref. [34]. The freestream static pressure was taken as the reference for all the pressure ports. The chordwise locations of the pressure ports are shown in Fig. 6. Integrated with the airfoil was a 20% chord trailing edge flap. Due to the confining space and rotating nature of the flap, it was not pressure instrumented.

A second NACA 0012 airfoil with a chord of 0.1 m was located upstream of the main airfoil and was attached to a stepper motor. This airfoil was used as a vortex generator to produce a simulated vortex which would convect downstream and interact with the main airfoil. Vortex generation by this airfoil was achieved by rapid deployment with the stepper motor. Additionally, the vertical position of the entire vortex generating assembly could be varied from approximately 0.038 m below to 0.038 m above the leading edge of the main airfoil, thus allowing for different miss distances to be examined.

US Digital E2 Series Quick Assembly optical encoders were attached to the trailing edge flap and the vortex generator to provide time histories of their angular deflections. These optical encoders were of the incremental type with 1024 pulses per revolution. Utilizing quadrature we increased the resolution to 4096 pulses per revolution, which, combined with the data-acquisition system discussed later, resulted in an angular resolution and accuracy of 0.088°.

Control and data collection of the wind tunnel setup was carried

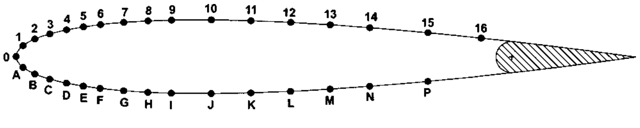

PORT	x/c	PORT	x/c
0	0.0	9/I	0.250
1/A	0.011	10/J	0.314
2/B	0.030	11/K	0.378
3/C	0.054	12/L	0.442
4/D	0.081	13/M	0.506
5/E	0.108	14/N	0.570
6/F	0.135	15/P	0.664
7/G	0.173	16	0.750

Fig. 6 Surface pressure port locations

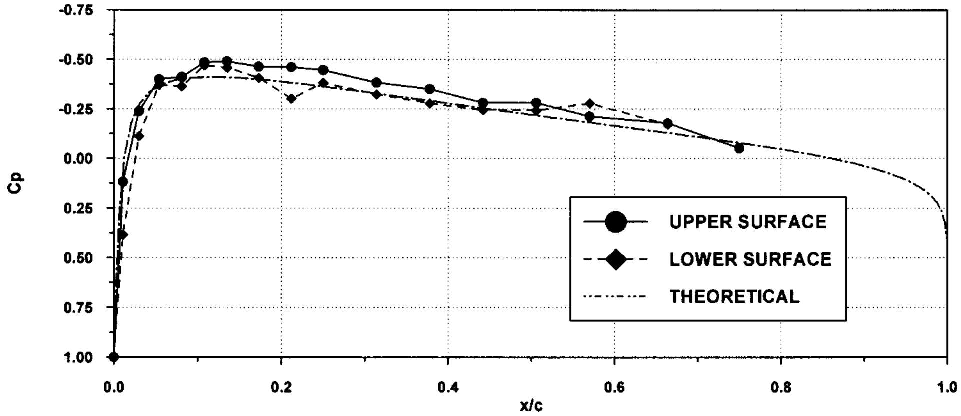

Fig. 7 Pressure distribution of experimental setup with no TEF or vortex generator deployment

out using three computers as shown in Fig. 5. Computer A contained a Computer Boards DIO-DAS08 Analog-to-Digital board interfaced to the ESP-32 pressure scanner and was used to acquire the surface pressure data on the main airfoil. The A/D board had 12-bit resolution. The pressure scanner used was calibrated during data-acquisition, every one hour. A five-point calibration was performed which accounted for transducer nonlinearities. The reference manometer used for calibration had an uncertainty of 0.005 Torr for the range of pressures used here. This combined with a one-count A/D conversion uncertainty of the 12-bit A/D board, yielded a pressure measurement "worst case" error of 0.03 Torr or 4 Pa. For the minimum and maximum freestream velocities tested in this work ($U=13$ m/s and $U=22.6$ m/s, respectively), this corresponds to a "worst case" error in the calculation of the pressure coefficients of 0.04 and 0.013, respectively. On board counters–timers were used to pace the data acquisition rate, which was set to 500 scans/s. Each scan sampled all 32 pressure ports, which was done at the fastest possible ESP sampling rate, i.e., 20 kHz.

Computer B was used to read the optical encoders. This was done by utilizing two LS7166 encoder-to-microprocessor interface chips obtained from US Digital. These chips contain 24-bit up–down counters, which continually keep track of the optical encoder outputs. By using a Computer Boards CIO-DIO24H Digital Input-Output board, the LS7166 chips were programmed and read by Computer B to provide the angle histories of the trailing-edge flap and the vortex generator motion.

Computer C was used to deploy both the trailing edge flap and the vortex generator. Trailing edge flap deployments consisted of rapidly switching the electromagnets off and then back on. This was done by routing the power supply to the electromagnets through a relay switch, which could be controlled by the parallel port of Computer C. The vortex generator deployments were controlled by interfacing the serial port to a Velmex NF90 stepper motor controller. This piece of hardware allowed for direct control of the stepper motor, which drove the vortex generator, thus allowing for a variety of deployment schedules to be programmed.

Synchronization of all three computers was carried out through their parallel ports. During a typical data acquisition run, Computers B and C were placed in a holding state, waiting for a trigger signal from Computer A. When Computer A gave the trigger signal, it instantly started acquiring data from the pressure scanner. "Instantly" here means within a few microseconds, since such a time delay is at least two orders of magnitude smaller than the time scales of interest here (order of milliseconds). When Computer B received the trigger signal, it instantly started acquiring data from the optical encoders. When Computer C received the trigger signal, it carried out the deployments of the vortex generator and trailing edge flap.

Evaluation of the construction quality of the main airfoil section was done by measuring the surface pressure for the simple case of zero trailing-edge flap angle and no vortex generator deployment. The resulting pressure distribution should be that for a NACA 0012 at zero angle of attack, for which the actual pressure distribution is well known as given in Abbott and Von Doenhoff [35] or can be easily computed by a number of methods. The resulting distribution is shown in Fig. 7 and shows that the experimental data is in relatively good agreement with the expected results. If one considers the pressure measurement uncertainty discussion above, one can conclude that the variations that do exist are attributed to flaws in the construction of the airfoil section.

Aeroelastic Response of the Flap Using Unsteady Linear Theory

It should be clarified that the objective of this section is not to address the question: "How are the optimum flap deployment schedules determined?" This is an extensive optimization problem and beyond the scope of the present work. However, even after the optimal deployment schedules are determined, the AFDS parameters will need to be determined in order to achieve these deployment schedules, which is what the present theory–formulation addresses. The fact that, in the experimental part of the present work, the optimal flap deployment schedules for pressure impulse alleviation were determined heuristically was due to the fact that the experiments predated the development of the aeroelastic model.

The formulation is presented here for the case of an airfoil with one degree of freedom (pitch) in a uniform freestream. The formulation is directly applicable to a flap, within the assumptions of linear theory. The flap response is theoretically modeled in the context of linear unsteady aerodynamic theory based on indicial function concepts [36]. The formulation assumes that the problem is governed by the linearized partial differential equations and linearized boundary conditions.

Figure 8 defines the kinematic and dynamic quantities involved in the analysis. The location of the pivot point has been assumed general. The airfoil pitch angle $\delta(t)$ is governed by the equation

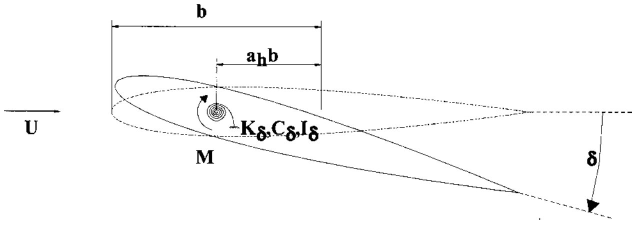

Fig. 8 Parameter definition for the unsteady flap response formulation

of motion of the airfoil, i.e., Eq. (1). The aerodynamic moment $M(t)$, or equivalently $M(s)$, where s is nondimensional time defined as $s=Ut/b$ (where $b=c/2$ is half of the airfoil chordlength), is derived from linearized unsteady theory, for arbitrary flap motion, by means of Duhamel's superposition integral and the Wagner indicial response $\phi_w(s)$:

$$\begin{aligned} M(s)=&\left(\frac{1}{2}+a_h\right)2\pi\rho b^2U^2\int_{-\infty}^{s}\phi_w(s-\sigma)\left[\delta'(\sigma)+\left(\frac{1}{2}\right.\right. \\ &\left.\left.-a_h\right)\delta''(\sigma)\right]d\sigma-a_h^2\pi\rho b^2U^2\delta'(s)-\left(\frac{1}{2}\right. \\ &\left.-a_h\right)\pi\rho b^2U^2\delta'(s)-\frac{\pi\rho b^2U^2}{8}\delta''(s) \end{aligned} \tag{2}$$

where the terms in the second line are the noncirculatory components accounting for fluid "apparent mass" effects. The circulatory terms involve the Wagner function $\phi_w(s)$, which gives the growth of circulation about the airfoil due to a sudden increase of downwash. The exact form of $\phi_w(s)$ is:

$$\begin{aligned} \phi_w(s)=1-\int_0^{\infty}&\{(K_0(\tau)-K_1(\tau))^2+\pi^2(I_0(\tau) \\ &+I_1(\tau))^2\}^{-1}e^{-\tau s}\tau^{-2}d\tau \end{aligned} \tag{3}$$

where $K_0(\tau)$, $K_1(\tau)$; $I_0(\tau)$, $I_1(\tau)$ are modified Bessel functions of the first and the second kind, respectively. Since the exact form of Wagner's function involves Bessel functions, it is tedious to implement. Much simpler estimates to Wagner's function have been developed and these are often used in place of the exact equation. Several of these estimates, as well as the exact form, can be found in Fung [36], from which the following is taken and is accurate to within 2%:

$$\phi_w(s)=1-A_1\exp(-b_1s)-A_2\exp(-b_2s) \tag{4}$$

where A_1, A_2, b_1, b_2 are constants [36]. $A_1=0.165$, $A_2=0.335$, $b_1=0.0455$, $b_2=0.3$.

The first approach taken to model the transient response of the flap system was derived from that used by Lee and Desrochers [37]. This approach uses Houbolt's finite difference scheme [38] to provide estimates for the first and second derivatives as a function of previous values of the primary function. Also, by using the three-term approximation for Wagner's function given above, a recursion formula can be derived for the convolution integral in Eq. (2). Incorporating these numerical techniques, the equations become algebraic and can be solved at discrete time steps thus providing a time marching solution for the response of the system. This approach is referred to as CODE A.

In a different approach and in order to gain insight into the relative significance of the terms (circulatory and noncirculatory) that comprise the aerodynamic moment M, $\phi_w(s)$ was approximated with a constant $\phi_w(s)=\Phi=\text{const}$, $0.5<\Phi<1.0$. It should be noted that $\phi_w(s)$ varies between about 0.5 for $s=0$ to 1 for $s\rightarrow\infty$. The convolution integral in Eq. (2) can then be analytically evaluated and Eq. (1) reduces to that of a simple mass-spring-damper free-oscillation system:

$$I_{\text{mod}}\ddot{\delta}+C_{\text{mod}}\dot{\delta}+K_{\text{mod}}\delta=0 \tag{5}$$

where:

$$I_{\text{mod}}=I_\delta+\left(\frac{1}{8}+a_h^2\right)\pi\rho b^4$$

$$C_{\text{mod}}=C_\delta-\left(\frac{1}{4}-a_h^2\right)2\pi\rho b^3U\Phi+\left(\frac{1}{2}-a_h\right)\pi\rho b^3U$$

$$K_{\text{mod}}=K_\delta-\left(\frac{1}{2}+a_h\right)2\pi\rho b^2U\Phi$$

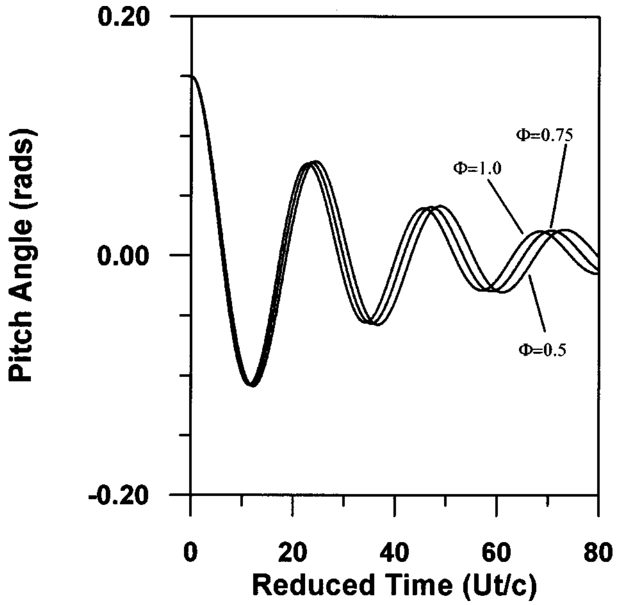

Fig. 9 Comparison of CODE B results for different values of Φ

A closed form solution for Eq. (5) is easily derived and the transient response can be readily determined. This approach is referred to as CODE B.

The effect of the choice for the values of the constant Φ in CODE B is shown in Fig. 9. Within the first period, it can be seen that the responses never vary by more than 10%, for the entire range of possible Φ's. The curves slowly diverge which can be attributed to the accumulated error differences resulting from the constant Φ approximation. However, as it was discussed in the "Active Flap Deployment System" section and will be experimentally demonstrated in the subsequent sections, the flap of the AFDS only performs a single oscillation. At the end of the first oscillation it is held by the electromagnets at its undeflected position. Therefore our prediction interest is focusing on the first oscillation only, and thus this divergence, observed in Fig. 9 at later oscillations, is of little predictive significance. It is noted here that within a single blade revolution many BVI–BDI events could take place, therefore, several such single flap oscillation deployments may be required.

Comparison of the predicted responses from the two modeling approaches (CODE A and CODE B) is shown in Fig. 10. This figure shows that there is a relatively small difference between the two codes (worst case discrepancy during the first oscillation does not exceed 10%). It should also be noted that only the first period of the response is of interest for application to the AFDS. Therefore, the growing disagreement of the two codes is of little concern here.

Comparison of the two codes to experimental data taken from the flutter apparatus described in Ref. [39] is show in Fig. 11. The experimental parameters were: Inertia $I=0.046\,\text{kgr-m}^2$, spring constant $K=6.86\,\text{N-m/rad}$, damping $C=0.036\,\text{kg-m}^2/\text{s}$. In the first period of the response (which is of interest here) the maximum discrepancy is 15%. Thus, once the optimum deployment schedules of the trailing edge flap for BDI or BVI reduction have been determined, these codes (modified to account for compressibility effects) can provide a reasonably accurate tool by which the system parameters for the AFDS can be designed.

Results From the Distrurbance Alleviation Experiments

A typical time history of the vortex generator deployment is shown in Fig. 12. Baseline noise is the result of generating a holding torque by having the stepper motor continuously cycle through ±1° steps around the zero-deflection position. This is also

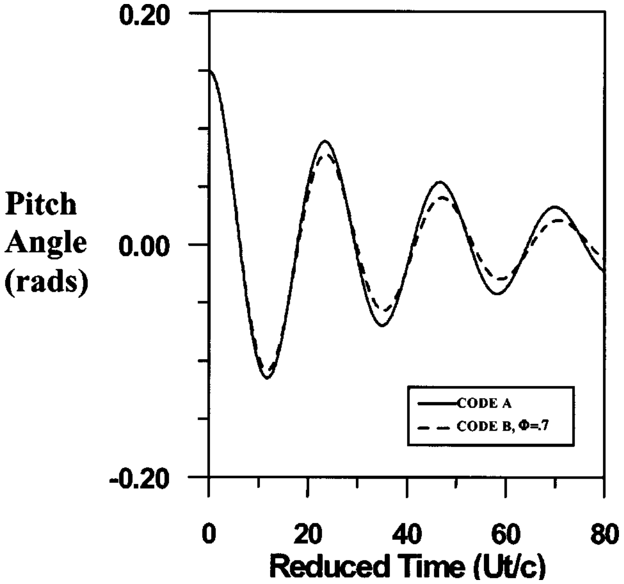

Fig. 10 Comparison of results from two different codes

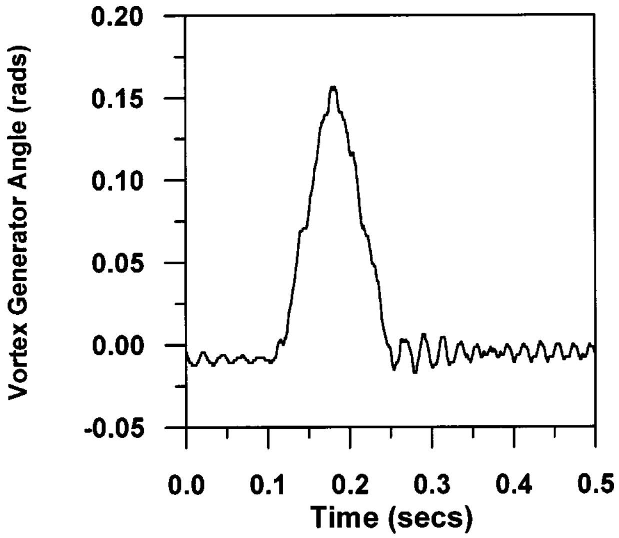

Fig. 12 Typical vortex generator deployment used in the experiments

the source of some of the baseline noise in the pressure distributions over the airfoil, as it will be seen shortly. In order to achieve the highest possible reduced frequencies, allowed by our hardware, the vortex generator was oscillated at the maximum rate that the hardware permitted, for all of the test cases presented here. This corresponded to a minimum duration of vortex generator oscillation around 100 millis. Although the reduced frequency could be increased by further reducing the freestream velocity, this was avoided in order to ensure reasonable accuracy of the pressure measurements. This resulted in disturbance reduced frequencies varying from 0.05 to 0.1 (depending on the freestream velocity) based on the blade chord length.

The optimal flap deployment schedules for pressure impulse alleviation were determined heuristically via an iterative process. The design of the flap deployment schedules was guided by first observing the magnitude and duration of the pressure impulses on the airfoil caused by the disturbance coming from the upstream vortex generator. Then, the actuation parameters of the AFDS were adjusted so that the duration of the flap oscillation matched that of the pressure impulses and the oscillation amplitude was initially decided based on steady-state pressure distribution considerations. For every iteration, the parameters we adjusted were tension in the two springs, flap moment of inertia and timing of the electromagnet actuation. In an on-board system, the former two would be adjusted by linear actuation of the SMA positioners shown in Fig. 2, while the latter would be adjusted the same way as in the experiment, via electronic timing. Subsequent to each parameter adjustment, the flap was actuated, the pressure data was collected and was evaluated for pressure impulse attenuation. This, in turn, guided an optimization of the flap actuation parameters for achieving the best possible pressure impulse alleviation. In our experimental setup, the iterative optimization process took on the order of a few hours, due to the fact that it was not automated; i.e., the parameter adjustments were performed manually and in a heuristic/trial-and-error manner and every time a new adjustment was made the pressure distribution was collected and visually inspected for disturbance alleviation. For an in-flight system, all these processes are envisioned to be automated and the optimization process should take a few rotor revolutions.

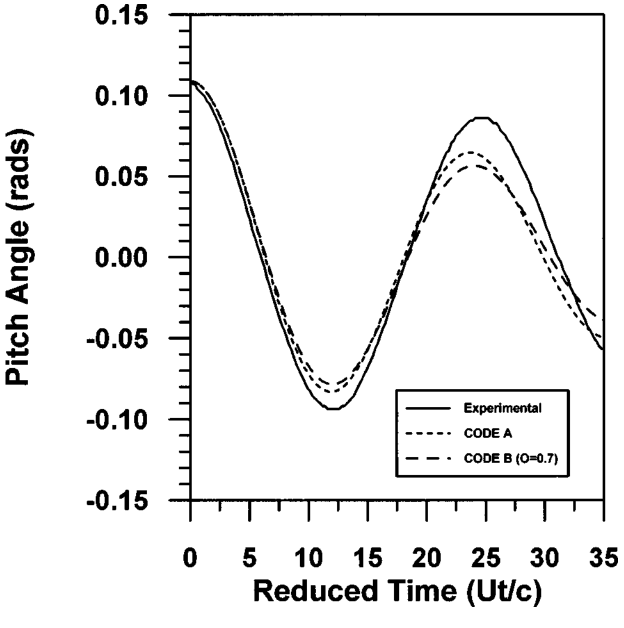

Fig. 11 Comparison of experimental and theoretical results for the aerodynamic models

Figure 13 shows the pressure signature generated by several separate BDI events (three in each case), for a single realization, and their subsequent reduction achieved with deployment of the AFDS. These plots represent the pressure histories at individual ports on the airfoil surface and at several free stream values. It can be seen that there is significant attenuation of the BVI pressure impulses. These results serve to further validate the use of the trailing edge flap approach towards BDI–BVI noise reduction and illustrate the successfulness of the AFDS.

For each of the different conditions tested (freestream velocity and vortex generator amplitude) an optimum flap deployment schedule could be identified. An example of a typical deployment is shown in Fig. 14. Although in the present work this was achieved by manually modifying the AFDS dynamic parameters (and thus modifying the deployment period and amplitude), parameter variation principles such as those illustrated in Fig. 2 can render the system fully self-adaptable in the future.

A more complete representation of the BDI events is shown in Fig. 15. Here, the pressure histories for several ports (1, 2, 4, and 6 as indicated), for a single realization, are shown for pure BDI events with no AFDS deployment [Fig. 15(*a*)], pure AFDS

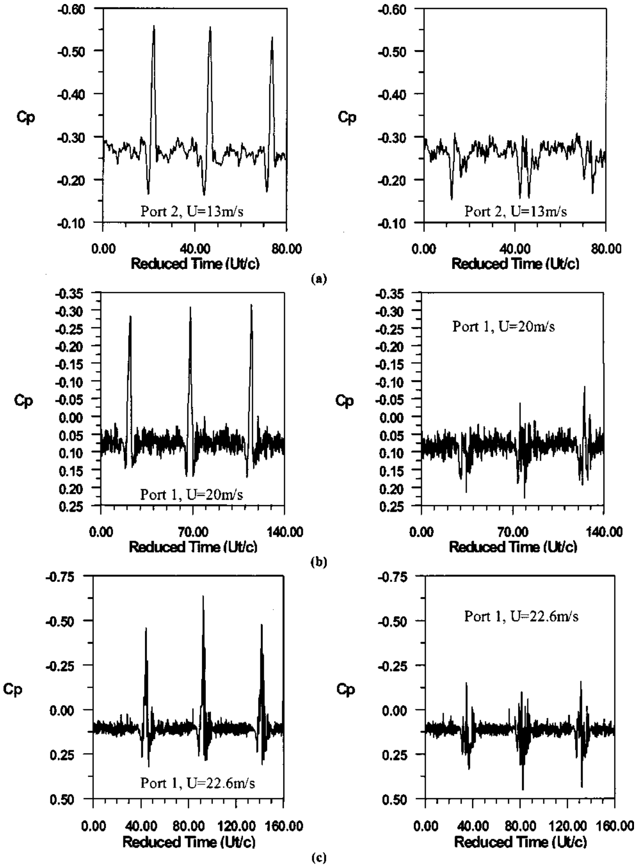

Fig. 13 Comparison of BDI pressure signatures with and without AFDS deployment for (*a*) pressure port 2, $U=13$ m/s (*b*) pressure port 1, $U=20$ m/s and (*c*) pressure port 1, $U=22.6$ m/s

deployment with no BDI events [Fig. 15(*b*)], and the combination of the two [Fig. 15(*c*)]. From these graphs the limitations of the TEF approach can be seen. In the first of the graphs, the BDI induced pressure spikes are observed predominantly in the leading edge region. Conversely, the pressure impulses generated from the AFDS deployment have a significant impact over the entire airfoil. Thus, complete elimination of the BDI impulses over the whole surface cannot be expected from the AFDS alone. However, significant alleviation of the disturbance signature can be achieved in the leading-edge area. Trailing–leading edge flap combinations could possibly provide higher flexibility in "shaping" the pressure history over the majority of the blade surface.

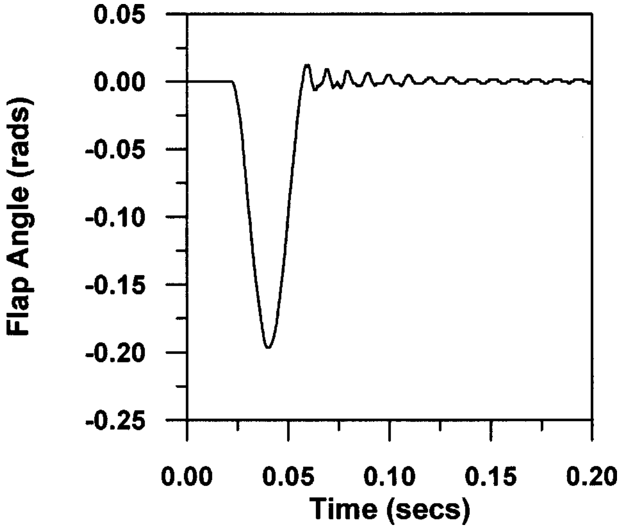

Fig. 14 An example of a typical AFDS deployment schedule

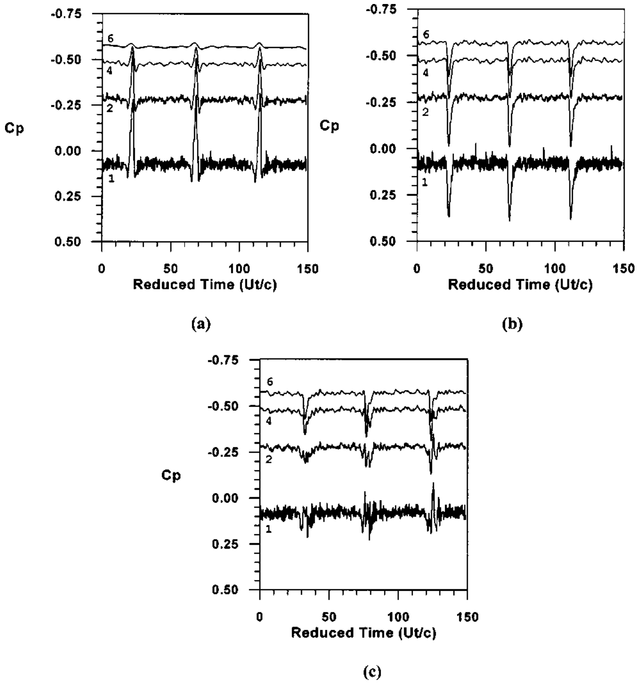

Fig. 15 Pressure histories for $U=22.6$ m/s and several ports during: (*a*) During BDI interaction, (*b*) AFDS deployment, and (*c*) combination of both

Conclusions

Significant attenuation of BDI events has been shown to be possible through the use of an Active Flap Deployment System (AFDS). An simple implementation of an innovative actuation system for trailing edge flap deployment was successfully demonstrated. The results of the current work are significant enough to warrant continuing work on refining the design of the original concept presented here.

While attenuation of the characteristic BDI pressure impulse was achieved, it was also noted that complete cancellation of the pressure fluctuations over the entire blade surface is not possible by a TEF alone. This is due to the difference in the chordwise changes in the BDI pressure distribution compared to those obtainable by the trailing edge flap deployments. However, it is believed that the reduction in the BDI disturbances that was achieved warrants continuing investigation of the TEF.

Two aerodynamic models of the AFDS were also developed. Both show adequate agreement with experimental results (especially during the first period of oscillation) to justify their use as prediction tools to aid in the refinement of the AFDS design. The results of CODE B show that, for the Reynolds numbers tested, the contribution of the circulatory aerodynamic terms is small.

Acknowledgments

This work was partly supported through Dr. Dimitris Lagoudas by the Army Research Office under Grant No. DAAL 03-92-G-0123, Dr. Gary Anderson, monitor.

References

[1] George, A. R., 1978, ''Helicopter Noise: State-of-the-Art,'' J. Aircr., **15**, No. 11, November, pp. 707–714.

[2] Widnall, S. E., 1971, ''Helicopter Noise due to Blade-Vortex Interaction,'' J. Acoust. Soc. Am., **50**, No. 1, Pt. 2, pp. 354–365.

[3] Widnall, S. E., and Martinez, R., 1983, ''An Aeroacoustic Model for High-Speed, Unsteady, Blade–Vortex Interaction,'' AIAA J., **21**, No. 9, September, pp. 1225–1231.

[4] Hardin, J. C., and Mason, J. P., 1985, ''A New Look at Sound Generation by Blade–Vortex Interaction,'' Trans. ASME, J. Vib., Acoust., Stress, Reliab. Des., **107**, No. 2, April, pp. 224–229.

[5] Hardin, J. C., and Lamkin, S. L., ''Aeroacoustic Interaction of a Distributed Vortex With a Lifting Joukwoski Airfoil,'' AIAA Paper 84-2287, October 1984.

[6] Hardin, J. C., and Lamkin, S. L., 1987, ''An Euler Code Calculation of Blade–Vortex Interaction Noise,'' Trans. ASME, J. Vib., Acoust., Stress, Reliab. Des., **109**, No. 1, January, pp. 29–35.

[7] Hardin, J. C., and Lamkin, S. L., 1987, ''Concepts for Reduction of Blade–Vortex Interaction Noise,'' J. Aircr., **24**, No. 2, February, pp. 120–125.

[8] Lee, Soogab, 1994, ''Reduction of Blade–Vortex Interaction Noise Through Porous Leading Edge,'' AIAA J., **32**, No. 3, March, pp. 480–488.

[9] Hassan, Ahmed A., Sankar, L. N., and Tadghighi, H., 1994, ''Effects of Leading and Trailing Edge Flaps on the Aerodynamics of Airfoil–Vortex Interactions,'' J. Am. Helicopter Soc., April, pp. 35–46.

[10] Lorber, Peter F., 1993, ''Blade–Vortex Interaction Data Obtained From a Pressure-Instrumented Model UH-60A Rotor at the DNW,'' J. Am. Helicopter Soc., July, pp. 26–34.

[11] Lorber, Peter F., 1991, ''Aerodynamic Results of a Pressure-Instrumented Model Rotor Test at the DNW,'' J. Am. Helicopter Soc., October, pp. 66–76.

[12] Splettstoesser, W. R., Schultz, K. J., and Martin, R. M., 1990, ''Rotor Blade–Vortex Interaction Impulsive Noise Source Localization,'' AIAA J., **28**, No. 4, April, pp. 593–600.

[13] Martin, R. M., Elliot, J. W., and Hoad, D. R., ''Comparison of Experimental and Analytical Predictions of Rotor Blade–Vortex Interactions Using Model Scale Acoustic Data,'' AIAA Paper 84-2269, October 1984.

[14] Booth, Earl R., 1990, ''Experimental Observations of Two-Dimensional Blade–Vortex Interaction,'' AIAA J., **28**, No. 8, August, pp. 1353–1359.

[15] Booth, Earl R., ''Surface Pressure Measurement During Low Speed Two-Dimensional Blade–Vortex Interaction,'' AIAA Paper 86-1856, July 1986.

[16] Booth, E. R., and Yu, J. C., ''Two-Dimensional Blade–Vortex Interaction Flow Visualization Investigation,'' AIAA Paper 84-2307, October 1984.

[17] Straus, J., Renzoni, P., and Mayle, R. E., 1990, ''Airfoil Pressure Measurements During a Blade Vortex Interaction and a Comparison With Theory,'' AIAA J., **28**, No. 2, February, pp. 222–228.

[18] Seath, D. D., Kim, Jai-Moo, and Wilson, D. R., 1989, ''Investigation of the Parallel Blade–Vortex Interaction at Low Speed,'' J. Aircr., **26**, No. 4, April, pp. 328–333.

[19] Lee, S., and Bershader, D., 1994, ''Head-On Parallel Blade–Vortex Interaction,'' AIAA J., **32**, No. 1, January, pp. 16–22.

[20] Kalkhoran, I., Wilson, D., and Seath, D., ''An Experimental Investigation of the Parallel Vortex–Airfoil Interaction at Transonic Speeds,'' AIAA Paper 89-1833, June 1989.

[21] Smith, D., and Sigl, D., ''Helicopter Rotor Tip Shapes for Reduced Blade–Vortex Interaction an Experimental Investigation,'' AIAA Paper 95-0192, Reno, Nevada, Jan. 1995.

[22] Brooks, Thomas F., and Booth, Earl R., 1993, ''The Effects of Higher Harmonic Control on Blade–Vortex Interaction Noise and Vibration,'' J. Am. Helicopter Soc., July, pp. 45–54.

[23] Dawson, S., and Straub, F., ''Design, Validation and Test of a Model Rotor With Tip Mounted Active Flaps,'' AHS 50th Annual Forum, May 1994, Washington DC.

[24] Marcolini, M., Booth, E., Tadghighi, H., Hassan, A., Smith, C., and Becker, L., ''Control of BVI Noise Using an Active Trailing Edge Flap,'' Presented at the 1995 AHS Vertical Lift Aircraft Design Conference, San Francisco, CA, January 1995.

[25] Simonich, J., Lavrich, P., Sofrin, T., and Topol, D., 1993, ''Active Aerodynamic Control of Wake–Airfoil Interaction Noise—Experiment,'' AIAA J., **31**, No. 10, October, pp. 1761–1768.

[26] Nelson, C. T., ''Effects of Trailing Edge Flap Dynamic Deployment on Blade–Vortex Interactions,'' MS Thesis, Aerospace Engineering Department, Texas A&M University, August 97.

[27] Walz, C., and Chopra, I., ''Design and Testing of a Helicopter Rotor Model With Smart Trailing Edge Flaps,'' AIAA Paper 94-1767, April 1994.

[28] Webb, G., Wilson, L., Lagoudas, D. C., and Rediniotis, O. K., 2000, ''Adaptive Control of Shape Memory Alloy Actuators for Underwater Biomimetic Applications,'' AIAA J., **38**, No. 2, Feb., pp. 325–334.

[29] Rediniotis, O., Wilson, L., Lagoudas, D., and Khan, M., 2002, ''Development of a Shape-Memory-Alloy Actuated Biomimetic Hydrofoil,'' J. Intell. Mater. Syst. Struct., **13**, No. 1, Jan., pp. 35–49.

[30] Jun, H., ''Development of a Fuel-Powered, Compact SMA Actuator System,'' Ph.D. Dissertation, Aerospace Engineering Department, Texas A&M University, College Station, Texas, October 2003.

[31] Garner, L., Wilson, L., Lagoudas, D., and Rediniotis, O., 2000, ''Development of a Shape Memory Alloy Actuated Underwater Biomimetic Vehicle,'' J. Smart Mater. Struct., **9**, No. 5, Oct., pp. 673–683.

[32] Lagoudas, D. C., and Miller, D. A., ''Experiments of Thermomechanical Fatigue of SMAs,'' *Proceedings of the 1999 Conference on Smart Structures and Materials*, SPIE, 1999, pp. 275–282.

[33] Rae, W. H., and Pope, A., *Low-Speed Wind Tunnel Testing*, John Wiley & Sons, New York, 1984.

[34] Rediniotis, O. K., and Pathak, M. M., 1999, ''A Simple Technique for Frequency Response Enhancement of Miniature Pressure Probes,'' AIAA J., **37**, No. 7, July, pp. 897–899.

[35] Abbott, I. H., and Von Doenhoff, A. E., *Theory of Wing Sections*, Dover Publications, Inc., New York, 1959.

[36] Fung, Y. C., *An Introduction to the Theory of Aeroelasticity*, Dover Publications Inc., New York, 1993.

[37] Lee, B. H. K., and Desrochers, J., ''Flutter Analysis of a Two-Dimensional Airfoil Containing Structural Nonlinearities,'' National Research Council Canada, LR-618, May, 1987.

[38] Houbolt, J. C., 1950, ''A Recurrence Matrix Solution for the Dynamic Response of Elastic Aircraft,'' J. Aeronaut. Sci., **17**, No. 9, pp. 540–550.

[39] O'Neil, Todd, and Strganac, T. W., Nonlinear Aeroelastic Response—Analyses and Experiments, AIAA Paper 95-1404, April, 1995.

Effects of Elevated Free-Stream Turbulence on Actively Controlled Separation Bubble[1]

E. Halfon
Research Assistant

B. Nishri
Research Associate

A. Seifert
Senior Lecturer
e-mail: Seifert@eng.tau.ac.il

I. Wygnanski[2]
Professor

Department of Fluid
Mechanics and Heat Transfer,
Faculty of Engineering,
Tel-Aviv University, Israel

The effects of elevated free-stream turbulence (FST) on natural and periodically excited separation bubbles were examined experimentally at low Reynolds numbers. The bubble was formed at the leading edge of a flat plate and the FST level was altered by placing a grid across the flow at different locations upstream of the plate. The mixing across the separated shear-layer increased due to the elevated FST and the two-dimensional periodic excitation, flattening, and shortening the bubble. Periodic excitation at frequencies that were at least an order of magnitude lower than the initial Kelvin–Helmholtz instability of the separated shear-layer were very effective at low FST. The fundamental excitation frequency and its first harmonic were amplified above the bubble. High frequency excitation ($F^+ \approx 3$, based on the length of the natural low FST bubble that served as a reference baseline) affected the flow near the leading edge of the bubble but it rapidly decayed in the reattachment region. Lower frequencies ($F^+ \approx 1$) were less effective and they decayed at a slower rate downstream of reattachment. An increase in FST level reduced the net effect of the periodic excitation on mixing enhancement and subsequent reattachment process. This was probably due to a destructive interference between the nominally 2D excitation and the random, in space and in time, FST. High FST is known to reduce the spanwise coherence in free shear layers [e.g., Chandrasuda, C., Mehta, R. D., Weir, A. D., and Bradshaw, P., 1978, "Effects of free-stream turbulence on large structures in turbulent mixing layers," J. Fluid Mech., ***85****, pp. 693–704] and therefore also the effectiveness of the current control strategy, this not withstanding 2D periodic excitation accelerated the reattachment process and the recovery rate of the attached boundary layer, reducing its momentum loss.* [DOI: 10.1115/1.1839933]

1 Introduction

Boundary layers are prone to separation when subjected to strong, adverse pressure gradient, but separation may also occur wherever the flow encounters large surface discontinuities. Laminar flow is much more prone to separation than turbulent one and sometimes laminar separation is followed by transition that leads to reattachment of the turbulent flow. This is so because the laminar shear layer is highly unstable and rolls-up into large (Kelvin–Helmholz-type) vortices. At higher Reynolds numbers the shear layer undergoes a "mixing transition," that is associated with the appearance of streamwise vortices and small scales that appear to be random. The large eddies transport momentum and mass across the mixing-layer, enhancing its entrainment capability that may result in reattachment. The abovementioned sequence of separation and reattachment frequently occurs on airfoils and low-pressure turbine blades at low Reynolds numbers (typically smaller than 10^5 based on chord or presently on bubble length). In both applications, the bubble is not desirable because it increases the drag and generates unsteady loads. If the bubble "bursts," i.e., the separation is not followed by a turbulent reattachment, a catastrophic loss of performance takes place. Elevated free-stream turbulence (FST), resulting from multiple rows of rotor-stator stages in turbomachinery, promotes earlier mixing transition in the shear layer bounding the separation bubble, increasing mixing rate across it and resulting in earlier reattachment [1–3]. However, in most low Reynolds number applications, and in particular where the surface discontinuity results in separation, the elevated FST does not eliminate the bubble. Therefore, one may reduce the losses and the unsteady loads by actively reducing the size of the bubble through the introduction of periodic excitation.

Earlier investigations have shown that laminar, transitional and turbulent separation bubbles can be very effectively controlled (i.e., reduced in size) through the addition of nominal 2D periodic perturbations provided the FST level is low [4–9]. This bubble control method relies on successive generation of spanwise-coherent structures that result in a small number (1–4) of transverse vortices being present in the bubble shear layer at any instance in time. The velocity perturbations associated with the vortices amplify, and the vortices grow in size while propagating downstream, enhancing mixing and accelerating reattachment [6,7]. While an elevated FST [1–3] has a similar effect on the bubble, the mechanism by which it is achieving the control over the bubble is different. This difference is attributed to the wide spectrum of scales and different orientation of eddies that are associated with the elevated FST. It was therefore decided to superimpose controlled but elevated FST on periodically excited, plane bubble flow while keeping both inputs properly controlled and documented. Past experience of periodic excitation or "Active Flow Control" (AFC) of fully turbulent mixing-layers [5–11] in the absence of elevated FST served as a basis for the present investigation. A feasibility study was carried out by Bachar, Ashpis and Wygnanski, (APS/DFD meeting, November 1998) in which active separation control was shown not to be hindered by the presence of elevated FST, gave another impetus for the present investigation.

The current tests are carried out on a large, transitional (at low FST) or turbulent (at larger FST) separation bubble that is situated near an elliptical leading edge of a long flat-plate. As a result of the leading edge shape, the separation location is not fixed, as it is also variable on low Re airfoils and *not* as it was in several in-

---

[1] Presented in the 1st AIAA Flow Control conference, June 2002, AIAA paper 2002-3169.

[2] Also at AME Department, University Of Arizona, Tucson, AZ.

Contributed by the Fluids Engineering Division for publication in the JOURNAL OF FLUIDS ENGINEERING. Manuscript received by the Fluids Engineering Division July 15, 2002; revised manuscript received April 15, 2004. Associate Editor: Michael W. Plesniak.

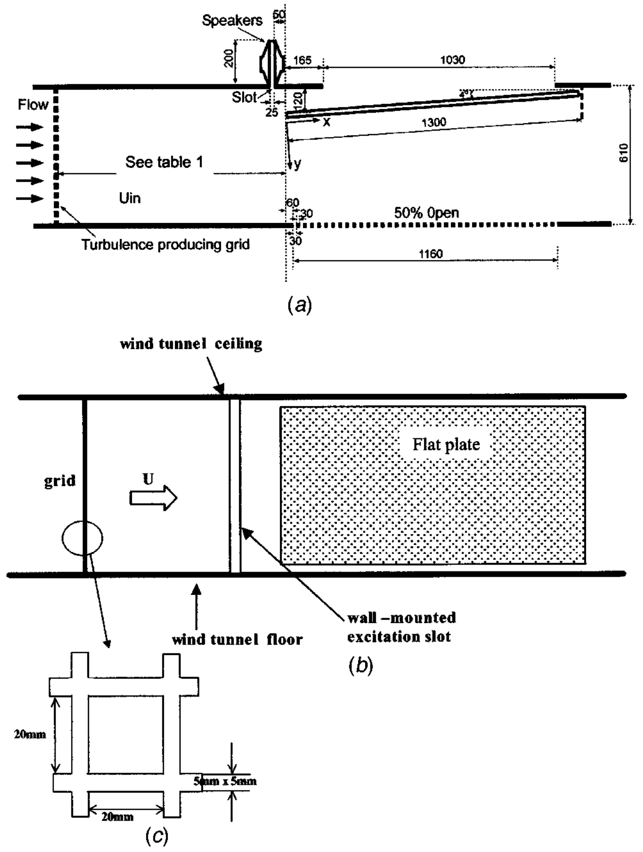

Fig. 1 (***a***) **Top view of the experimental set-up. All dimensions in mm.** (***b***) **Side view of the experimental set-up.** (***c***) **A typical cell of the turbulence generating gri**

Table 1 Turbulence levels and integral length scales in the streamwise (*Lx*) and spanwise (*Lz*) directions for different turbulence generating grid locations

Grid x [mm]	Tu [%]	Lx [mm]	Lz [mm]
No grid	0.4±7.5%		
−1500	1.9±2.5%	20	14
−600	4.2±2.5%	12	7
−300	11.0±2.5%	8	4

vestigations (i.e., flow over sharp corners [1,2] or turbulent flow over a flat plate [3]). Active Flow Control, using nominally 2D periodic acoustic excitation (termed AFC for the reminder of this manuscript) reduced the mean size of the bubble. The FST was then increased from 0.4% to 11% by placing a grid upstream of the test plate's leading edge. The spectral content of the oscillations in the free-stream and in the separated shear layer, were documented in the presence and in the absence of AFC. The effect of the elevated FST on the modification of the separated shear layer that was already affected by the periodic excitation was documented as well. Additional measurements included surface pressure distributions as well as mean and fluctuating velocity profiles.

2 Experiment Setup

2.1 Description of the Apparatus. A transitional separation bubble was formed on a flat plate due to a combination of its inclination and flow bleed out of the opposite tunnel sidewall. The test plate was mounted vertically [as shown in Fig. 1(***a***)] in the 914 mm (height) by 609 mm (width) and 6000 mm (long), test section of the low speed, closed-circuit wind tunnel at Tel-Aviv University. The plate dimensions were, length: $L_f=1300$ mm, height: $W=849$ mm, and thickness of 20 mm. The plate had a 1:4 elliptic leading edge.

The plate trailing edge was hinged to allow a limited variation in incidence (α) relative to the oncoming flow. The opposite sidewall of the wind tunnel was replaced by adjustable vertical louvers. The combination of adjustable louvers and the variation in the plate incidence was intended to cause divergence of the mean streamlines near the plate leading edge, and thus induce a controllable size of a separation bubble. The louvers were not essential for the mere purpose of controlling the bubble size, they also enabled convenient access for boundary layer traverses. The distance between the plate and the nearby tunnel wall was sufficient to bleed that wall's boundary layer through a special slot that was located farther downstream.

For all experiments reported herein, the plate incidence angle was fixed at 4 deg, the free-stream reference velocity was maintained at 5 m/s±5% and the vertical louvers were equally spaced resulting in solidity of 50% of the wind tunnel wall opposite to the test surface. The openings between the vertical louvers also allowed an external hot-wire traverse to reach the test area.

The plate was equipped with 27 pressure taps placed along the mid-span. The pressure taps were connected to a sensitive, fast responding, multichannel pressure scanner having a range of ±20 mm water, full scale. A single velocity component hot-wire anemometer was used for detailed boundary layer measurements above the plate surface. The initial distance of the hot wire from the plate was 0.5±0.5 mm. A 0.05 mm thick tape was glued to the plate in order to avoid an accidental contact with the hot-wire and also reduce the heat transfer to the wall. The uncertainty in the velocity measurements was 2% while the uncertainty in the measured pressures was 1% of the full scale or 0.2 mm water.

A two-dimensional excitation slot of 25 mm width that spanned the height of the test section was located on the wind tunnel wall, 50 mm upstream of the plate leading edge [see Figs. 1(*a*) and 1(*b*)]. Periodic excitation was generated by six acoustic drivers mounted onto a sealed box located outside the tunnel wall. The distance between the excitation slot and the plate leading edge was 130 mm. The acoustic drivers were activated by a function generator through a power amplifier.

2.2 Generation and Documentation of the Free-Stream Turbulence (FST). Elevated free stream turbulence was generated by placing an accurately machined metal grid [Fig. 1(*c*)], made of 5 mm thick/Aluminum plate, at various upstream distances from the plate leading edge [Figs. 1(*a*) and 1(*b*)]. The inflow conditions for each test were measured and defined for the baseline (without grid) and for three additional locations of the metal grid: 1500 mm, 600 mm, 300 mm upstream of the plate's leading edge. Inflow turbulence levels (based on the fluctuating, streamwise velocity component) measured 100 mm upstream of the plate leading edge, in the center of the test section are presented in Table 1, for the free-stream reference velocity of 5 m/s. Also shown are the streamwise integral length scales, calculated from the autocorrelation function (integrated from unity to the first zero crossing) by assuming a convection velocity that is equal to the free stream for Lx.

The decay rate of the streamwise turbulence level measured at $x=-100$ mm, with the grid positioned at increasing distance upstream of the plate LE are shown in Fig. 2. The data suggests that the decay rate of the power spectral density is linear with distance, in agreement with published data for grid generated turbulence [12]. The spatial variations of the turbulence levels in the $Y-Z$ plane at $x=-100$ mm were also measured and the variation were less than ±2.5% with the exception of the base flow that was approximately 3 times higher. The power spectra of the FST measured at the above location are presented in Fig. 3. The spectra measured with the grid being present, are typical to turbulence spectra in low speed, grid generated turbulence. For FST>4%,

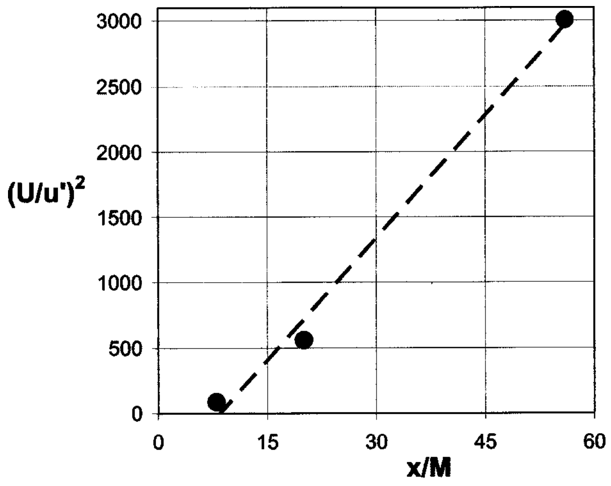

Fig. 2 The effect of grid position on normalized turbulence levels, measured 100 mm upstream of the plate LE. $M=25$ mm, rectangular grid and bars. Here x is the distance between the grid and the measurement location

one may observe an inertial subrange spanning at least one decade of the midrange wave numbers (corresponding to frequencies between 80 Hz and 800 Hz). At higher frequencies the negative slope of the power spectrum increases, indicating the effects of dissipation, while at lower frequencies the slope approaches zero. The absence of peaks in these spectra suggest that the turbulence generated by these grids is reasonably homogeneous although its integral scale increases in the direction of streaming as it always does in such cases. One may therefore assume that this turbulence is also reasonably isotropic in spite of the fact only one velocity component was measured.

Two point spanwise cross correlations, $R_{uu}(\Delta z)$, and the autocorrelation $R_{uu}(\Delta \tau)$, are plotted in [Figs. 4(*a*) and 4(*b*), respectively]. The $R_{uu}(\Delta z)$ correlations decay with increasing Δz reaching a plateau within $\Delta z<25$ mm for all the cases corresponding to the grid cell size. The autocorrelations $R_{uu}(\Delta \tau)$ measured at 20, 50, and 140 cm downstream of the grid (and 10 cm upstream of the plate's leading edge) intercept the $\Delta \tau$ axis at $\Delta \tau \approx 7$, 11, 18 ms, respectively.

The integral scales cited in Table 1 were calculated from the integral of the correlation coefficients from unity to the zero crossing (or extrapolated to it). The free stream velocity was used to convert the temporal to spatial integral scale. Both sets of correlations suggest that the integral scales increase linearly with increasing distance from the turbulence-generating grid.

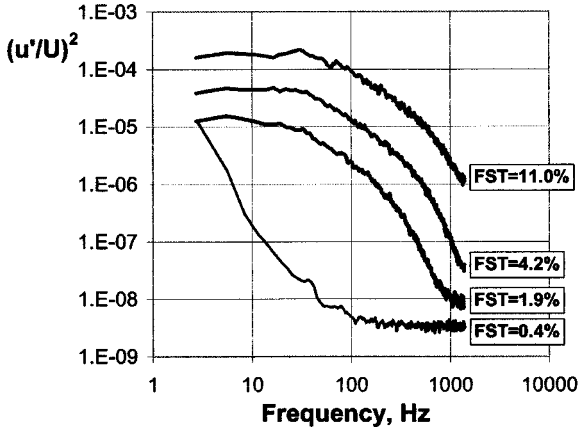

Fig. 3 The effect of grid position (determining the FST level) on FST turbulence spectra, measured 100 mm upstream of the plate LE. $M=25$ mm, rectangular grid, rectangular bars. Data was acquired at $z=0$ and $y=100$ mm

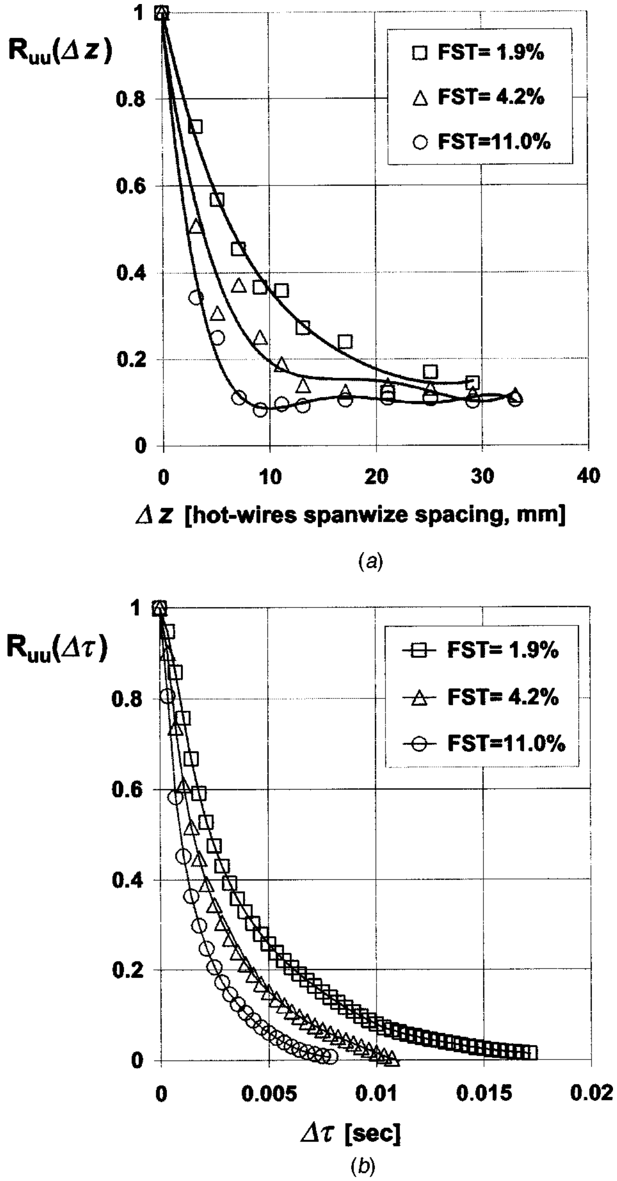

(*a*)

(*b*)

Fig. 4 (*a*) The effect of grid position (determining FST level) on turbulent scales using two wire correlations. Note that the initial spanwise separation between the hot-wire centers was about 3 mm while each HW was about 2 mm wide. (*b*) The effect of grid position (determining FST level) on streamwise turbulent scales

The power spectra of the u' component of velocity measured 20 mm downstream of the leading edge and inside the mixing layer bounding the bubble are shown in Fig. 5. The presence of the grid not only increased the turbulence level thus elevating the power spectrum but it also eliminated the spectral peaks observed in its absence. These spectral peaks are associated with the rollup of the large eddies that are generated by the Kelvin–Helmholtz instability mechanism. Since the size of the bubble was affected by the presence of the grid, the disappearance of the spectral peaks at FST=1.9% and higher may be attributed in part to the change in the location of the probe relative to the dividing streamline.

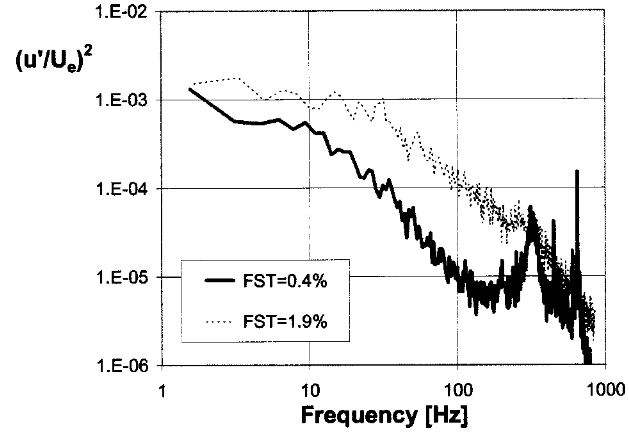

Fig. 5 The effect of elevated FST on velocity spectra inside the separated shear layer close to the plate LE ($x=10$ mm). Ue is the local free stream velocity

2.3 Introduction of Periodic Excitation. The objective of the present study was to identify the effects of the two-dimensional excitation on the characteristics of the separation bubble in the presence of elevated FST. The excitation method consisted of an acoustic disturbance that was introduced from a slot in the tunnel wall [Figs. 1(*a*) and 1(*b*)]. This method of actuation relies on acoustic receptivity of the leading edge to the excitation emanating from the tunnel wall upstream of the test plate. Six 40-W acoustic drivers connected to a single cavity were used to introduce the periodic perturbations through the slot. The following method for quantifying the nondimensional periodic addition of momentum (momentum coefficient), C_μ was used in order to be consistent with the well-known excitation method, in which an oscillatory jet emanates from a slot on the test surface (see [13], and references therein). In the latter case, the following definition was used [14]

$$C_\mu=\frac{2h}{L}\left(\frac{\overline{u_j}}{U_i}\right)^2, \tag{2.1}$$

where $\overline{u_j^2}$ was the mean square of the slot velocity perturbation and U_i was the undisturbed, free-stream velocity, L is a reference length scale, and h is the slot width. When excitation emanated from the slot in the wind-tunnel wall, the boundary layer response close to the test plate leading edge was quantified by integrating the oscillatory momentum coefficient defined as

$$C_\mu=\frac{1}{1/2U_i^2L}\cdot\int_0^\infty\langle u'\rangle^2dy, \tag{2.2}$$

where $\langle u'\rangle$ was the phase locked fluctuating component of velocity measured near the plate leading edge. Unless otherwise stated, the characteristic length scale ($L\equiv L_b$) is the length of the baseline bubble in the absence of the grid at low FST. Although intrinsic differences exist between the two methods of actuation, we regarded their net effect on the flow by considering the total coherent fluctuating momentum across the boundary layer. An example illustrating the validity of this calibration method was provided in [10] (and in the Ph.D. thesis by Nishri), who compared the effects of excitation provided by an acoustic driver located in a cavity and emanating from a slot to an excitation generated by a vibrating ribbon on the surface. It was concluded that for the same levels of fluctuation at identical frequencies, the effects on the flow were also identical.

Amplitude calibration was performed by scanning the flow without the turbulence generating grid, using a hot wire placed at $x=-2$ mm from the leading edge (up stream) and integrating the amplitude of the ensemble averaged fluctuations $\langle u'\rangle$. The integration limit was taken as $y=100$ mm, where the amplitudes reached an asymptotic limit with a reasonable accuracy. The receptivity of the plate LE flow to the excitation emanating from the slot in the tunnel wall was very high. The fluctuation levels of frequencies considered (25 Hz and 80 Hz) decayed with the distance from the slot in the tunnel wall to a similar low value and achieved a plateau around 100 mm from the test plate. A flat frequency response of the excitation was achieved by adjusting the excitation voltage at different frequencies to obtain the same $C\mu$.

Before attempting to quantify the effects of elevated FST on the effectiveness of AFC in controlling a separation bubble, one needs to consider the possibility that FST interacts with the excitation and alters its magnitude or spanwise coherence near the LE. To evaluate this effect, amplitude calibrations were repeated at two FST levels ($Tu\approx0.4\%$ and 3.0%) and at two frequencies, $F=25$ Hz and $F=80$ Hz. These were the frequencies used throughout the reported investigation. It was found that the mean velocities measured 2 mm upstream of the LE, increased due to the presence of the elevated FST (both data sets were acquired with AFC activated), corresponding to the reduction of the LE Cp. The RMS values of the velocity fluctuation and more specifically the velocity fluctuations at the excitation frequency increased as well. This indicates that the excitation emanating from the slot in the side-wall of the tunnel and penetrating into the leading edge bubble scales with the external mean velocity and it is not significantly altered by the presence of elevated FST (as will also be discussed later with respect to the data of Fig. 13). This finding eliminates the possibility that the effectiveness of the AFC was reduced as the FST level was increased because the magnitude of the separated shear layer excitation has diminished. The FST effect on the spanwise coherence of the excitation will be discussed in detail in Sec. 3.3, but it could be stated that it also did not deteriorate in the vicinity of the leading edge, due to elevated FST. The tunnel free-stream reference velocity was 5 m/s for all reported experiments.

3 Discussion of Results

3.1 Overview. Several indicators were used to characterize the bubble and the effects of the FST and AFC on it. The bubble height was characterized by $Y_{1/2}$, the distance in the wall normal direction in which the mean velocity was 50% of the velocity at the outer edge of the boundary layer. Mean static wall pressures provided another indicator for some bubble characteristics. The *variation* in the mean reattachment location was established from the *x* location where the second derivative of the wall pressure (d^2Cp/dx^2) was equal to zero, while the mean pressure inside the bubble is an indicator for the curvature of the reattaching streamline. The skin friction, C_f, downstream of reattachment was evaluated from the mean velocity profiles assuming the universality of the "law of the wall," although the validity of this approach was not tested. Another possible indication for reattachment is the *x* location in which the fluctuating part of the wall pressures reached a maximum [15,16]. This indication provides a reliable criterion for flow reattachment in uncontrolled flow, but was not used presently for the controlled flow due to the inadequate frequency response and additional flow related complications, such as an observed secondary peak in the wall pressure fluctuations related to the maximum amplitude of the periodic excitation above the bubble. The boundary layer recovery rate downstream of reattachment was evaluated using the boundary layer shape factor and the effects of FST and AFC on the total drag was estimated from the boundary layer momentum thickness. A measure of the boundary layer unsteadiness is provided by the variation of the maximum RMS values of the normalized fluctuating boundary layer velocity ($u'_{\max}/U_{\max}$) in the streamwise direction, *x*.

3.2 The Effects of the FST on the Uncontrolled Bubble. Although the flow in the separated shear layer is extremely un-

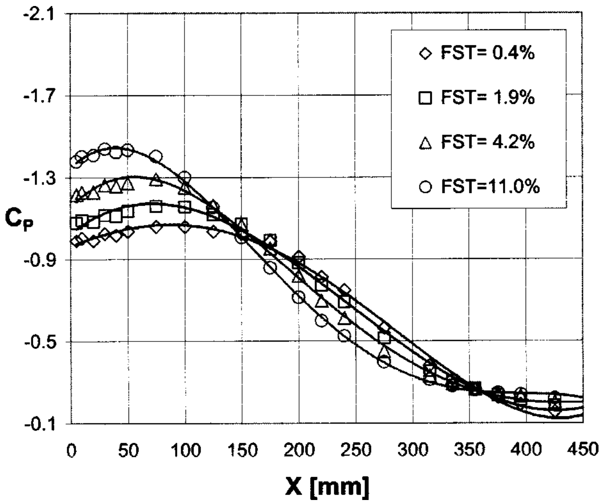

Fig. 6 The effect of FST level on mean wall pressures. No AFC

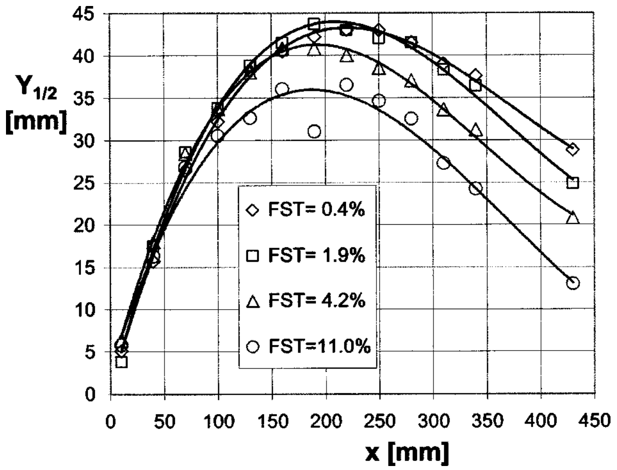

Fig. 7 The effect of FST level on $Y_{1/2}$ (the wall normal direction in which the local mean velocity is half the external velocity). No AFC

stable with a critical Re≈50 (based on the initial momentum thickness of the mixing layer and the velocity difference across it [17] and probably undergoes natural transition soon thereafter, the superposition of the grid turbulence elevated the turbulence level in this shear layer by an order of magnitude. This is particularly evident at scales that are commensurate with the integral scales of the grid near the plate leading edge (i.e., frequencies between 50 Hz and 350 Hz in Fig. 5). The grid generated turbulence also interferes with the eddies associated with the Kelvin–Helmholtz instability, eliminating the presence of the peaks in the spectra shown in Fig. 5 when the FST was 0.4%. The added FST did not have a pronounced effect on the mean separated flow near the LE, as indicated by the indifference of $Y_{1/2}$ at $x<100$ mm to the FST (Fig. 7), but the reattachment process was accelerated. Consequently, the earlier reattachment increased the curvature of the separating streamline and accelerated the flow around the LE, as seen in the pressure distributions of Fig. 6. It is therefore speculated that vortical structures associated with the FST increased the mixing across the shear layer accelerating reattachment. The effect of the elevated FST on the Mean Cp's could be seen in Fig. 6. Even though the Cp next to the LE became more negative, the pressure recovery is faster because dCp/dx has also increased at higher levels of FST.

The boundary of the bubble, as deduced from $Y_{1/2}$ (the y location at which the mean velocity is equal to 50% of the external velocity), is plotted in Fig. 7. It shows that close to the LE, $Y_{1/2}$ was not affected by the FST, but farther downstream $Y_{1/2}$ was reduced by the increased FST level. The maximum bubble height was reduced by about 10% for FST≈11%, while near the end of the measurement domain the reduction in $Y_{1/2}$ was more significant. The spreading rate of the separated shear layer, as indicated by the vorticity thickness, increased from 0.175 corresponding to FST=0.4% to 0.20, 0.236, and 0.242, for FST of 1.9%, 4.2%, and 11%, respectively. This is in agreement with the data of [18].

The reattachment location (as evaluated from the location of $d^2Cp/dx^2\approx X0$) [16] is plotted in Fig. 8 for the range of FST used in the present experiment. Increased FST, in the absence of periodic excitation, reduced the size of the bubble from $Xr=260$ at FST=0.4% to $Xr=170$ at FST=11%. Also plotted on this figure the results of periodic excitation for the four FST levels considered, but these will be discussed later.

The change in the shape factor of the boundary layer downstream of the bubble reattachment region [Fig. 9(*a*)] provides an indication of the rate at which the boundary layer approaches equilibrium, while its value is an indicator for the possible reoccurrence of separation. It may be noticed that an increase in the FST reduces the shape factor, H. This was accompanied by a reduction in dH/dx, that is indicative of the tendency toward equilibrium. The final value of H at the furthest downstream x station that was measured is about 2.0 for $Tu\approx 0.4\%$ while it is about 1.7 for $Tu\approx 11\%$. These values are still higher than $H\approx 1.4$ that is expected for an equilibrium turbulent boundary layer at zero pressure-gradient. (Note that the pressure gradient is small at $x>375$ mm, Fig. 6.)

The boundary layer momentum thickness downstream of reattachment is plotted in Fig. 9(*b*). This parameter is used to evaluate the total drag experienced by the flow due to the presence of the bubble and the skin friction downstream of reattachment to the end of the measurement domain. It was found that the elevated FST increased the momentum loss downstream of reattachment due to increased C_f.

3.3 The Combined Effect of FST and AFC. The AFC had a pronounced effect on the pressure distribution close to the LE at low FST, the suction peak increased as did the pressure recovery rate further downstream. High frequency excitation was more effective in increasing the suction than low frequencies at all FST levels. The optimal reduced frequency, F^+, is in agreement with the findings of Sigordson [8] who investigated the flow on a blunt faced cylinder with acoustic excitation emanating from the upstream corners and found out that the optimal reduced frequency is $F^+=3$. (Note that we are rescaling the results of [8] according

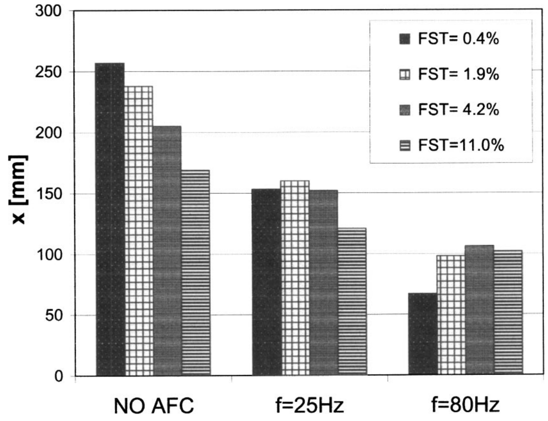

Fig. 8 The reattachment distance, based on the inflection point in the *Cp* distributions for the baseline and for the controlled bubbles

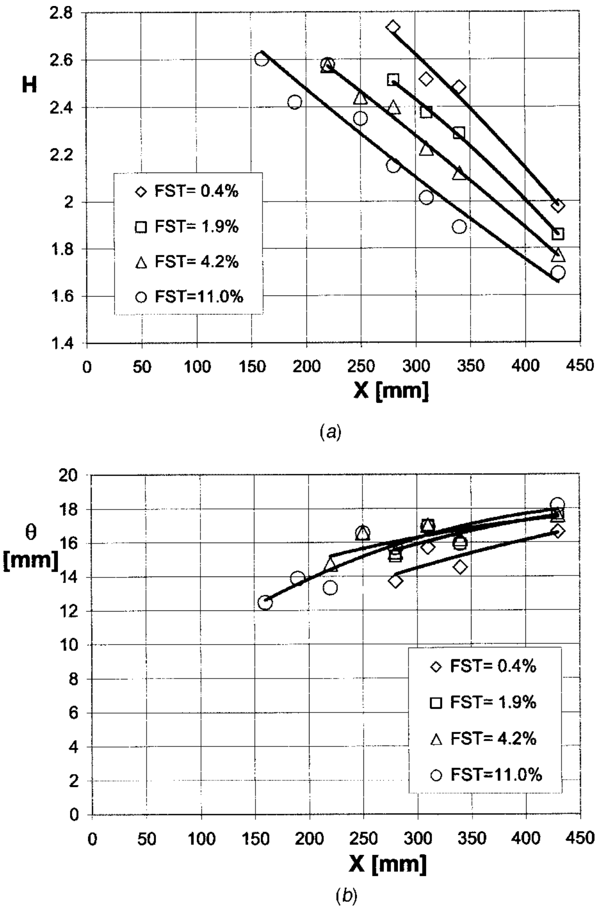

Fig. 9 (*a*) The effect of FST level on H (the boundary layer shape factor) downstream of reattachment. (*b*) The effect of FST level on *θ* (the boundary layer momentum thickness) downstream of reattachment

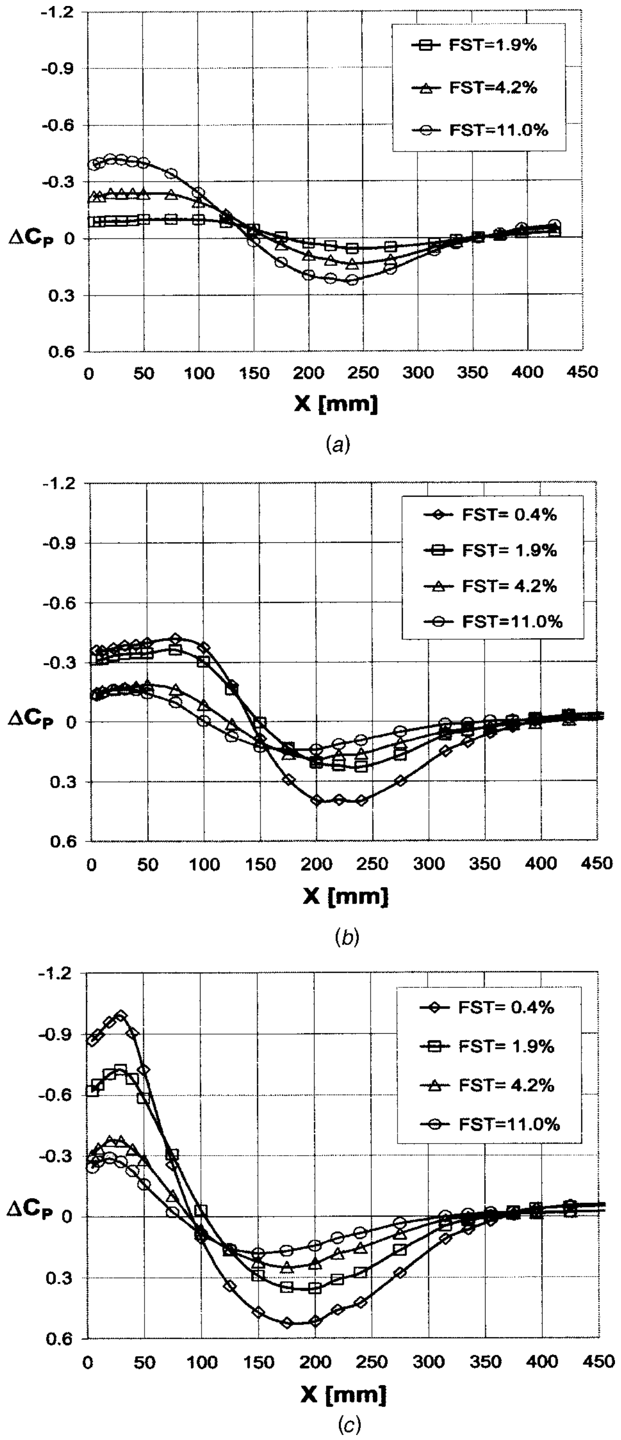

Fig. 10 (*a*) The effect of FST level on uncontrolled (no AFC) mean wall *Cp deviations* from the *Cp* of FST=0.4% (of Fig. 4) when the flow was uncontrolled. (*b*) The effect of FST level on controlled (AFC activated) mean wall *Cp deviations* from the uncontrolled *Cp* (of Fig. 4) when the flow was excited at $F+\approx 1$ ($F=25$ Hz). (*c*) The effect of FST level on controlled (AFC activated) mean wall *Cp deviations* from the uncontrolled *Cp* (of Fig. 4) when the flow was excited at $F+\approx 3$ ($F=80$ Hz)

to our following definition of F^+, to be based on the bubble length and free stream velocity.) The reduced frequency, $F^+ = fL_b/U_e$, used presently is proportional to the ratio of the bubble length in the absence of the grid ($L_b = 250$ mm) to the excited wavelength. Since the length of the bubble was altered by both FST and AFC, the actual frequencies (i.e., 25 Hz and 80 Hz) are mentioned throughout the paper rather than the reduced frequencies. The growth-rate of the separated shear layer vorticity-thickness, has increased by 34% and 50% (relative to its unperturbed value of 0.175 at FST=0.4%) as a consequence of the excitation at 25 Hz and 80 Hz, respectively. The effect of introducing the AFC on the reattachment distance decreased with increasing FST (Fig. 8). FST shortened the bubble from 255 mm at FST=0.4% to 165 mm at FST=11% in the absence of external excitation, and thus the introduction of AFC can not reduce the bubble as much at high FST as it does at low FST. Increasing the level of FST also increased the deviation of ΔCp from its reference measured in absence of the grid (FST=0.4%), reducing again the potential for improvement by AFC [Fig. 10(*a*)]. Controlled ΔCp distributions (from which the $F=0$ Cp of Fig. 6 *for the same FST levels were subtracted*) at $F=25$ Hz and $F=80$ Hz are presented in Figs. 10(*b*) and 10(*c*), respectively, in order to evaluate the *net effect* of the AFC. The excitation momentum coefficient for both frequencies was $1.25\times10^{-4}\pm25\%$, regardless of the FST level. The AFC accelerated the flow close to the LE and increased the pressure recovery rate further downstream. Excitation at $F=80$ Hz was clearly more effective at all FST values. The Cp variations due to the application of AFC were large and the pressure recovery was initiated at smaller distances, *x*. As the level of the FST increased from 0.4% to 11.0%, the uncontrolled bubble length decreased as well [Figs. 8, 10(*b*)–10(*c*)]. The net effect of AFC seems to have been overwhelmed by FST that exceeded 4.2%. Nevertheless, the excitation frequency

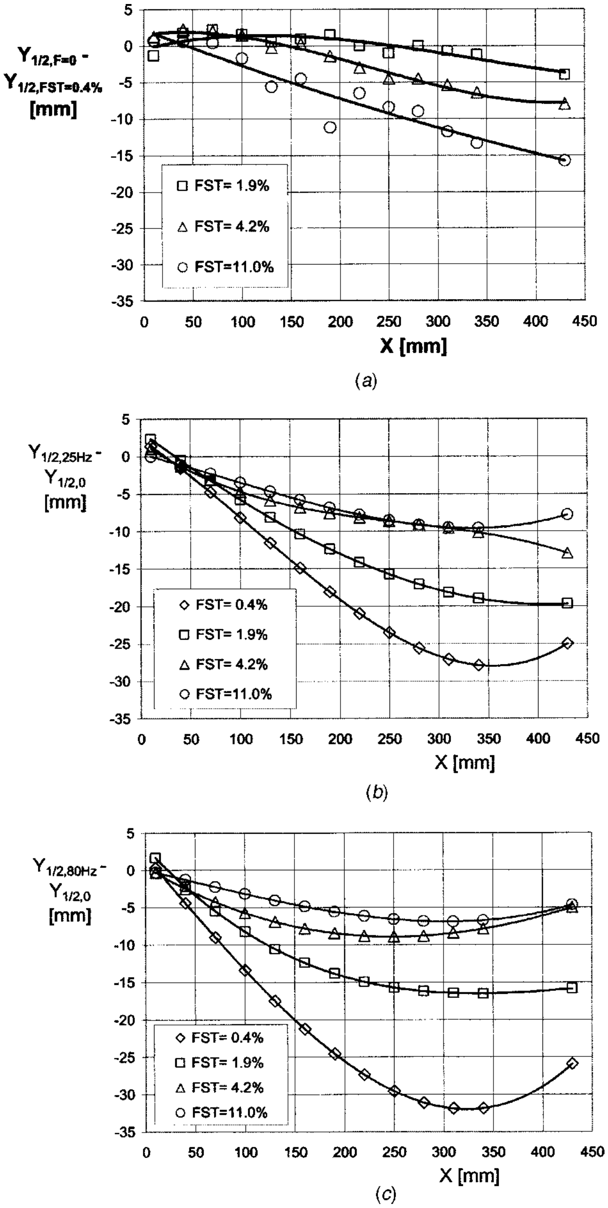

Fig. 11 (*a*) The effect of FST level on uncontrolled (no AFC) $Y_{1/2}$ (referenced) to the $Y_{1/2}$ of the $Tu=0.4\%$ data (of Fig. 7). (*b*) The effect of FST level on controlled (AFC activated) $Y_{1/2}$ *deviations* from the uncontrolled $Y_{1/2}$ (shown in Fig. 7) using $F^{+}\approx 1$ (25 Hz). (*c*) The effect of FST level on controlled (using $F=80$ Hz) $Y_{1/2}$ *deviations* from the uncontrolled $Y_{1/2}$ (of Fig. 7) using $F^{+}\approx 3$ (80 Hz)

plays an important role since at $F=80$ Hz the ΔCp is larger than that corresponding to $F=25$ Hz regardless of the FST level [Figs. 10(*b*) and 10(*c*)].

Figures 11(*a*)–11(*c*) present the combined effects of FST and AFC on $Y_{1/2}$. This parameter is indicative of the height of the bubble above the surface. The sole effect of increasing the FST level could be evaluated from Fig. 11(*a*). Note that Fig. 11(*a*) presents the *difference* between the $Y_{1/2}$ measured at low FST and that measured at higher FST levels in the absence of AFC. The bubble height increases very rapidly close to the LE, regardless of the FST. The $Y_{1/2}$ of the bubble at FST of 0.4% reaches about 43 mm at $x=230$ mm (see Fig. 7). The bubble height was slightly increased and the location of its maximum height moved upstream when FST≈1.9% (Fig. 7). The maximum bubble height was decreased to 41 mm and 37 mm, respectively, for FST levels of 4.2% and 11.0%, while the *x* location of the maximum height was decreased from 230 mm to 190 mm and 180 mm, respectively. Note that there is a gradual decrease in the bubble height as the FST level increases and that for FST≈11% it monotonically decreases for all *x* stations [Fig. 11(*a*)].

The $\Delta Y_{1/2}$ for the controlled bubbles are presented in Figs. 11(*b*) and 11(*c*) for $F=25$ Hz and $F=80$ Hz, respectively. The data for $Y_{1/2}$ of $F=0$ (Fig. 7) were subtracted from the controlled $Y_{1/2}$ data (for each imposed FST) to help identify the clear trends of the AFC, as the level of FST was increased. The most noticeable effect of AFC on $Y_{1/2}$ is at $F=80$ Hz and FST≈0.4%. Elevated FST combined with AFC reduces the bubble height, but it is not capable of eliminating it altogether (Figs. 7 and 8). AFC has a very strong effect in reducing the bubble height, but this effect diminished as the FST level was increased [Figs. 11(*b*) and 11(*c*)]. FST alone had a similar but weaker effect on $\Delta Y_{1/2}$ [compare Fig. 11(*a*) to Figs. 11(*b*) and 11(*c*)]. It was found that $F=80$ Hz [Fig. 11(*c*)] had a stronger effect on reducing $Y_{1/2}$ closer to the leading edge than $F=25$ Hz did [Fig. 11(*b*)], however the lower frequency was more effective at large distances and at elevated FST. At low FST, AFC reduced the bubble height by more than 75%, while the AFC effect persisted at increased FST levels but the magnitude of the effect diminished. At large *x* stations ($x>275$ mm) and large FST levels (4% and 11%), $F=25$ Hz was more effective than $F=80$ Hz.

A comparison of the reattachment location indicator (i.e., based on the inflection point in Cp [16]) is presented in Fig. 8. The net effect of the FST with $F=0$ provides a reduction in *x* location of reattachment, from $Xr=260$ at FST=0.4% to $Xr=170$ at FST =11%. The data further indicates that the reattachment location was reduced from $x\approx 260$ mm in the uncontrolled flow to $x\approx 150$ mm by $F=25$ Hz excitation and to $x\approx 60$ mm by $F=80$ Hz excitation. The relative reduction in reattachment location due to AFC decreased as the FST level was increased and excitation at $F=80$ Hz was more effective than $F=25$ Hz, however, the $F=80$ Hz excitation was also more sensitive to the FST level. There was qualitative agreement between several methods of identifying reattachment also at elevated FST levels. According to the Cp inflection point criterion, reattachment location for $F=80$ Hz and FST≈0.4% was $x\approx 70$ mm and it was shifted downstream to $x\approx 100$ mm for higher FST levels (Fig. 8). At low FST, the location of the maximum wall pressure fluctuations roughly coincides with the location of the Cp inflection point. However with AFC activated, the uncertainty in using the maximum of Cp_{rms} as an indication for reattachment became large, since there were more than one Cp_{rms} peaks observed in the streamwise Cp_{rms} distributions and the frequency response of the pressure scanning system was no longer flat even between 25 Hz and 80 Hz.

The recovery rate of the boundary layer downstream of reattachment can be evaluated from the rate at which the shape factor approaches an equilibrium value (i.e., H=constant). It was found [Fig. 9(*a*) for uncontrolled flow and Figs. 12(*a*) and 12(*b*) for FST=0.4% and FST=11%, respectively] that as the FST level was increased, H was reduced and the H recovery rate was relaxed, due to the smaller difference to equilibrium flow. AFC had also a strong effect in reducing H, and the minimum H of about 1.5 was obtained for both excitation frequencies at FST of 0.4% [Fig. 12(*a*)]. As the FST level was increased [Fig. 12(*b*)], AFC became less effective in reducing H, where again $F=80$ Hz was more sensitive to the FST level. Excitation with $F=25$ Hz proved to be more effective at large distances from the leading edge than $F=80$ Hz and therefore should be more effective in reducing the probability that the flow will separate again downstream of the bubble, if an adverse pressure gradient will be encountered.

The boundary layer momentum thickness may serve as an indicator for the total drag coefficient from the LE to the *x* location of the measurement in the absence of pressure gradient. It was noticed [Fig. 9(*b*)] that elevated FST increased the momentum loss, presumably due to a change in pressure gradient and an

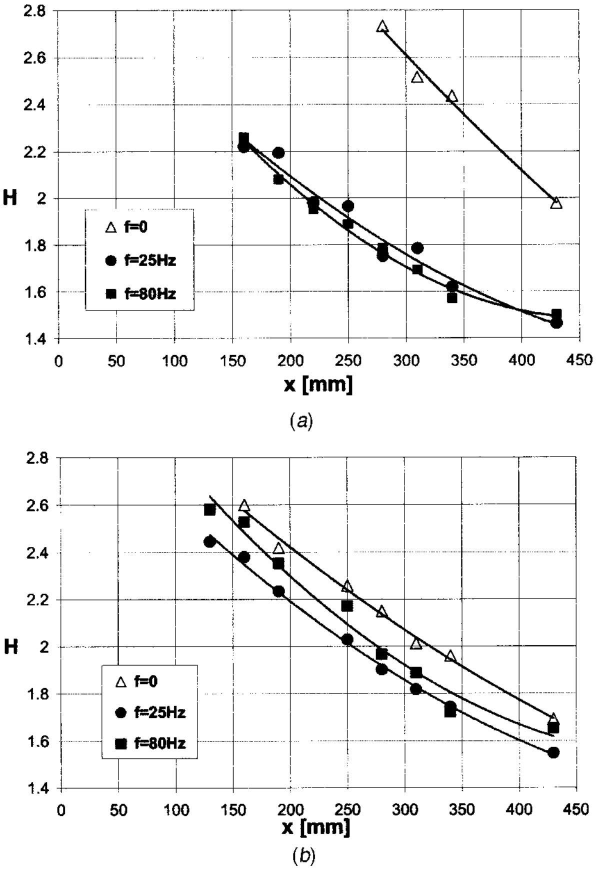

Fig. 12 The effect of periodic excitation on the boundary layer shape factor downstream of reattachment at two FST levels: (a) FST=0.4%, (b) FST=11%

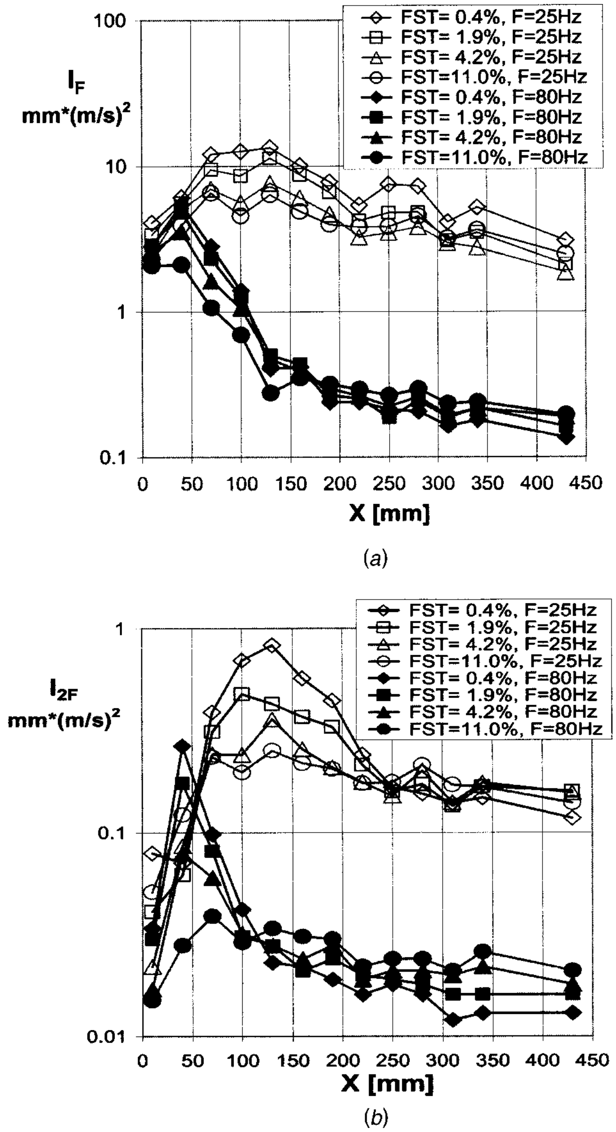

Fig. 13 The effect of FST level on oscillating *x* momentum integrated across the shear layer at the fundamental excitation frequency (a) and its harmonic (b), using $F+\approx 1$ (25 Hz) and $F+\approx 3$ (80 Hz)

increased C_f downstream of reattachment. AFC reduced the momentum loss, presumably due to a reduction in the bubble size and by affecting the Cp, distribution thus reducing the form-drag. As the FST level was increased, the relative reduction in the momentum thickness diminished, in agreement with previous observations, with the largest reduction in effectiveness noted between FST of 0.4% and FST of 1.9%. $F=80$ Hz was again more sensitive than $F=25$ Hz to elevated FST levels.

One of the benefits of using AFC for controlling the separation bubble is generating a steadier flow downstream of reattachment. An indication of this effect was found when the maximum boundary layer turbulence level vs x was evaluated [19]. At low FST and small x stations (i.e., where there was a significant reverse flow), the AFC increased the turbulence level. This was expected because the separated shear layer amplified the excitation (as will be shown in Fig. 13 and discussed in the context of that data). Furthermore, the shear layer is closer to the surface and thus pressure fluctuations will increase even if the coherent structures are not changed. The boundary layer turbulence level peaked at the reattachment region and decayed to below the maximum FST level of the uncontrolled flow downstream of reattachment. Excitation at $F=80$ Hz was more effective than excitation at $F=25$ Hz in reducing the maximum boundary layer turbulence level, but the difference between the two frequencies (and between those and the uncontrolled flow) diminished as the FST level was increased.

The magnitude of the squared streamwise velocity fluctuation associated with the fundamental excitation frequency (u_F) and its harmonic (u_{2F}) were integrated across the boundary layer in the form $I_{nF} \equiv \int_0^\delta u_{nF}^2 dy$ and are presented in Figs. 13(*a*) and 13(*b*). The boundary layer thickness is δ and $n=1$ marks the fundamental and $n=2$ its harmonic. These parameters are evaluated since they might be considered as the cause for the effectiveness of the entire AFC method. At $x=10$ mm the intensity of the fundamental excitation frequencies (Fig. 13) was similar, regardless of the frequency of excitation or the FST level. Both frequencies were amplified up to $x\approx 40$ mm and FST$<$11%. Elevated FST reduced the amplification rates (most notably those of $F=80$ Hz at FST=4% and 11%). This observation can partially explain the reduction in the effectiveness of the AFC at large FST levels. The differences between the amplitude evolution of $F=25$ Hz and that of $F=80$ Hz are very significant. However, the maximum takes place at x stations roughly corresponding to the frequency ratio (i.e., the higher frequency saturates at a lower x, in agreement with the data shown in Ref. [6]). The amplitude of $F=25$ Hz was increased up to $x=130$ mm while, $F=80$ Hz amplitudes decays for all FST levels at x greater than 40–50 mm. These differences are explained by a combination of at least two effects. First, the higher excitation frequency becomes neutrally stable closer to the LE (as shown for a free mixing layer in Ref. [6]). Second, the nonlinear modification of the mean flow which the excitation at $F=80$ Hz generates, alters the stability characteristics of the mean flow that in return causes an earlier saturation of the perturbations.

The intensities of the first harmonic of the excitation frequency [i.e., 50 Hz for $F=25$ Hz and 160 Hz for $F=80$ Hz, Fig. 13(*b*)], behave in a similar way to the fundamental suggesting that it is tied to the amplitude of the fundamental and it is probably not an independent manifestation of an instability.

The diminishing amplification of high frequencies with increasing FST level, suggests the possibility of destructive interference between the forced, predominantly two-dimensional, excitation and the random FST structures. This is especially important at the high frequencies that posses similar scales as those of the FST. In order to check this hypothesis, pairs of velocity signals were measured at varying spanwise spacing in the separated shear layer, just upstream of the leading edge (i.e., at $x=-2$ mm and $y=0$), and where the excitation reached its peak amplitude farther downstream. These data were used to evaluate the cross spectra in an attempt to quantify the effects of the elevated FST on the spanwise coherence of the excitation. The downstream measurement locations were $x=40$ mm and $y=20$ mm for $F=80$ Hz and $x=70$ mm and $y=45$ mm for $F=25$ Hz, where the amplitudes peaked. One of the hot wires was stationary at $z=-200$ mm and the other was traversed in the region $z=-195$ mm to $z=0$ mm at 10 mm increments. The minimal spanwise separation between the two wires was about 3 mm. Initially we considered the cross correlation coefficient between the two signals where the amplitudes peaked. A clear reduction in the maximum correlation coefficient, as the spanwise spacing was increased, was noted for increasing levels of FST. $F=80$ Hz was more sensitive than $F=25$ Hz to the increase of FST according to this criteria. The cross spectra of each pair of velocity signals was also calculated in order to evaluate the FST effect on the spanwise coherence of the nominally two-dimensional excitation. It could be seen that the phase of the cross spectra at $F=80$ Hz [Fig. 14(*b*)] become significantly more scattered with increased FST level than a similar phase corresponding to $F=25$ Hz [Fig. 14(*a*)]. The standard deviation of the phase about the spanwise averaged mean for $F=25$ Hz was approximately 0.04-rad for FST≈0.4%, 0.077 rad at FST≈1.9%, and it increased to about 0.13 rad at FST≈4.2% and 11.0%. For $F=80$ Hz the standard deviation of the phase about the spanwise averaged mean was about 0.05 rad for FST≈0.4%, 0.09 rad at FST≈1.9%, and it increased to 0.25 rad at 11.0% (note that only the FST=0.4% and 11% FST data are shown in Fig. 14). The FST had a negligible effect on the scatter of the phase coherence at the leading edge [Figs. 14(*a*) and 14(*b*), $x=-2$ mm data] especially for $F=80$ Hz excitation that is otherwise more sensitive to FST. This indicates a possibility of destructive interference between the free-stream turbulence and the excitation, reducing its spanwise coherence particularly when the scales of the excitation and the FST are comparable. The amplitudes of the cross spectra and the power spectral densities of the excitation amplitude were not reduced. It could only be speculated that the decrease of the spanwise coherence due to the elevated FST reduced the effectiveness of the periodic excitation in controlling the separation bubble. It should be noted that the velocity fluctuations associated with the excitation are of the same order as the typical vortices in the free stream, for the highest FST level tested. Therefore, a nonlinear interaction is possible.

4 Conclusions

The effects of elevated Free-Stream Turbulence (FST) on controlling a separation bubble through the use of periodic excitation (AFC) were studied experimentally. It was found that the bubble is very receptive to two-dimensional periodic excitation. The bubble dimensions were significantly reduced with effective excitation at reduced frequencies (based on the bubble length and free stream velocity) in the range 1–3. The bubble height and length are also reduced by elevated FST. However, even at the highest FST level of 11%, the bubble was still present in the uncontrolled flow. The effectiveness of the current AFC method, using periodic excitation was noticeable even at the highest FST levels, but the efficacy of the AFC was reduced due to the elevated FST. The reduced effectiveness is attributed to a phase randomization by the FST on the coherence of the nominally two-dimensional periodic excitation.

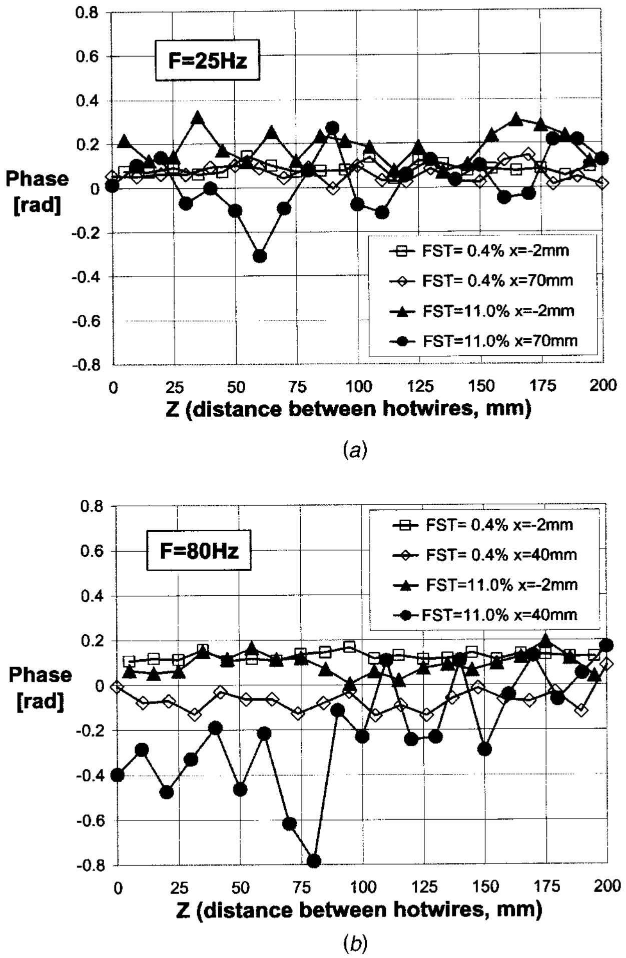

(*a*)

(*b*)

Fig. 14 The effect of FST level on the phase of the velocity cross spectral density at the excitation frequency. Data taken at maximum amplitude location [$x=70$ mm for $F=25$ Hz, (a) and $x=40$ mm for $F=80$ Hz, (b)] and just upstream of the LE ($x=-2$ mm)

Future research could include a real-time identification scheme to capture the structure of the incoming FST and adjust the amplitude and phase of the periodic excitation to generate an effective closed-loop control needed to overcome the phase-randomization by the FST. If higher control authority would be available (i.e., higher 2D amplitudes or 3D unsteady excitation modes), it is possible that the excitation will maintain its effectiveness even at high FST. Additionally, it is worth exploring a 2D excitation that emanates from the plate rather than from the sidewall in order to eliminate any possibility of phase randomization upstream of the leading edge and to investigate separation bubble that forms farther downstream of the leading edge, with a thicker laminar boundary layer upstream of separation.

Acknowledgments

The experiments were conducted in the Steve and Mary Meadow Aerodynamics laboratory at Tel-Aviv University and sponsored in part by the Lazarus and Meadow funds. This project was also sponsored in part by a contract from NASA Glenn Research Center (C-72101-K) and monitored by Dr. David Ashpis.

References

[1] Hillier, R., and Cherry, N. J., 1981, ''The Effects of Stream Turbulence on Separation Bubbles,'' J. Wind. Eng. Ind. Aerodyn., **8**, pp. 49–58.

[2] Castro, I. P., and Haque, A., 1988, ''The Structure of a Shear Layer Bounding a Separation Region. Part 2: Effects of Free-Stream Turbulence,'' J. Fluid Mech., **192**, pp. 577–595.

[3] Kalter, M., and Fernholz, H. H., 2001, ''The Reduction and Elimination of a Closed Separation Region by Free Stream Turbulence,'' J. Fluid Mech., **446**, pp. 271–308.

[4] Chang, P. K., 1976, *Control of Separation*, McGraw–Hill, New York.

[5] Oster, D., and Wygnanski, I., 1982, ''The Forced Mixing Layer Between Parallel Streams,'' J. Fluid Mech., **123**, p. 91.

[6] Roos, F. W., and Kegelman, J. T., 1986, ''Control of Coherent Structures in Reattaching Laminar and Turbulent Shear Layers,'' AIAA J., **24**, pp. 1956–1963.

[7] Fiedler, H. E., and Fernholz, H. H., 1990, ''On Management and Control of Turbulent Shear Flows,'' Prog. Aerosp. Sci., **27**, pp. 305–387.

[8] Sigordson, L. W., 1995, ''The Structure and Control of a Turbulent Reattaching Flow,'' J. Fluid Mech., **298**, pp. 139–165.

[9] Kiya, M., Shimizu, M., and Mochizuki, O., 1997, ''Sinusoidal Forcing of a Turbulent Separation Bubble,'' J. Fluid Mech., **342**, pp. 119–139.

[10] Nishri, B., and Wygnanski, I., 1998, ''Effects of Periodic Excitation on Turbulent Separation From a Flap,'' AIAA J., **36**, pp. 547–556.

[11] Seifert, A., and Pack, L. G., 2002, ''Active Control of Separated Flow on a Wall-Mounted Hump at High Reynolds Numbers,'' AIAA J., **40**, pp. 1363–1372.

[12] Hinze, *Turbulence*, 1975, 2nd ed., Fig. 3-25b, p. 271.

[13] Greenblatt, D., and Wygnanski, I., 2000, ''Control of Separation by Periodic Excitation,'' Prog. Aerosp. Sci., **37**, pp. 487–545.

[14] Seifert, A., Bachar, T., Koss, D., Shepshelovits, M., and Wygnanski, I., 1993, ''Oscillatory Blowing, a Tool to Delay Boundary Layer Separation,'' AIAA J., **31**, pp. 2052–2060.

[15] Mabey, D. G., 1972, ''Analysis and Correlation of Data on Pressure Fluctuations in Separated Flow,'' J. Aircr., **9**, pp. 642–645.

[16] Kiya, M., and Sasaki, K., 1983, ''Free Stream Turbulence Effects on a Separation Bubble,'' J. Wind. Eng. Ind. Aerodyn., **14**, pp. 375–386.

[17] Ho, C. H., and Huerre, P., 1984, ''Perturbed Free Shear Layers,'' Annu. Rev. Fluid Mech., **16**, pp. 365–424.

[18] Cherry, N. J., Hillier, R., and Latour, M. E. M. P., 1984, ''Unsteady Measurements in a Separated and Reattaching Flow,'' J. Fluid Mech., **144**, pp. 13–46.

[19] Halfon, E., Nishri, B., Seifert, A., and Wygnanski, I., 2001, ''Effects of Elevated Free Stream Turbulence on Active Flow Control of a Separation Bubble,'' Final report on contract C-72101-K submitted to NASA GRC (Dr. D. Ashpiz).

Mark F. Tachie
Department of Mechanical and Industrial Engineering,
University of Manitoba,
Winnipeg, Canada R3T 5V6
e-mail: tachiemf@cc.umanitoba.ca

Donald J. Bergstrom
Department of Mechanical Engineering,
University of Saskatchewan,
Saskatoon, Canada S7N 5A9

Ram Balachandar
Department of Civil & Environmental Engineering,
University of Windsor,
Windsor, Canada N9B 3P4

Roughness Effects on the Mixing Properties in Open Channel Turbulent Boundary Layers

This paper investigates the effects of surface roughness on the transport and mixing properties in turbulent boundary layers created in an open channel. The measurements were obtained on a smooth and two different types of rough surfaces using a laser Doppler anemometer. The results show that surface roughness enhances the levels of the turbulence kinetic energy, turbulence production, and diffusion over most of the boundary layer. The distributions of the eddy viscosity and mixing length are also strongly modified by surface roughness. Furthermore, the extent to which surface roughness modifies the turbulence structure depends on the specific geometry of the roughness elements.

[DOI: 10.1115/1.1792265]

Introduction

Many systems of environmental and engineering interest have surfaces that are rough. Examples include flow over turbine blades, aircraft wings, riverbeds, and flow in heat exchangers and piping networks. Surface roughness, in addition to increasing the skin friction characteristics, has significant effects on convective heat and mass transport rates in the flow. Therefore, an adequate understanding of roughness effects on the mean and turbulence characteristics is required to improve engineering design practices.

The analysis of turbulent flow over rough surfaces is significantly more complex than that for a smooth surface. For example, the protrusion of the roughness elements into the surrounding flow complicates its interaction with the flow both in terms of the mean velocity and turbulence quantities. The problem of roughness is further complicated by the fact that the geometry and length scales of the roughness elements encountered in practice vary widely, e.g., from well-defined geometry such as regularly spaced ribs to random roughness such as terrain roughness and manufacturing roughness of turbine blades [1]. For these reasons, the structure of rough-wall turbulent flows becomes difficult to generalize in a way that requires a minimal description of the surface geometry. In spite of the complex characteristics of surface roughness mentioned above, the wall similarity hypothesis proposed by Townsend [2] and modified by Raupach, Antonia, and Rajagopalan [3] suggests that roughness effects are confined to the roughness sublayer (about five roughness heights) so that the mixing properties in smooth- and rough-wall turbulent flows should be similar outside the roughness sublayer.

Given their practical importance and complexity, several experimental studies have been conducted to advance our understanding of rough wall turbulent flows, e.g., Krogstad and Antonia [4], Tachie, Bergstrom, and Balachandar [5], Ligrani and Moffat [6,7], and Mazouz, Labraga, and Tournier [8]. However, conclusions drawn in prior works regarding roughness effects on the mean and turbulence quantities are not consistent. For example, the measurements reported by Krogstad and Antonia [4], Tachie Bergstrom, and Balachandar [9] and Bergstrom, Kotey, and Tachie [10] over different types of rough surfaces indicate that surface roughness increases the strength of the wake parameter, π, and the levels of the turbulence intensities and Reynolds shear stress. On the other hand, several other studies including the measurements obtained in rough-wall channel flows by Mazouz, Labraga, and Tournier [8] and Bakken and Krogstad [11] conclude that roughness reduces the level of the Reynolds stresses. In most of the prior rough wall measurements, only mean velocity and Reynolds stresses were reported, and so roughness effects on turbulence diffusion and other mixing characteristics in turbulent boundary layers are still poorly understood.

Numerical prediction of rough-wall turbulent flows has also received considerable research attention over the past three decades. Cebeci and Chang [12], Krogstad [13], and many others applied mixing length and eddy viscosity models to predict the characteristics of the mean flow over rough surfaces. More recently, Zhang, Faghri, and White [14], Patel [15], Durbin et al. [16], and Akinlade and Bergstrom [17] applied two-equation turbulence models, i.e., k-ε and k-ω, to predict the mean and turbulence characteristics in rough-wall turbulent flows. However, a critical review of the present state of knowledge will indicate that our ability to accurately predict the turbulence quantities in rough-wall turbulent flow is deficient compared with the success achieved in modeling turbulent flows over a smooth surface.

Most of the previous experimental and numerical works on surface roughness dealt with zero-pressure gradient turbulent boundary layers and duct flows. Although an adequate understanding of roughness effects on the transport and mixing of pollutants such as wastewater and oil discharged from industries or catastrophes into river systems is important from environmental point of view, only little information is available. In our previous work [5] we reported mean and fluctuating components of the streamwise velocity over smooth and three geometrically different types of surface roughness (sand grains, wire mesh, and perforated plate) in an open channel. The present study documents the effects of surface roughness on the Reynolds stresses, turbulence kinetic energy, turbulence production and diffusion, and the distributions of eddy viscosity and mixing length in an open channel flow.

Experimental Setup and Procedure

The experiments were performed in an open channel flume. The channel was 10 m long, 0.8 m wide and 0.6 m deep. A schematic of the channel is shown in Figs. 1*a* and 1*b*. The sidewalls of the flume were made of tempered glass to facilitate optical access and flow visualization. To ensure a rapid development of turbulent boundary layer, a trip was located 4 m downstream of the contraction spanning the width of the flume. The trip was composed of 3 mm (median diameter) pebbles glued to the bottom of the channel as a 40 mm long strip. The measurements were obtained on a hydraulically smooth surface and the following two different types of surface roughness: (1) a 1.2-mm medium diameter sand

---

Contributed by the Fluids Engineering Division for publication in the JOURNAL OF FLUIDS ENGINEERING. Manuscript received by the Fluids Engineering Division October 25, 2002; revised manuscript received April 5, 2004. Associate Editor: M. W. Plesniak.

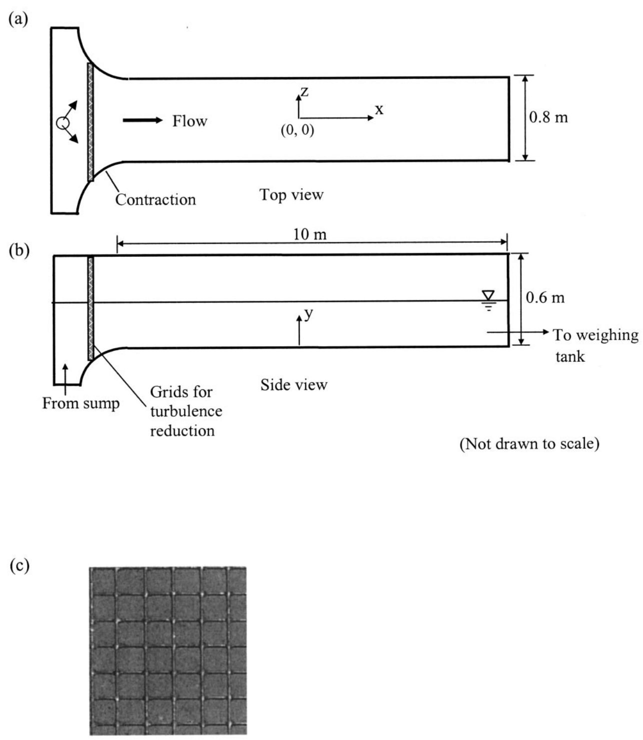

Fig. 1 (***a***), (***b***) **Schematics of the open channel; (*c*) photograph of wire-mesh roughness**

Table 1 Typical uncertainty estimates

Measured quantity	Uncertainty
y	± 0.025 mm
δ	± 2.5 mm
θ	$\pm 5\%$
U	$\pm 1\%$
U_τ	$\pm 2.5\%$ for smooth surface $\pm 5\%$ for a rough surface
π	± 0.05
u^2, v^2, $\langle uv \rangle$	$\pm 10\%$
$\langle u^2 v \rangle$, $\langle v^3 \rangle$	$\pm 12\%$

grain roughness coated on to a 1.75-m-long plywood sheet using double-sided tape, and (2) a 1.3-m-long (welded) stainless-steel wire mesh made of 0.6-mm wires with 7.0-mm centerline spacing, giving a ratio of centerline spacing to wire diameter of about 12. A photograph of a section of the wire mesh is shown in Fig. 1*c*. The sand grains were packed on the tape to yield the most dense arrangement.

The velocity measurements were obtained using four-beam two-component fiber-optic LDA (Dantec Inc.) system operated in a backscatter mode. The system was powered by a 300-mW argon-ion laser (Ion Laser Technology). The optical elements included a 40-MHz Bragg cell, a 1.96 beam expansion unit and a 500-mm focusing lens. The probe volume for the present configuration was $0.12 \times 0.12 \times 1.4$ mm^3. The fiber optic probe was mounted on a three-dimensional traversing mechanism. Each direction of the traversing mechanism was stepper-motor driven and controlled by a computer. Because of the four-beam arrangement of the LDA system, it was not possible to obtain a two-component LDA system close to the wall. Therefore, in addition to two-component measurements, one-component measurements were also made so that the streamwise component of the velocity field could be measured close to the wall. Detailed uncertainty analysis was carried out and typical estimates at 95% confidence level are shown in Table 1.

The depth of flow was kept at $h = 120$ mm in all the experiments. The freestream velocity was $U_e \approx 50$ cm/s so as to minimize Froude number effects. The acceleration parameter $K = (\nu/U_e^2)(dU_e/dx)$ was estimated to be 0.15×10^{-6}, and the turbulence intensity at the edge of the boundary layer was approximately 2.2%. A summary of the important flow parameters is given in Table 2, where U_e is the local maximum velocity, δ and θ are the boundary layer and momentum thickness, respectively, Re_θ is the Reynolds number based on U_e and θ, U_τ is the friction velocity, π is the Coles wake parameter, Re_k is the roughness Reynolds number based on the average roughness height and U_τ, ΔU^+ is the downward shift in the logarithmic profile due to wall roughness, and $k_s^+ (= k_s U_\tau/\nu)$ is the dimensionless equivalent sand-grain roughness height. Using the equivalent sand-grain roughness heights, we estimate $5k_s/\delta \approx 0.1$ for the sand grains and $5k_s/\delta \approx 0.2$ for the wire mesh. Therefore, the effect of the wire mesh roughness is expected to extend further into the outer layer than the sand grains although the physical size of the sand grains (1.2 mm) is twice the wire diameter (0.6 mm).

For the smooth wall, the friction velocity, U_τ, was determined by fitting to mean velocity data in the viscous sublayer [10,18]. For the sand grains and wire mesh roughness, a profile matching technique, following Krogstad, Antonia, and Browne [19], was used to determine U_τ, π, and the location of the virtual origin (y_o). That is, a mean-velocity defect profile that describes the logarithmic region and the wake component was written in the form below:

$$\frac{U}{U_e} = 1 + \frac{U_\tau}{\kappa U_e}\left\{ \ln\left(\frac{y+y_o}{\delta}\right) - (1+6\pi)\left[1-\left(\frac{y+y_o}{\delta}\right)^2\right] + (1+4\pi) \times \left[1-\left(\frac{y+y_o}{\delta}\right)^3\right]\right\}, \qquad (1)$$

where $\kappa = 0.41$. For each data set, the values of y_o, U_τ, and π were optimized (in a least-square sense) to achieve a good agreement between Eq. (1) and the experimental data set. Additional details of the profile matching techniques are available in Krogstad, Antonia, and Browne [19] and Tachie, Bergstrom, and Balachandar [5]. Because the profile-matching technique allows data over the entire boundary layer (i.e., $y \leqslant \delta$) to be fitted and the value of π to be optimized, it provides more reliable estimates of U_τ and π than would be obtained from the classical logarithmic law or Hama's formulation. Equation (1) was also applied to determine the value of U_τ and π for the smooth-wall data. The value of $\pi = 0.1$ obtained for the smooth surface is lower than values reported for zero-pressure gradient turbulent boundary layers at similar Reynolds numbers. The value of $\pi = 0.1$ is, however, consistent with previous open channel flow measurements [20,21]. The values of π for the rough surfaces (Table 2) are higher than for the smooth surface. This is an indication that surface roughness effects extend into the outer region of the mean flow.

Results and Discussion

Mean Velocity Profiles. The mean velocity profiles in outer coordinates are shown in Fig. 2*a*. The effect of surface roughness on the mean velocity profile in the wall region of an open channel flow is the same as observed in zero-pressure gradient turbulent boundary layers [4,9]. That is, the rough-wall profiles are "less full" compared with the smooth-wall profile. Close to the free surface, however, each profile shows a slight dip so that the local maximum velocity, U_e, occurs below the free surface. The mean velocity gradient $\partial U/\partial y$ is slightly negative in the region $y > \delta$.

Figure 2*b* shows the mean velocity profiles in inner coordinates. The dashed lines represent the logarithmic profiles, with the appropriate roughness shift (ΔU^+) for the rough-wall data. The logarithmic law constants used in this study are $\kappa = 0.41$ and $B = 5.0$. The solid lines represent polynomial fits to the experimen-

Table 2 Test conditions and boundary layer parameters

Test	U_e (cm/s)	δ (mm)	θ (mm)	Re_θ	U_τ (cm/s)	ΔU^+	π	Re_k	k_s^+
Smooth	49.2	38	3.87	1900	2.23		0.10		
Sand grains	53.1	37	4.11	2180	2.73	4.0	0.30	33	20
Wire mesh	53.4	38	4.91	2600	2.90	6.5	0.52	17	44

tal data. The curve fits match the experimental data reasonably well, and were differentiated and smoothed to obtain estimates of $\partial U^+/\partial y^+$. Consistent with the values of ΔU^+ and π summarized in Table 2, deviation of the experimental data from the smooth-wall logarithmic profile and the wake region is higher for the wire mesh than for the sand grains. The values of $\partial U^+/\partial y^+$ are higher for the rough-wall data than for the smooth-wall data outside the overlap region.

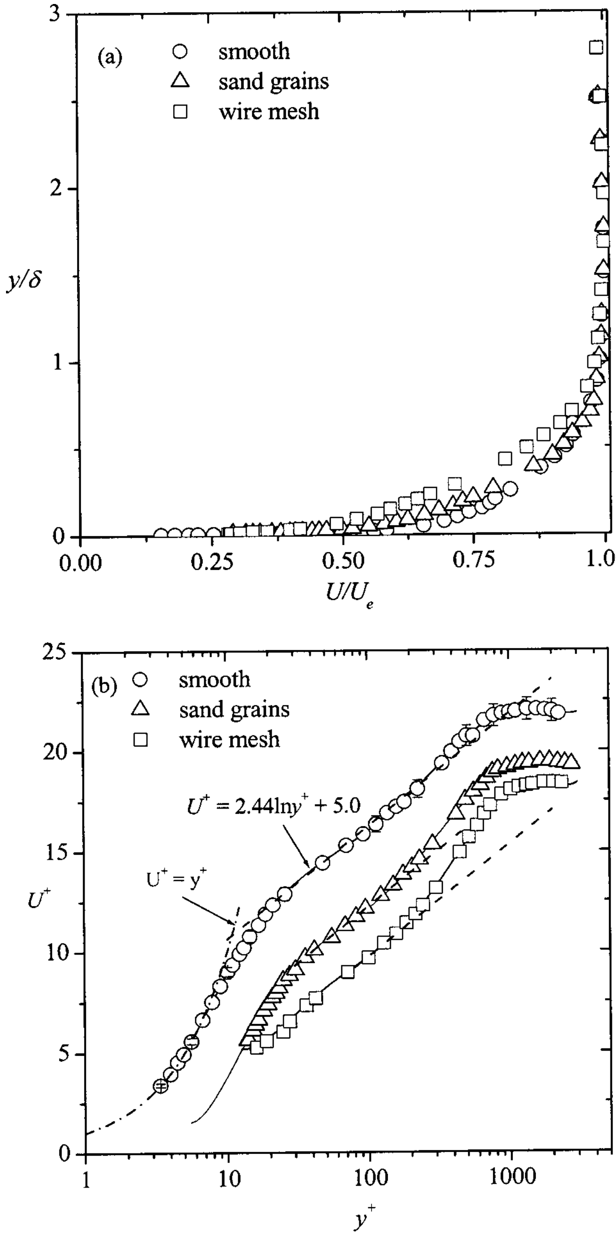

Fig. 2 Effects of surface roughness on the mean velocity profiles: (*a*) outer coordinates (uncertainty in U/U_e: ±2%, y/δ: ±5%); (*b*) inner coordinates (uncertainty in U^+: ±5%, y^+: ±5%). Dashed lines denote logarithmic profiles; solid lines are polynomial fits to data.

Reynolds Stresses. The velocity scale, U_τ^2, is generally used to normalize the Reynolds shear stress $(-\langle uv\rangle)$; however, there is no consensus on the correct scaling parameter for the Reynolds normal stresses (u^2,v^2,w^2). In most of the prior boundary layer studies, U_τ^2 was applied to normalize the normal stresses as well. George and Castillo [22] used the asymptotic invariance principle to show that, for a smooth-wall zero-pressure gradient (ZPG) turbulent boundary layer, U_e^2 is the correct scaling parameter for the normal stresses. On the other hand, the recent comprehensive local density approximation (LDA) measurements by DeGraaff and Eaton [23] demonstrated that mixed scaling (U_eU_τ) is better for the streamwise normal stresses (u^2), and U_τ^2 is appropriate for scaling the wall-normal normal stresses (v^2). In this work, we applied U_τ^2 to normalize the Reynolds shear stresses. For the normal stresses, U_τ^2, U_e^2 and U_eU_τ are used to interpret the data. As noted earlier, the four-beam LDA system used in this study did not permit reliable v^2 and $\langle uv\rangle$ data to be obtained in the very near-wall region.

The normal stresses (u^2 and v^2) normalized by U_τ^2 are shown in Fig. 3*a*. For the present smooth-wall data, u^2 profiles obtained using one-component (dashed lines) and two-component (symbols) LDA systems are plotted. With the one-component system, the peak and very near-wall region of u^2 could be measured. The two u^2 datasets (i.e., u^2 obtained using one-component and two-component systems) collapse within measurement uncertainties. The ZPG smooth-wall data reported by DeGraaff and Eaton [23] (Re_θ=1430) and previous wire-mesh data [4] (also in ZPG) are shown for comparison. It should be noted that the specific geometry of the wire mesh used in this and that used in Ref. [4] are different. That is, welded wire-mesh was used in this study, while woven wire mesh was used in Ref. [4]. Also, the ratio of centerline spacing to wire diameter is 12 in the present study and 4.6 in Ref. [4]. The smooth-wall u^2/U_τ^2 profiles obtained in this study and prior study [23] are in good agreement in the inner region $(y/\delta<0.15)$. The present wire-mesh profile is higher than the other datasets, including previous [4] wire-mesh data, in the region $0.1<y/\delta<0.4$.

Figure 3*a* also demonstrates that values of v^2/U_τ^2 obtained by DeGraaff and Eaton [23] are only slightly higher than the present smooth-wall data. The sand-grain data do not deviate significantly from the smooth-wall data set, but the wire-mesh profiles (both present and previous [4]) are distinctly higher than the smooth-wall data in the region $y/\delta<0.3$.

Figure 3*b* shows the distributions of u^2/U_e^2 and v^2/U_e^2 obtained in the present work and by DeGraaff and Eaton [23]. The use of U_e^2 as scaling parameter demonstrates more pronounced roughness effects on the normal stresses than U_τ^2, and the level of enhancement due to surface roughness occurs over most of the boundary layer $(y/\delta\leqslant 0.5)$. Furthermore, the shape of the u^2 profiles varies from one surface to the other. Application of the mixed scaling (Fig. 3*c*) also indicates that surface roughness increases the level of u^2/U_eU_τ compared to the smooth-wall case.

Figure 3*d* shows $-\langle uv\rangle/U_\tau^2$ profiles obtained in this work and

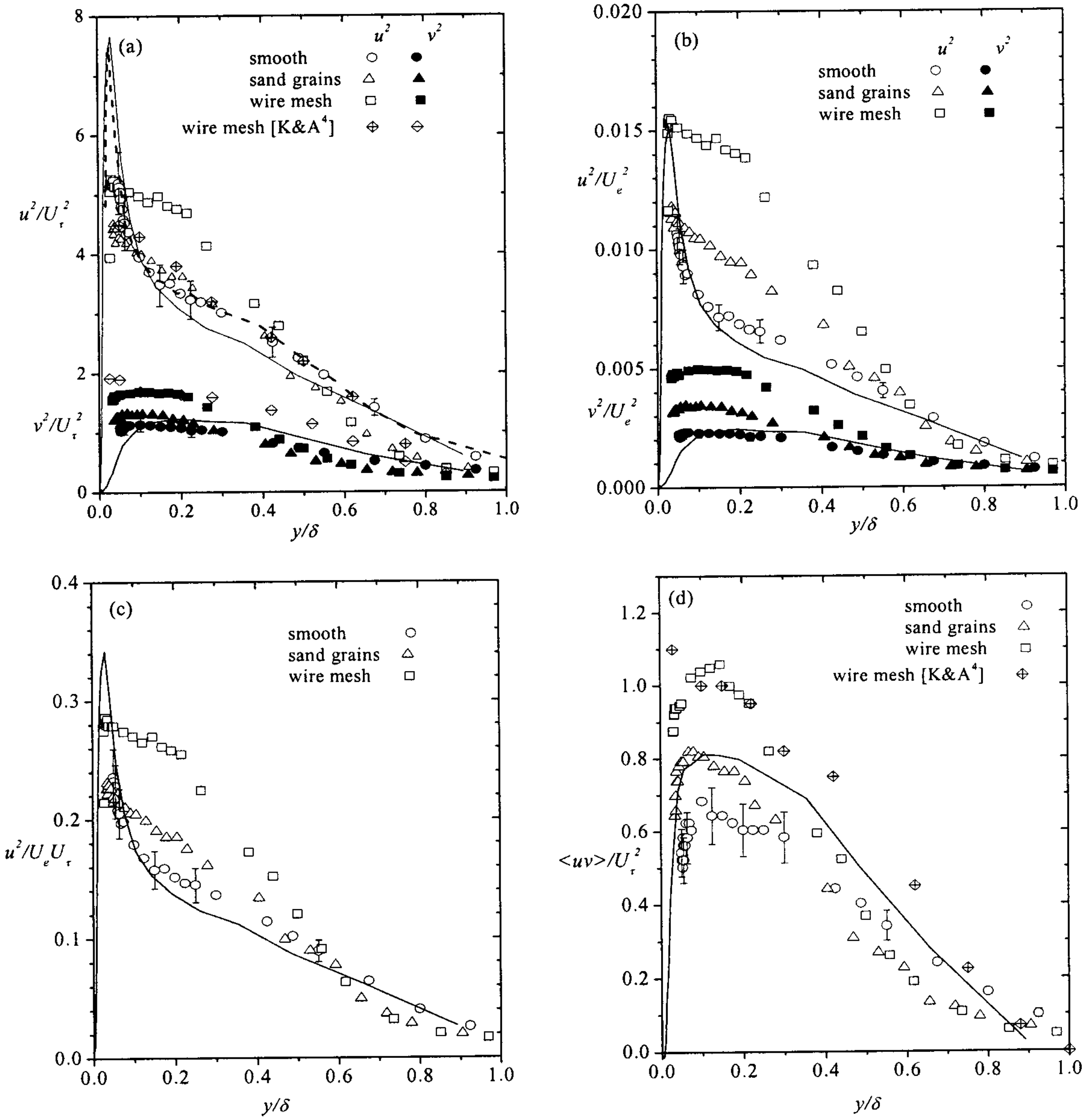

Fig. 3 Distributions of Reynolds stresses on smooth and rough surfaces (uncertainty in normalized u^2, v^2, $\langle uv \rangle$: ±12%, y/δ: ±5%). K&A denotes Krogstad & Antonia [4]. Dashed line denotes u^2/U_τ^2 obtained using one-component LDA system; solid line denotes data by DeGraaff and Eaton [23].

previous smooth-wall [23] and wire-mesh [4] data sets. The peak value of the present smooth-wall profile is 0.65 compared with 0.8 in Ref. [23]. At high Reynolds numbers, the peak value of $\langle uv \rangle/U_\tau^2$ should be approximately 1. Because the smooth-wall normal stresses (u^2/U_τ^2 and v^2/U_τ^2) in this study and in Ref. [23] compare reasonably well in the near-wall region, the low level of $\langle uv \rangle/U_\tau^2$ is not due to error in U_τ. In a previous study, Johnson and Barlow [24] studied the effects of spanwise extent of LDA probe volume on u/U_τ, v/U_τ, and $\langle uv \rangle/U_\tau^2$. They concluded that a larger probe volume underestimates $\langle uv \rangle/U_\tau^2$ in the wall region, but u/U_τ and v/U_τ are not affected by the probe volume dimension. For the probe volume dimension used in this study, the results of Johnson and Barlow [24] would indicate a 12% underestimation of $\langle uv \rangle$ in the wall region of our smooth- and rough-wall data. Such a correction would marginally improve the agreement between the present smooth-wall data and the previous LDA data [23], but the corrected data will still be much lower than those obtained in typical high-Reynolds-number experiments. The low level of $\langle uv \rangle/U_\tau^2$ in the near-wall region of the present smooth data may be partly due to large probe volume extent, low-Reynolds-number effect, and probably secondary flow. Because the same probe was used in all the present experiments, and the Reynolds numbers for the smooth- and rough-wall data do not vary much, the differences among the profiles in Fig. 3*d* may be attributed to roughness effect. Thus, we conclude from Fig. 3*d* that surface roughness increases the Reynolds shear stress over a significant portion of the flow, with the wire-mesh data sets (present and in Ref. [4]) showing the largest increase.

Turbulence Kinetic Energy and Triple Correlations. The turbulence kinetic energy ($2k$) is shown in Fig. 4*a*. Because the spanwise stress (w^2) was not measured in the present study, only the sum of the streamwise and wall-normal components (i.e., $2k \approx u^2+v^2$) is reported. The shape of the smooth-wall profile is similar to classical boundary layer measurements (e.g., Fig. 7–20 in Hinze [25]). The rough-wall profiles are distinctly different

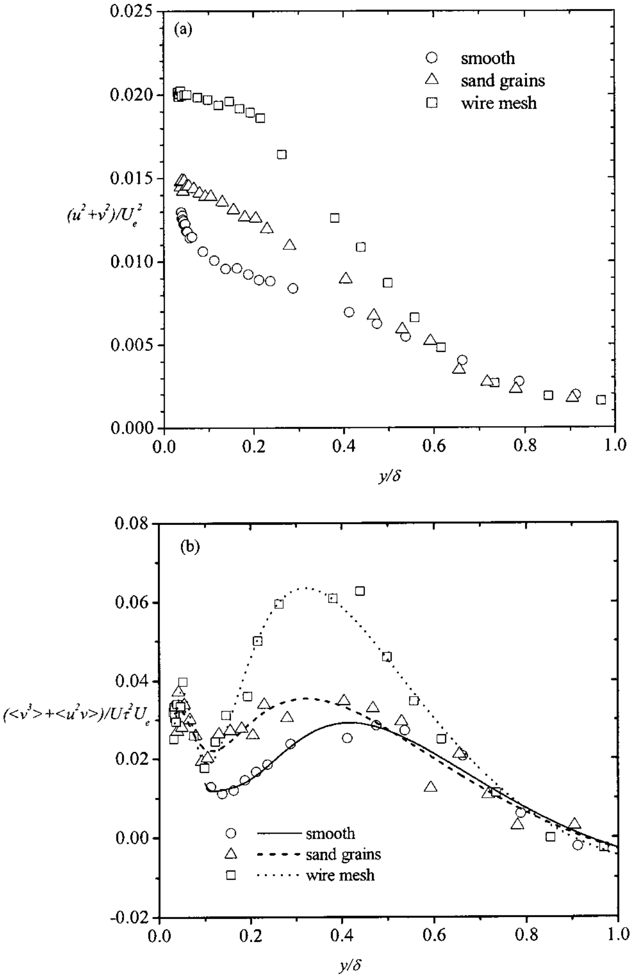

Fig. 4 (*a*) Distribution of approximate turbulence kinetic energy ($2k\approx u^2+v^2$) (uncertainty in normalized k: ±12%, y/δ: ±5%). (*b*) Distribution of major turbulence diffusion terms ($\langle v^3\rangle+\langle u^2v\rangle$) (uncertainty: ±15%).

from the smooth-wall data both in shape and magnitude. For instance, the levels of turbulence kinetic energy on the rough surfaces are higher than those for the smooth surface, and these differences persist up to $y/\delta\approx 0.5$.

The triple correlations are important turbulence statistics because their gradients are associated with the transport of turbulence kinetic energy. The following triple products were measured and reported by Tachie [18]: $\langle u^3\rangle$, $\langle v^3\rangle$, $\langle u^2v\rangle$, and $\langle v^2u\rangle$. In this work only the term ($\langle u^2v\rangle+\langle v^3\rangle$), which represents turbulence transport of $\langle u^2\rangle$ and $\langle v^2\rangle$, respectively, in the wall-normal direction, is shown. This term is also the major contributor to the turbulence diffusion term in the energy budget. As shown in Fig. 4*b*, the profiles have two peaks; one inside the inner region and the other in the outer region. The rough-wall profiles are higher than the smooth-wall data over most of the boundary layer. It appears roughness effects on the triple correlation are more pronounced in the intermediate region where the outer peak for the wire-mesh data is, for example, more than twice as high as the corresponding smooth wall value. The figure also shows that as the roughness effect increases, the location of the outer peak is closer to the wall.

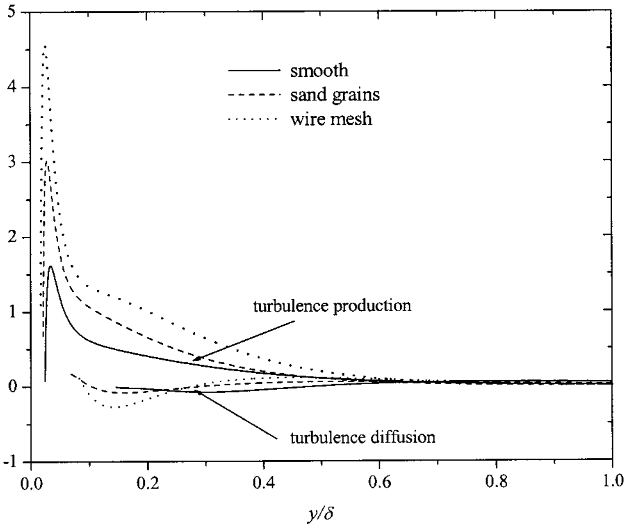

Fig. 5 Effects of surface roughness on turbulence production ($-\langle uv\rangle\partial U/\partial y$) and diffusion [$0.75\partial(\langle u^2v\rangle+\langle v^3\rangle)/\partial y$] (uncertainty in budget terms: ±15%)

Turbulence Production and Diffusion. Because a two-component LDA system was used in this study, all the terms in the energy budget could not be measured directly. Therefore, only the turbulence production and diffusion terms were estimated and reported. The mean flow was approximately two-dimensional and so continuity requires that $\partial U/\partial x\approx -\partial V/\partial y$. The production terms $u^2\partial U/\partial x(\approx -u^2\partial V/\partial y)$, $v^2\partial V/\partial y$, and $-\langle uv\rangle\partial U/\partial y$ were measured directly. It was found that the sum of the terms $-u^2\partial V/\partial y$ and $v^2\partial V/\partial y$ is negligible compared with the shear production $-\langle uv\rangle\partial U/\partial y$ [18]. Thus, only the main contributor to turbulence production ($-\langle uv\rangle\partial U/\partial y$) is reported. Following previous turbulent boundary layer studies [4], the turbulence diffusion term was approximated by $0.75\partial(\langle u^2v\rangle+\langle v^3\rangle)/\partial y$, which was measured directly. Although the set of measurements reported in this study is not complete enough to evaluate all of the terms in the transport equation for the turbulent kinetic energy, *k*, given the general scarcity of data on roughness effects and the strong effects of roughness observed on the Reynolds stresses, turbulence kinetic energy, and triple products, it was thought appropriate to estimate the effect of roughness on the diffusion and production terms in the turbulence kinetic energy equation. This information would be helpful for modelers as they begin to introduce roughness effects in two-equation and Reynolds stress transport equation closures. The terms considered in the following discussion are obtained by fitting curves to the experimental data. Following the analysis by George and Castillo [22], the terms are normalized by $U_\tau^2U_e/\delta$.

Figure 5 shows that surface roughness significantly increases the level of turbulence production over most of the boundary layer. This may be partly due to the higher Reynolds shear stress observed for the rough surfaces (Fig. 3*d*) and higher values of $\partial U^+/\partial y^+$ outside the overlap region. Although the diameter of the wire mesh is only 50% of the nominal diameter of the sand grains, the production term obtained over the wire mesh is distinctly higher than that over the sand grains. This clearly demonstrates that the specific geometry of the roughness elements has an important effect on the mechanism responsible for turbulence production. The diffusion term is also strongly modified by surface roughness. This term is negative, i.e., loss, in the region $0.2\leq y/\delta\leq 0.5$ for the smooth surface, and $0.1\leq y/\delta\leq 0.3$ for the rough surfaces. Outside these regions, the profiles are positive (gain). In each case, the diffusion term cannot be neglected close to the wall.

Mixing Length and Eddy Viscosity. Although the methodology of modeling turbulent flows via the mixing length and eddy viscosity fails to incorporate the exact physical processes, it has

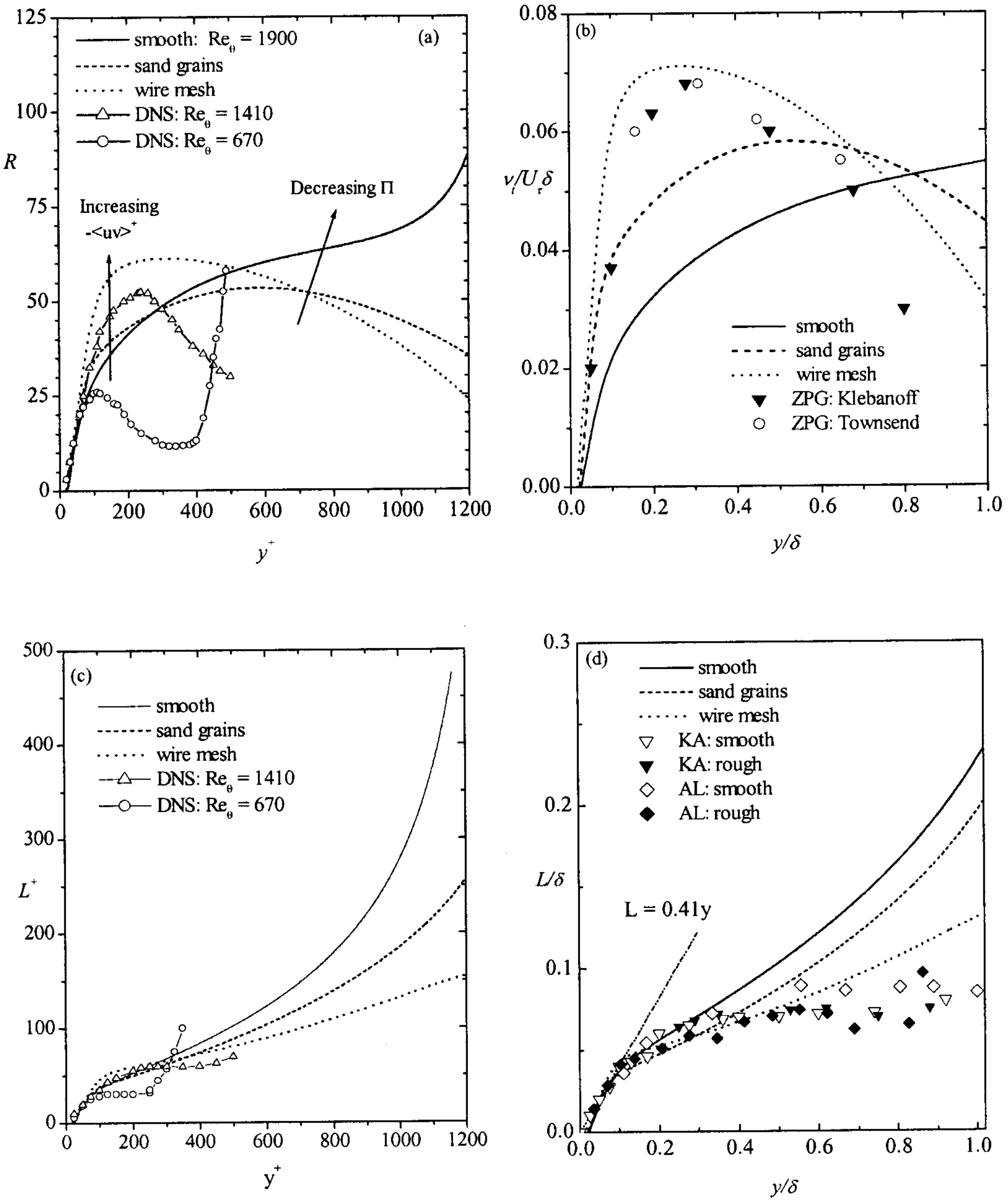

Fig. 6 (***a***), (***b***) **Distribution of eddy viscosity on smooth and rough surfaces (uncertainty: ±15%).** (***c***), (***d***) **Distribution of mixing length on smooth and rough surfaces (uncertainty: ±15%). K&A denotes Krogstad & Antonia [4]; AL denotes Antonia and Luxton [23].**

been successful in predicting some of the flow characteristics in simple shear flows on smooth and rough surfaces [26,27]. Furthermore, one-equation eddy-viscosity models have recently regained popularity as components of two-layer turbulence models, where an eddy viscosity model is used to resolve the near-wall region and more general models such as Reynolds-stress-equation models are employed outside the wall region [28]. Within this context, the present study also documents the effects of surface roughness on the distributions of the mixing length and eddy viscosity. Since the mixing length and eddy viscosity depend on the relative magnitude of $\langle uv \rangle$ and $\partial U/\partial y$, we first discuss roughness effects on the parameter $R = -\langle uv \rangle^+/\partial U^+/\partial y^+$. The parameter R can also be interpreted as the ratio of eddy viscosity (ν_t) to molecular viscosity (ν), i.e. $R = \nu_t/\nu$. According to Rodi, Mansour, and Michelassi [26], this quantity is an indicator of the influence of viscous effects in simple shear flows, i.e., whether Reynolds-number effects are important or not. Within the context of two-layer turbulence models, the value of $R = \nu_t/\nu$ is sometimes used to establish the interface between the one-equation and two-equation regions. For example, Rodi [28] proposed a value of $R \geqslant 36$ for the changeover from one- to two-equation region.

The values of R for the present data sets and those deduced from Spalart's DNS results at $\mathrm{Re}_\theta = 670$ and 1410 (Rodi, Mansour, and Michelassi [26]) are shown in Fig. 6*a*. As mentioned earlier, $\langle uv \rangle$ data could not be obtained very close to the wall in the present work due to hardware limitation. It should be noted that the DNS data at $\mathrm{Re}_\theta = 670$ never attained a value of $R = 36$ in the wall region; this suggests a significant low-Reynolds-number effect. Compared with the DNS results at $\mathrm{Re}_\theta = 1410$, the present smooth-wall profile indicates a low-Reynolds-number effect over most of the wall region. This observation is consistent with the data shown in Fig. 3*d* where we observed that the peak of

$\langle uv \rangle/U_\tau^2$ is less than the asymptotic value observed in high-Reynolds-number near-wall turbulent flows over a smooth surface.

Some important similarities and differences can be noted in Fig. 6*a*. For example, all the data sets are in good agreement in the immediate vicinity of the wall. The rough wall profiles and the DNS data at $\mathrm{Re}_\theta = 1410$ have similar shape. These two profiles show a peak in the intermediate region and then decrease monotonically toward the outer surface. It should be pointed out that these data sets have relatively higher values of $-\langle uv \rangle/U_\tau^2$ and π (and presumably higher values of $\partial U^+/\partial y^+$ outside the overlap region) compared with the present smooth-wall data. On the other hand, the present smooth-wall profile and the DNS data at $\mathrm{Re}_\theta = 670$ increase dramatically as the edge of the boundary layer is approached. The higher values of R observed in the wall region for the wire-mesh and DNS results at $\mathrm{Re}_\theta = 1410$ in comparison with the smooth-wall and DNS data at $\mathrm{Re}_\theta = 670$ are certainly due to the high levels of $-\langle uv \rangle/U_\tau^2$. The higher levels of R for the present smooth wall and DNS results at $\mathrm{Re}_\theta = 670$ in the outer region imply that $\partial U^+/\partial y^+$ tends to zero faster than $-\langle uv \rangle/U_\tau^2$. It was noted that (Fig. 2*b*) at similar y^+ locations outside the logarithmic region, the values of $\partial U^+/\partial y^+$ for the smooth surface are significantly lower than those for the rough surfaces because of the higher π values in the latter. Therefore, for low Reynolds number or noncanonical turbulent boundary layers, one must take into account the specific shape of the mean velocity profiles in the outer region in order to obtain the correct level of the eddy viscosity.

Figure 6*b* compares the eddy viscosity obtained in this work to the ZPG data of Klebanoff at $\mathrm{Re}_\delta = 7.5 \times 10^4$ and Townsend at $\mathrm{Re}_\delta = (3-4) \times 10^4$, as reproduced by Hinze [25]. The ZPG data are distinctly different from the present smooth-wall profile, but are in reasonable agreement with the wire-mesh data. The good agreement between the wire mesh and the ZPG data is to be expected for the following reason: the value of $\pi = 0.52$ for the wire mesh is similar to typical value of $\pi = 0.55$ for canonical turbulent boundary layer and so the values of $\partial U^+/\partial y^+$ should be similar for the two sets of data. Furthermore, it was shown in Ref. [29] that the $\langle uv \rangle/U_\tau^2$ profiles for the present wire mesh and typical canonical turbulent boundary layer agree fairly well in the region $y/\delta < 0.5$. As already explained, the lower level of the eddy viscosity for the smooth data in the region $y/\delta < 0.6$ can be attributed to low level of $\langle uv \rangle/U_\tau^2$; the higher level close to the free surface is due to low values of $\partial U^+/\partial y^+$.

The mixing length $L = -\langle uv \rangle^{1/2}/(\partial U/\partial y)$ is shown in Fig. 6*c* using inner scaling. Rodi, Mansour, and Michelassi [26] computed the mixing length distributions for the DNS results of Spalart; these profiles are also shown. With the exception of the DNS results at $\mathrm{Re}_\theta = 670$, all the data sets show good agreement in the region $y^+ < 300$. The smooth-wall profile is higher than the rough-wall profiles in the outer region of the boundary layer, which may be due to the significantly lower values of $\partial U^+/\partial y^+$ for the smooth surface.

The smooth- and rough-wall measurements obtained by Antonia and Luxton [30] and Krogstad and Antonia [4] are compared with the present data sets in Fig. 6*d*. Close to the wall, $y/\delta \leqslant 0.1$, all the data sets (both earlier and present) are approximately described by the relation $L/\delta = 0.41 y/\delta$. The present and earlier measurements show good agreement in the region $y/\delta < 0.3$. Although $\langle uv \rangle$ for the present smooth wall profile is lower than the smooth-wall results in Refs. [4], [30], the present data are higher in the outer region due their characteristic low values of $\partial U/\partial y$ in the outer region. Since the $\langle uv \rangle$ profile for the wire mesh and the previous data are similar and the π values (or $\partial U/\partial y$) are also comparable, the close agreement between wire mesh and the previous data up to $y/\delta \approx 0.6$ is not surprising. Figure 6*d* clearly demonstrates that compared with the smooth-wall data, surface roughness significantly decreases the mixing length distribution in the outer two-thirds of the open channel turbulent boundary layer.

Conclusions

The present measurements show that surface roughness significantly enhances the levels of the Reynolds stresses, turbulence kinetic energy, and turbulence diffusion in a way that depends on the specific geometry of the roughness elements. The higher level of kinetic energy due to surface roughness may be partly explained by an increase in turbulence production levels. The present data demonstrate that surface roughness increases the level of the eddy viscosity and mixing length in the inner region, but decreases the mixing length in the outer two-thirds of the boundary layer, where the effect of the mean velocity gradient becomes important. Therefore, roughness effects must be accounted for in even these relatively simplistic modeling methodologies. The higher values of the wake parameter obtained for the rough surfaces, and the fact that surface roughness enhances the level of the Reynolds stresses over most of the boundary layer, suggest a stronger interaction between the inner and outer region of a turbulent boundary layer than would be implied by the wall similarity hypothesis.

Acknowledgment

The support of the Natural Sciences and Engineering Research Council of Canada is gratefully acknowledged.

References

[1] Cui, J., Patel, V. C., and Lin, C.-L., 2000, "Large-Eddy Simulation of Turbulent Flow Over Rough Surfaces," IIHR Tech. Report No. 413, Iowa Inst. of Hydr. Res., University of Iowa, USA.

[2] Townsend A. A., 1976, *The Structure of Turbulent Shear Flow*, Cambridge University Press, Cambridge.

[3] Raupach, M. R., Antonia, R. A., and Rajagopalan, S., 1991, "Rough-Wall Turbulent Boundary Layers," Appl. Mech. Rev., **108**, pp. 1–25.

[4] Krogstad, P. A., and Antonia, R. A., 1999, "Surface Roughness Effects in Turbulent Boundary Layers," Exp. Fluids, **27**, pp. 450–460.

[5] Tachie, M. F., Bergstrom, D. J., and Balachandar, R., 2000, "Rough Wall Turbulent Boundary Layers in Shallow Open Channel Flow," ASME J. Fluids Eng., **122**, pp. 533–541.

[6] Ligrani, P. M., and Moffat, R. J., 1985, "Structure of Transitionally Rough and Fully Rough Turbulent Boundary Layers," J. Fluid Mech., **162**, pp. 69–98.

[7] Ligrani, P. M., and Moffat, R. J., 1985, "Thermal Boundary Layers on a Rough Surface Downstream of Steps in Wall Temperature," Boundary-Layer Meteorol., **31**, pp. 127–147.

[8] Mazouz, A., Labraga, L., and Tournier, C., 1998, "Anisotropy Invariant of Reynolds Stress Tensor in a Duct Flow and Turbulent Boundary Layer," ASME J. Fluids Eng., **120**, pp. 280–284.

[9] Tachie, M. F., Bergstrom, D. J., and Balachandar, R., 2002 "The Effect of Wall Roughness on an Open Channel Boundary Layer," 5th Int. Symp. on Eng. Turbulence Modelling and Measurements, Mallorca, Spain, Rodi, W. and Fueyo, N, eds. pp. 455–453.

[10] Bergstrom, D. J., Kotey, N. A., and Tachie, M. F., 2002, "The Effects of Surface Roughness on the Mean Velocity Profile in a Turbulent Boundary Layer," ASME J. Fluids Eng., **124**, pp. 664–670.

[11] Bakken, O. M., and Krogstad, P.-A., 2001, "Quandrant Analysis of Rough and Smooth Surface Channel Flow," Turbulence and Shear Flow Phenomena, Second Int. Symp., KTH, Stockholm, Sweden, Lindborg, E., Johanson, A., Eaton, J., Humphrey, J., Kasagi, N., Leschziner, M., and Sommerfield, M., eds. Vol. I, pp. 335–340.

[12] Cebeci, T., and Chang, K. C., 1978, "Calculation of Incompressible Rough-Wall Boundary-Layer Flows," AIAA J., **16**(**7**), pp. 730–735.

[13] Krogstad, P.-A., 1991, "Modification of the van Driest Damping Function to Include the Effects of Surface Roughness," AIAA J., **29**, pp. 688–694.

[14] Zhang, H., Faghri, M., and White, F. M., 1996, "A New Low-Reynolds-Number k-ε Model for Turbulent Flow Over Smooth and Rough Surfaces," ASME J. Fluids Eng., **118**, pp. 255–259.

[15] Patel, V. C., 1998, "Perspective: Flow at High Reynolds Numbers and Over Rough Surfaces-Achilles Heel of CFD," ASME J. Fluids Eng., **120**, pp. 434–444.

[16] Durbin, P. A., Medic, G., Seo, J.-M., Eaton, J. K., and Song, S. 2001, "Rough Wall Modification of Two-Layer k-ε," ASME J. Fluids Eng., **123**, pp. 16–21.

[17] Akinlade, O. G., and Bergstrom, D. J., 2002, "The Prediction of Turbulent Duct Flow With Surface Roughness Using k-ε Models," 5th Int. Symp. on Eng. Turbulence Modelling and Measurements, Mallorca, Spain, Rodi, W., and Fueyo, N., eds., pp. 197–205.

[18] Tachie, M. F., Open Channel Turbulent Boundary Layers and Wall Jets, 2001, Ph.D. thesis, University of Saskatchewan, Canada.

[19] Krogstad, P.-A., Antonia, R. A., and Browne, L. W. B., 1992, ''Comparison Between Rough- and Smooth-wall Turbulent Boundary Layers,'' J. Fluid Mech., **245**, pp. 599–617.

[20] Nezu, I., and Rodi, W., 1986, ''Open-Channel Flow Measurements With a Laser Doppler Anemometer,'' J. Hydraul. Eng., **112**(**5**), pp. 335–355.

[21] Nezu, I., and Nakagawa, H., 1993, *Turbulence in Open-Channel Flows*, A. A. Balkema, Rotterdam.

[22] George, W. K., and Castillo, L., 1997, ''Zero Pressure Gradient Turbulent Boundary Layer,'' Appl. Mech. Rev., **50**(**11**), pp. 689–729.

[23] DeGraaff, D. B., and Eaton, J. K., 2000, ''Reynolds-Number Scaling of the Flat-Plate Turbulent Boundary Layer,'' J. Fluid Mech., **422**, pp. 319–346.

[24] Johnson, P. L., and Barlow, R. S., 1990, ''Effect of Measuring Volume Length on Two-Component Laser Velocimeter Measurements in a Turbulent Boundary Layer,'' Exp. Fluids, **8**, pp. 137–144.

[25] Hinze, J. O., 1975, *Turbulence*. McGraw-Hill, New York.

[26] Rodi, W., Mansour, N. N., and Michelassi, V., 1993, ''One-Equation Near-Wall Turbulence Modeling With the Aid of Direct Simulation Data,'' ASME J. Fluids Eng., **115**, pp. 196–205.

[27] Antonia, R. A., Bisset, D. K., and Kim, J., 1991, ''An Eddy Viscosity Calculation Method for a Turbulent Duct Flow,'' ASME J. Fluids Eng., **113**, pp. 616–619.

[28] Rodi, W., 1991, ''Experience With Two-Layer Models Combining the k-ε Model With a One-Equation Model Near the Wall,'' AIAA Paper 29-0216, AIAA 29th Aerospace Sciences Meeting, Reno, U.S.A.

[29] Tachie, M. F., Bergstrom, D. J., and Balachandar, R., 2003, ''Roughness Effects in Low-Re_θ Open-Channel Turbulent Boundary Layers,'' Exp. Fluids, **35**, pp. 338–346.

[30] Antonia, R. A., and Luxton, R. E., 1971, ''The Response of a Turbulent Boundary Layer to a Step Change in Surface Roughness, Part 1. Smooth to Rough,'' J. Fluid Mech., **48**, pp. 721–761.

S. He
BSc MSc PhD CEng MIMechE
e-mail: s.he@rgu.ac.uk
School of Engineering,
The Robert Gordon University,
Aberdeen AB10 1FR, U.K.

J. A. Gotts
BSc CEng
e-mail: jim.gotts@british-energy.com
Engineering Division,
British Energy Generation Ltd,
Gloucester GL4 3RS, U.K.

Calculation of Friction Coefficients for Noncircular Channels

This paper presents a method for estimating a hydraulic resistance multiplier to enable approximate values of friction coefficients to be calculated for turbulent flows in noncircular channels of arbitrary shape using correlations developed for the circular pipe. Unlike most other methods, no preknowledge on the flow channels, such as the laminar shape factor or characteristic length, is required. Good agreement between predictions using the new method and experiments was achieved. [DOI: 10.1115/1.1845479]

1 Introduction

Friction coefficient correlations developed for turbulent flows in circular tubes are widely used for noncircular flow passages. For such flows, the hydraulic diameter (D_e) defined as $4A/P_r$ (where A is the area and P_r the perimeter) is used to substitute for the pipe diameter. However the friction calculated this way can be too high when the flow passage has sharp corners. The flow in these corners is often significantly slower than in the core of the channel. Therefore the friction calculated based on the mean velocity and the hydraulic diameter will not be a good representation of the true flow.

One approach to resolve the problem is to introduce a multiplier (called the *hydraulic resistance multiplier*, λ) to provide a correction. The multiplier is defined as the ratio of the friction coefficient of a noncircular passage over the friction coefficient of a circular tube of the same hydraulic diameter. Since the friction coefficient for a noncircular passage is generally less than that calculated using the circular tube correlation, the hydraulic resistance multiplier is normally less than unity. This paper presents a method for estimating the hydraulic resistance multiplier for noncircular flow passages of arbitrary geometry.

2 Review of Methods Available in the Literature

Much work has been carried out to determine the hydraulic resistance in noncircular passages and has led to the development of various correlations for friction coefficient; see for example the review by Kakac et al. [1]. More recent work includes Lee [2] and Vijayan et al. [3]. Most methods fall into one of the following groups: (a) the laminar flow shape factor approach; (b) the characteristic length scale approach; or (c) the multiplier approach. A brief review of these methods is given below.

2.1 The Laminar Flow Shape Factor Approach. For a laminar flow, the friction can always be correlated using $f\,\mathrm{Re}=C$, where C is a constant for a particular geometry, and Re is based on the hydraulic diameter D_e and cross-sectional mean velocity. The constant C is called the ''laminar flow shape factor.'' For a circular tube, $C=16$. One approach to calculating the turbulent friction coefficient is to relate it to the laminar flow shape factor. Examples of work following this approach include Gunn and Darling [4], Rehme [5], and Malàk et al. [6]. One disadvantage of this approach is that the laminar flow shape factor is needed for the calculation, but it is not always available.

2.2 The Characteristic Length Approach. Some workers have chosen to directly use the friction correlations developed for a circular tube in noncircular tube flow calculations. To do this, they replace the hydraulic diameter with a new characteristic length scale. Good results have been obtained for a number of geometries, such as triangular and square ducts, etc. However, there is no general formulation for the characteristic length scale for all noncircular ducts. Therefore the characteristic length scale has to be developed each time when a new duct is considered. Examples of work adopting the characteristic length approach include Bandopadhayay and Ambrose [7] for isosceles triangles, Jones [8] for rectangular ducts, and Ahmed and Brundrett [9] for equilateral triangles.

2.3 The Multiplier Approach and the Miller Method Another approach that makes use of the circular pipe friction correlations is the multiplier approach, one to be used in this paper as described in the introduction. Clearly the hydraulic resistance multiplier, which is expected to be unique to a particular geometry, needs to be derived, usually from experimental data. Miller [10] described a method which can be used to estimate the multiplier for any noncircular channel when there is a lack of such data. The method is outlined below.

When the friction coefficient correlation for a circular tube is used in conjunction with the hydraulic diameter to estimate the pressure drop in a noncircular channel with sharp corners, the values calculated are often too high. Under such a condition, Miller's method considers a new channel formed of only the central part of the original channel, i.e., the side corners are blocked. It is obvious that the pressure drop in the new channel is expected to be higher than in the original channel in reality because of the reduced size. However, the pressure drop calculated using the circular tube friction correlation for the new reduced channel is often lower than that calculated for the original channel. The reason for this result is that the circular tube correlation can be very inaccurate when used for channels with sharp corners. A much more reasonable result can often be achieved for the new channel with the sharp corners removed.

The above discussion can be illustrated by considering the pressure drop expression for a circular channel

$$\Delta p=4f_c\frac{L}{D_e}\frac{1}{2}\rho U^2. \tag{1}$$

where f_c is the friction coefficient calculated using the circular tube correlation. Considering $D_e=4A/P_r$ and $W=\rho AU$, the above equation becomes

$$\Delta p=\frac{1}{2}f_cL\frac{W^2}{\rho}\frac{P_r}{A^3} \tag{2}$$

Contributed by the Fluids Engineering Division for publication in the JOURNAL OF FLUIDS ENGINEERING. Manuscript received by the Fluids Engineering Division January 7, 2003; revised manuscript received June 4, 2004. Associate Editor: Jeffrey S. Marshall.

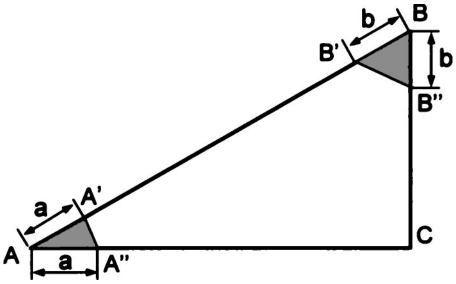

Fig. 1 Demonstration of subchannel partition

where A is the flow area, P_r is the wetted perimeter, L the length of the passage, and W the mass flow rate. It can be seen from Eq. (2) that the pressure drop calculated will indeed be reduced if, by blocking the sharp corners, a new passage can be formed which has a smaller P_r/A^3.

The procedure suggested by Miller [10] is rather straightforward. To start with, the corners of a noncircular channel are blocked to define a new flow passage within the original one, see Fig. 1, for example, where the new channel is shown as A′B′B″CA″. The sizes of the blocked areas can be varied (i.e., varying a and b in Fig. 1) to find a new imaginary channel with a minimized P_r/A^3. If P_r/A^3 applies to the original passage and P_{r1}/A_1^3 is the minimal value, it follows:

$$P_{r1}/A_1^3=\lambda(P_r/A^3) \tag{3}$$

where λ is a factor by which P_r/A^3 can be reduced. If a pressure drop Δp_1 is now associated with the flow in the imaginary channel, then

$$\Delta p_1=\frac{1}{2}f_cL\frac{W^2}{\rho}\frac{P_{r1}}{A_1^3} \tag{4}$$

Hence, combining Eqs. (2)–(4)

$$\Delta p_1=\lambda\Delta p \tag{5}$$

where the factor λ is the *hydraulic resistance multiplier* mentioned earlier, which can be expressed as

$$\lambda=\frac{P_{r1}}{P_r}\left(\frac{A}{A_1}\right)^3. \tag{6}$$

The pressure drop can then be calculated using Eq. (1) by replacing f_c with λf_c. The latter is named as the *modified friction coefficient*, denoted by *f*, i.e.,

$$f=\lambda f_c \tag{7}$$

where f_c is the friction coefficient for a circular tube of the same hydraulic diameter (D_e) and λ the *hydraulic resistance multiplier*. Note that the hydraulic diameter D_e referred to here [and that used in Eq. (1)] is based on the original channel.

3 Development of a New Method—the Multichannel Approach

The Miller method has proved to be very useful in some engineering applications when the friction factor of a particular channel is not available. However, the Miller method still substantially over predicts pressure drop for many channels. In the following paragraphs, an improved method will be presented, which enables a more realistic friction to be calculated.

Following Miller's basic idea, but instead of having the corners blocked, the noncircular passage is split into a few subchannels and flow is allowed to pass through all those subchannels. The split will be done in a way that the sharp corners are separated from the central (main) channel. Examples of the split of a number of typical channels are shown in Fig. 2.

After the splitting, the channel consists of a main (sub) channel and a number of side (sub) channels. Similar to the Miller method, the idea is then to vary the locations of the partition of the subchannels to minimize the pressure drop calculated. To guarantee the calculation procedure meaningful, the new channel configuration should be done in such a way that the pressure drop in it is always higher than that in the original channel and therefore searching for a minimum friction would mean approaching the "true" value. This is consistent with the Miller method. To comply with this requirement, when calculating the wetted perimeter Pr_i for the main channel, the imaginary interfaces should be taken as solid walls, i.e., they will be included in the perimeter calculation. But for the side channels on the other hand, the imaginary interfaces can be seen as free surfaces, i.e., not accounted for in the perimeter calculation. The reason for this can be explained as follows:

It is not difficult to imagine that the velocity in the "main" channel is faster than that in the surrounding "side" channels (sharp corners). Consequently, at the imaginary interfaces between the subchannels, the flow in the main channel is dragged back by the flows in the side channels. In the procedure of forming the subchannels, the imaginary interfaces can be represented either with solid walls or free surfaces. If these interfaces were replaced with free surfaces, i.e., no shear forces on them, then the flow in the main channel would be subject to less friction than in reality. This would invalidate the assumption made in the above paragraph: The friction in the new channel configuration is always higher than that in the original channel. On the other hand when the interfaces are replaced with solid walls, the flow in the main channel will be subjected to greater shear, clearly an appropriate treatment.

For the side channels on the other hand, as the flow is always pulled by the main channel flow (since the latter is faster), replacing the imaginary interfaces with free surfaces (i.e., ones with zero shear), will leave the side channels with higher frictions and therefore comply with the assumption made earlier.

Consider the triangular duct shown in Fig. 1 again as an example to derive the formula for the multiplier λ. Assuming the passage is divided into three subchannels as shown in the figure, the pressure drop in each can be written as

$$\Delta p_1=\frac{1}{2}f_{c1}L\frac{W_1^2}{\rho}\frac{P_{r1}}{A_1^3} \tag{8}$$

$$\Delta p_2=\frac{1}{2}f_{c2}L\frac{W_2^2}{\rho}\frac{P_{r2}}{A_2^3} \tag{9}$$

$$\Delta p_3=\frac{1}{2}f_{c3}L\frac{W_3^2}{\rho}\frac{P_{r3}}{A_3^3}. \tag{10}$$

The middle (main) passage is always referred to as passage 1. The pressure drop in the complete passage is expressed as

$$\Delta p=\frac{1}{2}f_cL\frac{W^2}{\rho}\frac{P_r}{A^3}. \tag{11}$$

It is now assumed that the friction coefficient for each of the subchannels can be estimated using the friction correlation for circular tubes based on the hydraulic diameter concept. The Blasius correlation (valid in the range: $3000<\mathrm{Re}<10^5$) is used here, i.e.,

$$f_c=0.079\,\mathrm{Re}^{-1/4}, \tag{12}$$

or

$$f_c=0.079\left(\frac{4W}{\mu P_r}\right)^{-1/4}. \tag{13}$$

Substituting f_c with the above expression, Eq. (11) now becomes

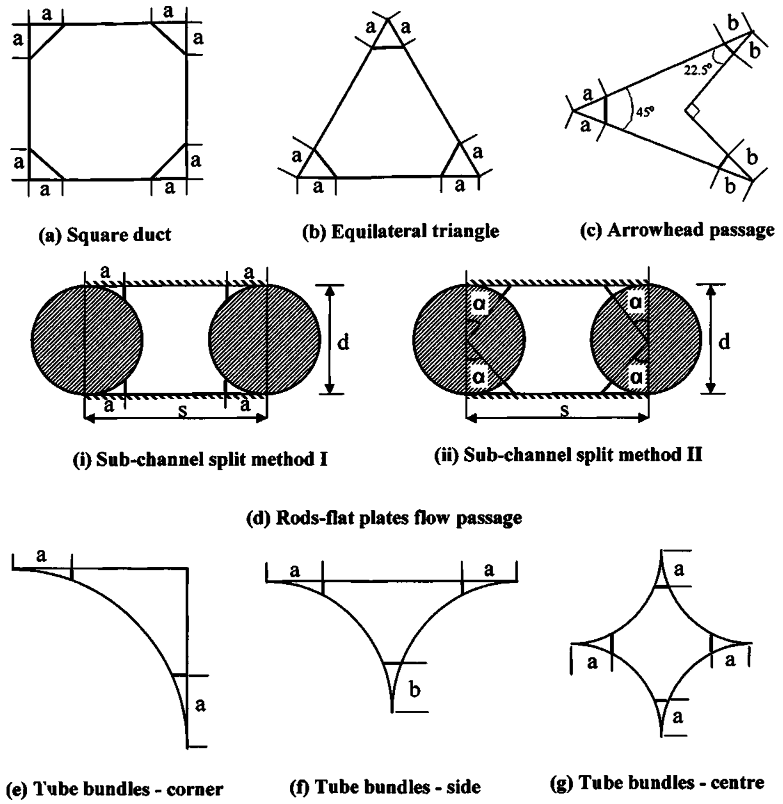

(a) Square duct

(b) Equilateral triangle

(c) Arrowhead passage

(i) Sub-channel split method I

(ii) Sub-channel split method II

(d) Rods-flat plates flow passage

(e) Tube bundles - corner

(f) Tube bundles - side

(g) Tube bundles - centre

Fig. 2 Partition of various flow passages

$$\Delta p = \frac{0.079\mu^{1/4}}{2\sqrt{2}} L \frac{W^{7/4}}{\rho} \frac{P_r^{5/4}}{A^3}. \tag{14}$$

The pressure drop in the side channels can also be expressed in a similar form by substituting f_{c1}, f_{c2}, f_{c3} in Eqs. (8) to (10) with Eq. (13). The three subchannels must all have an equal pressure drop, which may be different from that in the original channel, i.e.,

$$\Delta p_1 = \Delta p_2 = \Delta p_3 = \alpha \Delta p \tag{15}$$

Also,

$$W = W_1 + W_2 + W_3. \tag{16}$$

$$A = A_1 + A_2 + A_3 \tag{17}$$

From Eqs. (14) to (17),

$$\alpha = \left(\frac{W_1}{W}\right)^{7/4} \left(\frac{A}{A_1}\right)^3 \left(\frac{Pr_1}{Pr}\right)^{5/4} \tag{18}$$

and

$$\frac{W_1}{W} = \frac{1}{1 + (A_2/A_1)^{12/7}(Pr_1/Pr_2)^{5/7} + (A_3/A_1)^{12/7}(Pr_1/Pr_3)^{5/7}}. \tag{19}$$

Although α is expressed as a function of parameters of channel 1 in Eq. (18), this is of no significance. Effects of other channels are taken into account through Eq. (19).

For a general case, when the channel is split into n sub-channels, Eq. (18) remains the same but Eq. (19) becomes

$$\frac{W_1}{W} = \frac{1}{1 + \Sigma_{i=2}^{n}[(A_i/A_1)^{12/7}(Pr_1/Pr_i)^{5/7}]}. \tag{20}$$

The next step is to vary the positions of the partition (i.e., varying the partition parameters *a* and *b*) shown in Fig. 1 and find the minimum α which will be the *hydraulic resistance multiplier* λ for the particular geometry, i.e.,

$$\begin{aligned}\lambda &= \min(\alpha) \\ &= \min\left[\left(\frac{W_1}{W}\right)^{7/4}\left(\frac{Pr_1}{Pr}\right)^{5/4}\left(\frac{A}{A_1}\right)^3\right]_{\text{varying boundaries of splitting}}\end{aligned} \tag{21}$$

A discussion on how the minimization can be achieved is given in Sec. 4. The modified friction coefficient for the noncircular flow passage can now be expressed as

$$f = \lambda f_c \tag{22}$$

The pressure drop can be calculated using Eq. (1) by replacing the friction coefficient f_c for a circular tube with the modified friction coefficient *f*.

It is worth emphasizing at this stage the rules for the calculation of the perimeters Pr_i for the sub-channels: When the perimeter for the main channel (Pr_1) is calculated, the imaginary interfaces between the main channel and the various sub-channels are taken as solid walls, i.e., they will be included as walls in the perimeter calculations. For other subchannels, these interfaces will be taken as free surfaces. Therefore, they will be excluded in the calculation of Pr_i, $i=2,\ldots,n$. The perimeter of the original channel (Pr) is calculated as normal, i.e., all the physical side walls are included in its calculation.

It should be noted that, although the Blasius equation used in the derivation is strictly speaking only valid in the range $3000 < \mathrm{Re} < 10^5$, Eq. (21) is not limited to this Reynolds range. The Blasius equation has been used in determining the ratio of the friction coefficient of the subchannels which is only one of the factors that affect the distribution of flow rate between the various subchannels. The final value of λ has been found not very sensitive to the choice of the correlation for friction used in the derivation.

The *hydraulic resistance multiplier* determined using the multichannel method is independent of the Reynolds number. That is, referring to Eq. (22), the dependency of the friction coefficient on Reynolds number in the noncircular channel is assumed to be the same as that in a circular channel. This assumption has been adopted by most previous methods [7,8,10]. Many experimental results on non-circular channels showed little dependency of λ on Reynolds number [12], although some did show some relatively weak dependency on Reynolds number [4].

4 Comparisons of Calculations With Experimental Data and Predictions of Other Methods

The multichannel method was used to calculate the hydraulic resistance multipliers for a number of common geometries, including, a square and an equilateral triangular duct, an arrowhead passage, isosceles triangles with different apex angles, and various tube bundle sections. The calculations were done using the following procedures:

1. Decide a pattern of the split of the flow passage considered. The split should be done in a way that the sharp corners are separated from the main channel. The patterns of split that have been used in the example calculations are shown in Fig. 2. Theoretically speaking, there are infinite number of ways of constructing the subchannels by selecting different inclination of the interfaces of the sub-channels. However, such variation will normally have little effect on the final result. For example, Fig. 2(*d*) shows two obvious ways of the split of the flow passage between two rods and flat plates. The difference between the multipliers calculated using the two patterns of partition were always less than 0.3% for $1.05<s/d<2.0$. Therefore the main rule for determining the shape of the split is easy calculation of the perimeters and areas of the sub-channels, i.e., Pr_i and A_i. The choice is often very obvious, as shown in Fig. 2. It is worth noting that the number of the split parameters can be reduced by using the same split parameter for geometrically similar corners. For example, "*a*" is used for both corners in Figs. 2(*a*) and 2(*b*). By doing this the minimisation process will be simplified.
2. Express A_i, Pr_i, $i=1,\dots n$, and then W_i/W, as a function of the split parameters, *a*, *b*, . . . , etc.
3. Express α as a function of the split parameters using Eqs. (18) and (20), i.e., $\alpha=f(a,b,\dots,)$.
4. Minimize α through varying the split parameters *a*, *b*, . . . , etc. to find the hydraulic resistance multiplier λ. Effectively, this means varying the split parameters by a small step each time in a reasonable range. (A reasonable range means, for example, for the geometry in Fig. 2, $a+b$ should be less than the length of any of the sides of the triangle to be physically meaningful). Then, for any set of the split parameters, calculate α using Eqs. (18) and (20). The smallest α is then the multiplier λ to be found.

In this study, the Excel Spreadsheets was used for the calculation. The minimization was achieved using the Excel function: Solver. This function enables a minimization of the value of a cell (i.e., the one contains Eq. (18) for α, which is a function of the split parameters) to be achieved by varying the values of a number of other cells (say, those contains the split parameters, *a*, *b*, *c*, . . . ,) in a range specified by the user. The minimized value of α will be the hydraulic resistance multiplier λ.

Figure 3 shows the variation of the hydraulic resistance multipliers with the apex angle of an isosceles triangle calculated using the Miller and the multichannel methods, compared with experimental data by Carlson and Irvine [11]. These data were obtained from experiments for a Reynolds number range between 4000 and 10,000. A margin of 5% above and below the data is shown in the figure to facilitate the comparison. Also shown in the figure are predictions using a characteristic length approach due to Bandopadhayay and Ambrose [7] for comparison. It can be seen that the Miller method produces multipliers that are much higher than the experimental data. The multipliers calculated using the multichannel approach are significantly improved and are well within the 5% margin of the data. These results are also better than the multipliers calculated using the characteristic length approach [7] for ducts with lower apex triangles.

Figure 4 shows the variation of the hydraulic resistance multipliers with the normalized distance between the rods for a flow channel formed from two circular rods and flat plates calculated using the Miller and the multichannel approaches. Also shown in the figure are the multipliers obtained from the experimental data due to Mohandes and Knudsen [12], together with a margin of 5% above and below the data to facilitate the comparison. These experimental results showed no Reynolds number dependency when Re>5000. Again the hydraulic resistance multipliers predicted by

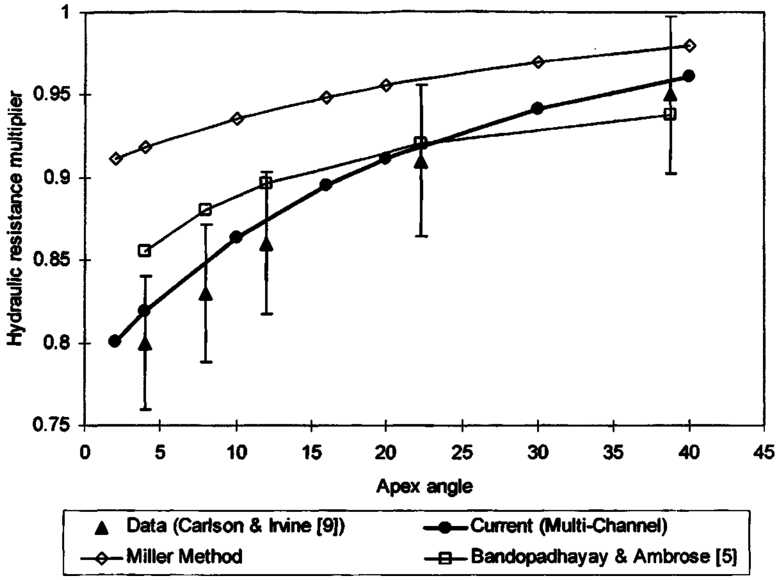

Fig. 3 Hydraulic resistance multiplier for isosceles triangle flow passages

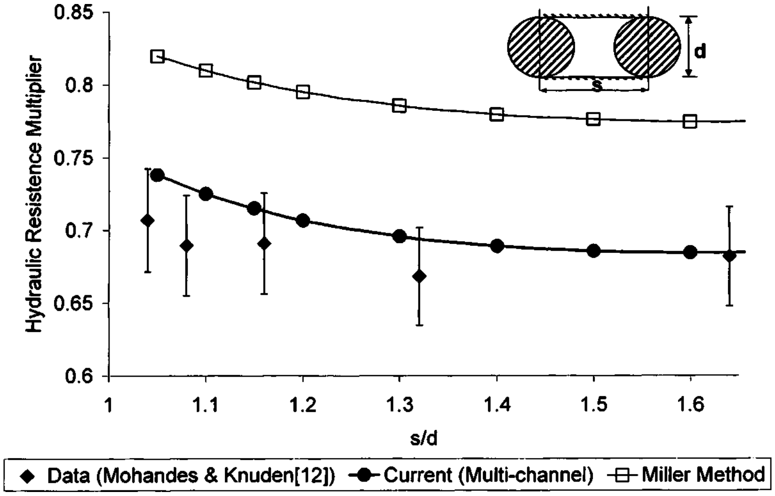

Fig. 4 Hydraulic resistance multiplier for two rods-flat plates passage

the multichannel model are very close to the experimental data, all but one are within the 5% margin. Those calculated using the Miller method are again much too high.

Calculations of hydraulic resistance multipliers have also been performed for a number of other non-circular channels. These include, as shown in Fig. 2, a square and an equilateral triangular duct, an arrowhead channel, and a number of flow passages formed by tube bundles and walls. The results are compared with experimental data and/or calculations using other methods in Table 1. The results shown in the "Data" column of the table were obtained from experimental data or correlations directly derived from experimental data. These shown in the "Other Models" column are results calculated using previous models based on either the laminar flow shape factor or the characteristic length approach. It is worth noting that the correlation for the passage between tube bundles [4] and that for the equilateral triangles [6] are weakly dependent on the Reynolds number. The results shown in the table are based on a middle ranged Reynolds number of 30,000. Also to be noted is that the experimental results for the arrowhead [13] were given with only one significant digit, i.e., 0.8 and 0.9 for Re=30,000 and 110,000, respectively. It was considered appropriate that a mean value should be used for comparison. As discussed in Section 3, the *hydraulic resistance multiplier* calculated using the multichannel approach is independent of Reynolds number.

It can be seen from Table 1 that the hydraulic resistance multipliers calculated using the Miller model are consistently much higher than the corresponding experimental data. These calculated using the multichannel model are significantly improved. The difference between the predictions using the multichannel model and the corresponding experimental data is always less than 5%. Good agreement has also been achieved between predictions using the current method and those using previous methods from the literature ("Other Models" column in Table 1).

It should be noted that the multichannel method is an approximate estimation method. It is based on the idea of approximating the friction of a noncircular channel with correlations for circular tubes. Some of the discrepancies between the predictions of the multichannel method and the data seen above can be attributed to this fundamental reason. However, the results shown above clearly demonstrate that by splitting a noncircular channel into subchannels and isolating sharp corners from the main channel, the multichannel method can reduce the error associated with the approximating procedure significantly. Another source of error that is likely to contribute to the discrepancies between the predictions and data is the use of the Blasius correlation.

Although there is no obvious theoretical method to estimate the uncertainty of the multichannel method, for the many cases considered in this study, the discrepancies between the estimated hydraulic resistance multipliers and these derived from experimental data have almost always been found to be less than 5% (with only one exception which is only marginally outwith this range). As a variety of common geometries have been covered in the current study, it is considered appropriate to conclude that an uncertainty

Table 1 Hydraulic resistance multiplier for flow between tube bundles

		Data	Other models	Miller	Multichannel
Equilateral triangle		0.901[a]	0.904[d]	0.971	0.947
Square			0.971[e]	0.985	0.975
Arrowhead		0.85[b]		0.938	0.875
Tube bundles —corner		0.700[c]		0.783	0.683
Tube bundles —side		0.674[c]		0.765	0.661
Tube bundles —center		0.674[c]		0.764	0.669
Flow between three-rods ($P/D=1.02$)	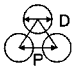		0.89[f]	1.0	0.880

[a] Reference [6].
[b] Reference [13].
[f] Reference [4].
[d] Reference [9].
[e] Reference [8].
[f] Reference [2].

of about 5% on the estimation of the hydraulic resistance multiplier can normally be expected for the multichannel method.

5 Conclusions

An approach has been developed for estimating the hydraulic resistance multiplier for arbitrary shaped noncircular flow passages. This enables a friction coefficient to be calculated. The method has been applied to a number of common geometries and the results are mostly within 5% of experimental data. The main advantage of the method is that it can readily be used for any noncircular flow passages, unlike most previous methods, which always require preknowledge (either from experiments or numerical simulations) on the flow shape factor or the characteristic length for the specific channel in question.

Acknowledgments

The work reported here was conducted while the first author was employed by British Energy Generation Ltd (BE). The contributions by M. Wyatt and M. Nicholls at early stages of this work are gratefully acknowledged.

Nomenclature

A, A_i = area of the main and subchannel i, respectively, m^2
C = laminar flow shape factor
De, De_i = hydraulic diameter ($4A/P_r$) of the main and subchannel i, respectively, m
f = fanning friction coefficient
f_c = fanning friction coefficient for circular pipes
L = length, m
P_r, P_{ri} = wetted perimeter of the main and subchannel i, respectively, m
Δp = frictional pressure drop, pa
Re = Reynolds number, UD_e/ν
U = velocity, m/s
W, W_i = mass flow rate of the main and subchannel i, respectively, kg/s
α = pressure ratio, $\Delta p_1/\Delta p$
λ = hydraulic resistance multiplier
μ = dynamic viscosity, kg s^{-1} m^{-1}
ρ = density, kg/m^3

Subscripts

1,2,3 = subchannel numbers

References

[1] Kakaç, S., Shah, R. K., and Aung, W., 1987, *Handbook of Single-Phase Convective Heat Transfer*, Wiley, NY.
[2] Lee, K. B., 1995, ‘‘Analytical Prediction of Subchannel Friction Factor for Infinite Bare Rod Square and Trianglar Arrays of Low Pitch to Diameter Ratio in Turbulent Flow,’’ Nucl. Eng. Des., **157**, pp. 197–203.
[3] Vijayan, P. K., Pilkhwal, D. S., Saha, D., and Raj, V. V., 1999, ‘‘Experimental Studies on the Pressure Drop Across the Various Components of a PHWR Fuel Channel,’’ Exp. Therm. Fluid Sci., **20**, pp. 34–44.
[4] Gunn, D. J., and Darling, C. W. W., 1963, ‘‘Fluid Flow and Energy Losses in Non-Circular Conducts,’’ Trans. Inst. Chem. Eng., **41**, pp. 163–173.
[5] Rehme, K., 1973, ‘‘Simple Method of Predicting Friction Factors of Turbulent Flow in Non-Circular Channels,’’ Int. J. Heat Mass Transfer, **16**, pp. 933–950.
[6] Malàk, J., Hejna, J., and Schmid, J., 1975, ‘‘Pressure Losses and Heat Transfer in Non-Circular Channels With Hydraulically Smooth Walls,’’ Int. J. Heat Mass Transfer, **18**, pp. 139–149.
[7] Bandopadhayay, P. C., and Ambrose, C. W., 1980, ‘‘A Generalized Length Dimension for Non-Circular Ducts,’’ Lett. Heat Mass Transfer, **7**, pp. 323–328.
[8] Jones, Jr., O. C., 1976, ‘‘An Improvement in the Calculation of Turbulent Friction in Rectangular Ducts,’’ ASME J. Fluids Eng., **98**, pp. 173–181.
[9] Ahmed, S., and Brundrett, E., 1971, ‘‘Characteristic Lengths for Non-Circular Ducts,’’ Int. J. Heat Mass Transfer, **14**, pp. 157–159.
[10] Miller, D. S., 1996, *Internal Flow Systems*, 2nd ed., BHR Group Limited, Bedfordshire, UK.
[11] Carlson, L. W., and Irvine, T. F., 1961, ‘‘Fully Developed Pressure Drop in Triangular Shaped Corners,’’ ASME J. Heat Transfer, **83**, pp. 441–444.
[12] Mohandes, A., and Knudsen, J. G., 1979, ‘‘Friction factors in Non-Circular Ducts With Sharp Corners,’’ Can. J. Chem. Eng., **57**, pp. 109–111.
[13] France, J., Pardy, A., and Ellaby, G., 1971, ‘‘Friction Factor Measurements on a Hinkley ‘B’ AGR Interbrick Gas Coolant Passage,’’ AEA TRG Report 2002(R).

Frictional Resistance of Antifouling Coating Systems

Michael P. Schultz
Department of Naval Architecture and Ocean Engineering,
United States Naval Academy,
Annapolis, MD 21402

An experimental study has been made to compare the frictional resistance of several ship hull coatings in the unfouled, fouled, and cleaned conditions. Hydrodynamic tests were completed in a towing tank using a flat plate test fixture towed at a Reynolds number (Re_L) range of 2.8×10^6–5.5×10^6 based on the plate length and towing velocity. The results indicate little difference in frictional resistance coefficient (C_F) among the coatings in the unfouled condition. Significant differences were observed after 287 days of marine exposure, with the silicone antifouling coatings showing the largest increases in C_F. While several of the surfaces returned to near their unfouled resistance after cleaning, coating damage led to significant increases in C_F for other coatings. The roughness function ΔU^+ for the unfouled coatings showed reasonable collapse to a Colebrook-type roughness function when the centerline average height ($k=0.17R_a$) was used as the roughness length scale. Excellent collapse of the roughness function for the barnacle fouled surfaces was obtained using a new roughness length scale based on the barnacle height and percent coverage. [DOI: 10.1115/1.1845552]

Introduction

The settlement and subsequent growth of flora and fauna on surfaces exposed in aquatic environments is termed biofouling. Biofouling on ship hulls leads to increased surface roughness, frictional resistance, and fuel consumption, e.g. [1–6]. A recent paper by Townsin [7] provides a comprehensive review of much of the research in this area. In order to control the problem, antifouling (AF) coatings are used. Most of these coatings incorporate biocides which are toxic to marine organisms. The environmental impact of tributyl tin (TBT) biocides in AF coatings has led to their ban on vessels of length <25 m in most industrialized countries [8], and a worldwide ban on the application of TBT AF coatings on all vessels was imposed by the International Maritime Organization in 2003 [9]. Copper-based coatings are the primary replacement for TBT coatings, but they are less effective in controlling fouling and may also become the target of environmental legislation. For this reason, there has been a great deal of interest in developing non-toxic replacements, e.g., [10,11]. The most promising alternatives to date are polydimethylsiloxane (PDMS) silicone elastomer coatings [12,13]. These coatings, termed fouling release, do not prevent fouling settlement [14] but reduce the adhesion strength of the fouling organisms by an order of magnitude or more compared to traditional AF coatings [15]. Since fouling-release coatings do not prevent fouling, they must be easily cleaned mechanically or be self-cleaning at operational speeds in order to be effective [16].

The effect of hull condition is of great importance to the performance of marine vehicles. Skin friction on some hull types can account for as much as 90% of the total drag even when the hull is free of fouling [17]. For this reason, understanding and predicting frictional drag has been the focus of a substantial body of research. Several previous investigations have looked at the effect of surface roughness on the frictional drag of unfouled marine paints. These include studies by Musker [18], Townsin et al. [19], Granville [20], Medhurst [21], and Grigson [22]. Most of this work centered on characterizing the change in roughness and drag of the self polishing copolymer (SPC) TBT systems. No effort to address the effect of fouling was made. This was likely due to the fact that the TBT systems provided long term fouling control with minimal fouling settlement.

A great deal of research has also been devoted to studying the effects of fouling on drag. Much of this has addressed calcareous macrofouling (e.g., barnacles, oysters, etc.) and is reviewed in *Marine Fouling and Its Prevention* [23]. Similar studies focusing on the effect of plant fouling and biofilms date back to McEntee [24]. Further work to better quantify the effect that slime films have on drag was carried out by Benson et al. [2], Denny [3], Watanabe et al. [5], and Picologlou et al. [25]. More recently, Lewthwaite et al. [4] and Haslbeck and Bohlander [26] conducted full-scale ship tests to determine the effect of fouling on the drag of copper-based coatings. Schultz and Swain [27] and Schultz [28] used laser Doppler velocimetry to study the details of turbulent boundary layers developing over biofilms and filamentous algae, respectively. The results of all these studies indicate that relatively thin fouling layers can significantly increase drag.

Despite the fairly large body of research that has been conducted, there are little if any reliable data available to compare the hydrodynamic performance of the nontoxic, fouling-release surfaces with the biocide-based systems over the coating life cycle. Some preliminary data from Candries et al. [11] seem to indicate that in the unfouled condition, fouling-release systems may have slightly less frictional resistance than traditional AF coatings despite having a larger mean roughness. These results have yet to be validated and no data were offered for fouled coatings or for fouled coatings that have been cleaned. The purpose of the present research is to compare the performance of fouling-release coatings with biocide-based AF coatings in the unfouled, fouled, and cleaned conditions.

Background

The mean velocity profile in the inner portion of a turbulent boundary layer, outside of the viscous sublayer, can be expressed as the classical log law

$$U^+=\frac{1}{\kappa}\ln(y^+)+B. \tag{1}$$

Clauser [29] contended that the mean velocity profile in the inner layer of rough wall flows also exhibits a log law with the same slope as that of the smooth wall outside the roughness sublayer. The log-law intercept, however, is shifted downward from that of

---

Contributed by the Fluids Engineering Division for publication in the JOURNAL OF FLUIDS ENGINEERING. Manuscript received by the Fluids Engineering Division March 21, 2004; revised manuscript received June 12, 2004. Review conducted by: Steven L. Ceccio.

the smooth wall. The downward shift is called the roughness function ΔU^{+}, and can be used to express the log law over rough walls as follows:

$$U^{+}=\frac{1}{\kappa}\ln(y^{+})+B-\Delta U^{+}. \tag{2}$$

ΔU^{+} is a function of the roughness Reynolds number k^{+} defined as the ratio of the roughness length scale k to the viscous length scale ν/U_{τ}.

Clauser [29] and Hama [30] both proposed that the outer region of the boundary layer for both smooth and rough walls obeys the velocity defect law given as

$$\frac{U_e-U}{U_\tau}=f\left(\frac{y}{\delta}\right). \tag{3}$$

The physical implication of a universal defect law is that the mean velocity in the outer layer is independent of surface condition except for the effect that it has on U_τ. Experimental support for a universal velocity defect profile on smooth and rough walls can be found in recent studies by Krogstad and Antonia [31] and Schultz and Flack [32]. Hama [30] showed that by evaluating Eqs. (1)–(3) for $y=\delta$ at the same value of the displacement thickness Reynolds number $\mathrm{Re}_{\delta*}$, the roughness function can be expressed as

$$\Delta U^{+}=\left(\sqrt{\frac{2}{c_f}}\right)_S-\left(\sqrt{\frac{2}{c_f}}\right)_R. \tag{4}$$

Granville [20] offers an alternative method for determining the roughness function indirectly. In this method, the overall frictional drag of a flat plate covered with a given roughness is related to the local wall shear stress and mean velocity profile at the trailing edge of the plate. The analysis is based on the assumption of boundary layer similarity for rough and smooth walls as expressed in Eqs. (1)–(3). Granville's procedure involves comparing the C_F values of smooth and rough plates at the same value of $\mathrm{Re}_L\, C_F$. The resulting equations for k^{+} and ΔU^{+} are given in Eqs. (5) and (6), respectively.

$$k^{+}=\left(\frac{k}{L}\right)\left(\frac{\mathrm{Re}_L\, C_F}{2}\right)\left(\sqrt{\frac{2}{C_F}}\right)_R\left[1-\frac{1}{\kappa}\left(\sqrt{\frac{C_F}{2}}\right)_R+\frac{1}{\kappa}\left(\frac{3}{2\kappa}-\Delta U^{+\prime}\right)\left(\frac{C_F}{2}\right)_R\right] \tag{5}$$

$$\Delta U^{+}=\left(\sqrt{\frac{2}{C_F}}\right)_S-\left(\sqrt{\frac{2}{C_F}}\right)_R-19.7\left[\left(\sqrt{\frac{C_F}{2}}\right)_S-\left(\sqrt{\frac{C_F}{2}}\right)_R\right]-\frac{1}{\kappa}\Delta U^{+\prime}\left(\sqrt{\frac{C_F}{2}}\right)_R \tag{6}$$

Further details of the development of these equations are given in [20]. Recent results by Schultz and Myers [33] show good agreement between the roughness functions determined by Granville's method and those measured directly using the local mean velocity profile. It is of note that once $\Delta U^{+}=f(k^{+})$ for a roughness, it can be used in a computational boundary layer code or a similarity law analysis [34] to predict the drag of any body covered with that roughness.

Experimental Facilities and Method

The experiments were conducted in the 115 m long towing tank facility at the United States Naval Academy Hydromechanics Laboratory, Annapolis, Maryland. The experimental facilities and method used in the present study were similar to those used by Schultz [35]. The width and depth of the tank are 7.9 m and 4.9 m, respectively. The towing carriage has a velocity range of 0–7.6 m/s. In the present study, the towing velocity was varied between 2.0 and 3.8 m/s ($\mathrm{Re}_L=2.8\times10^{6}-5.5\times10^{6}$). The velocity of the towing carriage was measured and controlled using an encoder on the rails that produce 4000 pulses/m. Using this system, the precision uncertainty in the mean velocity measurement was <0.02% over the entire velocity range tested. The working fluid in the

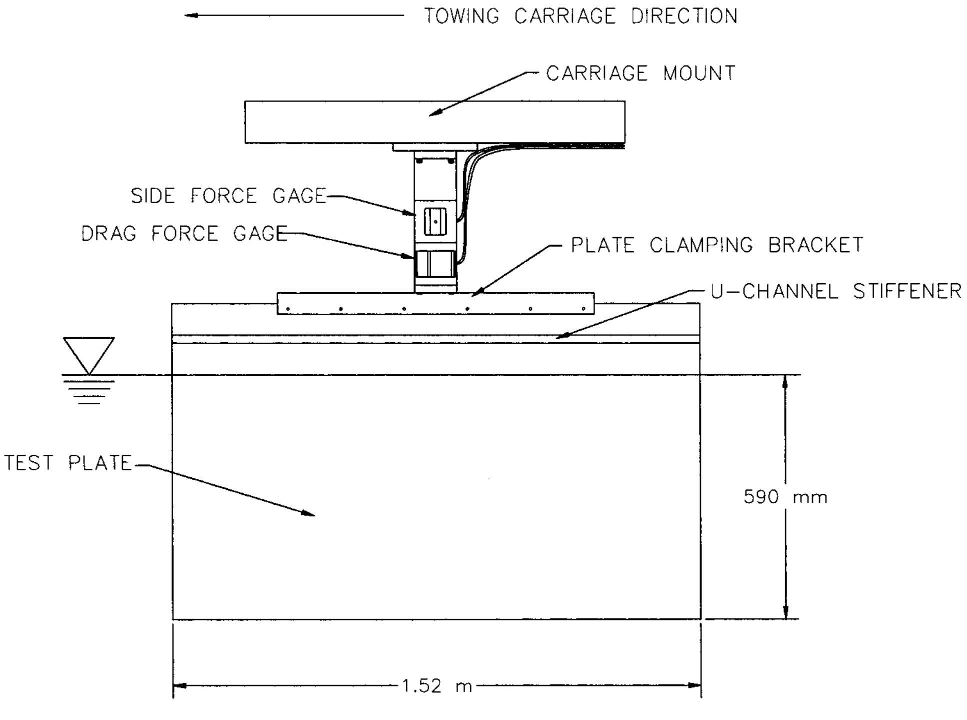

Fig. 1 Schematic of the flat plate test fixture

Table 1 Fouling coverage for the AF surfaces after 287 days exposure. Results are expressed in accordance with ASTM D3623 [36].

Test surface	Total fouling coverage (%)	Slime (%)	Hydroids (%)	Barnacles (%)	Fouling description
Silicone 1	75	10	5	60	Uniform coverage of barnacles (~6 mm in height)
Silicone 2	95	15	5	75	Uniform coverage of barnacles (~7 mm in height)
Ablative copper	76	75	0	1	Dense layer of diatomaceous and bacterial slime with very isolated barnacles (~5 mm in height)
SPC copper	73	65	3	4	Moderate layer of diatomaceous and bacterial slime with isolated barnacles (~5 mm in height)
SPC TBT	70	70	0	0	Light layer of diatomaceous and bacterial slime (~1 mm in height)

experiments was fresh water, and the temperature was monitored to within ±0.05°C during the course of the experiments using a thermocouple with digital readout.

Figure 1 shows a schematic of the test fixture and plate. The flat test plate was fabricated from 304 stainless steel sheet stock and measured 1.52 m in length, 0.76 m in width, and 3.2 mm in thickness. Both the leading and trailing edges were filleted to a radius of 1.6 mm. No tripping device was used to stimulate transition. The overall drag of the plate was measured using a Model HI-M-2, modular variable-reluctance displacement force transducer manufactured by Hydronautics Inc. An identical force transducer, rotated 90° to the drag gauge, was included in the test rig to measure the side force on the plate. The purpose of the side force gage was to ensure precise alignment of the plate. This was accomplished by repeatedly towing the plate at a constant velocity and adjusting the yaw angle of the test fixture to minimize the side force. Once this was done, no further adjustments were made to the alignment over the course of the experiments. The side force was monitored throughout to confirm that the plate alignment did not vary between test surfaces. Both of the force transducers used in the experiments had load ranges of 0–110 N. The combined bias uncertainty of the gages is ±0.25% of full scale. Data were gathered at a sampling rate of 100 Hz and were digitized using a 16-bit analog-to-digital converter. The sampling duration ranged from 30 s per test run at the lowest Reynolds number to 10 s per test run at the highest Reynolds number. The overall drag was first measured with 590 mm of the plate submerged. This was repeated with 25 mm of the plate submerged in order to find the wavemaking resistance tare. The difference between the two was taken to be the frictional resistance on the two 565 mm wide by 1.52 m long faces of the plate. The tests were repeated three times for each surface and Reynolds number. The results presented are the means of these runs.

Five antifouling coating systems were tested. Two of these were PDMS silicone AF systems, which will be referred to as silicone 1 and 2. One was an ablative copper AF system, typical of that presently used by the U.S. Navy on its surface combatants. SPC copper and SPC TBT paint systems were also tested. All of the paints were applied as directed by the paint manufacturer using the suggested surface preparation, primer, and tiecoat. The paint application was carried out by the Naval Surface Warfare Center-Carderock, Paints and Processes Branch (Code 641) using airless spray. Three control surfaces were also tested. These included test plates covered with 60-grit and 220-grit wet/dry sandpaper and a polished smooth surface. The surface profiles of all the test plates before exposure in the marine environment and after cleaning were measured using a Cyber Optics laser diode point range sensor laser profilometer system mounted to a Parker Daedal two-axis traverse with a resolution of 5 μm. The resolution of the sensor is 1 μm with a laser spot diameter of 10 μm. Data were taken over a sampling length of 50 mm and were digitized at a sampling interval of 25 μm. Ten linear profiles were taken on each of the test surfaces. A single three-dimensional topographic profile was made on each of the surfaces by sampling over a square area 2.5 mm on a side with a sampling interval of 25 μm.

The antifouling coatings were tested in three different conditions; unfouled, fouled, and cleaned. The unfouled condition was the as-applied painted surface, prior to marine exposure. The fouled condition was after exposure in the Severn River (Annapolis, Maryland) from September 16, 2002 until June 30, 2003 (287 days). The cleaned condition was the test surface after removal of the fouling using a nylon brush. It should be noted that the control test surfaces were not exposed in the marine environment. The exposure site at the U.S. Naval Academy was located near the confluence of the Severn River and the Chesapeake Bay (Annapolis, Maryland). The test plates were held vertically at ~0.2 m

Table 2 Roughness statistics for all test surfaces in the unfouled and cleaned condition

	Unfouled			Cleaned		
Test surface	R_a (μm)	R_q (μm)	R_t (μm)	R_a (μm)	R_q (μm)	R_t (μm)
Silicone 1	12±2	14±2	66±7	10±2	13±2	76±11
Silicone 2	14±2	17±2	85±8	19±1	23±1	142±21
Ablative copper	13±1	16±1	83±6	11±1	14±1	77±5
SPC copper	15±1	18±1	97±10	18±2	23±2	112±5
SPC TBT	20±1	24±2	129±9	22±2	27±2	135±7
60-grit SP	126±5	160±7	983±89	NA	NA	NA
220-grit SP	30±2	38±2	275±17	NA	NA	NA
Smooth	<1	<1	<1	NA	NA	NA

Note: Uncertainties represent 95% confidence precision error bounds.

below the mean low water level. The plates were exposed and the fouling coverage was evaluated according to ASTM D3623 [36]. The water temperature at the exposure site ranged from 1°C to 27°C and the salinity from 4 ppt to 10 ppt during the exposure period. The fouling coverage after 287 days is given in Table 1. After hydrodynamic testing, the fouled plates were cleaned using a nylon brush and a garden hose. The surface roughness of the test surfaces in the unfouled and cleaned condition is given in Table 2.

Uncertainty Estimates

Precision uncertainty estimates for the frictional drag measurements were made through repeatability tests using the standard procedure outlined by Moffat [37]. Three replicate towing tests were made with each surface at each Reynolds number. The standard error for C_F was then calculated. The 95% precision confidence limits for a mean statistic were obtained by multiplying the standard error by the two-tailed t value ($t = 4.303$) for two degrees of freedom given by Coleman and Steele [38]. The resulting precision uncertainties in C_F were $\leqslant \pm 1\%$ for all the tests. The overall precision and bias error was dominated by the systematic error due to the combined bias of the force gages ($\pm 0.25\%$ of full scale). The resulting precision and bias uncertainty in C_F ranged from $\pm 5\%$ at the lowest Reynolds number to $\pm 2\%$ at the highest Reynolds number. To insure the accuracy of the results, the control sandpaper and smooth test plates were run periodically throughout the experiments to check that the resulting mean C_F value was within the precision uncertainty bounds that had previously been obtained. The overall precision and bias error for the roughness function ΔU^+ ranged from $\pm 16\%$ or 0.2 (whichever is larger) at the lowest Reynolds number to $\pm 6\%$ or 0.1 (whichever is larger) at the highest Reynolds number.

Results and Discussion

The presentation of the results and discussion will be organized as follows. First, the frictional resistance results will be presented for the test surfaces in the unfouled, fouled, and cleaned conditions. These results will then be used to develop a relationship between the physical surface roughness and the roughness function ΔU^+. Finally, the frictional resistance will be scaled up to ship scale using similarity law analysis to determine the likely effect of these forms of roughness on ship frictional resistance.

Frictional Resistance, C_F. The results of the frictional resistance tests for the surfaces in the unfouled condition are presented in Fig. 2. The Kármán-Schoenherr friction line for a smooth plate is also shown for comparison [39]. This friction line is defined as

$$\frac{0.242}{\sqrt{C_F}} = \log(\mathrm{Re}_L\, C_F). \tag{7}$$

The present smooth plate results agree within ~1% with the Kármán-Schoenherr friction line as was also observed in a previous investigation in this facility [35]. At the lowest Reynolds number, the AF test surfaces all showed an increase in C_F compared to the smooth control. Silicone 1 and 2 had the smallest increase (1%), while the SPC TBT surface had the largest one (4%). It should be noted that while all of the AF surfaces had higher frictional resistance at the lowest Reynolds number than the smooth control, the differences were within the experimental uncertainty of the measurements. The 60-grit and 220-grit sandpaper controls exhibited increases in C_F of 66% and 17%, respectively, compared to the smooth test surface at the lowest Reynolds number. The effect of the surface roughness became larger with increasing Reynolds number. The increase in C_F for the AF surfaces ranged from 4% for silicone 1 to 8% for the SPC TBT surface at the highest Reynolds number. These differences are beyond the combined experimental uncertainty of the measurements and can be considered significant. The 60-grit and 220-grit sandpaper controls had increases in C_F of 83% and 31%, respectively, at the highest Reynolds number. Although the silicone fouling-release surfaces tended to have lower frictional resistance than the other AF surfaces over the entire range of Reynolds number tested, the differences observed were within the experimental uncertainty. A trend of lower drag on silicone fouling-release surfaces than for traditional AF paints was also noted by Candries et al. [11]. In the present case, the lower drag can be explained by the fact that the silicone surfaces were smoother than the other AF surfaces (Table 2). However, Candries et al. [11,40] noted lower drag even when the silicones were rougher than traditional AF surfaces. They attributed the lower drag to the longer wavelength of the roughness inherent for silicone coatings. Figure 3 shows representative surface profiles for Silicone 1 and the ablative copper coating that illustrate the differences in the roughness between silicones and traditional biocide-based AF coatings. It can be seen that the silicone roughness is populated by longer wavelengths than the copper surface. The wave-number spectra for the two surfaces presented in Fig. 4 clearly show a greater contribution to the roughness from the low wave-number scales on the silicone as compared to the copper surface. The relationship between the surface roughness and the increase in drag will be discussed further in the roughness function section.

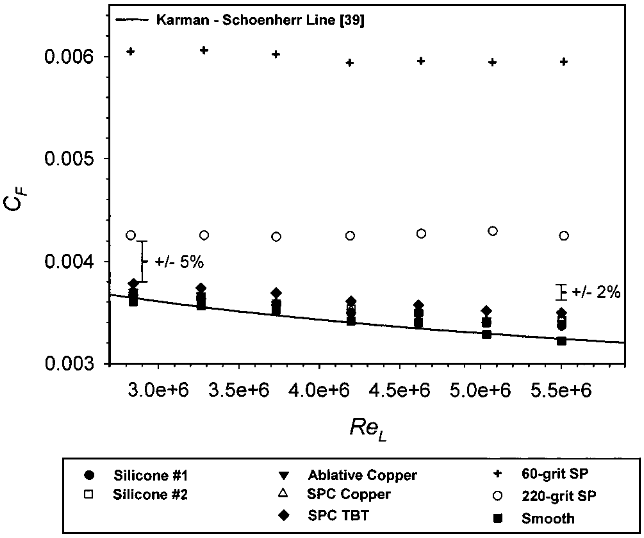

Fig. 2 Overall frictional resistance coefficient versus Reynolds number for all test surfaces in the unfouled condition. (Overall uncertainty in C_F: ±2% at highest Reynolds number; ±5% at lowest Reynolds number.)

The results of the frictional resistance tests for the surfaces in the fouled condition are presented in Fig. 5. All of the fouled surfaces exhibited a significant increase in frictional resistance compared to the smooth control over the entire Reynolds number range. The increase was greatest for the two silicone plates, which had C_F values three to four times higher than the smooth surface. These surfaces, not surprisingly, had the heaviest coverage of barnacles. These results indicate that if silicones are to be effective ship hull coatings they must be capable of hydrodynamic self-cleaning or be easily cleaned mechanically. The towing speeds in the present study were not high enough to cause significant self-cleaning of the coating. Further studies are needed in which the coated surfaces are towed at higher speeds in order to address the possible effect of self-cleaning on the drag. The ablative copper and SPC copper surfaces, which showed much lighter barnacle fouling (1%–4%), had increases in C_F that ranged from 87%–138%. The present results support findings of the classic pontoon resistance experiments carried out by Kempf [1] which also showed very large increases in frictional resistance with barnacle fouling. Recently, similar results were obtained in uncoated pipe flow experiments over barnacles by Leer-Andersen and Larsson

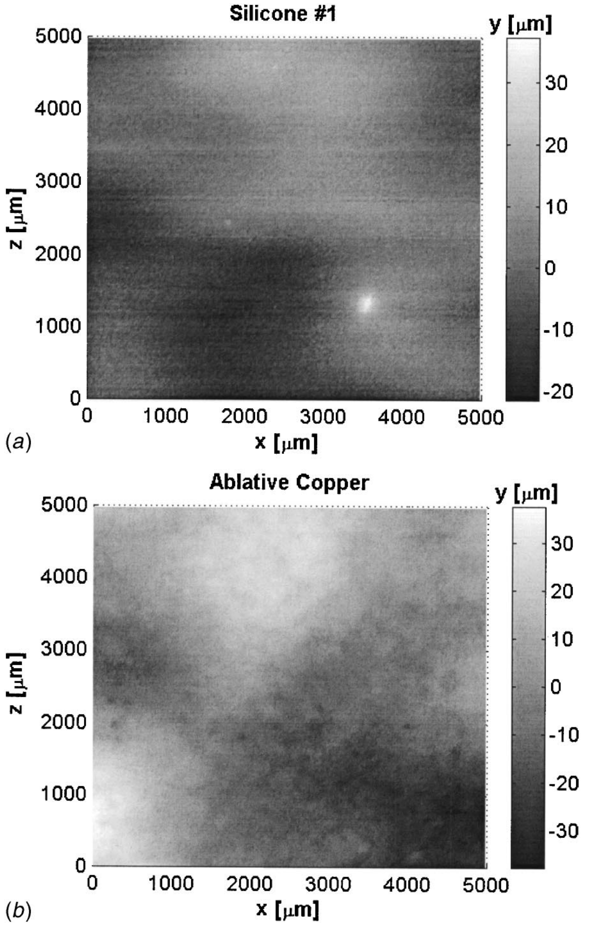

(*a*)

(*b*)

Fig. 3 Plan view of the surface waveform for (a) silicone 1 specimen; (b) Ablative copper specimen. (Overall uncertainty: *y* direction, ±1 *μ*m; *x* and *z* directions, ±5 *μ*m.)

[6]. It is of note that the SPC TBT surface showed an increase in C_F of 58%–68%, despite being covered with only a thin layer of slime. This supports the observations of Schultz and Swain [27] and Haslbeck and Bohlander [26] that show that surfaces covered with a light biofilm, otherwise free of calcareous fouling, can exhibit a significant increase in drag. The relationship between the fouling coverage and the increase in drag will be discussed further in the roughness function section. It should be noted that the present drag tests were carried out in fresh water, not the estuarine water that the fouling developed in. However, there was little difference visually in the fouling before and after exposure to the fresh water, and the invertebrate organisms, such as barnacles, remained alive. Also, since the salinity of the estuarine water was low, it is not felt that testing in fresh water caused undue stress on the fouling or significantly affected the results.

The results of the frictional resistance tests for the surfaces in the cleaned condition are presented in Fig. 6. All the AF surfaces showed an increased C_F as compared to the smooth control at the lowest Reynolds number. Silicone 1 and the ablative copper showed the smallest increase (3%), while the SPC TBT surface had the largest drag increment (7%). However, these differences were within the experimental uncertainty of the measurements. The effect of the surface roughness was more pronounced at

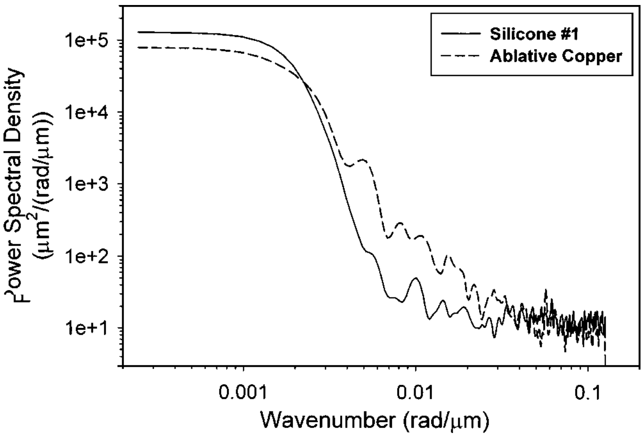

Fig. 4 Wave-number spectra of the surface waveforms for silicone 1 and ablative copper

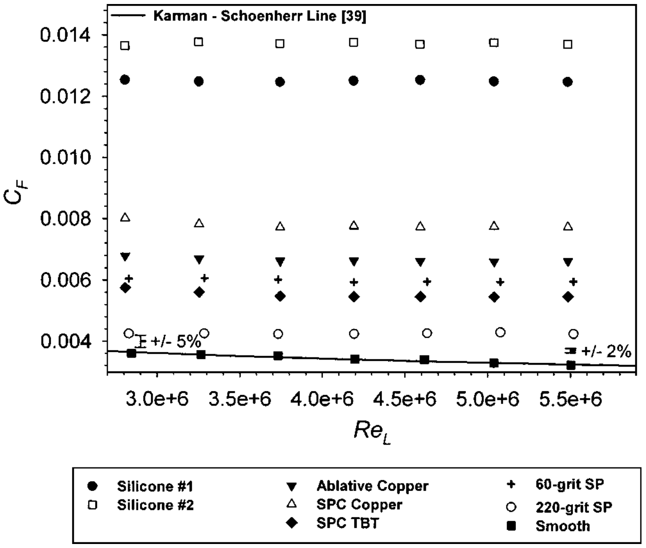

Fig. 5 Overall frictional resistance coefficient versus Reynolds number for all test surfaces in the fouled condition after 287 days exposure. (Overall uncertainty in C_F: ±2% at highest Reynolds number; ±5% at lowest Reynolds number.)

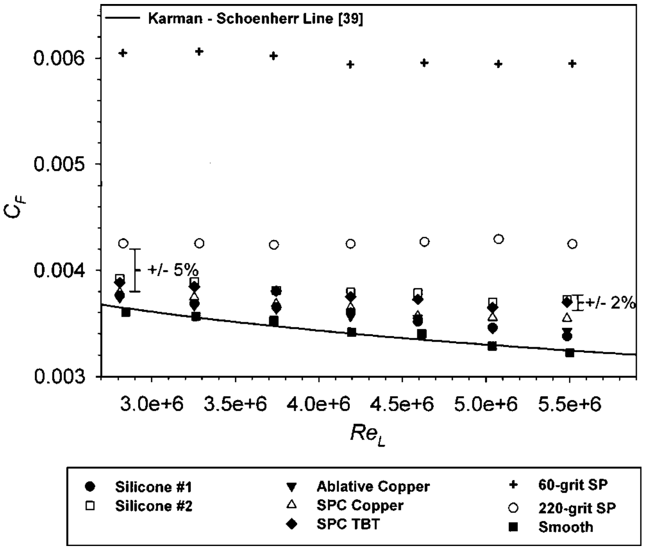

Fig. 6 Overall frictional resistance coefficient versus Reynolds number for all test surfaces in the cleaned condition. (Overall uncertainty in C_F: ±2% at highest Reynolds number; ±5% at lowest Reynolds number.)

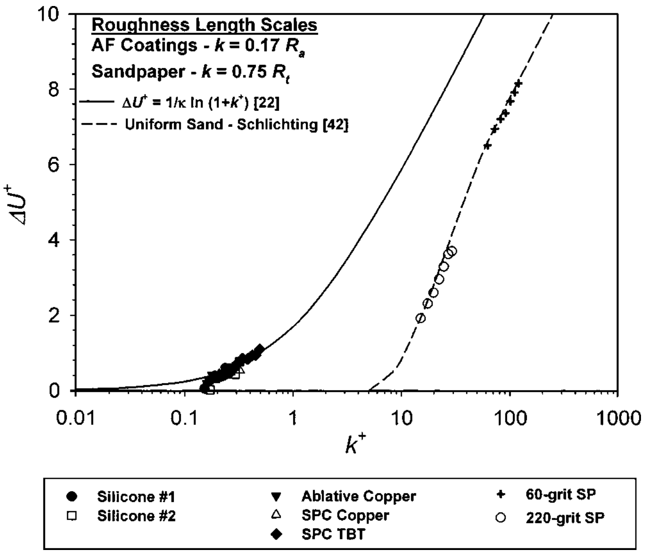

Fig. 7 Roughness function for all test surfaces in the unfouled condition. [Overall uncertainty in ΔU^+: ±6% or ±0.1 (whichever is larger) at highest Reynolds number; ±16% or ±0.2 (whichever is larger) at lowest Reynolds number.]

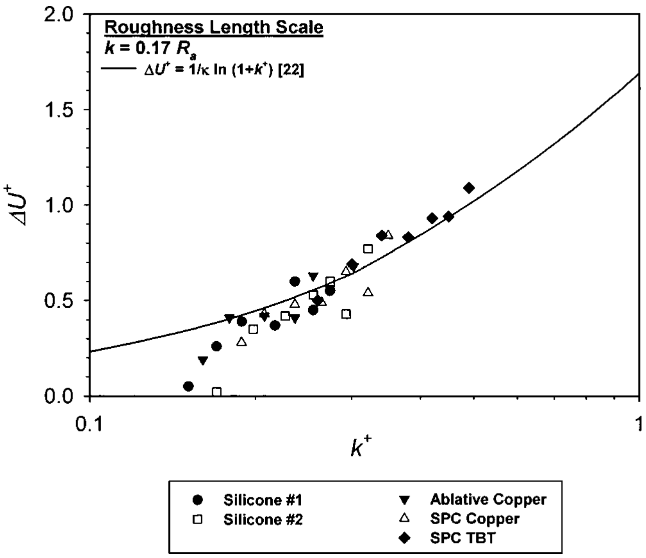

Fig. 8 Roughness function for the AF test surfaces in the unfouled condition. [Overall uncertainty in ΔU^+: ±6% or ±0.1 (whichever is larger) at highest Reynolds number; ±16% or ±0.2 (whichever is larger) at lowest Reynolds number.]

higher Reynolds number. The increase in C_F for the AF surfaces ranged from 5% for silicone 1 to 15% for silicone 2 compared to the smooth control at the highest Reynolds number. These differences are greater than the combined experimental uncertainty of the measurements and are considered significant. The ablative copper and silicone 1 both returned to nearly their unfouled frictional resistance, while silicone 2 and the SPC TBT showed significant increases in resistance. The roughness on the ablative copper, silicone 1, and the SPC TBT did not change from the unfouled to the cleaned conditions (Table 2), while the roughness on silicone 2 increased. It is believed that isolated coating damage due to exposure and cleaning led to increased drag on the SPC TBT surface, although it was isolated enough not to significantly affect the measured roughness statistics. The differences in surface roughness and how they relate to the frictional resistance will be discussed further in the roughness function section.

Roughness Function ΔU^+. The roughness functions ΔU^+ for the test surfaces in the unfouled, fouled, and cleaned condition were found by means of the similarity law analysis of Granville [20] developed for flat plates. This was carried out by solving Eqs. (5) and (6) iteratively for k^+ and ΔU^+, respectively. It should be noted that the choice of k for a given roughness has no effect on the calculated ΔU^+ despite its apparent dependence on k through the $\Delta U^{+\prime}$ term in Eqs. (5) and (6). This is because the effect of changing k on ΔU^+ is to simply move the curve along the abscissa without changing its slope. The roughness function results for all the test surfaces in the unfouled condition are shown in Fig. 7 and for the unfouled AF surfaces in Fig. 8. Shown for comparison is the roughness function for uniform sand given by Schlichting [41] based on the classical experiments of Nikuradse [42] and a Colebrook-type roughness function of Grigson [22] for random roughness given as

$$\Delta U^+ = \frac{1}{\kappa}\ln(1+k^+). \tag{8}$$

The roughness functions for the rough sandpaper controls show excellent agreement with a Schlichting uniform sand roughness function using $k = 0.75R_t$. This was also observed in previous investigations by the present author using a range of direct and indirect methods to obtain ΔU^+ [32,33]. All of the roughness length scales in Table 2, as well as moments of the wavenumber spectra (i.e., Townsin et al. [19]), the mean absolute roughness slope (i.e., Musker [18]) and combinations thereof, were considered as possible roughness length scales for the unfouled AF surfaces. The best fit of these results was found using a simple multiple of the centerline average height, R_a, as k. R_a was suggested to be a suitable roughness scaling parameter for sanded paint surfaces by Schultz and Flack [32]. With $k = 0.17R_a$, 75% of the variance (i.e., $R^2 = 0.75$) in ΔU^+ could be explained using a Colebrook-type roughness function [Eq. (8)]. The results presented in Figs. 7 and 8 show that reasonable agreement is obtained using this scaling considering the relatively large uncertainty in ΔU^+ as $k^+ \to 0$. Candries et al. [40] assert that a roughness parameter based on both R_a and the mean absolute slope adequately collapses a range of unfouled AF surfaces. This scaling was tried in the present study, but did no better job of collapsing the results than R_a alone. It is of note that the scatter in ΔU^+ in the study of Candries et al. was larger than in the present study. The results seem to indicate that the differences in roughness wavelength observed between the silicones and traditional AF paints in this study (see Figs. 3 and 4) are not large enough to significantly influence the frictional drag.

The roughness functions for the fouled surfaces are presented in Fig. 9. In order to develop suitable scaling parameters for the fouled surfaces it was decided to divide the surfaces into those with barnacle fouling and those without (only the SPC TBT surface). In developing a scaling parameter for the surfaces with barnacle fouling, it was assumed that the largest roughness heights (i.e., the height of the largest barnacles) have the dominant influence on drag and that effect of increased percent coverage of barnacles on drag is largest for small coverage and smaller for large coverage. These assumptions were gleaned from the present results and the pipe flow experiments of Leer-Andersen and Larsson [6], as well as the observations of Bradshaw for typical roughness types [43]. Based on this, the following roughness length scale was developed for the barnacle-fouled surfaces:

$$k = 0.059R_t(\%\ \text{Barnacle Fouling})^{1/2}. \tag{9}$$

R_t here is taken to be the height of the largest barnacles, given in the last column of Table 1. Using this scaling, excellent collapse ($R^2 = 0.98$) is obtained for the present results with a Colebrook-type roughness function [Eq. (8)]. Further study is needed to assess the validity of this scaling on a range of fouled surfaces and

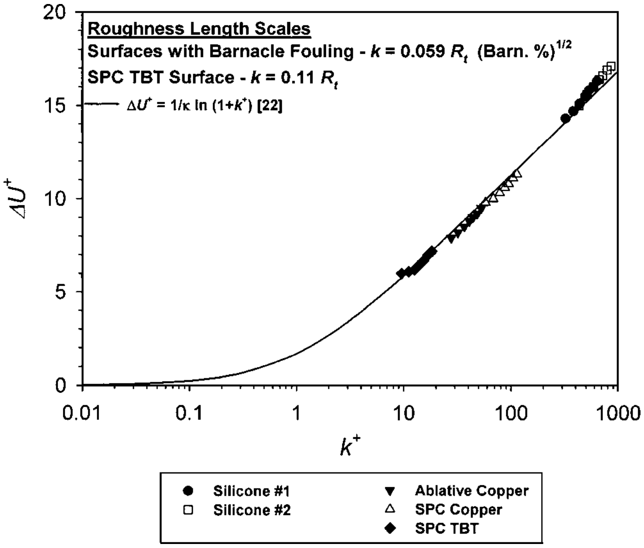

Fig. 9 Roughness function for the AF test surfaces in the fouled condition after 287 days exposure. [Overall uncertainty in ΔU^+: ±6% or ±0.1 (whichever is larger) at highest Reynolds number; ±16% or ±0.2 (whichever is larger) at lowest Reynolds number.]

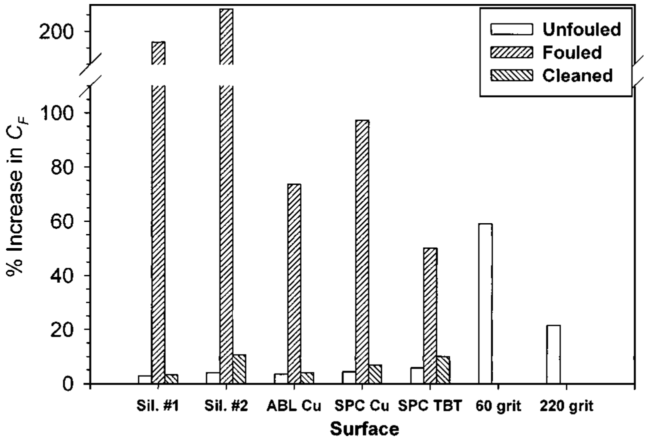

Fig. 11 Increase in C_F at ship-scale ($L=150$ m) for the test surfaces in the unfouled, fouled, and cleaned conditions for $U \approx 6.2$ m/s (12 knots)

its applicability to other calcareous fouling types. The SPC TBT remained free of barnacle fouling over the course of exposure and was covered with only a light slime film. The roughness function for this surface collapsed well ($R^2=0.90$) with a Colebrook-type roughness function [Eq. (8)] using $k=0.11R_t$, where R_t is the estimated thickness of the slime film using a wet film paint thickness gauge, given in the last column of Table 1. The slime film thickness measurement procedure is described in greater detail in Schultz and Swain [27].

The roughness functions for the cleaned surfaces are presented in Fig. 10. It was decided to use the same roughness scaling for the cleaned AF surfaces as for the unfouled surfaces ($k=0.17R_a$). As can be seen in Fig. 10, this choice of k gives poor collapse of the results. Other choices did not yield significant improvement. It is felt that the inability to collapse results for the cleaned surfaces stems from small areas of coating damage due to exposure in the marine environment and subsequent cleaning. The likelihood of these areas being randomly sampled when the roughness height measurements are made is small. However, the effect of the damage on the overall frictional resistance of the surface is quite significant. Further work is, therefore, needed to identify a robust roughness scaling parameter and sampling routine suitable for a wider range of coating types and conditions.

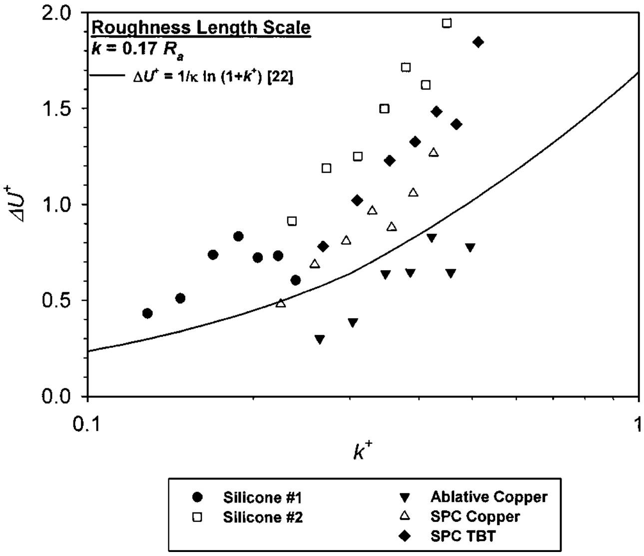

Fig. 10 Roughness function for the AF test surfaces in the cleaned condition. [Overall uncertainty in ΔU^+: ±6% or ±0.1 (whichever is larger) at highest Reynolds number; ±16% or ±0.2 (whichever is larger) at lowest Reynolds number.]

Frictional Resistance, C_F, at Ship-Scale. Granville [34] gives a similarity law procedure for calculating the effect of a given roughness on the frictional resistance of a planar surface of arbitrary length using the roughness function obtained for a flat plate in a lab. This was carried out using the present highest Reynolds number results for a plate length, L, of 150 m. This length was selected because it is representative of many midsized merchant ships as well as Naval surface combatants such as frigates and destroyers. Figure 11 shows the results of the similarity law analysis for all surfaces in the unfouled, fouled, and cleaned conditions for U≈6.2 m/s (12 knots). The results are presented as percent increase in C_F compared to a smooth surface. The increase in C_F for the AF surfaces in the unfouled condition ranged from 3% for silicone 1 to 6% for the SPC TBT surface. This indicates that only small differences in the performance of these coatings are likely when a ship is freshly out of drydock. The 60-grit and 220-grit sandpaper controls had increases in C_F of 59% and 22%, respectively.

The increase in C_F for the AF surfaces in the fouled condition ranged from 50% for SPC TBT to 217% for the silicone 2. The two silicone surfaces had the largest increase in frictional resistance with the biocide-based AF systems showing smaller increase. This indicates that silicones will likely provide significantly poorer performance than biocide-based systems if hydrodynamic self-cleaning is not possible or if mechanical cleaning is not utilized. The increase in C_F for the AF surfaces in the cleaned condition ranged from 3% for silicone 1 to 11% for silicone 2. It is of note that the frictional resistance for silicone 1, ablative copper, and SPC copper returned to within 1% of the unfouled condition, while silicone 2 and SPC TBT had increases of 7% and 4%, respectively, compared to the unfouled resistance. This difference is likely due to small areas of coating damage that were discussed previously.

Conclusion

An experimental study of the surface roughness and frictional resistance of a range of modern antifouling paint systems has been made. The results indicate little difference in C_F among the paint systems in the unfouled condition. Significant differences, however, were observed in C_F among the paint systems in the fouled condition, with the silicone surfaces showing the largest increases. While some of the antifouling systems returned to near their unfouled resistance after cleaning, coating damage led to significant increases in C_F for some coatings. The roughness function ΔU^+ for the unfouled coatings shows reasonable collapse to a Colebrook-type roughness function when the centerline average height ($k=0.17R_a$) is used as the roughness length scale. Excellent collapse of the roughness function for the barnacle fouled surfaces was obtained using a new roughness length scale based on the barnacle height and percent coverage. Poor collapse of the roughness function for the cleaned coatings was likely due to isolated damage.

Acknowledgments

The author would like to thank the Office of Naval Research for financial support under the direction of Dr. Steve McElvaney. Many thanks to Mr. Steve Enzinger, Mr. Don Bunker, and the rest of the USNA Hydromechanics Lab staff for providing technical support.

Nomenclature

B = smooth wall log-law intercept=5.0
C_F = overall frictional resistance coefficient $=(F_D)/(1/2\rho U_e^2 S)$
c_f = local frictional resistance coefficient$=(\tau_o)/(\frac{1}{2}\rho U_e^2)$
F_D = drag force
k = arbitrary measure of roughness height
L = plate length
N = number of samples in surface profile
Re_{δ^*} = displacement thickness Reynolds number$=U_e\delta^*/\nu$
Re_L = Reynolds number based on plate length$=U_e L/\nu$
R_a = centerline average roughness height$=1/N\Sigma_{i=1}^{N}|y_i|$
R_q = root mean square roughness height$=\sqrt{1/N\Sigma_{i=1}^{N}y_i^2}$
R_t = maximum peak to through height$=y_{\max}-y_{\min}$
S = wetted surface area
U = mean velocity in the x direction
U_e = freestream velocity relative to surface
U_τ = friction velocity$=\sqrt{\tau_o/\rho}$
ΔU^+ = roughness function
x = streamwise distance from plate leading edge
y = normal distance from the boundary measured from roughness centerline
δ = boundary layer thickness
δ^* = displacement thickness$=\int_0^\delta(1-U/U_e)dy$
κ = von Karman constant=0.41
ν = kinematic viscosity of the fluid
ρ = density of the fluid
τ_o = wall shear stress

superscript

$+$ = inner variable (normalized with U_τ or U_τ/ν)

subscript

min = minimum value
max = maximum value
R = rough surface
S = smooth surface

References

[1] Kempf, G., 1937, "On the Effect of Roughness on the Resistance of Ships," Trans. Institution of Naval Architects **79**, pp. 109–119.

[2] Benson, J. M., Ebert, J. W., and Beery, T. D., 1938, "Investigation in the NACA Tank of the Effect of Immersion in Salt Water on the Resistance of Plates Coated With Different Shipbottom Paints," N.A.C.A. Memorandum Report C&R C-S19-1(3).

[3] Denny, M. E., 1951, "B.S.R.A. Resistance Experiments on the Lucy Ashton: Part I—Full-Scale Measurements," Trans. Institution of Naval Architects **93**, pp. 40–57.

[4] Lewthwaite, J. C., Molland, A. F., and Thomas, K. W., 1985, "An Investigation Into the Variation of Ship Skin Frictional Resistance With Fouling," Trans. Royal Institute of Naval Architect., **127**, pp. 269–284.

[5] Watanabe, S., Nagamatsu, N., Yokoo, K., and Kawakami, Y., 1969, "The Augmentation in Frictional Resistance Due to Slime," J. Kansai Society of Naval Architects, **131**, pp. 45–51.

[6] Leer-Andersen, M., and Larsson, L., 2003, "An Experimental/Numerical Approach for Evaluating Skin Friction on Full-Scale Ships With Surface Roughness," J. Marine Sci. Technol., **8**, pp. 26–36.

[7] Townsin, R. L., 2003, "The Ship Hull Fouling Penalty," Biofouling, **19**(**Supplement**), pp. 9–16.

[8] Swain, G., 1998, "Biofouling Control: A Critical Component of Drag Reduction," *Proceedings of the International Symposium on Seawater Drag Reduction*, Newport, RI, pp. 155–161.

[9] Champ, M. A., 2003, "Economic and Environmental Impacts on Port and Harbors From the Convention to Ban Harmful Marine Anti-Fouling Systems," Mar. Pollution Bull., **46**, pp. 935–940.

[10] Swain, G. W., and Schultz, M. P., 1996, "The Testing and Evaluation of Non-Toxic Antifouling Coatings," Biofouling, **10**, pp. 187–197.

[11] Candries, M., Atlar, M., and Anderson, C. D., 2000, "Considering the Use of Alternative Antifoulings: the Advantages of Foul-Release Systems," *Proceedings ENSUS 2000*, Newcastle, UK, pp. 88–95.

[12] Brady, R. F., and Singer, I. L., 2000, "Mechanical Factors Favoring Release From Fouling Release Coatings," Biofouling, **15**, pp. 73–81.

[13] Schultz, M. P., Finlay, J. A., Callow, M. E., and Callow, J. A., 2003, "Three Models to Relate Detachment of Low Form Fouling at Laboratory and Ship Scale," Biofouling, **19**(Supplement), pp. 17–26.

[14] Swain, G. W., Nelson, W. G., and Preedeekanit, S., 1998, "The Influence of Biofouling and Biotic Disturbance on the Development of Fouling Communities on Non-Toxic Surfaces," Biofouling, **12**, pp. 257–269.

[15] Kavanagh, C. J., Schultz, M. P., Swain, G. W., Stein, J., Truby, K., and Darkangelo Wood, C., 2001, "Variation in Adhesion Strength of Balanus Eburneus, Crassotrea Virginica and Hydroides Dianthus to Fouling-Release Coatings," Biofouling, **17**, pp. 155–167.

[16] Kovach, B. S., and Swain, G. W., 1998, "A Boat-Mounted Foil to Measure the Drag Properties of Antifouling Coatings Applied to Static Immersion Panels," *Proceedings of the International Symposium on Seawater Drag Reduction*, Newport, RI, pp. 169–173.

[17] Lackenby, H., 1962, "Resistance of Ships, With Special Reference to Skin Friction and Hull Surface Condition," *Proceedings of the Institution of Mechanical Engineers*, **176**, pp. 981–1014.

[18] Musker, A. J., 1980–1981, "Universal Roughness Functions for Naturally-Occurring Surfaces," Trans. Can. Soc. Mech. Eng., **1**, pp. 1–6.

[19] Townsin, R. L., Byrne, D., Svensen, T. E., and Milne, A., 1981, "Estimating the Technical and Economic Penalties of Hull and Propeller Roughness," Trans. SNAME, **89**, pp. 295–318.

[20] Granville, P. S., 1987, "Three Indirect Methods for the Drag Characterization of Arbitrarily Rough Surfaces on Flat Plates," J. Ship Res., **31**, pp. 70–77.

[21] Medhurst, J. S., 1989, "The Systematic Measurement and Correlation of the Frictional Resistance and Topography of Ship Hull Coatings, With Particular Reference to Ablative Antifoulings," Ph.D. Thesis, University of Newcastle-upon-Tyne, Newcastle, UK.

[22] Grigson, C. W. B., 1992, "Drag Losses of New Ships Caused by Hull Finish," J. Ship Res., **36**, pp. 182–196.

[23] Anon, 1952, *Marine Fouling and Its Prevention*, Woods Hole Oceanographic Institution.

[24] McEntee, W., 1915, "Variation of Frictional Resistance of Ships With Condition of Wetted Surface," Trans. SNAME, **24**, pp. 37–42.

[25] Picologlou, B. F., Zelver, N., and Characklis, W. G., 1980, "Biofilm Growth and Hydraulic Performance," J. Hydraul. Div., Am. Soc. Civ. Eng., **HY5**, pp. 733–746.

[26] Haslbeck, E. G., and Bohlander, G., 1992, "Microbial Biofilm Effects on Drag—Lab and Field," *Proceedings 1992 SNAME Ship Production Symposium*.

[27] Schultz, M. P., and Swain, G. W., 1999, "The Effect of Biofilms on Turbulent Boundary Layers," ASME J. Fluids Eng., **121**, pp. 733–746.

[28] Schultz, M. P., 2000, "Turbulent Boundary Layers on Surfaces Covered With Filamentous Algae," ASME J. Fluids Eng., **122**, pp. 357–363.

[29] Clauser, F. H., 1954, "Turbulent Boundary Layers in Adverse Pressure Gradients," J. Aeromaut. Sci. , **21**, pp. 91–108.

[30] Hama, F. R., 1954, "Boundary-Layer Characteristics for Rough and Smooth Surfaces," Trans. SNAME, **62**, pp. 333–351.

[31] Krogstad, P. Å., and Antonia, R. Å., 1999, "Surface Roughness Effects in Turbulent Boundary Layers," Exp. Fluids, **27**, pp. 450–460.

[32] Schultz, M. P., and Flack, K. A., 2003, "Turbulent Boundary Layers Over Surfaces Smoothed by Sanding," ASME J. Fluids Eng., **125**, pp. 863–870.

[33] Schultz, M. P., and Myers, A., 2003, "Comparison of Three Roughness Function Determination Methods," Exp. Fluids, **35**, pp. 372–379.

[34] Granville, P. S., 1958, "The Frictional Resistance and Turbulent Boundary Layer of Rough Surfaces," J. Ship Res., **2**, pp. 52–74.

[35] Schultz, M. P., 2002, "The Relationship Between Frictional Resistance and Roughness for Surfaces Smoothed by Sanding," ASME J. Fluids Eng., **124**, pp. 492–499.

[36] ASTM D3623, 1994, ‘‘Standard Test Method for Testing Antifouling Panels in Shallow Submergence,’’ Vol. 6.02.

[37] Moffat, R. J., 1988, ‘‘Describing the Uncertainties in Experimental Results,’’ Exp. Therm. Fluid Sci., **1**, pp. 3–17.

[38] Coleman, H. W., and Steele, W. G., 1995, ‘‘Engineering Application of Experimental Uncertainty Analysis,’’ AIAA J., **33**(10), pp. 1888–1896.

[39] Schoenherr, K. E., 1932, ‘‘Resistances of Flat Surfaces Moving Through a Fluid,’’ Trans. SNAME, **40**, pp. 279–313.

[40] Candries, M., Atlar, M., Mesbahi, E., and Pazouki, K., 2003, ‘‘The Measurement of the Drag Characteristics of Tin-Free Self-Polishing Co-Polymers and Fouling Release Coatings Using a Rotor Apparatus,’’ Biofouling, **19**(Supplement), pp. 27–36.

[41] Schlichting, H., 1979, *Boundary-Layer Theory*, 7th ed., McGraw-Hill, New York.

[42] Nikuradse, J., 1933, ‘‘Laws of Flow in Rough Pipes,’’ *NACA Technical Memorandum 1292*.

[43] Bradshaw, P., 2000, ‘‘A Note on ‘‘Critical Roughness Height’’ and ‘‘Transitional Roughness’’,’’ Phys. Fluids, **12**, pp. 1611–1614.

Added Mass of an Oscillating Hemisphere at Very-Low and Very-High Frequencies

Mario A. Storti*
Jorge D'Elía†

Centro Internacional de Métodos
Computacionales en Ingeniería (CIMEC)
INTEC, UNL-CONICET. Güemes 3450,
3000-Santa Fe, Argentina
http://www.cimec.org.ar,
e-mail: cimec@ceride.gov.ar
Telephone: +54 342 4556673;
Fax: +54 342 4550944

A floating hemisphere under forced harmonic oscillation at very-low and very-high frequencies is considered. The problem is reduced to an elliptic one, that is, the Laplace operator in the exterior domain with Dirichlet and Neumann boundary conditions. Asymptotic values of the added mass are found with an analytic prolongation for the surge mode, and with a seminumerical computation with spherical harmonics for the heave one. The general procedure is based on the use of spherical harmonics and its derivation is based on a physical insight rather than a mathematical one. This case can be used to test the accuracy achieved by numerical codes based on other formulations as finite or boundary elements. [DOI: 10.1115/1.1839932]

1 Introduction

This work is concerned with a computation of the added mass of a floating hemispherical body due to a forced oscillatory motion of the body in the free surface of an inviscid incompressible fluid. Two canonical cases are considered, namely those of heave and surge motions, where these nautical terms are used to describe a vertical or horizontal oscillation of the body.

The present problem has several applications. For example, the oscillation of the body implies wave radiation and then it has interest in wave energy conversion (e.g., see Falnes [1]). Another case arise in seakeeping hydrodynamics (e.g., see Ohkusu [2], Huang–Sclavounos [3]), where the hydrodynamic characteristics of a vessel due to action of surface waves when the wave motion is small enough compared to the body length can be computed adopting a linearized theory. Then, the response of a body to incident waves can be determined from the added-mass and damping coefficients associated to the forced motions of the body in the absence of waves, for example, the heave motions of a semisubmersible platform due to the influence of ocean waves, e.g., see Hulme [4]. Besides, added mass effects can be recognized in ship vibrations. Although Lamb [5] investigated the accelerated motion of a submerged cylinder, its relevancy in ship vibrations was only properly recognized from the experimental work of Nicholls [6] and the mathematical one (using conformal mapping) of Lewis [7].

From a physical point of view, the added mass effect comes from the inertia of an incompressible fluid. For instance, when a floating shiplike body performs a heave motion and the fluid is assumed as incompressible, there will be fluid motion between the hull and the free surface on the downbeat and back again on the upbeat, see Fig. 1. The added mass effects in this case come from the pressures transmitted to the hull arising from the inertia of the fluid. A similar analysis can be made for the surge motion, e.g., see Llloyd [8] and Jennings [9].

The formulation of problems involving floating hemispheres is analogous to that for the corresponding two-dimensional ones involving circular cylinders and perhaps, as Hulme [10] says, this is the reason why they have received rather comparatively little attention in the literature. The modern history of this subject began with Ursell [11] who formulated and solved the boundary value problem for a semi-immersed heaving circular cylinder, where the velocity potential is represented as the sum of an infinite set of multipoles, each satisfying linearized free-surface boundary condition and each being multiplied by a coefficient determined by requiring the series to satisfy the kinematic boundary condition at a finite number of points on the cylinder. Grim [12] used a variation of the Ursell method to solve for the two-parameter Lewis-form cylinders by conformal mapping onto a circle. Tasai [13] and Porter [14] using the Ursell approach, obtained the added mass and damping for oscillating contours mappable onto a circle by the more general Theodorsen transformation, whereas Ogilvie [15] computed the hydrodynamics forces on a completely submerged heaving circular cylinder. Frank [16] used an integral formulation where the velocity potential is represented by a distribution of sources over the submerged cross section; the density of the sources is an unknown function of the position along the contour to be determined from integral equations found by applying the kinematic boundary condition on the submerged part of the cylinder.

Havelock [17] gives an account of the heaving-hemisphere case, where the solution is found with a method similar to that used by Ursell for the circular cylinder, that is, the velocity potential is expressed, in spherical polar coordinates, as the sum of a wave source at the sphere center together with an infinite series of wave-free potentials. Then, the velocity potential satisfies all the boundary conditions except for the body surface, and the latter is used to generate an infinite linear system of equations for the infinite number of unknowns appearing in the expansion of the velocity potential. Hulme [10] used an essentially equivalent approach to Havelock's one but with several modifications and more rigorous justification, where the solution is found by means of an expansion for the velocity potential in terms of an infinity series of spherical harmonics from which the relevant forces may be computed.

As it is usual in seakeeping flow problems, the forces exerted on oscillating bodies are given as the added mass and damping coefficients, which measure the components of the wave force in phase with the acceleration and velocity of the body, respectively. In this work only the former case is considered. The proposed method is nearly exact in the sense that the numerical solution can be done with a very high precision, and the results used to determine the accuracy achieved by other methods, e.g., finite or boundary elements, that can be used to treat more general body geometries, e.g., see Nigro et al. [18], Storti et al. [19,20], and D'Elía et al. [21–23].

In this work, the heave and surge modes at very low and very high frequencies of the unit hemisphere are reformulated as

---

*Conicet Senior Researcher; e-mail: mstorti@intec.unl.edu.ar
†Conicet Graduate Researcher; e-mail: jdelia@intec.unl.edu.ar

Contributed by the Fluids Engineering Division for publication in the JOURNAL OF FLUIDS ENGINEERING. Manuscript received by the Fluids Engineering Division October 15, 2003; revised manuscript received August 5, 2004. Associate Editor: S. Balachandar.

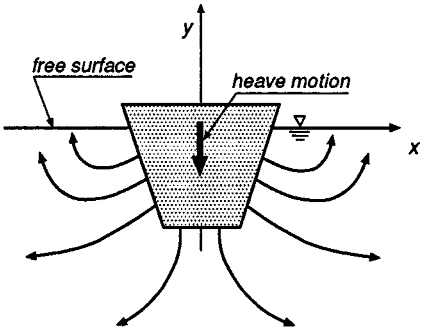

Fig. 1 Sketch of the movement of an incompressible fluid in shiplike vibration due to a heave motion

boundary value problems extended to the all space, they are solved by orthogonal expansion by means of spherical harmonics. In the Hulme's work, the derivation of the asymptotic form for the surge-mass coefficient at very high frequencies ($\omega \rightarrow \infty$) is, as Hulme says, *suggestive* rather than conclusive so, an alternative derivation is given here for the same coefficient where the present estimation is found closely related to Hulme's estimate.

2 The Oscillating Unity Hemisphere

An oscillating unity hemisphere in a forced motion is considered. The unit hemisphere is the open surface $r=1$, $0 \leqslant \theta \leqslant \pi/2$, $0 \leqslant \varphi \leqslant 2\pi$, where r is the radius, θ is the azimuthal angle and φ is the circumferential one. Its edge is on the free surface of an irrotational and incompressible fluid, without a mean flow, the fluid depth is assumed as infinity, the z-axis positive downward and the hydrostatic equilibrium plane is $z=0$, see Fig. 2. Due to the symmetry, the Cartesian coordinates (x,y,z) are transformed to the spherical ones (r,θ,φ) as

$$\begin{aligned} x &= r \sin\theta \cos\varphi, \\ y &= r \sin\theta \sin\varphi, \\ z &= r \cos\theta, \end{aligned} \tag{1}$$

see Fig. 3. In this work a whole linearized analysis is performed and for this reason the linearized surface boundary condition at $z=0$ is only used. As it is well known (e.g., see Newman [24], Ogilvie [25], Ohkusu [2], Stoker [26]), the standard free surface boundary condition of linearized water-wave theory for sinusoidal time dependence is given by

$$\phi_{,n} = \frac{\omega^2}{g}\phi \quad \text{at } z=0; \tag{2}$$

where ϕ is the velocity potential, $\phi_{,n} \equiv \partial\phi/\partial n$ is the normal velocity, n is the unit normal, $z=0$ is the hydrostatic free surface, ω is the circular frequency of the sinusoidal oscillation, and g is the gravity acceleration.

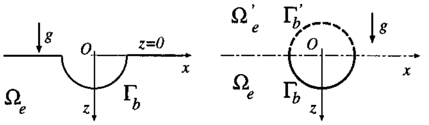

Fig. 2 Geometrical description of a seakeeping-like flow: Original problem (left) and extended to the upper plane (right)

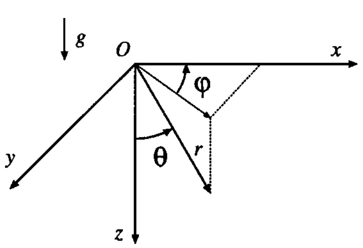

Fig. 3 Cartesian coordinates (x,y,z) and spherical ones (r,θ,φ)

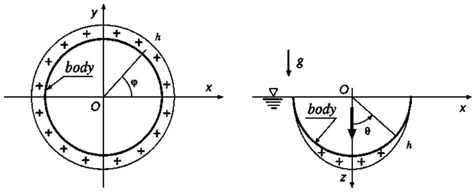

Fig. 4 The heave load $h(\theta,\varphi)=\cos\theta$, with $0 \leqslant \theta \leqslant \pi/2$

2.1 Limits at Very-Low and Very-High Frequencies. In both limit process $\omega \rightarrow 0$ and $\omega \rightarrow \infty$ for the linearized free-surface boundary condition given by Eq. (2), it will be assumed that the velocity potential ϕ, the normal velocity $\phi_{,n}$ and the gravity acceleration g remain finites and bounded. Then, on one hand, at very-low frequencies ($\omega \rightarrow 0$) the free-surface boundary Eq. (2) shrinks to the homogeneous Neumann one $\phi_{,n}=0$ at $z=0$, that is,

$$\omega \rightarrow 0: \begin{cases} \Delta\phi = 0 & \text{in } \Omega; \\ \phi_{,n} = 0 & \text{at } z=0; \\ \phi_{,n} = h & \text{at } \Gamma_b; \\ |\phi| \rightarrow 0 & \text{for } |x| \rightarrow \infty. \end{cases} \tag{3}$$

On the other hand, at very-high frequencies ($\omega \rightarrow \infty$) the free-surface boundary Eq. (2) shrinks to the homogeneous Dirichlet one $\phi=0$ at $z=0$, then

$$\omega \rightarrow \infty: \begin{cases} \Delta\phi = 0 & \text{in } \Omega; \\ \phi = 0 & \text{at } z=0; \\ \phi_{,n} = h & \text{at } \Gamma_b; \\ |\phi| \rightarrow 0 & \text{for } |x| \rightarrow \infty. \end{cases} \tag{4}$$

In Eqs. (3) and (4), Δ is the Laplace operator, $h=h(\theta,\varphi)$ is the load given by the normal displacement of the mode under consideration, and the last condition is the radiation boundary condition at infinity. For simplicity, it is assumed that the load $h=h(\theta,\phi)$ is real, that is, the body motion is in phase with the fluid velocity. It should be noted that the original linearized flow problem is defined only in the lower region $z \leqslant 0$ but the analysis performed for the two limit processes of the linearized surface boundary condition at $z=0$, that is, for $\omega \rightarrow 0$ [Very Low Frequencies (VLF)] and for $\omega \rightarrow \infty$ [Very High Frequencies (VHF)], suggests that the boundary conditions $\phi_{,n}=0$ at VLF and $\phi=0$ at VHF, respectively, could be taken into account at the plane $z=0$.

2.2 The Heave and Surge Modes. The heave-mode excitation of the body (vertical oscillation) produces a symmetrical displacement around the vertical axis z and it can be written as $h=\cos\theta$, with $0 \leqslant \theta \leqslant \pi/2$, see Fig. 4. Analogously, the surge-mode excitation (horizontal oscillation) produces an antisymmetrical displacement with respect to the plane $x=0$ and it can be written as $h=\sin\varphi$, with $0 \leqslant \varphi < 2\pi$, see Fig. 5. Once the velocity potential ϕ is solved for each mode (i.e., the surge ϕ^1 and the heave ϕ^3 ones), the added mass A_{ij} in the i degree of freedom due to a harmonic unity excitation on the j-direction is computed as the surface integral

$$A_{ij} = -\rho \int_{\Gamma_b} d\Gamma \; \phi^i \phi^j_{,n}, \tag{5}$$

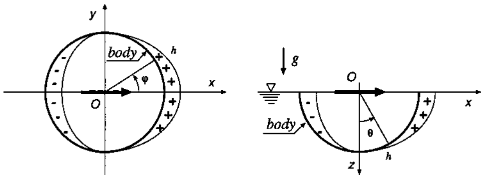

Fig. 5 The surge load $h(\theta,\varphi)=\sin\varphi\sin\theta$, with $0\leqslant\varphi<2\pi$ and $0\leqslant\theta<\pi/2$

over the body surface Γ_b, where $i=j=1$ for the surge mode and $i=j=3$ for the heave one, e.g., see Ohkusu [2], Newman [24]. Then, the added mass coefficient is obtained as $A'_{ij}=A_{ij}/(\rho V)$, where $V=(\frac{2}{3})\pi R^3$ is the body volume of the hemisphere and ρ is the fluid density.

3 The Extended Flow Problems

By symmetry, Eqs. (3) and (4) can be reproduced extending the flow problem to upper region $z<0$ by means of a reflection with respect to the plane $z=0$ and extending the load $h=h(\theta,\phi)$ in an appropriate way. For instance, the homogeneous Neumann boundary condition is obtained when the load h is extended in a symmetrical way, i.e., $h(x,y,z)=h(x,y,-z)$, while the homogeneous Dirichlet one is obtained when the load h is extended in an anti-symmetrical way, i.e., $h(x,y,z)=-h(x,y,-z)$. It should be noted that the plane $z=0$ is not really necessary in the subsequent analysis since the surface load extension *automatically* satisfied the suggested linearized boundary conditions $\phi_{,n}=0$ at VLF and $\phi=0$ at VHF, respectively.

3.1 The Extended Heave-Modes at VLF and VHF. The extended heave loads at VLF and VHF are obtained from the sphere ones as

$$\begin{aligned} &h=|\cos\theta| \quad \text{for low frequencies } (\omega\rightarrow 0),\\ &h=\cos\theta \quad \text{for high frequencies } (\omega\rightarrow\infty), \end{aligned} \tag{6}$$

where now $0\leqslant\theta\leqslant\pi$ due to the extension to upper region $z<0$. Then, the boundary value problem of the heave-mode at very-low frequencies ($\omega\rightarrow 0$) is written as

extended heave-mode at VLF

$$(\omega\rightarrow 0):\begin{cases}\Delta\phi=0 & \text{in } \Omega';\\ \phi_{,n}=|\cos\theta| & \text{at } \Gamma'_b;\\ \phi_{,n}=0 & \text{at } z=0;\\ |\phi|\rightarrow 0 & \text{for } |\mathbf{x}|\rightarrow\infty;\end{cases} \tag{7}$$

see Fig. 6, where $\Omega'=\Omega_e\cup\Omega'_e$ is the extended flow domain, Ω_e and Ω'_e are the flow domain exterior to the hemisphere and its extension through the reflection plane $z=0$, respectively, and Γ'_b is extended hemisphere surface through the same plane. Due to the module on source term, $|\cos\theta|$, this case does not have, in general, a closed solution, and whence it must be found with other resources like spherical harmonics, as considered in this work.

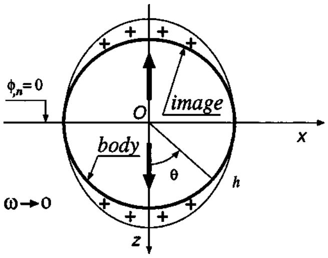

Fig. 6 Symmetrical load extension $h=|\cos\theta|$ for the heave-mode at very-low frequencies $\omega\rightarrow 0$

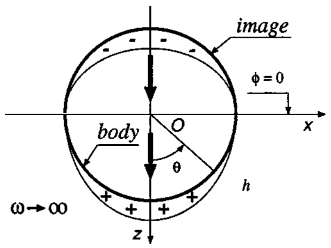

Fig. 7 Antisymmetrical load extension $h=\cos\theta$ for the heave-mode at very-high frequencies $\omega\rightarrow\infty$

Analogously, the boundary value problem of the heave-mode at very-high frequencies ($\omega\rightarrow\infty$) is written as

extended heave-mode at VHF

$$(\omega\rightarrow\infty):\begin{cases}\Delta\phi=0 & \text{in } \Omega';\\ \phi_{,n}=\cos\theta & \text{at } \Gamma'_b;\\ \phi=0 \quad \text{at} & \text{at } z=0;\\ |\phi|\rightarrow 0 & \text{for } |\mathbf{x}|\rightarrow\infty;\end{cases} \tag{8}$$

see Fig. 7 where, since the free surface boundary condition for VHF is $\phi=0$, its right hand side term has been extended in an anti-symmetric way and, then, it is equivalent to a sphere in infinite medium.

3.2 The Extended Surge-Mode. On the other hand, the extended surge loads at the VLF and VHF, e.g., see Figs. 8 and 9, are

$$\begin{cases} h=\sin\varphi\sin\theta & \text{for low frequencies } (\omega\rightarrow 0);\\ h=\sin\varphi\sin\theta\,\text{sign}\{\cos\theta\} & \text{for high frequencies } (\omega\rightarrow\infty).\end{cases} \tag{9}$$

Then, the boundary value problem of the surge-mode at very-low frequencies ($\omega\rightarrow 0$) is written as

extended surge-mode at VLF

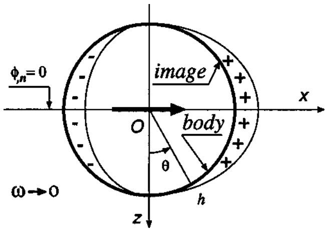

Fig. 8 The load extension $h=\sin\varphi\sin\theta$ for the surge-mode at Very Low Frequencies (VLF) ($\omega\rightarrow 0$)

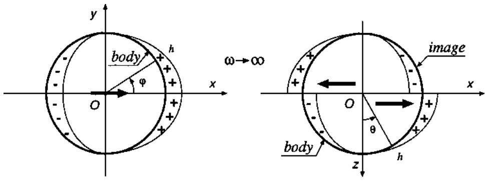

Fig. 9 The load extension $h=\sin\varphi\sin\theta\,\text{sign}\{\cos\theta\}$ for the surge-mode at Very High Frequencies (VHF) ($\omega\rightarrow\infty$)

$$(\omega\rightarrow 0):\begin{cases}\Delta\phi=0 \quad \text{in } \ in\ \ \Omega';\\ \phi_{,n}=\sin\varphi\sin\theta \quad \text{at } \ \Gamma'_e;\\ \phi_{,n}=0 \quad \text{at } \ z=0;\\ |\phi|\rightarrow 0 \quad \text{for } \ |\mathbf{x}|\rightarrow\infty;\end{cases} \tag{10}$$

and the boundary value problem at very-high frequencies ($\omega\rightarrow\infty$) is written as

extended surge-mode at VHF

$$(\omega\rightarrow\infty):\begin{cases}\Delta\phi=0 \quad \text{in } \ \Omega';\\ \phi_{,n}=\sin\varphi\sin\theta\,\mathrm{sign}\{\cos\theta\} \quad \text{at } \ \Gamma'_e;\\ \phi=0 \quad \text{at } \ z=0;\\ |\phi|\rightarrow 0 \quad \text{for } \ |\mathbf{x}|\rightarrow\infty.\end{cases} \tag{11}$$

4 Solution of the Extended Flow Problems

The extended flow problems can be solved, for instance, in an analytical way or by series. The solutions for the extended flow problems corresponding to the heave-mode at VHF ($\omega\rightarrow\infty$) and surge-mode at VLF ($\omega\rightarrow 0$), are the same of a sphere in an infinity medium and uniform velocity, so the additional mass is half the displaced mass, that is,

$$\begin{cases}A_{33}(\omega\rightarrow\infty)=\dfrac{\pi}{3}\rho R^3;\\[2ex] A_{11}(\omega\rightarrow 0)=\dfrac{\pi}{3}\rho R^3.\end{cases} \tag{12}$$

In the other two cases, the heave-mode at VLF ($\omega\rightarrow 0$) and the surge-mode at VHF ($\omega\rightarrow\infty$), are not that easy to obtain, so the solutions are found expanding the sources by means of spherical harmonics.

5 Spherical Harmonics

The exterior potential problem

$$\begin{cases}\Delta\phi=0 \quad \text{for } \ r>1;\\ \phi=f(\theta,\varphi) \quad \text{at} \quad \text{at } \ r=1;\end{cases} \tag{13}$$

where $\phi=\phi(\theta,\varphi)$ is solved expanding the function $f(\theta,\varphi)$ in terms of the harmonics

$$f(\theta,\varphi)=\sum_{n=0}^{\infty}a_{n0}P_n(\cos\theta)+\sum_{n=0}^{\infty}\sum_{m=1}^{n}[a_{nm}\cos(m\varphi)+b_{nm}\sin(m\varphi)]P_n^m(\cos\theta), \tag{14}$$

where $P_n(u)$ are the Legendre polynomials, with $u=\cos\theta$, $P_n^m(u)=(1-u^2)^{m/2}d^mP_n/du^m$ are the associated ones, while the coefficients are given by

$$a_{n0}=\frac{2n+1}{4\pi}\int_{r=1}d\Gamma\ f(\theta,\varphi)P_n(\cos\theta), \tag{15}$$

$$a_{nm}=\frac{2n+1}{2\pi}\frac{(n-m)!}{(n+m)!}\int_{r=1}d\Gamma\ f(\theta,\varphi)P_n^m(\cos\theta)\cos m\varphi, \tag{16}$$

$$b_{nm}=\frac{2n+1}{2\pi}\frac{(n-m)!}{(n+m)!}\int_{r=1}d\Gamma\ f(\theta,\varphi)P_n^m(\cos\theta)\sin m\varphi, \tag{17}$$

where $d\Gamma=\sin\theta\, d\varphi\, d\theta$ is the differential of the solid angle in spherical coordinates. Once this expansion is computed, the exterior potential can be written as

$$\phi(r,\theta,\varphi)=\sum_{n=0}^{\infty}Y_n(\theta,\varphi)r^{-(n+1)}, \tag{18}$$

where

$$Y_n(\theta,\varphi)=a_{n0}P_n(\cos\theta)+\sum_{m=1}^{n}[a_{nm}\cos(m\varphi)+b_{nm}\sin(m\varphi)]P_n^m(\cos\theta). \tag{19}$$

Then, the Neumann problem can be solved taking derivatives with respect to r and evaluating at $r=1$, that is, $h\equiv\phi_{,r}|_{r=1}$, obtaining the expression

$$h(\theta,\varphi)=-\sum_{n=0}^{\infty}(n+1)Y_n(\theta,\varphi), \tag{20}$$

from which analogous relations are obtained

$$a_{n0}=\frac{2n+1}{4\pi(n+1)}\int_{r=1}d\Gamma\ h(\theta,\varphi)P_n(\cos\theta), \tag{21}$$

$$a_{nm}=\frac{2n+1}{2\pi(n+1)}\frac{(n-m)!}{(n+m)!}\int_{r=1}d\Gamma\ h(\theta,\varphi)P_n^m(\cos\theta)\cos(m\varphi), \tag{22}$$

$$b_{nm}=\frac{2n+1}{2\pi(n+1)}\frac{(n-m)!}{(n+m)!}\int_{r=1}d\Gamma\ h(\theta,\varphi)P_n^m(\cos\theta)\sin(m\varphi), \tag{23}$$

Once the coefficients of the expansion are obtained, the added mass can be found from

$$A_{jj}=-\rho\int_{r=1}d\Gamma\ \phi\phi_{,r}=-\rho\int_0^{2\pi}G(\varphi)d\varphi\int_0^{\pi}H(\theta)d\theta, \tag{24}$$

where $G(\varphi)=\{1,\sin^2\varphi\}$ for the heave and surge motions, respectively, and

$$H(\theta)=\sum_{n=0}^{\infty}\left\{2a_{n0}^2[P_n(\cos\theta)]^2+\sum_{m=1}^{n}(a_{nm}^2+b_{nm}^2)\times[P_n^m(\cos\theta)]^2\right\}, \tag{25}$$

where the orthogonality property of the spherical harmonics was taken into account. Finally, using properties of the Legendre polynomials

$$A_{jj}=\rho\alpha\sum_{n=1}^{\infty}\frac{n+1}{2n+1}\left[2a_{n0}^2+\sum_{m=1}^{n}(a_{nm}^2+b_{nm}^2)\frac{(n+m)!}{(n-m)!}\right]; \tag{26}$$

where $\alpha=\{2\pi,\pi\}$, for the heave and surge motions, respectively.

6 Hemisphere in Heave-Mode at Very-Low Frequencies

The load in the heave-mode at VLF is $h(\theta,\varphi)=|\cos\theta|$, so

$$a_{n0}=\frac{2n+1}{4\pi(n+1)}\int_{-1}^{1}|\mu|P_n(\mu)d\mu\int_0^{2\pi}d\varphi, \tag{27}$$

where $\mu=\cos\theta$. As the $P_n(\mu)$ are even (odd) for n even (odd), only remains its even terms and then

$$a_{n0}=\frac{2n+1}{n+1}\int_0^1\mu P_n(\mu)d\mu, \tag{28}$$

for n even. For computing this integral, the P_n terms are generating in a recursive way with the initial conditions $P_0=1$, $P_1=\mu$, and the next terms $P_2, \ldots, P_n$ are obtained by solving

$$(n+1)P_{n+1}(\mu)-(2n+1)\mu P_n(\mu)+nP_{n-1}(\mu)=0. \quad (29)$$

The coefficients of the polynomials $\mu P_n(\mu)$ are obtained from the $P_n(\mu)$ ones, and the integral is made in a semianalytical way. The final result for the added mass in the heave-mode at VLF for the sphere is

$$A_{33}(\omega\to 0)=1.740\,335\,785\,143\rho R^3, \quad (30)$$

corresponding to $A'_{33}(\omega\to 0)=0.830\,949\,128\,536$, that is, the nondimensional coefficient with respect to the hemisphere mass $\frac{2}{3}\pi\rho R^3$.

7 Hemisphere in Surge-Mode at Very-High Frequencies

In this case, due to the load $h=\sin\varphi\sin\theta\,\mathrm{sign}\{\cos\theta\}$, the only no-null coefficients are the b_{n1} terms. For obtaining them an integral from $\mu=-1$ to $\mu=1$ must be made, with a function which includes the $P_n^1(\mu)$ terms. These terms have a factor $\sqrt{1-\mu^2}$, so it is more convenient to perform a seminumerical integration (e.g., see the Appendix). The final result is

$$A_{11}(\omega\to\infty)=0.570\,136\,261\,149eR^3\ldots, \quad (31)$$

corresponding to $A'_{11}(\omega\to\infty)=0.272\,220\,012\,593$, that is, the nondimensional coefficient with respect to the hemisphere mass $\frac{2}{3}\pi\rho R^3$.

8 Discussion

As it can be seen, the solutions to these problems have somewhat different properties according to whether the body oscillates in heave (vertically) or in surge (horizontally). On one hand, at Very Low Frequencies (VLF), if the body oscillates in heave its image moves oppositely (see Fig. 6) so that the two act together somewhat as a *pulsating source*, while if the body oscillates in surge its image moves in the same direction (see Fig. 8) and the total effect on the pressure load is the same as for an *horizontal dipole* in an infinite fluid. On the other hand, at Very High Frequencies (VHF), if the body oscillates in heave its image moves in the same direction (see Fig. 7) so that the two act together somewhat as a *vertical dipole*, while if the body oscillates in surge its image moves oppositely (see Fig. 9) and the total effect on the pressure load is the same as a *pair* of *horizontal dipoles* oriented in *opposite* directions. Furthermore, the intensity of the velocity potentials ϕ^j, with $j=1$ (surge) and $j=3$ (heave), are proportional to the source terms of the corresponding governing differential equations which, in turn, are fixed by these pressures loads. As the added mass is proportional to the integral of the fluid velocity at the surface of the extended body, then the resulting added mass can be expected to be greater for heave motion at Very Low Frequencies (VLF) (since its pressure load is always positive on the extended surface) than for the surge one at Very High Frequencies (VHF) (since its pressure load has both positive and negative values). In any case, the added mass at any frequency in heave motion is always greater than in the surge one (since the displaced fluid is greater in heave than in surge), as it is well known from the corresponding plots as functions of the frequency obtained, for instance, by numerical computations, e.g., see Papanikolau [27] or D'Elía [28]. A comprehensive analysis of relations between added masses and sources and doublets are given, for example, by Ogilvie [25] and Landweber [29].

The present estimates for the added mass coefficients with respect to the hemisphere mass $\frac{2}{3}\pi\rho R^3$, for the surge mode ($i=1$, longitudinal oscillation) and for the heave one ($i=3$, vertical oscillation), at VLF ($\omega\to 0$) and VHF ($\omega\to\infty$) limits, are summarized in Table 1 and compared to some literature values found (i) for the surge−sway mode, e.g., see Sierevogel [30], Prins [31] (where only the intervals [0.25,1.50] and [0.6,1.5] are, respectively, considered and so the extrapolations are rather doubtful); (ii) for the heave one, e.g., see Korsmeyer [32] and Liapis [33]; and (iii) Hulme [10]. The Sierevogel, Prins, and Liapis results are obtained with a panel method and Kelvin source; Korsmeyer used a panel method with Fourier transform and complex impedance extended to very-low frequencies, while the Hulme's numerical results are obtained by spherical harmonics but with a rather different derivation and implementation.

Table 1 Added mass coefficients at Very-Low Frequencies (VLF) ($\omega\to 0$) and Very-High Frequencies (VHF) ($\omega\to\infty$) for the surge mode $i=1$ (longitudinal oscillation) and the heave one $i=3$ (vertical oscillation) on the unit hemisphere

VLF ($\omega\to 0$)		VHF ($\omega\to\infty$)		
surge A'_{11}	heave A'_{33}	surge A'_{11}	heave A'_{33}	Reference
0.5	0.8	0.20	0.40	Sierevogel [30], Prins [31]
0.5	0.8	0.25	0.45	Korsmeyer [32], Liapis [33]
0.5	0.830 951	0.273 239	0.50	Hulme [10]
0.5	0.830 930	0.272 220	0.50	present work

In Hulme's work, the solution for each mode is expressed in terms of infinite series of spherical harmonics and then it is found solving truncated infinite linear system of equations. Hulme notes that its procedure is successful for slow oscillations of the body, i.e., small Ka, where a is the hemisphere radius (here Hulme's notation is employed) but, for high frequencies Ka the system is ill-conditioned so, for such cases, the problems are re-formulated as integral equations whose kernels become small as $Ka\to\infty$. This same procedure is also used by Ursell [34] and Davis [35] but, as a rigorous treatment of the surge case involves a significant amount of mathematical labor, Hulme gives a plausible procedure from which the surge-added mass coefficient is approximated as

$$A^{(1)}\sim C_1-\frac{C_2}{Ka} \quad \text{as} \quad Ka\to\infty, \quad (32)$$

with

$$C_1=-\frac{3}{2}\sum_{n=1}^{\infty}\alpha_n I\{2n,1;1\}; \quad C_2=+\frac{3}{2}\sum_{n=1}^{\infty}\beta_n I\{2n,1;1\}, \quad (33)$$

[Eqs. (5.14)–(5.16), p. 460, op. cit.] where the terms in the series for C_1 and C_2 decay as $1/n^3$ and $\log(n)/n^2$, respectively, so the C_2 coefficient is neglected by Hulme and, then, the surge-mass coefficient at VHF is assumed equal to $A^{(1)}\approx C_1\approx 0.273\,239\ldots$ which is closely related to the present estimate.

In conclusion, an alternative derivation of the added mass coefficients for the heave and surge motions of the unit floating hemisphere at very-low and very-high frequencies was shown. As a particular case, the numerical value obtained by the present procedure for the surge-mass coefficient at very high frequencies ($\omega\to\infty$) is closely related to Hulme's *suggestive* one. Other modeling efforts would be focused on its extension to other analytic body shapes which can be extended to the upper region as spheroids or ellipsoids. These simpler geometries can be used as test cases for validation of related numerical codes, as those used in ship-hydrodynamics or fluid−solid interaction.

Acknowledgments

This work was partially performed with the Free Software Foundation/GNU-Project resources, as GNU/Linux OS and GNU/Octave, and supported through Grant Nos. CONICET-PIP-198/98 (*Germen-CFD*), SECyT-FONCyT-PICT-51 (*Germen*), and CAI +D-UNL-94-004-024. The authors thank the referees for noticing

an error in the original manuscript (Appendix), through their constructive suggestions and careful reading of the manuscript.

Appendix

The load in the surge-mode at VHF is $h = \sin\varphi \sin\theta \operatorname{sign}\{\cos\theta\}$. The only no-null coefficients are the b_{n1} terms, that is,

$$b_{n1} = \frac{2n+1}{2\pi} \frac{1}{n(n+1)^2} \int_0^{2\pi} \sin^2 \varphi d\varphi \times \int_0^{\pi} \sin\theta \operatorname{sign}\{\cos\theta\} P_n^1(\cos\theta) \sin\theta d\theta, \qquad (A1)$$

introducing $\mu = \cos\theta$ and integrating in φ,

$$b_{n1} = \frac{2n+1}{2} \frac{1}{n(n+1)^2} \int_{-1}^{1} \sqrt{1-\mu^2} \operatorname{sign}\{\mu\} P_n^1(\mu) d\mu, \qquad (A2)$$

only the even terms are no-nulls, so

$$b_{n1} = \frac{2n+1}{n(n+1)^2} \int_0^1 (1-\mu^2) \frac{dP_n}{d\mu} d\mu, \qquad (A3)$$

integrating by parts,

$$b_{n1} = \frac{2n+1}{n(n+1)^2} \left[|(1-\mu^2) P_n(\mu)|_0^1 + 2\int_0^1 \mu P_n(\mu) d\mu \right], \qquad (A4)$$

or

$$b_{n1} = \frac{2n+1}{n(n+1)^2} \left[-P_n(0) + 2\int_0^1 \mu P_n(\mu) d\mu \right], \qquad (A5)$$

which is computed with a seminumerical procedure, for instance, with Octave [36].

References

[1] Falnes, J., and McIver, P., 1985, ''Surface Wave Interactions With System of Oscillating Bodies and Pressure Distributions,'' Appl. Ocean. Res., **7**(4), pp. 225–234.
[2] Ohkusu, M., *Advances in Marine Hydrodynamics*, Computational Mechanics Publications, 1996.
[3] Huang, Y., and Sclavounos, P. D., 1998, ''Nonlinear Ship Motions,'' J. Ship Res., **42**(2), pp. 120–130.
[4] Hulme, A., 1985, ''The Heave Added-Mass and Damping Coefficients of a Submerged Torus,'' J. Fluid Mech., **155**, pp. 511–530.
[5] Lamb, H., *Hydrodynamics*, Dover, New York, 6th edition, 1993.
[6] Nicholls, F. W., 1924, ''Vibration of Ships,'' Trans RINA, **66**, pp. 141–163.
[7] Lewis, F. M., 1929, ''The Inertia of the Water Surrounding a Vibrating Ship,'' Trans. Soc. Nav. Arch, **37**, pp. 1–20.
[8] Lloyd, A. R. J. M., *Seakeeping. Ship Behavior in Rough Weather*, Ellis Horwood Limited, Chichester, 1989.
[9] Jennings, A., 1985, ''Added Mass for Fluid-Structure Vibration Problems,'' Int. J. Numer. Methods Eng., **5**, pp. 817–830.
[10] Hulme, A., 1982, ''The Wave Forces Acting on a Floating Hemisphere Undergoing Forced Periodic Oscillations,'' J. Fluid Mech., **121**, pp. 443–463.
[11] Ursell, F., 1949, ''On the Heave Motion of a Circular Cylinder on the Surface of a Fluid,'' Q. J. Mech. Appl. Math., **2**, pp. 218–231.
[12] Grim, O., 1953, ''Berechnung der durch Schwingungen eines Schiffskoerpers Erzeugten Hydrodynamischen Kraefte,'' Jahbuch der Schiffsbautechnischen Gesellshaft, **47**, pp. 277–299.
[13] Tasai, F., 1959, ''On the Damping Force and Added Mass of Ships Heaving and Pitching,'' J. Zosen Kiokai, **105**, pp. 47–56.
[14] Porter, W. R., ''Pressure Distributions, Added Mass and Damping Coefficients for Cylinders Oscillating in a Free Surface,'' Technical Report, Report 82-16, University of California, Institute of Engineering Research, Berkeley, 1960.
[15] Ogilvie, T. F., 1963, ''First and Second Order Forces on a Cylinder Submerged Under a Free Surface,'' J. Fluid Mech., **16**, pp. 451–472.
[16] Frank, W., ''Oscillation of Cylinders in or Below the Free Surface of Deep Fluids,'' Technical report, Naval Ship Research and Development Center, 1967.
[17] Havelock, T. H., 1955, ''Waves Due to a Floating Hemi-Sphere Making Periodic Heaving Oscillations,'' Proc. R. Soc. London, Ser. A, **231**, pp. 1–7.
[18] Storti, M., D'Elía, J., Bonet, R., Nigro, N., and Idelsohn, S., 2000, ''The DNL Absorbing Boundary Condition. Applications to Wave Problems,'' Comput. Methods Appl. Mech. Eng., **182**(3–4), pp. 483–498.
[19] Storti, M., D'Elía, J., and Idelsohn, S., 1998, ''Algebraic Discrete Non-Local (DNL) Absorbing Boundary Condition for the Ship Wave Resistance Problem,'' J. Comput. Phys., **146**(2), pp. 570–602.
[20] Storti, M., D'Elía, J., and Idelsohn, S., 1998, ''Computing Ship Wave Resistance From Wave Amplitude With the dnl Absorbing Boundary Condition,'' Commun. Numer. Methods Eng., **14**, pp. 997–1012.
[21] D'Elía, J., Storti, M., and Idelsohn, S., 2000, ''A Panel-Fourier Method for Free Surface Methods,'' J. Fluids Eng., **122**(2), June, pp. 309–317.
[22] D'Elía, J., Storti, M., and Idelsohn, S., 2000, ''Iterative Solution of Panel Discretizations for Potential Flows the Modal/Multipolar Preconditioning,'' Int. J. Numer. Methods Fluids, **32**(1), pp. 1–27.
[23] D'Elía, J., Storti, M., Oñate, E., and Idelsohn, S., 2002, ''A Nonlinear Panel Method in the Time Domain for Seakeeping Flow Problems,'' Int. J. Comput. Fluid Dyn., **16**(4), pp. 263–275.
[24] Newman, J. N., *Marine Hydrodynamics*, The MIT Press, Cambridge, 1977.
[25] Ogilvie, T. F., 1977, ''Singular-Perturbation Problems in Ship Hydrodynamics,'' Adv. Appl. Mech., **17**, pp. 91–188.
[26] Stoker, J. J., *Water Waves*, Interscience Publishers, New York, 1957.
[27] Papanikolau, A., 1985, ''On the Integral-Equation-Methods for the Evaluation of Motions and Loads of Arbitrary Bodies in Waves,'' Ingenieur-Archiv, **55**, pp. 17–29.
[28] D'Elía, J., and Storti, M., ''A Kelvin-Source Mixed Computation in Ship Hydrodynamics,'' Technical report, CIMEC, 2000.
[29] Landweber, L., *Handbook of Fluid Dynamics*, chapter Motion of Immersed and Floating Bodies. McGraw-Hill, New York, 1961.
[30] Sierevogel, L., ''Time-Domain Calculations of Ship Motions,'' PhD thesis, Technische Universiteit Delft, 1998.
[31] Prins, H. J., ''Time-Domain Calculations of Drift Forces and Moments,'' PhD thesis, Technische Universiteit Delft, 1995.
[32] Korsmeyer, F. T., and Sclavounos, P. D., 1989, ''The Large-Time Asymptotic Expansion of the Impulse Response Function for a Floating Body,'' Appl. Ocean. Res., **11**(2), pp. 75–88.
[33] Liapis, S. J., ''Time-Domain Analysis of Ship Motions,'' PhD thesis, University of Michigan, 1986.
[34] Ursell, F., 1953, ''Short Surface Waves Due to an Oscillatin Inmersed Body,'' Proc. R. Soc. London, Ser. A, **220**, pp. 90–103.
[35] Davis, A. M., 1971, ''Short Surface Waves Due to an Oscillating Half-Inmersed Sphere,'' Mathematika, **18**, pp. 20–39.
[36] Octave 2.1.33 General Public License, GNU project, i386-redhat-linux-gnu, 2001.

Characterization of Turbulent Flow in a Flume with Surfactant

Roi Gurka
Department of Mechanical Engineering, The Johns Hopkins University, Baltimore, MD, USA
e-mail: gurka@pegasus.me.jhu.edu

Alex Liberzon
Institute of Hydromechanics and Water Resources Management, ETH, Zurich
e-mail: liberzon@ihw.baug.ethz.ch

Gad Hetsroni[1]
Multiphase Flow Laboratory, Department of Mechanical Engineering, Technion, Haifa, 32000, Israel
e-mail: hetsroni@tx.technion.ac.il

[DOI: 10.1115/1.1845511]

Introduction

Drag reduction in turbulent flow, by low concentrations of polymers, is well known since the publication on the phenomenon by Toms [1]. Recently, biodegradable surface active agents (surfactants) have become a more appropriate choice as drag reducing additives. These surfactants are environmental friendly and, in addition, they are less susceptible to mechanical degradation [2]. The influence on turbulent flow characteristics could be spectacular with only few parts per million of surfactant solution, added to the solvent [3,4]. The general belief is that surfactants, like other additives, act directly on the small turbulent scales ([4–6] and references therein).

The drag reduction effect is due to the modification of the turbulence structure. A significant decrease of the Reynolds stresses was observed [7], however without a substantial reduction of the rms values of the velocity fluctuations. In addition, the turbulent kinetic energy production, and the dissipation, were measured and found to be strongly reduced in the drag reduced flow [8]. Most researchers have reported an increase of anisotropy for surfactant solution flows, characterized by a considerable suppression of the wall-normal velocity fluctuations. The common agreement is that the decorrelation of the streamwise (u) and wall-normal (v) components is the main manifestation of the drag reduction effect, which leads to the reduction of Reynolds stresses [6]. Theoretical models of drag reduction flows concern the stretching of the polymers by the turbulent flow in certain areas, and consequential the local viscosity changes, as the major mechanisms of drag reduction (see review in [4]).

Recently, the influence of the additives was investigated experimentally by using motion pictures of dye injection [9], real-time hologram interferometry [10], and dye visualization [11]. The researchers found an increase in the spanwise spacing of low-speed streaks and decrease of "bursting events" in drag reduced flows. In the present research, we investigated experimentally the influence of the nonionic, biodegradable, nontoxic surfactants, on the turbulent flow in a flume, by means of particle image velocimetry (PIV) [19]. Similar experimental studies with PIV were recently performed by Warholic et al. [12] and White et al. [13], and in both studies polymers were used as drag reducing additives. The drag reduction in surfactant solution flows exceed Virk's maximum drag reduction limit [14] for polymers, for relatively low concentrations [15]. Therefore, these nontoxic and biodegradable materials that are also shown to be good drag reducers, have a great potential for many engineering and industrial applications.

Experimental Facility

Test Loop. The experiments were performed in a flume with dimensions of $4.9\times 0.32\times 0.1$ m, shown in Fig. 1. The entrance and the following part of the flume, up to 2.8 m downstream, were made of glass. All necessary precautions were taken: the eddies and recirculating currents were dampened by means of narrow slits in the inlet tank (as presented by dotted lines in the Fig. 1), baffles were installed in the pipe portion of the tank, the inlet to the channel was a converging channel in order to have a smooth entrance, the 0.75 HP, 60 RPM centrifugal pump was isolated from the system by means of rubber joints fitted to the intake and discharge pipes. A flowmeter, with an accuracy of 0.5% of the measured flow rate, continuously recorded the flow rate. In order to make the measurement area long enough and to avoid a flow-depth decrease at the end of the flume, flow restrictors (in the form of an array of cylinders) were placed at the outlet portion. The working fluid was treated and filtered tap water. A detailed description of the flume is given in [16].

Surfactant Solution. In the present study we used the dilute solution of Agnique PG 264-U surfactant (also known as Agrimul PG 2062), which is clustered under the alkyl polyglycosides family. The surfactant is based on plant-derived chemicals (carbohydrate molecular structure), it is readily biodegradable, nontoxic, nonionic, and does not add to the Earth's CO_2 burden. It has a density of $1070\ \mathrm{kg/m^3}$ and a dynamic viscosity of 17 kg/m s at 25°C. The surfactant molecules consist of a hydrophobic and a hydrophilic part. In water these molecules tend to assemble to aggregates called micelles. Above a certain value of concentration, defined as the critical micelle concentration, globular micelles are usually formed, resulting in drag reduction [4]. The critical micelle concentration value for the Agnique PG 264-U is 20 ppm. A semidilute surfactant solution was prepared by mixing of Agnique PG 264-U with 500 mL of water, heated up to 80°C and stirred for 30 min, then added to the outlet water tank.

Particle Image Velocimetry

The PIV system included a double pulsed Nd:YAG laser (170 mJ/pulse, 15 Hz) operating at 532 nm, sheet forming optics, and 8 bit, 1024×1024 pixels, 30 frames-per-second charge-coupled device camera. The camera was located 0.2 m under the flume, with imaging axis normal to the laser light sheet, as shown in Fig. 2. The velocity fields were measured in the streamwise-spanwise plane. The laser sheet was located 0.01 m above the bottom, which is equivalent to $y^+=80$ (the friction velocity was estimated in the streamwise-wall normal plane by [17]). The time separation between the two laser pulses was adjusted according to the mean streamwise velocity value and was equal to 2×10^{-3} s. Hollow glass spherical particles with an average diameter of 11.7 μm and a density of $1100\ \mathrm{kg/m^3}$, were used for seeding. The calibration procedure and the PIV cross-correlation analysis were performed by using INSIGHT 5.10 software [18]. In all the cases an interrogation area of 32×32 pixels with 50% overlapping was used. The spatial resolution of the camera was 80 μm per pixel, and the field of view was approximately $80\ \mathrm{mm}\times 80\ \mathrm{mm}$. The analysis produced about 3000 vectors per map, filtered by using standard median and global outlier filters. About 5% of the erroneous vectors were removed during the post-processing analysis. The statistical analysis was based on 50 image pairs, resulting in 50 two-component velocity vector fields for each experimental case. The acquisition time of each experiment was $50/15\approx 3.3$ s.

---

[1] Corresponding author.

Contributed by the Fluids Engineering Division for publication in the JOURNAL OF FLUIDS ENGINEERING. Manuscript received by the Fluids Engineering Division January 13, 2003; revised manuscript received July 27, 2004. Review conducted by: M. Plesniak.

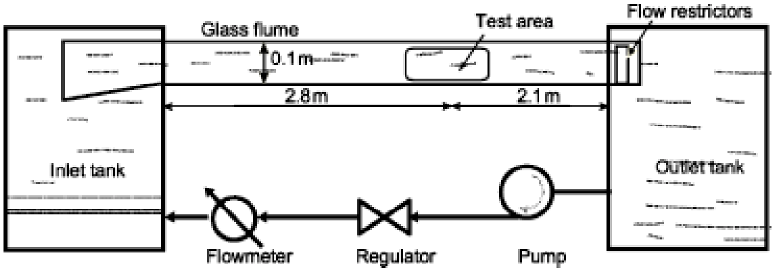

Fig. 1 Schematic drawing of the experimental facility

Results and Discussion

The influence of the surfactant solution on the turbulent flow field is demonstrated by means of the comparative results for water and drag reduced flow. The results were compared for the same flow-rate velocity $U_q = Q/A$, where Q is the flow rate and A is the cross-sectional area of the flow. All the experiments were conducted for a constant flow rate of 5.8×10^{-3} $\mathrm{m^3/s}$, which is equivalent to $U_q = 0.2$ m/s and $\mathrm{Re}_h = U_q h/\nu = 20{,}000$, where h is the water height, and ν is the kinematic viscosity of the water.

Figure 3 presents the two fluctuating velocity fields: of water flow (left) and of the flow with surfactant (right). The flow direction is from top to bottom, and the coordinates in the streamwise and the spanwise directions are normalized with the water height, h. Arrows represent the two-component fluctuating velocity vector field, $u' - w'$. The colors emphasize the high- and low-speed regions: The blue stands for fluctuating streamwise velocity which is higher than the ensemble averaged velocity field, and red is for the low speed regions. A negative value corresponds to a high speed region, since the positive x is defined from left to right and the positive z direction is from the bottom to the top. The effect of surfactant is shown qualitatively in Fig. 3, where one can observe weaker streamwise velocity fluctuations, than in the solvent counterpart.

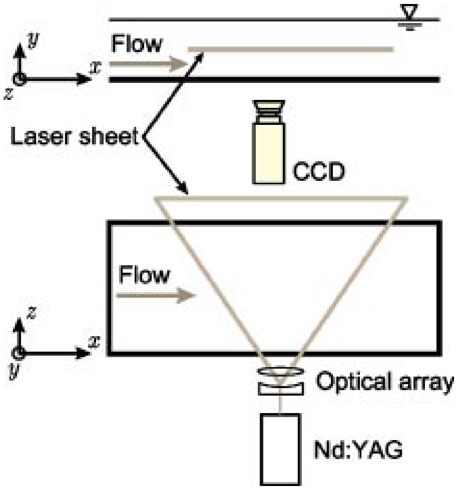

Fig. 2 Schematic view of the PIV configuration and the optical setup

The average root-mean-square value of the streamwise velocity fluctuations, calculated as $u'_{\mathrm{rms}} = \sqrt{\langle u'^2 \rangle}$, is shown as the probability density function in Fig. 4. The rms of the streamwise fluctuations of the surfactant flow is reduced, as compared to that of water. This result shows the effect of the surfactant, which suppresses the turbulent activity. This result is in a good agreement with the literature (e.g., [6] and references therein). Note that the rms values are compared as they are normalized by means of the flow-rate velocity U_q, which is the constant quantity in this experiment. Since the profile is altered as a part of the drag reducing effect, the mean streamwise velocity $\langle U \rangle$, calculated as the ensemble average of the PIV realizations at some constant wall normal location y, is not appropriate for the normalization.

The spatial characteristics are shown through two-point spatial correlation functions. The autocorrelation function of the streamwise velocity fluctuations along the streamwise axis is defined as $R_{uu}(x) = \langle u(x,z) \otimes u(x+\Delta x, z) \rangle$ and along the spanwise coordinate $R_{uu}(z) = \langle u(x,z) \otimes u(x, z+\Delta z) \rangle$. The autocorrelation function $R_{uu}(x)$, shown in Fig. 5, clearly demonstrates that the surfactant additive does not change the longitudinal length scale. In contrast, the spanwise correlation, statistically demonstrates the effect of the modification of the spanwise structure. In the case of water flow, the transversal correlation $R^{\mathrm{w}}_{uu}(z)$ crosses the zero

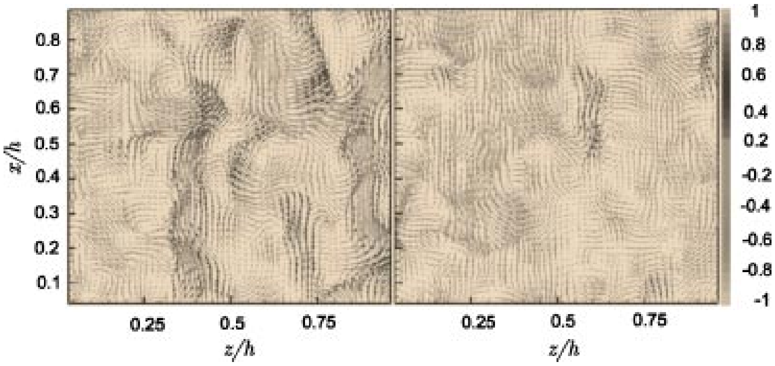

Fig. 3 The fluctuating velocity field in the streamwise-spanwise plane of the water flow (left) and the flow with surfactant (right). The gray scale represents the values of the streamwise velocity fluctuations in cm s^{-1} (i.e., $-1 \leqslant u' \leqslant 1$ cm s^{-1})

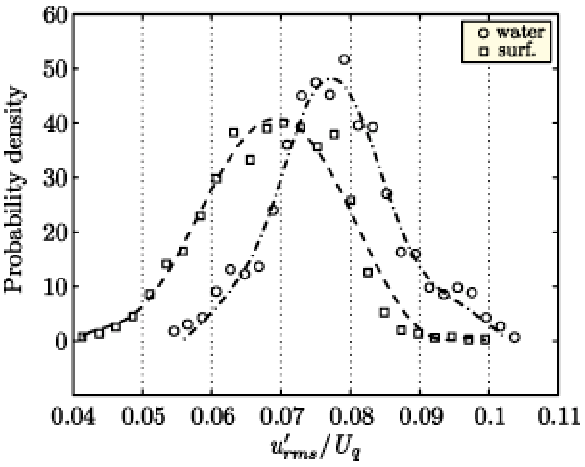

Fig. 4 PDF's of the u'_{rms}/U_q for water (circles) and surfactant (squares). $u'_{rms}(x,z)=\langle (u(x,z)-\langle u(x,z)\rangle)^2\rangle$ and the PDF is representing the spatial distribution of the rms values, normalized by the flow-rate velocity U_q.

axis, corresponding to the anticorrelation of the positive and negative velocity fluctuation values. In contrast, the function $R^s_{uu}(z)$ in the case of flow of surfactant solution, shows that the distance between high- and low-speed regions increases. This result is in good agreement with the experimental results of Warholic et al. [12] and Oldaker and Tiederman [11].

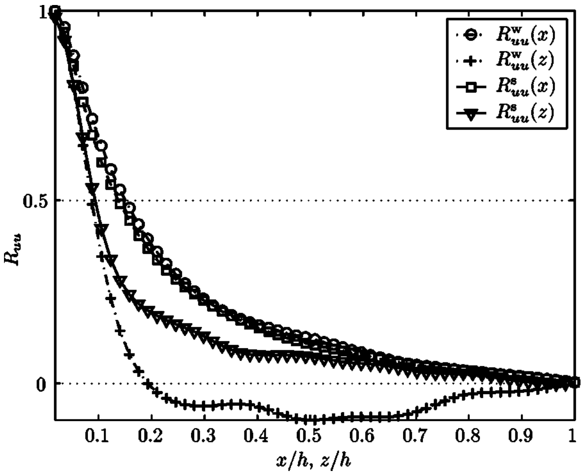

Fig. 5 Two-point (auto)correlation function R_{uu} of the streamwise velocity along the streamwise x and spanwise z coordinates, for water (circles and plus symbols) and for surfactant (square and triangular markers), respectively.

It is known that polymers, in addition to the scale modification effect, strongly decrease the one-point correlations between the streamwise and the wall-normal fluctuating velocities. In the present study we present comparative experimental results of the Reynolds stress component $-\langle u'w'\rangle$, summarized in Table 1. The first two rows in the Table 1 demonstrate the so-called "decorrelation" effect of u' and w' velocity components. The magnitude of the Reynolds stress more often approaches zero: The average value is the one order of magnitude smaller, and the distribution of values is less (e.g., standard deviation). In addition, the distribution for water flow includes larger values of the Reynolds stress (normalized by the square of the flow-rate velocity), shown by maximum values: i.e., 0.05 for water and only 0.03 for surfactant solution. The most important difference between water and surfactant solution flows is apparently the skewness factor, that emphasizes the fact of the decorrelation. This is consistent with the PIV results obtained by Kawaguchi et al. [20], in which the influence of surfactants was investigated in the streamwise-wall normal plane in a channel flow. Since the strong suppression of the Reynolds stress takes place without substantial reduction of the turbulent fluctuations (e.g., Fig. 4), we might conclude that the reduction is, for the most part, due to the decorrelation of the velocity components, which is in agreement with the previous results ([6] and references therein).

Table 2 presents the turbulent energy production term in the kinetic energy balance equation, $-\langle u'w'\rangle S_{uw}$. The effect of the surfactant on this quantity is even more pronounced, as production reaches lower values, compared to water flow, and the skewness factor changes the sign from the positive (i.e., productive) to the negative sign. The result implies that in addition to the decorrelation between the velocity fluctuations, the surfactant reduces the momentum transfer and the kinetic energy production. Similar results are presented by Wei and Willmarth [21], in which the LDV measurements were performed in a channel flow with polymer additives. They showed a dramatic reduction of the turbulent kinetic energy production in the $x-y$ plane, in a wall region between $40<y^+<200$. The mean rate-of-strain component in the streamwise-spanwise plane is defined as $S_{uw}=\langle \partial u/\partial z+\partial w/\partial x\rangle$ and in the production it represents the energy contribution of the large scale motions. This leads to the conclusion that the significant decrease of the turbulent energy production is not solely due to the decrease of the Reynolds stress, neither due to the decrease of the rate-of-strain component itself, but it is associated with an additional decorrelation effect. This effect was previously reported, but only by DNS results of den Toonder et al. [22], where the effect of polymer additives was investigated by using the "dumb-bell" model.

Summary

The drag reducing effect of a surfactant additive from the alkyl polyglycosides family was investigated experimentally. In the present study, PIV measurements were done to investigate the turbulent flow in the streamwise-spanwise plane of a flume at $y^+=80$, in the buffer zone, where about 80% of the energy pro-

Table 1 Statistical properties of the Reynolds stress $-\langle u'w'\rangle/U_q^2$.

Statistics	Maximum	Minimum	Average	Std. dev.	Skewness
Water	0.05	-0.035	0.35×10^{-3}	0.0045	0.93
Surfactant	0.03	-0.035	0.35×10^{-4}	0.0032	0.003

Table 2 Statistical properties of the turbulent energy production term $-\langle u'w'\rangle S_{uw}/U_q^2$.

Statistics	Maximum	Minimum	Average	Std. dev.	Skewness
Water	2×10^{-4}	-1.8×10^{-4}	-0.21×10^{-6}	0.1×10^{-4}	0.21
Surfactant	1.4×10^{-4}	-1.1×10^{-4}	-0.06×10^{-6}	0.06×10^{-4}	-0.27

duction takes place. The influence of the surfactant solution on the turbulent flow and its structure is presented by means of the correlation and the probability density functions. The biodegradable surfactant was shown to be an efficient drag reducing solution. The results support the explanation of the mechanisms responsible for the drag reduction, reviewed by [6]. The qualitative and quantitative results, that demonstrate the effect of the surfactant are summed up as follows:

- The analysis of the fluctuating velocity and its distribution suggest that the fluctuations in the drag reducing flow are decreased;
- The Reynolds stress is suppressed more than the rms of the streamwise velocity fluctuations, and this effect is considered as a decorrelation effect;
- The turbulent kinetic energy production term in the streamwise-spanwise plane diminishes, similar to the known effect in the streamwise-wall normal plane.

Nomenclature

x,y,z = Streamwise, wall normal, and spanwise coordinate, respectively, m
u,v,w = Instantaneous streamwise, wall normal, and spanwise velocity components, respectively, m/s
U,V,W = Ensemble average velocity components, m/s
u',v',w' = Fluctuating velocity components, m/s
u'_{rms} = Root-mean-square (rms) value of the fluctuating streamwise velocity, m/s
Q = Flow rate, m^3/s
U_q = ''Flow-rate'' velocity per unit length, the ratio of the flow-rate and the cross-sectional area, m/s
h = Water level, m
S_{uw} = Mean stress tensor component in the streamwise-spanwise plane, 1/s
$\langle \cdot \rangle$ = Ensemble averaging operator

References

[1] Toms, B. A., 1948, ''Some Observation on the Flow of Linear Polymer Solutions Through Straight Tubes at Large Reynolds Numbers.'' *Proc. 1st Int. Congress on Rheology*, North, Holland, Vol. II, 135–141.

[2] Zakin, J. L., and Lui, H. L, 1983, ''Variables Affecting Drag Reduction by Nonionic Surfactant Additives,'' Chem. Eng. Commun., **23**, pp. 77–80.

[3] Ohlendorf, D., Inherthal, W., and Hoffman, H., 1986, ''Surfactant Systems for Drag Reduction: Physico-Chemical Properties and Rheological Behaviour,'' Rheol. Acta, **26**, pp. 468–486.

[4] Gyr, A., and Bewersdorff, H.-W., 1995, ''Drag Reduction of Turbulent Flows by Additives,'' *Fluid Mechanics and its Applications*, Kluwer, Netherlands.

[5] Nieuwstadt, F. T. M., and den Toonder, J. M. J., 2001, ''Drag Reduction by Additives: A Review,'' *Turbulence Structure and Modulation*, edited by A. Soldati and R. Monti, Springer, NY, pp. 269–316.

[6] Tsinober, A., 2001, *An Informal Introduction to Turbulence*, Kluwer, Netherlands.

[7] Warholic, M. D., Gavin, M. S., and Hanratty, T. J., 1999, ''The Influence of a Drag-Reducing Surfactant on a Turbulent Velocity Field,'' J. Fluid Mech., **388**, pp. 1–20.

[8] Tsinober, A., 1990, ''Turbulent Drag Reduction Versus Structure of Turbulence,'' *Structure of Turbulence and Drag Reduction*, edited by A. Gyr, Springer, NY, pp. 313–334.

[9] Donohue, G. L., Tiederman, W. G., and Reischman, M. M., 1972, ''Flow Visualization of the Nearwall Region in a Drag-Reducing Channel Flow,'' J. Fluid Mech., **56**, pp. 559–57.

[10] Achia, B. U., and Thompson, D. W., 1977, ''Structure of the Turbulent Boundary in Drag-Reducing Flow,'' J. Fluid Mech., **81**, pp. 439–464.

[11] Oldaker, D. K., and Tiederman, W. G., 1977, ''Structure of the Turbulent Boundary Layer in Drag Reducing Pipe Flow,'' Phys. Fluids, **20**, pp. S133–S144.

[12] Warholic, M. D., Heist, D. K., Katcher, M., and Hanratty, T. J., 2001, ''A Study with Particle-Image Velocimetry of the Influence of Drag-Reducing Polymers on the Structure of Turbulence,'' Exp. Fluids, **31**, pp. 474–483.

[13] White, C. M., Somandepalli, V. S. R., and Mungal, M. G., 2004, ''The Turbulence Structure of Drag-Reduced Boundary Layer Flow,'' Exp. Fluids, **36**, pp. 62–69.

[14] Virk, P. S., 1971, ''Drag Reduction in Rough Pipes,'' J. Fluid Mech., **45**, pp. 225–246.

[15] Myska, J., and Chara, Z., 2001, ''The Effect of a Zwitterionic and Cationic Surfactant in Turbulent Flows,'' Exp. Fluids, **30**, pp. 229–236.

[16] Hetsroni, G., and Rozenblit, R., 1994, ''Heat Transfer to Liquid-Solid Mixture in a Flume,'' Int. J. Multiphase Flow, **20**, pp. 671–689.

[17] Liberzon, A., Gurka, R., and Hetsroni, G., 2004, ''XPIV—Multi-Plane Stereoscopic Particle Image Velocimetry,'' Exp. Fluids, **36**(2), pp. 355–362.

[18] TSI Inc. INSIGHT™ *5.10 PIV Evaluation Software*, 2002, TSI Inc., Shoreview, MN.

[19] Raffel, M., Willert, C. E., and Kompenhans, J., 1998, *Particle Image Velocimetry: A Practical Guide*, Springer-Verlag, Berlin.

[20] Kawaguchi, Y., Segawa, T., Feng, Z. P., and Li, P. W., 2002, ''Experimental Study on Drag-Reducing Channel Flow with Surfactant Additives—Spatial Structure of Turbulence Investigated by PIV System,'' Int. J. Heat Fluid Flow, **23**(**5**), pp. 700–709.

[21] Wei, T., and Willmarth, W. W., 1992, ''Modifying Turbulence Structure with Drag-Reducing Polymer Additives in Turbulent Channel Flow,'' J. Fluid Mech., **245**, pp. 619–641.

[22] den Toonder, J. M. J., Hulsen, M. A., Kuiken, G. D. C., and Nieuwstadt, F. T. M., 1997, ''Drag Reduction by Polymer Additives in a Turbulent Pipe Flow: Numerical and Laboratory Experiments,'' J. Fluid Mech., **337**, pp. 193–231.

Effects of Gas Content in Fluid on Oscillating Frequencies of Self-Excited Oscillation Water Jets

Yiyu Lu*
e-mail: Luyiyu@hotmail.com

Xiaohong Li
e-mail: xhLi@cqu.edu.cn

Education Ministry's Key Lab for the Exploitation of
Southwestern Resources & Environmental Disaster Control
Engineering, Chongqing University, Chongqing,
400044 P.R. China

Lin Yang
e-mail: Yang_Lin1970@hotmail.com
Zhuzhou Institute of Technology, Zhuzhou, Hunan,
412008 P. R. China

[DOI: 10.1115/1.1839925]

1 Introduction

The unsteady flow in and near cavity-type geometries, which belongs to a basic class of flow susceptible to self-excited oscillations, occurs in a variety of applications such as slotted-wall wind and water tunnels. Despite the diversity of types of cavity oscillations, several common features can be observed. According to the inducement cause of self-excited oscillations, Rockwell and Naudascher [1,2] categorized self-excited oscillations into three groups: (a) fluid-dynamic; (b) fluid-resonant; and (c) fluid-elastic. It is necessary to investigate the characteristics of self-excited oscillations in flow in order to utilize or avoid the self-excited oscillations in practical engineering situation.

Morel [3] experimentally studied a jet-driven Helmholtz oscillator. The amplitude of pressure oscillations may reach values of up to 5.6 times the jet dynamic pressure. Johnson, Conn and Chahine [4,5] developed self-resonating jets. Their comparative testing had shown that self-resonating cavitating jets can cut rock and perform underwater cleaning more effectively and efficiently than either conventional jets or nonresonating cavitating jets. Liao, Tang, and Shen [6–8] explored the relationships between structural parameters of the device of self-excited oscillation jets and its amplitude and frequencies. They designed the self-excited oscillation pulsed nozzle for oil well jetting drilling. The penetration rates and the footages of the bits have been increased by up to 50% and 15%, respectively, over the rates for similar bits with conventional jet nozzles.

The oscillating frequencies of water jets, which directly influence the cavitation intensity and erosive ability of water jets, are related to the chamber structure and water jet parameters [7]. Fluid in the oscillation chamber was generally treated as a single media and the sound speed of pressure perturbations was considered as a constant in the past research [9,10]. However, in fact, the fluids in the oscillation chamber contain air, water, and vapor. They cannot be treated as a single media. It should belong to two-phase flow of gas and liquid. The sound speed in the oscillation chamber has different characteristics from the single phase flow, hence would influence the oscillating frequencies.

The purpose of this work is to investigate the sound speed in the shear layer in the oscillation chamber and effects of gas content in fluid on oscillating frequencies. This is achieved by the theoretical computations and experiments.

2 Sound Speed in Shear Layer

The motion of disturbance wave in the shear layer satisfies the continuity equation and momentum equation:

$$\rho_m\left(\frac{\partial u}{\partial t}+u\,\frac{\partial u}{\partial x}\right)=-\frac{\partial p}{\partial x} \tag{1}$$

$$\frac{\partial}{\partial t}(\rho_m A)+\frac{\partial}{\partial x}(\rho_m uA)=0 \tag{2}$$

where u is velocity of disturbance fluid, p-pressure, t-time, A-section area, and $\rho_m=\rho_m(p)=\alpha\rho_g+(1-\alpha)\rho_l$ is mean density of the mixture. ρ_g-gas density, ρ_l-fluid density, and α-gas content in the fluid.

Solving Eqs. (1) and (2) with neglecting the square terms results in:

$$\frac{\partial^2 p}{\partial x^2}=\frac{1}{A_0}\,\frac{\partial^2(\rho_m A)}{\partial t^2} \tag{3}$$

where $A_0=A(p=0)$ is the section area of the mixture fluid when there is no disturbance. Equation (3) can be expressed as:

$$\frac{\partial^2 p}{\partial x^2}=\frac{1}{a^2}\,\frac{\partial^2 p}{\partial t^2} \tag{4}$$

where

$$\frac{1}{a^2}=\frac{1}{A_0}\left[\frac{d(\rho_m A)}{dp}\right]_{p=0} \tag{5}$$

i.e.,

$$\frac{1}{\rho_{m0}a^2}=\left[\frac{1}{\rho_m A}\,\frac{d(\rho_m A)}{dp}\right]_{p=0}=\left[\frac{1}{\rho_m}\,\frac{d\rho_m}{dp}+\frac{1}{A}\,\frac{dA}{dp}\right]_{p=0}=\frac{1}{K_m}+\frac{1}{D_m} \tag{6}$$

Rewriting Eq. (6) results in:

$$a=\frac{1}{\sqrt{\rho_m\left(\dfrac{1}{K_m}+\dfrac{1}{D_m}\right)}} \tag{7}$$

where

$$K_m=\frac{dp}{d\rho_m/\rho_m}=-\frac{dp}{dV/V} \tag{8}$$

$$D_m=\frac{dp}{dA/A} \tag{9}$$

a is sound speed in fluid, $\rho_{m0}=\rho_m(p=0)$ is the density of the mixture fluid when there is no disturbance and V is the mixture fluid volume.

The control volume in Fig. 1 is taken in the form of a small cylinder with length ΔL and section area A. Then the change in volume of liquid (ΔV_l) in the control volume can be expressed approximately using the definition of bulk modulus of elasticity of liquid (K_l):

---

*Correspondence to: Mr. Yiyu Lu, College of Resources and Environmental Science, Chongqing University, Chongqing, 400044 China; Email: LUYIYU@HOTMAIL.COM; Telephone: 86-23-65106640, Fax: 86-23-65106640.

Contributed by the Fluids Engineering Division for publication in the JOURNAL OF FLUIDS ENGINEERING. Manuscript received by the Fluids Engineering Division October 31, 2003; revised manuscript received July 7, 2004. Associate Editor: Georges L. Chahine.

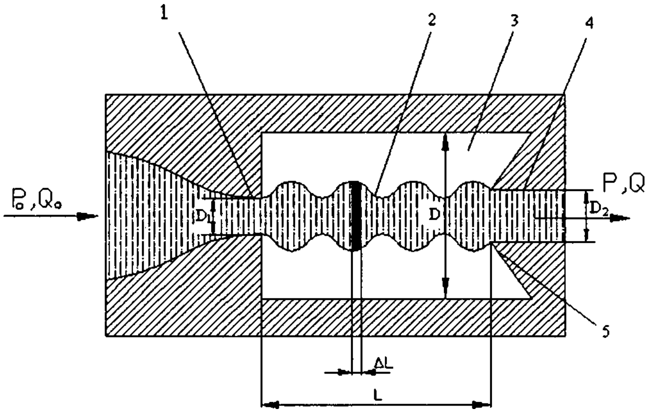

Fig. 1 Schematic of self-excited oscillation nozzle. 1—upstream nozzle, 2—mixture fluid boundary, 3—oscillation chamber, 4—downstream nozzle, 5—impinging edge

$$K_l=\frac{\Delta p}{\dfrac{\Delta V_l}{(1-\alpha)A\Delta L}} \tag{10}$$

$$\Delta V_l=\frac{\Delta p}{K_l}(1-\alpha)A\Delta L \tag{11}$$

where Δp is the change in pressure caused by pressure perturbations.

In the same way, the change in volume of gas (ΔV_g) in the control volume can also be expressed as:

$$\Delta V_g=\frac{\Delta p}{K_g}\alpha A\Delta L \tag{12}$$

where K_g is the bulk modulus of elasticity of gas.

Now, using Eqs. (10)–(12) in Eq. (8), K_m becomes

$$K_m=\frac{\Delta p}{(\Delta V_l+\Delta V_g)/V}=\frac{K_l}{1-\alpha+\alpha\dfrac{K_l}{K_g}} \tag{13}$$

Assume that there is some gas in the mixture fluid and is compressed isothermally, then

$$K_g=p \tag{14}$$

Solving Eqs. (7) and (13) for a results in

$$a=\sqrt{\frac{K_l/\rho_m}{1-\alpha+K_l/D_m+\alpha K_l/p}} \tag{15}$$

Equation (15) shows that the sound speed in the shear layer is relevant to gas content α, pressure p, mixture density and fluid boundary characteristics in the oscillation chamber. This is different from the usually used formula by previous researchers:

$$a_o=\sqrt{\frac{dp}{d\rho}}=\sqrt{\frac{K_l}{\rho_l}} \tag{16}$$

in which the effects of gas and liquid boundary in the fluids were neglected.

The bulk modulus of elasticity of the mixture fluid K_m is related to the bulk modulus of elasticity of liquid and gas in the mixture and gas content α. The inflation modulus of mixture fluid boundary D_m is related to the chamber structure, fluid velocity and pressure, etc. In the closed oscillation chamber, the density and modulus of elasticity of mixture fluid are different from a single media. The sound speed in the oscillation chamber cannot be considered as a constant.

3 Effects of Gas Content on Oscillating Frequencies of Self-Excited Oscillation Water Jets

Figure 1 shows a schematic of a self-excited oscillation nozzle. The self-excited oscillations of the flow emerging from the cavity will be strongly influenced by the chamber geometry. Assuming that n vortices are traveling simultaneously between the inlet and exit sections, the pressure disturbance wave arriving at the upstream face of the chamber, in order to induce optimum vorticity fluctuations, would have to travel upstream the length L of the chamber at the sound speed a, thus one has [11]

$$f=\frac{n}{L\left(\dfrac{1}{a_+}+\dfrac{1}{a_-}\right)} \tag{17}$$

where f is oscillating frequency and n is mode number of fluid dynamic oscillation ($n=1,2,3,\ldots$). a_+ and a_- are the downstream and upstream propagation speed of pressure disturbance waves respectively.

Preliminary analyses of the characteristics of shear layer instability have shown that the selective amplification of unstable fluctuations in the cavity shear layer is not related to the amplitude of original fluctuations, Mach number and Reynolds number, but dependent on the dimensionless frequencies—Strouhal number, S_l [1,2]

$$S_l=\frac{fL}{u_0} \tag{18}$$

When $p\geqslant 10$ MPa, it is reasonable to assume the sound speed a is of the same order as the original velocity u_o of water jets as there is some gas in the fluids. In this situation, the velocity of water jets should not be neglected in determining the upstream and downstream propagation speed of unstable fluctuation waves. Then

$$\begin{aligned} a_+&=a+u_0\\ a_-&=a-u_0 \end{aligned} \tag{19}$$

Using Eqs. (17) and (19) in Eq. (18), f and S_l become

$$f=\frac{n(a^2-u_0^2)}{2aL} \tag{20}$$

$$S_l=\frac{n(a^2-u_0^2)}{2au_0} \tag{21}$$

Equations (15) and (20) in a nondimensional form can be expressed as

$$a^*=\frac{a}{a_o}=\sqrt{\frac{\rho_l/\rho_m}{1-\alpha+K_l/D_m+\alpha K_l/p}} \tag{22}$$

$$f^*=\frac{f}{f_0}=\frac{\dfrac{n(a^2-u_0^2)}{2aL}}{\dfrac{na_0}{2L}}=\frac{a}{a_0}-\frac{u_0^2}{a_0^2}\frac{a_0}{a}=\frac{a}{a_0}-\frac{2p}{\rho a_0^2}\frac{a_0}{a} \tag{23}$$

Variations of dimensionless sound speed a^*, dimensionless frequency f^* and Strouhal number S_l with gas content α for the mode number ($n=3$) and two pressures ($p=10$ MPa, 15 MPa) are illustrated in Fig. 2.

As shown in Fig. 2, the increase of gas content α in fluids in the oscillation chamber leads to the decrease of the sound speed a and the oscillating frequencies. Especially when the gas content is relatively small, the sound speed and oscillating frequencies decrease rapidly. For the same gas content, the sound speed and oscillating frequencies increase with water jet pressure increase. As mentioned above, the sound speed in the shear layer is relevant to the bulk modulus of elasticity of the mixture and fluid boundary

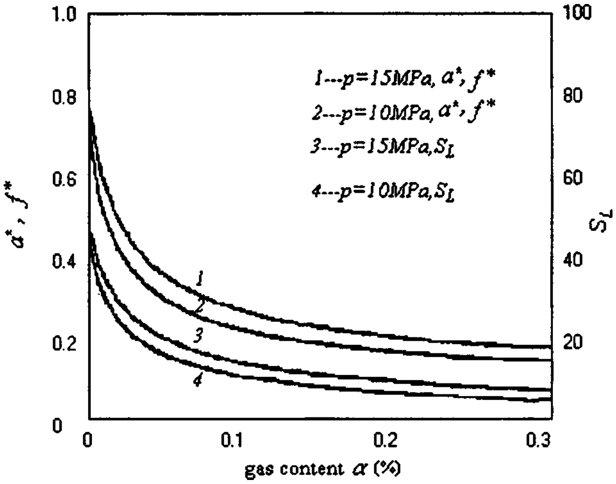

Fig. 2 Variation of dimensionless sound speed a^* and Strouhal number S_l with gas content α for the same mode number $(n=3)$ and two pressures $(p=10\,\mathrm{MPa},\ 15\,\mathrm{MPa})$

characteristics in the oscillation chamber, and the bulk modulus of elasticity of gas is much smaller than that of liquid. Even very little gas in the fluids would affect the pressure fluctuation wave significantly.

4 Experimental Facility and Procedures

A schematic of the components contained in this facility are shown in Fig. 3. An air hole was drilled in the oscillation chamber wall and a flowmeter, which was used to measure the air volume sucked in by self-excited oscillation water jets, was connected to the air hole. Air volume was controlled by a ball-valve connected with the flowmeter. The flow rates of air and water (Q_g and Q_l) flowing in the nozzle were measured by the flowmeters. The pressures of water jets were measured with pressure transducers and frequency analyses of pressure fluctuation were done utilizing a Fast Fourier Transform routine. The flow rate and pressure were found to have measurement error less than 3% and the uncertainty of fluctuation frequencies was estimated to be smaller than 15%.

The schematic of the self-excited oscillation nozzle is shown in Fig. 1. Major dimensions were as follows: $D_1=1.8\,\mathrm{mm}$, $D/D_1=8$, $L/D_1=2.4$, $D_2/D_1=1.2$ and diameter of air hole $d=4\,\mathrm{mm}$.

It is impossible to directly measure the gas content in the shear layer. However, since air is sucked in through the ball valve and flows out with the jet through the outlet, according to the mass continuity, the gas content in the shear layer should be proportional to the flow rate Q_g of the sucked air. Q_g is used to express the gas content to investigate the variation of the principal frequency of the pressure fluctuations with gas content and verify whether the experimental results have the same type of trends that the theory predicts in Fig. 2.

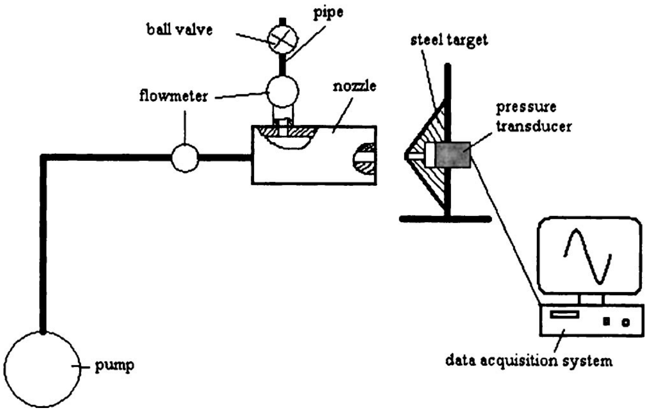

Fig. 3 Experimental setup

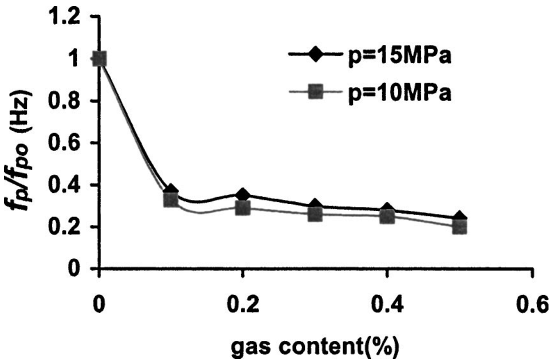

Fig. 4 The principal frequency of the pressure fluctuations f_p versus gas content α

If the gas produced by cavitations in the fluids is neglected, the gas content in the fluids can be calculated by the following equation:

$$\alpha \approx \frac{Q_g}{Q_l+Q_g} \tag{24}$$

5 Experimental Results

The gas content was changed by adjusting the ball-valve to change the flow rate of sucked air in the chamber. And the corresponding principal frequencies of the pressure fluctuations (f_p) were obtained by analyzing the pressure spectrums with a Fast Fourier Transform routine. Figure 4 shows f_p/f_{po} versus gas content α. f_{po} is the principal frequency of the pressure fluctuations when $Q_g=0$.

As shown in Fig. 4, increasing the gas content decreases the principal frequencies of the pressure fluctuations, and the principal frequencies of the pressure fluctuations increase with the pressure increases. The experimental results showed the same type of trends as the theoretical results.

6 Conclusion

Theoretical and experimental investigations have been conducted on the effects of gas content on the oscillating frequencies of self-excited oscillation water jets. The conclusions are summarized below. The sound speed in the shear layer is relevant to gas content, pressure, the bulk modulus of elasticity of the mixture, mixture density and fluid boundary characteristics in the oscillation chamber.

(1) The increase of gas content in fluids in the oscillation chamber leads to the decrease of the sound speed and the oscillating frequencies. Especially when the gas content is relatively small, the sound speed and oscillating frequencies decrease rapidly. For the same gas content, the sound speed and oscillating frequencies increase with water jet pressure increase.

(2) Experimental results showed the same trends as the theoretical results.

Acknowledgments

This work is jointly supported by the NSFC (No. 50334060). The authors are grateful to Dr. Z. Qin of CRC Mining in Queensland for helpful discussions.

References

[1] Rockwell, D., and Naudascher, E., 1978, ‘‘Review—Self-Sustaining Oscillations of Flow Past Cavities,’’ ASME J. Fluids Eng., **100**, pp. 152–165.

[2] Rockwell, D., 1977, ‘‘Prediction of Oscillation Frequencies for Unstable Flow Pas Cavities,’’ ASME J. Fluids Eng., **99**, pp. 294–300.

[3] Morel, T., 1979, ‘‘Experimental Study of a Jet-Driven Helmholtz Oscillator,’’ ASME J. Fluids Eng., **101**, pp. 383–390.

[4] Johnson, V. E., and Conn, A. F., 1982, ‘‘Self-Resonating Cavitating Jets,’’ *Proceedings of the 6th International Symposium on Jet Cutting Technology*, pp. 1–25.

[5] Chahine, G. L. et al., 1983, ‘‘Cleaning and Cutting With Self-Resonating Pulsed Water Jets,’’ *Proceedings of the second US water jet conference*, pp. 195–207.

[6] Liao, Z. F., Tang, C. L., and Wang, G. H., 1991, ‘‘A New Type of Nozzle for Oil Well Drill Bits,’’ *Proceedings of the 10th International Conference on Jet Cutting Technology*, pp. 135–144.

[7] Liao, Z. F., and Tang, C. L., 1987, ‘‘Theoretical Analysis and Experimental Study of the Self-Excited Oscillation Pulsed Jet Device,’’ Proceedings of the fourth US water jet conference, pp. 46–61.

[8] Shen, Z. H., Li, G. S., Wang, Z., and Xu, Y., 1991, ‘‘New Jet Theory and Prospects of Its Application in Drilling Engineering,’’ *13th World Petroleum Congress*, pp. 397–405.

[9] Williams, M., 1992, ‘‘A Helmholtz Pressure Equation Method for the Calculation of Unsteady Incompressible Viscous Flows,’’ Int. J. Numer. Methods Heat Fluid Flow, **14**, pp. 1–12.

[10] Zhu, Z., and Strokes, N., 1997, ‘‘Simulation of Two-Phase Flows in a Stirred Mixing Tank,’’ *Inter Conf on CFD in Mineral & Metal Processing and Power Generation*, pp. 387–394.

[11] Samis, S., and Anderson, C., 1984, ‘‘Helmhotz Oscillator for the Self-Modulation of a Jet,’’ *Proceedings of the 7th International Symposium on Jet Cutting Technology*, pp. 91–98.